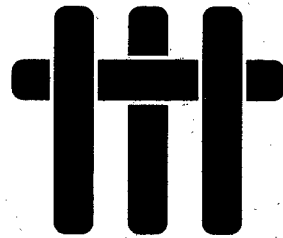


FINAL REPORT

University Research Initiative

Contract No.: N00014-92-J-1808

May 1996 - September 1997



Mechanism-Based Design for High-Temperature, High-Performance Composites

by

A.G. Evans & F.A. Leckie
University of California,
Santa Barbara, CA

and

J.W. Hutchinson
Harvard University,
Cambridge, MA

Cambridge University
Harvard University
Washington State University
University of Pennsylvania
University of Virginia

DISTRIBUTION STATEMENT A

Approved for public release,
Distribution Unlimited

19980721 080

QUALITY INSPECTED

Book 3 of 4:

SECTION A: CONSTITUENT PROPERTIES AND MACROSCOPIC PERFORMANCE OF MMC
SECTION B: CONSTITUTIVE LAWS AND DESIGN

**SUMMARY
OF
TABLE OF CONTENTS**

EXECUTIVE SUMMARY

BOOK 1: CONSTITUENT PROPERTIES AND MACROSCOPIC PERFORMANCE OF CMC - I

BOOK 2: CONSTITUENT PROPERTIES AND MACROSCOPIC PERFORMANCE OF CMC - II

BOOK 3:

Section A: CONSTITUENT PROPERTIES AND MACROSCOPIC PERFORMANCE OF MMC

Section B: CONSTITUTIVE LAWS AND DESIGN

BOOK 4: MEASUREMENT AND MICRO-MECHANISMS

BOOK 3

Section A

CONSTITUENT PROPERTIES AND MACROSCOPIC PERFORMANCE OF MMC

Creep of Metal-Matrix Composites with Elastic Fibers — Part I: Continuous Aligned Fibers	C. Cheng N. Aravas	1
Creep of Metal-Matrix Composites with Elastic Fibers — Part II: A Damage Model	C. Cheng N. Aravas	37
Measurement of the Cyclic Bridging Law in a Titanium Matrix Composite and Its Application to Simulating Crack Growth	S.J. Connell F.W. Zok	61
Power-Law Matrix Creep in Fiber Composites Due to Transverse Stress Gradients	Z.-Z. Du A.C.F. Cocks R.M. McMeeking	71
The Effects of a Single Mode III Loading Cycle on Mode I Crack Initiation and Growth Toughnesses in a Cross-Ply $[90^\circ/0^\circ]_{2s}$ Ti-6Al-4V/SiC _f Composite	S.V. Kamat J.P. Hirth F.W. Zok	93
A Shear Lag Model for a Broken Fiber Embedded in a Composite with a Ductile Matrix	C.M. Landis R.M. McMeeking	109
The Influence of Particle Size and Particle Fracture on the Elastic/Plastic Deformation of Metal Matrix Composites	C.-W. Nan D.R. Clarke	143
Modeling the Elastic-Plastic Deformation of Al/Al ₂ O ₃ Particulate Composites	C.W. Nan D.R. Clarke	155
Experimental Assessment of Fatigue Life and Failure Modes in a SiC/Ti Composite	T.E. Steyer F.W. Zok D.P. Walls	159
Strength Variability in Alumina Fiber-Reinforced Aluminum Matrix Composites	U. Ramamurty F.W. Zok F.A. Leckie H.E. Déve	197
Inelastic Deformation of Fiber Composites Containing Bridged Cracks	F.W. Zok M.R. Begley T.E. Steyer D.P. Walls	209

Section B

CONSTITUTIVE LAWS AND DESIGN

The Role of Scarf Angle in the Performance of Aluminum Matrix Composite Joints	D.D. Brink C.G. Levi A.C.F. Cocks F.A. Leckie	223
On Kink-Band Propagation in Fiber Composites	B. Budiansky N.A. Fleck J.C. Amazigo	235
Singularities in Bi-materials: Parametric Study of an Isotropic/Anisotropic Joint	R. Desmorat F.A. Leckie	253
Design and Life Prediction Issues for High-Temperature Engineering Ceramics and their Composites	A.G. Evans	273
Effect of Interface Undulations on the Thermal Fatigue of Thin Films and Scales on Metal Substrates	A.G. Evans M.Y. He J.W. Hutchinson	291
Failures at Attachment Holes in Brittle Matrix Laminates	G.M. Genin J.W. Hutchinson	303
Effect of Cyclic Thermal Loading on the Inplane Shear Strength of Fiber Reinforced MMC's	S. Jansson F. Leckie	333
Design Considerations and Mechanical Properties of SCS6/Ti 15-3 Metal Matrix Composite After Debond	S. Jansson K. Kedward	345
On the Behaviour of Metal Matrix Composites Subjected to Cyclic Thermal Loading	A.R.S. Ponter F.A. Leckie	355
Shakedown Limits for a Metal Matrix Composite	A.R.S. Ponter K.F. Carter J.M. Duggan	385
Effects of Cladding on the Tensile Properties of Titanium Matrix Composites	U. Ramamurty F.W. Zok F.A. Leckie	407
Role of Cladding in the Notched Tensile Properties of a Titanium Matrix Composite	U. Ramamurty F.W. Zok F.A. Leckie	413

Strength-Limited Design of Composite/Monolith
Transitions in Metallic Structures

F.W. Zok
M.Y. He
A.G. Evans
F.A. Leckie
H.E. Déve

423

Section A

CONSTITUENT PROPERTIES AND MACROSCOPIC PERFORMANCE OF MMC

CREEP OF METAL-MATRIX COMPOSITES WITH ELASTIC FIBERS — PART I: CONTINUOUS ALIGNED FIBERS

Cao Cheng and N. Aravas
Department of Mechanical Engineering
and Applied Mechanics
University of Pennsylvania
Philadelphia, PA 19104
USA

Abstract

Three-dimensional constitutive equations are developed for the time-dependent (transient) creep behavior of metal-matrix composites reinforced by continuous elastic fibers. The composite model is developed in two steps: i) one in which shear loads relative to the fibers are applied and the response is matrix-dominated, and ii) another in which the composite is subjected to axisymmetric loads relative to the fibers and the response is fiber-dominated. The predictions of the model are compared with the solutions of a number of 'unit cell' problems; periodic boundary conditions, consistent with the requirements of homogenization theory, are imposed on the unit cell, and the solutions are obtained by using the finite element method. A method for the numerical integration of the developed constitutive equations is presented and the material model is implemented in general-purpose finite element program.

1 Introduction

Metal-matrix composites reinforced by continuous fibers have attracted a lot of attention recently, in view of their potential as high-temperature structural materials. Several *one-dimensional* models that can be used to predict the *creep* behavior of fiber-reinforced composites under simple types of loading are already available in the literature; we mention amongst these the work of Mileiko (1970), Kelly and Street (1972), McLean (1985, 1988, 1989), Goto and McLean (1991a,b), and McMeeking (1993a,b). However, little progress has been made in the development of *three-dimensional* constitutive equations for the behavior of metal-matrix composites at high temperatures.

When both the matrix and the fibers are capable of creeping, the composite exhibits steady-state creep. Three-dimensional constitutive equations for such composites have been developed by Johnson (1977), and more recently by Aravas *et al.* (1995).

When the fibers do not creep, transient creep of the composite is observed (Weber *et al.*, 1993). When such a composite system is subjected to uniaxial tension in the fiber direction, the creeping matrix relaxes, and load is transferred continuously from the matrix to the fibers. Therefore, when the applied macroscopic stress is constant, the axial strain rate decreases with time; eventually, when the matrix stress is completely relaxed, all of the applied load is carried by the fibers and the strain approaches a constant value limited by the elastic deformation of the fibers. McLean (1985, 1988, 1989) developed a model for the response of such composites under uniaxial tension.

In this paper, we develop *three-dimensional* constitutive equations for the *time-dependent* (transient) creep of metal-matrix composites reinforced by continuous elastic fibers. The macroscopic response of the composite is assumed to be transversely isotropic, with the axis of transverse isotropy defined by the direction of the fibers. The composite model is developed in two steps: i) one in which shear loads relative to the fibers are applied and the response is matrix dominated, and ii) another in which the composite is subjected to axisymmetric loads relative to the fibers and the response is fiber dominated. The predictions of the model are compared with the solutions of a number of 'unit cell' problems; periodic boundary conditions, consistent with the requirements of homogenization theory, are imposed on the unit cell problems, and the solutions are obtained by using the finite element method. A method for the numerical integration of the developed constitutive equations is presented. The 'linearization moduli' associated with the integration algorithm are computed, and the proposed new constitutive model is implemented in a general-purpose finite element program.

The effects of fiber failure on behavior of the composite are discussed in detail in Part II of this paper, where a constitutive model that accounts for 'material damage' is developed.

Standard notation is used throughout. Boldface symbols denote tensors the order of which is indicated by the context. All tensor components are written with respect to a fixed Cartesian coordinate system, and the summation convention is used for repeated indices, unless otherwise indicated. A superposed dot indicates the material time derivative, and a superscript T the transpose of a matrix. Let \mathbf{a} and \mathbf{b} be vectors, \mathbf{A} and \mathbf{B} second-order tensors, and \mathbf{C} and \mathbf{D} fourth-order tensors; the following products are used in the text: $(\mathbf{ab})_{ij} = a_i b_j$, $(\mathbf{A} \cdot \mathbf{a})_i = A_{ij} a_j$, $(\mathbf{a} \cdot \mathbf{A})_i = a_j A_{ji}$, $(\mathbf{A} \cdot \mathbf{B})_{ij} = A_{ik} B_{kj}$, $\mathbf{A} : \mathbf{B} = A_{ij} B_{ij}$,

$(\partial \mathbf{A} / \partial \mathbf{B})_{ijkl} = \partial A_{ij} / \partial B_{kl}$, $(\mathbf{A} \mathbf{B})_{ijkl} = A_{ij} B_{kl}$, $(\mathbf{C} : \mathbf{A})_{ij} = C_{ijkl} A_{kl}$, and $(\mathbf{C} : \mathbf{D})_{ijkl} = C_{ijmn} D_{mnkl}$.

2 Description of the material system

We consider a metal-matrix composite reinforced by continuous aligned fibers. The matrix is considered to exhibit power-law steady-state creep, plus elastic response, such that the tensile strain rate is

$$\dot{\epsilon} = \frac{\dot{\sigma}}{E_m} + B \sigma^n, \quad (1)$$

where ϵ and σ are the uniaxial strain and stress respectively, E_m is the Young's modulus, and (B, n) are the creep constants of the matrix. The fibers behave elastically and the uniaxial stress-strain relationship is

$$\epsilon = \frac{\sigma}{E_f}, \quad (2)$$

where E_f is the Young's modulus of the fibers. The corresponding three-dimensional version of the above equations is

$$\dot{\epsilon} = \mathbf{C}_m^{-1} : \dot{\sigma} + \frac{3}{2} B \sigma_e^{n-1} \sigma' \quad \text{for the matrix,} \quad (3)$$

and

$$\epsilon = \mathbf{C}_f^{-1} : \sigma \quad \text{for the fibers,} \quad (4)$$

where ϵ and σ are the strain and stress tensors, \mathbf{C}_m and \mathbf{C}_f are the fourth-order tensors of the elastic moduli for the matrix and the fibers respectively, a prime denotes the deviatoric part of a tensor, and $\sigma_e = (1.5 \sigma' : \sigma')^{1/2}$ is the von Mises equivalent stress.

It is a well known result that, when the *macroscopic* deformation of the composite is uniform with ϵ and σ being the corresponding uniform macroscopic fields, then the *average* stresses and strains in the matrix and the fibers are such that

$$\sigma = f \hat{\sigma}_f + (1 - f) \hat{\sigma}_m \quad \text{and} \quad \epsilon = f \hat{\epsilon}_f + (1 - f) \hat{\epsilon}_m, \quad (5)$$

where the subscripts m and f refer to the matrix and the fibers respectively, a caret indicates volume average over the phase, and f is the volume fraction of the fibers.

In the following, we let the x_3 coordinate axis coincide with the direction of the fibers, so that the x_1 and x_2 axes are on the transverse plane. An arbitrary macroscopic stress state σ can be written as

$$\begin{bmatrix} \sigma_{11} & \sigma_{12} & \sigma_{13} \\ \sigma_{12} & \sigma_{22} & \sigma_{23} \\ \sigma_{13} & \sigma_{23} & \sigma_{33} \end{bmatrix} = \begin{bmatrix} \frac{1}{2}(\sigma_{11} - \sigma_{22}) & \sigma_{12} & \sigma_{13} \\ \sigma_{12} & \frac{1}{2}(\sigma_{22} - \sigma_{11}) & \sigma_{23} \\ \sigma_{13} & \sigma_{23} & 0 \end{bmatrix} + \begin{bmatrix} \frac{1}{2}(\sigma_{11} + \sigma_{22}) & 0 & 0 \\ 0 & \frac{1}{2}(\sigma_{11} + \sigma_{22}) & 0 \\ 0 & 0 & \sigma_{33} \end{bmatrix}. \quad (6)$$

The first term on the right hand side of the above equation corresponds to shear loading relative to the fibers, and the last term is the superposition of lateral pressure and uniaxial loading. Therefore, it is always possible to choose the orientation of the x_1 and x_2 axes (say x'_1 and x'_2) so that an arbitrary stress σ can be represented by the superposition of the two states shown in Fig. 1. In terms of the components of the arbitrary stress state of equation (6), the quantities σ_n , σ_p , τ_n and τ_p shown in Figs. 1a and 1b are given by

$$\sigma_n = \sigma_{33}, \quad \sigma_p = \frac{1}{2}(\sigma_{11} + \sigma_{22}), \quad \tau_n^2 = \sigma_{13}^2 + \sigma_{23}^2, \quad \tau_p^2 = \frac{1}{4}(\sigma_{11} - \sigma_{22})^2 + \sigma_{12}^2, \quad (7)$$

and are independent of the orientation of the x_1 - and x_2 -axes.

The behavior of the composite is expected to be substantially different under shear (Fig. 1a) and axisymmetric (Fig. 1b) loading. In particular, the response to the shear loads shown in Fig. 1a will be ‘matrix dominated’, and the composite is expected to experience ‘steady-state’ creep, i.e., the creep strain rate is constant under constant applied shear loads; on the other hand, when constant axisymmetric loads are applied, the corresponding creep strain rate will be time-dependent due to matrix relaxation and load transfer from the matrix to the fibers (Weber *et al.*, 1993). In the following two Sections 3 and 4, we analyze the behavior of the composite under the two types of loading shown in Fig. 1, and the results are then combined in the constitutive model presented in Section 5.

3 The matrix dominated behavior for shear loading

The creep response of the composite under the shear loading shown in Fig. 1a is dominated by the matrix behavior. The elasticity of the matrix and the fibers are not expected to have a significant influence on the steady-state creep characteristics of the composite under shear. Therefore, for the rest of Section 3, we assume that the fibers are rigid and that the matrix deforms by creep only, i.e., $\mathbf{C}_m^{-1} = \mathbf{C}_f^{-1} = \mathbf{0}$ and $\epsilon_f = \mathbf{0}$. Referring to Fig. 1a, we assume that the only non-zero stress components are $\sigma_{31'} = \sigma_{1'3} = \tau_n \cos \phi$, $\sigma_{32'} = \sigma_{2'3} = \tau_n \sin \phi$, and $\sigma_{1'2'} = \sigma_{2'1'} = \tau_p$, where the angle ϕ is as shown in Fig. 1a.

In the following, we discuss first a model developed by deBotton and Ponte Castañeda (dB-PC) (1993) for fiber-reinforced nonlinear composites, and then develop a simple model based on statically admissible stress fields and a set of ‘unit cell’ calculations with periodic boundary conditions.

3.1 The model of deBotton and Ponte Castañeda

deBotton and Ponte Castañeda (1993) have presented recently a constitutive model for nonlinear composite materials reinforced by continuous aligned fibers. The derivation of the model is based on a variational principle that enables the expression of the effective energy functions of nonlinear composites in terms of optimization problems. For the case of rigid fibers and a power-law creeping matrix and with respect to the coordinate axes (x'_1, x'_2, x_3)

shown in Fig. 1, their model can be written as

$$[\dot{\epsilon}] = \frac{3}{2} B (1-f) (1+f)^{-(n+1)/2} \sigma_s^{n-1} \begin{bmatrix} 0 & \tau_p & \tau_n \cos \phi \\ \tau_p & 0 & \tau_n \sin \phi \\ \tau_n \cos \phi & \tau_n \sin \phi & 0 \end{bmatrix}, \quad (8)$$

where $\sigma_s^2 = 3(\tau_n^2 + \tau_p^2)$. For an arbitrary orientation of the x_1 and x_2 coordinate axes on the transverse plane, the above equations become

$$[\dot{\epsilon}] = \frac{3}{2} B (1-f) (1+f)^{-(n+1)/2} \sigma_s^{n-1} \begin{bmatrix} (\sigma_{11} - \sigma_{22})/2 & \sigma_{12} & \sigma_{13} \\ \sigma_{12} & (\sigma_{22} - \sigma_{11})/2 & \sigma_{23} \\ \sigma_{13} & \sigma_{23} & 0 \end{bmatrix}, \quad (9)$$

where now $\tau_n^2 = \sigma_{13}^2 + \sigma_{23}^2$ and $\tau_p^2 = \sigma_{12}^2 + (\sigma_{11} - \sigma_{22})^2/4$, so that

$$\sigma_s^2 = \frac{3}{4} (\sigma_{11} - \sigma_{22})^2 + 3(\sigma_{12}^2 + \sigma_{13}^2 + \sigma_{23}^2). \quad (10)$$

According to this model, constant applied stresses cause constant strain rates (steady-state creep). Also, the predicted response of the composite is identical under longitudinal (σ_{31} or σ_{32}) or transverse (σ_{12}) shear.

An alternative Reuss-type of model is presented in the following Section 3.2 and comparisons with unit cell calculations are presented in Section 3.3.

3.2 A simple Reuss model

We assume that the stress tensor in the matrix σ_m is *uniform* and equal to the macroscopic stress, i.e., $\sigma_m = \sigma$. The corresponding uniform strain rate in the matrix is

$$\dot{\epsilon}_m = \dot{\epsilon}_m = \frac{3}{2} B \sigma_e^{n-1} \sigma'. \quad (11)$$

In view of equation (5b), the macroscopic strain rate $\dot{\epsilon}$ is now

$$\dot{\epsilon} = (1-f) \dot{\epsilon}_m = \frac{3}{2} B (1-f) \sigma_e^{n-1} \sigma', \quad (12)$$

or

$$[\dot{\epsilon}] = \frac{3}{2} B (1-f) \sigma_s^{n-1} \begin{bmatrix} 0 & \tau_p & \tau_n \cos \phi \\ \tau_p & 0 & \tau_n \sin \phi \\ \tau_n \cos \phi & \tau_n \sin \phi & 0 \end{bmatrix}, \quad \sigma_s^2 = \sigma_e^2 = 3(\tau_n^2 + \tau_p^2), \quad (13)$$

with respect to the coordinate axes (x'_1, x'_2, x_3) shown in Fig. 1. When the orientation of the x_1 and x_2 coordinate axes on the transverse plane is arbitrary, the above equation for the macroscopic strain rate can be written as

$$[\dot{\epsilon}] = \frac{3}{2} B (1-f) \sigma_s^{n-1} \begin{bmatrix} (\sigma_{11} - \sigma_{22})/2 & \sigma_{12} & \sigma_{13} \\ \sigma_{12} & (\sigma_{22} - \sigma_{11})/2 & \sigma_{23} \\ \sigma_{13} & \sigma_{23} & 0 \end{bmatrix}, \quad (14)$$

where

$$\sigma_s^2 = \sigma_e^2 = \frac{3}{4}(\sigma_{11} - \sigma_{22})^2 + 3(\sigma_{12}^2 + \sigma_{13}^2 + \sigma_{23}^2). \quad (15)$$

It is interesting to note that the form of equation (14) is identical to that of (9), the only difference being the multiplicative constant $(1 + f)^{-(n+1)/2} < 1$ in (9).

3.3 Unit cell solutions

The predictions of the analytical models discussed in the previous subsections are compared with the results of periodic homogenization theory (Sanchez-Palencia, 1980; Bakhvalov and Panasenko, 1989). A number of ‘unit cell’ problems with periodic boundary conditions, consistent with the requirements of homogenization theory, are solved by using the finite element method. The distribution of the fibers is assumed to be periodic, with the fibers arranged in a hexagonal array. A detailed description of the formulation of the unit cell problems can be found in Aravas *et al.* (1993) and Cheng (1996) and will not be repeated here.

The macroscopic applied loads are combinations of transverse and longitudinal shear. Figure 2 shows the assumed hexagonal arrangement of the fibers in the matrix, and Fig. 3 shows the finite element mesh used in the two-dimensional calculations. The dark and white regions in Fig. 3 represent the fibers and the matrix respectively. A similar mesh is used in the three-dimensional calculations that involve longitudinal shear (Aravas *et al.*, 1993). Calculations are carried out for several values of the matrix creep exponent n and for different values of the fiber volume fraction f . The numerical solution is practically independent of the values of the elastic constants of the fibers and the matrix. It is found that the results of the unit cell calculations agree very well with a constitutive equation of the form

$$[\dot{\epsilon}] = \frac{3}{2} B (1 - f) \chi^n \sigma_s^{n-1} \begin{bmatrix} (\sigma_{11} - \sigma_{22})/2 & \sigma_{12} & \sigma_{13} \\ \sigma_{12} & (\sigma_{22} - \sigma_{11})/2 & \sigma_{23} \\ \sigma_{13} & \sigma_{23} & 0 \end{bmatrix}, \quad (16)$$

where $\chi = \chi(n, f)$, and the orientation of the x_1 and x_2 axes on the transverse plane is arbitrary. Note that $\chi = (1 + f)^{-(n+1)/(2n)}$ in the dB-PC model, and $\chi = 1$ in the Reuss model of Section 3.2.

It is noteworthy that the unit cell calculations predict that the response is identical under longitudinal and transverse shear as well. The results of the finite element solutions indicate that, for values of n and f in the range $1 \leq n \leq 10$ and $0 \leq f \leq 0.70$, the quantity χ^{-1} can be approximated by an equation of the form:

$$\chi^{-1} = 1 + a(n) f + b(n) f^2 + c(n) f^6, \quad (17)$$

where $a(n)$ is given by

$$a(n) = \frac{1}{4G(n)} \left(\frac{n+1}{n} \right)^2 - \frac{n+1}{2n^2}, \quad G(n) = \frac{1}{2} \left(\frac{n+1}{\sqrt{n}+1} \right), \quad (18)$$

and

$$b(n) = \frac{0.467}{n} - 0.248 - 0.009n, \quad c(n) = \frac{15.199}{n} + 1.132 + 0.248n. \quad (19)$$

For composite materials with a *statistically isotropic* (as opposed to period) microstructure, Ponte Castañeda (1996) obtained the following exact result for the dilute limit (small f):

$$\chi^{-1} = 1 + a(n)f. \quad (20)$$

For small values of f , the interaction between neighboring fibers is very weak, and equation (20) is also valid for composites with a *periodic* microstructure. Note that the expression for χ^{-1} in equation (17) is consistent with the exact result (20) in the limit of small f .

For the case of transverse macroscopic shear loading ($\sigma_{12} = \tau$), the above model predicts

$$\frac{\dot{\gamma}}{B\tau_0^n} = 3^{(n+1)/2} (1-f) \chi^n \left(\frac{\tau}{\tau_0} \right)^n, \quad (21)$$

where $\gamma = 2\epsilon_{12}$, and τ_0 is an arbitrary reference stress. Figure 4 shows the results of the unit cell calculations together with those of equations (17)–(21) for $f = 0.32$ and $n = 3$. The predictions of the analytical model agree well with the results of the finite element solutions.

4 The fiber dominated behavior for axisymmetric loading

In the case of the axisymmetric loading shown in Fig. 1b, the elasticity of the fibers is of major importance. In the following, we discuss first a simple model developed by McLean (1985, 1988) for uniaxial tension in the direction of the fibers, and then develop a three-dimensional version of it for the case of the axisymmetric loading shown in Fig. 1b.

4.1 McLean's model for uniaxial tension in the direction of the fibers

The macroscopic applied load is tensile in the direction of the fibers, i.e., $\sigma_{33} = \sigma$. Let $\epsilon_{33} = \epsilon$ be the corresponding macroscopic axial strain component.

McLean assumes that the stresses take *constant* values in the fibers and the matrix and that the only non-zero components are $\sigma_{f33} = \sigma_f$ and $\sigma_{m33} = \sigma_m$. He also assumes that the corresponding uniform axial strain in the fibers and the matrix equals the macroscopic axial strain ϵ . With these assumptions, equation (5a) implies that

$$\sigma = f\sigma_f + (1-f)\sigma_m, \quad (22)$$

and the axial strain rate can be written as

$$\dot{\epsilon} = \frac{\dot{\sigma}_f}{E_f} = \frac{\dot{\sigma}_m}{E_m} + B\sigma_m^n. \quad (23)$$

Using the last two equations we can readily show that McLean model can be written in the following form:

$$\dot{\epsilon} = \frac{\dot{\sigma}}{E} + B' (\sigma - \alpha)^n \quad \text{and} \quad \frac{\dot{\alpha}}{f E_f} = \frac{\dot{\sigma}}{E} + B' (\sigma - \alpha)^n, \quad (24)$$

where the 'back stress' $\alpha = f \sigma_f$ is the part of the total axial stress carried by the fibers (see equation (22)), $E = f E_f + (1 - f) E_m$, and $B' = B E_m / [(1 - f)^{n-1} E]$. The initial values of the strain (ϵ_0) and the back stress (α_0) at the start of the loading history (time $t = 0^+$) are

$$\epsilon_0 = \sigma(0^+)/E \quad \text{and} \quad \alpha_0 = f E_f \epsilon_0. \quad (25)$$

The first term on the right hand side of (24a) defines the elastic strain rate in the composite ($\dot{\epsilon}^e$), and the second term defines the macroscopic creep strain rate $\dot{\epsilon}^c$. Equation (24a) for the composite has a form similar to that of the matrix (23b) or (1), where now E_m is replaced by E in the elastic part, and B and σ by B' and $\sigma - \alpha$ respectively in the creep part of $\dot{\epsilon}$. The back stress α is a measure of the stress carried by the fibers and accounts for the strengthening effects of the fibers; i.e., whereas the creep strain rate is proportional to σ^n in the absence of fibers, $\dot{\epsilon}^c$ is proportional to $(\sigma - \alpha)^n$ when $f \neq 0$.

For the case of a 'creep test' in which a constant stress σ is applied in the direction of the fibers, equations (24) make it clear that the strain rate varies with time due to the evolution of the back stress α (transient or non-steady-state creep). In this case, equations (24) can be integrated to give

$$\epsilon(t) = \epsilon_c \left\{ 1 - \left(1 - \frac{\epsilon_0}{\epsilon_c} \right) \left[1 + (n-1) \left(1 - \frac{\epsilon_0}{\epsilon_c} \right)^{n-1} \frac{B' \sigma^n t}{\epsilon_c} \right]^{-1/(n-1)} \right\} \quad \text{for } n > 1, \quad (26)$$

$$\epsilon(t) = \epsilon_c \left[1 - \left(1 - \frac{\epsilon_0}{\epsilon_c} \right) \exp \left(- \frac{B' \sigma^n t}{\epsilon_c} \right) \right] \quad \text{for } n = 1, \quad (27)$$

and

$$\alpha(t) = f E_f \epsilon(t), \quad (28)$$

where $\epsilon_0 = \sigma/E$, and $\epsilon_c = \sigma/(f E_f)$. In the uniaxial creep test, as the matrix creeps, the corresponding stress σ_m relaxes, load is transferred from the matrix to the fibers and, as a consequence, the back stress α increases with time. The long time response of the system as $t \rightarrow \infty$ is such that

$$\dot{\epsilon} \rightarrow 0, \quad \epsilon \rightarrow \epsilon_c, \quad \sigma_m \rightarrow 0, \quad \text{and} \quad \alpha = f \sigma_f \rightarrow \sigma, \quad (29)$$

i.e., eventually the strain approaches the limiting value ϵ_c , the matrix is completely unloaded and the whole load is carried by the fibers. Figure 5 shows the variation of the normalized strain $\hat{\epsilon}$ with normalized time \hat{t} for values of $n = 3$ and $\epsilon_0/\epsilon_c = 0.6$, where

$$\hat{\epsilon} = \frac{\epsilon}{\epsilon_c} = \frac{\alpha}{\sigma} \quad \text{and} \quad \hat{t} = \frac{B' \sigma^n t}{\epsilon_c}. \quad (30)$$

4.2 A three-dimensional version of the McLean model

We consider next the case in which the applied macroscopic load is axisymmetric of the form shown in Fig. 1b, i.e., $\sigma_{1'1'} = \sigma_{2'2'} = \sigma_p$ and $\sigma_{33} = \sigma_n$. Note that this macroscopic stress state maintains its form for an arbitrary orientation of the x_1 - and x_2 -axes on the transverse plane, i.e., it is always true that $\sigma_{11} = \sigma_{22} = \sigma_p$.

Assumptions similar to those of McLean are used for this type of loading as well; i.e., it is assumed that

1. the stresses take constant values in the fibers and the matrix, i.e.,

$$[\sigma_f] = \begin{bmatrix} \sigma_p & 0 & 0 \\ 0 & \sigma_p & 0 \\ 0 & 0 & \sigma_f \end{bmatrix} \quad \text{and} \quad [\sigma_m] = \begin{bmatrix} \sigma_p & 0 & 0 \\ 0 & \sigma_p & 0 \\ 0 & 0 & \sigma_m \end{bmatrix}, \quad (31)$$

where the transverse normal stresses are taken to be equal to the macroscopic load σ_p , and

2. the corresponding axial strain in the fibers and the matrix is equal to the axial macroscopic strain $\epsilon_{33} = \epsilon$, i.e.,

$$\epsilon_{f33} = \epsilon_{m33} = \epsilon. \quad (32)$$

In view of equation (5a), the axial components σ_f and σ_m are such that

$$\sigma_n = f \sigma_f + (1 - f) \sigma_m. \quad (33)$$

Recalling equation (5b) we write $\dot{\epsilon} = f \dot{\epsilon}_f + (1 - f) \dot{\epsilon}_m$, and using the constitutive equations (3) and (4) for the matrix and the fibers respectively we find

$$\begin{aligned} \begin{Bmatrix} \dot{\epsilon}_{11} \\ \dot{\epsilon}_{22} \\ \dot{\epsilon}_{33} \end{Bmatrix} &= \frac{f}{E_f} \begin{bmatrix} 1 & -\nu_f & -\nu_f \\ -\nu_f & 1 & -\nu_f \\ -\nu_f & -\nu_f & 1 \end{bmatrix} \begin{Bmatrix} \dot{\sigma}_p \\ \dot{\sigma}_p \\ \dot{\sigma}_f \end{Bmatrix} + \\ &+ \frac{1-f}{E_m} \begin{bmatrix} 1 & -\nu_m & -\nu_m \\ -\nu_m & 1 & -\nu_m \\ -\nu_m & -\nu_m & 1 \end{bmatrix} \begin{Bmatrix} \dot{\sigma}_p \\ \dot{\sigma}_p \\ \dot{\sigma}_m \end{Bmatrix} + \\ &+ (1-f) \frac{B}{2} |\sigma_m - \sigma_p|^{n-1} (\sigma_m - \sigma_p) \begin{Bmatrix} -1 \\ -1 \\ 2 \end{Bmatrix}. \end{aligned} \quad (34)$$

Our goal is to eliminate the 'local' stresses σ_m and σ_f from the above equation and arrive at an expression for $\dot{\epsilon}$ in terms of the macroscopic stresses σ_n , σ_p and a back stress α . This is achieved as follows.

As before, we introduce the back stress $\alpha = f \sigma_f$, and using (33) we write

$$\sigma_m = \frac{\sigma_n - \alpha}{1 - f} \quad \text{and} \quad \sigma_f = \frac{\alpha}{f}. \quad (35)$$

Next, we use the strain continuity equation $\dot{\epsilon}_{f33} = \dot{\epsilon}_{m33}$ together with the constitutive equations for the fibers and the matrix and equations (35) to determine $\dot{\alpha}$ in terms of $\dot{\sigma}_n$, $\dot{\sigma}_p$, σ_n , σ_p , and α :

$$\frac{\dot{\alpha}}{fE_f} = \frac{\dot{\sigma}_n}{E_L} + 2(1-f) \left(\frac{E_m}{E_f} \nu_f - \nu_m \right) \frac{\dot{\sigma}_p}{E_L} + B'(1-f)^n \left| \frac{\sigma_n - \alpha}{1-f} - \sigma_p \right|^{n-1} \left(\frac{\sigma_n - \alpha}{1-f} - \sigma_p \right), \quad (36)$$

where

$$E_L = E = fE_f + (1-f)E_m \quad \text{and} \quad B' = \frac{B E_m}{(1-f)^{n-1} E_L}. \quad (37)$$

Finally, substituting equations (35) into (34) and using the expression for $\dot{\alpha}$, we obtain the following equation for the macroscopic strain rates:

$$\begin{aligned} \begin{Bmatrix} \dot{\epsilon}_{11} \\ \dot{\epsilon}_{22} \\ \dot{\epsilon}_{33} \end{Bmatrix} &= \begin{bmatrix} 1/E_T & -\nu_T/E_T & -\nu_L/E_L \\ -\nu_T/E_T & 1/E_T & -\nu_L/E_L \\ -\nu_L/E_L & -\nu_L/E_L & 1/E_L \end{bmatrix} \begin{Bmatrix} \dot{\sigma}_p \\ \dot{\sigma}_p \\ \dot{\sigma}_n \end{Bmatrix} + \\ &+ B'(1-f)^n \left| \frac{\sigma_n - \alpha}{1-f} - \sigma_p \right|^{n-1} \left(\frac{\sigma_n - \alpha}{1-f} - \sigma_p \right) \begin{Bmatrix} K' \\ K' \\ 1 \end{Bmatrix}, \end{aligned} \quad (38)$$

where

$$\frac{1}{E_T} = \frac{1-f}{E_m} + \frac{f}{E_f} + 2f(1-f) \frac{E_f}{E_L} \left(\frac{E_m}{E_f} \nu_f - \nu_m \right) \left(\frac{\nu_m}{E_m} - \frac{\nu_f}{E_f} \right), \quad (39)$$

$$\frac{\nu_T}{E_T} = (1-f) \frac{\nu_m}{E_m} + f \frac{\nu_f}{E_f}, \quad \nu_L = f \nu_f + (1-f) \nu_m, \quad (40)$$

and

$$K' = -\frac{1}{2} + f \left[\frac{E_f}{E_m} \left(\nu_m - \frac{1}{2} \right) - \left(\nu_f - \frac{1}{2} \right) \right]. \quad (41)$$

The initial value of the back stress α_0 is

$$\alpha_0 = \frac{f E_f}{E_L} \left[\sigma_n(0^+) - 2(1-f) E_m \left(\frac{\nu_m}{E_m} - \frac{\nu_f}{E_f} \right) \sigma_p(0^+) \right]. \quad (42)$$

The first term on the right hand side of (38) defines the elastic part $\dot{\epsilon}^e$ of the total strain rate and the second term defines the macroscopic creep strain rate $\dot{\epsilon}^c$. In order to make connection with equation (16) for $\dot{\epsilon}^c$ in the case of shear loading, we note that the second term on the right hand side of (38) can be also written as

$$[\dot{\epsilon}^c] = \frac{3}{2} B (1-f) |S|^{n-1} \begin{bmatrix} K S & 0 & 0 \\ 0 & K S & 0 \\ 0 & 0 & L S \end{bmatrix}, \quad \text{where} \quad S = \frac{\sigma_n - \alpha}{1-f} - \sigma_p, \quad (43)$$

and

$$K = \frac{2}{3} \frac{E_m}{E_L} \left\{ -\frac{1}{2} + f \left[\frac{E_f}{E_m} \left(\nu_m - \frac{1}{2} \right) - \left(\nu_f - \frac{1}{2} \right) \right] \right\}, \quad L = \frac{2}{3} \frac{E_m}{E_L}. \quad (44)$$

4.3 Unit cell solutions

The predictions of the model developed in the previous section are now compared with unit-cell finite element calculations. Periodic boundary conditions, similar to those described in Section 3.3, are imposed. The material properties used in the calculations are $E_f = 360$ GPa, $\nu_f = 0.3$, $E_m = 65$ GPa, $\nu_m = 0.3$, $n = 3$, and $B = 4.125 \times 10^{-13}$ MPa $^{-n}$ s $^{-1}$. The volume fraction of the fibers is $f = 0.32$.

Figure 6 shows the results of the finite element calculations together with the predictions of the model (38)–(42), when a constant axial macroscopic load $\sigma_n = 500$ MPa is applied. The corresponding results for a constant axisymmetric transverse macroscopic load $\sigma_p = 100$ MPa are shown in Fig. 7. The results of the unit cell calculations agree well with the predictions of the analytical model.

5 A proposed new model

The results derived in Sections 3 and 4 for shear and axisymmetric loadings respectively are now combined and constitutive equations for general types of loading are developed. Clearly, in view of the non-linearity of the problem, the equations developed for shear and axisymmetric loadings can not be superposed. Instead, our results are combined in such a way that the proposed general constitutive equations for $\dot{\epsilon}^{\sigma}$ reduce to equations (16) and (43) when the applied loads are shear or axisymmetric respectively.

The detailed description of the proposed model is presented in the following two subsections. The macroscopic response of the composite is transversely isotropic, and the unit vector \mathbf{n} in the direction of the fibers is used to define the axis of rotational symmetry. The total macroscopic strain in the composite is written as the sum of the elastic and creep parts:

$$\epsilon = \epsilon^e + \epsilon^{\sigma}. \quad (45)$$

Constitutive equations for ϵ^e and $\dot{\epsilon}^{\sigma}$ are presented in the following.

5.1 Elasticity

The elastic strain is written in terms of the stress tensor σ as

$$\epsilon^e = \mathbf{C}^e{}^{-1} : \sigma, \quad (46)$$

where \mathbf{C}^e is the fourth-order elasticity tensor for the homogenized transversely isotropic composite. When the fibers are aligned with the x_3 coordinate direction (i.e., $\mathbf{n} = \mathbf{e}_3$), equation (46) can be written in matrix form as

$$\{\epsilon^e\} = [\mathbf{C}^e]^{-1} \{\sigma\}, \quad (47)$$

where $\{\epsilon^e\}^T = \{\epsilon_{11}^e, \epsilon_{22}^e, \epsilon_{33}^e, \gamma_{12}^e, \gamma_{13}^e, \gamma_{23}^e\}$, $\{\sigma\}^T = \{\sigma_{11}, \sigma_{22}, \sigma_{33}, \sigma_{12}, \sigma_{13}, \sigma_{23}\}$,

$$[C^e]^{-1} = \begin{bmatrix} 1/E_T & -\nu_T/E_T & -\nu_L/E_L & 0 & 0 & 0 \\ -\nu_T/E_T & 1/E_T & -\nu_L/E_L & 0 & 0 & 0 \\ -\nu_L/E_L & -\nu_L/E_L & 1/E_L & 0 & 0 & 0 \\ 0 & 0 & 0 & 1/G_T & 0 & 0 \\ 0 & 0 & 0 & 0 & 1/G_L & 0 \\ 0 & 0 & 0 & 0 & 0 & 1/G_L \end{bmatrix},$$

E_L , E_T , G_L , ν_L and ν_T are the five independent elastic constants of the composite, and

$$G_T = \frac{E_T}{2(1 + \nu_T)}. \quad (48)$$

The constants E_L , E_T , ν_L and ν_T are defined by equations (37a), (39), and (40), and the shear modulus G_L is estimated as (Christensen, 1979, p. 84)

$$G_L = G_m \frac{G_f(1+f) + G_m(1-f)}{G_f(1-f) + G_m(1+f)}, \quad (49)$$

where G_f and G_m are the shear moduli of the fibers and the matrix respectively.

5.2 Creep

The general form of the constitutive equations during creep is

$$\dot{\epsilon}^c = \mathbf{g}(\boldsymbol{\sigma} - \boldsymbol{\alpha}, s), \quad \dot{\boldsymbol{\alpha}} = \mathbf{h}(\boldsymbol{\sigma} - \boldsymbol{\alpha}, \dot{\boldsymbol{\sigma}}, s), \quad (50)$$

where $\boldsymbol{\alpha}$ is the back stress tensor, \mathbf{g} and \mathbf{h} are tensor-valued isotropic functions, and s is the collection of material parameters, $s = \{E_f, \nu_f, E_m, \nu_m, B, n, f\}$. In the present model, the back stress tensor $\boldsymbol{\alpha}$ is assumed to be in the direction of the fibers, i.e., $\boldsymbol{\alpha} = \alpha \mathbf{nn}$; it should be noted, however, that more complicated forms may be necessary when effects such as the primary (transient) creep of the matrix must be accounted for.

In the following, we combine the results of Sections 3 and 4 and develop constitutive equations for general types of loading. The proposed model is such that equations (16) and (38) are recovered as special cases, when the applied loads are shear or axisymmetric respectively. With respect to the coordinate axes shown in Fig. 1 and for an arbitrary orientation of the x_1 - x_2 axes on the transverse plane, we write the following equations for the creep strain rate:

$$[\dot{\epsilon}^c] = \frac{3}{2} B (1-f) \Sigma_e^{n-1} \begin{bmatrix} \chi(\sigma_{11} - \sigma_{22})/2 + K S & \chi \sigma_{12} & \chi \sigma_{13} \\ \chi \sigma_{12} & \chi(\sigma_{22} - \sigma_{11})/2 + K S & \chi \sigma_{23} \\ \chi \sigma_{13} & \chi \sigma_{23} & L S \end{bmatrix}, \quad (51)$$

where $\Sigma_e^2 = S^2 + (\chi \sigma_s)^2$. For convenience, we repeat the definition of the quantities entering the above equation: $\sigma_n = \sigma_{33}$, $\sigma_p = (\sigma_{11} + \sigma_{22})/2$,

$$S = \frac{\sigma_n - \alpha}{1 - f} - \sigma_p, \quad \sigma_s^2 = \frac{3}{4}(\sigma_{11} - \sigma_{22})^2 + 3(\sigma_{12}^2 + \sigma_{13}^2 + \sigma_{23}^2), \quad (52)$$

$$K = \frac{2}{3} \frac{E_m}{E_L} \left\{ -\frac{1}{2} + f \left[\frac{E_f}{E_m} \left(\nu_m - \frac{1}{2} \right) - \left(\nu_f - \frac{1}{2} \right) \right] \right\}, \quad L = \frac{2}{3} \frac{E_m}{E_L}, \quad (53)$$

and recall that $\chi(n, f)$ is defined by equations (17)–(19). The evolution of the back stress is given by

$$\frac{\dot{\alpha}}{f E_f} = \frac{\dot{\sigma}_n}{E_L} + 2(1 - f) \left(\frac{E_m}{E_f} \nu_f - \nu_m \right) \frac{\dot{\sigma}_p}{E_L} + B' (1 - f)^n \Sigma_e^{n-1} \left(\frac{\sigma_n - \alpha}{1 - f} - \sigma_p \right), \quad (54)$$

where E_L and B' are defined by (37), and the initial value of α_0 of the back stress is given by equation (42).

5.3 Unit cell solutions

The predictions of the proposed new model are compared with the results of finite element calculations, in which a unit cell is subjected to a combination of axisymmetric and shear macroscopic loading. The material constants mentioned in Section 4.3 are used in the present calculations as well. Figure 8 shows the temporal variation of various strain components for the case where constant macroscopic stresses $\sigma_{11} = 20$ MPa, $\sigma_{12} = 20$ MPa, and $\sigma_{33} = 500$ MPa are applied to the unit cell. The results of the numerical calculations agree well with the predictions of the analytical model.

6 Finite element implementation of the constitutive model

In this section, we discuss the implementation of the general form of the proposed constitutive model in a finite element program. In a finite element environment, the solution of the creep problem is developed incrementally and the constitutive equations are integrated numerically at the element Gauss points. In a displacement based finite element formulation the solution is deformation driven. At a material point, the solution $(\sigma_n, \epsilon_n, \alpha_n)$ at time t_n as well as the strain ϵ_{n+1} at time $t_{n+1} = t_n + \Delta t$ are supposed to be known and one has to determine the solution $(\sigma_{n+1}, \alpha_{n+1})$.

6.1 Numerical integration of the constitutive equations

We start with the elasticity equation (46)

$$\sigma_{n+1} = \mathbf{C}^e : \epsilon_{n+1}^e = \mathbf{C}^e : (\epsilon_n^e + \Delta \epsilon - \Delta \epsilon^{cr}) = \sigma^e - \mathbf{C}^e : \Delta \epsilon^{cr}, \quad (55)$$

where $\Delta\epsilon = \epsilon_{n+1} - \epsilon_n$ and $\Delta\epsilon^{cr} = \epsilon_{n+1}^{cr} - \epsilon_n^{cr}$ are the total- and creep-strain increments, and $\sigma^e = \sigma_n + C^e : \Delta\epsilon$ is the (known) ‘elastic predictor’.

The constitutive equations (51) and (54) for $\dot{\epsilon}^{cr}$ and $\dot{\alpha}$ are integrated by using the backward Euler method:

$$\Delta\epsilon^{cr} = g(\sigma_{n+1} - \alpha_{n+1}) \Delta t, \quad (56)$$

$$\Delta\alpha = h(\sigma_{n+1} - \alpha_{n+1}, \Delta\sigma/\Delta t) \Delta t, \quad (57)$$

where $\Delta\sigma = \sigma_{n+1} - \sigma_n$.

Summarizing, we write

$$G(\Delta\epsilon^{cr}, \Delta\alpha) \equiv \Delta\epsilon^{cr} - \Delta t g(\sigma_{n+1} - \alpha_n - \Delta\alpha) = 0, \quad (58)$$

$$H(\Delta\epsilon^{cr}, \Delta\alpha) \equiv \Delta\alpha - \Delta t h\left(\sigma_{n+1} - \alpha_n - \Delta\alpha, \frac{\sigma_{n+1} - \sigma_n}{\Delta t}\right) = 0, \quad (59)$$

where

$$\sigma_{n+1}(\Delta\epsilon^{cr}) = \sigma^e - C^e : \Delta\epsilon^{cr}. \quad (60)$$

We choose $\Delta\epsilon^{cr}$ and $\Delta\alpha$ as the primary unknowns and treat (58) and (59) as the basic equations in which σ_{n+1} is defined by (60). The solution is obtained by using Newton’s method. The first estimate for $\Delta\epsilon^{cr}$ and $\Delta\alpha$ used to start the Newton loop are obtained by using a forward Euler scheme, i.e., $(\Delta\epsilon^{cr})_{\text{est}} = g(\sigma_n - \alpha_n) \Delta t$ and $(\Delta\alpha)_{\text{est}} = h(\sigma_n - \alpha_n, \Delta\sigma_n/\Delta t) \Delta t$, where $\Delta\sigma_n = \sigma_n - \sigma_{n-1}$.

Once $\Delta\epsilon^{cr}$ and $\Delta\alpha$ are found, equation (60) defines the stress σ_{n+1} , $\alpha_{n+1} = \alpha_n + \Delta\alpha$, and this completes the integration procedure.

We conclude this section with a brief discussion of the appropriate time increment used in the integration procedure. Let σ_{\max} be the maximum of the absolute values of the stress components (i.e., $\sigma_{\max} = \max|\sigma_{ij}|_{n+1}$) and define

$$\text{CETOL} = 0.1 \times \frac{\sigma_{\max}}{(E_L + E_T)/2}, \quad (61)$$

where E_L and E_T are the elastic moduli defined in Section 5.1. The time increment Δt is chosen so that the maximum difference in the creep strain increment calculated from the creep strain rate based on the conditions at the beginning and at the end of the increment is always less than CETOL, i.e.,

$$|g_{ij}(\sigma_{n+1} - \alpha_{n+1}) - g_{ij}(\sigma_n - \alpha_n)| \Delta t < \text{CETOL} \quad \text{for all } i, j. \quad (62)$$

6.2 Linearization moduli

In an implicit finite element code, the overall discretized equilibrium equations are written at the end of the increment, resulting in a set of nonlinear equations for the nodal unknowns. If a full Newton scheme is used to solve the global nonlinear equations, one needs to calculate the so-called ‘linearization moduli’ \mathcal{J}

$$\mathcal{J} = \frac{\partial \sigma_{n+1}}{\partial \epsilon_{n+1}}. \quad (63)$$

For simplicity, we drop the subscript $(n+1)$ with the understanding that all quantities are evaluated at the end of the increment, unless otherwise indicated. Starting with the elasticity equation (55), we find

$$\partial\sigma = \mathbf{C}^e : \partial\epsilon - \mathbf{C}^e : \partial\epsilon^{cr}, \quad (64)$$

where we took into account that $\partial\Delta\epsilon^{cr} = \partial(\epsilon^{cr} - \epsilon_n^{cr}) = \partial\epsilon^{cr}$.

The differential $\partial\epsilon^{cr}$ is evaluated from equations (56) and (57) as follows

$$\partial\epsilon^{cr} = \Delta t \frac{\partial \mathbf{g}}{\partial \mathbf{s}} : (\partial\sigma - \partial\alpha) \quad \text{where} \quad \mathbf{s} = \sigma - \alpha, \quad (65)$$

$$\partial\alpha = \Delta t \frac{\partial \mathbf{h}}{\partial \mathbf{s}} : (\partial\sigma - \partial\alpha) + \frac{\partial \mathbf{h}}{\partial \dot{\sigma}} : \partial\sigma. \quad (66)$$

Eliminating $\partial\alpha$ from the last two equations, we find

$$\partial\epsilon^{cr} = \mathbf{D} : \partial\sigma, \quad (67)$$

where

$$\mathbf{D} = \Delta t \frac{\partial \mathbf{g}}{\partial \mathbf{s}} : \left[\mathbf{J} - \left(\mathbf{J} + \Delta t \frac{\partial \mathbf{h}}{\partial \mathbf{s}} \right)^{-1} : \left(\Delta t \frac{\partial \mathbf{h}}{\partial \mathbf{s}} + \frac{\partial \mathbf{h}}{\partial \dot{\sigma}} \right) \right], \quad (68)$$

\mathbf{J} being the fourth-order identity tensor. Finally, substituting equation (67) into (64) and solving for $\partial\sigma/\partial\epsilon$, we find

$$\mathcal{J} = \frac{\partial\sigma}{\partial\epsilon} = (\mathbf{J} + \mathbf{C}^e : \mathbf{D})^{-1} : \mathbf{C}^e = (\mathbf{C}^{e-1} + \mathbf{D})^{-1}. \quad (69)$$

6.3 The case of plane stress

In this section, we consider the case in which the fibers are all parallel to the $x_3 = 0$ plane (i.e., $\mathbf{n} = n_1\mathbf{e}_1 + n_2\mathbf{e}_2$) and the applied loads are such that $\sigma_{33} = \sigma_{31} = \sigma_{32} = 0$. The stress and strain tensors are now of the form

$$\sigma = \sigma_{\alpha\beta}\mathbf{e}_\alpha\mathbf{e}_\beta \quad \text{and} \quad \epsilon = \epsilon_{\alpha\beta}\mathbf{e}_\alpha\mathbf{e}_\beta + \epsilon_{33}\mathbf{e}_3\mathbf{e}_3, \quad (70)$$

where Greek subscripts range over the integers (1,2).

In such problems, one has to integrate the constitutive equations for given values of the in-plane components $\Delta\epsilon_{11}$, $\Delta\epsilon_{22}$, and $\Delta\epsilon_{12}$; the out-of-plane component $\Delta\epsilon_{33}$ is not defined kinematically, and its value is determined so that the condition $\sigma_{33} = 0$ is met. Therefore, some modifications to the method described in Section 6.1 are needed.

The total-strain increment is written as

$$\Delta\epsilon = \Delta\hat{\epsilon} + \Delta\epsilon_{33}\mathbf{e}_3\mathbf{e}_3, \quad (71)$$

where $\Delta\hat{\epsilon} = \Delta\epsilon_{\alpha\beta}\mathbf{e}_\alpha\mathbf{e}_\beta$ is the known part of $\Delta\epsilon$. The plane stress condition $\sigma_{33} = 0$ requires that

$$C_{33ij}^e(\Delta\epsilon_{ij} - \Delta\epsilon_{ij}^{cr}) = 0 \quad \text{or} \quad \Delta\epsilon_{33} = (C_{33ij}^e \Delta\epsilon_{ij}^{cr} - C_{33\alpha\beta}^e \Delta\epsilon_{\alpha\beta}) / C_{3333}^e. \quad (72)$$

Using the above expression for $\Delta\epsilon_{33}$ in the elasticity equation (55), we find

$$\sigma_{n+1} = \hat{\sigma}^e - \hat{C}^e : \Delta\epsilon^{cr}, \quad (73)$$

where

$$\hat{C}_{ijkl}^e = C_{ijkl}^e - C_{ij33}^e C_{33kl}^e / C_{3333}^e, \quad \text{and} \quad \hat{\sigma}^e = \sigma_n + \hat{C}^e : \Delta\hat{\epsilon} = \text{known}. \quad (74)$$

In deriving equation (73), we took into account that $\hat{C}_{ijkl}^e \Delta\epsilon_{kl}^{cr} = \hat{C}_{ij\alpha\beta}^e \Delta\epsilon_{\alpha\beta}^{cr}$, since $\Delta\epsilon_{3\alpha}^{cr} = 0$ and $\hat{C}_{ij33}^e = 0$.

The integration procedure becomes now identical to that described in Section 6.1, with C^e and σ^e replaced by \hat{C}^e and $\hat{\sigma}^e$.

7 An example: a plate with a hole

The model developed in Section 5 is implemented in the ABAQUS general-purpose finite element program (Hibbitt, 1984). This code provides a general interface so that a specific constitutive model can be introduced as a ‘user subroutine’. The constitutive equations are integrated by using the method presented in Section 6.

Figure 9 shows a schematic representation of a plate with a hole. The plate is reinforced by continuous aligned fibers in the x_2 direction. Let $2w$ and l be the width and length of the specimen, and $2a$ be the diameter of the hole; the geometry analyzed is such that $2w/l = 6/25$ and $a/w = 1/6$.

The matrix material is assumed to be a Ti-6Al-4V alloy and is reinforced by continuous aligned SiC fibers. The fiber volume fraction is 32%, i.e., $f = 0.32$. Typical values of the elastic constants for the matrix and the fibers are $E_m = 65$ GPa and $\nu_m = 0.30$ for Ti-6Al-4V at 600°C, and $E_f = 360$ GPa and $\nu_f = 0.19$ for SiC at 600°C. The values of the corresponding five effective elastic constants of the composite are calculated from the formulae provided in Section 5.1; the following values are found: $E_L = 160$ GPa, $\nu_T = 0.373$, $\nu_L = 0.259$, $G_T = 34.5$ GPa, and $G_L = 40$ GPa. The effective elastic constants of the composite are also determined from the solution of a series of unit cell problems with periodic boundary conditions; the values found are in very good agreement with those calculated from the formulae of Section 5.1. The creep constants of the matrix are $n = 3$ and $B = 4.125 \times 10^{-13}$ MPa $^{-n}$ s $^{-1}$.

A tensile stress $\sigma_{app}=250$ MPa is applied in the direction of the fibers. The thickness of the specimen is assumed to be small, so that plane stress conditions prevail. The load is applied at time $t = 0$, and is kept constant. The instantaneous response of the material is elastic and the elastic stress distribution provides the initial condition for the creep problem.

Due to the symmetries of the structure and the applied loads only one fourth of the plate is analyzed. The finite element mesh used in the calculations is shown in Fig. 10. Four-node isoparametric elements with 2×2 Gauss integrations are used. The analysis is carried out incrementally and the maximum size of the time increment is controlled by the formula in equation (62).

Figure 11 shows the variations of the axial stress σ_{22} and axial strain ϵ_{22} ahead of the hole along the cross-fiber direction at time $t = 0^+$, 1, 5, and 8 hours. The maximum values of axial stress and strain appear at the root of the hole (point A in Fig. 9). The same problem is analyzed in Part II, where the possibility fiber failure is examined; it is found that the composite loses its load carrying capacity first in the neighborhood of point A, and eventually fails along the minimum cross-section, as expected. Figure 12 shows contours of the axial stress σ_{22} at time $t = 0^+$, and 8 hours. Contours of the several transversely isotropic invariants of the total strain ϵ at time $t = 0^+$ and 8 hours, are shown in Figs. 13–16; the invariants plotted in these figures are (deBotton and Ponte Castañeda, 1993):

$$\epsilon_p = \frac{1}{2} \epsilon : \beta = \frac{1}{2} (\epsilon_{11} + \epsilon_{33}), \quad (75)$$

$$\epsilon_n = \epsilon : \mathbf{a} = \epsilon_{22}, \quad (76)$$

$$\gamma_p^2 = \frac{1}{2} (\epsilon : \beta) : (\epsilon : \beta) - \frac{1}{4} (\epsilon : \beta)^2 = \epsilon_{13}^2 + \frac{1}{4} (\epsilon_{11} - \epsilon_{33})^2, \quad (77)$$

$$\gamma_n^2 = \epsilon^2 : \mathbf{a} - (\epsilon : \mathbf{a})^2 = \epsilon_{12}^2 + \epsilon_{23}^2, \quad (78)$$

where $\mathbf{n} = \mathbf{e}_2$, $\beta = \mathbf{I} - \mathbf{nn} = \mathbf{e}_1\mathbf{e}_1 + \mathbf{e}_3\mathbf{e}_3$, and the Cartesian components refer to the coordinate system shown in Fig. 9. The axial strain ϵ_n and the transverse ‘dilatational’ strain ϵ_p attain their maximum values at point A. Figures 15 and 16 show that the longitudinal (γ_n) and transverse (γ_p) shear strains reach their maximum values on the surface of the hole; fiber debonding is to be expected in those locations.

Acknowledgments

Fruitful discussions with Professor R. M. McMeeking of the University of California, Santa Barbara are gratefully acknowledged. This research was supported by the Office of Naval Research contract N00014-92-J-1808 through sub-agreement KK3006 from the University of California, Santa Barbara. The ABAQUS finite element code was made available under academic license from Hibbitt, Karlsson and Sorensen, Inc., Providence, RI.

References

- [1] Aravas, N., Cheng, C. and Ponte Castañeda, P., ‘Steady state creep of fiber-reinforced composites: constitutive equations and computational issues’, *Int. J. Solids Struct.*, **32**, 2219–2244 (1995).
- [2] Bakhvalov, N. and Panasenko, G., *Homogenization: Averaging Processes in Periodic Media*. Kluwer Academic Publishers, Dordrecht, The Netherlands (1989).
- [3] Cheng, C., ‘Creep of fiber-reinforced metal-matrix composites’, Ph.D. Thesis, Department of Mechanical Engineering and Applied Mechanics, University of Pennsylvania (1996).

- [4] Christensen, R. M., *Mechanics of Composite Materials*. Wiley, New York (1979).
- [5] deBotton, G. and Ponte Castañeda, P., 'Elastoplastic constitutive relations for fiber-reinforced solids', *Int. J. Solids Struct.*, **30**, 1865–1890 (1993).
- [6] Goto, S. and McLean, M., 'Role of interfaces in creep of fibre-reinforced metal-matrix composites – I. Continuous fibers', *Acta Metall. Mater.*, **39**, 153–164 (1991a).
- [7] Goto, S. and McLean, M., 'Role of interfaces in creep of fibre-reinforced metal-matrix composites – II. Short fibers', *Acta Metall. Mater.*, **39**, 165–177 (1991b).
- [8] Hibbitt, H. D., 'ABAQUS/EPGEN — A general purpose finite element code with emphasis on nonlinear applications', *Nucl. Eng. Des.*, **77**, 271–297 (1984).
- [9] Johnson, A. F., 'Creep characterization of transversely-isotropic metallic materials', *J. Mech. Phys. Solids*, **25**, 117–126 (1977).
- [10] Kelly, A. and Street, N., 'Creep of discontinuous fibre composites II. Theory for the steady state', *Proc. Roy. Soc. Lond. A*, **328**, 283–293 (1972).
- [11] McLean, M., 'Creep deformation of metal-matrix composites', *Comp. Sci. Tech.*, **23**, 37–52 (1985).
- [12] McLean, M., 'Mechanisms and models of high temperature deformation of composites', *Mat. Res. Symp. Proc.*, **120**, 67–79 (1988).
- [13] McLean, M., 'Creep of metal matrix composites', *Materials and Engineering Design: The Next Decade* (ed. B. F. Dyson and D. R. Hayhurst), p. 287, Institute of Metals, London (1989).
- [14] McMeeking, R. M., 'Models for the creep of ceramic matrix composite materials', *High Temperature Mechanical Behavior of Ceramic Composites* (ed. S. V. Nair and K. Jakus), p. 409, Butterworth-Heinemann, Stoneham, Mass. (1993a).
- [15] McMeeking, R. M., 'Power law creep of a composite material containing discontinuous rigid aligned fibers', *Int. J. Solids Struct.*, **30**, 1807–1823 (1993b).
- [16] Mileiko, S. T., 'Steady state creep of a composite material with short fibres', *J. Mat. Sci.*, **5**, 254–261 (1970).
- [17] Ponte Castañeda, P., 'Exact second-order estimates for the effective mechanical properties of nonlinear composite materials', *J. Mech. Phys. Solids*, **44**, 827–862 (1996).
- [18] Sanchez Palencia, E., *Non-homogeneous media and vibration theory*, Lecture Notes in Physics, Vol. 127. Springer-Verlag, Berlin (1980).
- [19] Weber, C. H., Löfvander, J. P. A. and Evans, A. G., 'The creep behavior of CAS/Nicalon continuous-fiber composites', *Acta Metall. Mater.*, **41**, 2681–2690 (1993).

Figure captions

1. Representation of an arbitrary stress state.
2. Hexagonal array of fibers and the corresponding unit cell.
3. Finite element mesh used in the unit cell calculations.
4. Shear solution for $f = 0.32$ and $n = 3$.
5. Uniaxial tension solution for $\epsilon_0/\epsilon_c = 0.6$ and $n = 3$.
6. Uniaxial tension solution for $f = 0.32$, $n = 3$, $B = 4.125 \times 10^{-13} \text{ MPa}^{-n} \text{ s}^{-1}$, and $\sigma_n = 500 \text{ MPa}$.
7. Biaxial tension solution for $f = 0.32$, $n = 3$, $B = 4.125 \times 10^{-13} \text{ MPa}^{-n} \text{ s}^{-1}$, and $\sigma_p = 100 \text{ MPa}$.
8. Combination of axisymmetric and shear macroscopic loading for $f = 0.32$, $n = 3$, $B = 4.125 \times 10^{-13} \text{ MPa}^{-n} \text{ s}^{-1}$, and $\sigma_{11} = \sigma_{12} = 20 \text{ MPa}$, $\sigma_{33} = 500 \text{ MPa}$.
9. A plate with a hole. The fibers are in the x_2 coordinate direction.
10. Finite element mesh for the plate and detailed mesh near the hole.
11. Variations of the normalized axial stress $\sigma_{22}/\sigma_{\text{app}}$, and the axial strain ϵ_{22} along the cross-fiber direction at time $t = 0^+$, 1, 5 and 8 hours.
12. Contours of axial stress σ_{22} at time $t = 0^+$ and 8 hours.
13. Contours of strain invariant ϵ_n at time $t = 0^+$ and 8 hours.
14. Contours of strain invariant ϵ_p at time $t = 0^+$ and 8 hours.
15. Contours of strain invariant γ_n at time $t = 0^+$ and 8 hours.
16. Contours of strain invariant γ_p at time $t = 0^+$ and 8 hours.

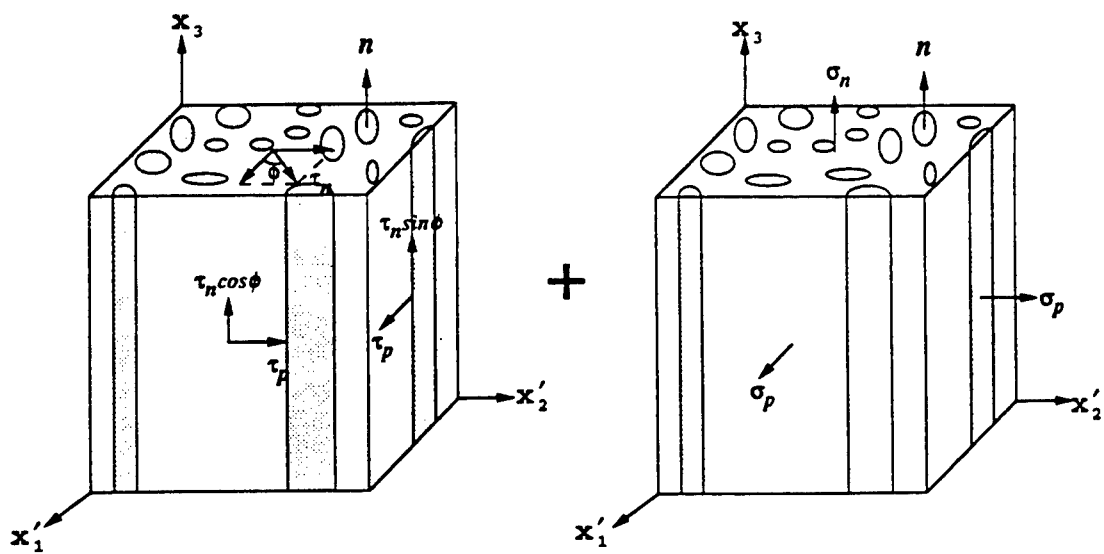


Figure 1

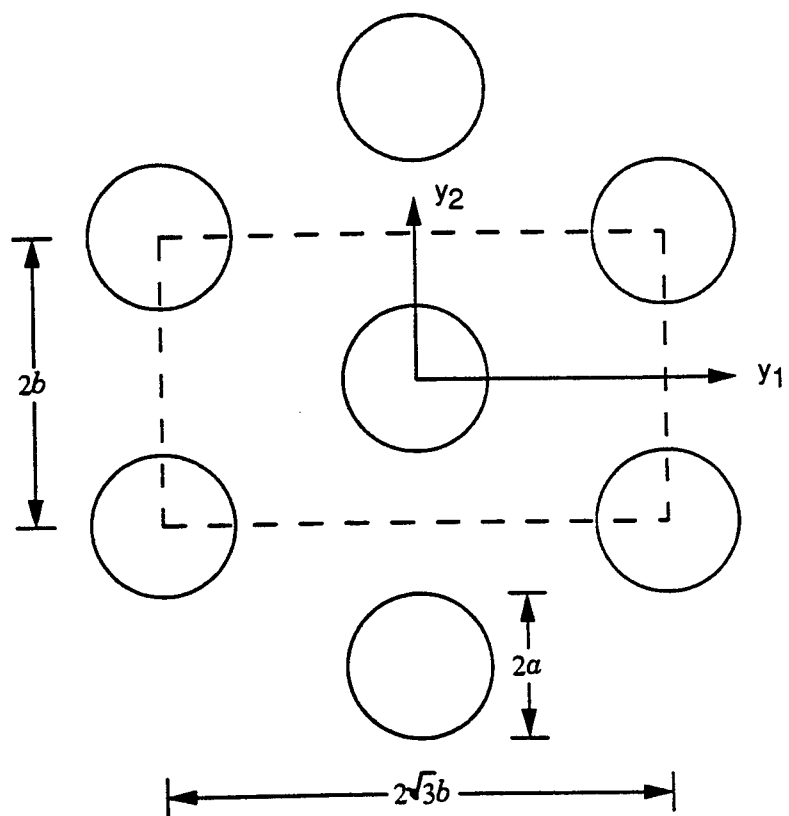


Figure 2

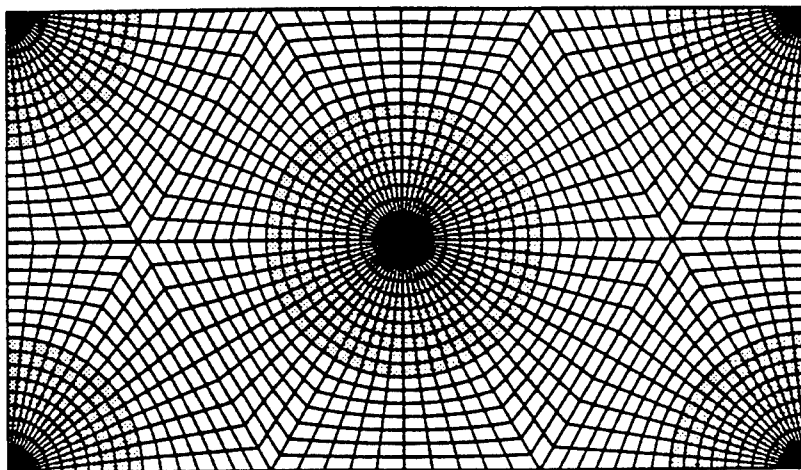


Figure 3

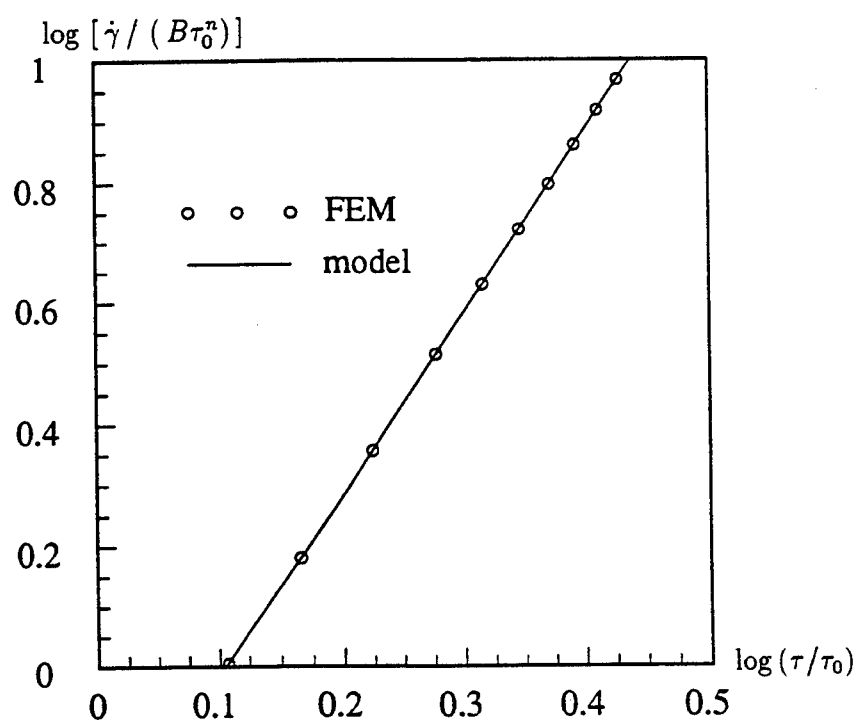


Figure 4

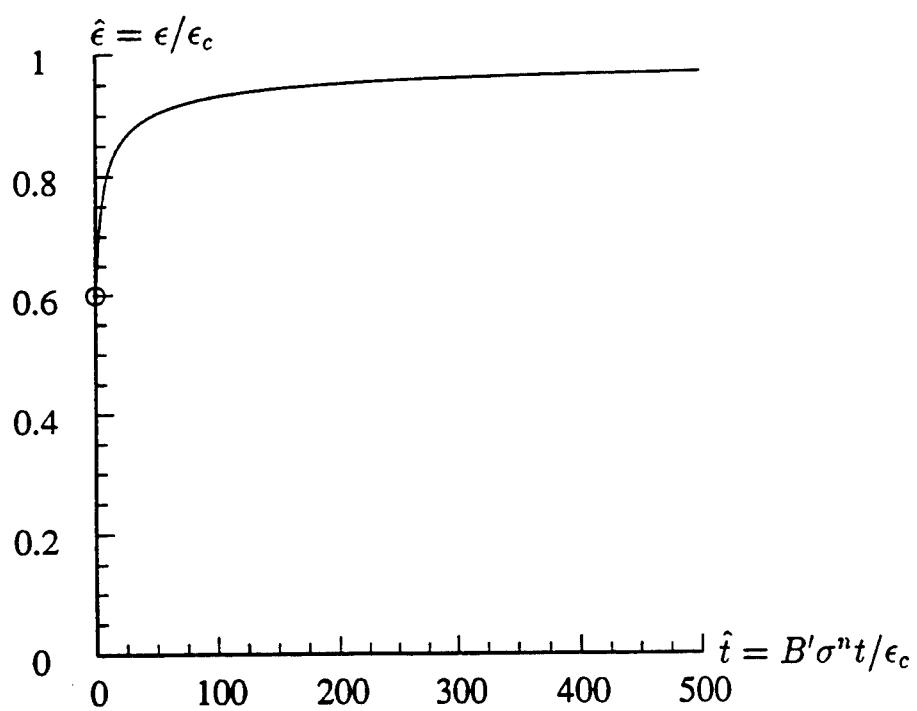


Figure 5

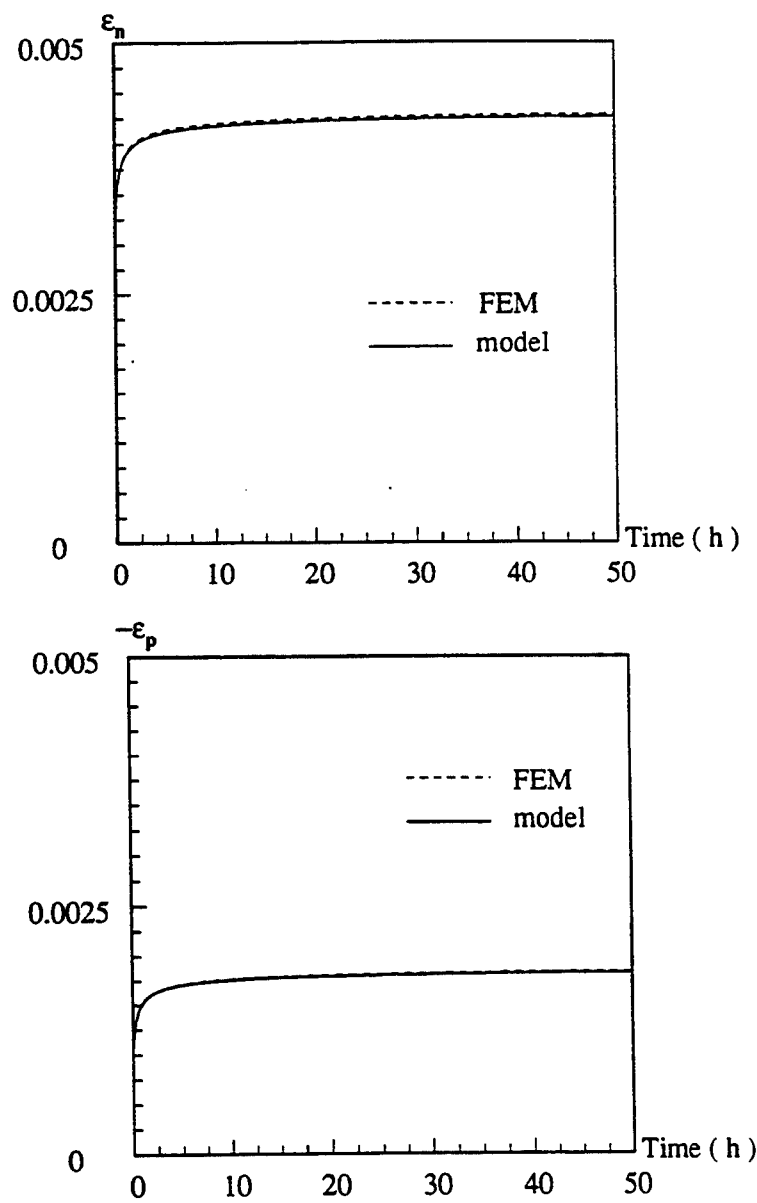


Figure 6

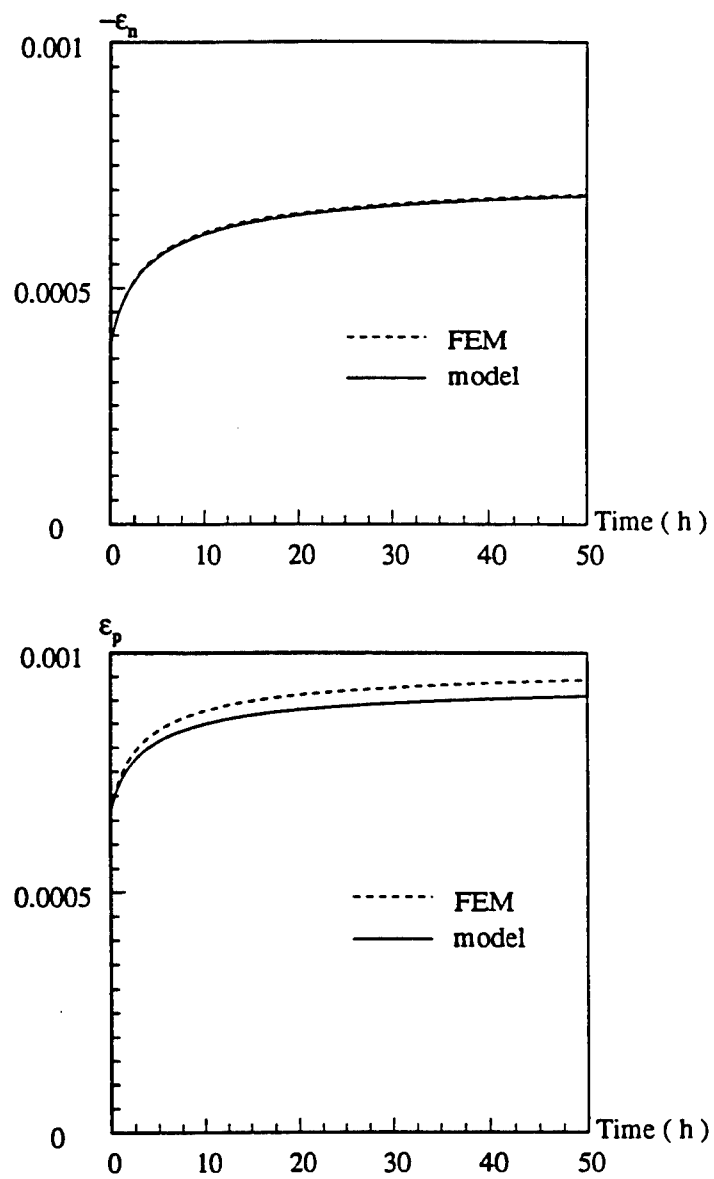


Figure 7

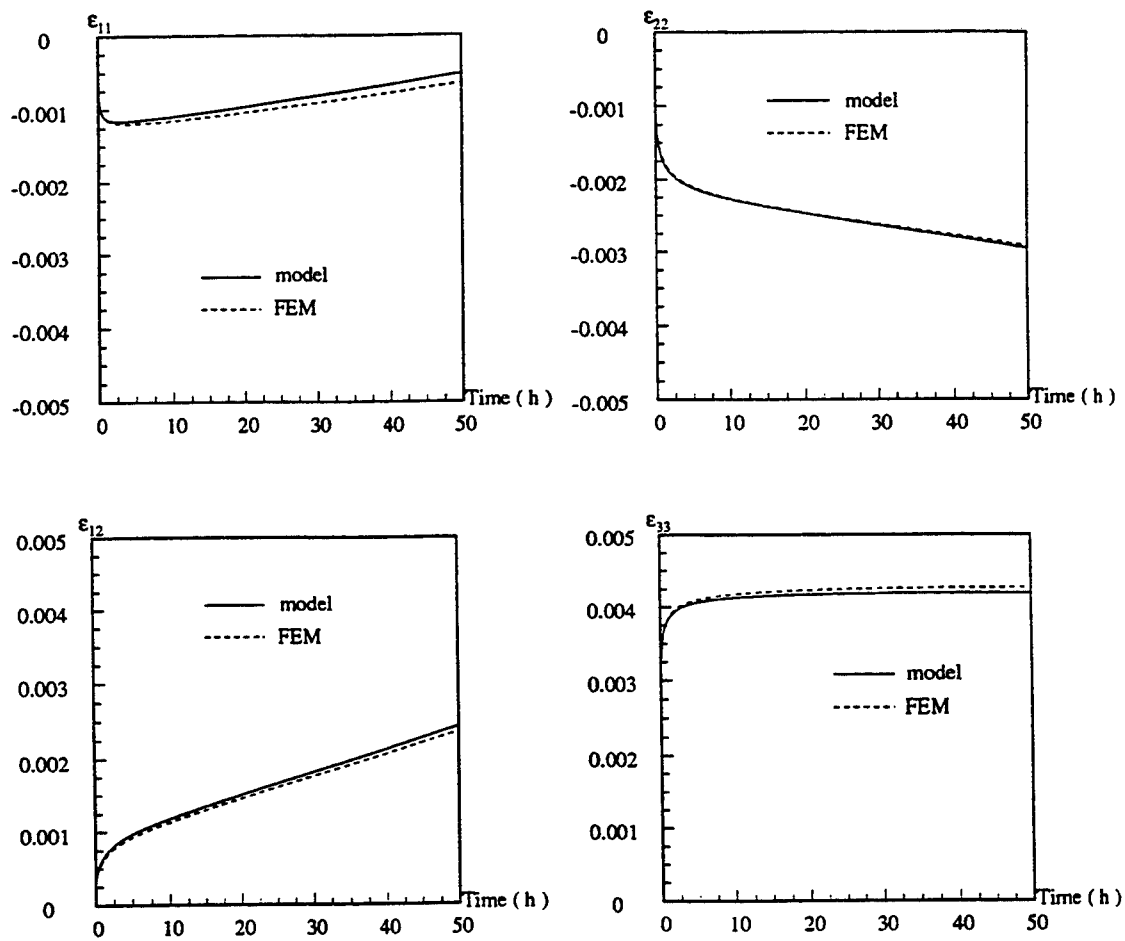


Figure 8

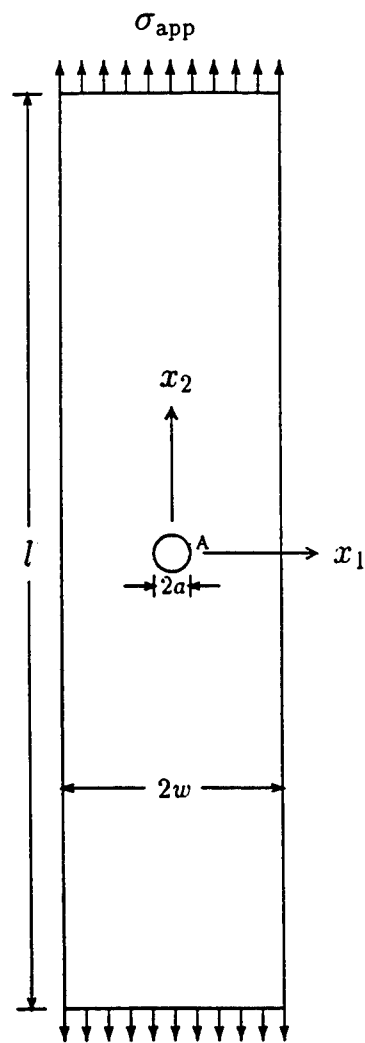


Figure 9

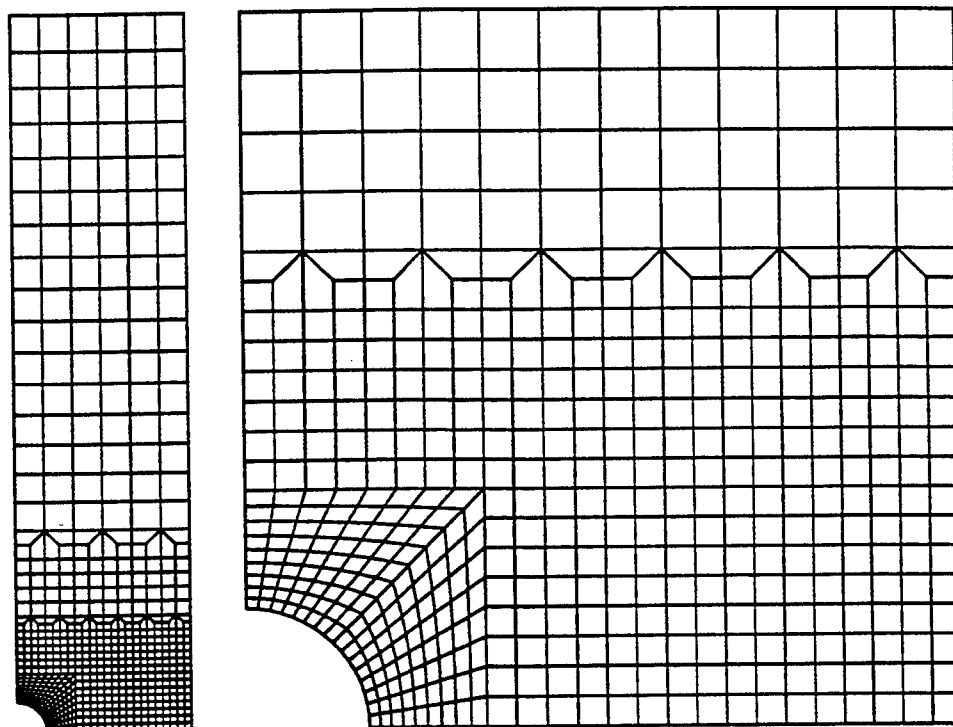


Figure 10

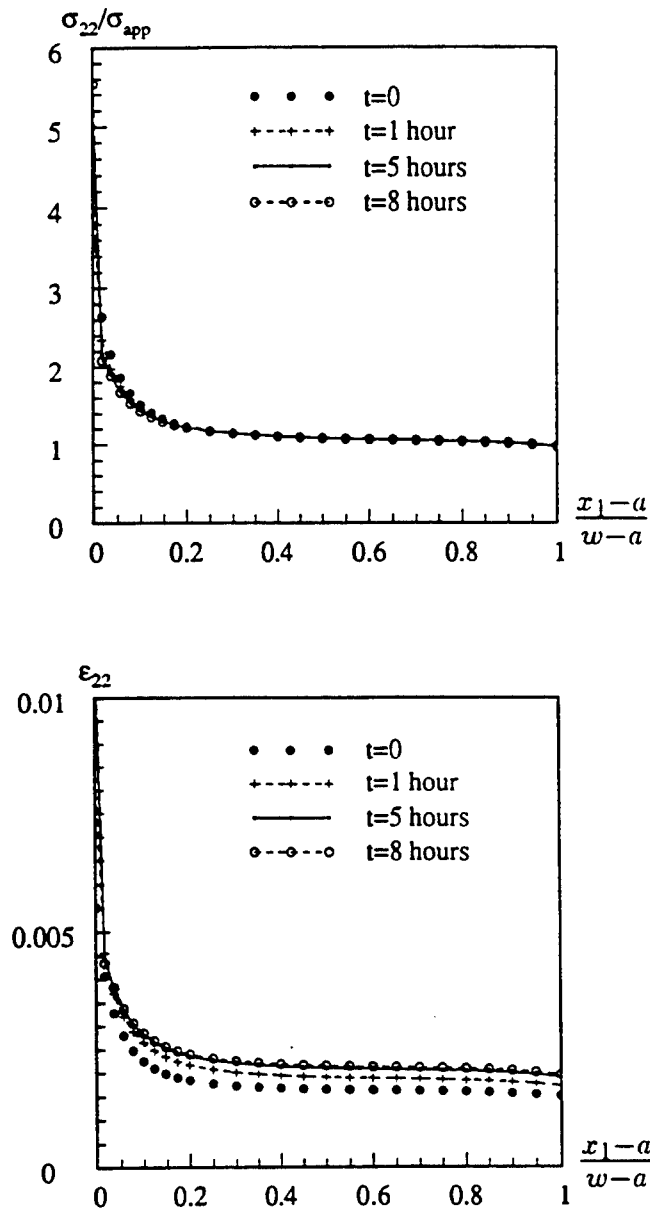
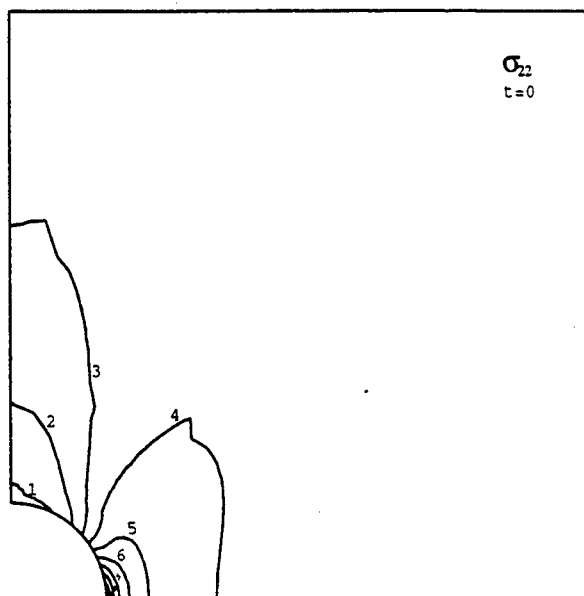


Figure 11

CONTOURS (MPa)

1	+0.00E-00
2	+1.00E+02
3	+2.00E+02
4	+3.00E+02
5	+4.00E+02
6	+5.00E+02
7	+6.00E+02
8	+7.00E+02
9	+8.00E+02
10	+9.00E+02
11	+1.00E+03



CONTOURS (MPa)

1	+0.00E-00
2	+1.00E+02
3	+2.00E+02
4	+3.00E+02
5	+4.00E+02
6	+5.00E+02
7	+6.00E+02
8	+7.00E+02
9	+8.00E+02
10	+9.00E+02
11	+1.00E+03

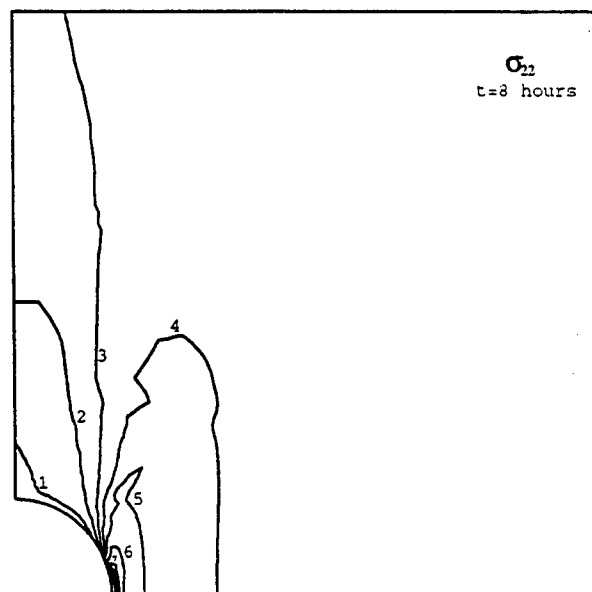
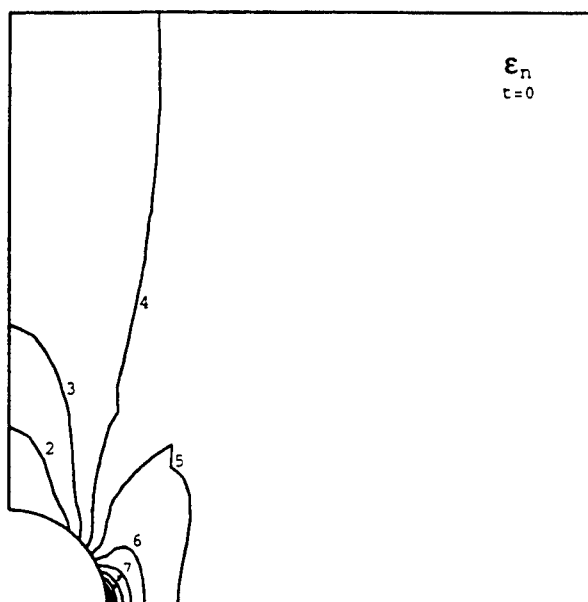


Figure 12

CONTOURS

1	+0.00E-00
2	+5.00E-04
3	+1.00E-03
4	+1.50E-03
5	+2.00E-03
6	+2.50E-03
7	+3.00E-03
8	+3.50E-03
9	+4.00E-03
10	+4.50E-03
11	+5.00E-03



CONTOURS

1	+0.00E-00
2	+5.00E-04
3	+1.00E-03
4	+1.50E-03
5	+2.00E-03
6	+2.50E-03
7	+3.00E-03
8	+3.50E-03
9	+4.00E-03
10	+4.50E-03
11	+5.00E-03

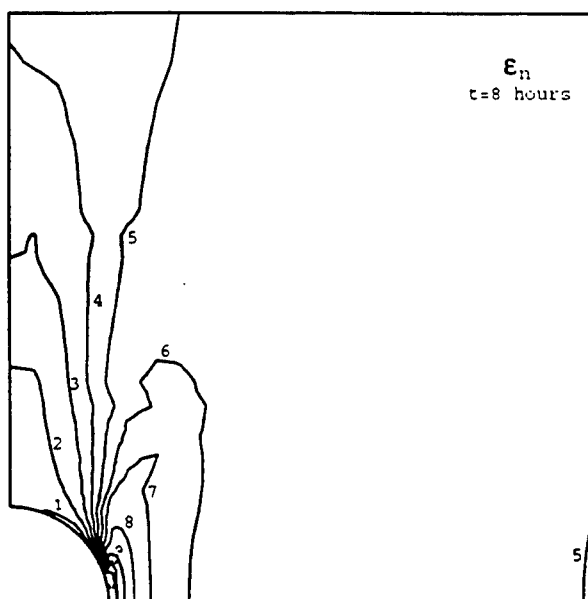
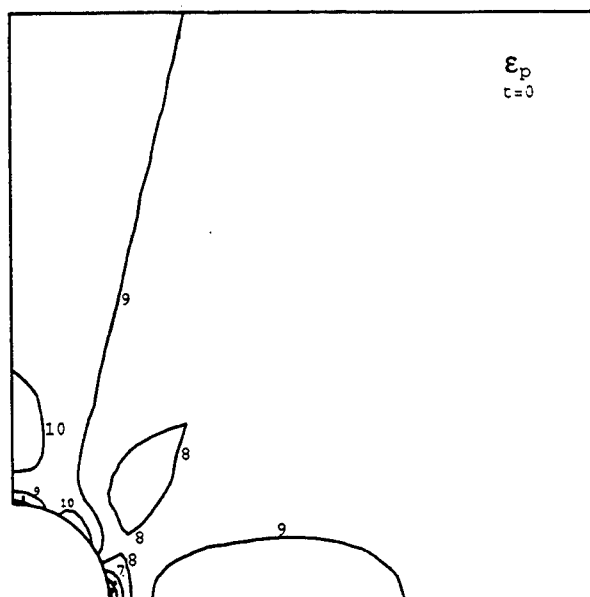


Figure 13

CONTOURS

1	-2.00E-03
2	-1.80E-03
3	-1.60E-03
4	-1.40E-03
5	-1.20E-03
6	-1.00E-03
7	-8.00E-04
8	-6.00E-04
9	-4.00E-04
10	-2.00E-04
11	+0.00E-00



CONTOURS

1	-2.00E-03
2	-1.80E-03
3	-1.60E-03
4	-1.40E-03
5	-1.20E-03
6	-1.00E-03
7	-8.00E-04
8	-6.00E-04
9	-4.00E-04
10	-2.00E-04
11	+0.00E-00

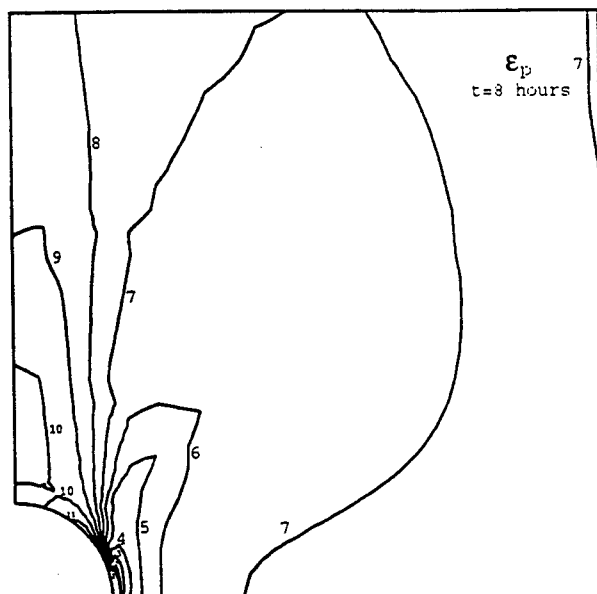
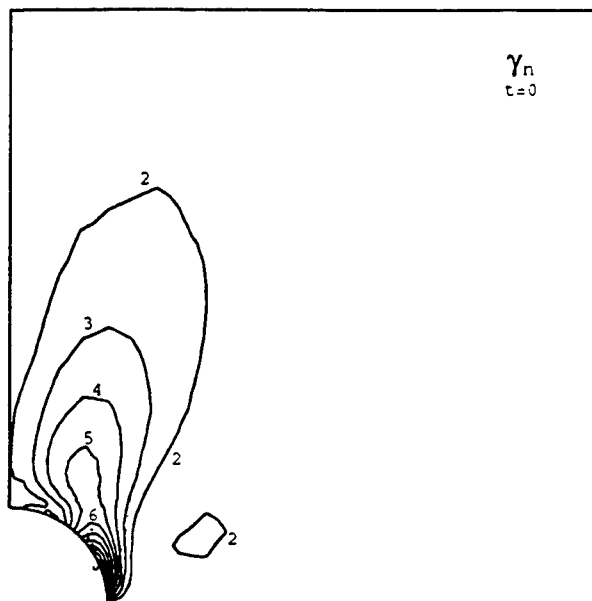


Figure 14

CONTOURS

1	+0.00E-00
2	+2.00E-04
3	+4.00E-04
4	+6.00E-04
5	+8.00E-04
6	+1.00E-03
7	+1.20E-03
8	+1.40E-03
9	+1.60E-03
10	+1.80E-03
11	+2.00E-03



CONTOURS

1	+0.00E-00
2	+5.00E-04
3	+1.00E-03
4	+1.50E-03
5	+2.00E-03
6	+2.50E-03
7	+3.00E-03
8	+3.50E-03
9	+4.00E-03
10	+4.50E-03
11	+5.00E-03

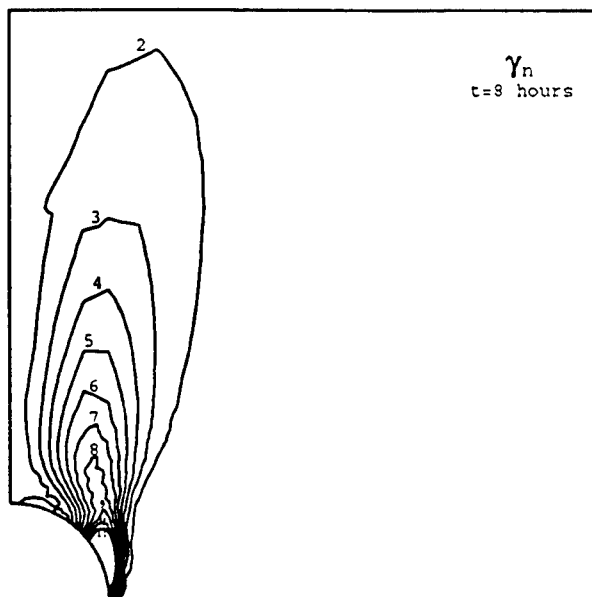
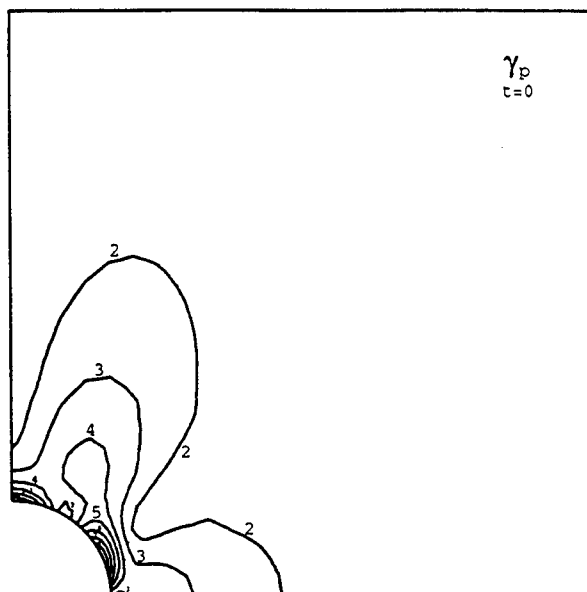


Figure 15

CONTOURS

1	+0.00E-00
2	+2.00E-04
3	+4.00E-04
4	+6.00E-04
5	+8.00E-04
6	+1.00E-03
7	+1.20E-03
8	+1.40E-03
9	+1.60E-03
10	+1.80E-03
11	+2.00E-03



CONTOURS

1	+0.00E-00
2	+5.00E-04
3	+1.00E-03
4	+1.50E-03
5	+2.00E-03
6	+2.50E-03
7	+3.00E-03
8	+3.50E-03
9	+4.00E-03
10	+4.50E-03
11	+5.00E-03

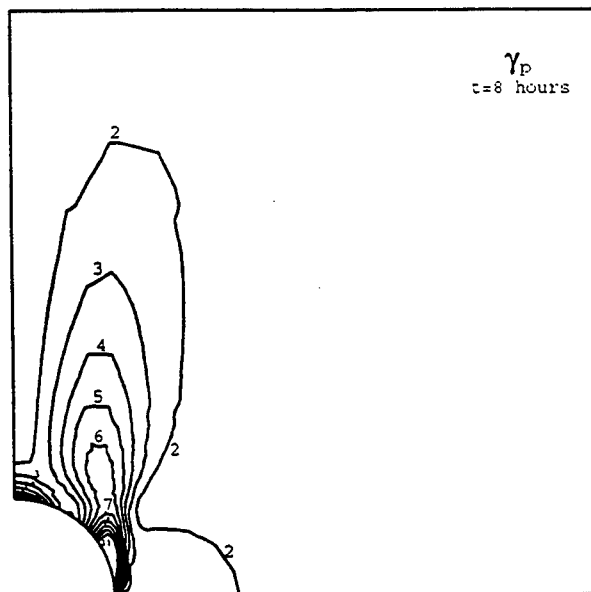


Figure 16

CREEP OF METAL-MATRIX COMPOSITES WITH ELASTIC FIBERS — PART II: A DAMAGE MODEL

Cao Cheng and N. Aravas

Department of Mechanical Engineering
and Applied Mechanics
University of Pennsylvania
Philadelphia, PA 19104
USA

Abstract

A constitutive model that accounts for the effects of fiber failure on the high temperature mechanical behavior of metal-matrix composites (MMC) reinforced by long brittle fibers is presented. Weibull statistics is used to describe the strength of the fibers and the assumption of 'global load sharing' is used to determine the average stress in the fibers. The developed three-dimensional constitutive model involves a 'damage parameter' that accounts for the accumulated fiber failure. A method for the numerical integration of the constitutive equations is developed. The proposed model is used together with the finite element method to predict the life of a plate with a hole loaded in tension in the direction of the fibers under creep conditions.

1 Introduction

A constitutive model for the mechanical behavior of metal-matrix composites reinforced by elastic fibers is presented in Part I. In developing that model, we assumed that the fibers remain intact as the composite deforms. However, it has been established that fibers in many composites experience strength degradation during deformation (Prewo, 1986; Thouless *et al.*, 1989). The effects of fiber failure on the creep behavior of metal-matrix composites are examined in detail in the present paper.

The material systems considered are the same as those of Part I. The response of the composite to shear loads relative to the fibers will be matrix-dominated, and fiber failure is not expected to affect significantly the performance of the composite under such loads. On the other hand, when axisymmetric loads are applied, fiber failure plays a very important role and can lead eventually to failure of the composite.

When a composite specimen is subjected to a uniaxial stress in the direction of the fibers, load is continuously transferred from the matrix to the fibers. When the applied stress is held constant and if the fibers remain intact, the corresponding axial strain rate decreases since the matrix stress relaxes due to matrix creep; as time progresses, the matrix is completely unloaded, the whole load is carried by the fibers, and the strain rate vanishes eventually. However, when fibers break, the fibers are locally unloaded, load is transferred back to the matrix, and the strain rate increases; this can cause, in turn, more fibers to break, and can lead eventually to failure of the composite component. A simple model that accounts for fiber breakage in a uniaxial tension test has been presented by McLean (1989). Theoretical studies on fiber failure stochastics within the framework of 'global load sharing', whereby the load shed from a broken fiber is shared nearly equally among all intact fibers, have been carried out by Curtin (1991) for composites with weak interfaces. More recently, Du and McMeeking (1995) made use of Curtin's results and studied in detail the effects of fiber breaks and the consequential stress relaxation in the broken fibers.

In this paper we study in detail the effects of fiber failure on the high temperature mechanical behavior of metal-matrix composites. In a way similar to that of Part I, a *three dimensional* constitutive model for the composite is developed in two steps: i) one in which shear loads relative to the fibers are applied, and ii) another in which the composite is subjected to axisymmetric loads relative to the fibers. For the case of the shear loads, it is assumed that equations (16)–(19) of Part I that describe the behavior of the composite under shear loads, are valid, even when the fibers fail. When axisymmetric loads are applied to the composite, Curtin's (1991) methodology is used to account for fiber failure. In fiber-reinforced metal-matrix composites, a weak fiber-matrix bond has been found to be essential to ensure good longitudinal strength (Jansson *et al.*, 1991). When a fiber breaks, the low shear strength of the interface diminishes any local stress concentrations, thus justifying the assumption of 'global load shearing'. The developed constitutive model involves a 'damage parameter' ω which takes values in the range $0 \leq \omega \leq 1$ and accounts for fiber failure. When $\omega = 0$, there is no fiber failure and the model reduces to that of Part I. Values of ω greater than zero account for the fact that, as fibers fail, the average stress in the unbroken fibers decreases, which in turn increases the stress carried by the matrix and

the corresponding creep strain rate. The limiting value $\omega = 1$ corresponds to the case where the local load-carrying capacity of the composite is reduced to zero and the corresponding strain rate becomes infinite. In deriving the model, we assumed that the fiber-matrix sliding stress is constant and ignored the effects of fiber relaxation near fiber breaks. A method for the numerical integration of the proposed model is presented and the developed constitutive equations are implemented in a general-purpose finite element program. The proposed constitutive equations are used together with the finite element method to study the evolution of damage in a plate with a hole loaded in tension in the direction of the fibers under creep conditions.

Standard notation identical to that of Part I is used in the present paper.

2 The fiber dominated behavior for axisymmetric loading with damage

2.1 McLean's model for uniaxial tension with damage

In Section 4.1 of Part I, we gave a detailed presentation of McLean's model for the case where the fibers remain *intact* while the composite deforms. For the case of uniaxial tension, McLean assumes that the axial strain in the matrix and the fibers equals the macroscopic axial strain ϵ , and that uniform stresses develop in the fibers and the matrix with the only non-zero components being $\sigma_{f33} = \sigma_f^{\text{un}}$ and $\sigma_{m33} = \sigma_m$. In the absence of any fiber failure, we have that

$$\sigma = f \sigma_f^{\text{un}} + (1 - f) \sigma_m \quad \text{and} \quad \dot{\epsilon} = \frac{\dot{\sigma}_f^{\text{un}}}{E_f} = \frac{\dot{\sigma}_m}{E_m} + B \sigma_m^n, \quad (1)$$

where $\sigma_f^{\text{un}} = E_f \epsilon$ is the stress in the unbroken fibers.

Curtin (1991) and Du and McMeeking (1995) used Weibull statistics to describe the strength of the fibers and carried out theoretical studies of fiber failure stochastics within the framework of global load sharing, for composites with weak interfaces. When the applied load in the direction of the fibers is such that the corresponding axial strain increases monotonically with time (i.e., no load reversals), they concluded that the average fiber stress $\bar{\sigma}_f$ is a nonlinear function of the macroscopic strain ϵ :

$$\bar{\sigma}_f = \left[1 - \frac{1}{2} \left(\frac{E_f \epsilon}{S_c} \right)^{m+1} \right] E_f \epsilon, \quad \text{where} \quad S_c = \left(\frac{2 S_0^m \tau_0 L_0}{D} \right)^{1/(m+1)}, \quad (2)$$

S_0 and L_0 are strength and length parameters of the Weibull distribution, m is the Weibull modulus, and τ_0 is the frictional sliding resistance between the fibers and the matrix. The derivation of equation (2a) can be found in Du and McMeeking (1995) (see their equation (10) on page 706) and will not be repeated here. Note that, if fiber failure is ignored, then

$$\bar{\sigma}_f = E_f \epsilon. \quad (3)$$

Equations (2a) and (3) make it clear that fiber failure reduces the stress carried by the fibers. The second term in the square brackets of equation (2a) can be viewed as a measure of the 'damage' in the composite; in fact, equation (2a) can be obtained from (3) if the elastic modulus E_f of the fibers is replaced by the secant modulus E_f^{sec} , i.e.,

$$\bar{\sigma}_f = E_f^{\text{sec}} \epsilon, \quad \text{where} \quad E_f^{\text{sec}} = \left[1 - \frac{1}{2} \left(\frac{E_f \epsilon}{S_c} \right)^{m+1} \right] E_f. \quad (4)$$

Using equation (2a) we can define the corresponding tangent modulus as

$$E_f^{\text{tan}} \equiv \frac{d\bar{\sigma}_f}{d\epsilon} = \left[1 - \frac{m+2}{2} \left(\frac{E_f \epsilon}{S_c} \right)^{m+1} \right] E_f. \quad (5)$$

Summarizing, we mention that, for the case of uniaxial tension with monotonically increasing ϵ , equations (1a,b) are replaced by

$$\sigma = f \bar{\sigma}_f + (1-f) \sigma_m \quad \text{and} \quad \dot{\epsilon} = \frac{\dot{\bar{\sigma}}_f}{E_f^{\text{tan}}} = \frac{\dot{\sigma}_m}{E_m} + B \sigma_m^n, \quad (6)$$

when fiber failure is taken into account.

Using the last two equations we can readily show that

$$\dot{\epsilon} = \frac{1}{1-\omega} \left[\frac{\dot{\sigma}}{E} + B' (\sigma - \alpha)^n \right] \quad \text{and} \quad \frac{\dot{\alpha}}{f E_f^{\text{tan}}} = \frac{1}{1-\omega} \left[\frac{\dot{\sigma}}{E} + B' (\sigma - \alpha)^n \right], \quad (7)$$

where ω is a 'damage parameter' defined as

$$\omega(\epsilon) = (m+2) \frac{f E_f}{2 E} \left(\frac{E_f \epsilon}{S_c} \right)^{m+1}, \quad (8)$$

the back stress α is defined as the part of the stress carried by the fibers, i.e., $\alpha = f \bar{\sigma}_f$, $E = f E_f + (1-f) E_m$, and $B' = B E_m / [(1-f)^{n-1} E]$. The damage parameter ω is proportional to the second term in the square brackets of equation (2a) and has been normalized in such a way that the strain rate $\dot{\epsilon}$ approaches infinity as $\omega \rightarrow 1$. When $\omega = 0$ (intact fibers), equations (7a,b) reduce to equations (24a,b) of Part I. A discussion of the physical meaning of ω is given in the Appendix.

The instantaneous response of the composite is elastic and the corresponding values of the strain, the back stress, and the damage parameter immediately after the application of the load are:

$$\epsilon_0 = \sigma(0^+)/E_0, \quad \alpha_0 = f E_{f0}^{\text{sec}} \epsilon_0, \quad \text{and} \quad \omega_0 = (m+2) \frac{f E_f}{2 E} \left(\frac{E_f \epsilon_0}{S_c} \right)^{m+1}, \quad (9)$$

where

$$E_0 = f E_{f0}^{\text{sec}} + (1-f) E_m \quad \text{and} \quad E_{f0}^{\text{sec}} = \left[1 - \frac{1}{2} \left(\frac{E_f \epsilon_0}{S_c} \right)^{m+1} \right] E_f. \quad (10)$$

Note that equation (9a) is a nonlinear equation that defines ϵ_0 . When the corresponding value of ω_0 is greater than one, then the composite fails instantaneously (see Appendix).

The response of the system as $\omega \rightarrow 1$ is such that

$$\epsilon \rightarrow \epsilon_{cr}, \quad \dot{\epsilon} \rightarrow \infty, \quad \alpha \rightarrow \alpha_{cr}, \quad \text{and} \quad \dot{\alpha} \rightarrow -\infty, \quad (11)$$

where

$$\epsilon_{cr} = \frac{S_c}{E_f} \left(\frac{2}{m+2} \frac{E}{f E_f} \right)^{1/(m+1)} \quad \text{and} \quad \alpha_{cr} = f E_f \left(1 - \frac{1}{m+2} \frac{E}{f E_f} \right) \epsilon_{cr}. \quad (12)$$

Equation (11d) shows that, at $\omega = 1$ the fibers are suddenly unloaded and the load is transferred instantaneously to the matrix.

We consider next the case of a 'creep test' in which a constant tensile stress σ is applied in the direction of the fibers. Equations (7) are integrated numerically and the evolution of the solution is determined until ω reaches the value of one. Figure 1 shows the temporal variation of ϵ , α , and ω for $E_f/E_m = 3$, $f = 0.35$, $n = 3$, $m = 5$, and $\sigma/S_c = 0.25$; the normalized quantities used in Fig. 1 are defined as

$$\hat{\epsilon} = \epsilon/\epsilon_{cr}, \quad \hat{\alpha} = \alpha/\alpha_{cr}, \quad \text{and} \quad \hat{t} = t B' E_f S_c^{n-1}. \quad (13)$$

We conclude this section with a discussion of the case where the applied uniaxial stress σ is such that the corresponding axial strain does not increase monotonically with time. In such a case, the fraction of broken fibers on any cross-section depends on both the current value of the applied stress σ and the maximum value of σ in the loading history of the specimen. Equation (2a) is now replaced by (Cheng, 1996)

$$\bar{\sigma}_f(\epsilon) = \left\{ 1 - \frac{\beta \sigma_f^{un}(\epsilon)}{2 S_c} \left[\frac{\sigma_f^{un \max}(\epsilon)}{S_c} \right]^m \right\} \sigma_f^{un}(\epsilon), \quad (14)$$

where $\sigma_f^{un}(\epsilon) = E_f \epsilon$, $\sigma_f^{un \max}(\epsilon)$ is the maximum tensile value of σ_f^{un} in the loading history of the specimen ($\sigma_f^{un \max} \geq 0$), and

$$\beta = \begin{cases} 1 & \text{if } \epsilon > 0, \\ 0 & \text{if } \epsilon \leq 0. \end{cases} \quad (15)$$

The conditions given in equation (15) above are based on the assumption that fiber breaks affect the material response in tension but have no effect when the specimen is loaded in compression along the fibers. The corresponding definitions of ω and E_f^{\tan} are

$$\omega(\epsilon) = (m+2) \frac{f E_f}{E} \frac{\beta \sigma_f^{un}(\epsilon)}{2 S_c} \left[\frac{\sigma_f^{un \max}(\epsilon)}{S_c} \right]^m, \quad (16)$$

and

$$E_f^{\tan} = \frac{d\bar{\sigma}_f}{d\epsilon} = \left(1 - \frac{\lambda m + 2}{m + 2} \frac{E}{f E_f} \omega \right) E_f. \quad (17)$$

Using the definition of ω , we can readily show that

$$\dot{\omega} = (\lambda m + 1) \omega \frac{\dot{\sigma}_f^{\text{un}}}{\sigma_f^{\text{un}}} \quad \text{where} \quad \lambda = \begin{cases} 1 & \text{if } \sigma_f^{\text{un}} = \sigma_{f \max}^{\text{un}} \text{ and } \dot{\epsilon} > 0, \\ 0 & \text{otherwise.} \end{cases} \quad (18)$$

In deriving equation (18a), we took into account that $\lambda \sigma_{f \max}^{\text{un}} = \lambda \sigma_f^{\text{un}}$. Finally, using the above results, we can show that the evolution equations for the axial strain and the back stress become

$$\dot{\epsilon} = \frac{\dot{\alpha}}{f E_f^{\text{tan}}} = \frac{\dot{\sigma}}{E_L} + \frac{B E_m}{(1-f)^{n-1} E_L} |\sigma - \alpha|^{n-1} (\sigma - \alpha), \quad (19)$$

where

$$E_L = f E_f^{\text{tan}} + (1-f) E_m = \left(1 - \frac{\lambda m + 2}{m + 2} \omega\right) E. \quad (20)$$

Note that, when $\epsilon > 0$, $\sigma_f^{\text{un}} \equiv E_f \epsilon = \sigma_{f \max}^{\text{un}}$ and $\dot{\epsilon} > 0$, then $\beta = \lambda = 1$, $E_L = (1 - \omega) E$ and equations (19) reduce to (7). Also, as the damage parameter ω approaches unity ($\omega \rightarrow 1$), $\lambda = 1$ and $E_L = (1 - \omega) E \rightarrow 0$, so that $\dot{\epsilon} \rightarrow \infty$.

2.2 A three-dimensional version of the McLean model with damage

Here, we proceed in a way similar to that used in Section 4.2 of Part I, where there was no damage. The applied macroscopic load is axisymmetric of the form shown in Fig. 1b of Part I, i.e., $\sigma_{1'1'} = \sigma_{2'2'} = \sigma_p$ and $\sigma_{33} = \sigma_n$. We assume again that the stresses in the fibers and the matrix are *uniform* and of the form

$$[\sigma_f] = \begin{bmatrix} \sigma_p & 0 & 0 \\ 0 & \sigma_p & 0 \\ 0 & 0 & \bar{\sigma}_f \end{bmatrix} \quad \text{and} \quad [\sigma_m] = \begin{bmatrix} \sigma_p & 0 & 0 \\ 0 & \sigma_p & 0 \\ 0 & 0 & \sigma_m \end{bmatrix}. \quad (21)$$

Using equation (5a) of Part I, we readily conclude that

$$\sigma_n = f \bar{\sigma}_f + (1-f) \sigma_m \quad \text{or} \quad \sigma_m = \frac{\sigma_n - \alpha}{1-f}, \quad (22)$$

where the back stress is defined again as $\alpha = f \bar{\sigma}_f$. It is also assumed that the corresponding axial strain component in the fibers and the matrix is equal to the axial macroscopic strain $\epsilon_{33} = \epsilon_n$, i.e.,

$$\epsilon_{f33} = \epsilon_{m33} = \epsilon_n. \quad (23)$$

Equation (5b) of Part I implies that

$$\begin{Bmatrix} \dot{\epsilon}_{11} \\ \dot{\epsilon}_{22} \\ \dot{\epsilon}_{33} \end{Bmatrix} = f \begin{Bmatrix} \dot{\epsilon}_{11}^f \\ \dot{\epsilon}_{22}^f \\ \dot{\epsilon}_{33}^f \end{Bmatrix} + (1-f) \begin{Bmatrix} \dot{\epsilon}_{11}^m \\ \dot{\epsilon}_{22}^m \\ \dot{\epsilon}_{33}^m \end{Bmatrix}. \quad (24)$$

The damage parameter ω is defined again as

$$\omega(\epsilon_n, \sigma_p) = (m+2) \frac{f E_f}{E} \frac{\beta \sigma_f^{\text{un}}(\epsilon_n, \sigma_p)}{2 S_c} \left[\frac{\sigma_f^{\text{un}} \max(\epsilon_n, \sigma_p)}{S_c} \right]^m, \quad (25)$$

so that

$$\dot{\omega} = (\lambda m + 1) \omega \frac{\dot{\sigma}_f^{\text{un}}}{\sigma_f^{\text{un}}}, \quad (26)$$

where now

$$\sigma_f^{\text{un}}(\epsilon_n, \sigma_p) = E_f \epsilon_n + 2 \nu_f \sigma_p, \quad (27)$$

and β and λ take the values of 1 or 0 according to equations (15) with $\epsilon = \epsilon_n$, and (18b) with σ_f^{un} defined by equation (27) above.

The average stress in the fibers is given by equation (14), which can be written as

$$\bar{\sigma}_f = (1 - c\omega) \sigma_f^{\text{un}} \quad \text{where} \quad c = \frac{1}{m+2} \frac{E}{f E_f}. \quad (28)$$

Using an argument similar to that used by Hild, Larsson and Leckie (1992), we readily conclude that the elastic constitutive equation for the damaged fibers can be written as

$$\begin{Bmatrix} \epsilon_{11}^f \\ \epsilon_{22}^f \\ \epsilon_{33}^f \end{Bmatrix} = \frac{1}{E_f} \begin{bmatrix} 1 & -\nu_f & -\nu_f \\ -\nu_f & 1 & -\nu_f \\ -\nu_f & -\nu_f & 1/(1-c\omega) \end{bmatrix} \begin{Bmatrix} \sigma_p \\ \sigma_p \\ \bar{\sigma}_f \end{Bmatrix}. \quad (29)$$

Since the damage parameter ω is a non-linear function of ϵ_n and σ_p (see equations (25) and (27) above), the last equation can be viewed as a non-linear transversely isotropic elastic constitutive equation that relates the average stress to the average strain in the fibers. Equation (24) now becomes

$$\begin{aligned} \begin{Bmatrix} \dot{\epsilon}_{11} \\ \dot{\epsilon}_{22} \\ \dot{\epsilon}_{33} \end{Bmatrix} &= \frac{f}{E_f} \begin{bmatrix} 1 & -\nu_f & -\nu_f \\ -\nu_f & 1 & -\nu_f \\ -\nu_f & -\nu_f & 1/(1-c\omega) \end{bmatrix} \begin{Bmatrix} \dot{\sigma}_p \\ \dot{\sigma}_p \\ \dot{\bar{\sigma}}_f \end{Bmatrix} + \\ &+ \frac{f}{E_f} \begin{bmatrix} 0 & 0 & 0 \\ 0 & 0 & 0 \\ 0 & 0 & c\dot{\omega}/(1-c\omega)^2 \end{bmatrix} \begin{Bmatrix} \sigma_p \\ \sigma_p \\ \bar{\sigma}_f \end{Bmatrix} + \\ &+ \frac{1-f}{E_m} \begin{bmatrix} 1 & -\nu_m & -\nu_m \\ -\nu_m & 1 & -\nu_m \\ -\nu_m & -\nu_m & 1 \end{bmatrix} \begin{Bmatrix} \dot{\sigma}_p \\ \dot{\sigma}_p \\ \dot{\sigma}_m \end{Bmatrix} + \\ &+ (1-f) \frac{B}{2} |\sigma_m - \sigma_p|^{n-1} (\sigma_m - \sigma_p) \begin{Bmatrix} -1 \\ -1 \\ 2 \end{Bmatrix}. \end{aligned} \quad (30)$$

Using a procedure similar to that of Part I, we substitute first the constitutive equations for the fibers and the matrix in the strain continuity equation $\dot{\epsilon}_{f33} = \dot{\epsilon}_{m33}$. Equations (22b),

(26) and (27) are used then to eliminate σ_m and $\dot{\omega}$, and the resulting equation is used to determine $\dot{\alpha}$ in terms of $\dot{\sigma}_n$, $\dot{\sigma}_p$, σ_n , σ_p , and α . Finally, substituting the expressions for $\dot{\alpha}$ into (30) and using (22b), (26) and (27) to eliminate σ_m and $\dot{\omega}$, we obtain the following equation for the macroscopic strain rates:

$$\begin{aligned} \begin{Bmatrix} \dot{\epsilon}_{11} \\ \dot{\epsilon}_{22} \\ \dot{\epsilon}_{33} \end{Bmatrix} &= \begin{bmatrix} 1/E_T & -\nu_T/E_T & -\nu_L/E_L \\ -\nu_T/E_T & 1/E_T & -\nu_L/E_L \\ -\nu_L/E_L & -\nu_L/E_L & 1/E_L \end{bmatrix} \begin{Bmatrix} \dot{\sigma}_p \\ \dot{\sigma}_p \\ \dot{\sigma}_n \end{Bmatrix} + \\ &+ \frac{3}{2} B (1-f) \left| \frac{\sigma_n - \alpha}{1-f} - \sigma_p \right|^{n-1} \left(\frac{\sigma_n - \alpha}{1-f} - \sigma_p \right) \begin{Bmatrix} K \\ K \\ L \end{Bmatrix}, \end{aligned} \quad (31)$$

where

$$E_L = f E_f^{\text{tan}} + (1-f) E_m, \quad \nu_L = f \tilde{\nu}_f + (1-f) \nu_m, \quad (32)$$

$$\frac{1}{E_T} = \frac{1-f}{E_m} + \frac{f}{E_f} + 2f(1-f) \frac{E_f^{\text{tan}}}{E_L} \left(\frac{E_m}{E_f} \nu_f - \nu_m \right) \left(\frac{\nu_m}{E_m} - \frac{\nu_f}{E_f} \right), \quad (33)$$

$$\frac{\nu_T}{E_T} = (1-f) \frac{\nu_m}{E_m} + f \frac{\nu_f}{E_f}, \quad (34)$$

$$E_f^{\text{tan}} = \left(1 - \frac{\lambda m + 2}{m + 2} \frac{E}{f E_f} \omega \right) E_f, \quad \tilde{\nu}_f = \left(1 - \frac{\lambda m + 2}{m + 2} \frac{E}{f E_f} \omega \right) \nu_f, \quad (35)$$

and

$$K = \frac{2}{3} \frac{E_m}{E_L} \left\{ -\frac{1}{2} + f \left[\frac{E_f^{\text{tan}}}{E_m} \left(\nu_m - \frac{1}{2} \right) - \left(\tilde{\nu}_f - \frac{1}{2} \right) \right] \right\}, \quad L = \frac{2}{3} \frac{E_m}{E_L}. \quad (36)$$

The evolution equation of the back stress ($\dot{\alpha} = f \dot{\sigma}_f$) is found to be

$$\frac{\dot{\alpha}}{f E_f^{\text{tan}}} = \frac{\dot{\sigma}_n}{E_L} + 2(1-f) \left(\frac{E_m}{E_f} \nu_f - \nu_m \right) \frac{\dot{\sigma}_p}{E_L} + \frac{B E_m (1-f)}{E_L} \left| \frac{\sigma_n - \alpha}{1-f} - \sigma_p \right|^{n-1} \left(\frac{\sigma_n - \alpha}{1-f} - \sigma_p \right). \quad (37)$$

3 A proposed new model

The results developed in the previous section are now incorporated in a three-dimensional constitutive model. As mentioned in the introduction, we assume that fiber failure does not affect significantly the response of the composite when shear loads relative to the fibers are applied, so that equations (16)–(19) of Part I can still be used for such types of loading.

The macroscopic response of the composite is assumed to be transversely isotropic, and the unit vector \mathbf{n} in the direction of the fibers is used to define the axis of rotational symmetry. The total strain in the composite is written as the sum of the elastic and creep parts:

$$\boldsymbol{\epsilon} = \boldsymbol{\epsilon}^e + \boldsymbol{\epsilon}^{\text{cr}}. \quad (38)$$

In the following, we discuss the constitutive equations for $\dot{\boldsymbol{\epsilon}}^e$ and $\dot{\boldsymbol{\epsilon}}^{\text{cr}}$ for the composite.

3.1 Elasticity

The elastic constitutive equation can be written in rate form as

$$\dot{\epsilon}^e = \mathbf{C}^e{}^{-1} : \dot{\sigma}, \quad (39)$$

where the fourth-order tangent elasticity tensor $\mathbf{C}^e(\omega, \lambda)$ for the homogenized transversely isotropic composite depends, in general, on the current value of the damage parameter ω and the direction of loading through λ .

When the fibers are aligned with the x_3 coordinate direction (i.e., $\mathbf{n} = \mathbf{e}_3$), equation (39) can be written in matrix form as follows

$$\{\dot{\epsilon}^e\} = [C^e]^{-1} \{\dot{\sigma}\}, \quad (40)$$

where $\{\dot{\epsilon}^e\} = \{\dot{\epsilon}_{11}^e, \dot{\epsilon}_{22}^e, \dot{\epsilon}_{33}^e, \dot{\gamma}_{12}^e, \dot{\gamma}_{13}^e, \dot{\gamma}_{23}^e\}$, $\{\dot{\sigma}\} = \{\dot{\sigma}_{11}, \dot{\sigma}_{22}, \dot{\sigma}_{33}, \dot{\sigma}_{12}, \dot{\sigma}_{13}, \dot{\sigma}_{23}\}$, and

$$[C^e]^{-1} = \begin{bmatrix} 1/E_T & -\nu_T/E_T & -\nu_L/E_L & 0 & 0 & 0 \\ -\nu_T/E_T & 1/E_T & -\nu_L/E_L & 0 & 0 & 0 \\ -\nu_L/E_L & -\nu_L/E_L & 1/E_L & 0 & 0 & 0 \\ 0 & 0 & 0 & 1/G_T & 0 & 0 \\ 0 & 0 & 0 & 0 & 1/G_L & 0 \\ 0 & 0 & 0 & 0 & 0 & 1/G_L \end{bmatrix},$$

where E_L , E_T , G_L , ν_L and ν_T are the five independent elastic moduli of the composite, and

$$G_T = \frac{E_T}{2(1 + \nu_T)}. \quad (41)$$

The moduli E_L , E_T , ν_L and ν_T are defined in equations (32)–(35); the shear modulus G_L is assumed to be independent of ω and is estimated by (Christensen, 1979, p. 84)

$$G_L = \frac{(1 + f) G_f + (1 - f) G_m}{(1 - f) G_f + (1 + f) G_m} G_m, \quad (42)$$

where G_m and G_f are the elastic shear moduli of the matrix and the fibers.

The constitutive equations developed here have a form similar to that of Part I. It should be emphasized though, that the effective elastic tangent moduli are now strong functions of the damage parameter ω . When $\omega = 0$, tangentthe above equations reduce to those presented in Part I; also, in the limit as $\omega \rightarrow 1$, the effective tangent modulus E_L approaches zero, and $\dot{\epsilon}^e$ becomes infinite.

3.2 Creep

The general form of the constitutive equations that account for fiber failure during creep is

$$\dot{\epsilon}^{cr} = \mathbf{g}(\boldsymbol{\sigma} - \boldsymbol{\alpha}, \omega, \lambda, s), \quad (43)$$

where α is the back stress tensor, ω is the damage tensor, \mathbf{g} is a tensor-valued isotropic functions, s is the collection of material parameters $s = \{E_f, \nu_f, E_m, \nu_m, B, n, f, S_c, m\}$.

In the present model, the back stress α and the damage tensor ω are assumed to be in the direction of \mathbf{n} , i.e., $\alpha = \alpha \mathbf{nn}$, $\omega = \omega \mathbf{nn}$; it should be noted, however, that more complicated forms may be necessary when effects such as fiber debonding must be accounted for.

In the following, we use the results of Section 3.3 of Part I for shear loads together with those of Section 2.2 in the present paper for axisymmetric loading and develop constitutive equations for general types of loading. These results are combined in a way similar to that used in Part I. With respect to the coordinate axes shown in Fig. 1 of Part I and for an arbitrary orientation of the x_1 - x_2 axes on the transverse plane, we write the following equations for the creep strain rate:

$$[\dot{\epsilon}^{\sigma}] = \frac{3}{2} B (1-f) \Sigma_e^{n-1} \begin{bmatrix} \chi(\sigma_{11} - \sigma_{22})/2 + K S & \chi \sigma_{12} & \chi \sigma_{13} \\ \chi \sigma_{12} & \chi(\sigma_{22} - \sigma_{11})/2 + K S & \chi \sigma_{23} \\ \chi \sigma_{13} & \chi \sigma_{23} & L S \end{bmatrix}, \quad (44)$$

where $\Sigma_e^2 = S^2 + (\chi \sigma_s)^2$. For convenience, we repeat the definition of the quantities entering the above equation: $\sigma_n = \sigma_{33}$, $\sigma_p = (\sigma_{11} + \sigma_{22})/2$,

$$S = \frac{\sigma_n - \alpha}{1-f} - \sigma_p, \quad \sigma_s^2 = \frac{3}{4}(\sigma_{11} - \sigma_{22})^2 + 3(\sigma_{12}^2 + \sigma_{13}^2 + \sigma_{23}^2). \quad (45)$$

The quantity $\chi(n, f)$ is given by equations (17)–(19) of Part I, and K and L are defined in equation (36) in the present paper.

The constitutive equations developed here have a form similar to that of Part I. It should be emphasized though, that K and L are now strong functions of the damage parameter ω . When $\omega = 0$, the above equations reduce to those presented in Part I; whereas, in the limit as $\omega \rightarrow 1$, the effective tangent modulus E_L approaches zero, and, as a consequence, K , L and $\dot{\epsilon}^{\sigma}$ become infinite.

3.3 The evolution of the back stress and the damage parameter

The general form of the constitutive equations for $\dot{\alpha}$ and $\dot{\omega}$ are

$$\dot{\alpha} = \mathbf{h}(\sigma - \alpha, \dot{\sigma}, \omega, \lambda, s), \quad \dot{\omega} = \mathbf{r}(\sigma, \epsilon, \text{history}, s), \quad (46)$$

where \mathbf{h} and \mathbf{r} are tensor-valued isotropic functions, and the argument ‘history’ in \mathbf{r} denotes dependence on the history of deformation.

As mentioned earlier, the back stress α and the damage tensor ω are assumed to be of the form $\alpha = \alpha \mathbf{nn}$, and $\omega = \omega \mathbf{nn}$.

The evolution of α is given by

$$\frac{\dot{\alpha}}{f E_f^{\text{tan}}} = \frac{\dot{\sigma}_n}{E_L} + 2(1-f) \left(\frac{E_m}{E_f} \nu_f - \nu_m \right) \frac{\dot{\sigma}_p}{E_L} + \frac{B E_m (1-f)}{E_L} \Sigma_e^{n-1} \left(\frac{\sigma_n - \alpha}{1-f} - \sigma_p \right), \quad (47)$$

where $\Sigma_e^2 = S^2 + (\chi \sigma_s)^2$.

The damage parameter ω is defined as

$$\omega(\epsilon_n, \sigma_p) = (m+2) \frac{f E_f}{E} \frac{\beta \sigma_f^{\text{un}}(\epsilon_n, \sigma_p)}{2 S_c} \left[\frac{\sigma_f^{\text{un}} \max(\epsilon_n, \sigma_p)}{S_c} \right]^m, \quad (48)$$

where

$$\sigma_f^{\text{un}}(\epsilon_n, \sigma_p) = E_f \epsilon_n + 2 \nu_f \sigma_p, \quad \text{and} \quad \beta = \begin{cases} 1 & \text{if } \epsilon_n > 0, \\ 0 & \text{if } \epsilon_n \leq 0. \end{cases} \quad (49)$$

The parameter λ that enters the expressions of E_f^{tan} and $\tilde{\nu}_f$ is defined as

$$\lambda = \begin{cases} 1 & \text{if } \sigma_f^{\text{un}} = \sigma_f^{\text{un}} \max \text{ and } \dot{\epsilon}_n > 0, \\ 0 & \text{otherwise.} \end{cases} \quad (50)$$

The instantaneous response of the composite to applied loads is ‘purely elastic’. The values of the strain $\epsilon_0 = \epsilon_0^e$, the back stress α_0 , and the damage parameter ω_0 immediately after the application of the load are determined from the integration of equations (39), (47), and the use of equation (48) respectively; these values are the three dimensional counterparts of the quantities in equation (9) for the case of uniaxial tension.

4 Finite element implementation of the constitutive model

In this section, we discuss the implementation of the general form of the constitutive model described in the previous section in a finite element program. In a finite element environment, the solution of the creep problem is developed incrementally and the constitutive equations are integrated at the element Gauss points. In a displacement based finite element formulation the solution is deformation driven. At a material point, the solution $(\sigma_n, \epsilon_n, \alpha_n, \omega_n)$ at time t_n as well as the strain ϵ_{n+1} at time $t_{n+1} = t_n + \Delta t$ are supposed to be known and one has to determine the solution $(\sigma_{n+1}, \alpha_{n+1}, \omega_{n+1})$.

4.1 Numerical integration of the constitutive equations

We use the backward Euler method to integrate the evolution equations for ϵ^e , ϵ^{cr} , and α . Starting with the elasticity equation (39) we write

$$\sigma_{n+1} = \sigma_n + \mathbf{C}^e(\omega_{n+1}, \lambda) : \Delta \epsilon^e = \sigma_n + \mathbf{C}^e(\omega_{n+1}, \lambda) : (\Delta \epsilon - \Delta \epsilon^{\text{cr}}), \quad (51)$$

where $\Delta \epsilon = \epsilon_{n+1} - \epsilon_n$ and $\Delta \epsilon^{\text{cr}} = \epsilon_{n+1}^{\text{cr}} - \epsilon_n^{\text{cr}}$ are the total- and creep-strain increments. The other constitutive equations are written as

$$\Delta \epsilon^{\text{cr}} = \mathbf{g}(\sigma_{n+1} - \alpha_{n+1}, \omega_{n+1}, \lambda) \Delta t, \quad (52)$$

$$\Delta \alpha = \mathbf{h}(\sigma_{n+1} - \alpha_{n+1}, \Delta \sigma / \Delta t, \omega_{n+1}, \lambda) \Delta t, \quad (53)$$

$$\omega_{n+1} = r(\sigma_{n+1}, \epsilon_{n+1}), \quad (54)$$

where $\Delta\sigma = \sigma_{n+1} - \sigma_n$. The value of λ for the increment is determined as described in the following. Let $\sigma_f^{\text{un}}_{\text{max}}$ be the maximum local non-negative value of σ_f^{un} in the history of deformation up to time t_n at the start of the increment. Then

$$\lambda = \begin{cases} 1 & \text{if } (\sigma_f^{\text{un}})_{n+1} > \sigma_f^{\text{un}}_{\text{max}}, \text{ and } \epsilon_{n+1} > \epsilon_n, \\ 0 & \text{otherwise} \end{cases} \quad (55)$$

where

$$(\sigma_f^{\text{un}})_{n+1} = E_f (\epsilon_n)_{n+1} + 2\nu_f (\sigma_p)_{n+1}, \quad (56)$$

$(\epsilon_n)_{n+1} = \mathbf{n} \cdot \epsilon_{n+1} \cdot \mathbf{n}$, $(\sigma_p)_{n+1} = (1/2) \sigma_{n+1} : (\mathbf{I} - \mathbf{nn})$, \mathbf{n} is the unit vector in the direction of the fibers, and \mathbf{I} is the second-order identity tensor. Also, the function $r(\sigma_{n+1}, \epsilon_{n+1})$ is defined as

$$r(\sigma_{n+1}, \epsilon_{n+1}) = (m+2) \frac{f E_f}{2 E} \frac{\beta (\sigma_f^{\text{un}})_{n+1}}{S_c} \left(\frac{\sigma_f^{\text{un}}_{\text{max}}}{S_c} \right)^m \quad (57)$$

where

$$\beta = \begin{cases} 1 & \text{if } (\epsilon_n)_{n+1} > 0, \\ 0 & \text{if } (\epsilon_n)_{n+1} \leq 0. \end{cases} \quad (58)$$

At the start of an increment the value of $(\sigma_p)_n$ is used in (56) instead of $(\sigma_p)_{n+1}$, and λ is set to either unity or zero according to (55). At the end of the integration the determined value of $(\sigma_p)_{n+1}$ is used in (56) in order to check the correctness of the used value for λ .

Summarizing, we write

$$\mathbf{G}(\Delta\epsilon^{\text{cr}}, \Delta\alpha, \omega_{n+1}) \equiv \Delta\epsilon^{\text{cr}} - \Delta t \mathbf{g}(\sigma_{n+1} - \alpha_n - \Delta\alpha, \omega_{n+1}, \lambda) = 0, \quad (59)$$

$$\mathbf{H}(\Delta\epsilon^{\text{cr}}, \Delta\alpha, \omega_{n+1}) \equiv \Delta\alpha - \Delta t \mathbf{h}\left(\sigma_{n+1} - \alpha_n - \Delta\alpha, \frac{\sigma_{n+1} - \sigma_n}{\Delta t}, \omega_{n+1}, \lambda\right) = 0, \quad (60)$$

$$R(\Delta\epsilon^{\text{cr}}, \Delta\alpha, \omega_{n+1}) \equiv \omega_{n+1} - r(\sigma_{n+1}, \epsilon_{n+1}) = 0, \quad (61)$$

where

$$\sigma_{n+1}(\Delta\epsilon^{\text{cr}}, \omega_{n+1}) = \sigma_n + \mathbf{C}^e(\omega_{n+1}, \lambda) : (\Delta\epsilon - \Delta\epsilon^{\text{cr}}). \quad (62)$$

We choose $\Delta\epsilon^{\text{cr}}$, $\Delta\alpha$, and ω_{n+1} as the primary unknowns and treat (59)–(61) as the basic equations in which σ_{n+1} is defined by (62). The solution is obtained by using Newton's method. The first estimates for $\Delta\epsilon^{\text{cr}}$ and $\Delta\alpha$ used to start the Newton loop are obtained by using a forward Euler scheme, i.e., $(\Delta\epsilon^{\text{cr}})_{\text{est}} = \mathbf{g}(\sigma_n - \alpha_n, \omega_n, \lambda_n) \Delta t$ and $(\Delta\alpha)_{\text{est}} = \mathbf{h}(\sigma_n - \alpha_n, \Delta\sigma_n/\Delta t, \omega_n, \lambda_n) \Delta t$, where $\Delta\sigma_n = \sigma_n - \sigma_{n-1}$; also the first estimate for ω_{n+1} is given by $(\omega)_{\text{est}} = r(\sigma_n, \epsilon_{n+1})$.

Once $\Delta\epsilon^{\text{cr}}$, $\Delta\alpha$, and ω_{n+1} are found, equation (62) defines the stress σ_{n+1} , $\alpha_{n+1} = \alpha_n + \Delta\alpha$, and this completes the integration procedure.

The case of plane stress is treated in a way similar to that described in Section 6.3 of Part I.

We conclude this section with a discussion of the numerical treatment of the limiting case $\omega = 1$. As ω approaches unity, the strain rate approaches infinity, thus introducing numerical difficulties. In our finite element calculations, the damage parameter ω was not permitted to grow beyond a critical value, say $\omega_{\text{cr}} = 0.99$. Once this critical value was reached at an

integration point, ω was kept equal to ω_{cr} and the corresponding back stress α was let to evolve until the value $\alpha = 0$, corresponding to complete fiber unloading, was reached; the calculations were continued beyond this point with $\omega = \omega_{cr}$ and $\alpha = 0$.

4.2 Linearization moduli

In an implicit finite element code, the overall discretized equilibrium equations are written at the end of the increment, resulting in a set of nonlinear equations for the nodal unknowns. If a full Newton scheme is used to solve the global nonlinear equations, one needs to calculate the so-called 'linearization moduli' \mathcal{J}

$$\mathcal{J} = \frac{\partial \sigma_{n+1}}{\partial \epsilon_{n+1}}. \quad (63)$$

For simplicity, we drop the subscript $(n+1)$ with the understanding that all quantities are evaluated at the end of the increment, unless otherwise indicated. Starting with the elasticity equation (51), we find

$$\partial \sigma = \frac{\partial C^e}{\partial \omega} : \Delta \epsilon^e \partial \omega + C^e : (\partial \epsilon - \partial \epsilon^{cr}), \quad (64)$$

where $\Delta \epsilon^e = \epsilon_{n+1}^e - \epsilon_n^e$. The differentials $\partial \epsilon^{cr}$, $\partial \alpha$ and $\partial \omega$ are evaluated from equations (52)–(54) as follows:

$$\partial \epsilon^{cr} = \Delta t \left[\frac{\partial g}{\partial s} : (\partial \sigma - \partial \alpha) + \frac{\partial g}{\partial \omega} \partial \omega \right], \quad (65)$$

$$\partial \alpha = \Delta t \left[\frac{\partial h}{\partial s} : (\partial \sigma - \partial \alpha) + \frac{1}{\Delta t} \frac{\partial h}{\partial \dot{\sigma}} : \partial \sigma + \frac{\partial h}{\partial \omega} \partial \omega \right], \quad (66)$$

$$\partial \omega = \frac{\partial r}{\partial \sigma} : \partial \sigma + \frac{\partial r}{\partial \epsilon} : \partial \epsilon, \quad (67)$$

where $s = \sigma - \alpha$. Using (67) to define $\partial \omega$, we can solve (65) and (66) for $\partial \alpha$ and $\partial \epsilon^{cr}$ to find

$$\partial \alpha = \mathbf{A} : \partial \sigma + \mathbf{B} : \partial \epsilon, \quad (68)$$

$$\partial \epsilon^{cr} = \mathbf{D} : \partial \sigma + \mathbf{E} : \partial \epsilon, \quad (69)$$

where

$$\mathbf{A} = \Delta t \left(\mathbf{J} + \Delta t \frac{\partial h}{\partial s} \right)^{-1} : \left(\frac{\partial h}{\partial s} + \frac{1}{\Delta t} \frac{\partial h}{\partial \dot{\sigma}} + \frac{\partial h}{\partial \omega} \frac{\partial r}{\partial \sigma} \right), \quad (70)$$

$$\mathbf{B} = \Delta t \left(\mathbf{J} + \Delta t \frac{\partial h}{\partial s} \right)^{-1} : \frac{\partial h}{\partial \omega} \frac{\partial r}{\partial \epsilon}, \quad (71)$$

$$\mathbf{D} = \Delta t \left[\frac{\partial g}{\partial s} : (\mathbf{J} - \mathbf{A}) + \frac{\partial g}{\partial \omega} \frac{\partial r}{\partial \sigma} \right], \quad \mathbf{E} = \Delta t \left(-\frac{\partial g}{\partial s} : \mathbf{B} + \frac{\partial g}{\partial \omega} \frac{\partial r}{\partial \epsilon} \right), \quad (72)$$

\mathbf{J} being the fourth-order identity tensor.

Finally, substituting the expression for $\partial\epsilon^{\sigma\tau}$ into (64) and solving for $\partial\sigma/\partial\epsilon$, we find

$$\mathcal{J} = \left(\mathbf{J} + \mathbf{C}^e : \mathbf{D} - \frac{\partial \mathbf{C}^e}{\partial \omega} : \Delta \epsilon^e \frac{\partial \tau}{\partial \sigma} \right)^{-1} : \left(\mathbf{C}^e - \mathbf{C}^e : \mathbf{E} + \frac{\partial \mathbf{C}^e}{\partial \omega} : \Delta \epsilon^e \frac{\partial \tau}{\partial \epsilon} \right). \quad (73)$$

5 An example: a plate with a hole

The model developed in Section 3 is implemented in the ABAQUS general-purpose finite element program (Hibbitt, 1984). The constitutive equations are integrated by using the method presented in Section 4.

The problem of a plate with a hole discussed in Section 7 of Part I is analyzed again, using the new constitutive model that accounts for fiber failure. The same geometry, material properties, and finite element mesh are used. The fiber diameter is assumed to be $D = 100 \mu\text{m}$. The Weibull modulus of the fibers is $m = 5$, and the gauge strength is $S_0 = 1.29 \text{ GPa}$ for a gauge length $L_0 = 1 \text{ m}$ at 600°C . The interface sliding stress τ_0 is sensitive to temperature, decreasing from about 120 MPa at ambient temperature to about 20 MPa at 600°C . The value of $\tau_0 = 20 \text{ MPa}$ at 600°C is used in the calculations. Using equation (2b), we find the characteristic stress for this fibrous system to be $S_c = 3.36 \text{ GPa}$ at 600°C . The critical value of the damage parameter used in the calculation is $\omega_{\text{cr}} = 0.99$.

Plane stress conditions are assumed, and a constant tensile stress of $\sigma_{\text{app}} = 250 \text{ MPa}$ is applied in the direction of the fibers. The load is increased linearly with time to its final value of 250 MPa in 20 seconds and is then kept constant. Again, due to the symmetries of the structure and the applied loads, we only consider a quarter of the plate. Four-node isoparametric elements with 2×2 Gauss integrations are used in the calculations.

Figure 2 shows the variations of the axial stress σ_{22} , the axial strain ϵ_{22} , and the damage parameter ω ahead of the hole along the x_1 -axis at time $t = 20$ seconds, 1, 5, and 8 hours. The stress concentration factor at the root of the hole just after the load is fully applied ($t = 20 \text{ s}$) is about 3.5, corresponding to a local tensile stress of about 875 MPa. The value of the damage parameter ω at the root of the hole is about 0.10 at that instant. As discussed in the Appendix, the elastic strength of the composite is about 1090 MPa. The damage parameter ω increases with time at the root of the hole and eventually causes local failure. The curves shown in Fig. 2 make it clear that a crack like defect is formed at the root of the hole and propagates along the x_1 -axis. The stress is relaxed in the fully damaged region due to fiber unloading; the small non-zero value of stress carried by the damaged region as shown in Fig. 2a, is due to the fact that the damage parameter is not let to grow beyond the critical value of $\omega_{\text{cr}} = 0.99$.

Figure 3 shows contours of the axial stress at time $t = 20$ seconds and 8 hours. The stress concentration moves with the ‘crack tip’ of the aforementioned defect. Figure 4 shows contours of the damage parameter ω at time $t = 8$ hours. The extent of ‘crack propagation’ is evident in that figure.

Acknowledgments

This research was supported by the Office of Naval Research contract N00014-92-J-1808 through sub-agreement KK3006 from the University of California, Santa Barbara. The ABAQUS finite element code was made available under academic license from Hibbitt, Karlsson and Sorensen, Inc., Providence, RI.

References

- [1] Aravas, N., Cheng, C. and Ponte Castañeda, P., 'Steady state creep of fiber-reinforced composites: constitutive equations and computational issues', *Int. J. Solids Struct.*, **32**, 2219-2244 (1995).
- [2] Cheng, C., 'Creep of fiber-reinforced metal-matrix composites', Ph.D. Thesis, Department of Mechanical Engineering and Applied Mechanics, University of Pennsylvania (1996).
- [3] Christensen, R. M., *Mechanics of Composite Materials*. Wiley, New York (1979).
- [4] Curtin, W. A., 'Theory of mechanical properties of ceramic matrix composites', *J. Am. Ceramic Soc.*, **74**, 2837 (1991).
- [5] Du, Z.-Z. and McMeeking, R. M., 'Creep models for metal-matrix composites with long brittle fibers', *J. Mech. Phys. Solids*, **43**, 701-726 (1995).
- [6] Hibbitt, H. D., 'ABAQUS/EPGEN — A general purpose finite element code with emphasis on nonlinear applications', *Nucl. Eng. Des.*, **77**, 271-297 (1984).
- [7] Hild, F., Larsson, P.-L. and Leckie, F. A., 'Localization due to damage in fiber-reinforced composites', *Int. J. Solids Struct.*, **29**, 3221-3238 (1992).
- [8] Jansson, S., Deve, H. E. and Evans A. G., 'The anisotropic mechanical properties of a Ti matrix composite reinforced with SiC fibers', *Metal. Trans.*, **22a**, 2975-2984 (1991).
- [9] McLean, M., 'Creep deformation of metal-matrix composites', *Comp. Sci. Tech.*, **23**, 37-52 (1985).
- [10] McLean, M., 'Mechanisms and models of high temperature deformation of composites', *Mat. Res. Symp. Proc.*, **120**, 67-79 (1988).
- [11] McLean, M., 'Creep of metal-matrix composites', *Materials and Engineering Design: The Next Decade* (ed. B. F. Dyson and D. R. Hayhurst), p. 287. Institute of Metals, London (1989).
- [12] Prewo, K., 'Tension and flexural strength of silicon carbide fiber-reinforced glass ceramics', *J. Mater. Sci.*, **21**, 3590-3600 (1986).

- [13] Thouless, M. D., Sbaizero, O., Sigl, L. S. and Evans, A. G., 'Effect of interface mechanical properties on pullout in a SiC-reinforced lithium aluminum silicate glass-ceramics', *J. Am. Ceram. Soc.*, **72**, 525-532 (1989).
- [14] Weber, C. H., Du, Z.-Z. and Zok, F. W., 'High temperature deformation and fracture of a fiber reinforced Titanium matrix composite', *Acta Metall. Mater.*, **44**, 683-695 (1996).

Appendix: The damage parameter ω

The physical meaning of the damage parameter ω is discussed in this section. The response of the composite is assumed to be purely elastic, i.e., both the fibers and the matrix can deform only elastically. For simplicity, we consider uniaxial loading in the direction of the fibers with a monotonically increasing axial strain ϵ .

Using the McLean assumptions, we can write

$$\sigma = f \bar{\sigma}_f + (1 - f) \sigma_m \quad \text{and} \quad \epsilon = \frac{\bar{\sigma}_f}{E_f^{\text{sec}}} = \frac{\sigma_m}{E_m}. \quad (74)$$

Equations (74b) can be written as

$$\bar{\sigma}_f = \left[1 - \frac{1}{2} \left(\frac{E_f \epsilon}{S_c} \right)^{m+1} \right] E_f \epsilon \quad \text{and} \quad \sigma_m = E_m \epsilon. \quad (75)$$

Using equation (74a), we find that the uniaxial stress-strain relationship of the composite is given by

$$\sigma = \left[1 - \frac{f E_f}{2 E} \left(\frac{E_f \epsilon}{S_c} \right)^{m+1} \right] E \epsilon, \quad (76)$$

where $E = f E_f + (1 - f) E_m$. Recalling the definition of ω :

$$\omega = (m + 2) \frac{f E_f}{2 E} \left(\frac{E_f \epsilon}{S_c} \right)^{m+1}, \quad (77)$$

we can readily show that

$$\sigma = \left(1 - \frac{\omega}{m + 2} \right) E \epsilon \quad \text{and} \quad \bar{\sigma}_f = \left(1 - \frac{E}{f E_f} \frac{\omega}{m + 2} \right) E_f \epsilon, \quad (78)$$

so that

$$\frac{d\sigma}{d\epsilon} = (1 - \omega) E \quad \text{and} \quad \frac{d\bar{\sigma}_f}{d\epsilon} = \left(1 - \frac{E}{f E_f} \omega \right) E_f. \quad (79)$$

The σ - ϵ and $\bar{\sigma}_f$ - ϵ curves have a maximum at

$$\omega = 1 \quad \text{and} \quad \omega = \frac{f E_f}{E} < 1, \quad (80)$$

respectively. The corresponding maximum stress values are

$$\sigma_{\max} = \frac{m + 1}{m + 2} \left(\frac{2}{m + 2} \frac{E}{f E_f} \right)^{1/(m+1)} \frac{E}{E_f} S_c, \quad \text{and} \quad \bar{\sigma}_{f\max} = \frac{m + 1}{m + 2} \left(\frac{2}{m + 2} \right)^{1/(m+1)} S_c, \quad (81)$$

and occur at strains

$$\epsilon_{\max} = \left(\frac{2}{m+2} \frac{E}{f E_f} \right)^{1/(m+1)} \frac{S_c}{E_f}, \quad \text{and} \quad \epsilon_{f\max} = \left(\frac{2}{m+2} \right)^{1/(m+1)} \frac{S_c}{E_f} < \epsilon_{\max}, \quad (82)$$

respectively.

Equation (80a) makes it clear that, when the response of the composite is purely elastic, the value $\omega = 1$ coincides with the point of instability on the σ - ϵ curve.

Figure 5 shows the variations of σ , $\alpha = f \bar{\sigma}_f$, σ_m , and ω with strain ϵ , for $E_f/E_m = 360/65$, $f = 0.32$, and $m = 5$; the points of maximum stress are marked on the σ and α curves.

For the material system used in the finite element calculations of Section 5 ($E_f = 360$ GPa, $E_m = 65$ GPa, $f = 0.32$, $m = 5$, $S_0 = 1.29$ GPa, $L_0 = 1$ m, $\tau_0 = 20$ MPa, $D = 100$ μm), we have $S_c = 3.36$ GPa, and the maximum stresses

$$\sigma_{\max} = 1.09 \text{ GPa} \quad \text{and} \quad \bar{\sigma}_{f\max} = 2.34 \text{ GPa}, \quad (83)$$

occur at

$$\epsilon_{\max} = 0.0080 \quad \text{and} \quad \epsilon_{f\max} = 0.0076, \quad (84)$$

respectively.

Figure captions

1. Temporal variations of the strain ϵ , the damage parameter ω , and the back stress α for uniaxial tension test with values of $E_f/E_m = 3$, $f = 35\%$, $n = 3$, $m = 5$, and $\sigma/S_c = 0.25$.
2. Variations of the axial stress $\sigma_{22}/\sigma_{\text{app}}$, the axial strain ϵ_{22} , and the damage parameter ω along the cross-fiber direction at times $t = 20$ seconds, 1, 5 and 8 hours.
3. Contours of the axial stress σ_{22} at time $t = 20$ seconds and 8 hours.
4. Contours of the damage parameter ω at time $t = 8$ hours.
5. Variations of stresses σ , $\alpha = f \bar{\sigma}_f$, σ_m , and the damage parameter ω with strain ϵ , for $E_f/E_m = 360/65$, $f = 0.32$, and $m = 5$.

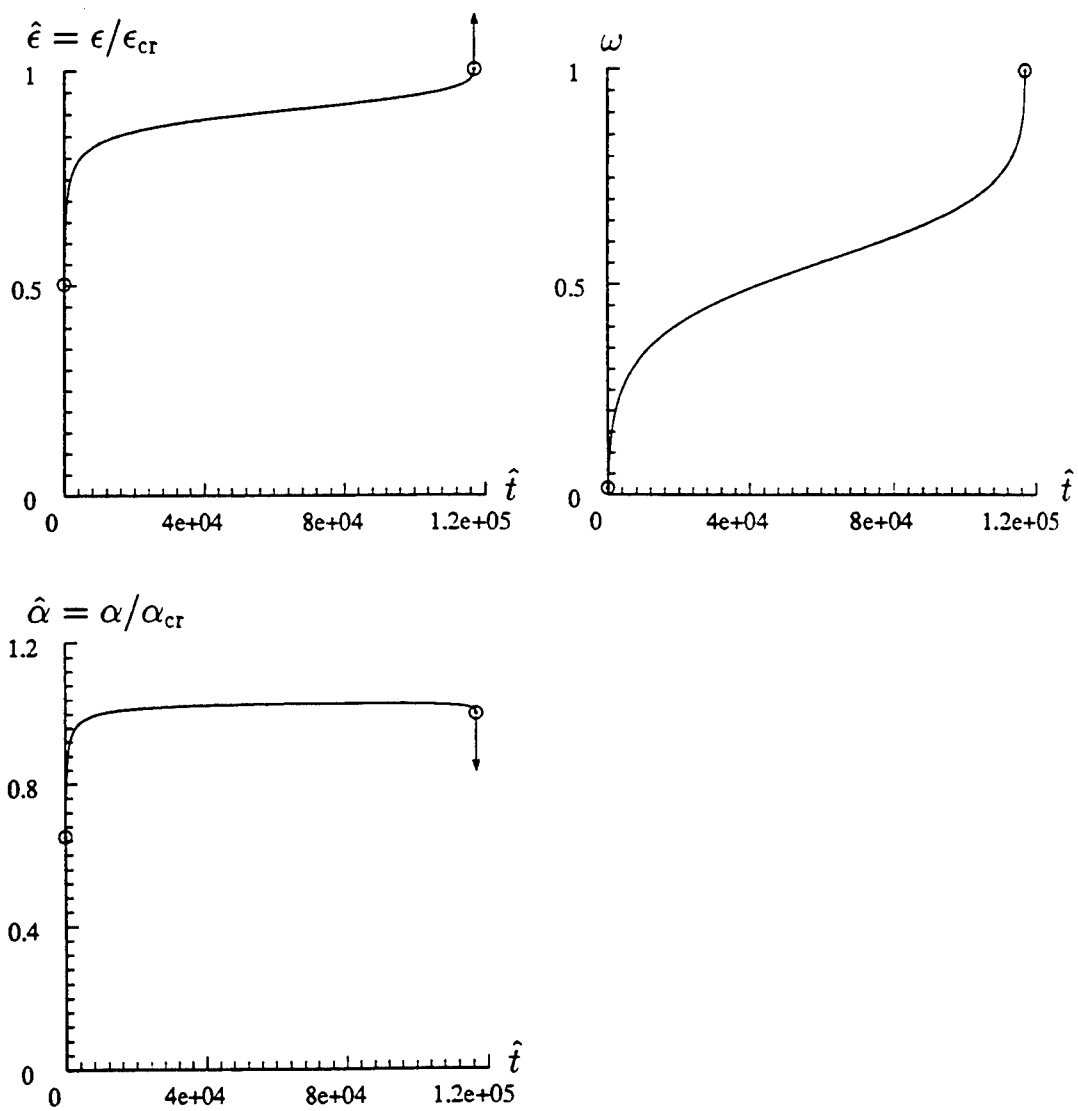


Figure 1

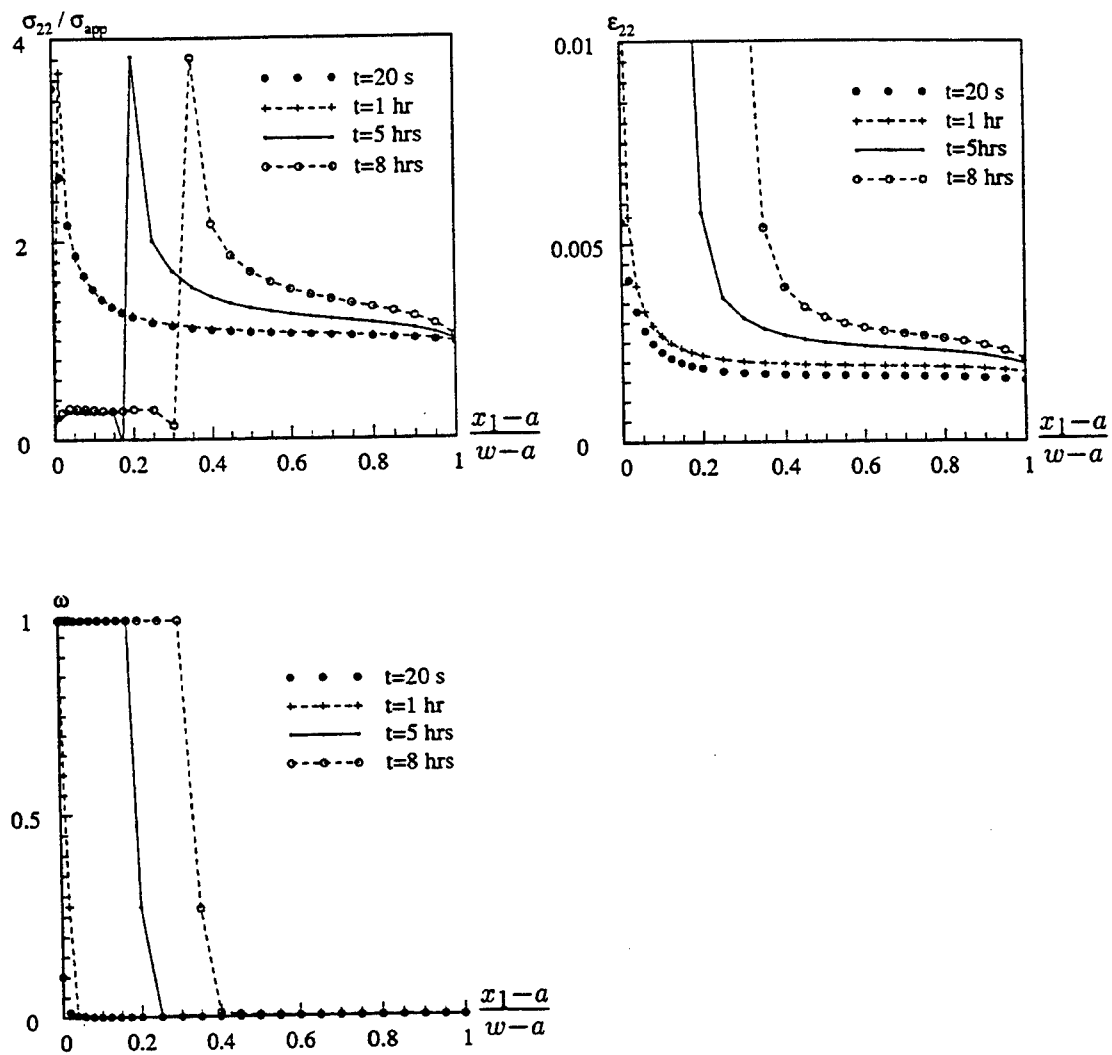
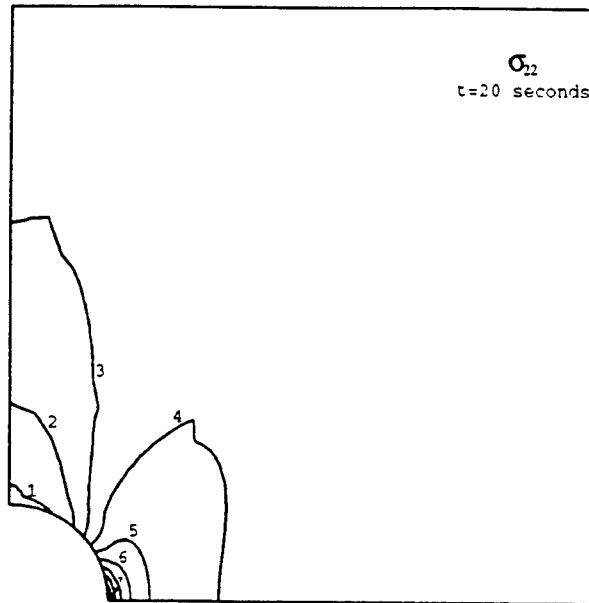


Figure 2

CONTOURS (MPa)

1	+0.00E-00
2	+1.00E+02
3	+2.00E+02
4	+3.00E+02
5	+4.00E+02
6	+5.00E+02
7	+6.00E+02
8	+7.00E+02
9	+8.00E+02
10	+9.00E+02
11	+1.00E+03



CONTOURS (MPa)

1	+0.00E-00
2	+1.00E+02
3	+2.00E+02
4	+3.00E+02
5	+4.00E+02
6	+5.00E+02
7	+6.00E+02
8	+7.00E+02
9	+8.00E+02
10	+9.00E+02
11	+1.00E+03

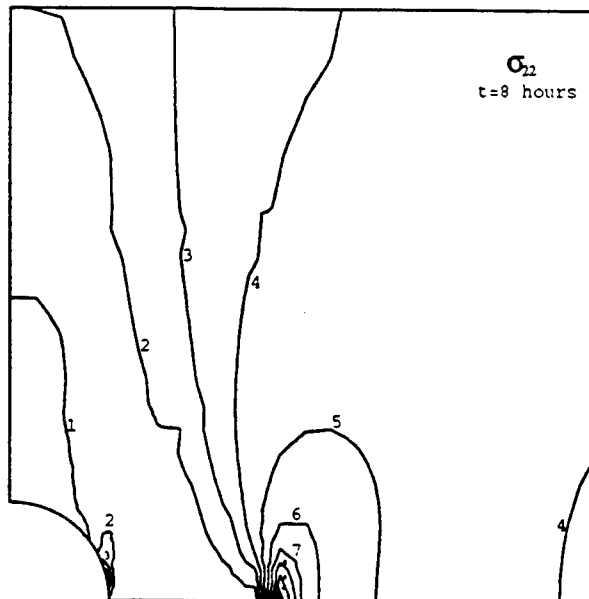


Figure 3

CONTOURS

1	+0.00E-00
2	+1.00E-01
3	+2.00E-01
4	+3.00E-01
5	+4.00E-01
6	+5.00E-01
7	+6.00E-01
8	+7.00E-01
9	+8.00E-01
10	+9.00E-01
11	+1.00E+00

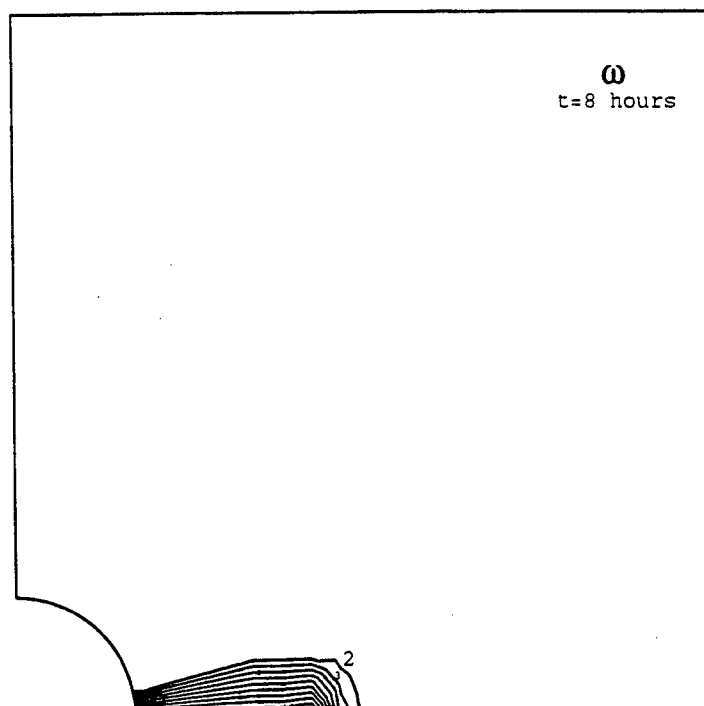


Figure 4

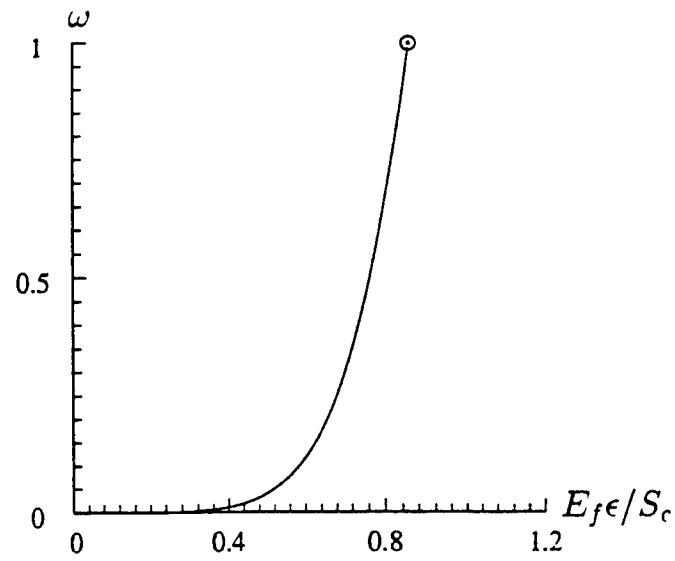
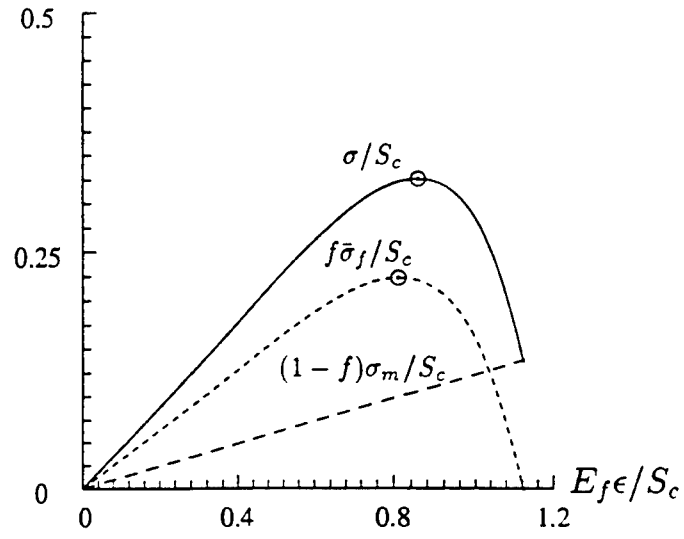


Figure 5

MEASUREMENT OF THE CYCLIC BRIDGING LAW IN A TITANIUM MATRIX COMPOSITE AND ITS APPLICATION TO SIMULATING CRACK GROWTH

S. J. CONNELL[†] and F. W. ZOK[‡]

Materials Department, University of California, Santa Barbara, CA 93106-5050, U.S.A.

(Received 28 January 1997; accepted 22 April 1997)

Abstract—The cyclic bridging traction law for a fiber reinforced titanium matrix composite (TMC) has been measured using a multiple fiber pullout specimen geometry. The test specimens were cut from fatigued specimens containing a single fully bridged matrix crack. The two key parameters obtained from such measurements are the interface sliding stress and the fiber bundle strength. The sliding stress was found to be considerably lower than the pristine values reported for other TMCs (by a factor of ~5), a result of wear of the fiber coatings. The fiber strength is also reduced following fatigue, by ~25%. The strength reduction is associated with the formation of new surface flaws, also due to cyclic sliding. Additionally, simulations of fatigue crack growth have been performed using the measured sliding stress and compared with experimental measurements over a range of applied stresses. Though excellent correlations are obtained between the experiments and the predictions, it is demonstrated that similar correlations can be obtained using sliding stress values that differ from the measured one by a factor of ~2 and by suitable adjustment of the Paris law parameter that characterizes the intrinsic fatigue resistance of the composite. © 1997 Acta Metallurgica Inc.

1. INTRODUCTION

Fatigue cracks in fiber-reinforced titanium matrix composites (TMCs) are often bridged by fibers [1–5]. The effect of fiber bridging on the crack tip stress intensity can be modeled by treating the fibers as a distribution of tractions acting on the crack faces [6–10]. The key property governing the effectiveness of the bridging is the cyclic traction law: the relationship between the bridging stress range, $\Delta\sigma_B$, and the range in the crack opening displacement, Δu . When the interface sliding stress, τ , is assumed to be constant along the sliding length of the fiber, the bridging law is [6]:

$$\Delta u = \lambda(\Delta\sigma_B)^2 \quad (1)$$

where λ is a bridging stiffness parameter defined by

$$\lambda = D(1-f)^2 E_m^2 / 8f^2 \tau E_f E^2 \quad (2)$$

Here E_f and E_m are the fiber and matrix Young's moduli, D is the fiber diameter, E is the longitudinal composite modulus and f is the fiber volume fraction. Of the various quantities governing λ , the one that is subject to the most uncertainty is the sliding stress, τ . Moreover, there is experimental evidence indicating that τ changes during cycling [4, 11, 12].

If the applied stress is sufficiently high, the bridging fibers begin to break when the crack reaches a critical length and the crack growth rate subsequently accelerates rapidly. The onset of fiber fracture can be viewed as a condition for composite failure since the remaining life is usually short. There exists a threshold stress below which no fiber failure occurs for any crack length and the fatigue life is essentially infinite [11, 13, 14]. The threshold stress depends on both the sliding stress and the fiber bundle strength. Figure 1 shows trends in the predicted threshold with the notch or flaw size, $2a_0$. In some instances, fatigue loading degrades the fiber strength through a fretting process along the fiber surfaces [15], thus reducing the threshold. Figure 1 illustrates the changes in the threshold stress with the degradation in fiber strength, characterized by the ratio of the current and pristine fiber strengths, S/S_0 .

The main objective of the present work is to experimentally determine the cyclic traction law in a TMC. The two key characteristics of the law are the sliding stress and the fiber strength. The measurements are based on cyclic tension tests performed on thin strips cut from within the bridged zones. A secondary objective is to demonstrate the overall utility of the crack bridging models by simulating fatigue crack growth at various levels of applied stress using the measured value of the sliding stress. In performing such simulations, it is demonstrated that good correlations can be

[†]Present address: Institute for Mechanics and Materials, University of California, San Diego, La Jolla, CA 92093-0404, U.S.A.

[‡]To whom all correspondence should be addressed.

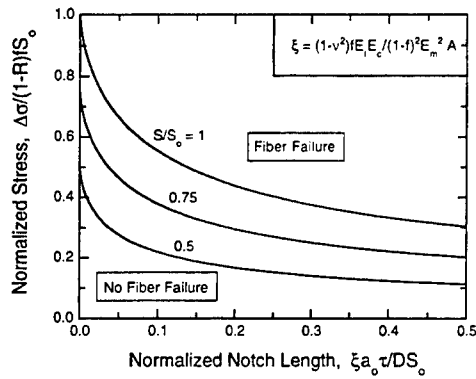


Fig. 1. Effects of the interface sliding stress, τ , and the fiber strength degradation (characterized by the strength ratio S/S_0), on the fatigue threshold in TMCs. (Data adapted from Ref. [13].)

obtained between the predictions and the experimental data using only a rough estimate of the sliding stress (within a factor of two of the measured value) and using the Paris law coefficient as a fitting parameter in the simulation. The analysis and modeling used to interpret the data are detailed in other papers; only the key equations are presented here.

2. EXPERIMENTS

The material used in this study was a Ti-6Al-4V matrix reinforced with unidirectional, continuous SiC fibers†, 100 μm in diameter. The composite panel was comprised of six plies, with a total thickness of 1.0 mm. The fiber volume fraction was 32%. Prior to consolidation, the fibers had been coated with two $\sim 0.5 \mu\text{m}$ layers of C, followed by $\sim 1 \mu\text{m}$ of TiB_2 . The TiB_2 coating serves as a diffusion barrier between the fiber and the matrix. During consolidation, the TiB_2 reacts with the matrix to form a layer of TiB needles, $\sim 0.7 \mu\text{m}$ thick. Upon fatiguing, matrix cracks deflect and propagate along the C-C interface. Some relevant constituent properties are given in Table 1.

Crack growth measurements were made up on $[0^\circ]$ coupons with a center-notch cut normal to the fiber direction. The notches were made by electro-discharge machining (EDM). In all cases, the notch length, $2a_0$, was 3 mm, the specimen width, $2w$, was 15 mm and the notch width was 300 μm . The longest cracks were grown to a length, $2a \sim 9 \text{ mm}$ ($a/w \sim 0.6$). The crack lengths were monitored optically using a stereo-microscope, at magnifications of 60–300X. The crack lengths on both sides of the notch were measured and averaged to obtain the crack extension, Δa . In all cases, single cracks formed on each side of the notch, and grew in a symmetric fashion.

Table 1. Summary of constituent properties

Fiber volume fraction	$f = 0.32$
Fiber modulus	$E_m = 400 \text{ GPa}$
Fiber CTE	$\alpha_f = 4.9 \times 10^{-6} \text{ K}^{-1}$
Matrix modulus	$E_m = 110 \text{ GPa}$
Matrix CTE	$\alpha_m = (9.0-10.4) \times 10^{-6} \text{ K}^{-1}$
Thermal misfit strain at 20°C	$\Omega_0 = 0.44\%$
Poisson's ratio	$\nu = 0.2$

The majority of the fatigue tests were conducted at room temperature at frequencies of 10–20 Hz. The stress range, $\Delta\sigma$, was varied from 200 to 400 MPa, with a fixed stress ratio, $R = 0.1$. A single test was conducted at 300°C, at an applied stress range of $\Delta\sigma = 300 \text{ MPa}$. An induction furnace was used for heating. The temperature was controlled by a thermocouple located at the crack plane; the temperature at this location varied by only $\pm 0.5^\circ\text{C}$ over the duration of the test. The temperatures at distances 2 mm above and below the crack plane were also monitored and found to remain within $\pm 5^\circ\text{C}$ of the crack-plane temperature.

In the room-temperature tests, acoustic emission was monitored by a transducer placed directly on the specimen. Events with an amplitude greater than 60 dB were counted as a single fiber failure [4]. This threshold level had been established from tensile tests performed on individual filaments extracted from the composite. Following some tests, the matrix material near the crack plane was dissolved in a concentrated HF solution to reveal the underlying pattern of fiber fracture.

The cyclic bridging law was measured using fiber pullout specimens. The specimens were made up by longitudinally sectioning the fatigue-cracked specimens at the notch root and at the crack tip, as shown in Fig. 2. The pullout specimen was thus comprised of a single, fully-bridged through-

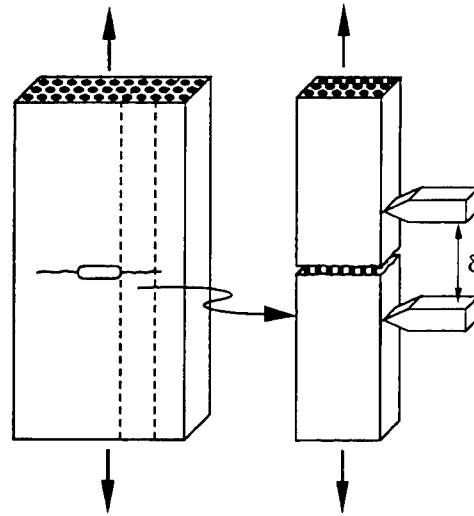


Fig. 2. Schematic showing the sectioning of the fatigue cracked specimens to obtain specimens for the pullout tests.

†Sigma fiber, produced by British Petroleum.

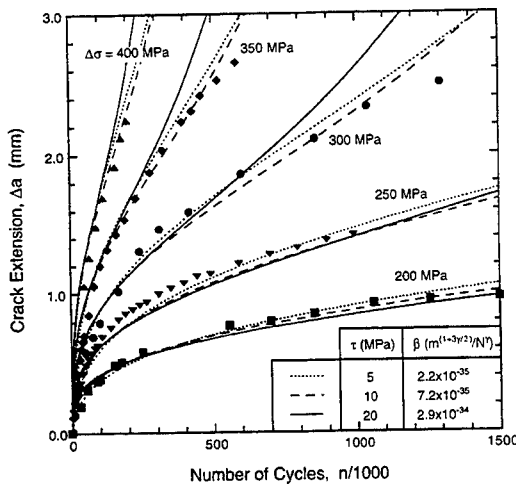


Fig. 3. Fatigue crack growth in $[0^\circ]$ notched coupons ($2a_0 = 3$ mm; $2w = 15$ mm). For the simulations, the Paris law exponent is taken as $n = 3.8$.

thickness matrix crack in an otherwise intact composite bar. Pullout specimens were cut only from fatigued specimens in which there had been minimal fiber failure during crack growth. Similar specimen geometries have been used previously to measure the traction law associated with grain bridging in ceramics [16–19].

The pullout specimens were loaded cyclically, starting at a stress range $\Delta\sigma = 400$ MPa and progressively increasing the stress by 50–100 MPa increments until fracture. Typically ~ 1000 loading cycles were applied at each stress level. The stress ratio was fixed at $R = 0.05$. The tests were periodically interrupted and the load–unload response measured at a loading rate of 1 MPa/s. The displacements across the crack were measured using a 10 mm extensometer with a resolution of ~ 0.1 μ m. One of the specimens was first cycled at ambient temperature at $\Delta\sigma = 400$ MPa, and then at temperatures of 100, 200 and 300°C at the same stress level. For the high temperature tests, the displacements were measured using a 12.7 mm high temperature contacting extensometer. Once at 300°C, the stress level was again incremented up to fracture. Following fracture, the pullout specimens were examined in a scanning electron microscope (SEM) and the pullout lengths of the fibers were measured.

The strengths of the individual fibers from within the bridging zone were measured also, using fibers that had been extracted from one of the pullout specimens. The fibers were extracted by dissolving the matrix in a concentrated HF solution. The extracted fibers were placed into one of four groups, according to their position along the crack. Each group consisted of ~ 20 fibers, representing a region along the crack of ~ 0.7 mm length. The extracted fibers were mounted individually in cardboard tabs with a 25 mm gauge length. The specimen from which fibers were extracted had been cut

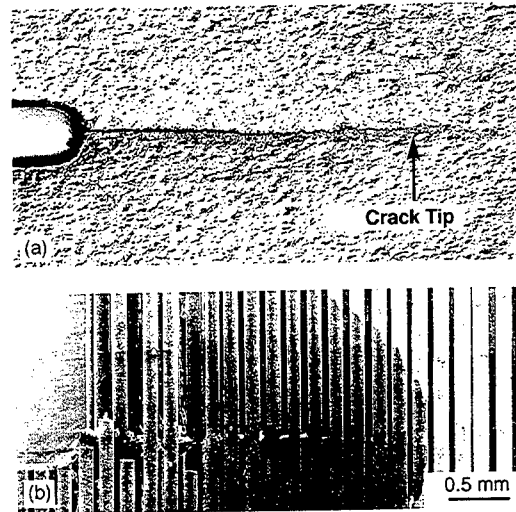


Fig. 4. (a) Matrix fatigue crack and (b) underlying bridging fibers, exposed following matrix dissolution. Fatigue test had been conducted at $\Delta\sigma = 400$ MPa.

symmetrically about the fatigue crack plane to the same total length as the cardboard tabs. In this way, the location of the matrix fatigue crack coincided precisely with the mid-point of the fiber gauge length. The location of fiber fracture could be correlated subsequently with the location of the matrix crack. The fibers were tested in a dedicated fiber testing machine. Approximately one half of the fibers shattered during fracture; in these cases the fracture origin could not be identified. The remaining fibers were examined in a SEM. The strength measurements were compared with those obtained on ~ 80 fibers extracted from the pristine composite [20].

3. FATIGUE CRACK GROWTH

The results of the room temperature $[0^\circ]$ fatigue crack growth experiments are summarized in Fig. 3. For all stress levels used in the present experiments, the crack growth rate decreased monotonically with increasing crack length over the entire loading history. This declaration is a manifestation of fiber bridging in the crack wake. The presence of bridging fibers was confirmed by examination of the specimens in the SEM; one such example is shown in Fig. 4. Similar results have been reported previously for other TMC systems. In the tests conducted at $\Delta\sigma = 300$ –400 MPa, a small number of fibers had failed (typically ≤ 20). In contrast, in the tests conducted at $\Delta\sigma = 200$ and 250 MPa, no fiber failures were measured. Consequently, only the latter specimens were used for making the pullout specimens. The results of the fatigue crack growth test performed at 300°C are shown in Fig. 5. Fatigue cracks had been initiated at room temperature and grown to a length of ~ 0.5 mm prior to heating. Once at 300°C, the crack growth rate increased by

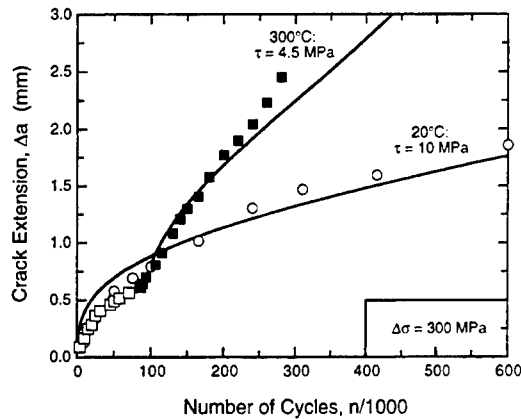


Fig. 5. Effect of temperature on fatigue crack growth.

a factor of ~ 3 . It decelerated slightly with further growth, though its final value (at $\Delta a = 2.5$ mm) was almost an order of magnitude higher than that at room temperature at the same crack length. Examination of the specimen following testing revealed no fiber failure in the crack wake. Moreover, studies on the Ti-alloy itself indicate that there is no detectable change in the fatigue resistance of the alloy over the range 20–300°C [21]. The inference from these results is that the increased crack growth rate is due to a reduction in the sliding stress and the associated reduction in the effectiveness of fiber bridging.

4. SLIDING STRESS

A typical hysteresis loop obtained from the fiber pullout tests is shown in Fig. 6(a). The measured displacement, δ , represents the sum of the elastic displacement, δ_e , of the intact portion of the composite within the extensometer gauge length and the displacement, δ_s , due to fiber/matrix sliding adjacent to the matrix crack. Two different methods were used to calculate the bridging parameter, λ , and, in turn, the sliding stress, τ , from these loops. The analysis is presented in [11].

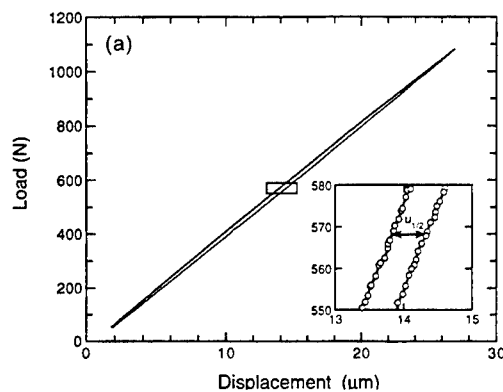


Table 2. Summary of sliding stress measurements at room temperature

Test	Average sliding stress, τ (MPa)		
	No. of measurements	Compliance method	Loop width method
1	8	8.9 ± 1.4	8.1 ± 3.9
2	14	12.3 ± 1.6	11.6 ± 2.2
Average	—	11.0 ± 2.2	10.3 ± 3.3

The first method is based on the variation in the instantaneous compliance, $d\delta/d\sigma$, with the stress difference from the last load reversal, $\bar{\sigma}$; it is predicted to follow the relation

$$d\delta/d\sigma = 2\lambda\bar{\sigma} + C \quad (3)$$

where C is the specimen compliance. The slope of a plot of $d\delta/d\sigma$ vs $\bar{\sigma}$ gives λ . Figure 6(b) shows a representative plot of the instantaneous compliance vs applied stress. The linearity is consistent with the assumption that the sliding stress is constant along the slip length. The second method is based on the width of the hysteresis loop, $u_{1/2}$, at one half of the peak load; it is given by

$$u_{1/2} = \frac{1}{2}\lambda(\Delta\sigma)^2 \quad (4)$$

The sliding stress measurements at room temperature are summarized in Table 2. The two methods of analysis yield similar results, with an average value $\tau = 10.7 \pm 2.8$ MPa. This value is much lower than those obtained in pristine Ti/SiC composites ($\tau \sim 60$ –80 MPa), also measured by fiber pullout [22,23]. The differences can be attributed to wear of the fiber coatings following repeated sliding. Similar conclusions have been reached from comparisons based on fiber *pushout* tests [4,12]. In the subsequent fatigue crack growth simulations, the sliding stress is taken to be 10 MPa.

The effect of temperature on the sliding stress is shown in Fig. 7. In this particular test, the sliding stress was ~ 9 MPa at ambient temperature and subsequently decreased approximately linearly with temperature to ~ 4 MPa at 300°C. This temperature dependence can be rationalized on the basis of the

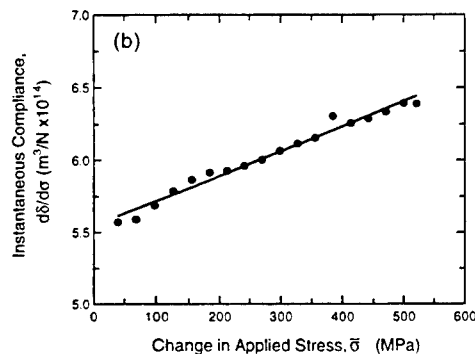


Fig. 6. (a) Hysteresis loop and (b) instantaneous compliance plot, measured on a pullout specimen.

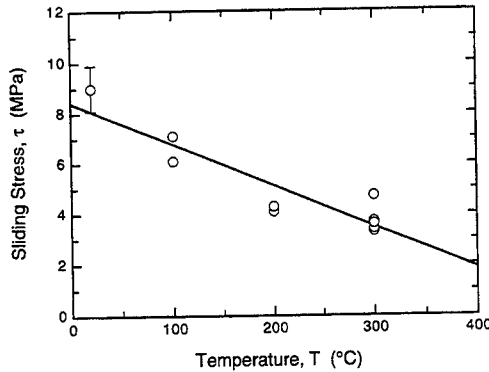


Fig. 7. Influence of temperature on the sliding stress.

relaxation of the thermal misfit strain through a modified form of the Coulomb friction law, as detailed in the Appendix. An analysis of the data yields a friction coefficient of $\mu \approx 0.06$. This value is considerably lower than the one inferred from the temperature dependence of the pristine sliding stress measured by fiber pushout ($\mu \approx 0.4$) [24], the difference again being attributed to coating wear following repeated sliding.

5. FIBER STRENGTH

The fiber bundle strengths, σ_B and the mean pullout lengths $\langle L \rangle$, are plotted in Fig. 8. One such specimen is shown in Fig. 9 and typical fiber fracture origins are shown in Fig. 1. Also shown in Fig. 8 are the predicted trends in the bundle strength and the pullout length with the sliding stress. The predictions assume that frictional coupling exists between the fibers and matrix and that the fiber strengths follow a Weibull distribution. The key results are [25, 26]:

$$\sigma_B = g(m)\sigma_c = g(m)\left(2\sigma_m^0 \tau L_0/D\right)^{1/(m+1)} \quad (5)$$

and

$$\langle L \rangle = h(m)\delta_c = h(m)\left(\sigma_0 D L_0^{1/m}/2\tau\right)^{m/(m+1)} \quad (6)$$

where σ_c and δ_c are the characteristic stress and characteristic length; m is the Weibull modulus; σ_0 is the reference strength corresponding to a reference length of L_0 ; and $g(m)$ and $h(m)$ are the functions plotted in Fig. 6(a) of [26] and Fig. 6 of [25], respectively. The calculated curves in Fig. 8 further assume that the fiber strength distribution is the same as that of the fibers extracted from the as-processed composite (Fig. 11). The predictions consistently overestimate the measured values: the strengths by $\sim 25\%$ and the pullout lengths by an order of magnitude. These discrepancies suggest that the fiber strength has been degraded *locally*, causing failure to occur preferentially in regions close to the matrix crack plane.

The fiber failure origins within the bundle were ascertained by examination of the test specimens in the SEM. Of ~ 80 fibers that were examined, $\sim 70\%$ had failed from flaws located in either the W core or at the W/SiC interface. The remaining 30% had failed from surface flaws. Examples of both types of fracture origins are shown in Fig. 10. Similar examinations were made on a specimen that had been tested in monotonic tension. In the latter case, $\sim 90\%$ of the fibers had failed from interior flaws and the remaining 10% from surface flaws. The larger proportion of surface flaws found in the fatigued specimen confirms that new surface flaws are introduced during the fatigue process.

The results of the individual fiber tensile tests provide further evidence of fiber strength degradation. A comparison of the strength distributions of the fatigued fibers and the pristine fibers is shown in Fig. 11. The mean strength of the fatigued fibers was $\sim 30\%$ lower than that of the pristine value. Moreover, of the ~ 30 fatigued fibers that had not shattered during testing, $\sim 80\%$ had failed within ± 2 mm of the prior matrix crack plane. The distribution of failure locations is plotted in Fig. 12.

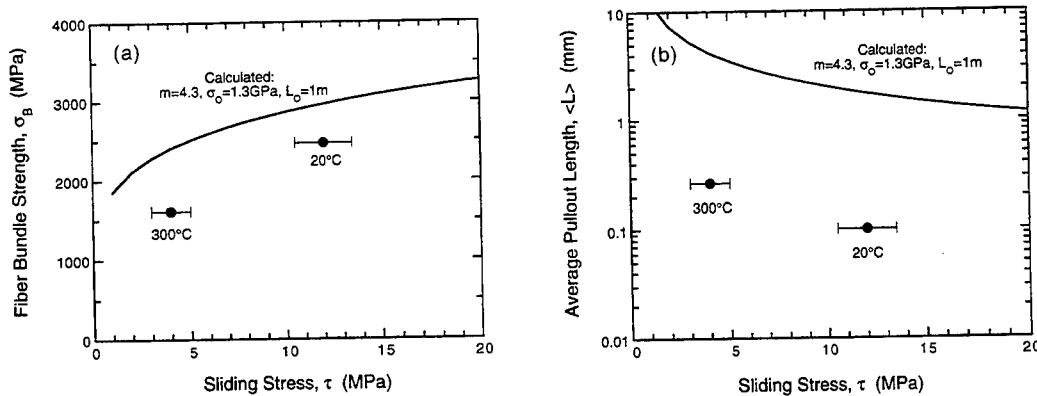


Fig. 8. Trends in (a) fiber bundle strength and (b) pullout length with the interface sliding stress.

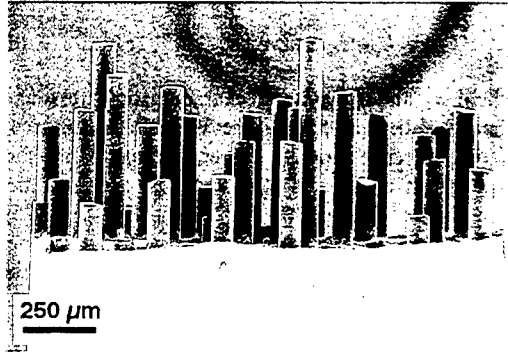


Fig. 9. Fractured pullout specimen (300°C).

Clearly, a disproportionately high number of these failures occurs near the crack plane. Had the failure process been truly random, only ~15% of fiber failures would have occurred in this region.

The Weibull parameters associated with the degraded fibers were calculated from a least squares fit of the strength data, assuming: (i) that the fibers in which failure was confirmed to occur near the

matrix crack represent a random sampling of the distribution associated with the bridging fibers (the remaining fibers being excluded from the analysis) and (ii) that the effective fiber gauge length within the bridging zone is 4 mm (the length over which the failures occurred).

The results are presented in Fig. 13. Evidently, the Weibull modulus (5.3) is slightly higher than that of the pristine fibers (4.3), though the reference strength is reduced by a factor of ~2 (from 1.30 to 0.68 GPa for $L_0 = 1$ m).

There was no apparent effect of the location of the fibers with respect to the crack tip on the fiber strength. The average strengths obtained over 0.7 mm increments (each containing ~20 fibers) are plotted against position in Fig. 14. Also shown are the corresponding number of fatigue cycles experienced by each group of fibers. The results suggest that the strength degradation occurs in the early stages of fatigue cycling ($\leq 3 \times 10^5$ cycles).

6. CRACK GROWTH SIMULATION

Crack growth simulations were performed by calculating the crack tip stress intensity factor range ΔK_t , in terms of the applied stress, the crack and notch lengths, and the constituent properties that govern the bridging law, and combining the solution with an empirical relation between ΔK_t and the crack growth rate, da/dn . The solutions for ΔK_t were obtained from [7]. The crack growth rate was assumed to follow a modified form of the Paris law:

$$\frac{da}{dn} = \beta_m (\alpha \Delta K_t)^m = \beta_c (\Delta K_t)^m \quad (7)$$

where $\alpha \Delta K_t$ is the stress intensity range acting in the matrix (ΔK_m); β_m and γ are constants that characterize the fatigue resistance of the matrix; and β_c is a composite property defined by

$$\beta_c = \beta_m \alpha^m \quad (8)$$

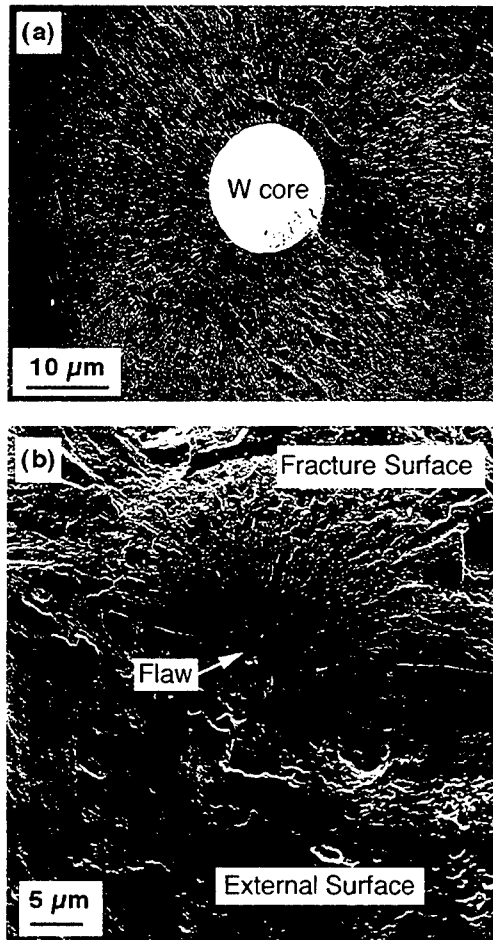


Fig. 10. Examples of the two types of fracture origins: (a) internal flaw (at W core) and (b) surface flaw.

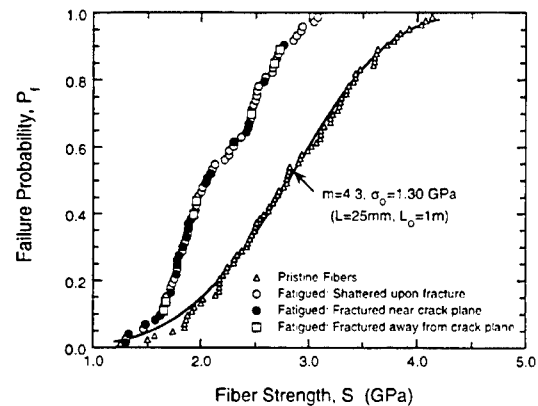


Fig. 11. Strength distributions of fatigued and pristine fibers. σ_0 is the reference strength corresponding to a reference length, L_0 , and m is the Weibull modulus.

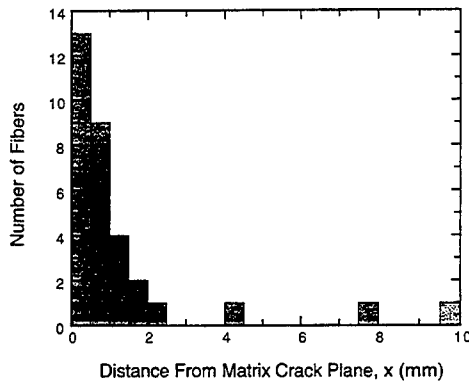


Fig. 12. Distribution of failure locations of fatigued fibers. The crack plane ($x = 0$) was located at the middle of the 25 mm gauge section. (Data based on fibers that had not shattered during testing.)

For monolithic Ti-6Al-4V alloys with microstructures similar to that in the present composite, $\gamma = 3.8$ and β_m ranges from $\sim 2 \times 10^{-35}$ to $2 \times 10^{-34} m^{(1 + 3\gamma/2)}/N^\gamma$ [24].

The crack growth simulations were performed using several different values of τ and β_c . The results are shown in Fig. 3. In the first case, the sliding stress was taken to be 10 MPa (the average measured value), and the simulations were performed using β_c as a fitting parameter. The value inferred from this fitting procedure is $\beta_c = 7.2 \times 10^{-35} m^{(1 + 3\gamma/2)}/N^\gamma$. Excellent correlations are obtained between the simulations and the experimental data for all stress ranges. To assess the sensitivity of the model predictions to the selection of τ , additional simulations were performed using sliding stresses that differ from the measured value by a factor of two and again using β_c as a fitting parameter. Excellent correlations were obtained using $\tau = 5$ MPa and $\beta_c = 2.2 \times 10^{-35} m^{(1 + 3\gamma/2)}/N^\gamma$. For $\tau = 20$ MPa and $\beta_c = 2.9 \times 10^{-34} m^{(1 + 3\gamma/2)}/N^\gamma$, the correlations were reasonably good over most of the range of data, with moderate differences at high stresses and crack lengths. Evidently, the crack growth simulations alone cannot be used to determine uniquely the values of τ and β_c , even when experimental data exist for several stress ranges. Conversely, the crack growth curves can be simulated quite accurately using a rough estimate of either τ and β_c and using the other as a fitting parameter. These features are attractive from the (practical) viewpoint of fatigue life prediction but not for inferring the pertinent constituent properties.

As a further assessment of the bridging model, the values of β_c inferred from the fitting procedure were compared with the reported values of β_m , through equation (8). To perform such comparisons, an estimate of α is required. At the simplest level, the effects of the fibers at the crack tip can be neglected, yielding $\alpha = \Delta K_m / \Delta K_t = 1$. Two alternate approaches for evaluating α have been proposed.

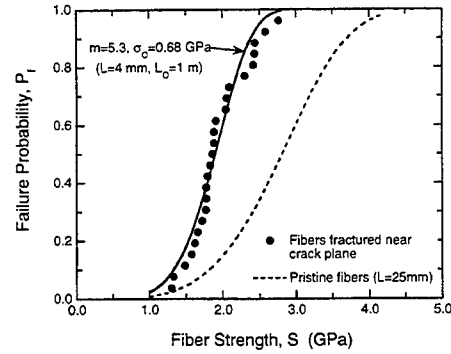


Fig. 13. Comparison of the strength distribution of the bridging fibers with the distribution measured on pristine fibers.

The first is based on the energy release rate within the matrix, accounting for the area fraction of matrix at the crack tip as well as the elastic anisotropy of the composite. The result is [13, 28]:

$$\alpha = \Delta K_m / \Delta K_t = \sqrt{E_m(1 - \nu^2) / (1 - f) A E} \quad (9)$$

where A is a dimensionless orthotropy factor. For the present Ti/SiC composite, $A = 0.925$ and thus $\alpha = 0.94$; similar to the previous estimate of $\alpha = 1$. The second alternative is based on the assumption that the fiber and matrix strains are equal to one another at the crack tip [29], yielding

$$\alpha = E_m / E = 0.55 \quad (10)$$

Strain compatibility is expected to be obtained at distances ahead of the crack tip that are greater than the fiber spacing. At shorter distances, strain differences may be present, depending on the mismatch in the elastic-plastic characteristics of the two constituents as well as the debonding and sliding characteristics of the interfaces. Arguably, the latter approach for evaluating α for TMCs is the least plausible. Typically, the amount of crack growth per cycle and hence the size of the cyclic

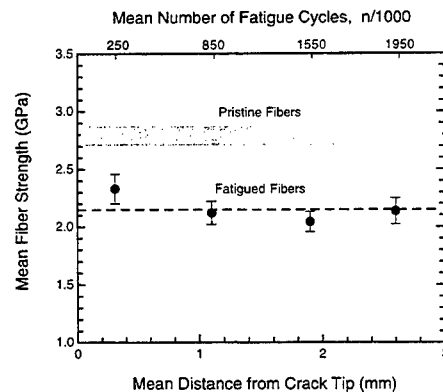


Fig. 14. Influence of number of loading cycles on fiber strengths. (Error bars represent the standard deviation of the mean.)

plastic zone is of the order 10^{-9} – 10^{-8} m. In comparison, the fiber spacing is $\sim 10^{-4}$ m. The vast difference between these quantities suggests that strain compatibility is not necessarily obtained over the distances relevant to the fatigue cracking process. Based on these arguments, α is expected to be in the range 0.94–1.0, and β_c in the range $\sim (0.8-1.0)\beta_c$. The latter range is considerably smaller than the uncertainty associated with β_c obtained from the fitting exercise, and for practical purposes, β_c and β_m can be assumed to be the same. Indeed, the inferred value of β_c using a sliding stress of 10 MPa falls within the range of values of β_m reported for the neat matrix (2×10^{-35} – $2 \times 10^{-34} m^{(1+3\nu/2)/N^c}$) [28].

Simulation of fatigue cracking at 300°C was performed assuming that the matrix figure resistance remains unchanged (which is consistent with the reported data for the Ti-6Al-4V alloy [21]), and using τ as a fitting parameter. The value of β_c was taken to be the one obtained from the simulations for the room temperature tests with $\tau = 10$ MPa ($\beta_c = 7.2 \times 10^{-35} m^{(1+3\nu/2)/N^c}$). Good correlation with the experimental data is obtained for $\tau = 4.5$ MPa (Fig. 5). This value is essentially identical to the one measured in the fiber pullout test at the same temperature (Fig. 7), confirming that the reduction in fatigue resistance with increasing temperature is due to the reduction in τ .

7. CONCLUDING REMARKS

The present study demonstrates that the interface sliding stress pertinent to crack bridging under fatigue loading is considerably lower than that obtained on pristine material, a result of cyclic sliding and wear of the fiber coatings. Moreover, the sliding stress decreases with increasing temperature, by a factor of ~ 2 over the range 20–300°C. This change can be rationalized on the basis of the relaxation in the thermal misfit strain. The fatigue crack growth behavior at 20°C and 300°C is consistent with the measured sliding stresses and the reported parameters characterizing the fatigue resistance of the matrix, and can be simulated using the crack bridging model.

During cycling, the fiber strength is reduced, a result of new surface flaws introduced by the sliding. This is manifested in a reduction in the measured strengths of the individual fibers as well as preferential fiber failure in the regions near the matrix crack plane. The implication is that the fatigue threshold, based on the onset of fiber failure, is diminished with cycling. However, the degradation appears to occur in the early stages of cracking. It is envisaged that the measured fiber strengths following fatigue might be used with the predictions of Fig. 1 to identify the allowable flaw or notch sizes and fatigue stresses to obtain infinite life.

Acknowledgements—Funding for this work was provided by the ARPA University Research Initiative Program at UCSB under ONR contract No. N00014-92-J-1808.

REFERENCES

1. Cox, B. N. and Marshall, D. B., *Fatigue Frac. Eng. Mater. Struct.*, 1991, **14**, 847.
2. Sensmeier M. D., Wright P. K., in *Fundamental Relationships Between Microstructure and Mechanical Properties of Metal Matrix Composites*, ed. P. K. Liaw, M. N. Gungor. The Minerals Metals and Materials Society, Warrendale, PA, 1990, pp. 441–457.
3. Wright P. K., Nimmer R., Smith G., Sensmeier M., Brun M. in *Interfaces in Metal-Ceramic Composites*, ed. R. Y. Lin, R. J. Arsenault, G. P. Martins, S. G. Fishman. The Minerals, Metals and Materials Society, Warrendale, PA, 1989, pp. 559–581.
4. Walls, D. P., Bao, G. and Zok, F. W., *Acta Metall. Mater.*, 1993, **41**(7), 2061.
5. Larsen, J. M., Jira, J. R., John, R. and Ashbaugh, N. E., in *Life prediction methodology for titanium composites ASTM STP 1253*, ed. W. S. Johnson, J. M. Larsen and B. N. Cox. ASTM, 1995.
6. McMeeking, R. M. and Evans, A. G., *Mech. Mater.*, 1990, **9**, 217.
7. Bao, G. and McMeeking, R. M., *Acta Metall. Mater.*, 1994, **42**(7), 2415.
8. Begley, M. R. and McMeeking, R. M., *Mat. Sci. Eng. A.*, 1995, **200**(1), 12.
9. Cox, B. N. and Lo, C. S., *Acta Metall. Mater.*, 1992, **40**(7), 1487.
10. Bakuckas, J. G. and Johnson, W. S., *J. Comp. Tech. Res.*, 1993, **15**(3), 242.
11. Walls, D. P. and Zok, F. W., *Acta Metall. Mater.*, 1994, **42**(8), 2675.
12. Warren, P. D., Mackin, T. J. and Evans, A. G., *Acta metall. mater.*, 1992, **40**, 1243.
13. Budiansky, B. and Cui, Y. L., *Acta metall. mater.*, **42** 1994.
14. Zok, F. W., Du, Z. Z. and Connell, S. J., *Mat. Sci. Eng. A.*, 1995, **200**, 103.
15. Kantzos, P. and Telesman, J., *Int. J. Fat.*, 1990, **12**, 409.
16. Hay, J. C. and White, K. W., *Acta metall. mater.*, 1992, **40**, 3017.
17. Hay, J. C. and White, K. W., *J. Am. Ceram. Soc.*, 1993, **76**, 1849.
18. White, K. W. and Hay, J. C., *J. Am. Ceram. Soc.*, 1994, **77**, 2283.
19. Hay, J. C. and White, K. W., *J. Am. Ceram. Soc.*, 1995, **78**, 1025.
20. Zok, F. W., Chen, X. Y. and Weber, C. H., *J. Am. Ceram. Soc.*, 1995, **78**, 1965.
21. Cunningham S. United Technologies Pratt & Whitney. Private communication.
22. Marshall, D. G., Shaw, M. C. and Morris, W. L., *Acta Metall. Mater.*, 1992, **40**, 443.
23. Marshall, D. B., Shaw, M. C., Morris, W. L. and Graves, J., *Key Engineering Materials*, 1996, **116/117**, 209.
24. Connell S.J., Zok F.W., *Mat. Sci. Eng.*, submitted.
25. Curtin, W. A., *J. Am. Ceram. Soc.*, 1991, **74**, 2837.
26. Curtin, W. A., *J. Mech. Phys. Solids*, 1993, **41**, 217.
27. *Damage Tolerant Design Handbook, Part 1, Metals and Ceramics Information Centre*. Batelle's Columbus Laboratories, Columbus, OH, 1975.
28. McCartney, L. N., *Proc. R. Soc. Lond. A.*, 1987, **409**, 329.
29. Marshall, D. B., Cox, B. N. and Evans, A. G., *Acta metall. mater.*, 1985, **33**, 2013.

30. Budiansky, B., Hutchinson, J. W. and Evans, A. G., *J. Mech. Phys. Solids*, 1986, **34**, 167.

APPENDIX

Analysis of sliding stress

The temperature dependence of the sliding stress can be rationalized on the basis of a modified Coulomb friction law. In the pristine material, the friction law can be written as

$$\tau = \mu(p_A + p_T) \quad (A1)$$

where μ is the coefficient of friction, p_T is the thermal residual stress acting normal to the interface (compression being positive) and p_A is the additional pressure that develops as a result of asperity mismatch during sliding. Using a concentric cylinder model, the thermal stress can be related to the misfit strain, Ω , by [30]

$$p_T = - \left[\frac{(1-f) E_m E_f}{E_f + E(1-2\nu)} \right] \Omega \equiv -\eta \Omega \quad (A2)$$

where

$$\Omega \equiv (\alpha_f - \alpha_m) (T - T_p) \quad (A3)$$

Here α_f and α_m are the thermal expansion coefficients of the fibers and the matrix, and T_p is the minimum stress free temperature. Assuming that the asperity pressure is independent of temperature, equation (A1) can be re-written as

$$\tau = \mu[p_A + \eta(\Omega_0 - (\alpha_f - \alpha_m)\Delta T)] \quad (A4)$$

where Ω_0 is the misfit strain at ambient temperature, T_0 , and ΔT is the temperature difference from ambient $T - T_0$.

It has been demonstrated previously that the fiber coatings undergo wear during cyclic sliding [4, 11, 12]. The removal of material during wear reduces the normal stress by an amount

$$p_w \approx -2E_f \Delta/D \quad (A5)$$

where Δ is the thickness of material removed. Equation (A4) can be modified accordingly to read:

$$\tau = \mu[p_A + \eta(\Omega_0 - (\alpha_f - \alpha_m)\Delta T) - 2E_f \Delta/D] \quad (A6)$$

An assessment of equation (A6) was made in the following way. The friction coefficient was obtained from the slope of the $\tau - T$ curve (Fig. 7); the two are related by

$$\mu = \frac{1}{\eta(\alpha_f - \alpha_m)} \frac{d\tau}{dT} \quad (A7)$$

From the linear regression analysis of the experimental data and the constituent properties summarized in Table 1, the result is $\mu = 0.06$. This value is much lower than the one obtained from the temperature-dependence of the sliding stress in the pristine material, measured using fiber pushout tests: $\mu \approx 0.4$. The sum of the contributions from asperity mismatch and coating wear was obtained from the sliding stress at ambient temperature, $\tau_0 = 9$ MPa, along with the measured value of μ . The result is $p_A + p_w \approx -80$ MPa. The asperity pressure in the pristine material has been estimated from pushout tests to be $p_A = p_A^0 \approx 50$ MPa [24]. Thus, the contribution due to wear is inferred to be $p_w \approx -130$ MPa. This change can be effected through only a small amount of material removed: $\Delta = -p_w D / 2E_f \approx 0.02 \mu\text{m}$.

Power-law matrix creep in fiber composites due to transverse stress gradients

Z.-Z. DU *¹, A. C. F. COCKS ** and R. M. McMECKING ***

ABSTRACT. – This paper extends the recent work of Du, McMeeking and Schmauder (1995) on transverse yielding when stress gradients are developed in metal matrix composites to include the effects of power-law creep of the matrix. The composites considered have a strongly bonded interface. A characteristic repeating cell is identified. Creep potentials in terms of transverse stress and stress gradient are calculated from the analysis of the response of a single cell for composites with different matrix creep properties and fiber volume fractions. A general constitutive relationship accounting for matrix yielding, creep and flow past the fibers is developed.

1. Introduction

Metal matrix composites (MMCs) reinforced by continuous fibers are increasingly used for the fabrication of turbine rings in the aerospace industry. These components are generally operated in high temperature environments and subjected to a complex multiaxial stress state. Since these components are circumferentially reinforced and subjected to centrifugal loading, transverse stress gradients will develop in them. This loading could cause the matrix to yield, creep and perhaps to flow past the fibers. The fibers deform elastically only and therefore, unless they break, they are anchored in place relative to a matrix which can flow past them. The radial stress gradients in the matrix are therefore balanced by shear drag from the fibers. The resulting loading of the fibers generates circumferential tension in them.

Previous modeling of the transverse behavior of metal matrix composites has not accounted for the effects of stress gradients. Instead, emphasis has been placed on the roles of interface and interphase properties between the fibers and the matrix (Nimmer *et al.*, 1991; Gunawardena *et al.*, 1993; Du and McMeeking, 1994). Other modeling has

* Materials Department and Mechanical Engineering Department, University of California, Santa Barbara, California 93106, U.S.A.

** Engineering Department, Leicester University, Leicester, LE1 7RH, U.K.

*** Mechanical Engineering Department, University of California, Santa Barbara, California 93106, U.S.A.

¹ Now at Hibbitt, Karlsson and Sorensen, Inc., 1080 Main Street, Pawtucket, RI 02860, U.S.A.

addressed the effects of fiber arrangement, fiber volume fraction and loading direction on the transverse strength (Brockbrough and Suresh, 1990; Zahl *et al.*, 1994).

Recently, Du *et al.* (1995) have examined plastic flow behavior in an elastic perfectly plastic matrix reinforced by continuous fibers when stress gradients are developed. Results were given for the influence of the fiber volume fraction, fiber arrangement and stress gradient. The yield surfaces in terms of mean stress and stress gradient were calculated. In addition, a constitutive relationship accounting for matrix plastic straining and matrix flow past the fibers was developed. It was found that the transverse limit strengths are sensitive to the stress gradient across the cell. The presence of the stress gradient in the composite reduces the transverse strength. In addition, a tensile stress can also develop in the fibers, which is required from overall equilibrium considerations, to balance the transverse stress gradient. When the stress in the fibers is above the effective strength of the fibrous system, fiber failure occurs, leading to a further reduction of the transverse strength as well as the longitudinal strength.

In the present work, we extend the work of Du *et al.* (1995) to include the effects of creep of the matrix when stress gradients are developed in the composite. As before, plane strain cell models are used. The repeating cells are subjected to unequal tractions at the top and bottom as shown in Figure 1. The fibers are treated as rigid and stationary and the matrix is characterized by power-law hardening behavior of the Ramberg-Osgood type. The resulting stress field is equivalent to that developed in a power-law creeping material. This equivalence is used here to develop constitutive laws when the matrix creeps. Equilibrium of the cells is depicted in Figure 1. A strong bond is assumed between the fibers and the matrix. As discussed in Du *et al.* (1995), plane strain is used to avoid the complications of diverging flow occurring in a ring geometry which would depend on the diameter of the ring. In a ring with a large diameter compared to the fiber diameter, plane strain is a good model. In such a ring, the shear forces depicted on AD and BC in Figure 1 would be replaced by tensile circumferential stresses in the fibers providing a component of reaction in the radial direction. If the diameter of a given fiber ring is not large compared to the fiber cross-sectional diameter, the plane strain model becomes suspect. Axisymmetric analysis rather than planar calculations would become necessary. Although the range of validity of the plane strain results is not known, we suspect that most turbine rings will have a large diameter compared to the fiber diameter so that our plane strain model becomes valid. A hexagonal fiber arrangement with a circular cross section is considered. Such a fiber arrangement has been found to be nearly isotropic in terms of transverse strength (Zahl *et al.*, 1994) so that the direction of loading in this case is chosen arbitrarily and is shown in Figure 1. Analyses are conducted for composites with a wide range of fiber volume fractions and matrix creep properties. The results of these calculations are used to develop the constitutive relationship.

When developing constitutive models, it often proves convenient to express the constitutive response using scalar stress and strain-rate potentials. If the potentials for the matrix materials are convex then equivalent convex potentials can be obtained for the macroscopic response, which are functions of suitably defined macroscopic stress or strain-rate quantities (*see for example* Hill, 1967). Cocks and Leckie (1987) and Cocks

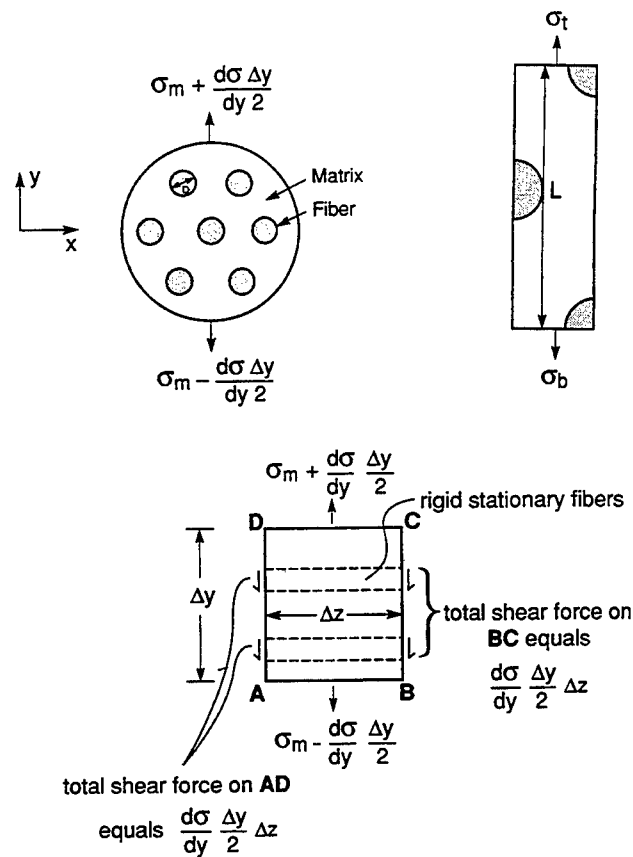


Fig. 1. – Schematic of the cell model.

(1989, 1994) have examined the general structure of constitutive laws for the situation where power-law creep is the dominant mechanism of deformation. The potentials governing the power law creep response of heterogeneous materials are often obtained from consideration of regular repeating structure and the response of a representative cell of the microstructure is analyzed. This approach has been adopted by Duva (1986), Cocks (1989) and Sofronis and McMeeking (1992) to determine constitutive relationships for porous materials and by Bao *et al.* (1991) for metals reinforced by ceramic particles. Cocks (1989) demonstrated that the strain-rate potential in general can be expressed in terms of a macroscopic effective stress. Surfaces of constant effective stress nest inside each other in stress space (Cocks, 1994; Calladine and Drucker, 1962), in order of increasing n , with the surface for $n \rightarrow \infty$ forming the inner surface.

In the present work, we analyze the response of the repeating cell of Figure 1 using the finite element method. Macroscopically, a zone of the material is considered to be subject to boundary velocities in the y -direction given by

$$(1) \quad v = v^0 + \dot{E}y$$

where v^0 is a uniform velocity and \dot{E} is a uniform strain rate. These velocities are supposed to be applied to the matrix, so the boundary of the macroscopic element being discussed must be drawn through the matrix. The fibers are required to be immovable in the y -direction, but are free to move with the matrix in the x -direction. Therefore, the velocities given by Eq. (1) will force the matrix to flow vertically past the fibers, given that many fibers will occupy the macroscopic region under consideration. The boundary conditions of the macroscopic element for the x -direction should be chosen to preserve incompressibility of the matrix material during creeping flow and, for the situation considered here, to avoid any average normal or shear stresses in the x -direction. Arguments of Hill (1967) then permit us to assert that in the core interior of the macroscopic element, the response of the matrix will be free of influence from the constraints imposed on the boundary of the macroscopic element except that the response will conform to the requirement that there be a net velocity and a net strain rate in the y -direction as invoked by Eq. (1). Let the actual velocity in the core interior of the macroscopic element be

$$(2) \quad v = v^0 + \dot{E}y + \hat{v}$$

where $\hat{v}(x, y)$ is the perturbation of the velocity from the long range net velocity and strain rate. Since the fibers are stationary in the y -direction, v in Eq. (2) must be zero on the boundary of the fibers due to the no-slip condition imposed there. Unfortunately, \hat{v} is in general unknown, and would only be determined by a full analysis of the macroscopic element. However, the statement in Eq. (2) applies algebraically to the lower and upper matrix boundaries of the repeating unit cell shown in Figure 1 and, tessellated by finite elements, in Figure 2. Periodicity and the conditions in the core interior of the macroscopic element permit us to deduce that the sides of the repeating unit cell parallel to the y -axis remain straight, free of shear tractions and on average free of load in the x -direction. A fiber will displace in the x -direction at the same rate as the cell boundary to which it is attached and, of course, has zero velocity in the y -direction.

With the macroscopic element recreated by joining together such deforming unit cells, no two unit cells will experience the same conditions of distortion. Therefore, the problem under consideration is somewhat different from the usual one of determining the behavior of a heterogeneous material from the characteristic response of a single cell which represents all repeating units of the material. However, for the problem tackled in this paper, each cell subjected to the conditions described in the previous paragraph will deform compatibly with its neighbors since they will be joined at boundaries with common values of velocities as given by Eq. (2). We argue therefore, that the response of the unit cell subject to boundary conditions given by Eq. (2), provides information relevant to the macroscopic constitutive response of a zone of the composite material experiencing conditions around its perimeter given by Eq. (1), but with the many fibers within the zone immobilized in the y -direction. We propose that the constitutive law developed from our calculations can be used for coarser scale analysis of the response of the composite material when the fibers are so held fixed, even though the stress gradients predicted will occur on a scale of the fiber spacing and diameter. Indeed, the

behavior we anticipate in components like turbine rings will inevitably involve stress gradients on this scale and methods must be developed which recognize this. It is an open question whether higher order terms beyond the strain rate in Eq. (1) become important in such components or whether they may be safely neglected in the way that Hill (1967) demonstrated for heterogeneous materials not having immobile reinforcements. We leave the study of such deeper questions of constitutive theory to future research.

A question which we must face to pursue our analysis is the form which \hat{v} should take on the upper and lower boundaries of our unit cell (*Fig. 2*). This point is similar to the issue which arises in any unit cell calculation where the constraint imposed on the boundary must be decided. In the problem we examine, it is not possible to equate the velocities on the upper boundary to the velocities on the lower, as is often done in the unit cell analyses. The equivalent to that approach would be to make \hat{v} at x on the top equal to \hat{v} at x on the bottom through appropriate constraints on the finite element equations and then ensure that the top and bottom velocities differ according to Eq. (2). Such an approach has not been used for this paper, but should be investigated in the future. Instead, we use a rudimentary technique and set $v = 0$ at the nodes attached to a fiber on the upper and lower boundaries and set $\hat{v} = 0$ at every other node on the upper and lower boundaries. This has the advantage of ensuring compatibility between the unit cells representing a macroscopic zone of the material; it is also simple and numerically efficient and the results allow us to provide an exposition of our ideas. The disadvantage is that the elements at the upper and lower boundaries of the unit cell adjacent to the fiber are forced to have an excessive shear strain rate. This is not a serious difficulty for high values of the creep exponent since a fairly uniform flow through the center of the gap between fibers can be expected with shear strain rate concentrations in the elements bordering the fibers. When the creep exponent has a low value, a non-uniform flow of

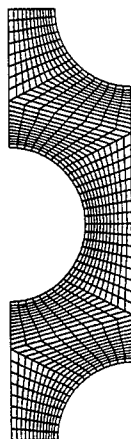


Fig. 2. – Typical finite element model for a cell which has a fiber volume fraction of 0.35 in the hexagonal arrangement.

matrix material through the gap between the fibers can be expected and setting \hat{v} to zero over most of the gap is not appropriate and only very approximate.

2. Creep potential

The strain-rate of an element of matrix material is given by

$$(3) \quad \dot{\epsilon}_{ij} = \frac{\partial \phi}{\partial \sigma_{ij}}$$

where

$$(4) \quad \phi = \frac{1}{n+1} \dot{\epsilon}_0 \sigma_0 \left(\frac{\sigma_e}{\sigma_0} \right)^{n+1}$$

$\dot{\epsilon}_0$ is the strain rate at a stress σ_0 , n is the power-law creep exponent and σ_e is the tensile equivalent effective stress. For the problem of Figure 1, there are two macroscopic measures of the applied load: the mean stress σ_m and the stress gradient $\frac{d\sigma}{dy}$, which we have multiplied by the fiber diameter D to provide a quantity with the dimensions of stress. We will refer to these quantities as generalized macroscopic stresses. The conjugate generalized strain-rates are then the mean strain-rate $\dot{\epsilon}_m$ and the velocity in the direction of flow v , which is normalized by the fiber diameter D to provide a quantity with the dimensions of strain-rate. Following Hill (1967) and Duva and Hutchinson (1984) we can define a macroscopic strain-rate potential Φ , such that

$$(5) \quad \dot{\epsilon}_m = \frac{\partial \Phi}{\partial \sigma_m}.$$

In addition,

$$(6) \quad \frac{v}{D} = \frac{\partial \Phi}{\partial \left(D \frac{d\sigma}{dy} \right)}$$

where

$$(7) \quad \Phi = \frac{1}{V} \int_{V_m} \phi dV$$

V is the total volume of the macroscopic element and V_m is the volume of matrix material.

Combining Eq. (3), (4) and (7) and making use of the principle of virtual power we obtain

$$(8) \quad \Phi = \frac{V^{-1}}{n+1} \int_{V_m} \dot{\epsilon}_e \sigma_e dV = \frac{V^{-1}}{n+1} \int_{V_m} \dot{\epsilon}_{ij} \sigma_{ij} dV = \frac{1}{n+1} \left(\sigma_m \dot{\epsilon}_m + D \frac{d\sigma}{dy} \frac{v}{D} \right).$$

Cocks (1989) demonstrated that the macroscopic potential Φ can be expressed in terms of a macroscopic effective stress $\bar{\Sigma}$, which is a homogeneous function of degree one in the macroscopic generalized stresses σ_m and $D \frac{d\sigma}{dy}$, such that

$$(9) \quad \Phi = \frac{1}{n+1} \dot{\epsilon}_0 \sigma_0 \left(\frac{\bar{\Sigma}}{\sigma_0} \right)^{n+1}.$$

Comparing Eq. (8) and (9) we obtain

$$(10) \quad \bar{\Sigma} = \sigma_0 \left(\frac{\sigma_m \dot{\epsilon}_m + D \frac{d\sigma}{dy} \frac{v}{D}}{\sigma_0 \dot{\epsilon}_0} \right)^{\frac{1}{n+1}}.$$

Use of Eq. (10) requires a knowledge of the exact solution to the problem of Figure 1. In the current paper we generate this solution by identifying a characteristic repeating cell within the macroscopic element and use the finite element method to obtain σ_m and $D \frac{d\sigma}{dy}$ for prescribed value of $\dot{\epsilon}_m$ and $\frac{v}{D}$. The parameter $\dot{\epsilon}_m$ is the mean strain rate in the unit cell and can be identified with \dot{E} of Eq. (1). The velocity v is the mean velocity in the y -direction and is equivalent to $v^0 + \dot{E} y_m$ from Eq. (1) where y_m is the y -coordinate of the center of the unit cell. The results of a series of calculations can then be conveniently presented as contours of constant macroscopic effective stress in generalized stress space, with the generalized strain-rate normal to the surface. The details of these calculations are described in the following sections.

In the limit as $n \rightarrow \infty$, $\bar{\Sigma}$ is the same as the flow potential for a perfectly plastic material. For a material obeying the von Mises yield criterion, a limit surface in stress space is therefore given by

$$(11) \quad F = \bar{\Sigma} - \sigma_0 = 0$$

where, now, σ_0 is the uniaxial yield strength of the material. Following the procedures employed by Cocks (1994) it can be shown that surfaces of constant $\bar{\Sigma}/\sigma_0$ nest inside each other in order of increasing n , with the limit surface for $n \rightarrow \infty$ forming the inner envelope. The solution in this limit is provided by Du *et al.* (1995), which can be compared directly with the current results when the above representation is employed.

3. Numerical model

A typical finite element grid used to discretize the problem of Figure 1 is shown in Figure 2 for the hexagonal arrangement of fibers for a fiber volume fraction of 0.35. Except for nodes attached to a fiber, all straight edges of the cell are required to remain straight and parallel to their original orientations and free of shear tractions during deformation. Deformation is induced by displacement boundary condition applied to the top and bottom edges of the cell. The sides of the cell are allowed to move in such a way that the average normal traction is zero. The fibers move in the x -direction with the side boundary to which they are attached. The finite element nodes on the surfaces of the

fibers are not permitted to move relative to the fiber, simulating a strong bond between the matrix and the rigid fiber. The deformation is plane strain. The resulting average normal stress is σ_t at the top of the cell and σ_b at the bottom, as shown in Figure 1.

Rather than employ the creep constitutive law of Eq. (3), in the computations it proves more convenient to use a plasticity model with a power-law hardening relationship of the Ramberg-Osgood type, such that in uniaxial tension

$$(12) \quad \frac{\varepsilon}{\varepsilon_0} = \frac{\sigma}{\sigma_0} + \alpha \left(\frac{\sigma}{\sigma_0} \right)^n.$$

In the computations presented in this paper, the coefficient α was taken to be $3/7$ and the yield strain ε_0 was set equal to $\sigma_0/E_m = 1.5 \times 10^{-3}$, where E_m is Young's modulus for the matrix. A value of $\nu = 0.33$ for Poisson's ratio of the matrix material was used in all the computations. Eq. (12) was generalized to multiaxial stress states using small strain J_2 flow theory. For deflections much greater than the elastic distortion of the body, the stresses and strains at a material point increase in proportion to each other and the resulting solution is equivalent to that for J_2 deformation theory. As demonstrated by Odqvist (1966), the resulting strain-field is then the same as the strain-rate field for a creeping material with the same power-law exponent n . We use this equivalence here to obtain the solution for the creep law of Eq. (3).

The two generalized stress measures, the mean stress σ_m and stress gradient $Dd\sigma/dy$, are given by

$$(13) \quad \sigma_m = \frac{\sigma_t + \sigma_b}{2}$$

$$(14) \quad D \frac{d\sigma}{dy} = D \frac{\Delta\sigma}{L} = D \frac{(\sigma_t - \sigma_b)}{L}$$

and the corresponding generalized strains are

$$(15) \quad \varepsilon_m = \frac{u_t - u_b}{L}$$

$$(16) \quad \frac{u}{D} = \frac{u_t + u_b}{D}$$

where u_t and u_b are the vertical displacements at the top and bottom of the cell respectively and L is the height of the cell, which equals $1.65 \frac{D}{\sqrt{f}}$ for the hexagonal fiber arrangement.

In the results presented in the next sections, attention is centered on the situation where both σ_m and $\Delta\sigma$ are positive, *i.e.* $\sigma_t \geq |\sigma_b|$. However, symmetry arguments can be used to obtain the solution in the other quadrants of stress space.

The commercial finite element code ABAQUS (1993) was used to carry out the computations on a Convex mainframe. Isoparametric second order hybrid elements with

reduced integration were used in order to avoid the problem of mesh locking associated with incompressible deformation.

4. Results

First we consider the situation where there is no stress gradient and the top and bottom surfaces of the cell are subjected to the same stress. In this limit, since there is only one generalized stress, $\bar{\Sigma}$ is proportional to σ_m for a power-law creeping material. For a given value of σ_m , $\bar{\Sigma}$ can be determined by calculating the generalized mean strain from the finite element analysis using Eq. (15), interpreting this as a strain-rate, and substituting the result into Eq. (10). The resulting variation of $\bar{\Sigma}$ with σ_m is plotted in Figure 3a for a matrix creep exponent of 3 and a range of fiber volume fractions. It is evident that there is not a linear relationship between $\bar{\Sigma}$ and σ_m as required by the homogeneity condition. This is because, at small strains, elastic deformation dominates the response and the analogy between flow theory and deformation theory, and hence power-law creep, is not valid. It is only at large strains, when the effects of elastic deformation can be ignored, that the results of the computations can be used to predict the power-law creep response. It is evident from Figure 3a that for values of σ_m in excess of about $2\sigma_0$ the plots are linear. We use the slope of this linear portion of the curve to determine the homogeneous relationship between $\bar{\Sigma}$ and σ_m for the creeping matrix.

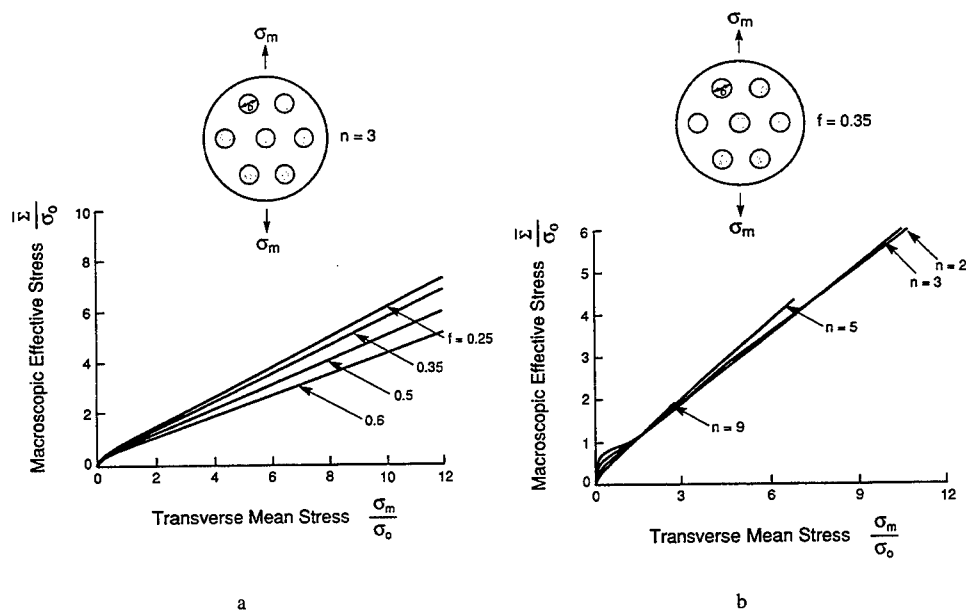


Fig. 3. - Macroscopic effective stress-transverse mean stress curves when $\Delta\sigma = 0$ for (a) materials with different fiber volume fractions when $n = 3$ and (b) materials with different creep exponents when $f = 0.35$.

The effect of varying the creep exponent n is shown in Figure 3b, where the value of $\bar{\Sigma}$ determined from the computations is plotted against σ_m for n in the range 2 to 9 and a fiber volume fraction of 0.35. Taking the slope of the linear portions of these and similar curves for a range of creep exponents and fiber volume fractions, we can determine an appropriate relationship between $\bar{\Sigma}$ and σ :

$$(17) \quad \bar{\Sigma} = \frac{\sigma_m}{h(n, f)}$$

where $h(n, f)$ is a dimensionless function of n and f . This function is plotted in Figure 4 for the range of conditions considered in the computations. These results are well approximated by the relationship

$$(18) \quad h(n, f) = \exp \left[\left(\frac{2.9}{n} - \frac{2.3}{n^2} \right) f^{\frac{1}{2}} \right] \frac{2(1 + 0.26f)}{\sqrt{3}}$$

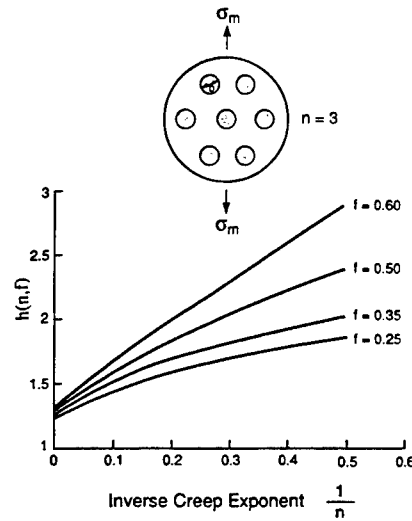


Fig. 4. – Normalizing parameter $h(n, f)$ as a function of the creep exponent for different fiber volume fractions.

which differs from the numerical results by no more than 8% for $f \leq 0.6$. In the limit $n \rightarrow \infty$ the power law creep response is equivalent to that of a perfectly plastic material of yield strength σ_0 . The limit strength of the composite is then given by

$$(19) \quad \bar{\Sigma} = \frac{\sigma_m}{h(\infty, f)} = \sigma_0.$$

This limit has been analyzed by Du *et al.* (1995) and Eq. (18), although slightly different to the relationship that they propose, also fits their results with an error of less than 8%.

It should be noted that in previous studies by Bao *et al.* (1991) and Zhal *et al.* (1994) on composites with a power-law hardening matrix, an asymptotic reference stress $\bar{\sigma}_n$ was often introduced to describe the deformation response of the material in the absence of stress gradients. The reference stress $\bar{\sigma}_n$ was obtained by normalizing the composite stress, σ_m with respect to the stress in the pure matrix at the same strain. This reference stress $\bar{\sigma}_n$ can be related to the quantity, $h(n, f)$ by the following:

$$(20) \quad h(n, f) = \left(\frac{\bar{\sigma}_n}{\sigma_0} \right)^{\frac{n}{n+1}} \alpha^{-\frac{n}{n+1}}.$$

The same procedure can be adopted to determine the material response in the other extreme of zero mean stress and positive stress gradient. The unit cell was subjected to a tensile stress along its top surface and a compressive stress of the same magnitude along the bottom. The difference between the displacements of these two surfaces was evaluated from the computations and the macroscopic effective stress was calculated using Eq. (14), (16) and (10). These calculations are summarized in Figure 5, where $\bar{\Sigma}/\sigma_0$ is plotted as a function of $\frac{D}{\sigma_0} \frac{d\sigma}{dy}$ for a range of values of n and f . Again, we focus on the linear portion of these curves to determine an expression for $\bar{\Sigma}$ for this loading condition:

$$(21) \quad \bar{\Sigma} = \frac{D \frac{d\sigma}{dy}}{g(n, f)}$$

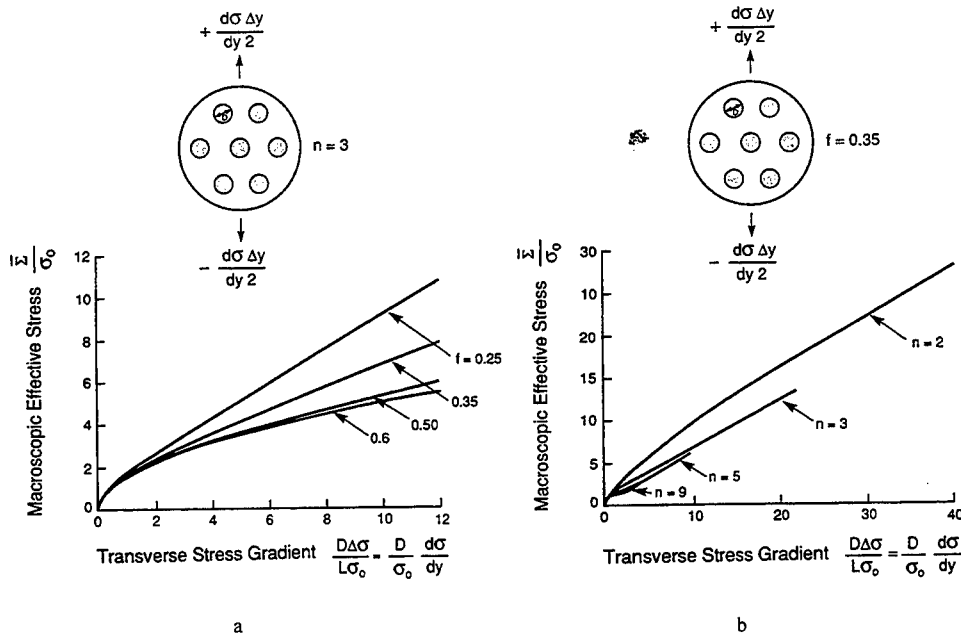


Fig. 5. – Macroscopic effective stress-transverse stress gradient curves when $\sigma_m = 0$ for (a) materials with different fiber volume fractions when $n = 3$ and (b) materials with different creep exponents when $f = 0.35$.

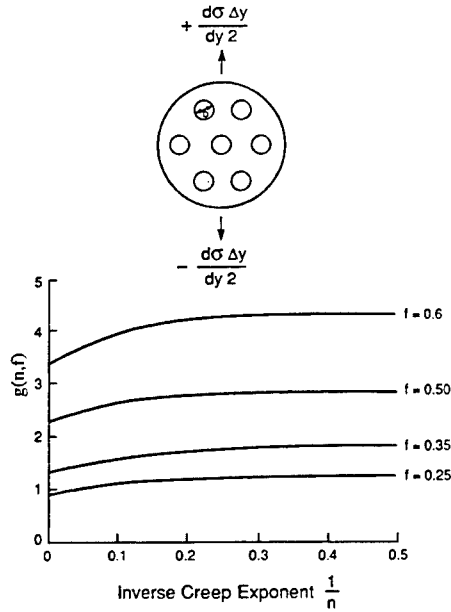


Fig. 6. – Normalizing parameter $g(n, f)$, as a function of the creep exponent for materials with different fiber volume fractions.

where $g(n, f)$ is plotted in Figure 6. These results are well approximated by

$$(22) \quad g(n, f) = 8.17 f - 20.4 f^2 + 30.8 f^3 \quad n \leq 3$$

$$(23) \quad g(n, f) = \left(0.76 + \frac{1.45}{n} - \frac{2.2}{n^2}\right)(8.17 f - 20.4 f^2 + 30.8 f^3) \quad n \leq 3.$$

The above equations provide a fit to the computations with an error of less than 5% for $f \leq 0.6$.

As before, the limit strength of the composite is given by

$$(24) \quad \bar{\Sigma} = \frac{\frac{D}{\sigma_0} \frac{d\sigma}{dy}}{g(\infty, f)} = \sigma_0.$$

The expression for $g(\infty, f)$ in this limit given by Eq. (24) is of the same form as that given by Du *et al.* (1995), with slightly different values of the coefficients to provide the best fit over all values of n .

When using the constitutive law of Eq. (12) to determine the macroscopic effective stress a radial loading path (either in load or displacement space) must be followed when performing the computations. For situations in which there is both a mean stress and a stress gradient it proves computationally convenient to prescribe the displacement rate. Figures 7a and 7b show plots of $\bar{\Sigma}/\sigma_0$ against σ_m/σ_0 and $\bar{\Sigma}/\sigma_0$ against $\frac{D}{\sigma_0} \frac{d\sigma}{dy}$ for a range of values of u_b/u_t , the ratio of the displacements applied to the top and bottom

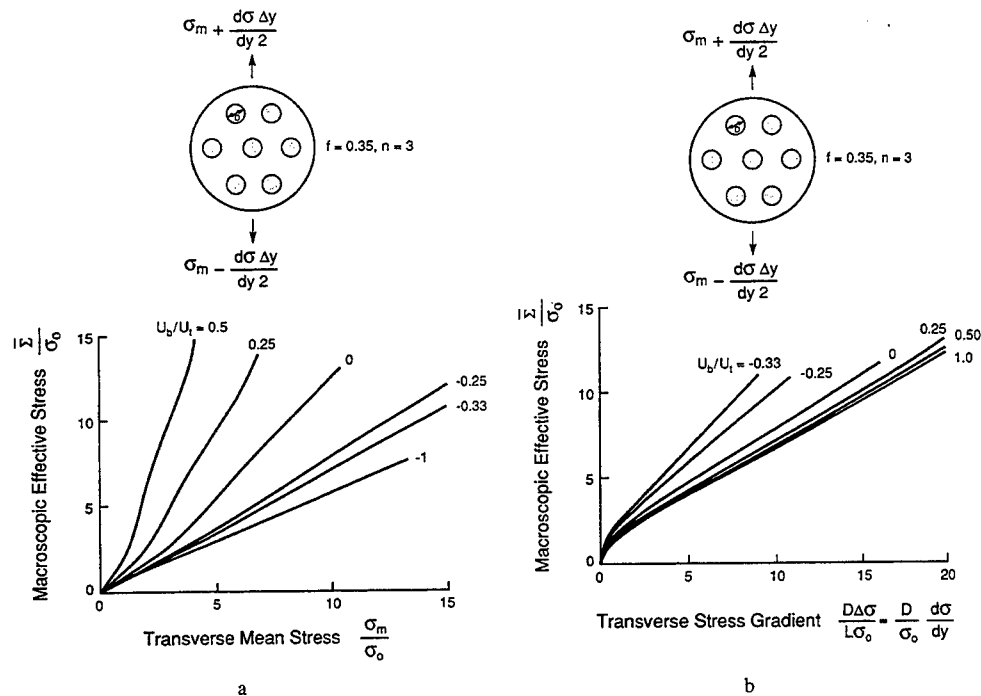


Fig. 7. – (a) Macroscopic effective stress-transverse mean stress curves and (b) macroscopic effective stress-transverse stress gradient curves for a fiber volume fraction of 0.35 and a creep exponent $n = 3$. The unit cell used for the calculations is subjected to a range of ratios of upward displacement u_b at the cell bottom to the upward displacement u_t at the top of the cell.

of the cell. The curves for a given value of u_b/u_t in Figures 7a and 7b were obtained from the same calculation. As in the extreme situations considered above, these curves become linear after an initial transient period, and we use the slope of these linear regions to determine the relationship between $\bar{\Sigma}$, σ_m and $D \frac{d\sigma}{dy}$. Linear fits were obtained by performing a least squares linear regression analysis for each curve in Figure 7 over the range in which the trend is linear. A convenient way of presenting the results of these calculations is as curves of constant $\bar{\Sigma}/\sigma_0$ in $\sigma_m/\sigma_0 - \frac{D}{\sigma_0} \frac{d\sigma}{dy}$ space. These can be constructed by first translating the linear portions of Figures 7a and 7b so that they pass through the origin. Then, for given values of n and f a value of $\bar{\Sigma}/\sigma_0$ can be specified and the values of σ_m/σ_0 and $\frac{D}{\sigma_0} \frac{d\sigma}{dy}$ corresponding to this value read off these plots for a range of values of u_b/u_t . The resulting surfaces for $\bar{\Sigma}/\sigma_0 = 1$ are plotted in Figure 8 for a range of values of n and a fiber volume fraction of 0.35. Use of this value of $\bar{\Sigma}/\sigma_0$ allows the surface for $n \rightarrow \infty$ to be plotted as the limit surface obtained by Du *et al.* (1995). It is evident from these curves that the nesting character predicted by Cocks (1994) is obtained for all fiber volume fractions. However, for states of generalized stress with a high stress gradient, decreasing the value of n does not result in any further expansion of the surface for $n < 3$, implying that these solutions provide a reasonable approximation for smaller values of n .

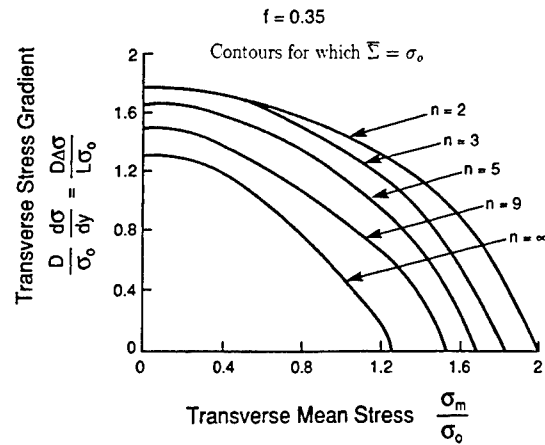


Fig. 8. – Constant macroscopic effective stress contours for materials with a range of creep exponents when $f = 0.35$.

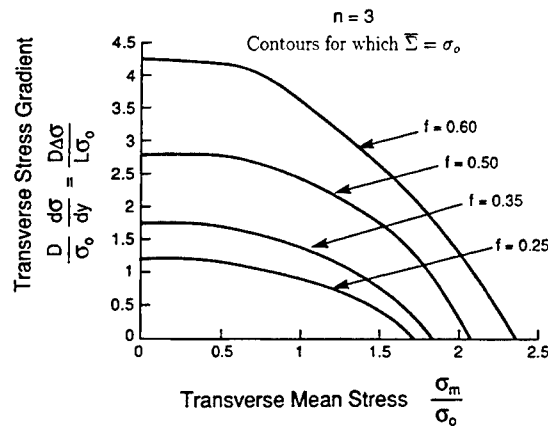


Fig. 9. – Constant macroscopic effective stress contours for materials with a range of fiber volume fractions when $n = 3$.

Surfaces of $\bar{\Sigma}/\sigma_0 = 1$ are plotted in Figures 9-11 for different fiber volume fractions when the matrix creep exponent equals, 3, 5 and ∞ respectively. It is evident from these plots that the surfaces of constant effective stress expand away from the origin as the volume fraction of fibers is increased. This is simply a reflection of the fact that the material becomes more difficult to deform as the fiber volume fraction is increased and a higher stress is required to achieve a given strain-rate.

5. Constitutive relationships

In the constitutive model development, it is instructive to represent the effective macroscopic stress in terms of elementary functions. Examination of the results in

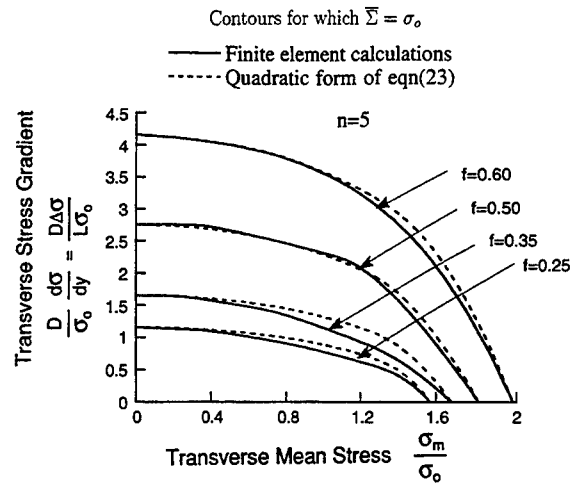


Fig. 10. – Constant macroscopic effective stress contours for materials with a range of fiber volume fractions when $n=5$. The solid line represents the finite element results and the dash line represents the quadratic form of Eq. (25).

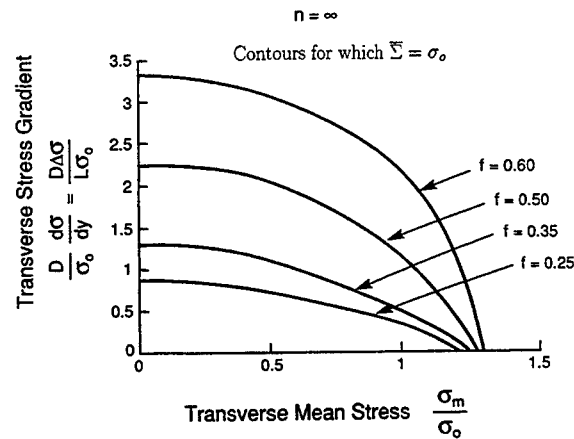


Fig. 11. – Constant macroscopic effective stress contours for materials with a range of fiber volume fractions when $n = \infty$.

Figures 8-11 reveals that the shape of the curves can be approximately represented by an ellipse. Indeed, elliptical forms for the representation of $\bar{\Sigma}$ in the absence of the stress gradient have been widely used (Duva, 1986; Cocks, 1989, 1994; Sofronis and McMeeking, 1992) to describe the response of power-law creeping materials containing voids. For the problems analyzed in this paper, for length scales larger than the fiber spacing, $\Delta\sigma/L$ is the stress gradient $d\sigma/dy$. In addition, the mean stress σ_m represents the stress σ averaged over scales larger than the fiber spacing. Henceforth, the symbol σ

will be used instead σ_m . The macroscopic effective stress is given by

$$(25) \quad \frac{\bar{\Sigma}}{\sigma_0} = \left[\left(\frac{\sigma}{\sigma_0 h(n, f)} \right)^2 + \left(\frac{D \frac{d\sigma}{dy}}{\sigma_0 g(n, f)} \right)^2 \right]^{\frac{1}{2}}$$

where $h(n, f)$ and $g(n, f)$ are given by Eq. (18) and Eq. (22) and (23) respectively. Surfaces with the elliptical approximation of Eq. (25) ($\sigma \equiv \sigma_m$) are superimposed on those obtained from the finite element calculations in Figure 10 for a range of fiber volume fractions when $n = 5$. It is found that the numerical results are well approximated by the quadratic form of Eq. (25). Since these surfaces of constant $\bar{\Sigma}$ are convex, the same arguments as used to derive the plastic flow in Du *et al.* (1995) provides, from Eqs. (6), (7) and (9).

$$(26) \quad \dot{\epsilon} = \frac{\partial \Phi}{\partial \bar{\Sigma}} \frac{\partial \bar{\Sigma}}{\partial \sigma}$$

and

$$(27) \quad \frac{v}{D} = \frac{\partial \Phi}{\partial \bar{\Sigma}} \frac{\partial \bar{\Sigma}}{\partial (D \frac{d\sigma}{dy})}.$$

Combination of these two equations with Eq. (25) gives

$$(28) \quad \dot{\epsilon} = \frac{\dot{\epsilon}_0}{h^2(n, f)} \frac{\sigma}{\sigma_0} \left[\left(\frac{\sigma}{\sigma_0 h(n, f)} \right)^2 + \left(\frac{D \frac{d\sigma}{dy}}{\sigma_0 g(n, f)} \right)^2 \right]^{\frac{n-1}{2}}$$

and

$$(29) \quad \frac{v}{D} = \frac{\dot{\epsilon}_0}{g^2(n, f)} \frac{D \frac{d\sigma}{dy}}{\sigma_0} \left[\left(\frac{\sigma}{\sigma_0 h(n, f)} \right)^2 + \left(\frac{D \frac{d\sigma}{dy}}{\sigma_0 g(n, f)} \right)^2 \right]^{\frac{n-1}{2}}.$$

These last two equations represent the flow-law for high temperature creep of materials which exhibit motion of the matrix past the fibers. Note, that in the limit $d\sigma/dy = 0$, when the stress gradient vanishes, Eq. (28) and (29) give the expected result for the transverse flow law

$$(30) \quad \dot{\epsilon} = \frac{\dot{\epsilon}_0}{h^{n+1}} \left(\frac{\sigma}{\sigma_0} \right)^n$$

with $v = 0$.

When $\sigma = 0$, the equations reduce to

$$(31) \quad \frac{v}{D} = \frac{\dot{\epsilon}_0}{g^{n+1}} \left(\frac{D \frac{d\sigma}{dy}}{\sigma_0} \right)^n$$

with $\dot{\epsilon} = 0$.

Another useful potential function is the dual or scalar stress potential, Ψ . The scalar stress potential and the strain-rate potential are related as follows:

$$(32) \quad \Phi + \Psi = \sigma_{ij} \dot{\epsilon}_{ij}$$

where Ψ is a function of the macroscopic generalized strain-rate quantities, such that

$$(33) \quad \sigma_m = \frac{\partial \Psi}{\partial \dot{\epsilon}}$$

and

$$(34) \quad D \frac{d\sigma}{dy} = \frac{\partial \Psi}{\partial \left(\frac{v}{D}\right)}$$

where

$$(35) \quad \Psi = \frac{n}{n+1} \dot{\epsilon}_0 \sigma_0 \left(\frac{\bar{E}}{\dot{\epsilon}_0} \right)^{\frac{n+1}{n}}.$$

In this expressions, \bar{E} is a macroscopic effective strain-rate which is a homogeneous function of degree one in the macroscopic generalized strain-rates $\dot{\epsilon}$ and v/D . Similar to the macroscopic effective stress, the macroscopic effective strain-rate can be conveniently presented as contours of constant $\bar{E}/\dot{\epsilon}_0$ in generalized strain-rate space, with the generalized stress normal to the surface. Combining Eqs. (28), (29) and (32) with Eq. (8) gives

$$(36) \quad \Psi = \frac{n}{n+1} \dot{\epsilon}_0 \sigma_0 \left[h^2(n, f) \left(\frac{\dot{\epsilon}}{\dot{\epsilon}_0} \right)^2 + g^2(n, f) \left(\frac{v}{D\dot{\epsilon}_0} \right)^2 \right]^{\frac{n+1}{2n}}.$$

Comparison of Eq. (35) with Eq. (36) gives

$$(37) \quad \frac{\bar{E}}{\dot{\epsilon}_0} = \left[h^2(n, f) \left(\frac{\dot{\epsilon}}{\dot{\epsilon}_0} \right)^2 + g^2(n, f) \left(\frac{v}{D\dot{\epsilon}_0} \right)^2 \right]^{\frac{1}{2}}.$$

The surfaces for $\bar{E}/\dot{\epsilon}_0 = 1$ are plotted in Figure 12 for a range of values of n and a fiber volume fraction of 0.35. It is evident from these curves that surfaces of constant effective strain-rate nest inside each other in strain-rate space, in order of decreasing n , with the surface for $n \rightarrow \infty$ forming the outer surface. This result is consistent with the general results of Calladine and Drucker (1962) on nesting surfaces. A general proof of this nesting character is given in the Appendix.

6. Concluding discussion

In this paper, the recent work of Du *et al.* (1995) on transverse yielding when stress gradients are developed has been extended to include the effects of power-law matrix creep. Macroscopic effective stress surfaces, expressed in terms of the mean stress and the

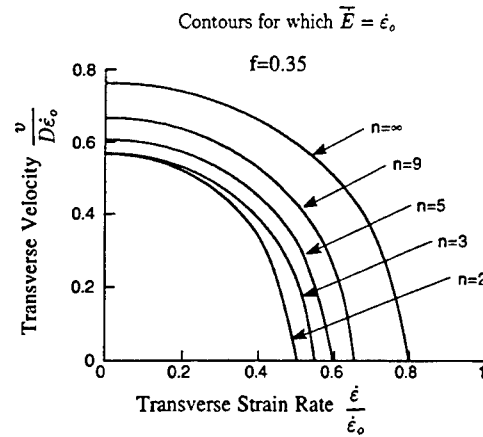


Fig. 12. – Constant macroscopic effective strain-rate contours for materials with a range of creep exponents when $f = 0.35$.

stress gradient, have been determined. Correspondingly, macroscopic effective strain-rate surfaces in terms of the strain-rate and the velocity have also been constructed. The transverse limit and reference stresses are found to be sensitive to the stress gradient across the cell. General constitutive relationships accounting for matrix yielding, creep and flow past the fibers have also been constructed, allowing the transverse creep strain-rate and the transverse velocity to be predicted.

A feature of the constitutive relationships is that a real length appears in the laws. The length appearing is the fiber diameter and therefore, this sets the scale for the influence of the stress gradient on the constitutive behavior. Since stress gradients are involved in the constitutive laws, a scaling length is an inherent feature, and therefore, the fact that the fiber diameter influences the macroscopic behavior of the material is not surprising. This feature will mean that large turbine rings with small diameter fibers will behave differently from small turbine rings with large diameter fibers. The question of which is best is an interesting design issue.

In this paper, it is assumed that fibers are intact and stationary due to elastic constraint so that the matrix flows past the fibers, eventually, leading to a steady state flow rate. As noted previously, a tensile stress may develop in the fibers as a result of the stress gradient. When the fiber tensile stress is above a critical (statistical) value, the fiber fails. With a sufficient number of breaks, the fibers will be able to elongate effectively and therefore provide less constraint against radial matrix flow. Therefore, the interaction of fiber failure and radial matrix flow should be studied.

Another issue which has not been addressed in this paper is that the composite may be subjected to a transverse multiaxial stress state. In this situation, macroscopic multiaxial deviatoric stresses may develop. This will influence the plastic flow, creep and matrix flow past the fibers. Therefore, a multiaxial generalization of the creep law derived in this paper is required. This development will permit the use of the stress gradient model in realistic boundary value problems.

Acknowledgements

The work was sponsored by the Advanced Research Projects Agency through the University Research Initiative at the University of California, Santa Barbara (ONR Contract N-00014-92-J-1808). The ABAQUS finite element code was made available by Hibbitt, Karlsson and Sorensen Inc., Pawtucket, R. I. through an academic licence.

APPENDIX

The nesting character of surfaces of constant \bar{E} in macroscopic strain-rate space

In this Appendix we examine the nesting character of surfaces of constant $\bar{E}/\dot{\epsilon}_0$ in generalized macroscopic strain-rate space. We assume that the body experiences a set of generalized macroscopic strain-rates \dot{E}_i and denote the set of conjugate stresses by Σ_i . Following Cocks (1994) we can identify a macroscopic stress potential

$$(A1) \quad \Psi = \frac{1}{V} \int_{V_m} \psi dV$$

where

$$(A2) \quad \Psi = \frac{n}{n+1} \dot{\epsilon}_0 \sigma_0 \left(\frac{\dot{\epsilon}_e}{\dot{\epsilon}_0} \right)^{\frac{n}{n+1}}$$

and $\dot{\epsilon}_e$ is the von Mises effective strain-rate. Combining Eqs. (A1) and (A2) with Eq. (31) gives

$$(A3) \quad \bar{E} = \left(V^{-1} \int_{V_m} \dot{\epsilon}_e^{\frac{n+1}{n}} dV \right)^{\frac{n}{n+1}}$$

The convexity condition for the potential ψ is given by the inequality (Cocks, 1994)

$$(A4) \quad (\dot{\epsilon}_{ij}^1 - \dot{\epsilon}_{ij}^2) \frac{\partial \psi^1}{\partial \dot{\epsilon}_{ij}} + \psi^2 - \psi^1 \geq 0$$

where $\dot{\epsilon}_{ij}^1$ and $\dot{\epsilon}_{ij}^2$ are two arbitrary strain-rates and ψ^1 and ψ^2 are the associated stress potentials.

Now consider the situation where $\dot{\epsilon}_{ij}^1$ is the strain-rate field for $n = n_1$ and $\dot{\epsilon}_{ij}^2$ is the field for $n = n_2$, where $n_1 > n_2$, and that each field results in the same macroscopic strain rate \bar{E} . Integrating Eq. (4) over the volume and employing the principle of virtual power gives

$$(A5) \quad (\dot{E}_i^1 - \dot{E}_i^2) \Sigma_i^1 - \frac{n_1}{n_1 + 1} \dot{\epsilon}_0 \sigma_0 V^{-1} \\ \times \left[\int_{V_m} \left(\frac{\dot{\epsilon}_c^1}{\dot{\epsilon}_0} \right)^{\frac{n_1+1}{n_1}} dV - \int_{V_m} \left(\frac{\dot{\epsilon}_c^2}{\dot{\epsilon}_0} \right)^{\frac{n_1+1}{n_1}} dV \right] \geq 0.$$

Now, according to Eq. (A3)

$$(A6) \quad V^{-1} \int (\dot{\epsilon}_c^1)^{\frac{n_1+1}{n_1}} dV = \bar{E}^{\frac{n_1+1}{n_1}}$$

and

$$(A7) \quad V^{-1} \int (\dot{\epsilon}_c^2)^{\frac{n_1+1}{n_1}} dV = V^{-1} \int [(\dot{\epsilon}_c^2)^{\frac{n_2+1}{n_2}}]^{\frac{n_1+1}{n_2+1} \frac{n_2}{n_1}} dV \\ \leq \left[V^{-1} \int [(\dot{\epsilon}_c^2)^{\frac{n_2+1}{n_2}} dV \right]^{\frac{n_1+1}{n_2+1} \frac{n_2}{n_1}} = \bar{E}^{\frac{n_1+1}{n_1}}$$

where the inequality arises from Hardy *et al.* (1934) "general properties of means". Inequality (A6) then becomes

$$(A8) \quad (\dot{E}_i^1 - \dot{E}_i^2) \Sigma_i^1 \geq 0.$$

This is simply a statement of the fact that all strain-rate states \dot{E}_i^2 corresponding to the surface of constant \bar{E} for $n = n_2 (< n_1)$ lie inside the corresponding surface for $n = n_1$, i.e. surfaces of constant \bar{E} nest inside each other, with the surface for $n \rightarrow \infty$ forming the outer envelop.

REFERENCES

- ABAQUS User Manual, 1993, Hibbitt, Karlsson and Sorensen, Inc., 1080 Main Street, Pawtucket, R.I.
- BAO G., HUTCHINSON J. W., McMECKING R. M., 1991, Particle reinforcement of ductile matrices against plastic flow and creep, *Acta Metall. Mater.*, **39**, 1871.
- BROCKENBROUGH J. R., SURESH S., 1990, Plastic-deformation of continuous fiber-reinforced metal matrix composites-effects of fiber shape and distribution, *Scripta Metall. Mater.*, **24**, 325.
- CALLADINE C. R., DRUCKER D., 1962, Nesting surfaces of constant rate of energy dissipation in creep, *Q. Applied Math.*, **20**, 79.
- COCKS A. C. F., 1989, Inelastic deformation of porous materials, *J. Mech. Phys. Solids*, **37**, 693.
- COCKS A. C. F., 1994, The structure of constitutive laws for the sintering of fine grained materials, *Acta Metall. Mater.*, **42**, 2191.
- COCKS A. C. F., LECKIE F. A., 1987, Creep constitutive equations for damaged materials, *Advances in Applied Mechanics*, **25**, 239.
- DU Z.-Z., McMECKING R. M., 1994, Control of strength anisotropy of metal matrix fiber composites, *J. Computer-Aided Materials Design*, **1**, 243.

- DU Z.-Z., McMEEKING R. M., SCHMAUDER S., 1995, Transverse yielding and matrix flow past the fibers in metal matrix composites, *Mech. Mater.*, **21**, 159.
- DUVA J. M., 1986, A constitutive description of nonlinear materials containing voids, *Mech. Mater.*, **5**, 137.
- DUVA J. M., HUTCHINSON J. W., 1984, Constitutive potentials for dilutely voided nonlinear materials, *Mech. Mater.*, **3**, 41.
- GUNAWARDENA S. R., JANSON S., LECKIE F. A., 1993, Modeling of anisotropic behavior of weakly bonded fiber reinforced MMC's, *Acta Metall. Mater.*, **41**, 3147.
- HARDY G., LITTLEWOOD J. E., POLYA G., 1934, *Inequalities*, Cambridge University Press.
- HILL R., 1950, *The mathematical theory of plasticity*, Oxford University Press.
- HILL R., 1967, The essential structure of constitutive laws for metal composites and polycrystals, *J. Mech. Phys. Solids*, **15**, 79.
- NIMMER R. P., BANKERT R. J., RUSSELL E. S., SMITH C. A., WRIGHT P. K., 1991, Micromechanical modeling of fiber/matrix interface effects in transversely Loaded SiC/Ti-6-4 metal matrix composites, *J. Composites Technology and Research*, **13**, 3.
- ODQVIST F. K. G., 1966, *The mathematical theory of creep and creep rupture*, Oxford University Press.
- SOFRONIS P., McMEEKING R. M., 1992, Creep of power-law material containing spherical voids, *J. Appl. Mech.*, **59**, S88.
- ZAHL D. B., SCHMAUDER S., McMEEKING R. M., 1994, Transverse strength of metal matrix composites reinforced with strongly bonded continuous fibers in regular arrangements, *Acta Metall. Mater.*, **42**, 2983.

(Manuscript received August 8, 1995;
revised and accepted May 15, 1996.)

The Effects of a Single Mode III Loading Cycle on Mode I Crack Initiation and Growth Toughnesses in a Cross-Ply $[90^\circ/0^\circ]_{2s}$ Ti-6Al-4V/SiC_f Composite

S. V. KAMAT* AND J. P. HIRTH

*School of Mechanical and Materials Engineering
Washington State University
Pullman, WA 99164-2920*

F. W. ZOK

*Materials Department
University of California
Santa Barbara, CA 93106*

(Received August 25, 1995)
(Revised June 3, 1996)

ABSTRACT: The effects of a single Mode III loading cycle on the subsequent Mode I crack initiation and growth toughnesses in a cross-ply $[90^\circ/0^\circ]_{2s}$ Ti-6Al-4V/SiC_f composite have been investigated. A Mode III cycle with $\Delta J_{III} = 8 \text{ kJ/m}^2$ was found to have no measurable effect on either the initiation or growth toughnesses. In contrast, a Mode III cycle with $\Delta J_{III} = 14 \text{ kJ/m}^2$ resulted in a significant decrease in the subsequent Mode I crack initiation toughness. It also caused a reduction in the crack growth toughness until the crack had extended beyond the damage zone produced during the Mode III excursion. The results are rationalized on the basis of the fracture mechanisms as well as the deformation field produced by Mode III loading. The Mode III damage effect has implications for failure criteria for composites under multiaxial loading.

KEY WORDS: cross-ply $[90^\circ/0^\circ]_{2s}$ Ti-6Al-4V/SiC_f composite, Mode III loading cycle, Mode I crack initiation and growth toughnesses.

1. INTRODUCTION

THERE HAS BEEN considerable interest in unidirectional continuous fiber-reinforced titanium matrix composites (TMCs) for use in advanced aerospace applications, motivated by their attractive specific properties in the longitu-

*Presently on leave from Defence Metallurgical Research Laboratory, Hyderabad, India 500058.

dinal direction at ambient and elevated temperatures. However, these composites exhibit poor transverse properties, often being inferior to those of the matrix alone. Cross-ply composites are being considered as a viable alternative for applications requiring an increase in transverse properties, though the increase in the transverse properties is achieved at the expense of the longitudinal properties.

The tensile behavior (e.g., modulus, strength) of TMCs is relatively well understood. In contrast, the damage tolerance behavior is less well understood. An understanding of damage tolerance is essential for ensuring the reliability of TMCs in structural applications. Most of the work in this field has been focused on unidirectional composites [1–5], with smaller efforts on cross-ply materials [6–8]. The results indicate that the crack initiation and propagation mechanisms are strongly dependent on the fiber strength, interfacial shear strength and matrix toughness. Backuckas and Johnson [9] have presented a correlation of interfacial shear strength and crack growth in titanium matrix composites. Crack splitting, interfacial debonding, matrix plastic deformation and multiple fiber breakage are the major mechanisms operating within the crack tip damage zone in such composites.

However, structures for aerospace applications often experience multiaxial loading cycles which, in principle, could lead to a mixed mode cracking failure or to an influence of Mode II or III loading on a Mode I cracking failure. In recent years, several investigations [10–13] have shown that the *simultaneous* superposition of Mode I and Mode III loadings, i.e., mixed Mode I/III loading, results in a substantial reduction in the crack initiation toughness in some ductile materials. Kumar [14] has also shown that, in a high purity rotor steel, an application of *one* Mode III load cycle with $\Delta J = J_{IIIc}$ and $R = 0$ prior to a Mode I test results in a significant reduction in both the crack initiation and growth toughnesses: here the R -ratio is displacement based, that is the reverse loading restores the original specimen geometry. Similar effects might be anticipated for a metal matrix composite. Hence, the objective of the present study was to investigate the effects of a single Mode III loading cycle on the subsequent Mode I crack initiation and growth toughness in a cross-ply $[90^\circ/0^\circ]_2$, Ti-6Al-4V/SiC_f composite.

2. EXPERIMENTAL PROCEDURE

The material used in this investigation was a cross-ply $[90^\circ/0^\circ]_2$, Ti-6Al-4V/SiC_f composite. It was obtained in the form of 1.3 mm thick panels. The diameter of the sigma SiC fiber was 100 μm and the volume fraction was 32%. Prior to consolidation, the fibers had been coated with $\sim 1 \mu\text{m}$ of C, followed by $\sim 1 \mu\text{m}$ of TiB₂. The TiB₂ coating serves as a diffusion barrier between the fiber and the matrix. During consolidation, the TiB₂ reacts with the matrix to form a layer of TiB needles $\sim 0.7 \mu\text{m}$ thick. The uniaxial tensile behavior of this cross-ply composite has been characterized by Connell et al. [15]. The stress-strain curve is shown in Figure 1. The curve does not exhibit a well-defined yield point. Deviations from linearity begin to occur at relatively low stresses ($\approx 200 \text{ MPa}$), though the changes in tangent modulus are initially small. The tangent modulus eventually reaches a saturation value at a stress of $\approx 200 \text{ MPa}$, indicating that

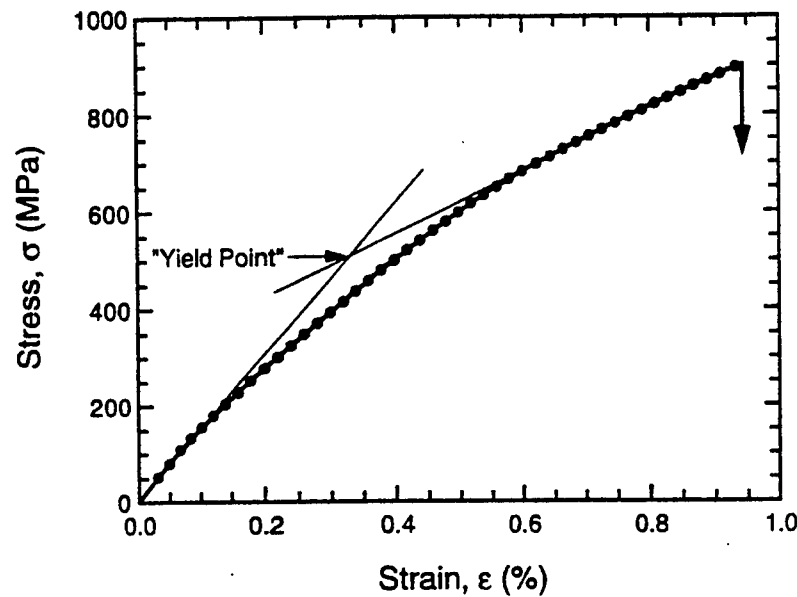


Figure 1. Tensile stress-strain curve.

the matrix has completely yielded and all additional stress is supported solely by the fibers aligned along the loading direction. Indeed, the saturation value ($d\sigma/d\epsilon = 60\text{--}65$ GPa) is in accord with the one calculated on the basis of the longitudinal fibers alone: $d\sigma/d\epsilon = fE_f/2 = 64$ GPa. In view of these complications, the yield point of the composite is defined as the intersection point between the two extrapolated linear portions of the curve, as shown by the lines in Figure 1. This yield point thus represents averages of the stress and strain at which yield occurs. The relevant tensile properties are summarized in Table 1.

The commonly used parameter for characterizing the toughness of fiber-reinforced composites is the work of rupture which is essentially the energy absorbed per unit area for the entire fracture process. This parameter is unable to distinguish the contributions to the total energy from the initiation and propagation stages. The present composite exhibits slow stable crack growth and small

Table 1. Tensile properties of cross-ply $[90^\circ/0^\circ]_2$, Ti-6Al-4V/SiC_f Composite.

Property	Value
Tensile strength	925 MPa
Yield stress	500 MPa
Yield strain	0.4%
Initial composite Young's modulus, E	155 GPa
Fiber Young's modulus, E_f	400 GPa
Poisson's ratio	0.19

scale bridging, i.e., the extent of bridging zone developed ahead of the crack is small [17]. Hence, a J -integral approach in accordance with the recommendations of ASTM standards E-813 [18] and E-1152 [19] for monolithic materials was adopted in this study.

A triple pant-leg specimen geometry, shown in Figure 2, was employed to determine the J - R curve. The specimens were pre-cracked by means of wire cut electrical discharge machining (EDM) which resulted in a notch root radius of 100 μm . As revealed in fractography presented subsequently, the initial crack tip position was predominantly in the matrix. The effects of notch root radius on the J - R curve for this composite have been discussed in an earlier study [17]. The primary reason for using a triple pant-leg specimen is that it is amenable to both Mode I as well as Mode III loading. When any two adjacent pant-legs are pin-loaded at holes A and B or B and C , as shown schematically in Figure 3, the triple pant-leg specimen becomes similar to a compact tension specimen used for conducting pure Mode I tests [18,19]. However, if the two outside pant-legs are fixed to a base using holes A and C , and the center leg is pulled, as shown schematically in Figure 4, pure Mode III loading is obtained at both crack tips.

An Instron 1361 testing machine was used for performing all the tests. A pure Mode III load was applied to the specimens, to either $J_{III}^{max} = 8 \text{ kJ/m}^2$ or 14 kJ/m^2 . The latter value was selected because it corresponds to a load where fiber cracking is audible. The loads were then reversed so that the displaced legs were restored to their original undeformed positions. This corresponds to essentially an application of one cycle of Mode III loading, with $\Delta J_{III} = 8 \text{ kJ/m}^2$ or 14 kJ/m^2 , respectively, at a displacement based R -ratio = 0. In both cases, there was no crack initiation as a result of the Mode III cycle. These specimens were

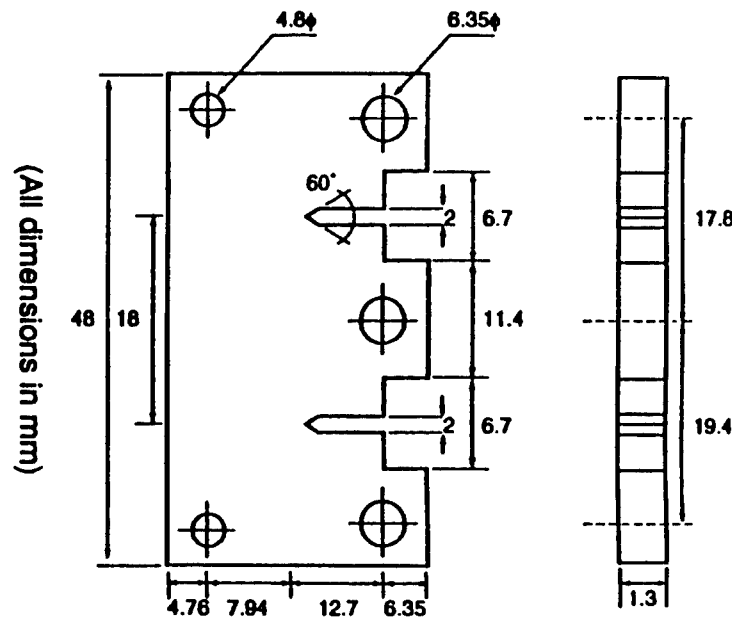


Figure 2. Triple pant-leg specimen geometry.

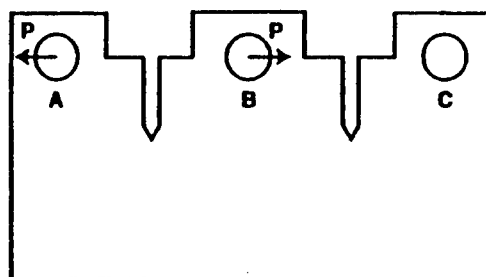


Figure 3. Schematic for applying Mode I loading to the triple pant-leg specimen.

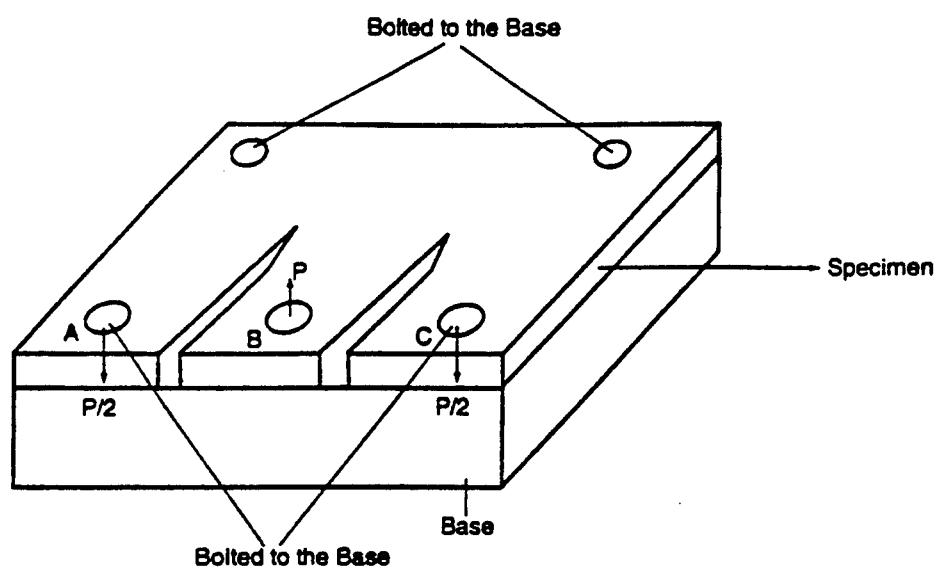


Figure 4. Schematic for applying Mode III loading to the triple pant-leg specimen.

then tested in pure Mode I loading to evaluate the effect of Mode III cycle on the Mode I fracture resistance curve. For comparison, one specimen was also tested in pure Mode I loading without any prior Mode III loading ($\Delta J_{III} = 0$).

The Mode I tests were performed by means of a single specimen unloading compliance technique, as per the recommendations of ASTM E-813 [18] and E-1152 [19] and the details are given in Reference [17]. The broken specimens were also examined in the scanning electron microscope to observe the fracture features.

3. RESULTS

The J - Δa plots for the three tests with $\Delta J_{III} = 0, 8$ or 14 kJ/m^2 are illustrated in Figure 5. A blunting line with a slope of $2\sigma_f = (\sigma_{ys} + \sigma_{UTS})$ was superimposed on this plot (σ_{ys} is the yield strength and σ_{UTS} is the ultimate tensile strength). Exclusion lines with the same slope as the blunting line offset by 0.15 mm, 0.20 mm and 1.5 mm were also superimposed on the plot. A power law equation was fit to the data points lying between the 0.15 mm and 1.50 mm exclusion lines. The intersection of the fitted power-law curve with the 0.20 mm exclusion line was taken as the crack initiation toughness (J_{IC}). For all cases, the condition for J -dominance

$$b, a \geq \frac{200J_{IC}}{\sigma_f} \quad (1)$$

where b is the ligament ahead of the crack and a is the crack length, as well as the condition for plane strain

$$B \geq \frac{25J_{IC}}{\sigma_f} \quad (2)$$

where B is the specimen thickness, were satisfied.

The effect of the prior Mode III excursion on the subsequent Mode I initiation toughness is shown in Figure 6. The Mode I data is for two tests which agreed within 10 percent, typical of tests of this type [15]. The other points are for one test. Hence, Figure 6 is presented as a trend line to emphasize the drop in toughness with $\Delta J_{III} = 14 \text{ kJ/m}^2$ and not as an extrapolated curve. The data show that a prior Mode III cycle with $\Delta J_{III} = 8 \text{ kJ/m}^2$ has no effect on the crack initiation toughness whereas a cycle with $\Delta J_{III} = 14 \text{ kJ/m}^2$ results in a reduction in the initiation toughness of $\sim 20\%$.

The crack growth toughness is characterized in terms of the slope of the J - Δa curve (dJ/da). The slope was evaluated by means of a power-law fit to the data in Figure 5, resulting in an equation that could be differentiated and plotted as a function of crack extension, Δa . The variation of dJ/da with Δa is illustrated in Figure 7 for the three tests: the data points are arbitrarily selected from the power law fit and therefore need not correspond to those in Figure 5. In all cases, the crack growth toughness is high initially and decreases gradually with increasing

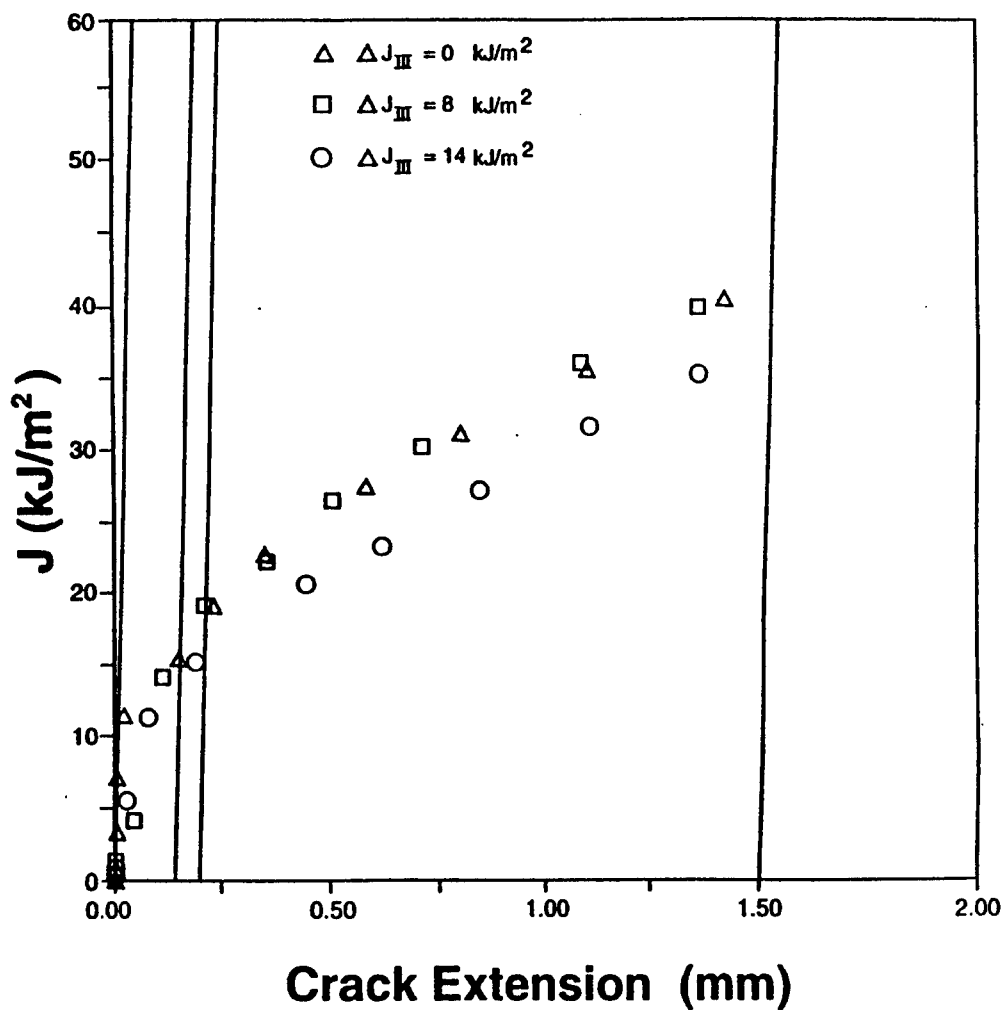


Figure 5. J- Δa plots for the three tests with different prior Mode III cycles.

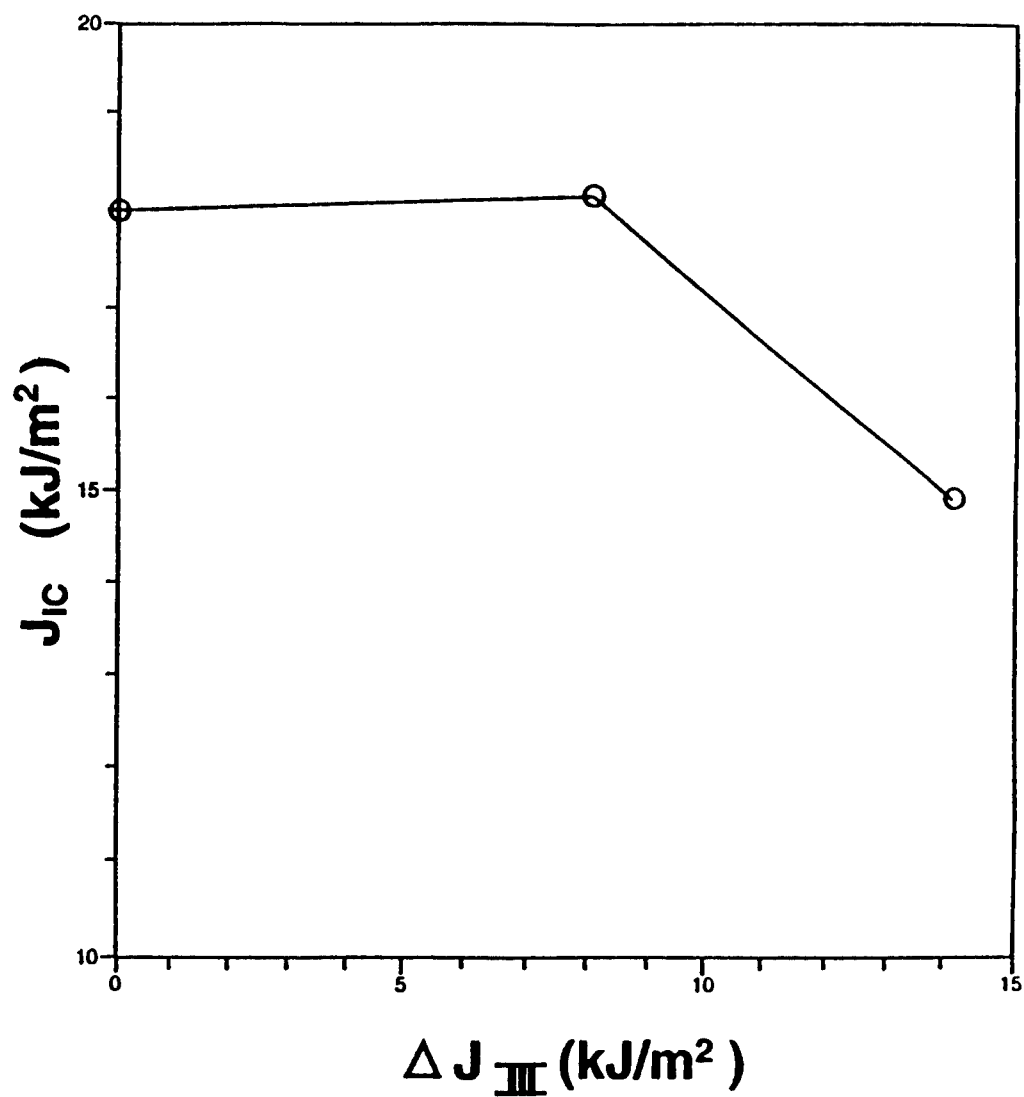


Figure 6. Mode I crack initiation toughness versus ΔJ_{III} .

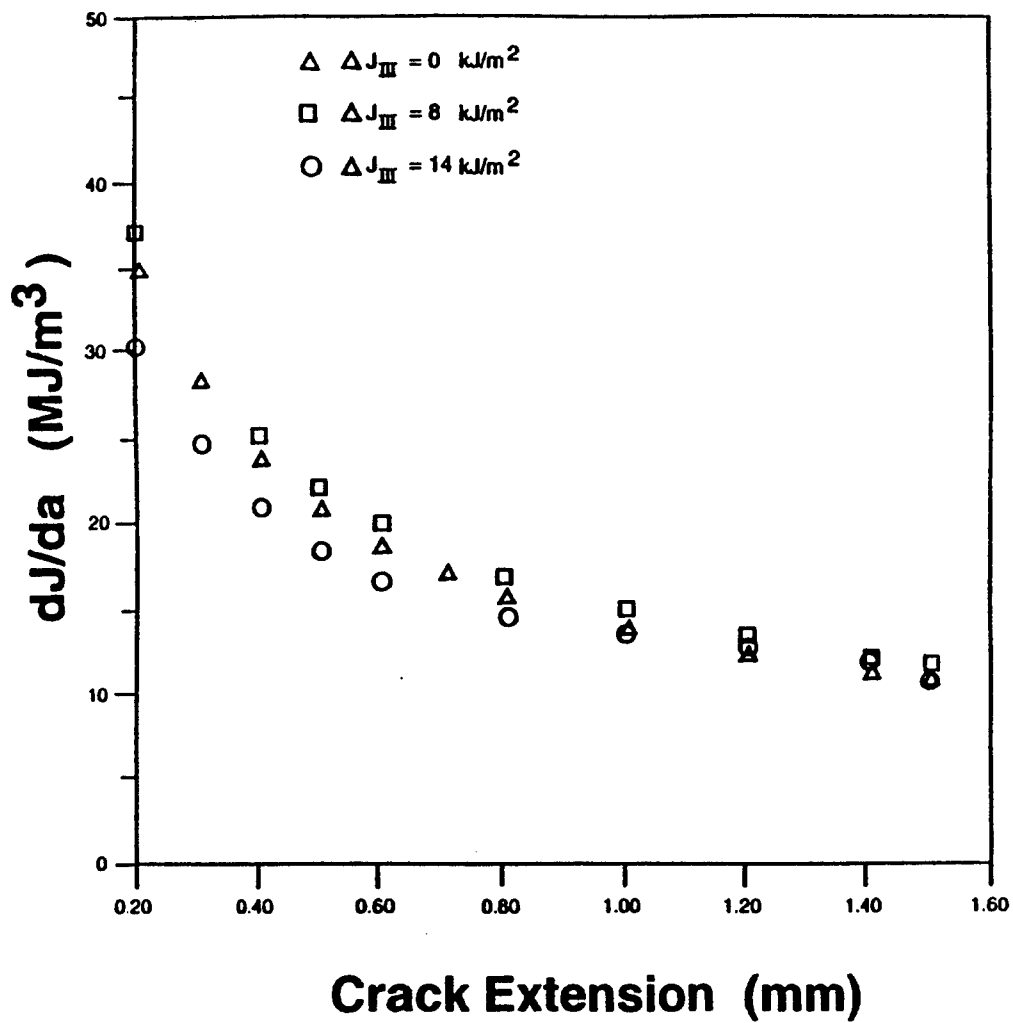


Figure 7. Crack growth toughness versus crack extension for the three tests with different prior Mode III damage.

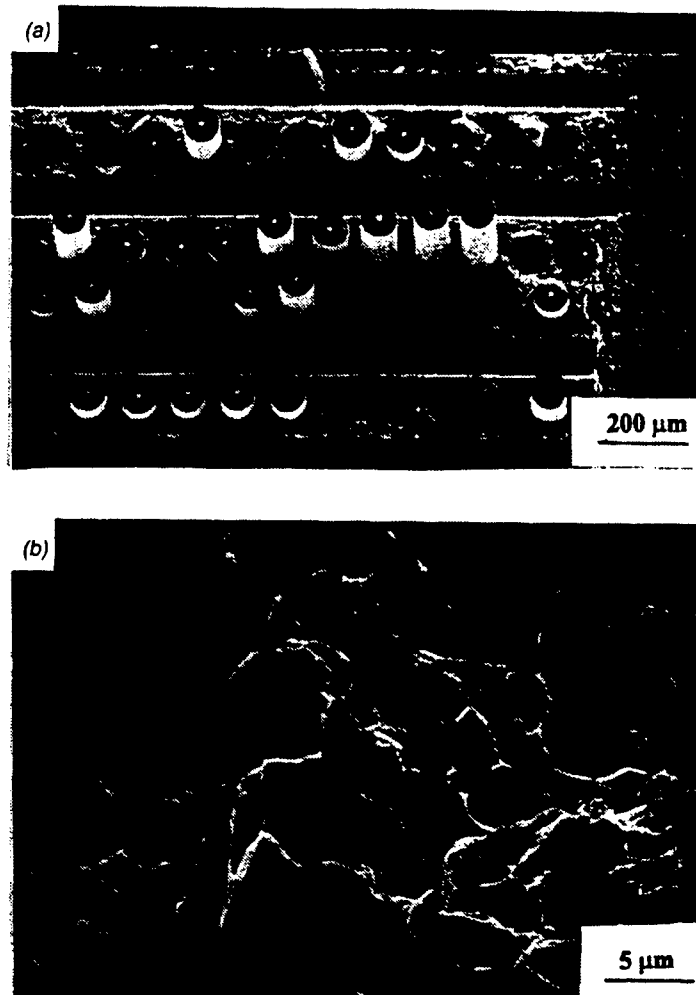


Figure 8. SEM fractographs for the specimen with $\Delta J_{III} = 0$; (a) low magnification and (b) high magnification.

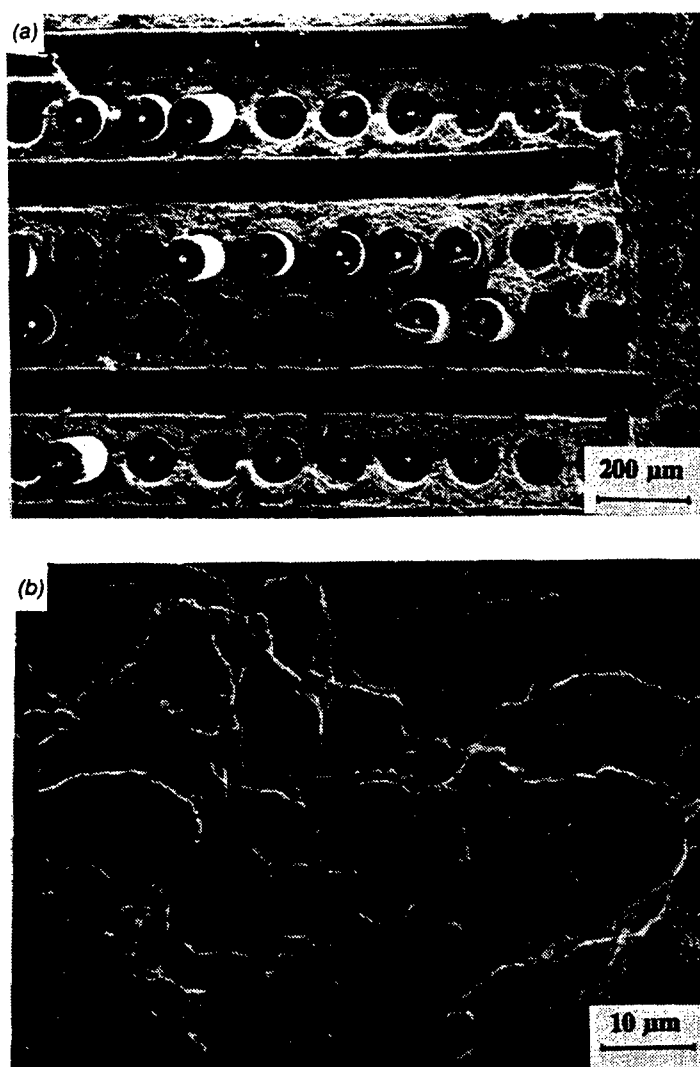


Figure 9. SEM fractographs for the specimen with $\Delta J_{III} = 14 \text{ kJ/m}^2$; (a) low magnification and (b) high magnification.

crack extension. In the specimen with $\Delta J_{III} = 8 \text{ kJ/m}^2$, the crack growth toughness is marginally higher than that in the specimen with $\Delta J_{III} = 0$, especially for small crack extensions; however, the differences are rather small ($\sim 5\%$). In contrast, a prior Mode III cycle with $\Delta J_{III} = 14 \text{ kJ/m}^2$ results in a reduction in the crack growth toughness (compared to that in the specimen with $\Delta J_{III} = 0$) in the initial stages of crack extension, by $\sim 15\%$. However, beyond a crack extension of $\sim 1 \text{ mm}$, the crack growth toughnesses for the two specimens become more or less the same. The strict condition for J_R -controlled crack growth [20]

$$-\frac{b}{J_{Ic}} \left(\frac{dJ}{da} \right) \geq 40 \quad (3)$$

is not quite satisfied for any of the specimens because b is not large enough. Hence, the magnitudes of the crack growth toughness should be considered only for the purpose of qualitative comparisons.

Representative scanning electron micrographs for specimens with $\Delta J_{III} = 0$ and $\Delta J_{III} = 14 \text{ kJ/m}^2$ are shown in Figures 8 and 9, respectively. The initial crack tip positions are shown at the right side of Figures 8(a) and 9(a). In both figures, a and b correspond to low and high magnifications, respectively. The fracture features for the specimen with $\Delta J_{III} = 8 \text{ kJ/m}^2$ are so closely similar to those shown in Figure 8 for $\Delta J_{III} = 0$ that a separate figure is not included. Figures 8(b) and 9(b) show that the matrix alloy (Ti-6Al-4V) fails by a ductile mechanism of void nucleation, growth and coalescence in all cases in the stable crack growth regime. There are minor variations in the matrix crack topography with regard to the presence of shear ridges and the degree of planarity, but these did not vary systematically with the different loading: the major difference is in the degree of fiber pullout. There is a clear difference in the degree of fiber pullouts in Figures 8(a) and 9(a), with only a few fibers failing near the crack plane for Figure 8(a) while most of those in Figure 9(a) exhibit little pullout. For specimens with $\Delta J_{III} = 0$ or 8 kJ/m^2 , the SiC fibers parallel to the Mode I loading direction generally fail away from the matrix crack plane and therefore undergo pullout prior to complete separation. The pullout length appears to be of the order of 1–2 fiber diameters on average. In contrast, in the specimen with prior $\Delta J_{III} = 14 \text{ kJ/m}^2$, most of the fibers parallel to the Mode I loading direction are fractured in the crack plane without any apparent pullout over a distance of $\sim 1 \text{ mm}$ from the notch tip [Figure 9(a)]. Beyond 1 mm, more fiber pullout similar to that seen in the other specimens is evident [Figure 9(a)]. In all specimens, the fibers normal to the Mode I loading direction debond from the matrix, leaving either the entire fiber or a corresponding matrix trough on the fracture surface.

4. DISCUSSION

The effects of Mode III excursions on the Mode I fracture resistance can be rationalized in terms of the deformation fields ahead of the crack as a result of Mode I and Mode III loading. The shear strains ahead of a Mode I and Mode III cracks have been calculated by Kumar [21] using the FEM stress distribution

results of Pan and Shih [22]. The variation of shear strains with the angular coordinate θ is shown in Figure 10. The shear strain associated with Mode I loading (ϵ_{xz}) is spread out in a fan inclined to the crack plane at $45^\circ < \theta < 135^\circ$ (producing the traditional kidney bean shaped plastic zone). In contrast, the shear strain (ϵ_{yz}) associated with Mode III loading is concentrated in the trajectory of the crack plane ($\theta = 0^\circ$). The magnitude of the shear strains scale with the applied J through the relations

$$\begin{aligned}\epsilon_{xz} &\propto (J_I)^{1/N+1} \\ \epsilon_{yz} &\propto (J_{III})^{1/N+1}\end{aligned}\quad (4)$$

where N is the strain hardening exponent.

The fracture surface observations (Figure 8) for the specimen with no prior Mode III damage indicated the crack initiation toughness is primarily governed by the matrix ductile fracture whereas the crack growth toughness is dependent on the matrix ductile fracture as well as the contributions from fiber pullout. Let us now consider the influence of a Mode III cycle on the fracture process. When a Mode III cycle is imparted on the specimen, a plastic zone is developed at the crack tip. The size of the plastic zone at the maximum load is given by

$$r_y^{max} = \frac{1}{6\pi} \left(\frac{J_{III}^{max} E}{\tau_f^2} \right) \frac{1}{1 - \nu^2} \quad (5)$$

where E is the elastic modulus, ν is the Poisson's ratio and $\tau_f = \sigma_f/2$ is the shear flow stress. The sizes of the plastic zones developed for the specimens with

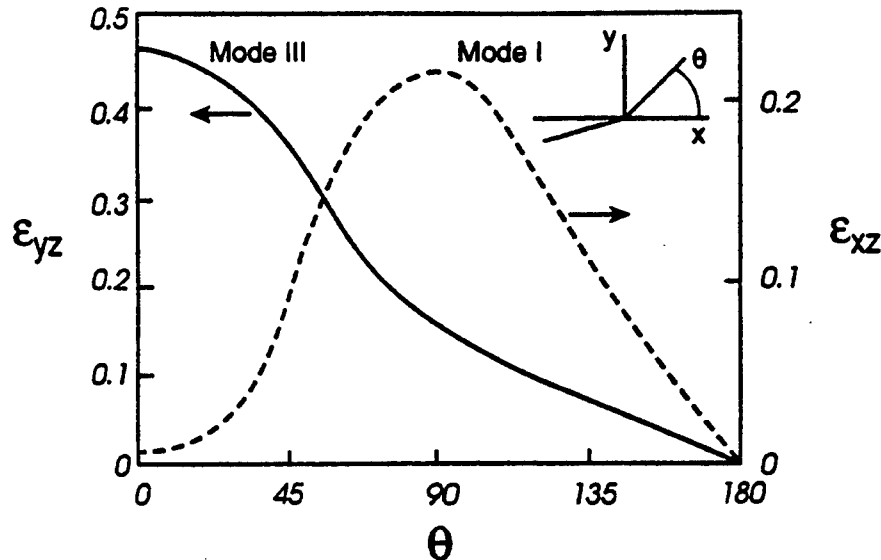


Figure 10. Normalized plastic shear strains plotted as a function of angular coordinate θ .

$\Delta J_{III} = 8 \text{ kJ/m}^2$ and 14 kJ/m^2 are approximately 0.56 mm and 1.0 mm, respectively. The localized shear strain (ϵ_{yz}) discussed earlier is effective within this plastic zone and can induce large stresses within SiC fibers in the trajectory of the crack because of strain incompatibility [23]. When the shear strain exceeds a critical value, the stresses become sufficiently large to cause fiber fracture. The fracture surface observations [Figures 8(a) and 9(a)] indicate that localized shear strain resulting from the Mode III excursion is sufficient to cause fiber fracture for $\Delta J_{III} = 14 \text{ kJ/m}^2$ but not for $\Delta J_{III} = 8 \text{ kJ/m}^2$. A second effect which can arise because of the Mode III cycle is the development of compressive residual stresses at the pre-crack tip because of the shrinking of the plastic zone on unloading. The magnitude of those stresses is expected to scale with the applied ΔJ_{III} .

The mode III loading affects the subsequent Mode I fracture resistance in the following way. For $\Delta J_{III} = 8 \text{ kJ/m}^2$, there is no damage zone formed, and thus the crack initiation and growth toughnesses should be similar to that of the undamaged specimen ($\Delta J_{III} = 0$), in accord with the experimental results (Figures 6 and 7). The marginally higher initiation and initial growth toughnesses may be attributed to the compressive residual stresses at the pre-crack tip, which cause a small closure effect. In contrast, for the specimen with $\Delta J_{III} = 14 \text{ kJ/m}^2$, the beneficial effect of the compressive residual stresses is outweighed by the deleterious effect of fiber fracture within the plastic zone. The fractured fibers act as favorable sites for void initiation and should thus cause a reduction in the crack initiation toughness. This is observed experimentally (Figure 6). The presence of the fractured fibers should also significantly reduce the contributions of fiber pullout and crack bridging towards the growth toughness. This, too, is observed experimentally (Figure 7). One would also expect, that once the crack extends beyond the Mode III damage zone, the growth toughness should match that for the undamaged specimen. Indeed, Figure 7 shows that, beyond 1 mm crack extension, the growth toughnesses for the two specimens become similar.

These results imply that a prior Mode III cycle can cause a reduction in the subsequent Mode I crack initiation and growth toughness of cross-ply $[90^\circ/0^\circ]_2$, Ti-6Al-4V/SiC_f composite provided that the amplitude of the Mode III cycle exceeds a critical value. At present this indication is not quantitative for growth because the condition for J -dominance was not satisfied since the requisite material was unavailable. In the future one could eliminate this problem by testing material with larger w so that Equation (3) would be satisfied.

5. CONCLUSIONS

1. A prior Mode III cycle with $\Delta J_{III} = 8 \text{ kJ/m}^2$ has only a marginal effect on the subsequent Mode I crack initiation and growth toughness in a cross-ply $[90^\circ/0^\circ]_2$, Ti-6Al-4V/SiC_f composite.
2. A prior Mode III cycle with $\Delta J_{III} = 14 \text{ kJ/m}^2$ results in a reduction in the subsequent Mode I crack initiation toughness. It also causes a reduction in the crack growth toughness until the Mode I crack extends beyond the damage zone produced as a result of the Mode III loading.

ACKNOWLEDGEMENT

The authors are grateful for the support of this work under the Advanced Research Project Agency, University Research Initiative, under Office of Naval Research Contract No. 00014-93-I-0213.

REFERENCES

1. Jeng, S. M., J.-M. Yang and C. J. Yang. 1991. *Mater. Sci. Eng.*, A138:181-190.
2. Jeng, S. M., P. Allassoeur and J.-M. Yang. 1992. *Mater. Sci. Eng.*, A154:11-19.
3. Yang, J.-M. and S. M. Jeng. 1992. *JOM*, 44(6):52-57.
4. Backuckas, J. G., Jr., J. Awerbuch, T. M. Tan and A. C. W. Lau. 1993. *ASTM STP 1189*, pp. 713-720.
5. Connell, S. J., F. W. Zok, Z. Z. Du and Z. Suo. 1994. *Acta Metall. Mater.*, 42:3451-3461.
6. Chiu, H. P., S. M. Jeng and J.-M. Yang. 1994. *J. Mater. Res.*, 9:1767-1774.
7. Backuckas, J. G., Jr., W. S. Johnson and C. A. Bigelow. 1993. *J. Eng. Mater. Tech.*, 115:404-409.
8. Johnson, W. S., S. J. Lubowinski and A. L. Highsmith. 1990. *ASTM STP 1080*, pp. 193-218.
9. Backuckas, J. G., Jr. and W. S. Johnson. 1994. *NASA Tech. Memorandum 109082*, NASA Langley Research Center.
10. Raghavachary, S., A. R. Rosenfield and J. P. Hirth. 1990. *Metall. Trans.*, 21A:2539-2545.
11. Gordon, J. A., J. P. Hirth, A. M. Kumar and N. E. Moody. 1992. *Metall. Trans.*, 23A:1013-1020.
12. Feng, X., A. M. Kumar and J. P. Hirth. 1993. *Acta Metall. Mater.*, 41:2755-2764.
13. Kamat, S. V. and J. P. Hirth. 1996. *Acta Metall. Mater.*, 44:1047-1054.
14. Kumar, A. M. Unpublished research.
15. Connell, S. J. and F. W. Zok. Unpublished research.
16. Jansson, S., H. E. Deve and A. G. Evans. 1991. *Metall. Trans.*, 22A:2975-2984.
17. Kamat, S. V., J. P. Hirth and F. W. Zok. 1996. *Acta Metall. Mater.*, 44:1831-1838.
18. ASTM E-813. 1994. *Annual Book of Standards*, Philadelphia, v. 3.01, pp. 628-642.
19. ASTM E-1152. 1994. *Annual Book of Standards*, Philadelphia, v. 3.01, pp. 744-754.
20. Broek, D. 1986. *Elementary Engineering Fracture Mechanics*. Dordrecht: Martinus Nijhoff Publishers, p. 249.
21. Kumar, A. M. Unpublished research.
22. Pan, J. and C. F. Shih. 1990. *J. Mech. Phys. Solids*, 38:161-181.
23. Lee, T. D., T. Goldberg and J. P. Hirth. 1979. *Metall. Trans.*, 14A:199-208.



A Shear Lag Model For a Broken Fiber Embedded in a Composite with a Ductile Matrix

by

Chad M. Landis

and

Robert M. McMeeking

Department of Mechanical and Environmental Engineering

University of California, Santa Barbara 93106

October 1997

ABSTRACT

A shear lag model is developed to predict the stress recovery in a broken fiber embedded in a ductile matrix composite. The model builds on the original shear lag model of Cox (1) by introducing plasticity constitutive behavior into the matrix. The matrix is assumed to be an elastic-perfectly plastic material that deforms according to J_2 flow theory. The use of a flow rule to govern the matrix deformation in this model differs from previous attempts to represent plasticity in the matrix. A non-linear partial differential equation is obtained from the model. Numerical solutions to the equations are obtained and compared to simpler shear lag models which assume sliding at the fiber-matrix interface controlled by a uniform shear stress. Axisymmetric finite element calculations were done to assess the validity of the shear lag model. It proves to be in good agreement with the finite element analysis. Predictions of the shear lag calculations suggest that the global load sharing strength model of Curtin (2) is valid for a composite with a yielding matrix that is elastically rigid.

I. INTRODUCTION

Fibrous composite materials utilize a weak matrix reinforced by strong, elastically stiff fibers. Predicting the mechanical properties of the composite requires a detailed understanding of the stress and strain states in the constituent materials. Due to the complex geometry of composite materials, it is a formidable endeavor to solve the governing equations of solid mechanics in closed form. Further complications arise when the statistical nature of the fibers is considered. During loading weak fibers will fail first, and an understanding of the resulting stresses in the reinforcements is required to predict the strength of the composite.

The term shear lag has been used to describe models that represent fibers as one dimensional axial load carrying springs. Other simplifications can be made, but the universal characteristic of shear lag models is that a three dimensional fiber or laminate is assumed to act like a one dimensional entity. Shear lag models of varying degrees of complexity have been used to determine the stresses in a broken fiber. The first model we discuss is the simple shear sliding model (Kelly and Tyson (3)). This version assumes that the stress in the broken fiber recovers to the far field applied stress through the action of a constant sliding stress. The slip length, L_s , axial stress, σ_f , and shear stress, τ , along the fiber are:

$$L_s = \frac{D E_f \epsilon}{4 \tau_0} \quad (1)$$

$$\sigma_f = \begin{cases} 4\tau_0 \frac{z}{D}, & 0 \leq z \leq L_s \\ E_f \epsilon, & L_s \leq z \leq \infty \end{cases} \quad (2)$$

$$\tau = \begin{cases} -\tau_0, & 0 \leq z \leq L_s \\ 0, & L_s \leq z \leq \infty \end{cases} \quad (3)$$

where D is the fiber diameter, E_f is the Young's modulus of the fiber, ϵ is the strain applied to the composite in the fiber direction, τ_0 is the level of the shear sliding resistance, and z is the axial coordinate along the fiber with the origin located at the break as shown in Figure 1. This model of the fiber stress distributions was used by Curtin (2) to predict the strength of a uniaxially reinforced composite under the assumptions of global load sharing.

However, the first shear lag model in the literature was developed by Cox (1), to determine the stresses in a fiber embedded in an elastic matrix. The results for the axial and shear stresses along an infinite fiber are:

$$\sigma_f = E_f \epsilon \left[1 - \exp \left(-2 \sqrt{\frac{G_m D}{E_f w}} \frac{z}{D} \right) \right] \quad (4)$$

$$\tau = -\frac{1}{2} E_f \epsilon \sqrt{\frac{G_m D}{E_f w}} \exp \left(-2 \sqrt{\frac{G_m D}{E_f w}} \frac{z}{D} \right) \quad (5)$$

where G_m is the shear modulus of the matrix, and w is a measure of the fiber spacing, also as shown in Figure 1. The Cox model assumes that the interface between the fiber and matrix is well bonded. Hedgepeth and van Dyke (4) modeled plasticity in a multiple fiber system by limiting the allowable shear stress on a fiber. Recently, Beyerlein and Phoenix (5) studied plasticity and debonding in a similar fashion in two dimensional composite systems. This type of model for plasticity does not require a flow rule and we will refer to it as shear sliding. Shear sliding can be added to Cox's model by limiting the shear stress at the interface to a prescribed value of τ_0 . The results for the slip length, and stresses for this model are:

$$L_s = \frac{D}{4} \left(\frac{E_f \epsilon}{\tau_0} - 2 \sqrt{\frac{E_f w}{G_m D}} \right) \quad (6)$$

$$\sigma_f = \begin{cases} 4\tau_0 \frac{z}{D}, & 0 \leq z \leq L_s \\ E_f \epsilon - 2\tau_0 \sqrt{\frac{E_f w}{G_m D}} \exp \left[2 \sqrt{\frac{G_m D}{E_f w}} \left(\frac{L_s}{D} - \frac{z}{D} \right) \right], & L_s \leq z \leq \infty \end{cases} \quad (7)$$

$$\tau = \begin{cases} -\tau_0, & 0 \leq z \leq L_s \\ -\tau_0 \exp \left[2 \sqrt{\frac{G_m D}{E_f w}} \left(\frac{L_s}{D} - \frac{z}{D} \right) \right], & L_s \leq z \leq \infty \end{cases} \quad (8)$$

Note that if $\epsilon \leq 2 \frac{\tau_0}{E_f} \sqrt{\frac{E_f w}{G_m D}}$ then $L_s=0$ and the axial stress and shear stress are given by (4) and

(5). While the model does limit the shear stress to a prescribed yield strength, no flow rule is used to determine the evolution of the deformation. In Cox's model equilibrium in the matrix requires that the shear stress in the matrix decreases with radial distance from the fiber. This implies that plasticity occurs in a very thin layer around the broken fiber, and that the rest of the matrix is elastic.

Alumina fibers in an aluminum matrix is an example of a composite that uses strong, brittle fibers to reinforce a weak, ductile matrix. During cooling from high temperatures after processing, the thermal expansion mismatch of the alumina fibers and the aluminum matrix causes the fibers to be in a state of residual compression, and the matrix to be in tension. When the composite is loaded no fibers will break at least until the residual compression is relieved. At the applied strain when the first fiber breaks it is very likely that the matrix has yielded in tension. In this system it is unrealistic to assume that the matrix is elastic, and that yielding only occurs locally near fiber breaks. In order to account for load redistribution around a broken fiber

in the presence of gross yielding, a flow rule must be introduced to govern the deformation of the matrix. This work attempts to introduce such a constitutive behavior in the context of the shear lag framework. The model is then compared to the other shear lag models, as well as to axisymmetric finite element calculations.

II. SHEAR LAG MODELS

In this section the basic shear lag governing equations are developed. The differences between shear lag models arise due to differences in the assumed matrix constitutive behavior (elastic, plastic, creeping), and the interface behavior (weakly bonded vs. well bonded). The assembly of a shear lag model results in a governing differential equation for the fiber displacement, u , as a function of the distance from the break, z , and possibly a time variable, t . Simplifications must be made such that all of the field variables, σ_{ij} , ϵ_{ij} , and u_i , can be related to the fiber displacement, u , and other variables that are parameters of the model.

2.1 Model Geometry

The derivation in this paper is for a cylindrical fiber system, but the equations are easily adapted to a two dimensional slab geometry, representative of laminated composites. Consider the cell shown in Figure 1. The fiber break is located at $z=0$. For a hexagonal array of fibers the cell is idealized to be circular and cylindrical. The outer surface of the cell just touches the edges of the six nearest neighbor fibers. The distance between fiber surfaces can be related to the fiber volume fraction, f , by

$$w = D \left(\frac{1}{\sqrt{f}} \sqrt{\frac{\pi}{2\sqrt{3}}} - 1 \right). \quad (9)$$

2.2 Equations common to all shear lag models

Equilibrium of forces acting on a differential element of fiber requires that

$$\frac{\partial \sigma_f}{\partial z} = -4 \frac{\tau}{D} \quad (10)$$

where σ_f is the average axial stress in the fiber, and τ is the shear stress acting on the interface between the fiber and the matrix. Hooke's Law for the fiber gives

$$\sigma_f = E_f \frac{\partial u}{\partial z} \quad (11)$$

where u is the axial displacement of the fiber, and $\frac{\partial u}{\partial z}$ is the axial strain in the fiber. The standard shear lag statement that relates the shear stress at the fiber/matrix interface, τ , to the fiber displacement, u , is obtained by substituting (11) into (10). It is given by

$$\tau = -\frac{1}{4} D E_f \frac{\partial^2 u}{\partial z^2}. \quad (12)$$

The fiber is considered to be a one dimensional entity such that the only quantities of interest are the axial stress, strain, and displacement. The radial, hoop, and shear stresses within the fiber are not considered in the model. Equations (11) and (12) characterize the stress states of the fiber and fiber/matrix interface in terms of the fiber displacement. To complete the model, the field quantities in the matrix must now be related to the fiber displacement.

The first approximation common to many shear lag models (Cox (1); Du and McMeeking(6)) is that the axial displacement at the outer boundary of the cell is equivalent to the displacement that would exist in an undamaged composite at the same applied strain. Taking the fiber break to be the origin of the z axis, as shown in Figure 1, this condition is given by

$$u_c = \epsilon z \quad (13)$$

where u_c is the displacement of the outer boundary, and ϵ is the nominal composite strain.

The second assumption involves approximating the shear strain at the fiber/matrix interface. The simplest approximation, used by Du and McMeeking (6), is that

$$\gamma = \frac{u_c - u}{w} \quad (14)$$

where γ is the shear strain at the interface. Equation (14) is an excellent approximation for a two dimensional geometry. Cox (1) accounted for the axisymmetric geometry in an approximate fashion by considering equilibrium of the matrix in the axial direction. The result is that in equation (14), w is replaced by $\frac{D}{2} \ln\left(\frac{2w + D}{D}\right)$. This is a small correction for high volume fractions. For simplicity, this correction has been left out of the model that will be presented.

Equations (9) through (14) are the starting point for any shear lag model that attempts to describe the stress distribution in a broken fiber. The remaining pieces of information needed to formulate a governing differential equation are the matrix constitutive law, and the fiber/matrix interface behavior. When the applied strain is high enough to cause fibers to break, the matrix has usually failed in tension by cracking or yielding. It is assumed therefore, that the matrix is not able to directly carry any of the load shed by the broken fiber, but can only transmit it by

shear stress to other fibers. Therefore, the purpose of the matrix constitutive law is to relate the shear stress in the matrix to the shear strain.

2.3 Shear Lag Constitutive Law for a Well Bonded Fiber in an Elastic-Perfectly Plastic Matrix

The constitutive law used is for an elastic-perfectly plastic material with deformation governed by J_2 flow theory (Hill (7)). The Young's modulus of the material is E_m , and the yield stress is σ_y . For simplicity it is assumed that the material is always on the yield surface. For most systems of interest this is a good assumption for one of two reasons. First, residual thermal stresses can cause the matrix to yield prior to any loading. Second, if it did not yield upon cooling, the matrix has usually yielded in tension when enough strain has been applied to break a fiber. A simple state of stress is assumed to exist in the matrix near the fiber/matrix interface, namely an axial stress acting in the z direction and a shear stress as depicted in Figure 1. Again, radial and hoop components of stress are not considered in the model. The yield condition is therefore,

$$\sigma_y = \sqrt{\sigma_m^2 + 3\tau^2} \quad (15)$$

where σ_m is the axial stress in the matrix and τ is the shear stress acting on the fiber/matrix interface. The strain rates in the matrix are given by J_2 flow theory and elasticity,

$$\dot{\epsilon}_m = \frac{\dot{\sigma}_m}{E_m} + \frac{2}{3}\sigma_m\lambda \quad (16)$$

$$\dot{\gamma} = \frac{\dot{\tau}}{G_m} + 2\tau\lambda \quad (17)$$

where ϵ_m is the axial strain in the matrix at the interface, γ is the shear strain in the matrix at the interface, λ is a proportionality factor enforcing normality of plastic strains to the yield surface, and the superposed dot represents differentiation with respect to time. Note that this time does not necessarily correspond to natural time, but is a loading parameter.

Equations (16) and (17) can be combined to eliminate λ , yielding an equation governing the matrix response

$$\frac{3\tau\dot{\sigma}_m}{E_m} - \frac{\sigma_m\dot{\tau}}{G_m} = 3\tau\dot{\epsilon}_m - \sigma_m\dot{\gamma}. \quad (18)$$

From (15), it can be shown that $\dot{\sigma}_m = \frac{-3\tau}{\sigma_m}\dot{\tau}$. With the use of $\epsilon_m = \frac{\partial u}{\partial z}$ at the interface and equations (12) through (14), equation (18) becomes the governing partial differential equation for $u(z,t)$

$$\left(\frac{9}{4}D \frac{E_f}{E_m} \tau^2 + \frac{1}{4}D \frac{E_f}{G_m} \sigma_m^2 \right) \frac{\partial^2 \dot{u}}{\partial z^2} - 3\tau\sigma_m \frac{\partial \dot{u}}{\partial z} - \frac{\sigma_m^2}{w} (\dot{u} - \dot{\epsilon}z) = 0 \quad (19)$$

It is important to note that $\dot{\epsilon}$ is the nominal composite strain rate. At first glance (19) may appear to be a linear partial differential equation for $u(z,t)$. However, all of the coefficients of the derivatives contain τ or σ_m . Equation (15) relates σ_m to τ , and τ is related to u by (12). Thus

the coefficients of the derivatives are actually non-linear functions of $\frac{\partial^2 u}{\partial z^2}$, and consequently equation (19) is highly non-linear.

Boundary conditions are needed at $z=0$ and at $z \rightarrow \infty$. At the fiber break the axial stress in the fiber is zero, and far from the break the fiber strain must be equal to the applied composite strain. Mathematically these boundary condition are:

$$E_f \frac{\partial u}{\partial z}(z = 0) = 0 \quad (20)$$

$$\frac{\partial u}{\partial z}(z \rightarrow \infty) = \epsilon. \quad (21)$$

A time history for the applied strain must also be specified. The key variables that must be specified in the time history are the strain at which the fiber breaks and the strain to which the composite is extended after the fiber breaks. Equation (19) is solved by a finite difference scheme that is described in the Appendix.

Figures 2 and 3 illustrate the stress profiles immediately after fracture for fibers that have broken at various different composite strain levels with $\frac{E_f}{E_m}=5$, and $f=0.5$. The shear stress versus distance from the break plots of Figure 2 consist of three regions. The slip zone is where the shear stress is almost uniform at the value $\tau = \tau_y = \frac{\sigma_y}{\sqrt{3}}$. The non-linear recovery region is where there is a non-linear transition from the maximum plateau shear stress to nearly zero shear stress. Finally, the third region is where the shear stress is essentially zero. The shear stress approaches τ_y only asymptotically near the break, and approaches zero asymptotically far from the break. Therefore, the entire curve actually lies in the non-linear region. For practical considerations the non-linear recovery region is taken to be finite with boundaries at the position where $\tau = 0.99\tau_y$ and $\tau = 0.01\tau_y$. Notice that the non-linear recovery zone does not change

size or shape as the applied strain when the break occurs is increased. At higher strains, the non-linear recovery region is located further from the break and the length of the slipped region increases. Similarly, the axial stress profiles of Figure 3 can be broken into three regions, a nearly linear region starting from the break, a non-linear recovery region, and a nearly uniform region. As with the shear stress, the axial stress approaches a uniform gradient near the break and a uniform value far from the break only asymptotically. The non-linear zone in the axial stress distribution also changes location with different breaking strains while its size and shape remain the same. The positions of the non-linear recovery zones for the shear and axial stresses are coincident. For a given moduli ratio and volume fraction, the location of the non-linear recovery region depends on the composite strain. Higher applied strain implies that the region is located at a position further from the break. Notice in Figure 2 that if the applied strain at which the break occurs is very low, then the initial uniform shear stress region will not exist and the non-linear recovery region will not be fully developed.

A closed form solution of equation (19) is not available so a numerical investigation was used to determine some of the characteristics of the recovery region. The size and shape of the non-linear recovery region does not depend on the applied strain (as long as the strain is sufficiently high), but it does depend on the parameters $\frac{E_f}{E_m}$ and $\frac{w}{D}$. Three parameters were chosen to describe the non-linear region: its length, L_n , the applied strain at which it is fully developed, ϵ_n , and the average axial stress in the region when the fiber breaks at an applied composite strain of ϵ_n , $\bar{\sigma}_n$. Figure 4 contains a schematic that illustrates each of these parameters. The slip length, L_s , can be obtained from the second parameter, ϵ_n , by the following formula,

$$L_s = \frac{D}{4} \left(\frac{E_f \varepsilon}{\tau_y} - \frac{E_f \varepsilon_n}{\tau_y} \right). \quad (22)$$

Notice the similarity to equation (6). Figure 4 shows a schematic of these parameters. For a given value of $\frac{w}{D}$, all of these parameters can be fitted to a power law of the form

$$P = A \left(\frac{E_f}{E_m} \right)^n \quad (23)$$

where P is one of the three parameters, A is a constant, and n is a power law exponent. The fits for L_n , ε_n , and $\bar{\sigma}_n$ have maximum errors between the fitted curves and the actual data points of 2%, 5%, and 7% respectively.

Figure 4 contains a table listing values of A and n for values of $\frac{w}{D}$ between 0.25 and 2.

Note that as $\frac{E_f}{E_m}$ or $\frac{w}{D}$ go to zero, L_n , ε_n , and $\bar{\sigma}_n$ also go to zero, corresponding to the simple

shear sliding approximation (equations 2 and 3). This becomes evident after careful

consideration of equation (19). As $\frac{E_f}{E_m}$ goes to zero, or $\frac{w}{D}$ goes to zero the only solution

available for (19) with the appropriate boundary conditions is a step function for the shear stress.

As $\frac{w}{D}$ goes to zero, the distance between fibers is zero. The description of the shear strain in the matrix, equation (14), can take on only two values. Either the shear strain is zero and the state of stress at the interface is uniaxial extension, or the shear strain is infinite and the state of stress is pure shear. This is the physical origin for the step function shape of the shear stress distribution

when $\frac{w}{D}$ goes to zero. As $\frac{E_f}{E_m}$ goes to zero the physical reasoning for the step function shape of the shear stress is not as simple. However, mathematically it is clear that a step function shape for the shear stress, and consequently a bilinear distribution for the axial stress, is the solution if the matrix is elastically rigid.

As noted above, the strain at which the break occurs and the strain to which the fiber is subsequently loaded must be specified. Due to the strain path dependence of J_2 flow theory, different loading conditions result in different stresses in the fiber. This has a small effect on the distribution of stress in the fiber, but it is interesting since the simpler model of equations (7) and (8) cannot predict it. Consider a fiber that is initially broken, i.e. the strain to cause the break is zero. The composite is then extended and stresses develop in the fiber. The stress distributions can be broken up into the same regions that were described for a fiber that breaks at finite strain. The axial and shear stress profiles will develop and then the non-linear region will move along the fiber. For a given set of parameters, $\frac{E_f}{E_m}$, $\frac{w}{D}$, and $\frac{E_f \epsilon}{\sigma_y}$, the length of the non-linear recovery

zone for a fiber that breaks at strain ϵ will be shorter than the same zone for a fiber that is initially broken in a composite then extended to strain ϵ . The dependence of the shear and axial stress distributions on the loading sequence arises from the load path dependence of a plastically deforming material.

Returning to fibers that break at finite strain, three parameters are needed to solve (19):

$\frac{E_f}{E_m}$, $\frac{w}{D}$, and $\frac{E_f \epsilon}{\sigma_y}$ (notice that v_m is taken to be $1/3$ and $G_m = \frac{3}{8}E_m$, otherwise $\frac{E_f}{G_m}$ would also

have to be specified). Figures 5 and 6 are plots that illustrate the influence of these parameters.

The axial coordinate normalization $\frac{4\tau_y}{E_f \epsilon} \frac{z}{D}$ maps a single simple shear sliding slip length, L_s , to one unit. The axial stress normalization $\frac{\sigma_f}{E_f \epsilon}$ in Figure 6 causes a value of unity to represent the far field stress in the fiber. The shear and axial stress profiles of the simple shear sliding model are shown as a comparison in Figures 5 and 6, i.e. equations (3) and (2) respectively. Also, equations (7) and (8) give very good approximations to the shapes of the axial and shear stress distributions respectively. As $\frac{E_f}{E_m} \rightarrow 0$, $\frac{w}{D} \rightarrow 0$, or $\frac{E_f \epsilon}{\sigma_y} \rightarrow \infty$ the shear and axial stress profiles from the solution of equation (19) approach the simple shear sliding curves. Note that the limits $\frac{E_f}{E_m} \rightarrow 0$ and $\frac{w}{D} \rightarrow 0$ will create a true step function for the shear stress distribution, while the limit $\frac{E_f \epsilon}{\sigma_y} \rightarrow \infty$ causes the approach to a step function due to the choice of the normalization.

III. FINITE ELEMENT MODEL

Finite element calculations were done to determine the validity of the shear lag model with the elastic/perfectly-plastic matrix constitutive behavior. The model does not consider the exact three dimensional geometry of the fiber composite system, but instead idealizes the geometry as axisymmetric (Du and McMeeking (8), He *et al.* (9), Nedele and Wisnom (10), Tripathi *et al.* (11)). Figure 7 is an illustration of the axisymmetric model along with the actual values used for volume fraction, moduli ratio, and applied strain to calculate solutions for the stresses. The model has a broken fiber at the center, an annulus of matrix of width w surrounding the broken fiber, an annulus of fiber material representing the nearest neighbor

fibers, an annulus of matrix, and finally an annulus of material that has the averaged composite properties. The width of the annulus of fiber material, denoted m in Figure 7, is chosen such that its volume is equal to the volume of the six nearest neighbor fibers. The width of the second annulus of matrix material is taken to be one half of w , and the thickness of the composite annulus is $2w$. The length of the model, L , is chosen such that the shear stress at the fiber/matrix interface is approximately zero at $z=2/3 L$ for the listed applied strain. The fiber material is elastic and the matrix material is elastic-perfectly plastic. The yield stress of the matrix, σ_y , is taken to be $E_m/1000$. The Poisson's ratio of all materials is taken to be one third. The loading conditions are for a fiber that has broken at a finite strain. The model is extended uniformly to the strain at which the fiber fails. This also causes the matrix to yield. Thereafter, the tractions on the end of the broken fiber are removed incrementally while the displacements of the remaining boundary of the model are held fixed. No further strain is applied to the model after this process is completed. The model was computed with four sets of moduli ratios and three volume fractions as shown in Figure 7. The commercial finite element package ABAQUS was used and the results for the shear stress at the fiber/matrix interface are compared to the shear lag model.

The shear lag results are shown to be in excellent agreement with the more detailed finite element results. Figures 8a and 8b plot the shear stress from the solution of equation (19) against the finite element results. Also shown are the results from equation (8), which is the shear lag model combining Cox's original elastic version with a shear sliding interface zone near the break. The zero point on the z axis is taken to be where the non-linear recovery region begins, i.e. where $\tau = 0.99\tau_y$. This is done for two reasons. First it is easier to compare the different non-linear recovery zones. Second, any shear stress distribution for a higher strain than ϵ_n can be

constructed by adding a uniform shear stress zone from $z=0$ to $z=L_s$ (where L_s is given by (22)), and moving the beginning of the non-linear recovery region to $z=L_s$. The value of ϵ_n is also given on Figures 8a and 8b. The composite properties represented were chosen such that a wide range of non-linear recovery lengths would be presented. Figures 8a and 8b show that there is good agreement over a wide range of moduli ratios and fiber volume fractions between equation (19) and the finite element calculations.

Equation (8) is also a good approximation to the shear stress distribution for most of the material systems considered. Equation (8) has a sharp kink in the plots of shear stress versus distance from the break distributions where the shear stress begins to drop off from the plateau stress. Equation (8) cannot predict differences in the stress distribution due to different loading conditions, as the solution of equation (19) is able to do as discussed in the previous section. In general (7) and (8) give a good approximation to the stresses in a broken fiber in a plastic matrix, but (7) and (8) do not show some of the finer details of the solution to (19).

IV. DISCUSSION

Modeling the strength of composite materials requires an understanding of how stresses are distributed around fiber breaks. A complete solution to the governing equations (equilibrium, compatibility, and constitutive behavior) for this complicated three dimensional system would require a great deal of numerical computation. However, the shear lag approximation has been shown to compare well with an axisymmetric finite element model, and is much less onerous in computation. The shear lag approximation allows all field quantities to be related to the axial displacement of the broken fiber. Depending on the complexity of the

matrix constitutive behavior, the solution of the shear lag model is either a closed form expression or requires minimal numerical calculations.

The model developed was one for continuous, brittle, elastic fibers well bonded to a ductile matrix with elastic-perfectly plastic constitutive behavior. The solutions to the model were compared to a simple version where the shear stress is assumed to be constant over a finite slip region around the break. Three parameters control the shape of the stress profiles in the fiber, $\frac{E_f}{E_m}$, $\frac{w}{D}$, and $\frac{E_f \epsilon}{\sigma_y}$. The first two parameters dictate the size and shape of the non-linear region of the shear stress and axial stress distributions, and the third parameter specifies where the non-linear region is located along the fiber. The simple sliding model for the stress profiles in the fiber serve as bounds to the stresses predicted by the shear lag model. For volume fractions where the fibers are not in contact, as the parameter $\frac{E_f}{E_m}$ goes to infinity, i.e. the matrix material is elastically rigid, the stress profiles approach those of the simple sliding model.

This is an interesting result when the assumptions of the global load sharing (GLS) composite strength model are considered (Curtin (2)). The GLS model assumes that the load shed by broken fibers is shared equally by all intact fibers on the plane of the break. No load is carried by the matrix. It is also assumed that shear sliding occurs at a uniform sliding stress over a finite distance around the break. It has been shown by the shear lag model that the latter assumption is true when the matrix is elastically rigid in shear and yielding occurs at the interface. It is interesting to note that the former assumption also holds when the matrix is rigid in shear. Hedgepeth and van Dyke (4) developed a model to predict stress concentrations in fibers adjacent to a broken fiber. They showed that stress in a fiber neighboring a break is

increased above the applied stress over a length proportional to $\sqrt{\frac{E_f}{G_m}}$, i.e. zero length when the matrix is rigid. Therefore the GLS composite strength model is a description of a composite with long brittle elastic fibers embedded in a matrix that will not carry axial loads, but is rigid in shear, and "yields" at a prescribed level of shear stress. This "yielding" can take the form of localized shear yielding for a ductile matrix, or interface sliding for a brittle matrix.

The main deficiency of this model is that it does not consider the stresses in fibers neighboring the break. While not done in this work, it is possible to generalize the governing equations developed here to include interactions with other fibers. In order to truly understand composite failure knowledge of the stress concentrations in neighboring fibers is needed. In future work (Landis and McMeeking (12)) we will show how the same parameters, specifically $\frac{E_f}{E_m}$ and $\frac{E_f \epsilon}{\sigma_y}$, that govern the shape of the stress profile in the broken fiber, also govern the stress concentrations in the neighboring fibers. While the model presented here does not increase our knowledge of stress concentrations in composites, it does develop the basic mechanics that are necessary to understanding failure in ductile matrix composites.

Often shear lag models are misconstrued as exact solutions. Shear lag models make many simplifying assumptions to the governing equations of solid mechanics. The elastic-perfectly plastic matrix response lends itself to the shear lag description. It has been shown here that the model is in good agreement with more detailed numerical calculations and a simpler shear lag model for a wide range of composite properties.

ACKNOWLEDGEMENT

The work was sponsored by the Advanced Research Projects Agency through the University Research Initiative at the University of California, Santa Barbara (ONR Contract N-0014-92-J-1808)

REFERENCES

1. Cox, H. L., The elasticity and strength of paper and other fibrous materials, *Br. J. Appl. Phys.* **3** 1952 pp. 72-79.
2. Curtin, W. A., Theory of mechanical properties of ceramic matrix composites, *J. Am. Ceram. Soc.*, **74** 1991 pp. 2837-2845.
3. Kelly, A. and Tyson, W., Tensile properties of fiber/reinforced metals: copper/tungsten and copper/molybdenum, *J. Mech. Phys. Solids*, **13** 1965 pp. 329-350.
4. Hedgepeth, J. M. and van Dyke, P., Local stress concentrations in imperfect filamentary composite materials, *J. Compos. Mater.*, **1** 1967 pp. 294-310.
5. Beyerlein, I. J. and Phoenix, S. L., Stress Concentrations around multiple fiber breaks in an elastic matrix with local yielding or debonding using quadratic influence superposition, *J. Mech. Phys. Solids* **44** 1996 pp. 1997-2039.
6. Du, Z.-Z. and McMeeking, R. M., Creep models for metal matrix composites with long brittle fibers, *J. Mech. Phys. Solids*, **43** 1995 pp. 701-726.

7. Hill, R., The Mathematical Theory of Plasticity, Oxford University Press, 1950, New York.
8. Du, Z.-Z. and McMeeking, R. M., Control of strength anisotropy of metal matrix fiber composites, *J. Computer-Aided Mater. Des.* , **1** 1994 pp. 243-264.
9. He, M. Y., Evans, A. G. and Curtin, W. A., The ultimate tensile strength of metal and ceramic-matrix composites, *Acta. Metall. Mater.* **41** 1993 pp. 871-878.
10. Nedele, M. R. and Wisnom, M. R., Stress concentration factors around a broken fibre in a unidirectional carbon fibre-reinforced epoxy, *Composites* , **25** 1994 pp. 549-557.
11. Tripathi, D., Chen, F. and Jones, F. R., The effect of matrix plasticity on the stress fields in a single filament composite and the value of interfacial shear strength obtained from the fragmentation test, *Proc. R. Soc. Lond. A*, **452** 1996 pp. 621-653.
12. Landis, C. M. and McMeeking, R. M., Stress concentrations in composites with interface sliding, matrix stiffness, and uneven fiber spacing using shear lag methodology. To be published, 1997.

APPENDIX: Finite Difference Scheme

In this appendix the finite difference scheme that was used to solve equation (19) of the main text is described. The stresses, strains, lengths, displacements, and moduli are normalized as follows:

$$\hat{\tau} = \frac{\tau}{\sigma_y}, \hat{\sigma}_m = \frac{\sigma_m}{\sigma_y}, \hat{\sigma}_f = \frac{\sigma_f}{\sigma_y}, \hat{\epsilon} = \frac{E_f \epsilon}{\sigma_y}, \hat{w} = \frac{w}{D}, z = \frac{z}{D}, \hat{u} = \frac{E_f u}{\sigma_y D}, \hat{E} = \frac{E_m}{E_f}, \text{ and } \hat{G} = \frac{G_m}{E_f}.$$

Equation (19) becomes

$$\left(\frac{9}{4} \frac{\hat{\tau}^2}{\hat{E}} + \frac{1}{4} \frac{\hat{\sigma}_m^2}{\hat{G}} \right) \frac{\partial^2 \hat{u}}{\partial \hat{z}^2} - 3 \hat{\tau} \hat{\sigma}_m \frac{\partial \hat{u}}{\partial \hat{z}} - \frac{\hat{\sigma}_m^2}{\hat{w}} (\hat{u} - \hat{\epsilon}) = 0. \quad A1$$

The fiber is discretized into $N-1$ equal segments of length $\Delta \hat{z} = \frac{\hat{L}}{N}$, where $\hat{L} = \frac{L}{D}$, and L is the total length of the fiber. For the calculations done in this paper, L is taken to be sufficiently long such that the solutions represent an infinite fiber. The time history of the loading is then broken into two segments. The first segment is when the fiber just breaks and the applied strain rate is zero. During this time segment the tractions at the broken end of the fiber are released gradually to zero. During the second time segment the applied strain rate is not zero, but the strain at the broken end of the fiber is always zero. Each of these time segments is discretized into a finite number of time steps Δt . It is assumed that the fiber displacements are known everywhere along the fiber at time t . A centered finite difference scheme yields

$$\frac{\partial^2 \hat{u}}{\partial \hat{z}^2} = \frac{\hat{u}_{i+1} - 2\hat{u}_i + \hat{u}_{i-1}}{\Delta \hat{z}^2} \quad A2$$

$$\frac{\partial \hat{u}}{\partial \hat{z}} = \frac{\hat{u}_{i+1} - \hat{u}_{i-1}}{2\Delta \hat{z}} \quad A3$$

$$\dot{\hat{u}} = \frac{\hat{u}^{t+1} - \hat{u}^t}{\Delta t} \quad A4$$

$$\hat{\tau}_i = -\frac{1}{4} \left(\frac{\hat{u}_{i+1}^t - 2\hat{u}_i^t + \hat{u}_{i-1}^t}{\Delta \hat{z}^2} \right) \quad A5$$

$$\hat{\sigma}_{m_i} = \sqrt{1 - 3\hat{\tau}_i^2} \quad A6$$

Let

$$\alpha_i = -\frac{1}{4\Delta \hat{z}} \left(\frac{9\hat{\tau}_i^2}{\hat{E}} + \frac{\hat{\sigma}_{m_i}^2}{\hat{G}} \right) + \frac{3}{2} \hat{\tau}_i \hat{\sigma}_{m_i} \quad A7$$

$$\beta_i = \frac{1}{2\Delta \hat{z}} \left(\frac{9\hat{\tau}_i^2}{\hat{E}} + \frac{\hat{\sigma}_{m_i}^2}{\hat{G}} \right) + \frac{\hat{\sigma}_{m_i}^2}{\hat{w}} \Delta \hat{z} \quad A8$$

$$\gamma_i = -\frac{1}{4\Delta \hat{z}} \left(\frac{9\hat{\tau}_i^2}{\hat{E}} + \frac{\hat{\sigma}_{m_i}^2}{\hat{G}} \right) - \frac{3}{2} \hat{\tau}_i \hat{\sigma}_{m_i} \quad A9$$

$$\delta_i = \frac{\hat{\sigma}_{m_i}^2}{\hat{w}} \dot{\hat{e}} \Delta t \hat{z}_i \Delta \hat{z} \quad A10$$

where the subscripts denote positions along the fiber in z space, and superscripts denote material times in t space. The solution of (19) results in the solution of a tridiagonal matrix for each time step. Notice that the coefficients α , β , γ , and δ change after each increment of time. The difference equation for an interior point on the fiber becomes

$$\alpha_i \hat{u}_{i+1}^{t+1} + \beta_i \hat{u}_i^{t+1} + \gamma_i \hat{u}_{i-1}^{t+1} = \alpha_i \hat{u}_{i+1}^t + \beta_i \hat{u}_i^t + \gamma_i \hat{u}_{i-1}^t + \delta_i \quad A11$$

Equation A11 is valid for $1 < i < N$.

The equation at $i=N$ is

$$\hat{u}_N^{t+1} = \hat{u}_N^t + \hat{\epsilon} \hat{L} \Delta t. \quad A12$$

For the node at the fiber break, $i=1$

$$\hat{\tau}_1 = -\frac{1}{4} \left(\frac{-7\hat{u}_1^t + 8\hat{u}_2^t - \hat{u}_3^t}{2\Delta \hat{z}^2} - \frac{3}{\Delta \hat{z}} \hat{\epsilon}_{\text{break}} \right) \quad A13$$

where $\hat{\epsilon}_{\text{break}}$ is the normalized strain at the break for time step t . For the first time segment when the fiber just breaks, $\hat{\epsilon}_{\text{break}}$ will be a positive value. For subsequent loading $\hat{\epsilon}_{\text{break}}$ will be zero. By defining

$$\beta_1 = \frac{1}{4\Delta \hat{z}} \left(\frac{9\hat{\tau}_1^2}{\hat{E}} + \frac{\hat{\sigma}_{m1}^2}{\hat{G}} \right) - \frac{3}{2} \hat{\tau}_1 \hat{\sigma}_{m1} + \frac{3}{8} \frac{\Delta \hat{z}}{\hat{w}} \hat{\sigma}_{m1}^2 \quad A14$$

$$\gamma_1 = -\frac{1}{4\Delta \hat{z}} \left(\frac{9\hat{\tau}_1^2}{\hat{E}} + \frac{\hat{\sigma}_{m1}^2}{\hat{G}} \right) + \frac{3}{2} \hat{\tau}_1 \hat{\sigma}_{m1} + \frac{1}{8} \frac{\Delta \hat{z}}{\hat{w}} \hat{\sigma}_{m1}^2 \quad A15$$

$$\delta_1 = \frac{\hat{\sigma}_{m1}^2}{\hat{w}} \hat{\epsilon} \Delta t \frac{\Delta \hat{z}^2}{4} - \frac{1}{4} \left(\frac{9\hat{\tau}_1^2}{\hat{E}} + \frac{\hat{\sigma}_{m1}^2}{\hat{G}} \right) \dot{\hat{\epsilon}}_{\text{break}} \Delta t \quad A16$$

where $\dot{\hat{\epsilon}}_{\text{break}}$ is the rate at which strain is increasing at the break, $\dot{\hat{\epsilon}}_{\text{break}}$ is negative during the break process, and zero during subsequent loading. The difference equation for the node at $i=1$ is

$$\beta_1 \hat{u}_1^{t+1} + \gamma_1 \hat{u}_2^{t+1} = \beta_1 \hat{u}_1^t + \gamma_1 \hat{u}_2^t + \delta_1 \quad A17$$

The shear stresses in A5 and A13 must not be allowed to exceed the shear yield strength.

Therefore if the value of τ is very close to τ_y then it is given the value τ_y so that the next time increment will not violate the yield condition.

The initial displacement profile is $\hat{u}_i^0 = \hat{\epsilon}_{\text{fracture}} \hat{z}_i$, where $\hat{\epsilon}_{\text{fracture}}$ is the normalized strain when the fiber breaks. Equations A11, A12, and A17 constitute a tridiagonal set of N linear algebraic equations to be solved for the displacements at time $t+1$. The updated displacements are used to calculate updated shear stresses, and the process continues until the applied strain reaches its final value.

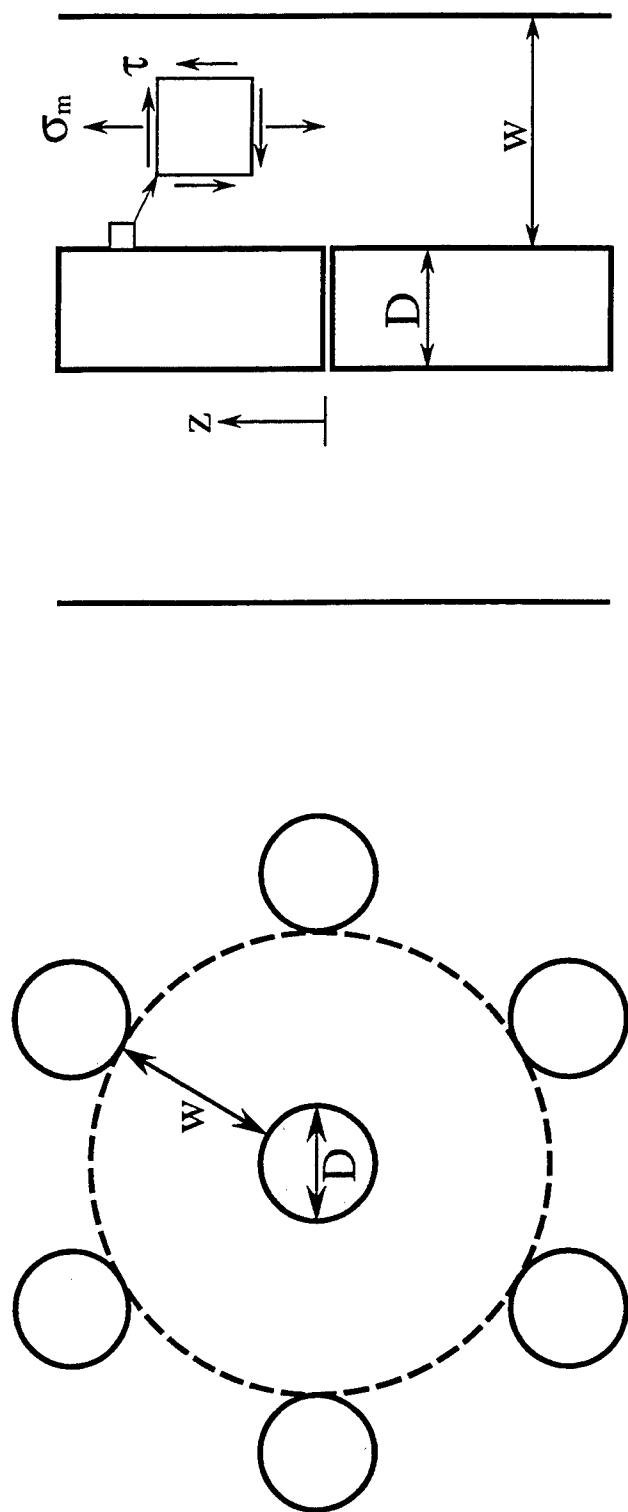


Figure 1. Top and side views of the unit cell used for the shear lag models. The assumed stress state in the matrix is shown on the right.

Shear Stress Distribution in a Broken Fiber

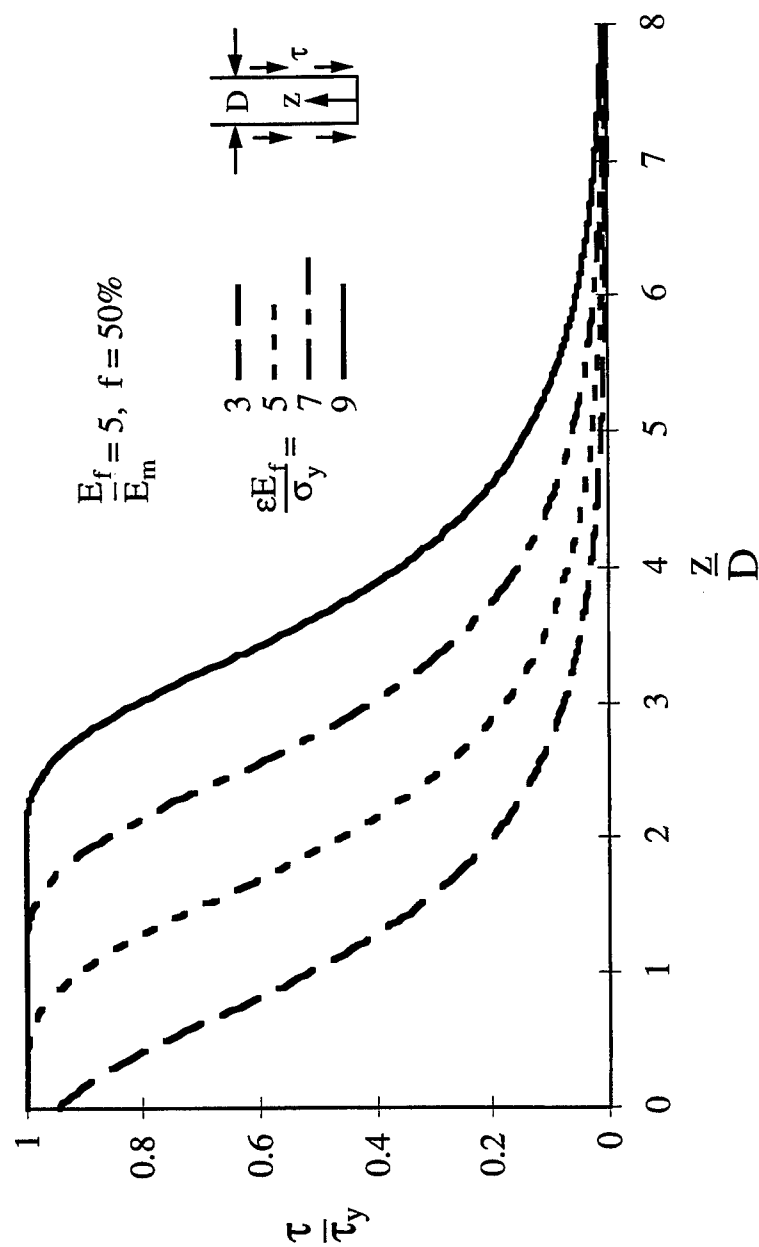


Figure 2. Solution of equation 19 for the shear stress distribution, $\tau(z)$, in a broken fiber as a function of distance from the break, z , for different values of applied far field strain.

Axial Stress Distribution in a Broken Fiber

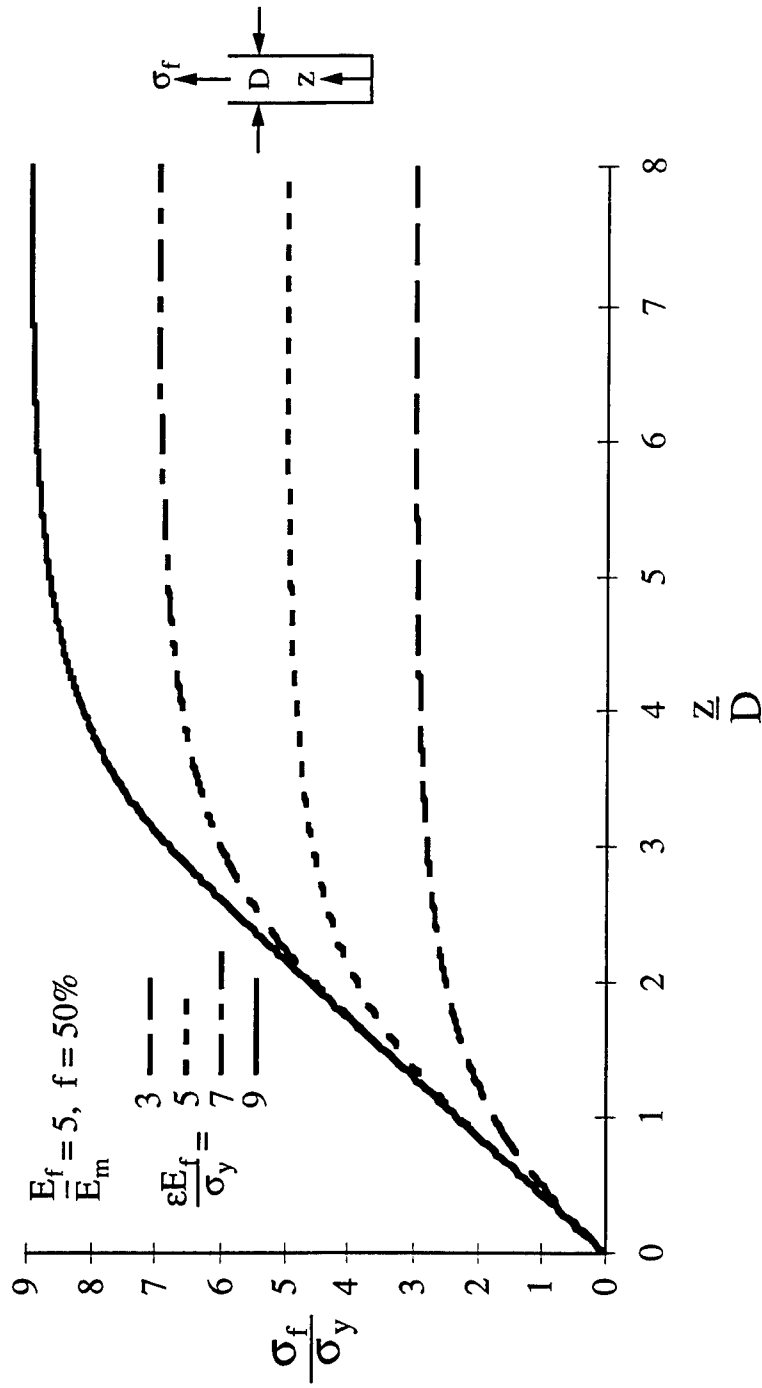
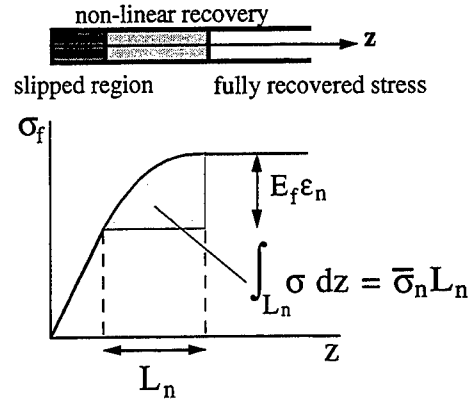


Figure 3. Solution of equation 19 for the axial stress distribution, $\sigma(z)$, in a broken fiber as a function of distance from the break, z , for different values of applied far field strain.

Power Law

$$P = A \left(\frac{E_f}{E_m} \right)^n$$



P	$\frac{w}{D}$ (f)	A	n
$\frac{L_n}{D}$	0.25 (0.58)	2.948	0.532
	0.5 (0.40)	3.963	0.544
	1 (0.23)	5.317	0.552
	2 (0.10)	7.149	0.554
$\frac{E_f \epsilon_n}{\sigma_y}$	0.25 (0.58)	1.342	0.600
	0.5 (0.40)	1.582	0.648
	1 (0.23)	1.865	0.680
	2 (0.10)	2.149	0.707
$\frac{\bar{\sigma}_n}{\sigma_y} \frac{L_n}{D}$	0.25 (0.58)	3.380	1.125
	0.5 (0.40)	5.409	1.183
	1 (0.23)	8.619	1.222
	2 (0.10)	13.450	1.250

Figure 4. A schematic of the three parameters characterizing the non-linear stress recovery region, and their fits to a power law for four values of fiber volume fraction.

Shear Stress Distribution in a Broken Fiber

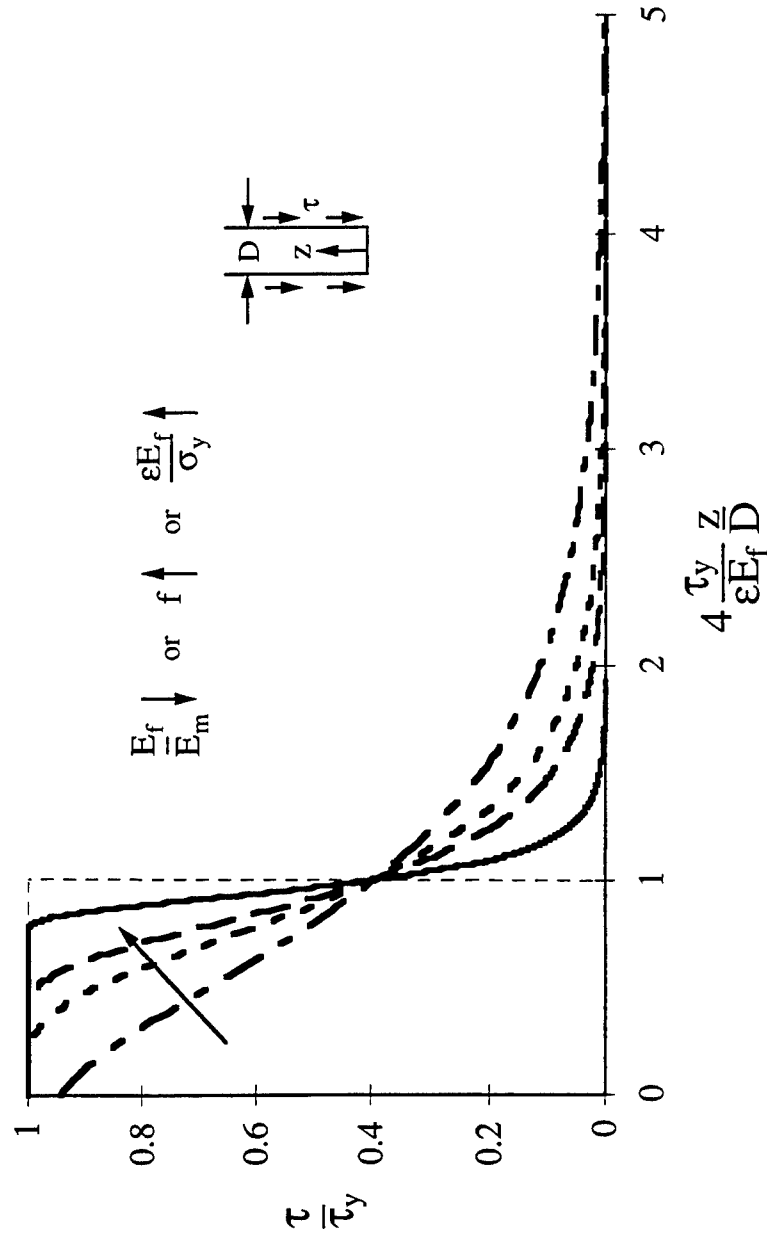


Figure 5. Shear stress distribution in a broken fiber as a function of distance (in slip lengths) from the break. The curves follow the arrow as the fiber to matrix moduli ratio decreases, the fiber volume fraction increases, or the applied strain increases.

Axial Stress Distribution in a Broken Fiber

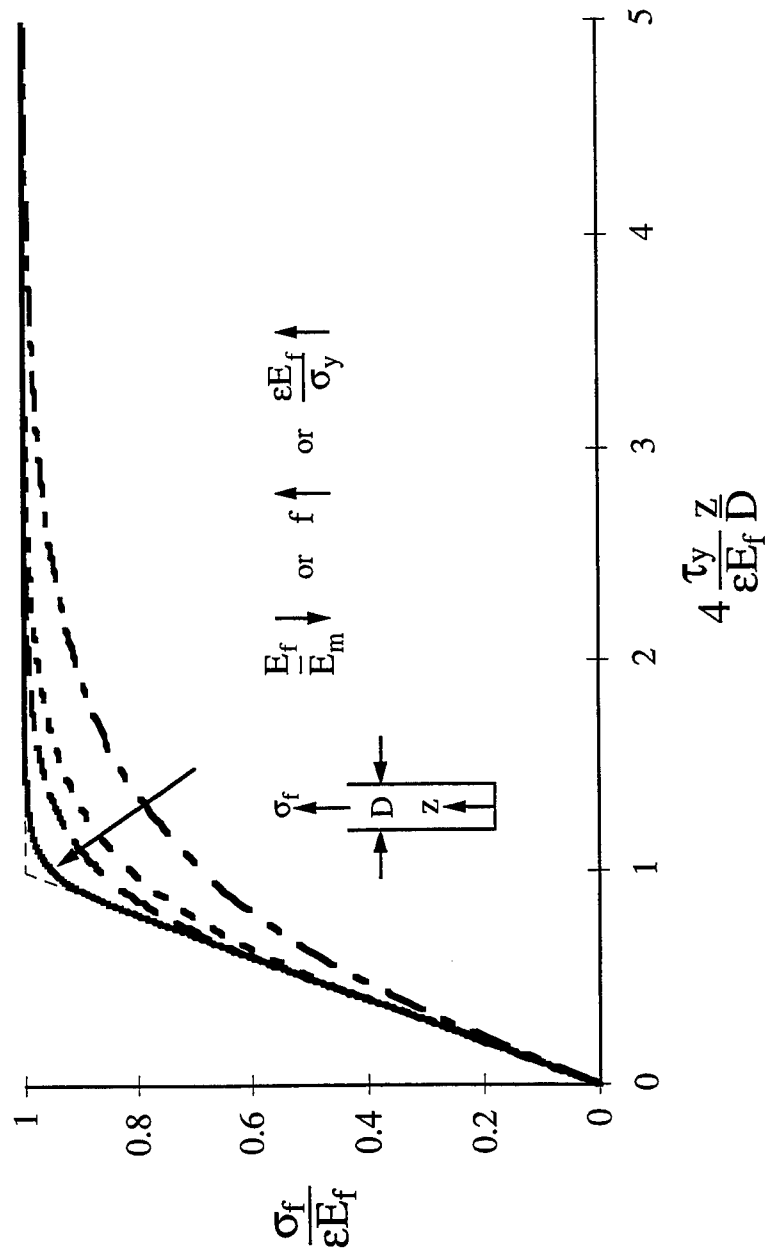
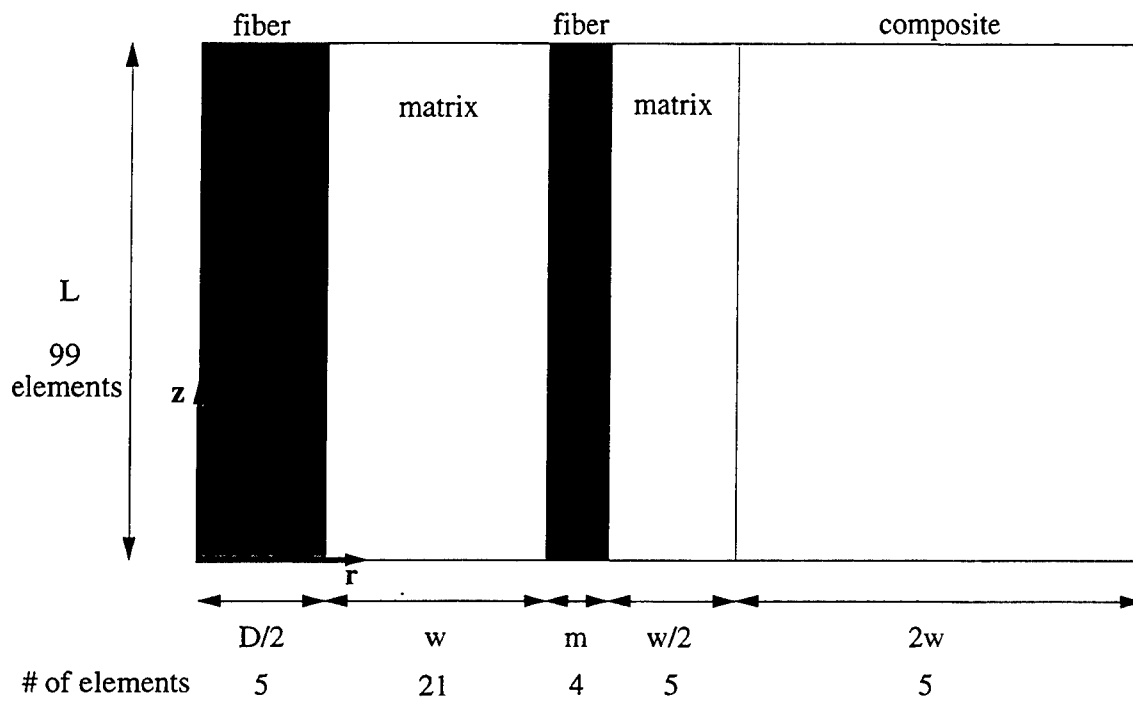


Figure 6. Axial stress distribution in a broken fiber as a function of distance (in slip lengths) from the break. The curves follow the arrow as the fiber to matrix moduli ratio decreases, the fiber volume fraction increases, or the applied strain increases.



$\frac{E_f}{E_m}$	f (%)	$\frac{E_f \epsilon}{\sigma_y}$
1	10	5.2
1	30	3.75
5	10	9.44
5	30	8.6
5	60	4.6
10	30	11.9
10	60	9.8
100	60	49.7

Figure 7. Geometry of the finite element mesh, and a list of the composite parameters and applied strain.

Shear Stress Distribution in a Broken Fiber

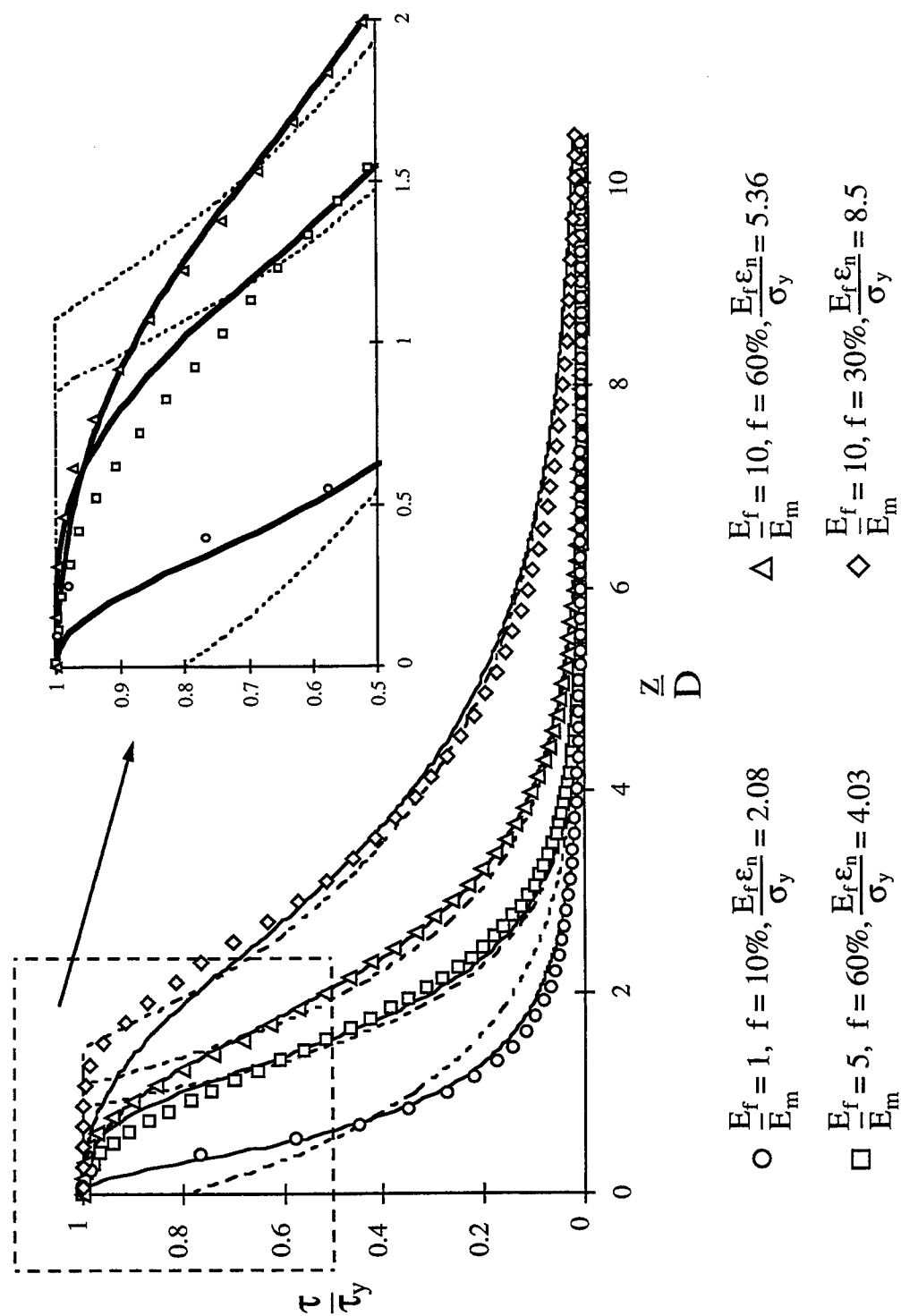


Figure 8a. Comparison of finite element calculations (discrete points) with the shear lag model presented in this paper (solid lines), and equation (8) (dashed lines). The shear stress is plotted as a function of distance from the break for 4 combinations of fiber volume fraction and fiber to matrix moduli ratio. The longest curve was taken out of the inset for clarity.

Shear Stress Distribution in a Broken Fiber

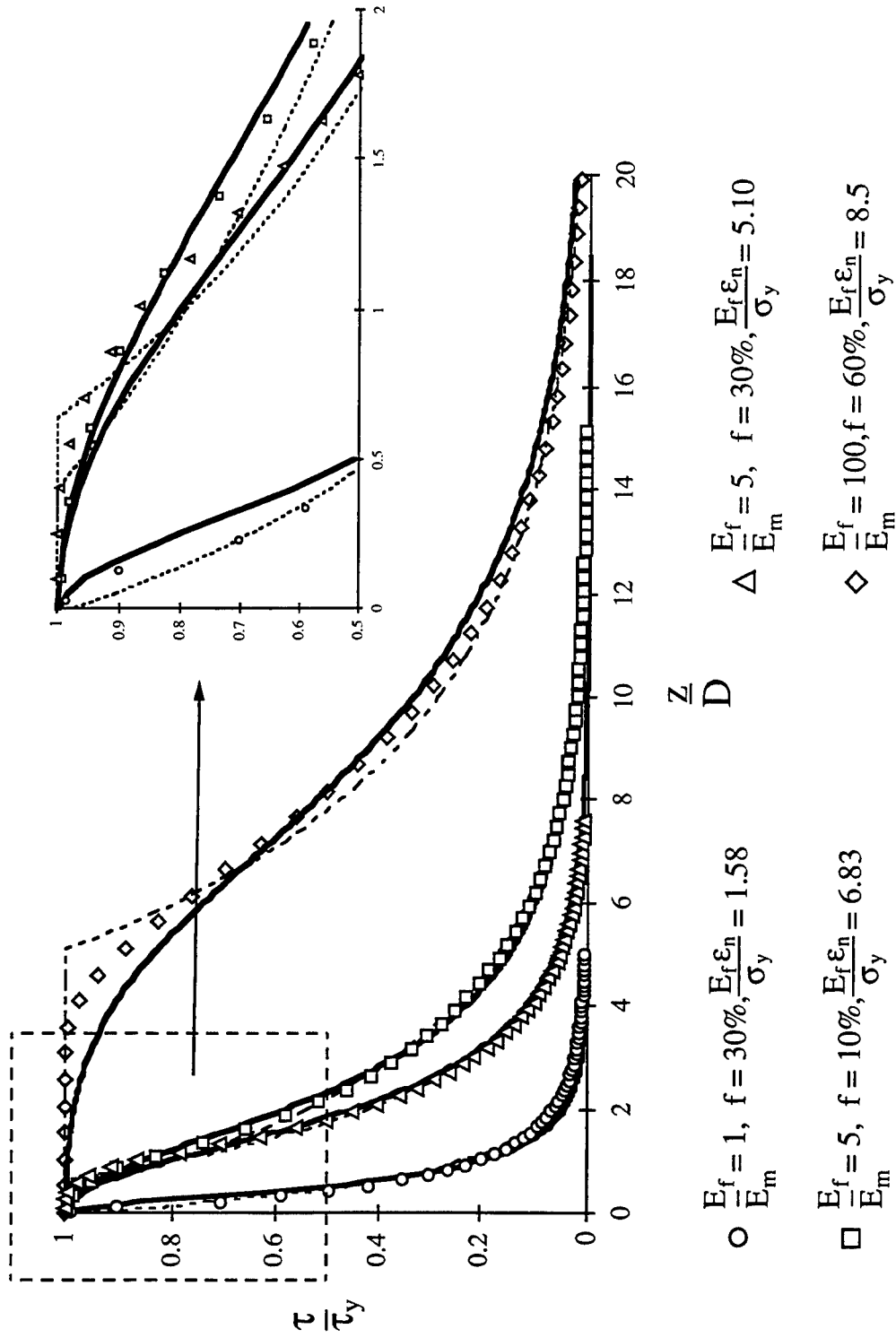


Figure 8b. Comparison of finite element calculations (discrete points) with the shear lag model presented in this paper (solid lines), and equation (8) (dashed lines). The shear stress is plotted as a function of distance from the break for 4 combinations of fiber volume fraction and fiber to matrix moduli ratio. The longest curve was taken out of the inset for clarity.



THE INFLUENCE OF PARTICLE SIZE AND PARTICLE FRACTURE ON THE ELASTIC/PLASTIC DEFORMATION OF METAL MATRIX COMPOSITES

C.-W. NAN[†] and D. R. CLARKE

Materials Department, College of Engineering, University of California, Santa Barbara,
 CA 93106-5050, U.S.A.

(Received 6 October 1995)

Abstract—A methodology is introduced for calculating the deformation response of particulate reinforced metal matrix composites in terms of an effective medium approach combined with the essential features of dislocation plasticity. By comparing the simulated and experimental stress-strain curves for two sets of SiC–Al composites, the effects of particle size and size distribution and volume fraction on the deformation response are given. A feature of the methodology is that the effects of particle cracking during deformation can be incorporated quantitatively. When included, the simulations lead to excellent agreement with experiments on the effects of particle cracking on both the overall deformation response and the tension–compression deformation asymmetry. Copyright © 1996 Acta Metallurgica Inc.

1. INTRODUCTION

With the ever greater sophistication in metals processing, a wide variety of two-phase metal based composites have been developed over the last 50 years ranging from precipitation hardened to dispersion hardened alloys [1, 2] to metal-matrix composites (MMCs) [3, 4] to interpenetrating phase composites [5]. These can all be described as metal matrix composites but with a variety of different particle sizes, volume fractions, reinforcement shapes and topologies that are dependent on the particular processing route used to fabricate the materials.

To account for the observed deformation behavior of this very broad class of composites, two quite distinct and successful but nevertheless incompatible theories have been developed. One, based on dislocation plasticity models [6–8], has been extremely successful in describing the deformation of composites containing a small concentration of sub-micron second-phase particles. The other, based on continuum plasticity and usually implemented by Eshelby-based approaches [9, 10] or finite element methods [11], has been successful for composites containing large ($> 10 \mu\text{m}$) particles. Whilst each has been successful within its own range of particle size, they both predict unrealistic behavior when extended outside of their range of applicability. For instance, dislocation based models predict a parabolic work-

hardening for all particle sizes and a much smaller increase in yield stress for large particle sizes than is observed. On the other hand, the continuum plasticity models do not lead to the large increases in yield stress, or the parabolic work-hardening rates, obtained with small volume fractions of small precipitates. There thus exists a range of particle size, roughly from 0.1 to $10 \mu\text{m}$, for which no existing theory satisfactorily describes the observed behavior. Although a number of approaches, such as the super-dislocation scheme of Hirth *et al.* [12], have been developed to bridge the gap, there nevertheless exists no substantive model that incorporates both the essential features of both continuum plasticity and the dislocation plasticity.

In the absence of any such complete theory, we adopt in this work a hybrid, analytical method for calculating the deformation behavior of metal matrix composites over the full range of particle sizes. The approach we describe is a combination of the key features of dislocation plasticity with a continuum mechanics approach based on effective medium approximations (EMA) [13]. This latter is preferred here over finite element computations because of the ease of the computation, the insensitivity to detailed geometrical arrangement of particles and because stochastic effects, such as the strain-dependent fracture of particles during tensile deformation, can be readily incorporated. In essence, the size effects explicit in dislocation plasticity are combined with the continuum approach, which whilst readily incorporating the effects of particle shape and volume fraction, have no intrinsic length scale and hence cannot accommodate size effects.

[†]On leave from Research Institute for Advanced Materials, Wuhan University of Technology, Wuhan, Hubei 430070, China.

The plan of the paper is as follows. First, the general methodology for the calculation of the elastic/plastic behavior of a two-phase composite within the framework of a relatively new effective medium approach is described. Then, our method of incorporating some of the key features of dislocation plasticity into the EMA is described. Finally, the effect of particles fracturing during deformation as a result of the stress in them exceeding a critical value is included. For illustrative and quantitative purposes, the calculations are compared with the results of two sets of experimental data on particulate reinforced aluminum alloys, those by Lloyd [14] and those by Kiser *et al.* [15]. Lloyd's data are for two different aluminum alloys (T4 and T6) plus two different sizes of SiC particles. Kiser *et al.*'s data are for one aluminum alloy but with two different volume fractions and slightly different sizes of Si particles. These two studies rather than others in the literature were chosen for comparison because they alone reported the deformation behavior of the unreinforced aluminum alloys as well as the composite behavior. This is essential, since the form of the EMA used in this work requires a knowledge of the deformation behavior of the unreinforced alloy as one of a limited number of input parameters. The objective of the present work is to introduce the hybrid methodology and also to compare the predictions of the theory with experimental results, demonstrating how particle size and size distribution as well as particle fracturing exert an influence on the deformation behavior of metal matrix composites.

2. EFFECTIVE MEDIUM APPROACH

Consider a MMC consisting of elastic reinforcements perfectly bonded to an elastoplastic metal matrix. For convenience, we use the following relation to describe the non-linear stress-strain (σ - ϵ) behavior of the metal matrix and the MMC

$$\sigma = C(\epsilon)\epsilon, \quad (1)$$

where C is the elastoplastic secant stiffness which is dependent upon the instantaneous strain ϵ . The effective secant modulus C^* of the MMC can be defined in terms of averaged stress $\bar{\sigma}$ and strain $\bar{\epsilon}$, namely,

$$\bar{\sigma} = C^*(\bar{\epsilon})\bar{\epsilon}. \quad (2)$$

To proceed, we introduce a homogeneous reference medium whose secant modulus C^0 depends on the homogeneous strain field ϵ^0 . In the case of homogeneous boundary conditions, the secant modulus C^0 does not vary spatially. The actual secant modulus, $C(\epsilon)$, varies with position and strain but can be written as a variation from that of the homogeneous reference medium

$$C(\epsilon) = C^0(\epsilon^0) + C'(\epsilon), \quad (3)$$

where $C'(\epsilon)$ is the variation from C^0 . Under any prescribed surface displacement, the local strain within the MMC can be obtained from equations (1) and (3), with the additional equilibrium condition, $\sigma_{ij,j} = 0$, as

$$\epsilon = (I + GT)\epsilon^0 = (I + GT)\langle I + GT \rangle^{-1}\bar{\epsilon}, \quad (4)$$

where

$$T(\epsilon) = C'(I - GC)^{-1}, \quad (5)$$

and where the angular bracket denotes averaging, I is the unit tensor, and G is the modified Green's function tensor [13]. From equations (1), (2) and (4), the effective secant modulus of the MMC can be obtained as

$$C^* = C^0 + \langle T \rangle \langle I + GT \rangle^{-1}. \quad (6)$$

For calculating the deformation response of MMC, we assume that the metal matrix itself can be taken as the homogeneous reference material, so that $C^0 = C^m$. The average strain and stress in the metal matrix can then be expressed in terms of the macroscopically average strain and stress in the MMC as

$$\epsilon^m = \langle I + GT \rangle^{-1}\bar{\epsilon}, \quad \sigma^m = C^m \langle I + GT \rangle C^* >^{-1}\bar{\sigma}. \quad (7)$$

For simplicity of expression, we consider an isotropic MMC with spherical particles although the methodology is capable of treating anisotropic MMCs with non-spherical particles. Characterizing the metal matrix composite by its secant bulk and shear moduli, k^* and μ^* , the moduli of the MMC can be written, using equation (6), as

$$\frac{k^* - k^m}{3k^* + 4\mu^m} = f \frac{k^p - k^m}{3k^p + 4\mu^m},$$

$$\frac{\mu^* - \mu^m}{\mu^* + y^s} = f \frac{\mu^p - \mu^m}{\mu^p + y^s}, \quad (8)$$

with

$$y^s = \frac{\mu^m(9k^m + 8\mu^m)}{6(k^m + 2\mu^m)},$$

k^m and μ^m are the secant bulk and shear moduli of the metal matrix; k^p and μ^p are the elastic bulk and shear moduli of the particles, and f is volume fraction of the particles. By decomposing the stress and strain into hydrostatic (σ_{kk} and ϵ_{kk}) and deviatoric (σ'_{ij} and ϵ'_{ij}) parts, equation (7) becomes

$$\epsilon'_{kk} = \frac{3k^* + 4\mu^m}{3k^m + 4\mu^m} \bar{\epsilon}_{kk}, \quad \sigma'_{kk} = \frac{3k^* + 4\mu^m}{3k^m + 4\mu^m} \frac{k^m}{k^*} \bar{\sigma}_{kk}, \quad (9)$$

$$\epsilon'_{ij} = \frac{\mu^* + y^s}{\mu^m + y^s} \bar{\epsilon}'_{ij}, \quad \sigma'_{ij} = \frac{\mu^* + y^s}{\mu^m + y^s} \mu^m \mu^* \bar{\sigma}'_{ij}. \quad (10)$$

Therefore, if the elastic moduli and the volume fraction of the particles and the stress-strain behavior of the matrix metal are all known, the mechanical behavior of the MMC can be predicted by using these rather simple effective medium equations (8)-(10).

The uniaxial stress-strain behavior for a range of metal matrix materials can be reasonably expressed by an empirical power law such as the Ramberg-Osgood equation

$$\epsilon^m = \frac{\sigma^m}{E^m} + \alpha \frac{\sigma_o^m}{E^m} \left(\frac{\sigma^m}{\sigma_o^m} \right)^{1/n} \quad (11)$$

where E^m is the Young's modulus of the matrix, σ_o^m is its yield strength, n is the strain hardening exponent, and α is a dimensionless constant (here $\alpha = 3/7$ is taken). (The uniaxial behavior can be generalized to triaxial stress state using the Mises invariant in the usual way.) The secant Young's modulus of the isotropic matrix metal, defined by the ratio of tensile stress to the tensile strain, is given by

$$E^{ms} = \frac{E^m}{1 + \alpha \left(\frac{\sigma_{11}^m}{\sigma_o^m} \right)^{n+1-n}} \quad (12)$$

The assumption of plastic incompressibility for the matrix metal results in the secant bulk modulus of the metal matrix being equal to its linear elastic bulk modulus and thus the secant shear modulus μ^{ms} can be written as

$$\mu^{ms} = \frac{E^{ms}}{3 - E^{ms}/3k^m} \quad (13)$$

In order to calculate the stress-strain curve of the MMC from those of its constituents, we adopt an iterative scheme. First, a value for σ_{11}^m is selected, from which the values of E^{ms} and μ^{ms} are calculated using equations (12) and (13). These values are then used to determine k^* and μ^* from equation (8). With these starting values, the average stress and strain of the MMC can be obtained from equations (9) and (10). Then the value of σ_{11}^m is increased and the same process repeated. In this way the entire stress-strain curve of the MMC can be determined.

To illustrate the predictions of the effective medium calculation, we compare them with the reported properties of the two Al matrix composites: the Al-15 v/o SiC composite (denoted as A356/SiC/15p in Ref. [14]) with different SiC particle sizes and different tempers (T4 or T6); and the Al-Si composite (T4) [15] with different volume fractions and slightly different particle sizes. The pertinent mechanical and physical properties of each phase used for the calculations are shown in Table 1. Table 2 shows the parameters in the Ramberg-Osgood law, n and σ_o^m , which we obtained by fitting equation (11) to the

Table 2. Ramberg-Osgood parameters

Matrix metal	n exponent	σ_o^m (MPa)
A356-T4	0.212	86
A356-T6	0.109	207
Al-T4	0.18	137

unreinforced matrix flow curves reported in Refs [14] and [15] for the different matrices (A356-T4 and A356-T6 [14], and Al-T4 [15]). The stress-strain curves calculated for these two different systems are shown in Figs 1 and 2, respectively. Comparison with the experiments show that the simple EMA predicts similar flow curves and trends concerning the effects of volume fraction of particles and properties of both phases. However, as expected it does not give any particle size dependence of the mechanical behavior of MMCs, as shown in experiment (Fig. 1) since there is no length scale in the effective medium formulations. Comparison with the tension/compression data for the Al-Si composites, indicates that the method does predict reasonable compressive flow curves but the calculated flow curves in tension diverge rapidly from their respective tensile flow curves, especially for the Al-20 v/o Si composite.

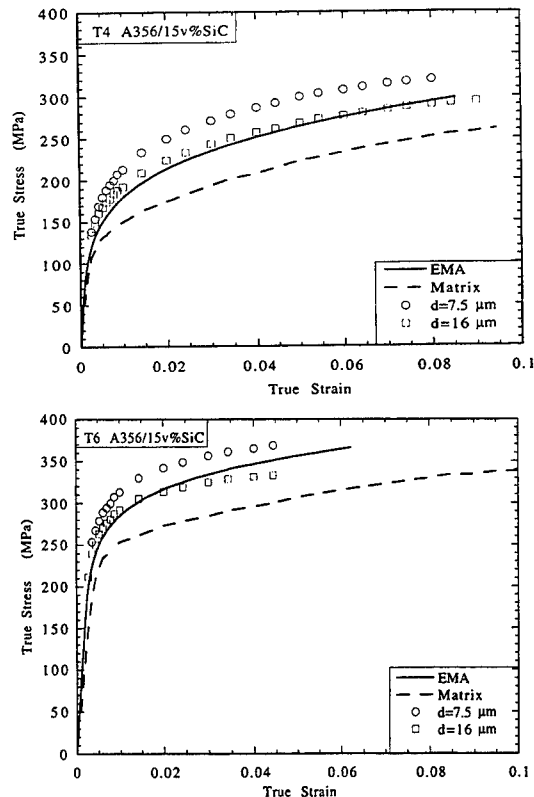


Fig. 1. Comparison between the experimental data (in tension) reported by Lloyd [14] for the Al-15 v/o SiC ($f = 0.15$) composite with different particle sizes and the calculated stress-strain curve based simply on the effective medium approximation (EMA). In (a) the aluminum matrix is in the T4 condition and in (b) in the T6 condition. The dashed line corresponds to the deformation behavior of the aluminum matrix alone.

Table 1. Materials properties

Parameter	Unit	Al matrix	SiC particles	Si particles
Young's modulus	GPa	70	427	165
Poisson's ratio	1	0.33	0.17	0.22
CTE	$\times 10^{-6}/^{\circ}\text{C}$	23.6	4.3	3.0
Burgers vector	nm	0.283		

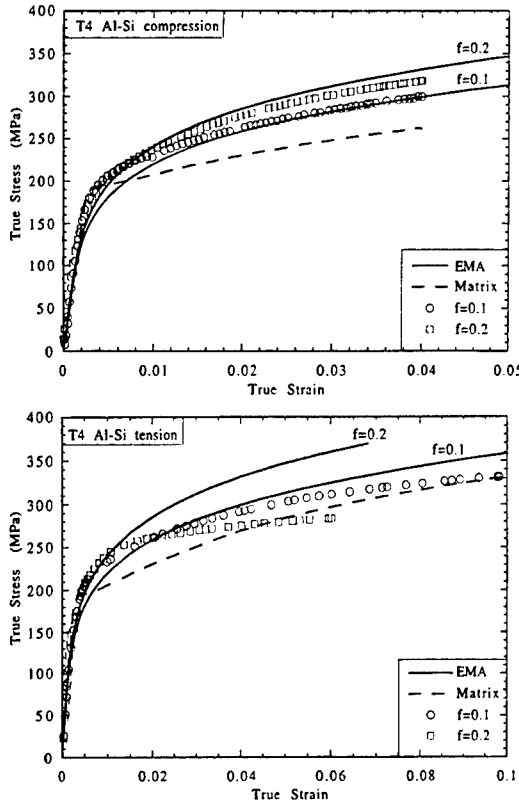


Fig. 2. Comparison between the experimental data of Kiser *et al.* [15] for the Al-Si (T4) composite with different particle volume fractions under (a) compressive and (b) tensile testing and the calculated deformation behavior based on the EMA alone. The data points shown are representative ones selected from the full data set of Kiser *et al.*

In the following section we introduce particle size effects into this EMA formulation by incorporating dislocation plasticity to alter the flow stress in the metal matrix.

3. EFFECT OF PARTICLE SIZE

3.1. Incorporation of dislocation plasticity

In the dislocation description of deformation in two-phase composites, four distinct contributions to the flow stress can be identified. The first is the Orowan stress, the stress to pass a dislocation through an array of impeding particles of average spacing, L .

$$\Delta\sigma_{or}^m = \alpha \frac{\mu^m b}{L} \quad (14)$$

where α is a constant of the order of 1, μ^m is the elastic shear modulus of the matrix and b is the Burgers vector of the matrix metal. The mean particle spacing is related to the particle size and volume fraction by the usual equation

$$L = (\pi d^2 / 4f)^{1/2}$$

where d is the particle diameter. The second and third contributions are those due to the strain gradient effects associated with geometrically necessary distributions of dislocations required to accommodate the plastic strain mismatch between the particles and the surrounding matrix [16]. The isotropic form of the strain gradient contribution to the flow stress can be written, following Brown [7, 17], as

$$\Delta\sigma_{iso}^m = \beta \mu^m \sqrt{\frac{f \epsilon_p b}{d}} \quad (15)$$

where β is a geometric factor, which according to Brown, has a numerical value of ~ 0.4 , ϵ_p is the plastic strain in the matrix metal. The kinematic strain gradient contribution has the form

$$\Delta\sigma_{kin}^m = \gamma \mu^m f \sqrt{\frac{\epsilon_p b}{d}} \quad (16)$$

where γ is another geometric factor with a numerical value of ~ 2.0 .

The fourth possible contribution is the strengthening due to the statistically stored density, ρ , of dislocations, introduced for instance as a result of processing and thermal expansion mismatch on cooling. This may be written quite generally as [18]

$$\Delta\sigma_{STE}^m = \eta \mu^m b \sqrt{\rho} \quad (17)$$

where η is another constant of order unity. For the particular case in which the dislocations are created by thermal expansion mismatch, $\Delta\alpha$, and the particles are again spherical, the dislocation density can be expressed [19, 20] as

$$\rho = \frac{6\Delta T \Delta \epsilon f}{bd(1-f)} \quad (18)$$

where ΔT is temperature change from the heat treatment temperature of the matrix to room temperature. It should be noted that the form of the thermal expansion contribution has the same functional dependence on particle size and volume fraction as does the isotropic strain gradient term.

These four contributions to the overall dislocation flow stress can be incorporated into the effective medium calculations by modifying the yield stress used in the Ramberg-Osgood equation. Thus, σ_o^m in equation (11) becomes

$$\sigma_o^* = \sigma_o^m + \Delta\sigma^m \quad (19)$$

where σ_o^m is the original yield strength of the unreinforced matrix and $\Delta\sigma^m$ is the net dislocation strengthening effect due to the presence of the particulates. The question arises, as in other areas of dislocation plasticity, of how to appropriately combine the individual flow stresses in equations (14)–(17). We have chosen to add them in quadrature [4, 21, 22]:

$$(\Delta\sigma^m)^2 = (\Delta\sigma_{or}^m + \Delta\sigma_{kin}^m)^2 + (\Delta\sigma_{iso}^m)^2 + (\Delta\sigma_{STE}^m)^2. \quad (20)$$

Replacing the matrix yield stress σ_0^m in equation (11) with the modified yield stress σ_0^{m*} to account for dislocation plasticity effects in the matrix therefore provides a particle size dependence for the calculated mechanical behavior of the composite. The calculational results for the Al-15 v/o SiC and Al-Si composites are shown in Figs 3 and 4. Comparison with the data for the Al-Si composites and the EMA results shown in Fig. 1 indicates that the calculated flow stresses in the low strain region (Fig. 3) are in reasonable agreement with experiment. However, in the large strain region, the calculated flow stress of the composites are noticeably higher than experiment and the difference between theory and experiment becomes progressively larger with increasing particle size. This can be attributed to the increasing contribution from the strain gradient terms. From Fig. 4 for the Al-Si (T4) composite, the calculated compressive stresses in the larger strain region are also higher than the experiment. For the Al-Si composite, the compressive behavior is mainly dependent on the volume fraction of the Si particles. Also, the calculations do not lead to the large tension-compression stress-strain asymmetry shown in the experiment (Fig. 4). The large deviations from the predictions in the case of the larger particle

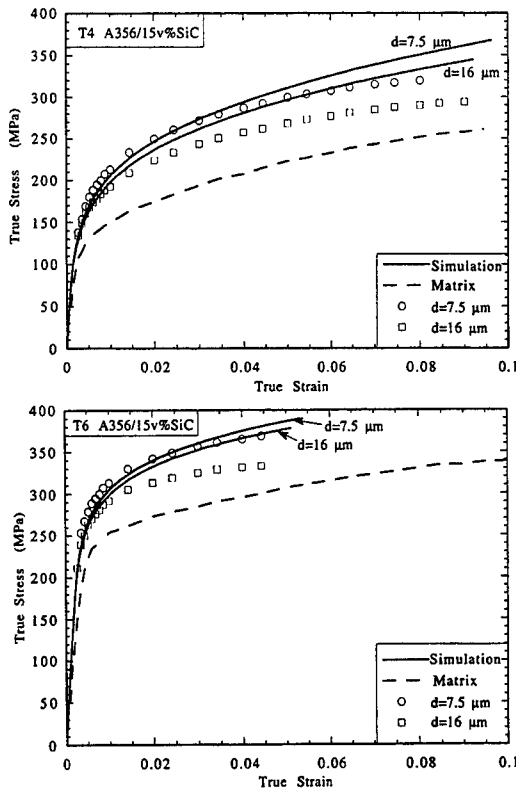


Fig. 3. Comparison between the experimental data for the Al-15 v/o SiC composites and those calculated using an EMA incorporating the full dislocation plasticity described by equations (19) and (20) in the text. (a) T4 aluminum matrix. (b) T6 aluminum matrix.

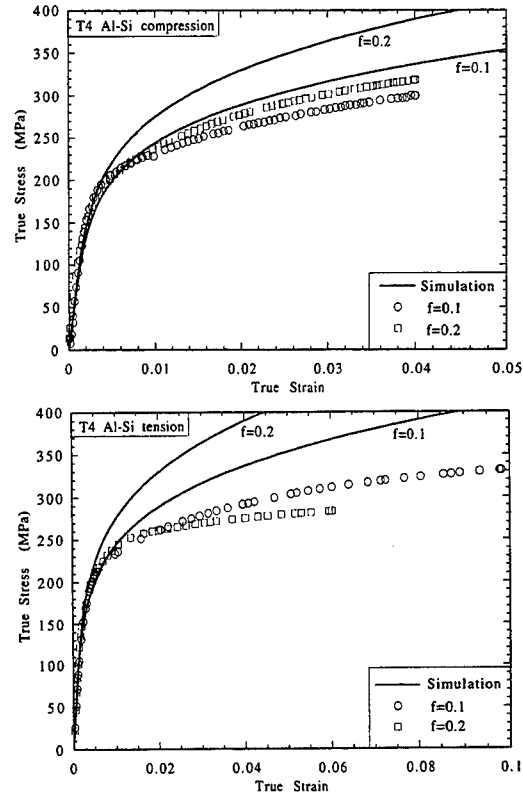


Fig. 4. Comparison between the experimental data for the Al-Si (T4) composite under compression (a) and tension (b) and the calculations using the EMA incorporating dislocation plasticity described by equations (19) and (20) in the text.

size (Fig. 3) and higher volume fraction (Fig. 4) composites are probably related to damage in the form of particle cracking [23, 24] as will be discussed later. However, in order to have a better understanding of the role of such damage on the deformation behavior of the metal matrix composites, we first take into account the effect of distribution in particle size.

Figure 5 shows the effect of the different values of a uniform particle size on stress-strain behavior of the Al-15 v/o SiC (T4) composite. When the particle size is large, e.g. $d > 10 \mu\text{m}$, there is only a slight dependence of the behavior on the particle size and so continuum plasticity dominates. In contrast, when the particle size is small, e.g. $d < 0.5 \mu\text{m}$, the dislocation strengthening dominates and the mechanical behavior has a strong dependence on particle size. In the intermediate particle size range, both mechanisms play a significant role in the deformation response of these metal matrix composites.

3.2. Incorporation of particle size distribution

To incorporate the effect of a distribution of particle sizes, we consider that the composite is made up of an assemblage of perfectly bonded composite

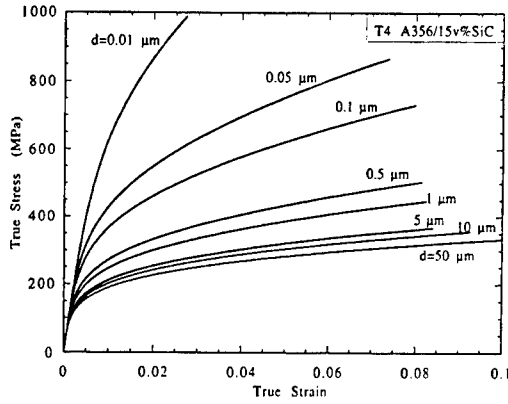


Fig. 5. Predictions for the effect of different uniform particle sizes on the flow behavior of the T4 Al-15 v/o SiC composite. The dislocation plasticity contribution is described by equations (19) and (20) in the text.

spheres in the spirit of Hashin's original approach to composite materials [25] (Fig. 6). In each composite unit, the volume fraction of the particle is f . By using the EMA results above, we can express the average strain and stress in any composite unit as

$$\bar{\epsilon}_{kk}^e = \frac{3k^m + 4\mu^{ms}}{3k^* + 4\mu^{ms}} \frac{1}{3k^m} \sigma_{kk}^m, \quad (21)$$

$$\bar{\sigma}_{kk}^e = \frac{3k^m + 4\mu^{ms}}{3k^* + 4\mu^{ms}} \frac{k^*}{k^m} \sigma_{kk}^m$$

$$\bar{\epsilon}_{ij}^{rc} = \frac{\mu^{ms} + \gamma^s}{\mu^* + \gamma^s} \frac{1}{2\mu^{ms}} \sigma_{ij}^{rm},$$

$$\bar{\sigma}_{ij}^{rc} = \frac{\mu^{ms} + \gamma^s}{\mu^* + \gamma^s} \frac{\mu^*}{\mu^{ms}} \sigma_{ij}^{rm} \quad (22)$$

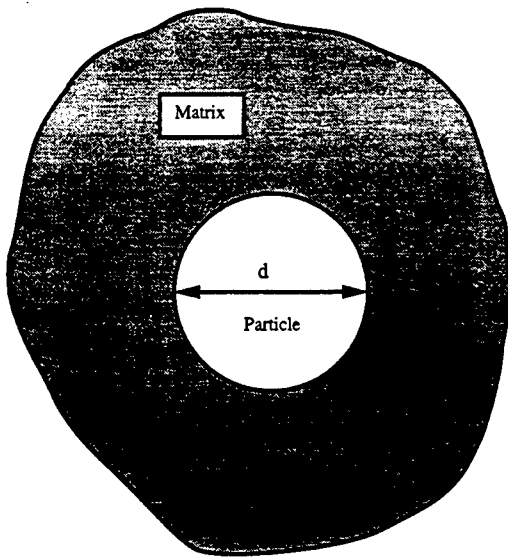


Fig. 6. A composite unit consisting of a particle, diameter d , and its surrounding matrix. The volume fraction of the particle is f .

where k^* and μ^* are still determined by equation (8). The macroscopically averaged stress and strain in the MMC are then the stochastic averages of the stress and strain in the individual composite units, namely

$$\bar{\sigma}_{kk} = \langle \bar{\sigma}_{kk}^e \rangle = \left\langle \frac{3k^m + 4\mu^{ms}}{3k^* + 4\mu^{ms}} \frac{k^*}{k^m} \right\rangle \sigma_{kk}^m \quad (23)$$

$$\bar{\sigma}_{ij}^{rc} = \langle \bar{\sigma}_{ij}^{rc} \rangle = \left\langle \frac{\mu^{ms} + \gamma^s}{\mu^* + \gamma^s} \frac{\mu^*}{\mu^{ms}} \right\rangle \sigma_{ij}^{rm} \quad (24)$$

$$\bar{\epsilon}_{kk} = \langle \bar{\epsilon}_{kk}^e \rangle = \left\langle \frac{3k^m + 4\mu^{ms}}{3k^* + 4\mu^{ms}} \right\rangle \frac{1}{3k^m} \sigma_{kk}^m \quad (25)$$

$$\bar{\epsilon}_{ij}^{rc} = \langle \bar{\epsilon}_{ij}^{rc} \rangle = \left\langle \frac{\mu^{ms} + \gamma^s}{\mu^* + \gamma^s} \frac{1}{2\mu^{ms}} \right\rangle \sigma_{ij}^{rm} \quad (26)$$

where the quantities within the angular brackets are functions of particle sizes. Given a distribution of particle size, the average $\langle F(d) \rangle$ is given by

$$\langle F(d) \rangle = \int F(d) P(d) dd \quad (27)$$

where $P(d)$ is the number frequency function of the particle size distribution which is usually expressed by a lognormal distribution function, i.e.

$$P(d) = \frac{1}{\sqrt{2\pi}\delta d} \exp \left[-\left(\frac{\ln(d/\bar{d})}{\delta} \right)^2 \right] \quad (28)$$

where \bar{d} and δ are the mean particle size and the standard deviation, respectively. By assuming an initial value for σ_{ij}^m , the entire stress-strain relation of the MMC can be calculated at a given particle volume fraction and size distribution from these averaging equations.

When the effect of a lognormal distribution in particle sizes is included in the simulations, it has little effect on the predicted deformation behavior. This conclusion is not the case when damage occurs as will be seen in the following section. Therefore it is sufficient to consider only the effects of the average particle size when no damage occurs during deformation. However, in practice, the larger particles tend to more easily crack than smaller particles during deformation, especially upon tensile testing. Recent investigations have indicated that there is a particle size dependence of particulate fracture, with a measurable increase in the number of particles fractured with increasing strain at low strains [23]. It transpires that the particle size distribution, $P(d)$ in equation (27), is very important for modeling particle cracking effects in the MMCs.

4. EFFECT OF REINFORCEMENT FRACTURE DURING DEFORMATION

As tensile deformation proceeds, the strain, and hence the stress, in the reinforcement phase increases.

Table 3. Particle size parameters

MMC	Average particle size d (μm)	Standard deviation δ	Size range (μm)
A356/SiC/15p	7.5	0.55	1-60
A356/SiC/15p	16	0.35	1-60
10% Si-Al	3.5	0.35	1-14
20% Si-Al	4.6	0.4	1-20

In some cases, particularly with large particles, the stress can exceed the fracture strength and the particles then break. Metallographic studies by a number of authors (see, for example, Refs [14, 23, 24]) have shown that particles are broken and that the proportion of particle fractures increases with increasing strain imposed on the composite. Such particle fracture will have the effect of decreasing the secant modulus of the composite. Also, if the fractures are localized it can lead to a necking instability of the composite.

To quantify the effects of particle fracture during deformation, we introduce particle fracture into the effective medium calculation in the following phenomenological manner: at each iteration in the deformation, the stress in the particles is calculated as a function of the size distribution, namely

$$\sigma_{kk}^p = \frac{3k^m + 4\mu^{ms} k^p}{3k^p + 4\mu^{ms} k^m} \sigma_{kk}^m \quad (29)$$

$$\sigma_{ij}^p = \frac{\mu^{ms} + \gamma^s \mu^p}{\mu^p + \gamma^s \mu^{ms}} \sigma_{ij}^m \quad (30)$$

Then, the particle is considered to break if the stress in the particle exceeds the Griffith criterion, where the fracture stress is given by

$$\sigma_c^p = K/\sqrt{d} \quad (31)$$

where K is a constant related to the fracture toughness of the particles together with geometrical factors. In the MMC, the value of the constant K is also related to the metal matrix. Particles in the MMC with high strength of the metal matrix generally have high fracture stress σ_c^p [15].

If the fracture stress is exceeded in a particle of a given size during an increment of deformation, those sized particles are then considered broken. Henceforth they are considered to be a void in the subsequent iterations. This is accomplished by setting their modulus to zero. Then the deformation is incremented according to equations (23)–(26) with the average strain and stress of the MMCs calculated to each iteration.

For illustration we re-calculate the flow behavior of the Al-15 v/o SiC and Al-Si (T4) composites using this procedure to account for particle fracture. The particle size parameters for these two systems are summarized in Table 3. The values of the parameter K in equation (31) are taken as $K = 2.4 \text{ MPa}\sqrt{\text{m}}$ for SiC in the A356 T4 aluminum matrix, $2.8 \text{ MPa}\sqrt{\text{m}}$ for Si in the A356-T6 aluminum matrix, and $1.1 \text{ MPa}\sqrt{\text{m}}$ for Si in the T4 matrix,

which are reasonable values considering the macroscopic fracture toughness of SiC and Si. The calculated results for these two sets of composites are shown in Figs 7 and 8. The comparison of Fig. 7 shows that the calculated flow curves for Al-15 v/o SiC composites correspond closely with experiment for both particle sizes. By comparison with Fig. 3, particle cracking in the larger particle size composite (Al-15 v/o SiC, $d = 16 \mu\text{m}$) leads to a larger degradation in the flow stress. The comparison of Fig. 8 also shows that the calculation is in good agreement with experiment for the Al-Si composite in tension. As no cracking is likely to occur in compression, the deformation behavior of the composite is expected to be the same as shown in Fig. 4(a). As might be expected the effect of particle size on the deformation behavior is greater at the

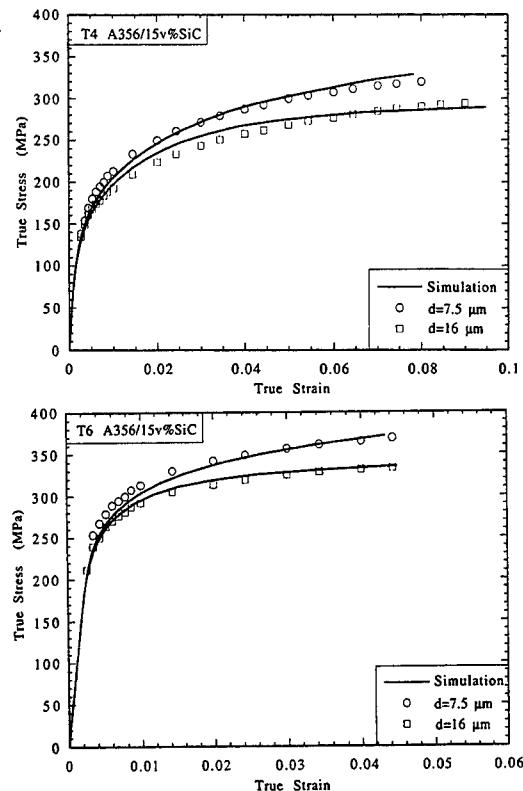


Fig. 7. The effects of particle fracture: comparison between the experimental data for the Al-15 v/o SiC composites and those calculated using EMA with incorporated dislocation plasticity and particle fracture effects. The values of the particle size parameters used are listed in Table 3. (a) T4 aluminum matrix. (b) T6 aluminum matrix.

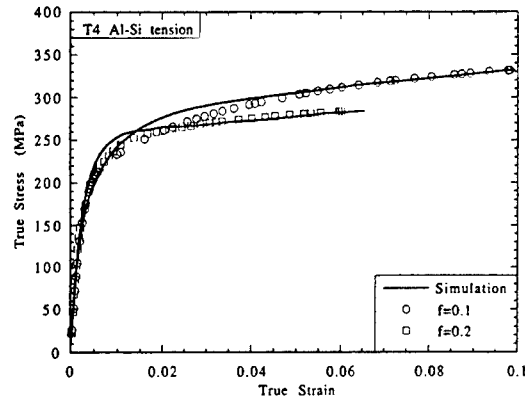


Fig. 8. The effects of the reinforcement fracture: comparison between the experimental data in tension for the Al-Si (T4) composite and the calculations based on the EMA incorporating dislocation plasticity and particle fracture effects.

higher particle volume fraction. These two examples show that the theory models the effect of the particle cracking during the composite deformation rather well. In addition, comparison of the Al-Si composite in tension and compression [Figs 4(a) and 8] indicate larger tension-compression stress-strain asymmetry.

In order to illustrate the effect of variations in particle size distribution on the deformation behavior when particle fracture is included, a series of simulations with increasing standard deviation, δ , in particle size were performed for the T4 Al-15v/oSiC composite. The effect of three different values for the standard deviation are shown in Fig. 9. According to the Griffith relation, the particles most susceptible to fracture are those at the larger size range of the population. Thus, with increasing standard deviation of the particle size distribution, the number of larger particles and hence of cracked particles at a given strain increase. As a result the calculated flow stress decreases as shown in Fig. 9.

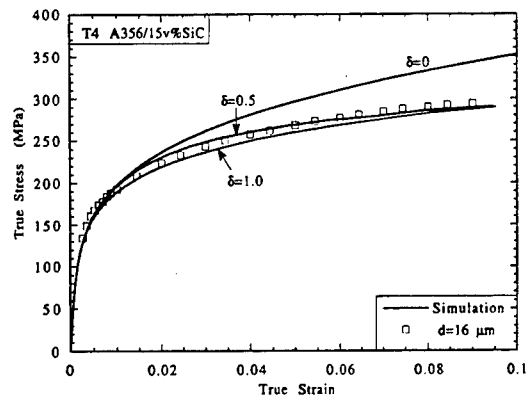


Fig. 9. Effect of the standard deviation δ of the particle size distribution on the flow curve for T4 Al-15 v/o SiC composite. Effective medium calculation with dislocation plasticity and particle fracture.

5. DISCUSSION

The calculations presented here demonstrate that the full stress-strain curves of two different sets of Al matrix composites can be reproduced by a single hybrid continuum and dislocation plasticity calculation incorporating particle fracture during deformation. Although the correspondence between experiment and the predictions is clearly not unique, since different numerical values for the constants in the individual dislocation contributions [equations (14)–(18)] and the fracture toughness of the particles could have been chosen, it is nevertheless a rather demanding test as reasonable values for all the numerical constants were adopted. Thus, whilst it could be argued that a correspondence between experiment and theory can always be obtained with a sufficient number of free parameters, it is important to emphasize that in the calculations presented here there were no adjustable parameters beyond those usually used in dislocation models. However, the real value of these calculations is that the influence of different contributions to the flow stress of a composite can be assessed, as is done in the following.

As anticipated, the stress-strain curves (Figs 1 and 2) calculated using the effective medium equations alone do not adequately describe the observed particle size dependence. However, the correspondence with the experimental data, especially at the larger particle size in the Al-SiC composites (Fig. 1) and in compression for the Al-Si alloys (Fig. 2), is nevertheless striking. This is especially so since the only input parameters are those used to describe the flow stress of the metal matrix material by the Ramburg-Osgood equation and the volume fraction and elastic moduli of the particulate phase. Some discrepancies appear at small strains but this is probably attributable to the inadequacies of the Ramburg-Osgood equation in describing the deformation behavior near the yield point rather than any underlying weakness of the effective medium equations. Although other continuum constitutive relations could have been used in implementing the effective medium calculations presented here, the Ramburg-Osgood equation was adopted since it is the one generally used in finite element computations thereby facilitating future comparisons. Furthermore, our choice of using the effective medium equations to calculate the continuum deformation behavior rather than the more conventional finite element approach was based on two factors. Firstly, it is insensitive to the detailed local geometric arrangement of the particles and hence samples all geometric arrangements equivalently. It thus avoids the accidental arrangements of particles that can lead to either unrepresentatively low or high flow stresses sometimes seen in finite element computations. Secondly, it is also considerably faster to compute. In addition to the volume fraction,

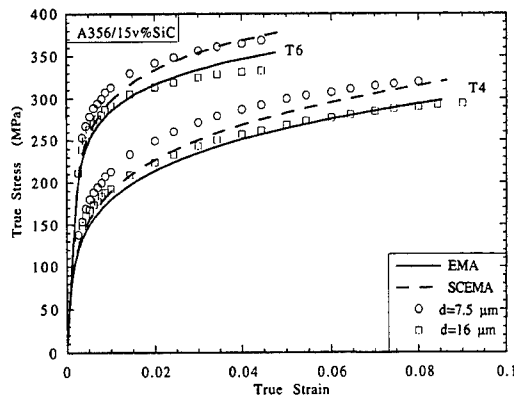


Fig. 10. Comparison between the predictions of both the effective medium approximation (EMA) and the self-consistent effective medium approximation (SCEMA) and the experimental flow curves for the two sets of Al-15 v/o SiC composites. No dislocation plasticity or particle fracture effects are included.

the EMA formulation [13] can also directly incorporate the effects of particle shape (i.e. platelet, whisker, particulate) and reinforcement distribution. Although these are not discussed in the present work they are expected to be of some importance when the methodology detailed here is extended to other metal matrix composites, for instance those consisting of aligned fibers such as the Cu-W system.

In this work we have in fact only used the first order form of the effective medium approximation, namely that in which the effective medium in which the particles are embedded corresponds to that of the metal matrix alone, i.e. $C^0 = C^m$. This is known to be a reasonable approximation when the volume fraction of particles is small and the particles are dispersed as with the two aluminum composites considered in this work. However, when the particle volume fraction is high and they can agglomerate, it is more reasonable to consider the particles embedded in a composite effective medium whose stiffness, C^* , must be obtained self-consistently. At low volume fractions the two forms of EMA solutions give only slightly different results but the difference becomes more marked with increasing volume fraction. For illustration, Fig. 10 shows a comparison between the predictions of the EMA and SCEMA calculations for the case of the two Al-SiC composites, which contain 15 v/o particles. The SCEMA predicts a consistently higher flow stress than the EMA solutions. However, given the relatively small differences for the volume fractions considered here the simpler EMA formulation is adequate for the illustrative purposes of this work.

The introduction of dislocation strengthening of the matrix has two effects as was anticipated. One, it introduces a particle size effect and, two, it increases the flow stress in each of the composites as shown by the simulations in Figs 3-5. The effect of dislocation plasticity has, of course, been introduced

into the effective medium calculation in an empirical fashion [equations (19)]. As a result the degree of strengthening depends, as might be expected, on the particular plasticity contribution included and on the particle size. The effect of the latter is shown by the curves in Fig. 5. The magnitude of the different dislocation contributions is more difficult to illustrate in a comprehensive manner. Also, the different dislocation strengthening mechanisms will vary in importance from one composite material to another depending on the particle sizes, volume fractions and shapes. Furthermore, the individual mechanisms may not contribute to the flow stress in the non-linear fashion assumed in equation (20). However, despite these complications, some appreciation of the relative contributions to the quantitative stress-strain behavior can be obtained by comparing the predictions with the deformation response of the T4 Al-Si composites in compression, as is shown in Fig. 11(a) and (b). Since no particle fracture is expected under compression testing, at least at the strains reported

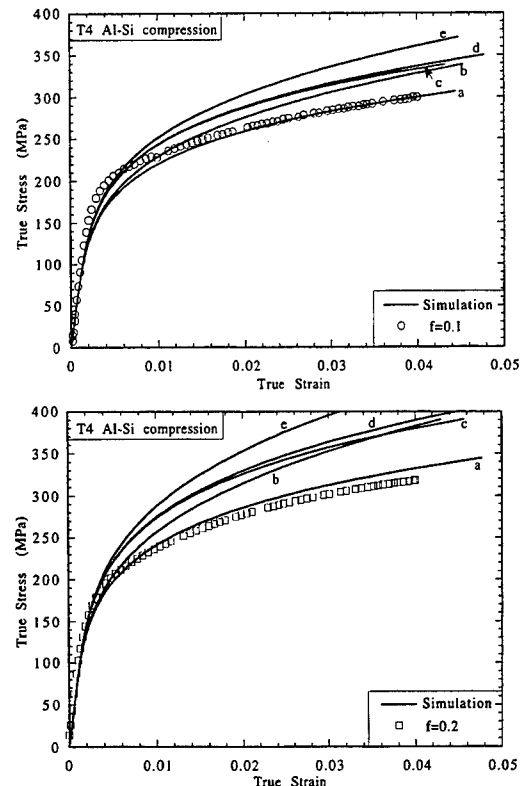


Fig. 11. The effect of including different dislocation plasticity contributions to the flow stress used in the EMA calculations of the T4 Al-Si composites under compression. (a) 0.1 and (b) 0.2 volume fraction of Si particles. Curves *a*, *b*, *c* correspond to the EMA calculation with Orowan strengthening, Orowan strengthening plus strain gradient plasticity and Orowan strengthening plus thermal expansion, respectively. Curve *d* is the full dislocation plasticity calculation given by equation (20). Curve *e* is that due to the linear addition of all the dislocation contributions.

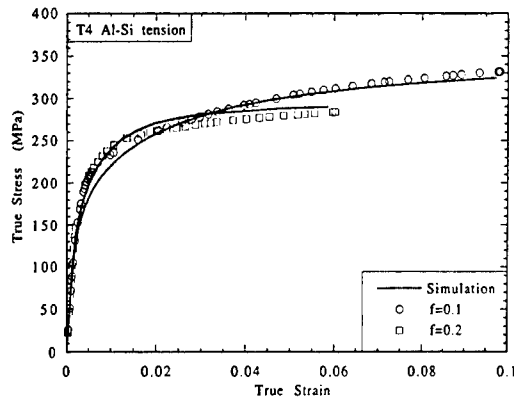


Fig. 12. The effects of the particle fracture. Comparison between the experimental data in tension for the Si-Al (T4) composite and the calculations based on the EMA with incorporated Orowan dislocation plasticity and particle fracture only.

by Kiser *et al.*, the different dislocation contributions can be assessed. As the Si particles in these composites are relatively large, the Orowan strengthening alone is not as significant as that due to the combined strengthening from the Orowan mechanism and either the strain gradient or thermal expansion terms. Also, as expected, when the individual contributions are added linearly to the matrix flow stress (curve e) the predicted flow stress is considerably larger than that when they were added in quadrature (curve d). Interestingly, at least for the Al-Si composite considered here, the inclusion of dislocation strengthening, other than the simple Orowan strengthening, leads to an over-estimate of the flow stress in compression. This would suggest that the numerical value of the geometric constant in the expressions for the dislocation strengthening are perhaps too large. However, this probably remains problematic until experimental data is available for composites with smaller particle sizes ($< 1 \mu\text{m}$) and with similar volume fractions. When only Orowan strengthening and particle fracturing is included in the EMA calculation of the tensile response of the same composites, there is very good correspondence between the simulated stress-strain curves and those reported (Fig. 12).

The comparison between the simulated stress-strain curves and the experimental deformation curves demonstrate that in the metal matrix composites considered here, particle cracking during deformation plays a significant role. The effect can be quite pronounced, especially for the larger particle sizes, as was deduced by Lloyd and Kiser *et al.* on the basis of their experiments. Indeed, since particle fracture is readily observed in most failed composites under tensile loading, it is usually assumed to be responsible for failure. The simulations presented here provide a justification for this assumption as well as quantitative description. The effect of particle fracture is two-fold. First, the decrease in flow stress

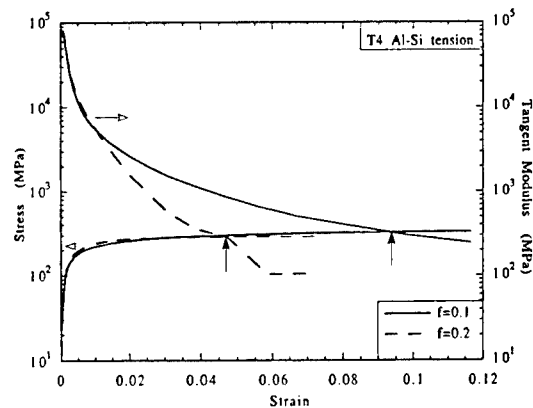


Fig. 13. The calculated tensile stress and tangent modulus as a function of strain for the Al-Si composites with 10 and 20 v/o Si. The point of intersection (arrowed) of the stress and tangent modulus curves corresponds to the predicted strain at which mechanical instability will occur.

caused by particle fracture lowers the tangent modulus. As a result, the condition for mechanical instability, the Considere condition, is attained at a smaller strain than would occur, in the absence of particle fracture. For illustration, this is shown in Fig. 13 in which the tangent modulus as well as the simulated stress-strain curve itself are plotted for both the 10 v/o and 20 v/o Si composites. The strains at which the composites are predicted to fail by mechanical instability are arrowed. The second, related, effect is that the simulations suggest that the decrease in flow stress due to particle fracture can be larger than the increase in flow stress due to dislocation strengthening. This is especially so for the larger particles since they are both more likely to fail, according to the Griffith criteria, and lead to a smaller contribution to dislocation strengthening. Using equations (29)–(31) it is possible to calculate the fraction of particles that break as a function of the deformation strain. The calculated results for the Al-SiC composites are shown in Fig. 14. The larger

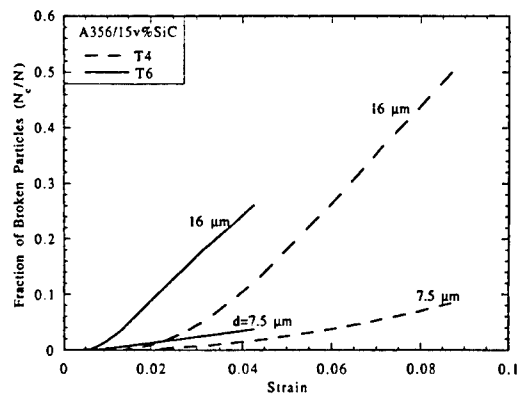


Fig. 14. Calculated fraction of broken particles as a function of deformation strain for the two sets of Al-15 v/o SiC composites.

the mean particle size, the higher the proportion of broken particles at any given strain. As a result, the decrease in flow stress is larger for the larger particle composites than for the smaller particle composites. This is consistent with the comparison between the flow curves in Figs 3 and 7 for the two different sizes in SiC particles. The higher flow stress of the T6 aluminum has the effect of causing the stress in the particles to reach their fracture stress at a smaller strain, thus the curves for the T6 Al-SiC composites are displaced to smaller strains relative to those for the T4 Al-SiC composites. The strain at which the first particles fracture appears to be independent of the mean particle size but this is probably a consequence of the larger standard deviation in the size of the smaller SiC particles than the larger ones (Table 3). From equations (29)–(31) it can be anticipated that the higher the volume fraction of particles in a composite, the lower the applied strain at which particles of a given size fracture. This is borne out by the comparison between the flow stress of the two Al-Si composites. The composite with the 20 v/o particles exhibits a greater decrease in flow stress than the 10 v/o particles, as seen in the comparison between the curves in Figs 8 and 12. A further consequence is that there will be a greater asymmetry between the tension and compression responses for the 20 v/o composite than for the 10 v/o composite. This is seen in both experiment and in the simulations.

6. CONCLUDING REMARKS

A simple calculational procedure for modeling the deformation response of particle reinforced metal matrix composites has been developed in terms of an effective medium approach combined with consideration of the essential features of dislocation plasticity. Comparison with experimental stress-strain curves shows that the procedure can predict the effects of the properties of the matrix metal and reinforcement, the particle size and size distribution and volume fraction on the deformation response of the MMCs. The only input parameters required for the calculation are the particle size, volume fraction, elastic constants and the stress-strain curve of the matrix metal. By incorporating a Griffith criteria for particle fracture, the methodology also successfully accounts for damage in the form of deformation-induced particle cracking and leads to excellent agreement with experiment in which particle cracking is reported to occur. A consequence of particle cracking is that it leads to a tension-compression deformation asymmetry which can be quantified.

Acknowledgements—The authors are grateful to Dr M. T. Kiser and Professors Frank Zok and David Wilkinson for providing details of their experimental results prior to publication, and to Professor L. M. Brown for invaluable discussions during the course of this work. The work was supported by the Advanced Research Projects Agency University Research Initiative at UCSB under contract N00014-92-J-1808. The work of C.W.N. was also supported by The State Education Commission of China.

REFERENCES

1. A. Kelly and R. B. Nicholson (eds), *Strengthening Methods in Crystals*. Elsevier, New York (1971).
2. A. Kelly, *Strong Solids*. Oxford University Press, Oxford (1966).
3. N. Hansen, D. J. Jensen, T. Leffers, H. Lilholt, T. Lorenten, A. S. Pedersen, O. B. Pedersen and B. Ralph (eds), *Metal-Matrix Composites: Processing, Microstructure and Properties*. Risø Nat. Lab., Denmark (1991).
4. T. W. Clyne and P. J. Withers, *An Introduction to Metal Matrix Composites*. Cambridge University Press, Cambridge (1993).
5. D. R. Clarke, *J. Am. Ceram. Soc.* **75**, 739 (1992).
6. M. F. Ashby, *Phil. Mag.* **14**, 1157 (1966).
7. L. M. Brown in *Strength of Metals and Alloys* (edited by P. Hassen, V. Gerold and G. Kostore), p. 1551. Pergamon Press, Oxford (1979).
8. F. J. Humphreys, in *Dislocations and Properties of Real Materials*, p. 175. Inst. of Metals, London (1985).
9. Y. P. Qiu and G. J. Weng, *Int. J. Solids Struct.* **27**, 1537 (1991).
10. S. F. Corbin and D. S. Wilkinson, *Acta metall. mater.* **42**, 1131 (1994).
11. G. Bao, J. W. Hutchinson and R. M. McMeeking, *Acta metall. mater.* **39**, 1871 (1991).
12. J. P. Hirth, *Appl. Mech. Rev.* **45**, 575 (1992).
13. C.-W. Nan and R.-Z. Yuan, *Phys. Rev.* **48**, 3042 (1993).
14. D. J. Lloyd, *Int. Mater. Rev.* **39**, 1 (1994).
15. M. T. Kiser, F. W. Zok and D. S. Wilkinson, *Acta metall. mater.* **44**, 3465 (1996).
16. N. A. Fleck, G. M. Muller, M. F. Ashby and J. W. Hutchinson, *Acta metall. mater.* **42**, 475 (1994).
17. L. M. Brown and W. M. Stobbs, *Phil. Mag.* **34**, 351 (1976).
18. N. Hansen, *Acta metall. mater.* **25**, 863 (1977).
19. R. J. Arsenault and N. Shi, *Mater. Sci. Engng* **81**, 175 (1986).
20. R. J. Arsenault, L. Wang and C. R. Feng, *Acta metall. mater.* **39**, 47 (1991).
21. H. Lilholt, in *Deformation of Multi-Phase and Particle Containing Materials* (edited by J. B. Bilde-Sørensen, N. Hansen, A. Horsewell, T. Leffers and H. Lilholt), p. 381. Risø Nat. Lab., Denmark (1985).
22. F. J. Humphreys, in *Mechanical and Physical Behavior of Metallic and Ceramic Composites*, p. 51. Risø Nat. Lab., Denmark (1988).
23. D. J. Lloyd, *Acta metall. mater.* **39**, 59 (1991).
24. W. H. Hunt, Jr, J. R. Brockebrough and P. E. Magnusen, *Scripta metall. mater.* **25**, 15 (1993).
25. Z. Hashin, in *Mechanics of Composite Materials* (edited by F. W. Wendt, H. Liebowitz and N. Perrone), p. 201. Pergamon Press, New York (1970).

Modeling the Elastic-Plastic Deformation of Al/Al₂O₃ Particulate Composites

Ce-Wen Nan and David R. Clarke*

Materials Department, University of California, Santa Barbara, California 93106-5050

Comparison is made between experimental measurements of the elastic-plastic deformation of a series of Al/Al₂O₃ particulate composites with a rather simple hybrid modeling method combining an effective medium approximation with the essential features of dislocation plasticity. Two different effective approximations—a simple, non-self-consistent and a self-consistent effective medium approximation—are employed depending on the volume fraction of particles. For a wide range of volume fractions of Al₂O₃ particles, there is good agreement between the full stress-strain curves measured and the predictions of the hybrid model.

I. Introduction

ONE of the most significant advances to have been made in recent decades in materials processing has been the ability to fabricate composites with large volume fractions of particulate reinforcement, significantly larger than can be obtained by the traditional dispersion or precipitation hardening approaches. Thus, the Dimox process,¹ the melt infiltration,² and the slurry-casting process³ have all been used to make aluminum alloy composites with Al₂O₃ particulate loadings up to 50 or 60 vol%. At these high volume fractions, the usual “rule-of-mixtures” approaches⁴ to modeling the deformation behavior are unreliable since they do not take into account the elastic interaction between the particulates. They are, in essence, dilute solution models and as such are strictly only applicable to low volume fractions of randomly dispersed particles in which the particles are widely spaced. They are, in essence, analogous to the Einstein equations for the viscosity of dilute suspensions. At large volume fractions, other modeling approaches are necessary and a number have been described in the literature. One such approach is to use finite element computations. This requires a detailed knowledge of the constitutive behavior of the individual phases in the composite as well as of the geometry of the particles and their spatial arrangements. Another approach is some form of a number of effective medium approximations in which the response of the composite is calculated on the basis of the deformation of a volume fraction of particles embedded in a matrix having deformation characteristics approximating those of the composite. Each of these approaches, however, neglects the contribution to work hardening of the matrix due to dislocation processes, which can be of significance when the spacing between particles is small. While dislocation plasticity has been extremely successful in model-

ing the plastic deformation of metals containing low volume fractions of small (submicrometer) inclusions and precipitates,^{5,6} it invariably overestimates the work hardening rate and underestimates the increase in yield stress of metals containing large (greater than micrometer) particles. In contrast, the continuum plasticity computations, whether based on finite element methods or effective medium calculations, when applied to dispersion-hardened materials generally underestimate the work-hardening. The failure of the presently developed dislocation models stems, in large part, from the fact that they do not adequately take into account the elastic interactions between particles. In this contribution, we utilize recent experimental results on the deformation behavior of Al₂O₃-particulate-loaded aluminum alloy matrix to compare two effective medium approximations and the contribution from dislocation plasticity. In contrast to the majority of studies of the deformation behavior of metal-matrix composites in the literature, the experimental data published by Aghajanian *et al.*⁷ are particularly suited for modeling since they not only include a range of volume fractions of particles (from 25% to 52%) but also present the full stress-strain curve of the metal used to form the matrix.

II. Effective Medium Approximations

In effective medium approaches, the composite is assumed to behave as a continuum in which the particles are perfectly bonded to the matrix material. Usually both the matrix and the particles are considered to respond elastically but in a recent formulation the method has been extended to treat an elastoplastic matrix.⁸ In such a material, the constitutive relation between the average stress and strain in the composite can be written in terms of its secant stiffness C^* , namely

$$\bar{\sigma} = C^*(\bar{\epsilon})\bar{\epsilon} \quad (1)$$

For the particular case of a composite containing spherical particles, the pertinent moduli are the effective secant bulk modulus, k^* , and the shear modulus, μ^* . The effective medium calculation for the effective moduli then reduces to the standard Eshelby expressions for a composite of spherical inclusions,⁹ and the two moduli can be expressed as

$$\frac{k^* - k^m}{3k^* + 4\mu^o} = f \frac{k^p - k^m}{3k^p + 4\mu^o} \quad (2a)$$

$$\frac{\mu^* - \mu^{ms}}{\mu^* + y^o} = f \frac{\mu^p - \mu^{ms}}{\mu^p + y^o} \quad (2b)$$

with

$$y^o = \frac{\mu^o(9k^o + 8\mu^o)}{6(k^o + 2\mu^o)}$$

where k^o and μ^o are the secant bulk and shear moduli of the effective reference medium. k^m and μ^{ms} are the secant bulk and the shear moduli of the metal matrix; k^p and μ^p are the elastic bulk and the shear moduli of the particles, and f is the volume fraction of the particles. By decomposing the stress and strain into hydrostatic (σ_{kk} and ϵ_{kk}) and deviatoric (σ'_{ij} and ϵ'_{ij}) parts,

W. D. Nix—contributing editor

Manuscript No. 191559. Received September 4, 1996; approved October 18, 1996. Supported by the Advanced Research Projects Agency University Research Initiative at the University of California, Santa Barbara, under Contract No. N00014-92-J-1808. The work of C.W.N. was also supported by The State Education Commission of China.

*Member, American Ceramic Society.

the average stress and strain in the metal matrix (Eq. (2)) can be expressed as

$$\epsilon_{kk}^m = \frac{3k^* + 4\mu^o}{3k^m + 4\mu^o} \bar{\epsilon}_{kk} \quad (3a)$$

$$\sigma_{kk}^m = \frac{3k^* + 4\mu^o k^m}{3k^m + 4\mu^o k^*} \bar{\sigma}_{kk} \quad (3b)$$

$$\epsilon_{ij}^m = \frac{\mu^* + y^o}{\mu^{ms} + y^o} \bar{\epsilon}_{ij} \quad (4a)$$

$$\sigma_{ij}^m = \frac{\mu^* + y^o \mu^{ms}}{\mu^{ms} + y^o \mu^*} \bar{\sigma}_{ij} \quad (4b)$$

From these equations, as in all formulations of the effective medium approach, two different approximations can be obtained depending on the choice of the constants k^o and μ^o describing the reference composite. One is the simple effective medium approximation (EMA) in which the reference state is the metal matrix alone, namely $k^o = k^m$ and $\mu^o = \mu^{ms}$. The second is that in which the reference material corresponds to the composite itself and the values are obtained self-consistently, $k^o = k^*$ and $\mu^o = \mu^*$. This is the self-consistent effective medium approximation (SCEMA). The former is generally valid when the concentration of particles is small and the latter when the concentration of particles is sufficiently high that elastic interactions between the particles are included. Therefore, with a knowledge of the elastic moduli and volume fraction of particles, and the stress-strain behavior of the matrix metal, the full deformation of the composite can be calculated using these two approximations.

To proceed, a constitutive relation between the stress and strain in the matrix is required. We adopt the Ramberg-Osgood equation:

$$\epsilon^m = \frac{\sigma^m}{E^m} + \alpha \frac{\sigma_0^m (\sigma^m)^{1/n}}{E^m} \quad (5)$$

It is commonly used in finite element computations since it adequately expresses the elastic-plastic response of most metals used as matrices. E^m is Young's modulus of the matrix, σ_0^m is its yield strength, n is the strain hardening exponent, and α is a dimensionless constant (here $\alpha = 3/7$ is taken). (The uniaxial behavior can be generalized to a triaxial stress state using the Mises invariant in the usual way.) The secant modulus of the isotropic matrix metal, defined by the ratio of tensile stress to the tensile strain, is given by

$$E^{ms} = \frac{E^m}{1 + \alpha \left(\frac{\sigma_0^m}{\sigma^m} \right)^{n/(1-n)}} \quad (6)$$

Further, making the standard assumption that a metal is plastically incompressible requires that the secant bulk modulus of the metal matrix be equal to its linear elastic bulk modulus. The secant shear modulus μ^{ms} can then be written as

$$\mu^{ms} = \frac{E^{ms}}{3 - E^{ms}/3k^m} \quad (7)$$

In order to calculate the full stress-strain curve of the composite, the following procedure is adopted. First, a value for the initial stress in the matrix, σ_{11}^m , is assumed and the values of E^{ms} and μ^{ms} are calculated using Eqs. (6) and (7). From these values, the composite moduli, k^* and μ^* , are calculated from Eq. (2). Having obtained these values the average stress and strain of the composite are calculated from Eqs. (3) and (4). This provides a point on the stress-strain curve. The value of σ_{11}^m is then increased incrementally and the process repeated until the entire stress-strain curve is computed.

III. Comparison with Experiment

According to the above scheme, the only parameters needed to describe the entire stress-strain curve of the composites are

the flow stress of the metal and the volume fraction and elastic properties of the particulate phase. By fitting the stress-strain curve of the unreinforced metal in the T4 condition presented by Aghajanian *et al.*,⁷ the parameters in the Ramberg-Osgood equation were found to be $n = 0.0507$ and $\sigma_0^m = 151.95$. The other data required for calculating the effective medium approximations are Young's modulus and Poisson's ratio of the metal and particles $E^m = 70$ GPa, $\nu^m = 0.33$, $E^p = 363$ GPa, and $\nu^p = 0.25$. Using these data, the computed effective medium and self-consistent effective medium approximations to the stress-strain curves are shown in Figs. 1(A) and (B), respectively, together with Aghajanian *et al.*'s experimental results. As might be expected, the simple effective medium approximation (EMA) consistently underpredicts the flow stress and exhibits a considerably smaller dependence on particle volume fraction than experiment. In contrast, the self-consistent effective medium approximation (SCEMA) predictions are clearly much closer to the experimental data, especially at the higher volume fractions. (The discrepancies at small strains are most probably attributable to the inadequacies of the Ramberg-Osgood equation in describing the deformation behavior near the yield stress rather than any underlying weakness of the effective medium equations.) Despite the similar form and trends of the calculated SCEMA stress-strain curves, they do, nevertheless, consistently underestimate the flow stress at all volume fractions and the difference becomes more marked with increasing plastic strain. This difference is attributed to the neglect of dislocation plasticity in contributing to the flow stress in the metal matrix and hence in the effective medium calculation.

IV. Inclusion of Dislocation Plasticity

Dislocation plasticity in the matrix has the effect of increasing the flow stress of the metal. As such, it can be readily incorporated into the effective medium approach by modifying the constitutive behavior assumed for the metal. This can be achieved by expressing the yield stress used in the Ramberg-Osgood relation as

$$\sigma_0^{m*} = \sigma_0^m + \Delta\sigma^m \quad (8)$$

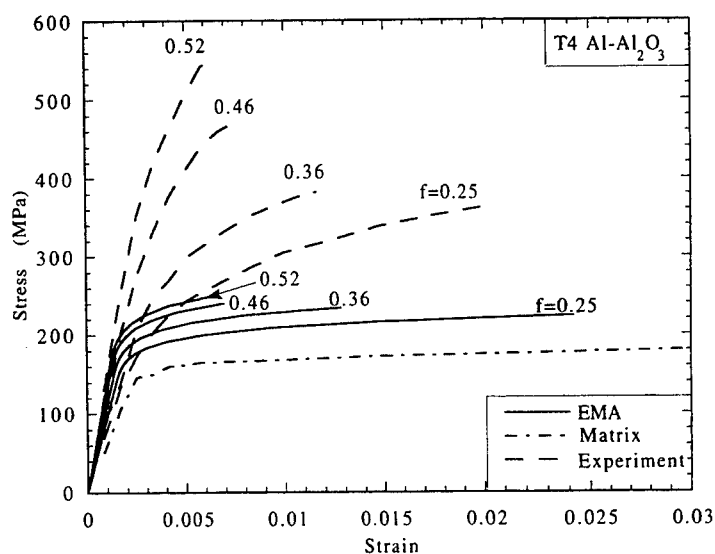
where σ_0^m is the original yield strength of the unreinforced matrix and $\Delta\sigma^m$ is the net dislocation strengthening effect due to the presence of the particles. Four principal contributions to the net dislocation strengthening can be envisaged:⁵ the stress required to bow dislocations between adjacent particles, the Orowan stress, σ_{OR}^m ; the strengthening due to isotropic and kinematical strain gradient effects, σ_{ISO}^m and σ_{KIN}^m ; and the additional strengthening resulting from interaction from dislocations punched in as a result of the thermal expansion mismatch between the metal and the particles, σ_{CTE}^m . Although there always remains the issue of how these individual contributions should be combined, we adopt the simplest approach, namely that they be added:

$$\Delta\sigma^m = \sigma_{OR}^m + \sigma_{ISO}^m + \sigma_{KIN}^m + \sigma_{CTE}^m \quad (9)$$

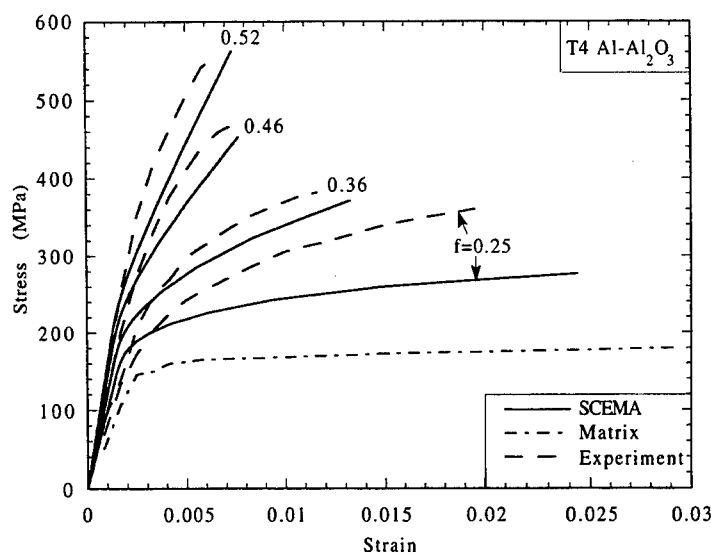
Since analytical expressions for the individual terms have been presented in the dislocation literature, together with justification for their formulation, we simply adopt them here. Using these expressions, the net dislocation strengthening can be written as

$$\Delta\sigma^m = K\mu b \sqrt{\frac{4f}{\pi d^2}} + \beta\mu \sqrt{\frac{fb\epsilon_p}{d}} + \gamma\mu f \sqrt{\frac{b\epsilon_p}{d}} + \eta\mu \sqrt{\frac{6fb\Delta T\Delta\alpha}{d(1-f)}} \quad (10)$$

where K and η are constants of order unity, $\beta \sim 0.4$ and $\gamma \sim 2.5$, d is the particle size and μ and b are the matrix shear modulus and the Burgers vector, respectively, and ϵ_p is the plastic strain in the matrix. ΔT is the temperature change on cooling from the



(A)



(B)

Fig. 1. Comparison between the experimental stress-strain curves of Al/Al₂O₃ particulate composites for a range of volume fractions and calculations based on (A) the effective medium approximation (EMA) and (B) the self-consistent effective medium approximation (SCEMA).

heat-treatment or fabrication temperature and $\Delta\alpha$ is the thermal expansion mismatch.

The effect of incorporating dislocation plasticity into the effective medium approximations is shown in Figs. 2(A) and (B) for the EMA and SCEMA, respectively. In calculating the curves, the mean particle size of 15 μm stated by Aghajanian *et al.*⁷ has been used in evaluating the dislocation strengthening (Eq. (10)). While the overall contribution from dislocation plasticity is not large, primarily because of the relatively large particle size, its incorporation into the self-consistent effective medium approximation does lead to substantially closer agreement with experiment, the exception being for the lowest volume fraction ($f = 0.25$) composite for which the models still underestimate the flow stress after yielding. Since comparison of the stress-strain curves indicates that the hardening rate remains underestimated, it suggests that the dislocation strengthening from the strain gradient terms has not been adequately accounted for in Eq. (10). However, given the uncertainties on how the different dislocation terms should be added together, as well as in the

actual values of the constants in the individual terms, further refinement is not considered justifiable.

V. Summary

In summary, a rather simple hybrid modeling method combining an effective medium approach with the essential features of dislocation plasticity closely matches the deformation response of a series of aluminum matrix composites containing large volume fractions of alumina particles. Neither the effective medium nor the dislocation models alone are adequate to describe the full deformation response. The incorporation of dislocation plasticity within the deformation response of the metal matrix not only provides an improvement over the self-consistent effective medium approximation but also introduces a particle size effect. Such size effects are absent in the continuum models of deformation since they are intrinsically size independent. This enables effects such as particulate cracking to be incorporated into the deformation response as well as

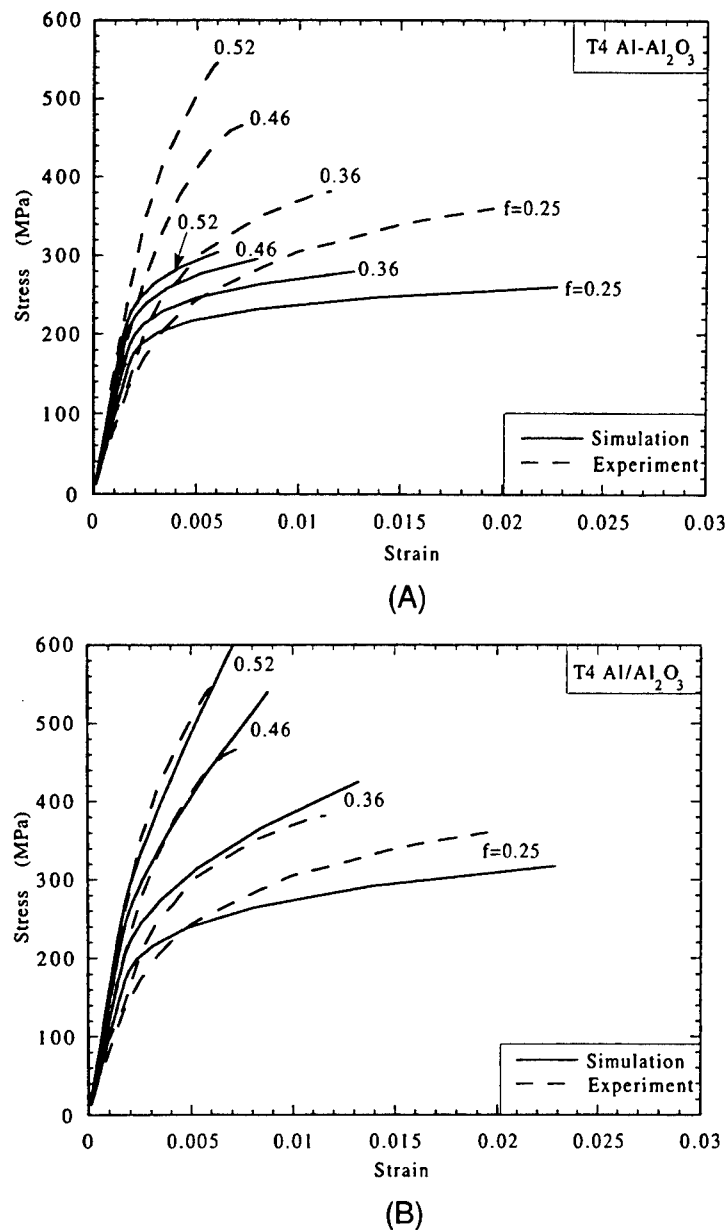


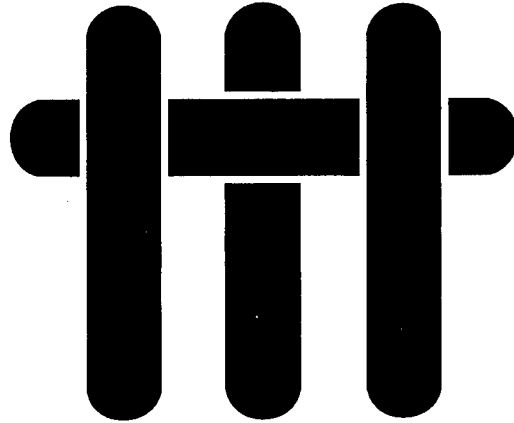
Fig. 2. Comparison between experimental results and the calculations based on a hybrid approach in which dislocation plasticity is incorporated into the effective medium approximations: (A) effective medium approximation and (B) self-consistent effective medium approximation.

introducing a tension-compression asymmetry, as is described elsewhere.¹⁰

References

- ¹M. K. Aghajanian, M. A. Rocazella, J. T. Burke, and S. D. Keck, "The Fabrication of Metal Matrix Composites by a Pressureless Infiltration Technique," *J. Mater. Sci.*, **26**, 447 (1991).
- ²R. Mehrabian, "New Pathways to Processing Composites"; pp. 3-22 in Materials Research Society Symposia Proceedings, Vol. 120, *High Temperature/High Performance Composites*. Materials Research Society, Pittsburgh, PA, 1988.
- ³P. K. Rohatgi, R. Asthana, and S. Das, "Solidification, Structures and Properties of Cast Metal-Ceramic Particle Composites," *Int. Met. Rev.*, **31**, 115-39 (1986).
- ⁴T. W. Clyne and P. J. Withers, *An Introduction to Metal Matrix Composites*. Cambridge University Press, Cambridge, U.K., 1993.
- ⁵L. M. Brown; pp. 1551-72 in *Strength of Metals and Alloys*. Edited by P. Hassen, V. Gerold, and G. Kostore. Pergamon Press, Oxford, U.K., 1979.
- ⁶A. Kelly and R. B. Nicholson (Eds.), *Strengthening Methods in Crystals*. Elsevier, New York, 1971.
- ⁷M. K. Aghajanian, R. A. Langensiepen, M. A. Rocazella, J. T. Leighton, and C. A. Andersson, "The Effect of Particulate Loading on the Mechanical Behavior of Al₂O₃/Al Metal-Matrix Composites," *J. Mater. Sci.*, **28**, 6683 (1993).
- ⁸C.-W. Nan and R.-Z. Yuan, "Multiple Scattering Solution to Nonlinear Mechanical Properties of Binary Elastic-Plastic Composite Media," *Phys. Rev.*, **48**, 3042 (1993).
- ⁹J. D. Eshelby, "The Determination of the Elastic Field of a Spheroidal Inclusion and Related Problems," *Proc. R. Soc. London*, **A241**, 376-96 (1957).
- ¹⁰C.-W. Nan and D. R. Clarke, "The Influence of Particle Size and Particle Fracture on the Elastic/Plastic Deformation of Metal Matrix Composites," *Acta Materialia*, **44** [9] 3801-11 (1996). □

M A T E R I A L S



EXPERIMENTAL ASSESSMENT OF FATIGUE LIFE AND FAILURE MODES IN A SiC/Ti COMPOSITE

T.E. Steyer and F.W. Zok

Materials Department
University of California
Santa Barbara, California 93106

and

D.P. Walls

United Technologies, Pratt & Whitney
Mail Stop 707-22; PO Box 109600
West Palm Beach, FL 33410-9600

Submitted to Composites Science and Technology

March, 1997

Revised September, 1997

ABSTRACT

An experimental investigation of the fatigue life and the associated failure modes in a fiber-reinforced Ti matrix composite (TMC) has been conducted. Tests have been performed over a wide range of loading conditions, characterized by stress ratios (minimum/maximum) of $R = 0$ to 0.8, and the results presented in the form of a Goodman diagram. The failure modes include: (i) catastrophic fracture following damage initiation; (ii) the formation and propagation of multiple bridged cracks, leading to the development of hysteresis and permanent strain and, in some instances, fiber bundle fracture; and (iii) the development of similar damage but without the occurrence of fiber bundle fracture. There exists a damage initiation threshold, associated with a critical value of the stress amplitude, below which there is no apparent microstructural damage and the fatigue life is effectively infinite. There is also a fracture threshold following matrix cracking which is dictated by the fiber strength distribution. The fibers degrade somewhat upon cycling in the presence of matrix cracks, as manifested in a slight reduction ($\sim 10\%$) in the mean strength of extracted fibers as well as the occurrence of composite fracture well after the attainment of a saturation in the matrix crack density. The results indicate that the damage initiation threshold is likely to be the single most important property from the viewpoint of design and life prediction under high cycle fatigue.

Keywords: A. Metal-matrix composites; B. Fatigue; C. Failure criterion;
D. Fractography

1. INTRODUCTION

SiC fiber-reinforced Ti matrix composites (TMCs) are strong candidates for use in aircraft engine components such as compressor fan blades. This selection is driven by the exceptional specific stiffness and strength of TMCs along the fiber direction. Successful implementation of TMCs into fan blades is dependent on two additional performance characteristics: (i) their ability to sustain the impact of foreign objects and retain mechanical integrity, and (ii) their ability to withstand high cycle fatigue (HCF) loading under conditions of moderately low cyclic stress (associated with aerodynamic vibrations) and relatively large mean stress (due to centrifugal forces). The present article focuses on the latter problem.

There exists an extensive body of literature pertaining to the growth of bridged matrix cracks in TMCs during fatigue [1-19]. The majority of this work emphasizes the effects of crack bridging on the crack tip stress intensity factor and the rate of crack extension under various loading configurations and notch geometries. The solutions for the fiber stresses within the bridged zones can be used to predict the onset of fiber fracture, subject to knowledge of the fiber strength [17-21]. The changes in the hysteresis behavior associated with multiple bridged cracks have been modeled also and successfully correlated with experimental data [22, 23].

Notwithstanding the maturity of the bridging mechanics field, there is an inadequate body of knowledge (theoretical or experimental) that can be used by designers to predict the fatigue life of TMC components. This deficiency is due in part to the complexity of the failure processes and the progressive change in some of the constituent properties, including the fiber strength [24] and the interfacial sliding resistance [9, 25, 26], upon fatigue cycling. Moreover, there is minimal information pertaining to crack initiation [27].

The present article represents an attempt to systematically document the sequence of damage and failure processes that occur in a TMC over a broad range of loading conditions, and to represent this information in a form that is familiar to designers, notably, through a Goodman diagram. The work includes a series of fatigue experiments at stress ratios, R , ranging from 0 to 0.8, and stress amplitudes, σ_A , that lead to fracture in $\sim 10^4$ - 10^8 cycles. (The regime of high R and low σ_A is most relevant to fan blades.) The fatigue experiments are augmented by measurements of fiber strengths, using fibers extracted from both pristine and fatigued specimens. These measurements provide information regarding the magnitude of fiber strength degradation associated with fatigue and the expected retained strength following complete matrix cracking. For the purpose of constructing the Goodman diagram, empirical relations are established between the fatigue life and the loading conditions. Although some insight into the factors limiting material performance is inferred from these relations, a completely mechanistic approach for life prediction in TMCs is still lacking.

Generally, Goodman diagrams are comprised of a series of contours, each with a prescribed number of cycles to failure, N_f , plotted on axes of stress amplitude, σ_A , and mean stress, σ_M . An example is illustrated schematically in Fig. 1. The upper limit of the diagram, corresponding to $N_f = 1$, is obtained by setting the maximum stress, σ_{\max} , equal to the ultimate tensile strength, σ_u , yielding*:

$$\sigma_{\max} = \sigma_A + \sigma_M = \sigma_u \quad (1)$$

This condition is represented by a line which has a slope of -1 and intersects both axes at σ_u . The contours for higher values of N_f lie below this line. The σ_A axis

* This assumes that the tensile strength is greater than the compressive strength. If this is not the case, an additional line must be included to account for compressive failure, given by $\sigma_M - \sigma_A = \sigma'_u$ where σ'_u is the compressive strength.

represents fully-reversed tension/compression loading ($R = -1$), and the line $\sigma_A = \sigma_M$ represents tension/zero loading ($R = 0$). Generally, the curves for $N_f > 1$ do not intersect the σ_M axis because of a fatigue threshold at a critical (positive) value of σ_A . The contours are calculated by interpolating experimental fatigue life data obtained over a broad range of loading conditions, characterized by R . Such diagrams are commonly used for design and life assessment of structural components [28, 29].

Monolithic metals and TMCs exhibit some fundamentally different fatigue characteristics, particularly in the regime of high cycle fatigue (HCF). In metals, HCF involves sub-critical growth of a small number of (unbridged) cracks. Up to the point of catastrophic fracture, the global response is essentially linear-elastic, with negligible change in modulus. Consequently, there is little warning from global modulus measurements that fracture is imminent. A positive attribute of this behavior is that the component continues to serve its function (e.g. support load and not deform excessively), until fracture. In this context, the appropriate criterion for failure is *fracture*. In contrast, HCF of TMCs involves the growth of numerous matrix cracks, each bridged by fibers. The bridging is extremely effective in preventing catastrophic fracture. However, once the cracks propagate across the entire cross section, almost all of the load is supported by the fibers, and the modulus is reduced to $\sim fE_f$, where f is the fiber volume fraction and E_f is the fiber modulus. Typically, the reduction in stiffness is $\sim 30\%$. Moreover, the cracks give rise to a permanent strain of ~ 0.1 - 0.2% . In these materials, the failure criterion is not well-defined and depends on the specific component of interest. For example, in stiffness-critical components, functional failure is considered to have occurred when the modulus reduction is deemed to be excessive. Consequently, the number of cycles to *failure* may be very much lower than the number of cycles to *fracture*. Recognizing these differences between metals and TMCs, it is envisioned that Goodman diagrams for TMCs could be constructed for a variety of failure criteria,

including fracture, modulus reduction and permanent strain, and subsequently superimposed on one another in order to identify the relevant failure modes and lifetimes within the stress domains pertinent to various components.

2. MATERIALS AND TEST METHODS

2.1 Composite Characterization

The material used in this study was a $[0^\circ]_8$ SCS-6/Ti-6Al-4V composite produced by Textron Specialty Materials. The fiber volume fraction, f , was 0.35. The mechanical tests were performed on flat dogbone specimens with a 50 mm gauge length and a 6.3 mm width. The specimens were cut by electro-discharge machining. No further conditioning (i.e. polishing) of the cut surfaces was performed prior to testing. Stainless steel tabs were affixed to the specimen ends with epoxy. The specimens were mounted onto a servohydraulic test machine using hydraulic wedge grips. The axial strain was measured using a 10 mm extensometer.

The majority of fatigue tests was conducted at a frequency of 10 Hz, up to 10^7 cycles. The one exception was a 100 Hz test performed at a low stress amplitude and run out to 10^8 cycles. The tests were interrupted periodically (typically, 3 to 4 times per decade of cycling, starting at 10^4 cycles) and the stress-strain hysteresis measured between the minimum and maximum loads at a loading rate of ~ 5 MPa/s. At each stage, surface replicas were made of one of the broad faces using cellulose acetate tape and subsequently examined in an optical microscope. The purpose of the replicas was to assess the nature and degree of matrix damage. The fatigue tests were performed at stress amplitudes between 120 and 600 MPa, and with stress ratios, $R = 0, 0.5$ and 0.8 . Some of the fractured specimens were examined in a scanning electron microscope in an attempt to identify the fracture origins of the fibers and determine whether new flaws were introduced during fatigue. Moreover,

measurements were made of the distributions in fiber pullout lengths and compared with the predicted values [30, 31].

2.2 Fiber Strength Characterization

The strength characteristics of the fibers were determined by testing ~ 20 individual filaments, 25 mm long, extracted from each of three representative specimens. Fiber extraction was accomplished by dissolving the matrix in a 49% HF solution. The cumulative failure probability, P_f , was determined by ranking the strength data in ascending order and using the probability estimator

$$P_f = \frac{i - 0.5}{n} \quad (2)$$

where i is the rank and n is the total number of tested fibers.

The first specimen was the pristine (as-processed) composite. Its fiber strength distribution was characterized by the Weibull function:

$$P_f(\sigma, L_f) = 1 - \exp \left[- \frac{L_f}{L_o} \left(\frac{\sigma}{\sigma_o} \right)^m \right] \quad (3)$$

where σ is the stress; L_f is the fiber length; L_o and σ_o are the reference values of length and strength; and m is the Weibull modulus.

The other two specimens from which fibers were extracted had been subjected to fatigue. The first of these was a specimen tested at $\sigma_A = 130$ MPa and $R = 0.8$. Fracture had occurred after 3.7×10^5 cycles with no apparent damage in the matrix remote from the fracture plane. The fibers were extracted from the longer one of the two broken halves. The tested length was ≥ 10 mm away from the fracture plane. Under these conditions, no relative sliding had occurred between the fibers and

matrix. Consequently, the fiber strength distribution is expected to be representative of the intrinsic fatigue degradation of the fiber due to subcritical cracking (if any). In comparing the pristine fibers with the fatigued ones, the strength distribution of the pristine fibers is modified to account for the "proof loading" of the fibers within the composite to a stress level, σ_p

$$\sigma_p = \epsilon_c E_f + \sigma_R \quad (4)$$

where ϵ_c is the axial composite strain at the load maximum, E_f is the fiber Young's modulus, and σ_R is the residual axial stress in the fibers (≈ -600 MPa [32]). The modified distribution is given by [33]

$$P'_f(\sigma, L_f) = \frac{P_f(\sigma, L_f) - P_f(\sigma_p, L_c)}{1 - P_f(\sigma_p, L_c)} \quad (5)$$

where L_f is the gauge length of the tested fibers (25 mm) and L_c is the composite gauge length from which the fibers had been extracted.

The second fatigued specimen had been tested at $\sigma_A = 200$ MPa and $R = 0.5$. In this case, multiple matrix cracks had formed and propagated across the entire cross-section, each fully bridged by fibers, and with a spacing of ~ 0.7 mm. The crack pattern had reached a saturation state after $\sim 2 \times 10^6$ cycles. The test was continued to 10^7 cycles, at which point the specimen was still intact. The fibers within this specimen are expected to provide insight into the effects of fiber/matrix sliding on the fiber strength. In making comparisons with the pristine strength distribution, Eqn. 5 was used again to account for "proof loading". Recognizing that the matrix does not support any stress following complete cracking, the relevant proof stress in this case is

$$\sigma_p \approx \sigma_{\max} / f \quad (6)$$

where σ_{\max} is the stress maximum (800 MPa). (Strictly, the assumption regarding the matrix stress only applies along those sections containing matrix cracks; load transfer by interface sliding leads to a tensile stress in the matrix segments between cracks and a corresponding reduction in the fiber stress. By performing a shear lag analysis of the fibers within the intact matrix segments, with a sliding stress, $\tau \approx 20$ MPa [23], the fiber stress at the center of such a matrix segment is found to be $\sim 10\%$ less than the value predicted by Eqn. 6. This produces only a very small effect on the modified strength distribution and is subsequently neglected.)

3. EXPERIMENTAL RESULTS AND ANALYSIS

3.1 Damage Progression

During cycling, the composite specimens exhibited several characteristic modes of damage and fracture, dependent on the loading conditions. The sequence, along with the corresponding numbers of cycles, are documented in Fig. 2 for the case of $R = 0$ and described below. Similar features were observed for tests performed at higher values of R .

At high stresses (≥ 1000 MPa), fracture occurs catastrophically without extensive matrix damage or reduction in stiffness. Apparently, the fatigue life is controlled by the damage initiation event. This is designated as "*damage-intolerant*" behavior.

At lower stresses, numerous matrix cracks initiate at the specimen edges and propagate stably through the composite. As this happens, the permanent strain increases and a non-linear hysteresis loop develops. Several representative loops are

shown in Fig. 3. The trends in crack density, permanent strain and hysteresis modulus with loading cycles are plotted in Fig. 4. In some instances, the cracks propagate to the mid-section of the specimen and either link with cracks emanating from the other side (when they are nearly coplanar) or arrest as they grow a short distance past one another (when they are not coplanar). An example of the crack pattern is shown in Fig. 5. Once the cracks arrest, the hysteresis loop achieves a steady-state, with no change upon further cycling. Fracture may or may not occur following the attainment of this steady-state. There is a fatigue threshold below which the steady-state hysteresis may continue through to runout (at $N = 10^7$) without fracture of the fiber bundle. In other instances, fracture occurs after crack initiation but before crack arrest. Both of these behavior types are termed "*damage-tolerant*". This behavior is preferred over damage-intolerant behavior since the material is capable of sustaining the cyclic stress in the presence of matrix damage. However, in practice, failure in this regime may be dictated by the loss in stiffness or the development of permanent strain rather than fracture, as suggested by Fig. 4.

At yet lower stresses, matrix cracks never form and fracture does not occur. The stress below which this behavior is obtained represents a fatigue threshold below which the life is effectively infinite and there is no change in the stress-strain response. Clearly, this behavior is the most desirable. This threshold was found in the high R-ratio tests and, as detailed below, occurs at a critical stress amplitude of ~130 MPa.

3.2 Influence of Loading Conditions on Damage Initiation and Fracture

The number of cycles to crack initiation, N_i , determined from both examinations of surface replicas and changes in hysteresis, are plotted on Fig. 6. The

combined effects of σ_A and σ_M were incorporated into an effective stress, $\bar{\sigma}$, defined by

$$\bar{\sigma} \equiv \left[\sigma_A \sigma_M^n \right]^{\frac{1}{1+n}} \quad (7)$$

where n is a weighting parameter. This effective stress is similar to the Smith-Watson-Topper parameter [34], which has been used previously to characterize fracture of TMCs in the low cycle fatigue (LCF) regime. Indeed, if the material response is linear and $n = 1$, the two are equivalent and given by the geometric mean: $(\sigma_A \sigma_M)^{1/2}$. The present form of this parameter is preferred since it allows different weightings to be assigned to σ_A and σ_M through the exponent n : the limiting cases being $\bar{\sigma} = \sigma_A$ for $n = 0$ and $\bar{\sigma} = \sigma_M$ for $n = \infty$. Upon plotting $\bar{\sigma}$ against N_i it was apparent that the best correlation among the data was obtained for $n = 0$. The implication of this result is that damage initiation is controlled exclusively by the cyclic stress ($\bar{\sigma} = \sigma_A$), independent of the mean stress. This is consistent with the view that initiation occurs by cyclic plasticity within the Ti matrix [28].

For the purpose of constructing the Goodman diagram (Section 4), the initiation conditions were fit to an empirical function of the form

$$\bar{\sigma} = A_1 \exp(p_1 N_i) + A_2 \exp(p_2 N_i) + \sigma_{th} \quad (8)$$

where p and A are fitting parameters and σ_{th} is the threshold stress for crack initiation. The best fit of Eqn. 8 to the experimental data is obtained for $n = 0$, with the fitting parameters being $A_1 = 228$ MPa, $A_2 = 300$ MPa, $p_1 = 8.8 \times 10^{-6}$, $p_2 = 4.0 \times 10^{-5}$ and $\sigma_{th} = 130$ MPa. The effect of n on the relative goodness of fit (ψ^2) is shown in Fig. 7. The best fit curve (for $n = 0$) is shown in Fig. 6.

The fatigue fracture data are presented in Fig. 8 in terms of both the stress amplitude and the stress maximum. Upon inspection of these plots, it is evident that neither one of these parameters alone determines the fatigue life. The data are found to be well described by the empirical relation

$$2\sigma_A = \sigma_u(1-R) \operatorname{sech} \left[b(1-R^q) \log N_f \right] \quad (9)$$

in the regime $\sigma_A > \sigma_{th}$. Here σ_u is the ultimate tensile strength (1760 MPa), and b and q are fitting parameters. The optimal fits (based on least squares regression analyses) are obtained for $b = 0.26$ and $q = 2.43$. For $N_f = 1$, Eqn. 9 reduces to the required limit (similar to Eqn. 1):

$$\frac{2\sigma_A}{1-R} = \sigma_{max} = \sigma_u \quad (10)$$

The correlations between the calculated curves and the experimental data are shown in Fig. 8. The quality of the fit is illustrated further by comparing the measured and calculated values of N_f (Fig. 9). The majority of the data lie within a band of ± 3 : comparable to typical statistical variations in N_f that are obtained in fatigue under nominally identical testing conditions [35].

3.3 Fiber Strength and Fiber Pullout

The strength distribution of the pristine fibers is shown in Fig. 10(a). The distribution was fitted to a Weibull function, yielding the results presented in Table 1. Also shown in Fig. 10(a) is the strength distribution of the fibers extracted from the composite that had failed after 3.7×10^5 cycles with no apparent matrix damage, as well as the distribution that would be expected if the fibers had not been degraded during cycling (through Eqn. 5). Evidently, the fibers extracted from the

fatigued specimen exhibit strength characteristics similar to those of the pristine fibers, indicating no degradation in strength during fatigue. In light of the fact that no relative sliding had occurred between the fibers and the matrix, as well as the fatigue-insensitivity of SiC, the lack of strength degradation is not altogether unexpected.

Figure 10(b) shows a comparison between the strength distribution of the pristine fibers and the one obtained from the specimen that had been fatigued to 10^7 cycles and had exhibited extensive matrix cracking. In this case, the fatigued fibers exhibit a slight strength reduction, with a difference of $\sim 10\%$ in the mean values. Using the student t-test, the confidence level associated with this difference was determined to be $\sim 68\%$. Although this confidence level is not particularly high, the observations and analyses presented below provide corroborating evidence of fiber degradation, particularly in the regions near the matrix cracks.

Additional insight is obtained from an analysis of fiber bundle strengths. Two approaches are considered. In the first, the flaws in the fibers are assumed to be distributed uniformly along the fiber length and the fibers are assumed to be coupled to the matrix through a friction stress, τ . The stress-strain response of the fiber bundle following complete matrix cracking is then computed using the approach described in [30]. This is accomplished by evaluating the number of flaws that have been activated at each stress and the inelastic displacement at each break location associated with fiber-matrix slip. The resultant stress-strain response exhibits progressive softening as the fibers fragment, ultimately reaching a maximum stress level. The predicted fiber bundle strength is [30]

$$\sigma_B = \left[\frac{\sigma_o^m \tau L_o}{r} \right]^{\frac{1}{m+1}} \left(\frac{2}{2+m} \right)^{\frac{1}{m+1}} \left(\frac{m+1}{m+2} \right) \quad (11)$$

and the corresponding composite strength, σ_u is:

$$\sigma_c = f \sigma_B \quad (12)$$

with r being the fiber radius (71 μm). The friction stress ($\tau \approx 23 \text{ MPa}$) was evaluated from the measured hysteresis loops following matrix crack saturation, as detailed in [23]. Using the Weibull parameters characterizing the pristine fiber, the composite strength is predicted to be 1160 MPa. In contrast, the strength that is estimated from the fatigue experiments (taking the lowest value of the stress maximum at which fracture occurs) is considerably lower: 600 MPa. Even when the Weibull parameters for the degraded fibers are used, the predicted strength ($\sim 950 \text{ MPa}$) is still considerably higher than the measured value.

The second approach for predicting the bundle strength assumes that strength-limiting flaws are located preferentially near the matrix crack planes, where the amount of relative sliding between the fibers and the matrix is greatest. The implication of this assumption is that the fibers ultimately fail in the plane of a matrix crack and therefore the contribution to the bundle strength derived from frictional sliding around broken fibers is negligibly small. In this limit, a lower bound estimate of the strength is the dry fiber bundle strength (in the absence of the matrix), given by [9]

$$\sigma_B = \sigma_o [m e L_f / L_o]^{-1/m} \quad (13)$$

Using the Weibull parameters for the degraded fibers yields a strength, $\sigma_c = 485 \text{ MPa}$. This value corresponds reasonably well to the one inferred from the fatigue tests ($\leq 600 \text{ MPa}$), thus supporting the postulate of preferential fiber degradation near the matrix cracks.

The measured distribution in the fiber pullout lengths, ℓ_p , also suggests localized strength reduction upon fatigue. One such distribution is shown in Fig. 11; its average value, $\bar{\ell}_p$, was $\sim 80 \mu\text{m}$. If the flaws were distributed uniformly along the fibers, the average pullout length would be expected to be [30]

$$\bar{\ell}_p = g(m) \left(\frac{\sigma_o r L_o^{1/m}}{\tau} \right)^{\frac{m}{m+1}} \quad (14)$$

where $g(m)$ is the function plotted in Fig. 6 of [30]. The predicted value is $\ell_p \approx 4.1 \text{ mm}$: more than an order of magnitude greater than measured value. This discrepancy is also consistent with local fiber degradation near matrix cracks, yielding anomalously low pullout lengths.

Examinations of broken fibers in the SEM proved to be somewhat inconclusive. The fracture origins could not be consistently identified and differences between the fracture surfaces of fatigued and pristine fibers could not be established. However, there is clear evidence of wear of some of the fiber surfaces following matrix cracking (Fig. 12). It is surmised that the reduction in fiber strength upon fatigue is associated with the presence of surface defects produced by fiber-matrix sliding.

4. GOODMAN DIAGRAM

The preceding results have been used to construct a Goodman diagram (Fig. 13) in the stress domain defined by $0 \leq \sigma_A \leq \sigma_M$ (i.e. $R \geq 0$). The line for $N_f = 1$ was calculated by setting the maximum stress equal to the ultimate tensile strength of the pristine composite (Eqn. 1). The dashed contours, corresponding to $N_f = 10^4$, 10^5 , 10^6 and 10^7 , were calculated using Eqn. 9 along with the relation

$$R = \frac{\sigma_M - \sigma_A}{\sigma_M + \sigma_A} \quad (15)$$

The *initiation* threshold, σ_{th} , is described by a critical value of the stress amplitude and therefore appears as a horizontal line ($\sigma_A = \sigma_{th} = 130$ MPa). The fracture threshold (following matrix cracking) was obtained by setting the stress maximum equal to $\sigma_c = f \sigma_B \approx 485$ MPa. Also shown is the boundary between damage-tolerant and damage-intolerant behaviors, calculated by setting the number of cycles for crack initiation (Eqn. 8) equal to the number of cycles for fracture (Eqn. 9).

The diagram reveals several notable features associated with fatigue failure.

- (i) The stress domains for damage-tolerant and damage-intolerant behavior are comparable in "size". The boundary between the two depends on both σ_A and σ_M , though it tends to be dominated by σ_M for low R values (approaching zero).
 - (ii) Within the damage-tolerant domain, the fatigue life is finite for most combinations of σ_A and σ_M ; there exists only a small triangular region (in the bottom left) in which extensive matrix damage occurs but does not lead to fracture.
 - (iii) In the lower domain ($\sigma_A < \sigma_{th}$), the fatigue life is infinite, and, because of the absence of matrix cracks, the material response remains unchanged throughout.
- Evidently, the small triangular region in which the composite is capable of sustaining damage without fracture provides only a modest expansion of the allowable stress domain for infinite life, beyond that associated with the initiation threshold. Consequently, for conservative designs of components subject to HCF, the initiation threshold represents the most critical boundary on the diagram.

5. CONCLUDING REMARKS

The Goodman diagram for a SiC fiber-reinforced TMC has been constructed, based on fatigue tests performed over a range of loading conditions as well as measurements of fiber strengths. Four types of behavior have been observed: (i) damage-intolerant, with fracture controlled by crack initiation; (ii) damage-tolerant, associated with the formation of multiple matrix cracks and followed, eventually, by fiber bundle fracture; (iii) damage-tolerant, without fiber bundle fracture, thus yielding a fracture threshold; and (iv) undamaged indefinitely, because of an initiation threshold. The fracture threshold is governed by the fiber bundle strength, which degrades somewhat during cycling. This degradation appears to be due to the formation of new surface flaws upon repeated fiber-matrix sliding.

Based on design and lifing considerations, the damage initiation threshold is arguably the single most important quantity governing fatigue, especially for HCF. Above the threshold, matrix cracks form and propagate readily. Even though these cracks are effectively bridged by fibers, they lead to rather significant changes in mechanical properties, including a loss in stiffness and the development of hysteresis and permanent strain. Moreover, there is only a small range of stresses over which damage can occur but not eventually lead to catastrophic fracture.

The estimate of the initiation threshold ($\sigma_A = \sigma_{th} = 130$ MPa) obtained from the present experiments is expected to be conservative in relation to that for real components, because of the presence of cut fibers along the specimen length and the lack of any special surface preparation prior to testing. TMC components such as fan blades are not expected to have exposed fibers and their surfaces are expected to be smoother than those of the present test coupons (at least initially). These differences highlight the importance of identifying the fatigue threshold in specimens that are fully encased by the Ti matrix alloy and investigating the role of surface condition.

ACKNOWLEDGMENTS

Funding for this work was provided by the ARPA University Research Initiative Program at UCSB under ONR contract No. N00014-92-J-1808.

REFERENCES

1. Johnson, W.S., Lubowinski, S.J., and Highsmith, A.L., *Thermal and Mechanical Behavior of Metal Matrix and Ceramic Matrix Composites*, ed. J.M. Kennedy, H.H. Moeller, and J.W. Johnson, American Society for Testing and Materials, 1990, pp. 193-218.
2. Hillberry, B.M. and W.S. Johnson, *J. Comp. Tech. Res.*, **14**[4] (1992) 221-24.
3. Barney, C., Beevers, C.J. and Bowen, P., *Composites*, **24**[3] (1993) 229-34.
4. Cotterill, P.J. and Bowen P., *Composites*, **24**[3] (1993) 214-21.
5. Hillberry, B.M. and Johnson, W.S., *J. Comp. Tech. Res.*, **15**[3] (1993) 210-6.
6. Ibbotson, A.R., Beevers, C.J. and Bowen, P., *Composites*, **24**[3] (1993) 241-7.
7. Greaves, I., Yates, J.R. and Atkinson, H.V., *Composites*, **25**[7] (1994) 692-7.
8. Jira, J.R. and Larsen, J.M., *Metall. Trans. A*, **25**[7] (1994) 1413-24.
9. Walls, D.P., Bao, G. and Zok, F.W., *Acta Metall. Mater.*, **41**[7] (1993) 2061-2071.
10. Brindley, P.K. and Bartolotta, P.A., *Mater. Sci. Eng.*, **A200** (1995) 55-67.
11. Majumdar, B.S. and Newaz, G.M., *Mater. Sci. Eng.*, **A200** (1995) 114-29.
12. Wang, P.C., Jeng, S.M., and Yang, J.-M., *Mater. Sci. Eng.*, **A200** (1995) 173-80.
13. Ward, G.T., Herrmann, D.J. and Hillberry, B.M., *J. Comp. Tech. Res.*, **17**[3] (1995) 205-11.
14. Lerch, B. and Halford, G., *Mat. Sci. Eng. A*, **200**[1-2] (1995) 47-54.
15. Wang, P.C., Jeng, S.M., Yang, J.-M. and Mal, A.K., *Acta Mater.*, **44**[3] (1996) 1097-108.
16. Cox, B.N. and Marshall, D.B., *Fatigue Frac. Eng. Mat. Struct.*, **14**[8] (1991) 847-861.
17. McMeeking, R.M. and Evans, A.G., *Mech. Mater.*, **9** (1990) 217-27.
18. Bao, G. and McMeeking, R.M., *Acta Metall. Mater.*, **42**[7] (1994) 2415-25.

19. Cox, B.N. and Marshall, D.B., *Acta Metall. Mater.*, **42**[2] (1994) 341-63.
20. Budiansky, B., Hutchinson, J.W. and Evans, A.G., *J. Mech. Phys. Solids*, **34** (1986) 167-89.
21. Begley, M.R. and McMeeking, R.M., *Comp. Sci. Tech.*, **53**[4] (1995) 365-82.
22. Walls, D.P., McNulty, J.C. and Zok, F.W., *Metall. Trans. A*, **27A**[7] (1996) 1899-907.
23. Zok, F.W., Begley, M.R., Steyer, T.E. and Walls, D.P., *Mech. Mater.*, (submitted).
24. Connell, S.J. and Zok, F.W., *Acta Mater.*, (submitted).
25. Kantzos, P., Eldridge, J., Koss, D.A. and Ghosn, L.J., *Mat. Res. Soc. Symp. Proc.*, **273** (1992) 135-142.
26. Walls, D.P. and Zok, F.W., *Acta Metall. Mater.*, **42**[8] (1994) 2675-2681.
27. Jeng, S.M., Allassoeur, P., Yang, J.-M. and Aksoy, S., *Mater. Sci. Eng.*, **A148** (1991) 67-77.
28. Suresh, S., *Fatigue of Materials* (1991) Cambridge University Press.
29. Nicholas, T. and Zuiker, J.R., *Int. J. Fract.*, **80**[2-3] (1996) 219-35.
30. Curtin, W.A., *J. Am. Ceram. Soc.*, **74**[11] (1991) 2837-45.
31. Curtin, W.A., *J. Mech. Phys. Solids*, **41**[2] (1993) 217-45.
32. Ramamurty, U., Dary, F.-C. and Zok, F.W., *Acta Mater.*, **44**[8] (1996) 3397-406.
33. Wiederhorn, S.M. and Tighe, N.J., *J. Mater. Sci.*, **13** (1978) 1781-93.
34. Smith, K.N., Watson, P. and Topper, T.H., *J. Mater.*, **5**[4] (1970) 767-78.
35. Nicholas, T., *Mater. Sci. Eng.*, **A200** (1995) 29-37.

Table 1 Weibull Parameters for Extracted Fibers

	Pristine Composite	Fatigued Composite*
Length, L_f (mm)	25	25
Reference Strength, σ_o (MPa), (for $L_o = 25$ mm)	3900	3580†
Weibull modulus, m	4.3	3.0†

* $\sigma_A = 200$ MPa, $R = 0.5$, runout at $N = 10^7$.

†In determining m and σ_o for the fatigued fibers, the probability estimator, P_f , (given in Eqn. 2) was adjusted to account for the fibers that had broken during fatigue. The approximate estimator for this case is $P_f = [(i-0.5)/n](1-n_B/n_T)$, where n_B is the number of broken fibers upon extraction and n_T is the total number of extracted fibers. No broken fibers were found in the pristine composite.

FIGURES

- Figure 1 Schematic of a Goodman diagram.
- Figure 2 Summary of the sequence of damage events occurring in fatigue for $R = 0$.
- Figure 3 Typical hysteresis loops following fatigue cycling ($R = 0$, $\sigma_A = 400$ MPa).
- Figure 4 Variations in (a) crack density, measured along the specimen edge, (b) hysteresis modulus, and (c) permanent strain with loading cycles for the representative tests performed at $R = 0$.
- Figure 5 Backscatter SEM image showing multiple matrix cracks in a fatigued specimen ($\sigma_A = 300$ MPa, $R = 0$, $N_f = 1.0 \times 10^7$ cycles).
- Figure 6 Optimal fit of Eqn. 8 ($n = 0$) to the crack initiation data.
- Figure 7 Influence of the mean stress exponent n on the relative goodness-of-fit of Eqn. 8 for crack initiation.
- Figure 8 Fatigue life presented in terms of (a) the stress maximum and (b) the stress amplitude. The lines are the fits obtained using Eqn. 9. The runout tests, indicated by the open symbols, were not used in the fitting procedure.
- Figure 9 Comparison of measured and calculated cycles to fracture. The band represents a variation of a factor of ± 3 .
- Figure 10 Comparisons of fiber strength distributions from pristine and fatigued fibers: (a) $\sigma_A = 130$ MPa, $R = 0.8$, $N_f = 3.7 \times 10^5$; (b) $\sigma_A = 200$ MPa, $R = 0.5$, runout at $N = 10^7$.
- Figure 11 Measured fiber pullout length distribution ($\sigma_A = 300$ MPa, $R = 0$, $N_f = 1.0 \times 10^7$).

Figure 12 SEM micrographs showing (a) a fractured fiber and (b) a close-up view of the fiber showing wear of both the fiber surface and the fiber coating following fatigue ($\sigma_A = 300$ MPa, $R = 0$, $N_f = 1.0 \times 10^7$).

Figure 13 Goodman diagram for the TMC.

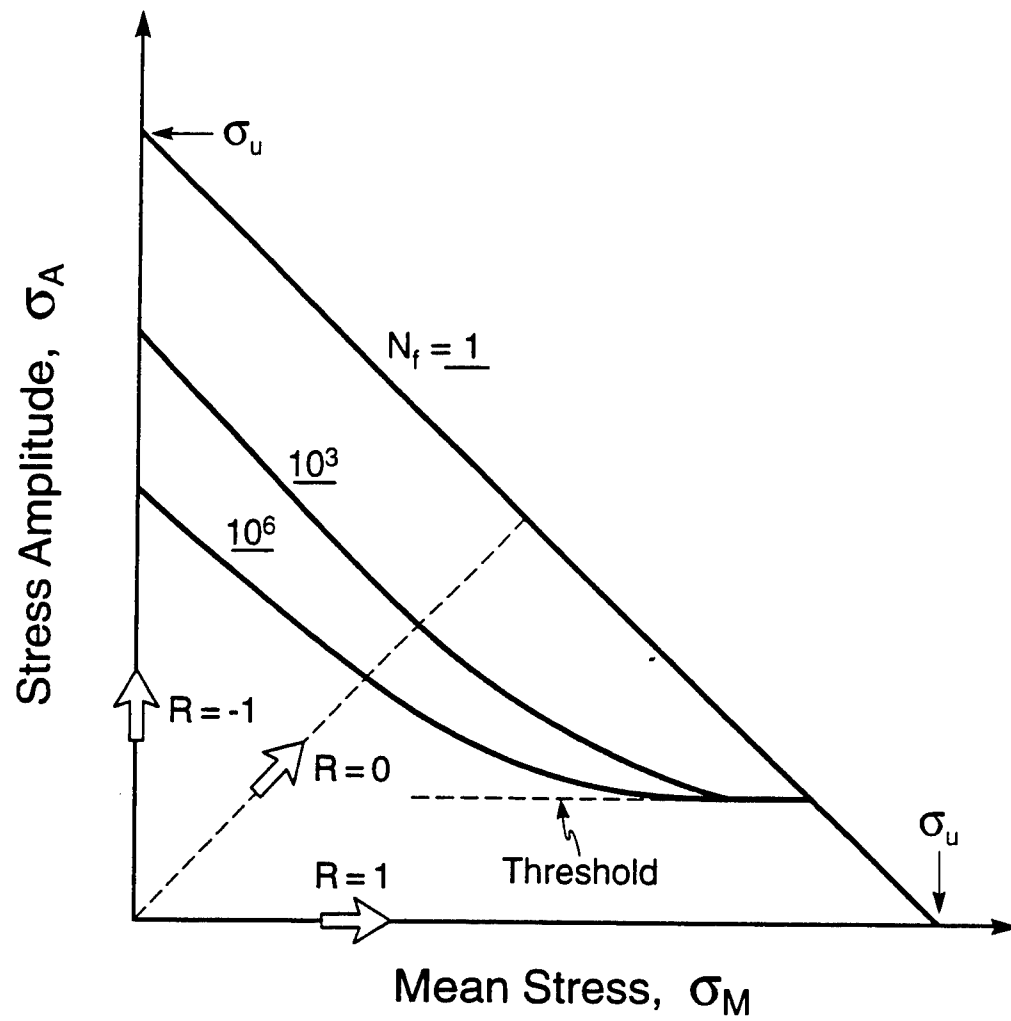


Figure 1

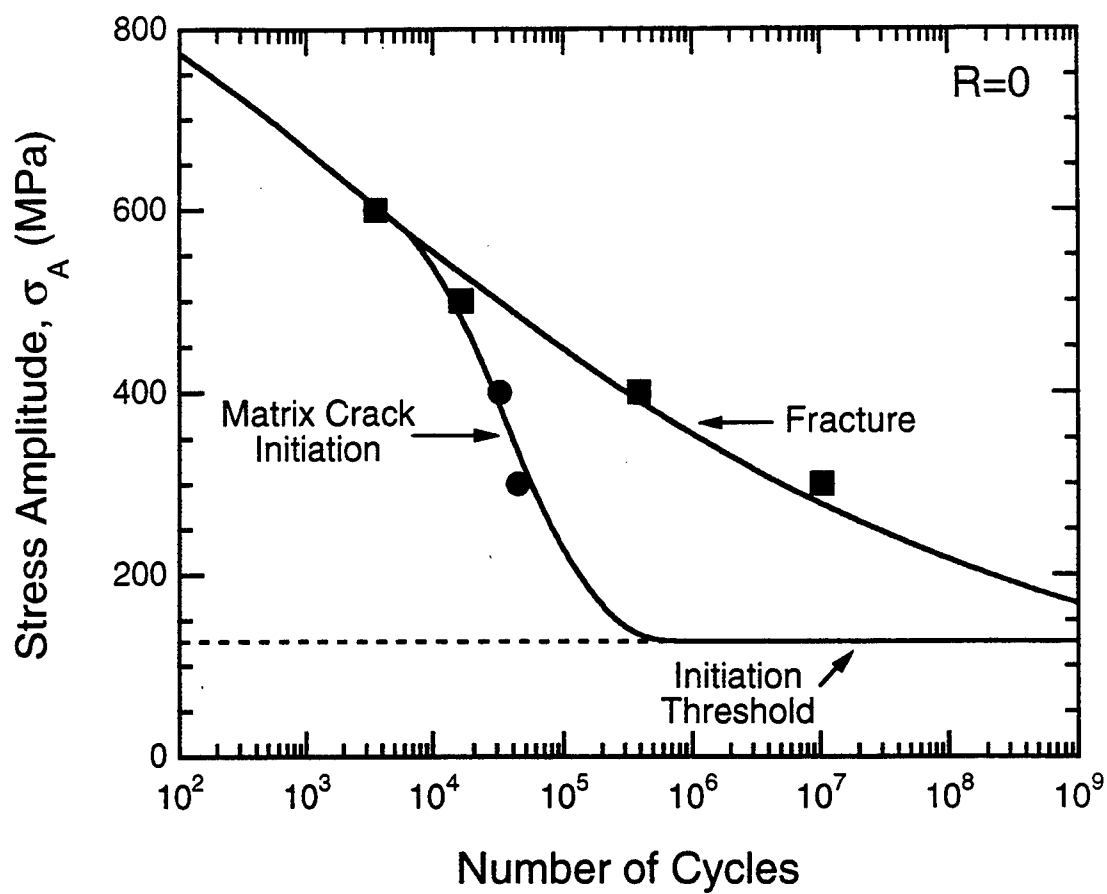


Figure 2

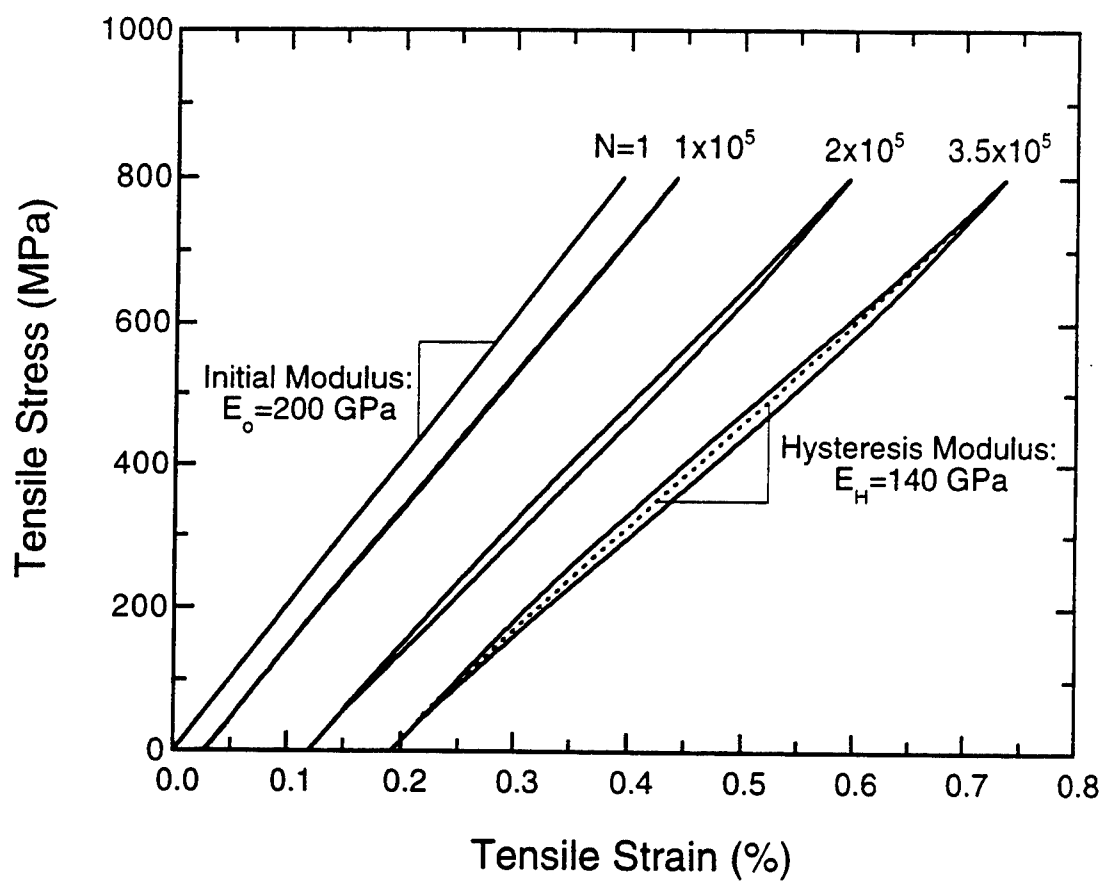


Figure 3

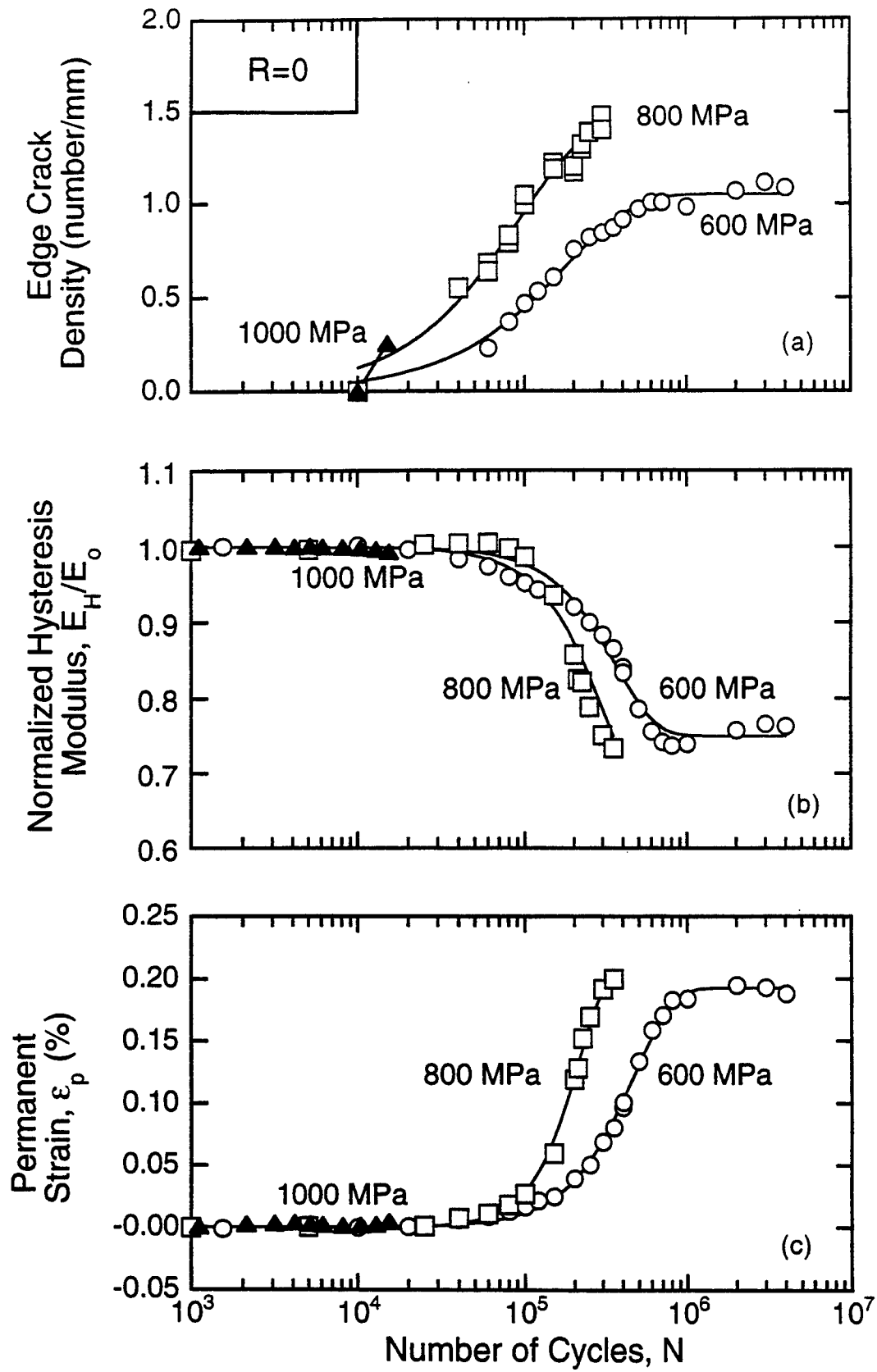


Figure 4

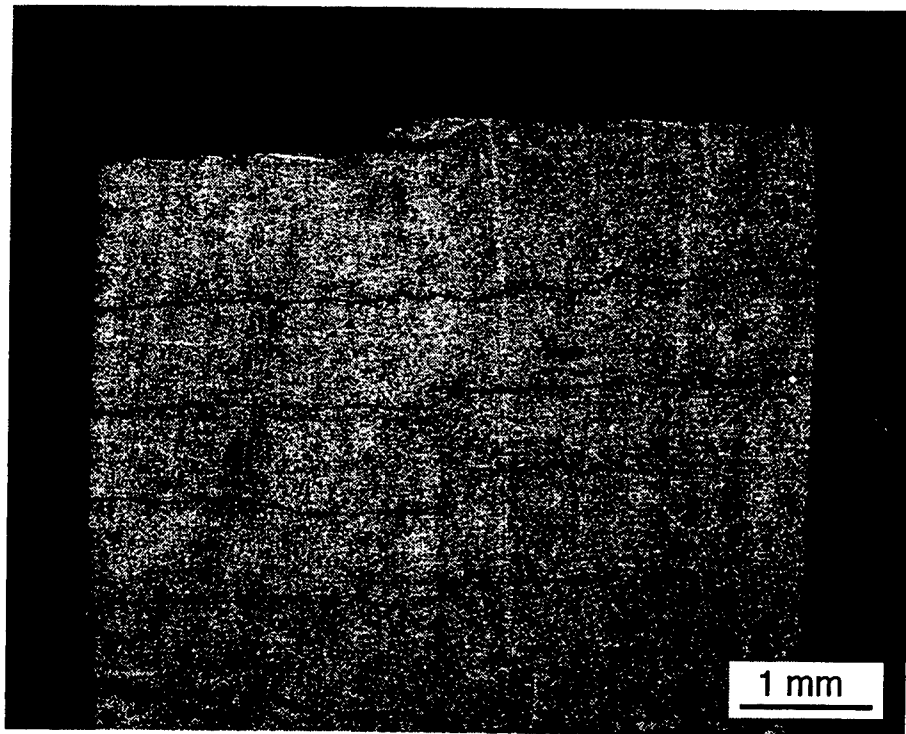


Figure 5

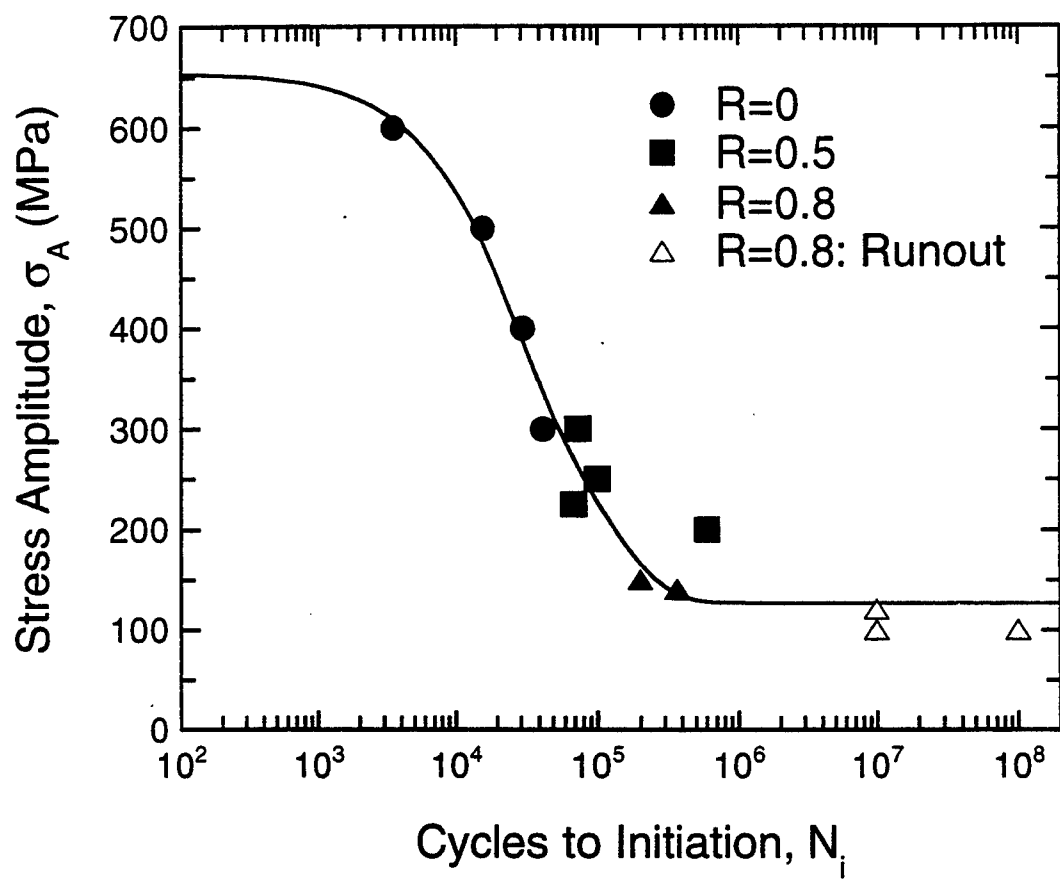


Figure 6

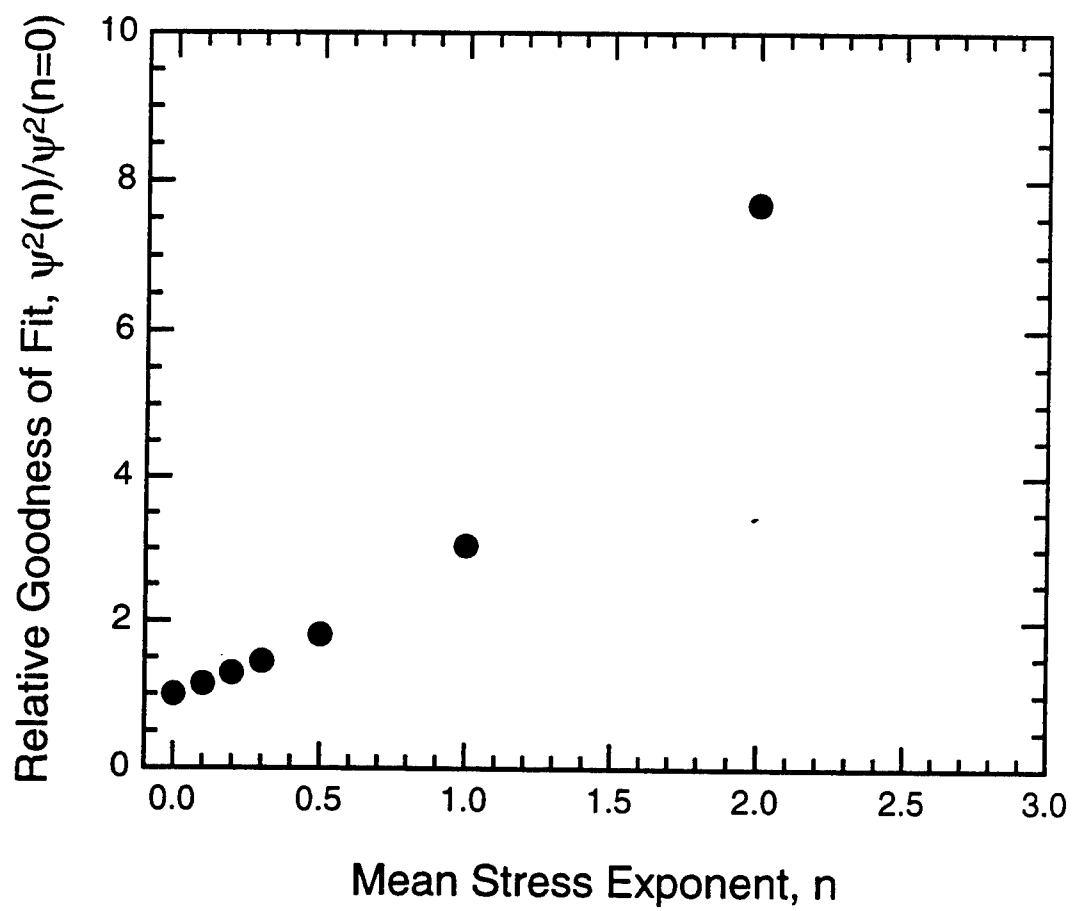


Figure 7

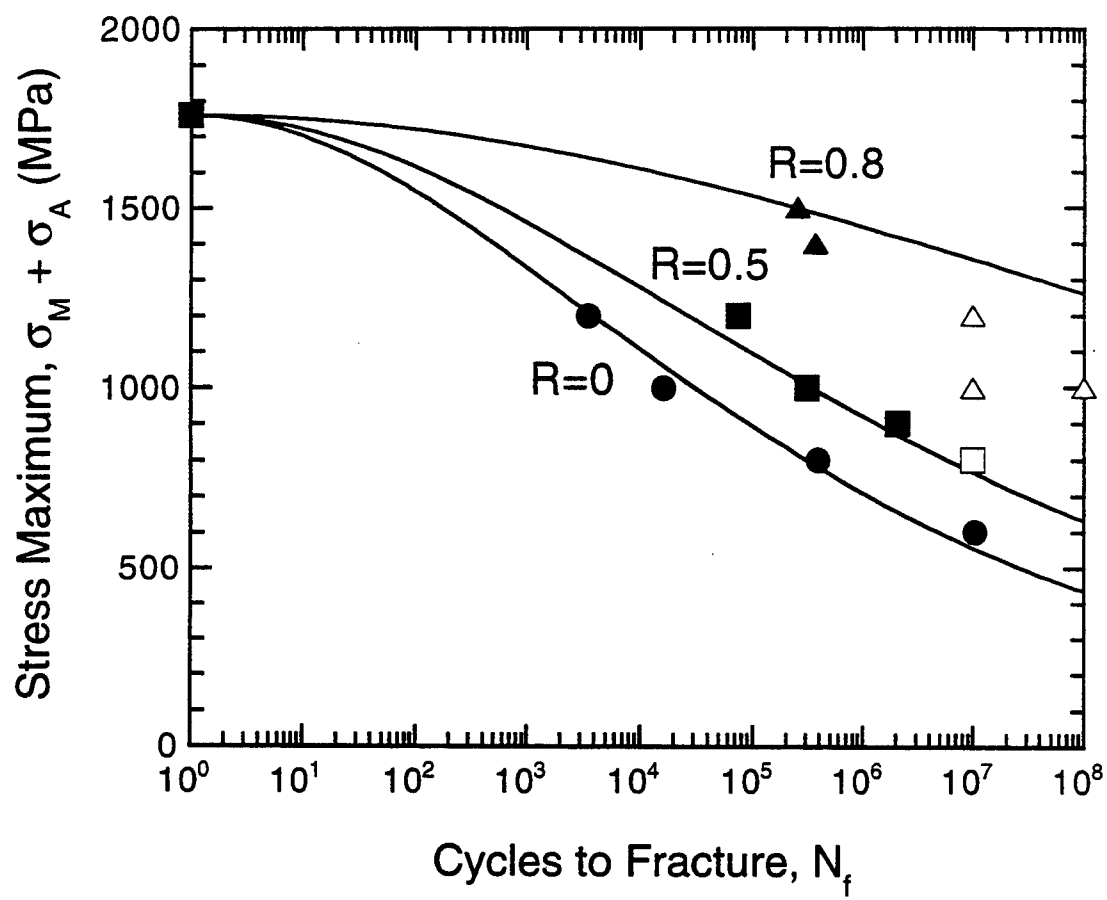


Figure 8(a)

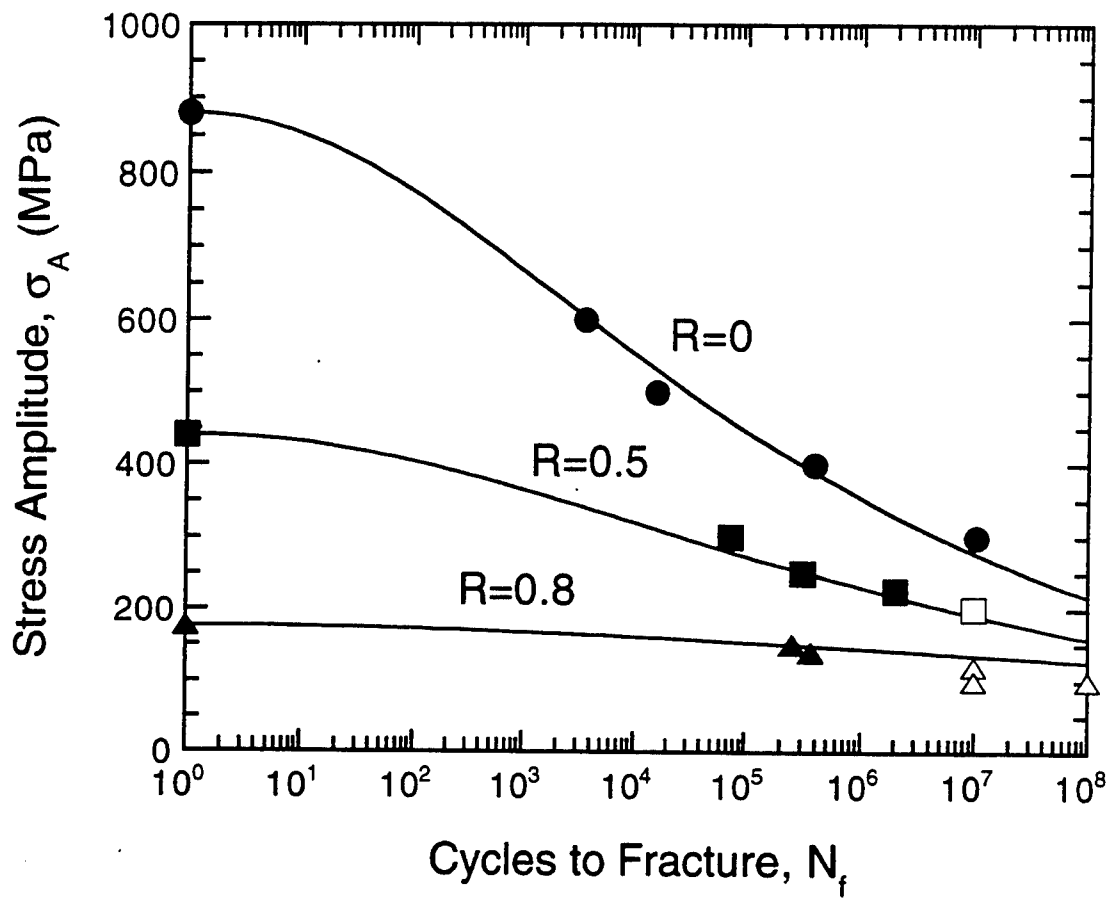


Figure 8(b)

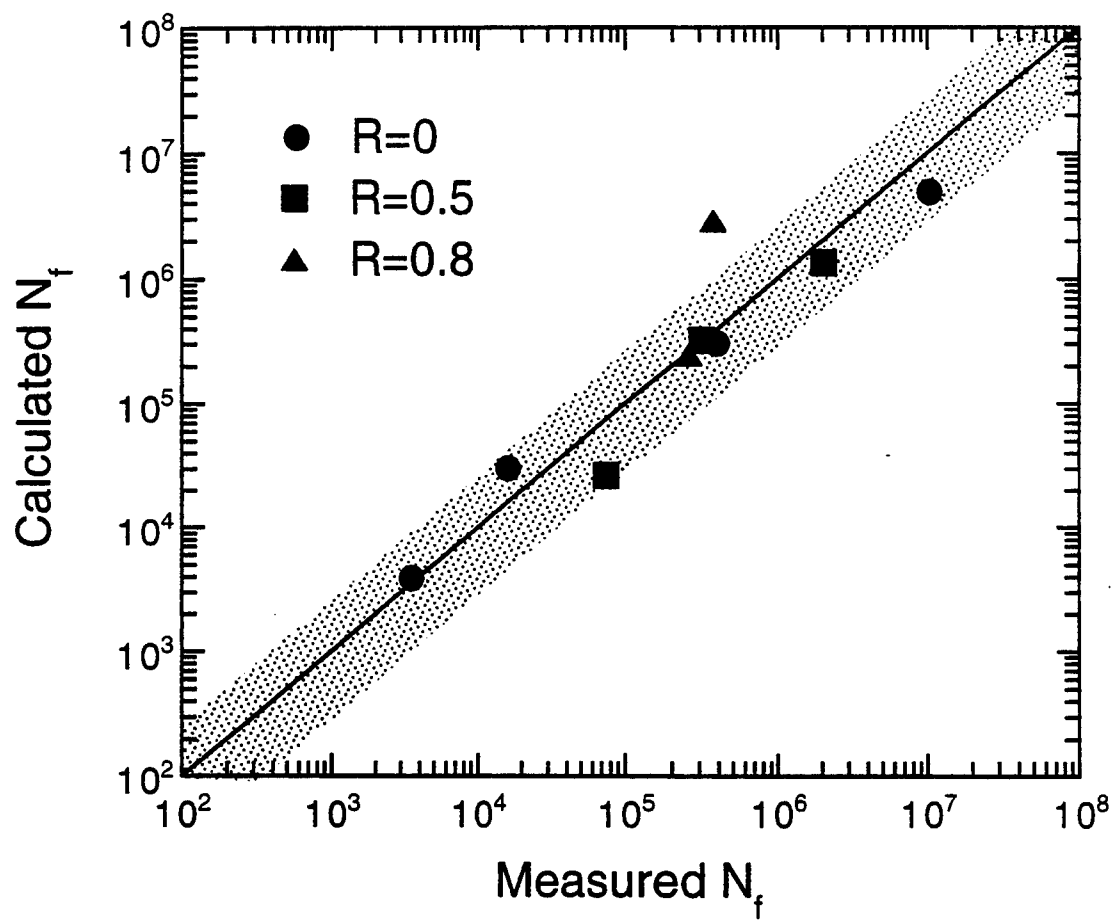


Figure 9

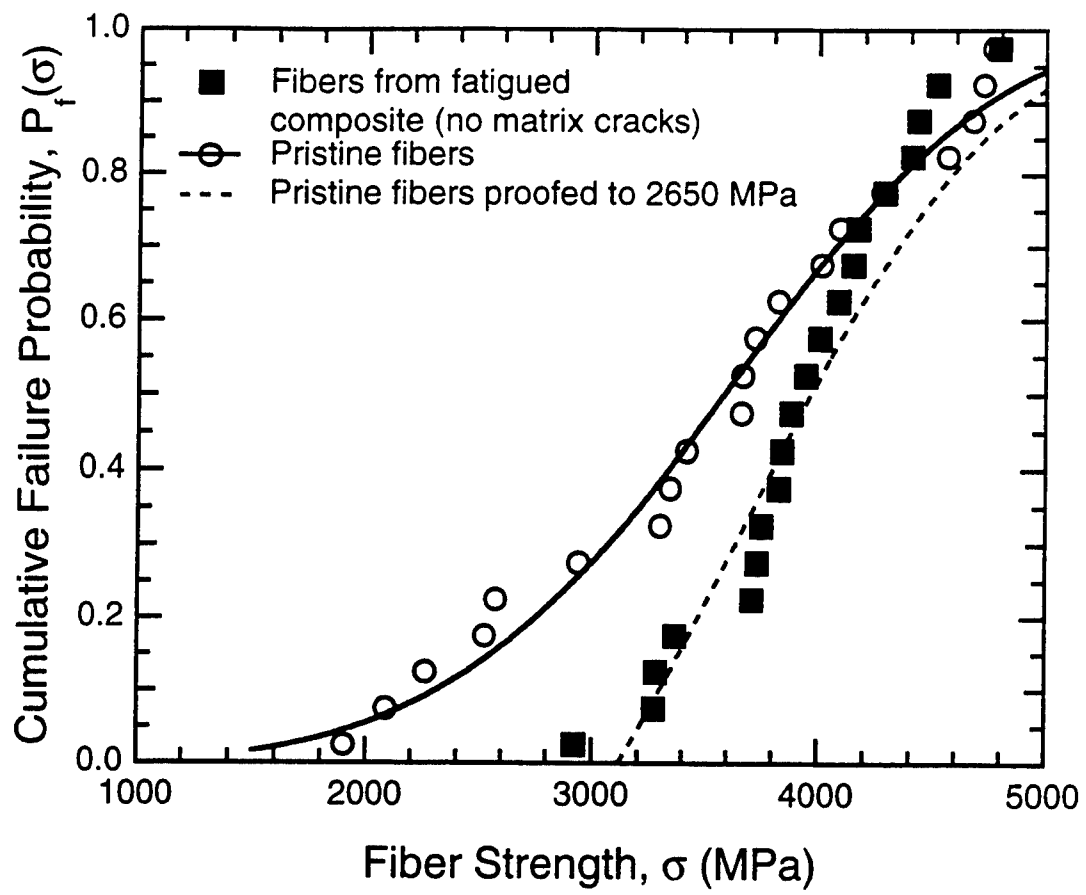


Figure 10(a)

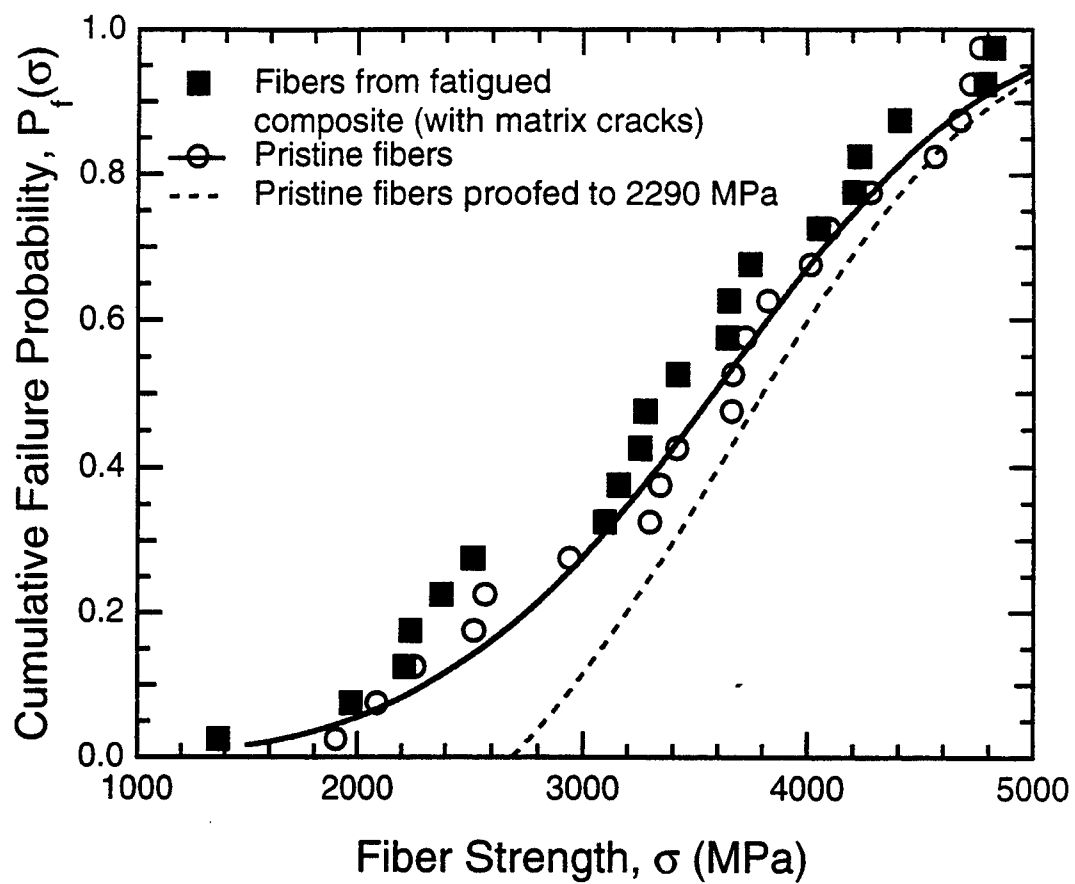


Figure 10(b)

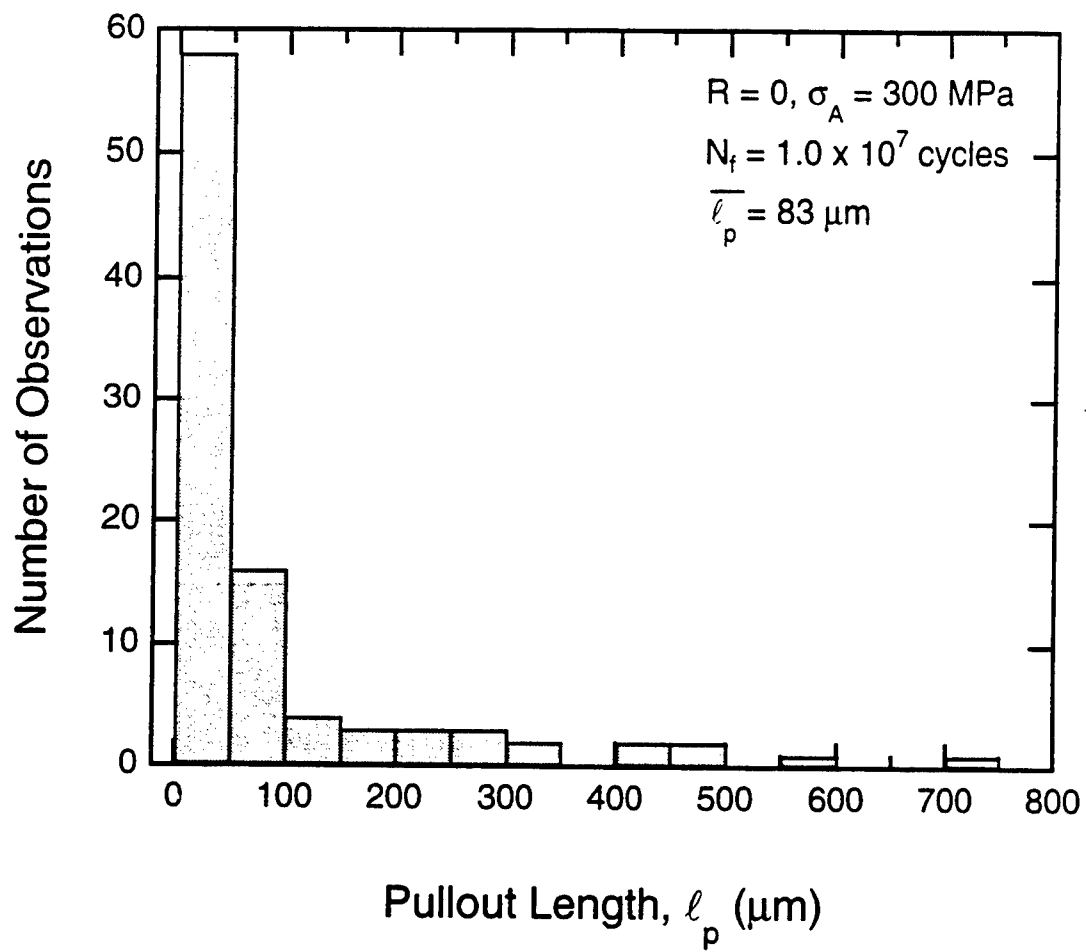


Figure 11

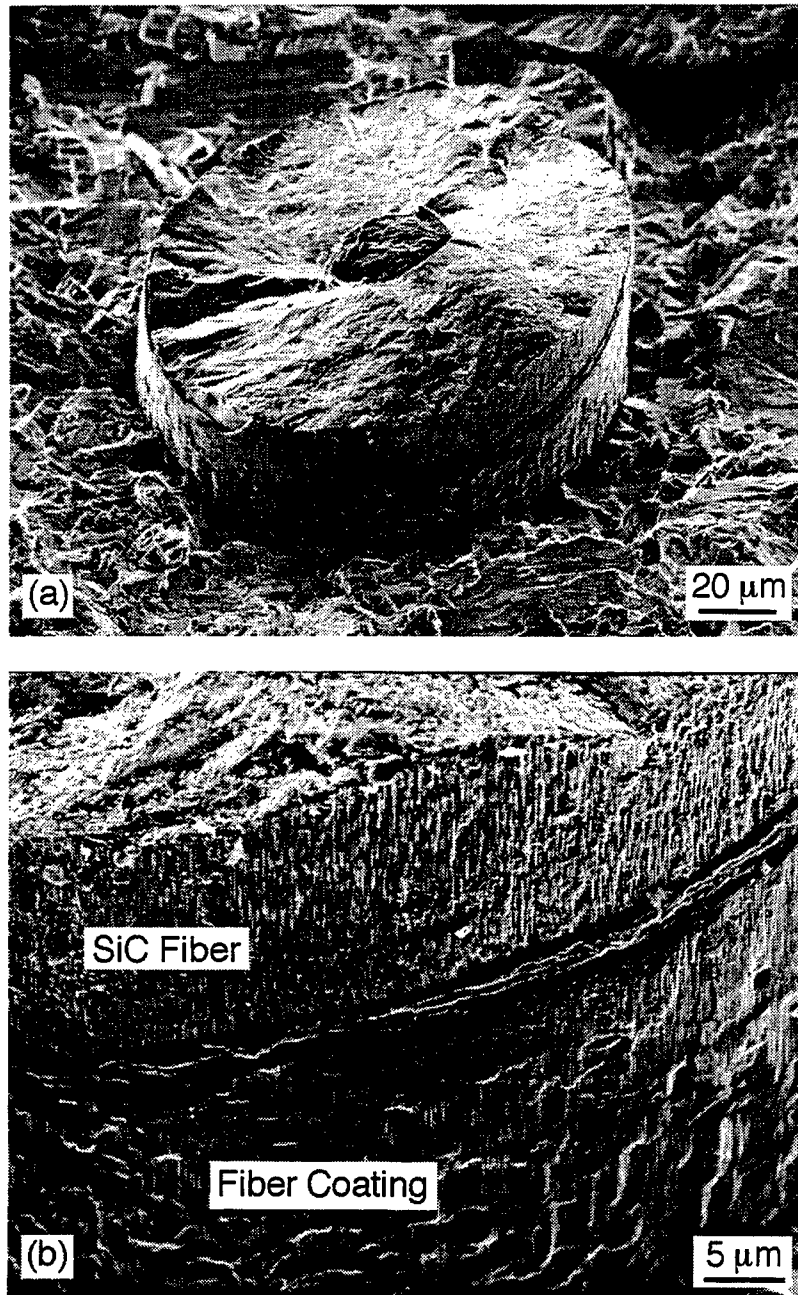


Figure 12

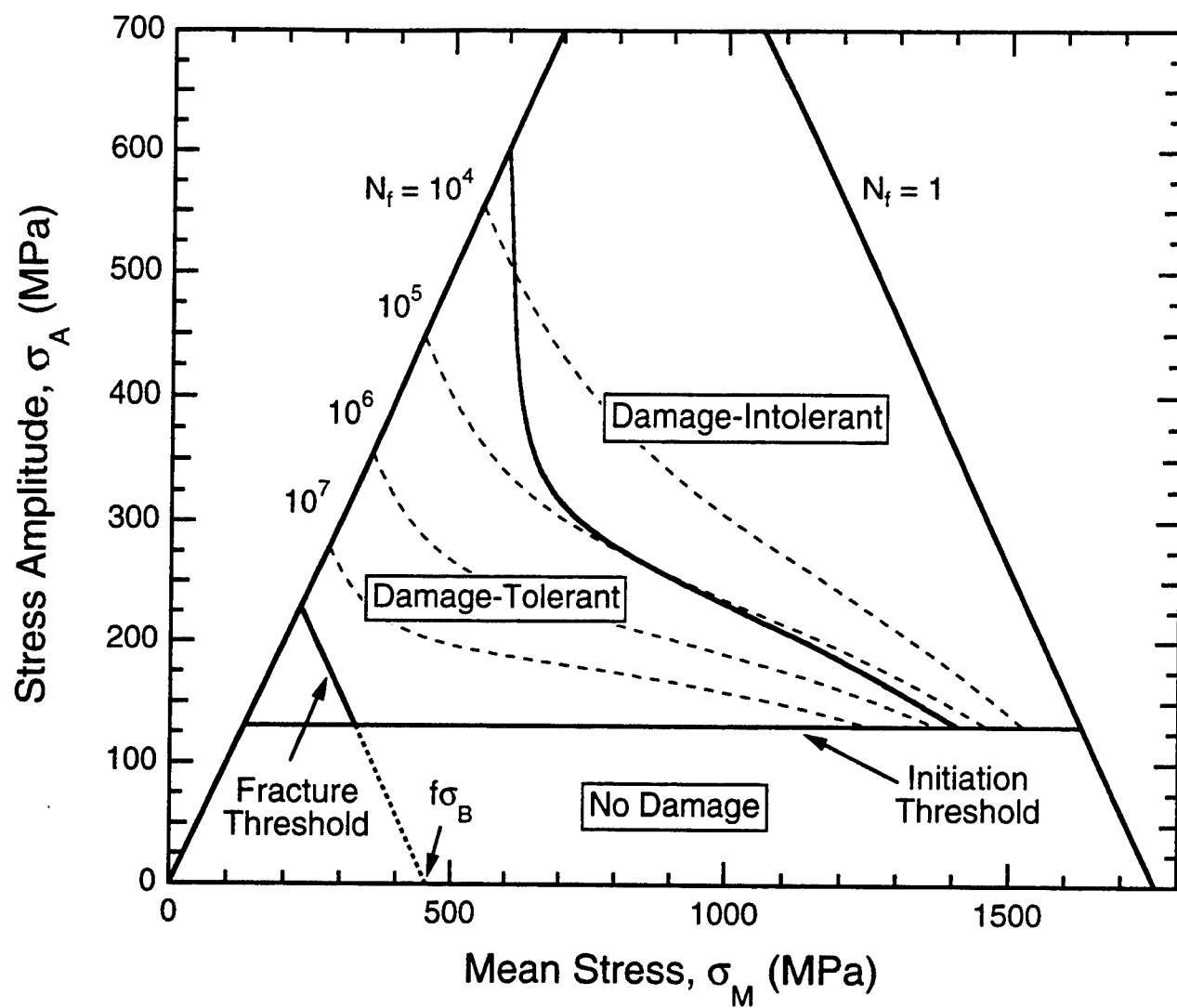


Figure 13



STRENGTH VARIABILITY IN ALUMINA FIBER-REINFORCED ALUMINUM MATRIX COMPOSITES

U. RAMAMURTY^{1*}, F. W. ZOK¹, F. A. LECKIE² and H. E. DÈVE³

¹Materials Department, ²Department of Mechanical and Environmental Engineering, University of California, Santa Barbara, CA 93106 and ³Metal Matrix Composites Program, 3M Company, Bldg. 60, 2465 S. Lexington Ave., Mendota Heights, MN 55120, U.S.A.

(Received 3 February 1997; accepted 21 March 1997)

Abstract—The strength variability of an Al–2% Cu alloy matrix reinforced with 65 vol.% Nextel-610 Al₂O₃ fibers has been investigated, with the aim of identifying and separating the contributions associated with the variabilities in both the fiber bundle strength and the fiber volume fraction. Strength distributions have been measured using three test geometries, including three- and four-point flexure and uniaxial tension. The measured distributions are rationalized on the basis of a fiber strength distribution that follows Weibull statistics and a fiber volume fraction distribution characterized by a Gaussian. The fiber bundle strength distribution is found to be extremely narrow, with a Weibull modulus in the range of ~50–60. In addition, the coefficient of variation in the fiber volume fraction distribution is inferred to be ~6%; by comparison, measurements made on relatively large specimens yield a coefficient of variation of ~3%. The differences in these values are attributed to local volume fraction variations which are not detectable by the global measurements. The measured strengths are compared with the predicted values based on the theoretical work of Curtin and co-workers, incorporating the effects of local load sharing between broken fibers and their neighbors. Good correlations are obtained between the experimental data and the model predictions. © 1997 Acta Metallurgica Inc.

1. INTRODUCTION

Continuous alumina-fiber-reinforced aluminum matrix composites (AMCs) exhibit attractive mechanical properties along the fiber direction. Young's moduli of ~250 GPa and tensile strengths approaching 2 GPa have been measured in some systems [1]; comparable to or exceeding the corresponding properties in SiC fiber-reinforced Ti matrix composites [2, 3]. These properties are attributable to the exceptional performance of recent generations of small diameter polycrystalline alumina fibers along with existing capabilities for producing AMCs with very high fiber volume fractions (60–70%) using fairly conventional metal casting processes. These have served as the motivation for considering AMCs in strength- and stiffness-critical components, including doors and landing gear for aircraft [1].

One of the critical issues involved in fail-safe design of engineering components made with AMCs relates to strength *variability*. Methods are needed for designing critical experiments to ascertain the nature and degree of strength variability in AMCs at the laboratory scale and subsequently extrapolating the results to predict strength and reliability of very large components.

The objective of the present paper is to present experiments and analyses that provide insight into strength variability of AMCs, especially the volume dependence of strength. The effects of volume are evaluated by performing mechanical tests on three different test geometries. It is demonstrated that the strength distributions obtained using one (fixed) test geometry are considerably broader than those inferred by comparing mean strengths from different test geometries. The variations in both the fiber bundle strength and the fiber volume fraction are combined in order to simulate the measured distributions in composite strength. Finally, the measured strengths are compared with the predictions obtained from computer simulations and analyses of fiber fragmentation and fiber bundle fracture, by Curtin and co-workers [4, 5].

2. BACKGROUND

2.1. Strength variability in metals and ceramics

The constituents of AMCs (a brittle ceramic and a ductile metal) exhibit markedly different characteristics in their strength variability. The strength of a ductile metal is governed by its resistance to plastic flow by dislocation motion, characterized by its yield stress, σ_y . It is dictated by an *average* characteristic of the microstructure, such as the grain size or the precipitate spacing, and, consequently, does not vary with specimen or component size. Usually, the

*Present address: School of Mechanical and Production Engineering, Nanyang Technological University, Nanyang Avenue, Singapore 2263

distribution in yield stress is rather narrow and can be described empirically by a Gaussian (or normal) distribution function, given by [6]

$$g(\sigma_y) = \frac{1}{\sqrt{2\pi}\gamma_\sigma} \exp\left[-\frac{1}{2}\left(\frac{\sigma_y - \bar{\sigma}_y}{\gamma_\sigma}\right)^2\right] \quad (1)$$

where $g(\sigma_y)$ represents the probability density at σ_y , $\bar{\sigma}_y$ is the average yield stress, and γ_σ is the standard deviation.

In contrast, the strength of a ceramic at ambient temperature is governed by the material's fracture toughness and the size of the *largest* flaw, via the Griffith relation. In this case, the strength is not dictated by an average microstructural characteristic but rather by an extreme value. As a result, the strength follows weakest link scaling laws, in accordance with [7]

$$P(\sigma) = 1 - \exp\left[-\int_0^\sigma q(\sigma) dV\right] \quad (2)$$

where $P(\sigma)$ is the cumulative failure probability at a stress σ , V is the volume and $q(\sigma)$ is a positive, monotonically increasing function of σ , governed by the flaw size distribution. The Weibull function is obtained when $q(\sigma)$ is taken to be a power law

$$q(\sigma) = \frac{1}{V_0} \left(\frac{\sigma}{\sigma_0}\right)^m \quad (3)$$

with σ_0 being a reference stress corresponding to the reference volume V_0 and m the Weibull modulus (or dispersion index). Combining equations (2) and (3) yields [7]

$$P(\sigma) = 1 - \exp\left[-k \left(\frac{V}{V_0}\right) \left(\frac{\sigma}{\sigma_0}\right)^m\right] \quad (4a)$$

where k is a dimensionless loading factor defined by

$$k = \frac{1}{V\sigma_{\max}^m} \int_0^\sigma \sigma^m dV \quad (4b)$$

and σ_{\max} is the maximum tensile stress in the body. For linear elastic materials, k is only a function of m and the specimen geometry. Expressions for k for typical test geometries are presented in Table 1.

Table 1. Loading factors for common test geometries (adapted from Ref. [7])

Geometry	Loading factor, k
Uniaxial tension	1
Pure bending	$\frac{1}{2(m+1)}$
Three-point flexure	$\frac{1}{2(m+1)^2}$
Four-point flexure	$\frac{m+2}{4(m+1)}$
(Outer span/inner span = 2)	

From equation (4) it follows that the ratio of mean strengths, $\bar{\sigma}_1$ and $\bar{\sigma}_2$, obtained from two different loading configurations with k -factors of k_1 and k_2 and volumes V_1 and V_2 is

$$\frac{\bar{\sigma}_1}{\bar{\sigma}_2} = \left(\frac{k_2 V_2}{k_1 V_1}\right)^{1/m} \quad (5)$$

For example, the ratio of mean strengths measured in pure bending, $\bar{\sigma}_b$, and in uniaxial tension, $\bar{\sigma}_t$, is given by (Table 1)

$$\frac{\bar{\sigma}_b}{\bar{\sigma}_t} = \left(2(m+1) \frac{V_t}{V_b}\right)^{1/m} \quad (6)$$

where V_t and V_b are the volumes under tension and bending,† respectively.

From the preceding analysis, there emerge two distinctly different approaches for determining the Weibull parameters of a material. The first (and most common) involves making a series of strength measurements on a fixed specimen geometry and volume, and subsequently fitting the measured distribution to equation (4). This approach tacitly assumes that the strength variability is associated exclusively with a single population of flaws. The second is based on comparisons of mean strengths of two or more test geometries, with either varying volumes or different k -factors [through equation (5)]. Though less commonly used, this approach is preferred over the first since the volume dependence of strength is measured directly. In the present study, comparisons are made between the two approaches and used to identify and separate the volume-dependent and volume-independent contributions to strength variability.

2.2. Strength variability in fiber reinforced metal matrix composites

The longitudinal tensile strength, σ_c , of a fiber-reinforced metal matrix composite is given by

$$\sigma_c = f\sigma_b + (1-f)\sigma_m \quad (7)$$

where f is the fiber volume fraction, σ_b is the in-situ fiber bundle strength, and σ_m is the stress borne by the matrix at the point at which the fiber bundle fails, usually taken to be its yield stress, σ_y . In general, the variability in composite strength is controlled by the variabilities in the constituent properties, σ_b and σ_y , and the fiber volume fraction, f .‡ In the specific case of AMCs, the variation in σ_y is expected to play only a small role, because of both the low variability in

†In the present context, V_b is the total volume subjected to bending, including the region that is under compression.

‡In uniaxial tension, the strength at each cross-section is governed by the local *area* fraction of fibers, rather than the volume fraction measured over some length of composite. Consequently, the relevant distribution in f is the one that would be obtained by measuring the area fraction of fibers, averaged over the entire cross-sectional area, at various locations along the specimen length.

yield strengths of metal alloys as well as the relatively small contribution that is derived from the matrix, i.e. typically, $(1-f) \sigma_y/\sigma_c \approx 0.01-0.03$. Consequently, the variations in σ_b and f are expected to dominate.

The fiber bundle strength is dictated by the strength distribution of the individual fibers as well as the load transfer characteristics between neighboring fibers. The extent of load transfer is governed by a shear resistance, τ . In systems containing fibers with weak coatings, τ is controlled by the sliding resistance of the interface; in contrast, in systems with well-bonded interfaces (as applies in the case of the AMCs tested in this study), it is controlled by the shear yield stress of the matrix, τ_y . In either case, if τ is sufficiently low, global load sharing (GLS) conditions are obtained [8-10]. In this regime, the load carried by a broken fiber is distributed equally to all fibers in the plane of the break with no attendant stress concentration in neighboring fibers. Consequently, fiber damage develops in a random fashion with no correlation between the damage sites. The GLS fiber bundle strength is dictated by a characteristic slip length, δ_o [8]:

$$\delta_o = \left(\frac{\sigma_{of} R L_o^{1/m_f}}{\tau} \right)^{m_f/(m_f+1)} \quad (8)$$

where R is the fiber radius, m_f is the Weibull modulus of the fibers and σ_{of} is the reference strength corresponding to a reference length, L_o . Provided the length of the composite is greater than $\sim 2\delta_o$ and the number of fibers is large, the bundle strength is deterministic and given by [8]

$$\sigma_b = S_o \left(\frac{1}{2 + m_f} \right)^{1/m_f+1} \left(\frac{m_f + 1}{m_f + 2} \right) \quad (9)$$

where S_o is a characteristic strength defined by

$$S_o = \left(\frac{\sigma_{of} \tau L_o}{R} \right)^{1/(m_f+1)} \quad (10)$$

When the sliding stress is large, the load from a broken fiber is distributed preferentially to its neighbors: the so-called local load sharing (LLS) condition [10]. In this regime, fiber damage spreads in a correlated manner and the fiber bundle strength is intrinsically stochastic in nature. One of the important implications is that the strength follows weakest-link statistics and hence exhibits a volume dependence [4, 5]. This volume dependence has been reported for a number of fiber-reinforced polymer matrix composites [11-14] and some ceramic matrix composites [15], but not in metal matrix systems.

A particularly notable feature of the composite strength distribution is the expected presence of both a volume-dependent contribution (through σ_b) as well as a volume-independent one (through f). One of the objectives of the present work is to demonstrate how

Table 2. Summary of constituents properties

Nextel 610™ fibers	
Volume fraction, f	0.652 ± 0.022
Density, ρ_f (g/cm ³)	3.9
Radius, R	5-6 μ m
Young's modulus, E_f (GPa)	380
Weibull modulus, m_f	9
Reference strength, σ_{of} (MPa)	2060
$(L_o = 1 \text{ m})$	
Al-2% Cu alloy	
Density, ρ_m (g/cm ³)	2.73
Young's modulus, E_m (GPa)	60
0.2% offset yield stress, σ_y (MPa)	100

these contributions can be separated using strength distributions obtained from various test geometries.

3. MATERIALS

The composite material used in this study was an Al-2% Cu alloy reinforced unidirectionally with Nextel™-610 fibers (99% α -Al₂O₃). The fiber properties are listed in Table 2. The composite panels were manufactured by laying up an array of aligned fiber tows in a mold and using pressure-assisted casting to infiltrate the molten matrix alloy. The panels were ~ 1.5 mm thick and had a nominal fiber volume fraction of 65%. A transverse cross-section of the composite is shown in Fig. 1. The composites were free of any residual porosity. Moreover, the fiber packing was uniform, with the exception of narrow matrix-rich channels, $\sim 10-20 \mu$ m wide, between the prior fiber tows. For comparison, an ingot of the neat matrix alloy was also cast and tested.

The panels were heat treated in order to peak-age the matrix. The treatment was comprised of solutionizing at 520°C for 16 h, quenching into water at 90°C, and aging for 100 h at 190°C. The appropriate aging time was determined by aging a series of specimens for various times at 190°C and subsequently measuring their transverse tensile strengths. The transverse strength is dictated by the matrix and hence the aging time corresponding to its peak value is expected to be the same as that for the matrix alone. The ingot of neat matrix was subjected to the same heat treatment.

The variability in the fiber volume fraction was determined from density measurements made on 12 of the fractured three-point flexure specimens, each with a volume of $\sim 150 \text{ mm}^3$. The density measurements were made using an immersion technique (based on Archimede's principle), with diethyl-phthalate as the immersion fluid. The precision of the measurements was $\sim 0.01\%$. The fiber volume fraction was calculated from the composite density, ρ_c , using the equation:

$$f = \frac{\rho_c - \rho_m}{\rho_f - \rho_m} \quad (11)$$

where ρ_m and ρ_f are the densities of the matrix (2.73 g/cm³) and the fibers (3.9 g/cm³), respectively [1]. Additionally, in one instance, the fiber volume

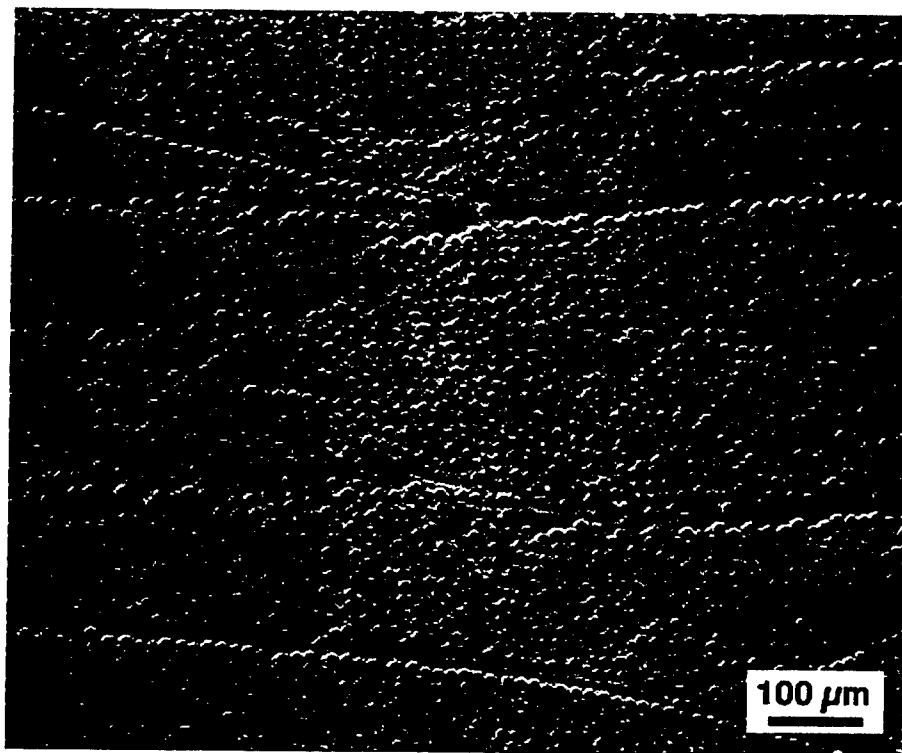


Fig. 1. Transverse cross-section through composite, showing the spatial distribution of fibers.

fraction was determined using quantitative metallography of a polished cross-section and found to be consistent with the result obtained from the density measurements.

The distribution in the fiber volume fraction is plotted in Fig. 2. Also shown is the curve obtained upon fitting the data to the normal distribution function. The average and standard deviations in the fiber volume fraction were $\bar{f} = 0.652$ and $\gamma_f = 0.022$, and the corresponding coefficient of variation, $\beta_f = \gamma_f/\bar{f} \approx 3\%$.

4. MECHANICAL MEASUREMENTS

Three types of mechanical test were performed on the composite panels: three- and four-point flexure and uniaxial tension. In all cases, the fibers were parallel to the direction of applied stress. A total of ~ 60 tests were performed. The flexure specimens were 6.3 mm wide. The loading span for the three-point flexure specimens was 26 mm. The inner and outer loading spans for the four-point specimens were 26 and 51 mm, respectively. The tensile tests were performed on straight specimens with a width of 9.5 mm and a gauge length of 80 mm. All tensile test results reported here were from gauge failures. In most cases, strains were measured using strain gauges of appropriate size mounted on the tensile faces of the specimens. The tensile behavior of the neat matrix was measured using standard dog-bone specimens.

The 0.2% offset yield stress was found to be $\sigma_y = 100$ MPa, and the corresponding shear strength is $\tau_y = \sigma_y/\sqrt{3} \approx 60$ MPa.

Figure 3(a) shows the typical tensile stress-strain behavior of the composites. The corresponding tangent modulus, $d\sigma/d\epsilon$, is plotted against strain in Fig. 3(b). The response is essentially linear over the entire strain range. The average tangent modulus, $d\sigma/d\epsilon \approx 230 \pm 10$ GPa, is comparable to the calculated value of $fE_f = 239$ –256 GPa, assuming that the fibers support all of the load. In some instances, the initial elastic modulus (~ 250 –260 GPa) was slightly higher and comparable to the value expected from the

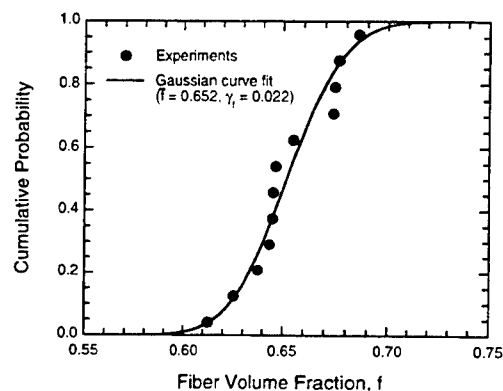


Fig. 2. Fiber volume fraction distribution.

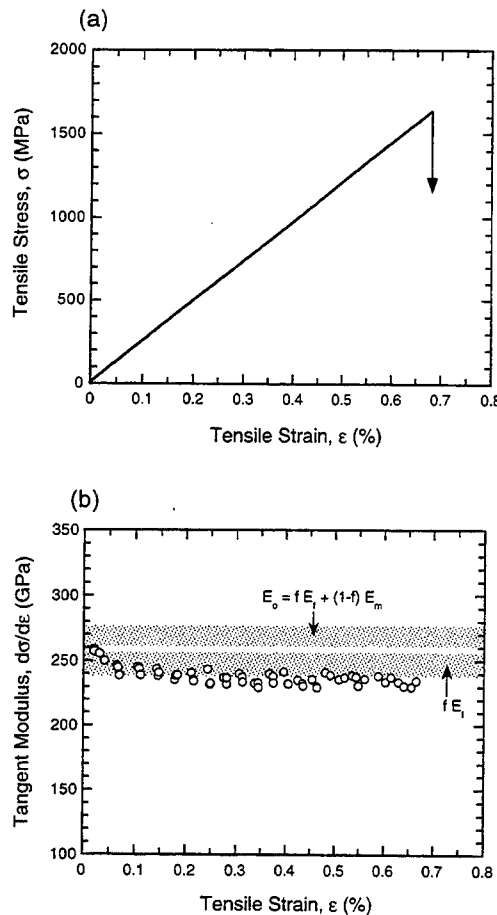


Fig. 3. (a) Typical tensile stress-strain response of the AMC. (b) Variation in the tangent modulus with tensile strain.

rule of mixtures: $E = fE_f + (1-f)E_m = 261 - 276$ GPa.† The slight changes in the tangent modulus are ascribed to matrix yielding and occur at relatively low stresses (typically <100 MPa). Moreover, the magnitude of these changes is so small that the deviation from linearity in the stress-strain curves is almost imperceptible. Similar stress-strain characteristics were obtained in the flexure tests, i.e. linear response with a slope $\approx fE_f$.

The absence of a reduction in tangent modulus prior to fracture indicates that there is little fiber failure prior to composite fracture and suggests that local load sharing (LLS) conditions are operative. This conclusion is supported by fractographic observations which reveal planar fracture surfaces, devoid of fiber pull-out (Fig. 4). The strength distributions are plotted on Fig. 5. The failure probabilities were obtained by ranking the strength data in ascending order and using the cumulative

probability estimator

$$P = \frac{i - 0.5}{I} \quad (12)$$

where i is the rank and I is the total number of datum points. The strengths of the flexure specimens were calculated assuming the material to be linear elastic. This assumption is justified on the basis of the nearly linear response measured in both tension and flexure.‡ The mean strengths increase in the order: tension \rightarrow four-point flexure \rightarrow three-point flexure. This trend is qualitatively consistent with the reduction in the effective volume subject to stress and suggests that weakest link scaling concepts might be used to rationalize the measurements.

5. ANALYSIS OF STRENGTH VARIABILITY

The suitability of the Weibull distribution function (equation 4) in describing the measured strength distributions was assessed in the following way. First, the values of m and σ_0 were obtained by fitting the Weibull function to the data sets for each of the three test geometries. If the distribution follows the Weibull function, the values of m and σ_0 should be the same in each of the test geometries. The results of this fitting are summarized in Fig. 5 and Table 3. Second, the mean strengths for each of the test geometries were calculated and their ratios used to determine the Weibull modulus, m , through equation (5). These results are presented graphically in Fig. 6. Comparisons were then made between the Weibull moduli obtained using the two methods.

The Weibull moduli obtained by fitting the three strength distributions are similar to one another, ranging from ~ 16 to 20, but the reference strengths vary by as much as a factor of ~ 2 . The latter inconsistency reveals an inadequacy in the Weibull function in describing the strength distributions. A further inconsistency is obtained from the mean strength comparisons. The ratio of mean strengths measured in three-point flexure (2170 MPa) and uniaxial tension (1820 MPa) yields $m \approx 59 \pm 6$: ~ 3 times the value obtained from fitting the individual distributions. The ratio of mean strengths measured in four-point flexure (2050 MPa) and uniaxial tension yields a similarly large value: $m \approx 51 \pm 10$.

The inconsistencies in the Weibull parameters obtained from the strength distributions are believed to be associated with variations in fiber volume fraction, superimposed on the intrinsic bundle strength distribution. As noted previously, the

†The ranges correspond to \pm one standard deviation in the fiber volume fraction distribution.

‡Strictly, this approach overestimates the true flexural strength. If the matrix within the composite undergoes yielding across the entire cross-section and the fibers remain elastic, the calculated composite stress exceeds the true tensile stress at the outer surface by an amount $(1-f)\sigma_y/2$. In the present system, this correction is only ~ 17 MPa, which is $<1\%$ of the measured composite strength, and can be safely neglected.

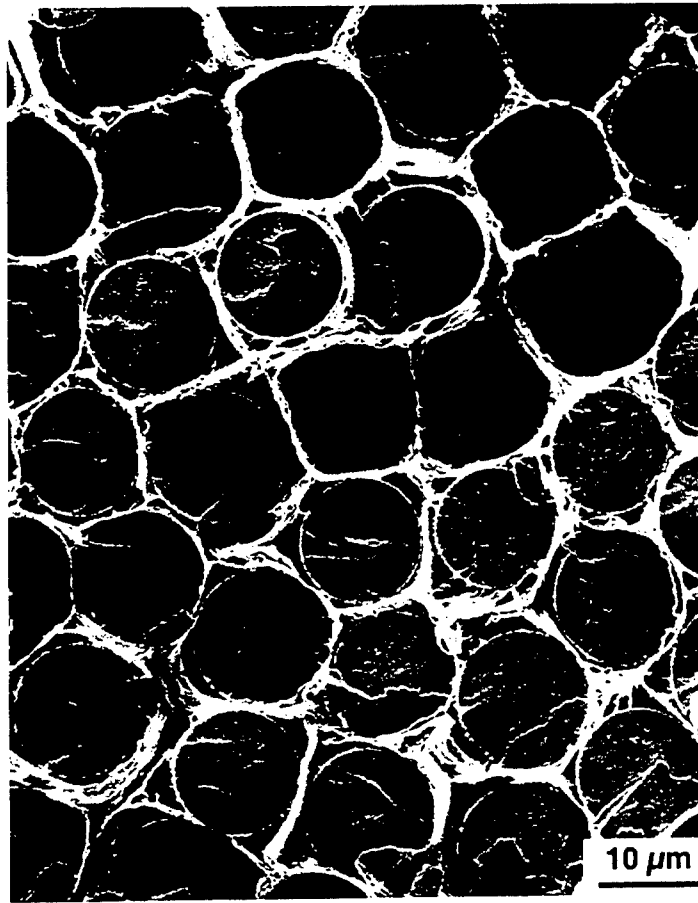


Fig. 4. Scanning electron micrograph of tensile fracture surface of the AMC, showing planar fracture and negligible fiber pull-out.

composite strength distribution is a convolution of the distributions of the fiber bundle strength and the fiber volume fraction. To first order, the fiber volume fraction is expected to be volume independent and follow a Gaussian distribution. In contrast, the fiber

bundle strength follows weakest link scaling laws and therefore exhibits a volume dependence. This distribution is assumed to follow the Weibull function.

The relevant parameters in these distributions were evaluated in the following way. The average Weibull modulus determined from the mean strength comparisons ($m = 55$) was taken to be representative of the variation in σ_b at the mean fiber volume fraction, f . An implicit assumption here is that the load sharing behavior remains unchanged over the range of f in the present composites. The corresponding reference strength for the bundle strength distribution was calculated from the tensile strength distribution and equation (4a). The result is $\sigma_{cb} = \sigma_{oc}/\bar{f} = 2198$ MPa, for a reference volume $V_o = 1 \text{ m}^3$.

In the initial calculations, the fiber volume fraction was assumed to follow a Gaussian distribution with the mean and standard deviation obtained from the experimental measurements. However, it should be noted that each of these measurements represents an average over a relatively large volume, whereas the distribution relevant to the composite strength is the

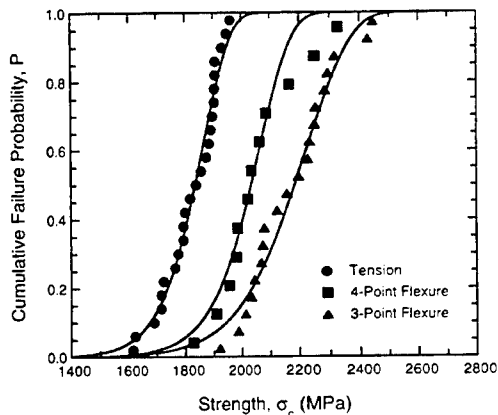


Fig. 5. Measured strength distributions and curve fits based on the Weibull distribution function.

Table 3. Summary of strength distributions

Test	Composite strength, σ_c (MPa)	Failure strain (%)	Apparent Weibull modulus, m_c	Apparent reference strength, σ_{c0} † (MPa)	Specimen volume, V (m ³)
Three-point flexure	2171 ± 144	0.907 ± 0.06	16.2 ± 1.1	588 ± 46	242 × 10 ⁻⁹
Four-point flexure	2051 ± 141	0.814 ± 0.037	20.1 ± 3	807 ± 104	474 × 10 ⁻⁹
Uniaxial tension	1821 ± 99	0.744 ± 0.029	20.4 ± 1.1	952 ± 33	1080 ± 10 ⁻⁹

†Extracted from the least-square fit of the Weibull function [equation (4)] to the experimental data.

one which would be obtained by measuring the area fraction of fibers at each cross-section through the composite. Clearly, the distribution in the *local* values of f must be at least as broad as that of the measured global distribution. Nevertheless, the *global* values provide for a useful preliminary assessment of the proposed methodology for simulating the composite strength distribution.

In convoluting the two distributions, it is assumed that the matrix contribution to the strength is negligible such that†

$$\sigma_c \approx f\sigma_b. \quad (13)$$

Furthermore, recognizing that the cumulative probability $P(\sigma_c)$ of a composite strength $\leq \sigma_c$ is equivalent to the cumulative probability of a bundle strength $\sigma_b \leq \sigma_c/f$, denoted $Q(\sigma_b) = Q(\sigma_c/f)$, leads to the result

$$P(\sigma_c) = \int_0^1 [Q(\sigma_c/f)][h(f)] df \quad (14)$$

where $h(f)$ is the probability density of f . Combining

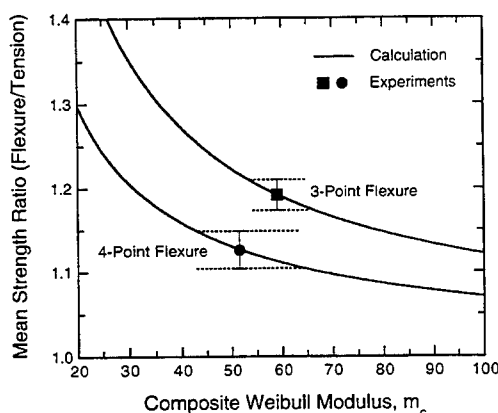


Fig. 6. Variation in the strength ratio (flexure/tension) with the Weibull modulus. The lines are calculated from equation (5) and the k -factors in Table 1. The solid symbols represent the measured strength ratios. The error bars were calculated using standard error propagation techniques.

†More rigorous numerical simulations that incorporate the matrix contribution [through equation (7)] have also been performed using the convolution theorem. The predicted distributions are essentially identical to the ones obtained using the approximation in equation (13), with the two lying within about the thickness of the lines in Fig. 7.

equations (1), (4a), and (13) yields

$$P(\sigma_c) = \frac{1}{\sqrt{2\pi}\gamma_f} \int_0^1 \left[1 - \exp \left(-\frac{V}{V_0} \left(\frac{\sigma_c}{f\sigma_{ob}} \right)^m \right) \right] \times \left[\exp \left(-\frac{1}{2} \left(\frac{f - \bar{f}}{\gamma_f} \right)^2 \right) \right] df. \quad (15)$$

The simulated strength distributions are plotted in Fig. 7. The three curves in each of these plots represent differing values of γ_f . For $\gamma_f = 0$, a simple Weibull distribution is obtained, with strength variations that are much lower than the measured ones. For $\gamma_f = 0.022$ (the value obtained from the global volume fraction measurements), the distributions are somewhat broader, though they remain narrower than the measured ones and suggest that the relevant value of γ_f is somewhat higher. As an alternate approach, γ_f was inferred from the strength distributions, assuming that the distributions are controlled solely by the variations in f and σ_b , and following the normal practices for summing the variances of two distributions to obtain the variance of the combined distribution. This calculation yields $\gamma_f = 0.04$. The predicted strength distributions using this value exhibit a closer correspondence to the experimental data than for the case of $\gamma_f = 0.022$ as shown in Fig. 7. Moreover, the relative goodness-of-fit, as measured by the ratio of the chi-square parameters obtained for the two fits, is ~ 3 times better for $\gamma_f = 0.04$ than for $\gamma_f = 0.022$. The inferred value of γ_f is taken to represent the standard deviation in the fiber *area* fraction distribution and, as expected, exceeds γ_f of the global volume fraction distribution.

The results indicate that the variability in the fiber bundle strength of the present composite is extremely low, as manifested by the high Weibull modulus (~ 50), and that a large portion of the composite strength variability can be attributed to fiber volume fraction variations. Indeed, the coefficient of variation of the fiber volume fraction distribution exceeds that of the fiber bundle strength distribution ($\sim 6\%$ vs $\sim 2\%$), suggesting that the breadth of the distribution obtained from any one test geometry is dominated by variations in f rather than the fiber bundle strength characteristics. Consequently, a strength distribution obtained from one test geometry can provide misleading information about the nature of the strength variability and its volume dependence.

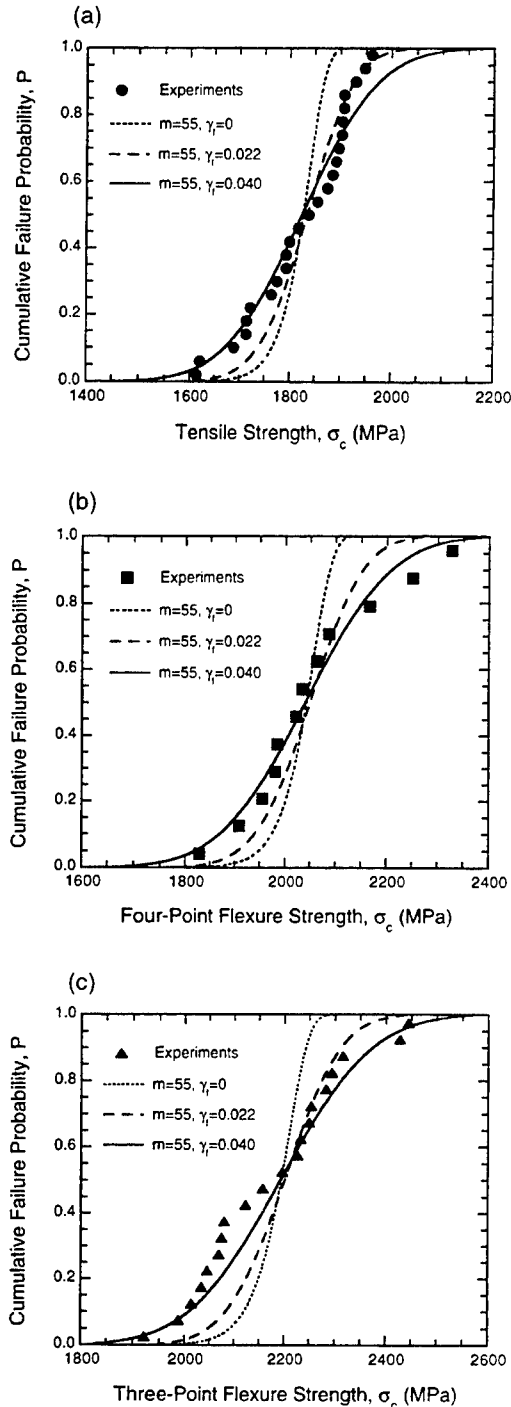


Fig. 7. Comparisons of measured and calculated strength distributions: (a) uniaxial tension, (b) four-point flexure, and (c) three-point flexure.

Separation of the volume-dependent and volume-independent contributions to strength variability can be obtained only by comparing strength distributions associated with substantially different volumes or test geometries.

6. COMPARISONS BETWEEN EXPERIMENT AND THEORY

The values of the fiber bundle strength and the corresponding coefficient of variation obtained from the experiments have been compared with the theoretical predictions of fiber bundle fracture under LLS conditions [4, 5]. The comparisons provide insight into the connections between the composite and fiber strength characteristics as well as the role of load transfer between fibers through matrix shearing. They also provide an assessment of the validity of the existing theories. The key results of the theory are presented below.

Ibnabdeljalil and Curtin [5] used a 3D-lattice Green's function method to simulate the evolution of fiber damage and ultimate fracture in a unidirectional composite under LLS conditions. The modeling parameters were selected to yield stress concentrations in the fibers around a fiber break of ≈ 1.14 (the same as the value obtained by Hedgepeth and VanDyke [16]). Upon comparison of the simulated strength distributions under LLS conditions [5] with the known strength distribution under GLS conditions [17], they demonstrated that there exists a characteristic volume (or "link"), comprised of n fibers of length $0.4\delta_o$, which exhibits the same strength distributions under both GLS and LLS conditions. The number of fibers in the link were found to vary with the fiber Weibull modulus in accordance with the empirical relation

$$n = 403m_i^{-1.28} \quad (16)$$

for $2 \leq m_i \leq 10$. With knowledge of the characteristic link size and its strength distribution, weakest link scaling laws were used to obtain approximate analytical solutions for the strength distribution of a fiber bundle comprised of N links. The bundle strength was found to follow a Weibull distribution, with reference strength σ_{ob} and Weibull modulus m_b given by†

$$\frac{\sigma_{ob}}{S_o} = \mu^* + \gamma^* \left[\frac{\ln(\ln N) + \ln(4\pi)}{\sqrt{8 \ln N}} - \sqrt{2 \ln N} \right] \quad (17)$$

and

$$m_b = \frac{\mu^* \sqrt{2 \ln N}}{\gamma^*} 0.5 [\ln(\ln N) + \ln(4\pi) - 4 \ln N] \quad (18)$$

where μ^* and γ^* are the normalized mean and standard deviation of the strength distribution of the characteristic link under GLS and are summarized in Table 1 of Ref. [5]. The mean and standard deviation

†Strictly, the strength does not follow a Weibull distribution, as manifest in the dependence of m_b on N . A slightly better fit is obtained by using a Gaussian to describe the strength distribution of the characteristic link, though the differences in the predicted mean strengths are extremely small.

Table 4. Comparison of measured and predicted strengths

Test	Effective volume, [†] kV (m ³)	Effective number of links, N	Predicted strength (MPa)
Three-point flexure	3.86×10^{-11}	79	2320
Four-point flexure	2.15×10^{-9}	5150	2190
Uniaxial tension	1.08×10^{-6}	2.2×10^6	2050

[†]Calculated using $m_c = 55$.

of the distribution are related to σ_{ob} and m_b through the usual relations [7]

$$\bar{\sigma}_b/\sigma_{ob} = \Gamma\left(1 + \frac{1}{m_b}\right) \quad (19)$$

and

$$\gamma_b/\sigma_{ob} = \sqrt{\Gamma\left(1 + \frac{2}{m_b}\right) - \Gamma^2\left(1 + \frac{1}{m_b}\right)} \quad (20)$$

where $\Gamma(\cdot)$ is the gamma function.

To perform comparisons with the experimental results, estimates are needed for S_0 and δ_0 . These have been calculated from equations (8) and (10) using the reported strengths of the pristine fibers [1] and an effective sliding stress of $\tau_y = \sigma_y/3 = 60$ MPa. The number of links in each of the tensile specimens was calculated from the average fiber volume fraction and the number of fibers in the characteristic link [equation (16)], yielding the results presented in Table 4. For the flexure specimens, an *effective* number of links was used, based on the effective volume, kV , that dictates the failure probability. These results are also given in Table 4. A comparison of the measurements and predictions is presented in Fig. 8.

Over the range of N relevant to the present experiments (~ 70 to 2×10^6), the predicted coefficient of variation diminishes from $\sim 2.1\%$ to $\sim 1.2\%$. By comparison, the measured value is $\sim 2\%$. Over the same range of N , the correlation in the mean strengths is similar, with the predicted strengths overestimating the measured strengths by only $\sim 10\%$. Indeed, by simply reducing S_0 by 10% in these calculations [indicated by the dashed line in Fig. 8(b)], an excellent correlation is obtained between the two. The overall capability of the model to predict the fiber bundle strength distribution is thus considered to be satisfactory.

Also shown for comparison in Fig. 8(b) is the predicted strength for GLS conditions [8]. (Strictly, the predicted value is a lower bound for finite values of N and is valid only for $N = \infty$.) The discrepancies between this prediction and the measurements further support the view that LLS conditions are operative in this system.

As a further assessment of the role of load transfer via matrix shear in the fiber bundle strength, the measurements are compared with the predicted strength of a dry fiber bundle in which no coupling

exists between fibers. When the number of fibers in such a bundle is large, the strength is given by

$$\sigma_d = \sigma_{of}(m_f e L/L_0)^{-1/m_f} \quad (21)$$

where L is the fiber length. Using the fiber properties given in Table 2 along with a gauge length of 80 mm (equal to the length of the composite tensile specimens), the dry bundle strength is calculated to be $\sigma_d = 1910$ MPa and the corresponding composite strength is $f\sigma_d \approx 1240$ MPa. The latter value is $\approx 2/3$ of the mean tensile strength of the composite. The difference reflects the effects of the matrix in transferring load around broken fibers. It should be emphasized that the matrix contribution is

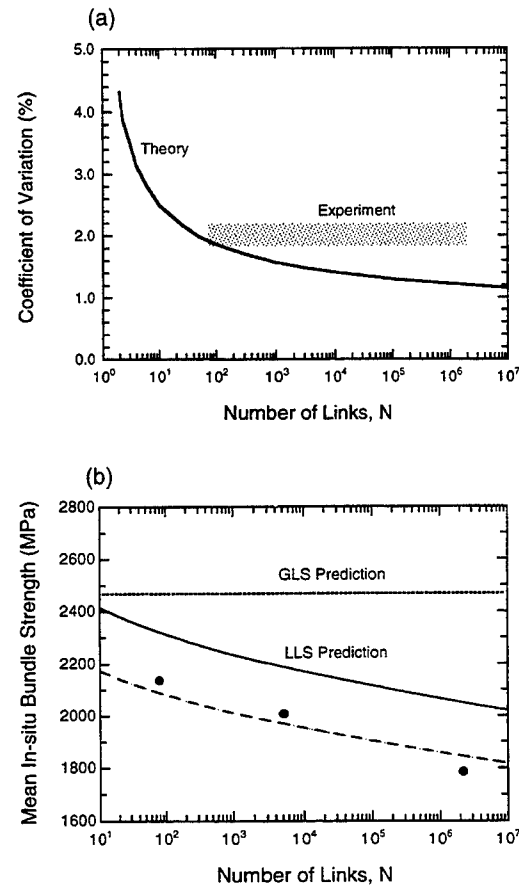


Fig. 8. Comparisons between experiment and theory: (a) the mean strength and (b) the coefficient of variation. The dashed line in (a) was calculated by reducing the estimate of S_0 by 10%.

not derived from the longitudinal stress that it supports, but rather from the plastic shearing process that occurs along the fiber direction around fiber breaks which allows broken fibers to support high loads at relatively short distances ($\sim \delta_0$) from the break locations. In this sense, the high composite strength is attributable in part to the synergistic interactions between the fibers and the matrix, and cannot be predicted through a simple rule-of-mixtures approach using the strengths of the two constituents alone.

7. CONCLUDING REMARKS

The present work has demonstrated how the contributions to strength variability from variations in the fiber volume fraction and the fiber bundle strength can be determined from experiments performed on several different test geometries. The separation of the contributions is crucial in extrapolating laboratory-scale test results to large components. By performing experiments on only one test geometry and assuming the variability in strength follows Weibull statistics may lead to a substantial underestimate of the true Weibull modulus of the fiber bundle and an overestimate of the volume dependence of strength.

One of the outstanding issues emanating from this work is the degree of *local* fiber volume fraction variations in AMCs. Though no direct measurements have been made, the strength distributions suggest local variations that are somewhat larger than the measured global variations, by a factor of ~ 2 . It is possible that this difference may be due in part to other factors that influence strength, including variations in the degree of fiber alignment, though additional experiments would be needed to determine the magnitude of such effects. Notwithstanding, the comparison between the value of γ_l inferred from the strength measurements and that obtained from the global volume fraction measurements supports the hypothesis that the volume-independent contribution to strength variation is associated mainly with variations in f .

The measured mean strengths and the corresponding coefficient of variation appear to be in good agreement with the existing theory of fiber fragmentation and fiber bundle fracture in LLS composites. The slight discrepancies between the measured and predicted mean strengths may be associated with numerous factors, including (i) uncertainties in the fiber properties, which may be exacerbated by fiber degradation during composite processing; (ii) the presence of extrinsic factors that influence strength, including manufacturing defects and surface flaws introduced by machining; and (iii) deficiencies in the theory.

Acknowledgements—This work was funded by DARPA University Research Initiative program at UCSB under

Office of Naval Research contract No. N00014-92-J-1808. The authors gratefully acknowledge Professor W. A. Curtin for many useful comments and discussions and Dr F. Dary for some experimental assistance.

REFERENCES

1. Dève, H. E. and McCullough, C., *J. Metals*, 1995, **47**(7), 33.
2. Jansson, S., Dève, H. and Evans, A. G., *Metall. Trans.*, 1991, **22A**, 2975.
3. Weber, C. H., Chen, X., Connell, S. J. and Zok, F. W., *Acta metall. mater.*, 1994, **42**, 3443.
4. Zhou, S. J. and Curtin, W. A., *Ibid.*, 1995, **43**, 3093.
5. Ibnabdeljalil, M. and Curtin, W. A., *Int. J. Solids Struct.*, 1997, **34**(21), 2649.
6. Ruff, P. E., *Metals Handbook*, Vol. 8, (9th edn). American Society of Metals, Metals Park, Ohio, 1984, p. 662.
7. DeSalvo, G. J., Theory and structure design applications of Weibull statistics. Westinghouse Electric Corporation Report, Pittsburgh, PA No. WANL-TME-2688, 1970.
8. Curtin, W. A., *J. Am. Ceram. Soc.*, 1991, **74**, 2837.
9. Curtin, W. A., *J. Mech. Phys. Solids*, 1993, **41**, 217.
10. He, M., Evans, A. G. and Curtin, W. A., *Acta metall. mater.*, 1993, **41**, 871.
11. Bullock, R. E., *J. Comp. Mater.*, 1974, **8**, 200.
12. Wisnom, M. R., *Composite Struct.*, 1991, **18**, 47.
13. Wisnom, M. R., *Composites*, 1991, **22**(1), 47.
14. Kortschot, M. T. and Beaumont, P. W. R., *Comp. Sci. Technol.*, 1990, **39**, 303.
15. McNulty, J. C. and Zok, F. W., *J. Am. Ceram. Soc.*, 1997, **80**(60), 1335.
16. Hedgepeth, J. M. and VanDyke, P., *Comp. Mater.*, 1967, **1**, 294.
17. Phoenix, S. L., Ibnabdeljalil, M. and Hui, C.-Y., *J. Solids Struct.*, 1997, **34**, 545.

APPENDIX

Nomenclature

E	elastic modulus
f	fiber volume fraction
$g(x)$	Gaussian probability density function [equation (1)]
$h(f)$	probability density of f
k	loading factor (Table 1)
L_0	reference length (1 m)
m	Weibull modulus
N	number of characteristic links
n	number of fibers in the characteristic link
P	cumulative failure probability of composite
Q	cumulative failure probability of fiber bundle
R	fiber radius
S_0	characteristic fiber strength [equation (10)]
V	volume
V_0	reference volume (1 m ³)
β	coefficient of variation (standard deviation/mean)
δ_0	characteristic slip length [equation (8)]
eI_u	composite failure strain
γ	standard deviation
μ	mean

r_l	density	subscripts f, m, c and b denote values for fibers, matrix, composite, and fiber bundle, respectively; B and T refer to bending and tension; and an overbar indicates the mean value.
s_l	strength	
s_{l_0}	reference strength	
τ	fiber/matrix sliding stress	

Inelastic deformation of fiber composites containing bridged cracks

F.W. Zok ^{a,*}, M.R. Begley ^b, T.E. Steyer ^a, D.P. Walls ^c

^a *Materials Department, University of California, Santa Barbara, CA 93106, USA*

^b *Division of Applied Sciences, Harvard University, Cambridge, MA 02138, USA*

^c *United Technologies, Pratt and Whitney, West Palm Beach, FL 33410, USA*

Received 5 April 1996; received in revised form 25 February 1997

Abstract

An analysis of the inelastic tensile deformation of a fiber composite containing multiple bridged cracks of finite length is presented. Composite strains are predicted by using crack opening areas to account for the additional inelastic strain due to the cracks. The analysis is based upon a line-spring representation of the crack surface tractions associated with bridging fibers, accounting for frictional sliding along the fiber–matrix interface with a constant shear stress. Approximate analytical solutions are derived based on the assumption that the near tip behavior of the crack dominates either the entire crack profile (for short cracks) or only a small portion of it (for long cracks). These results are compared to more detailed numerical solutions. The analysis is extended to the case of cyclic loading, incorporating the hysteresis that occurs as a result of reverse slip along the interfaces. © 1997 Elsevier Science Ltd.

1. Introduction

Fiber-reinforced titanium matrix composites (TMC) undergo multiple matrix cracking during cyclic tensile loading parallel to the fiber axis (Harmon and Saff, 1989; Walls et al., 1996). In uniform (unnotched) panels, the cracks usually initiate at the edges and propagate both through the thickness and across the width of the panel. Provided the applied stress is sufficiently low, the cracks grow past the fibers, leaving the fibers intact in the crack wake. This process is accommodated by debonding and sliding along the fiber–matrix interface.

Fig. 1 shows a typical sequence of crack patterns obtained from surface replicas taken at various stages of a fatigue test on a unidirectional Ti–6Al–4V/SCS-6 SiC composite (Steyer et al., 1997). As the cracks develop, the tensile response of the composite exhibits several changes, including: (i) a reduction in the longitudinal Young's modulus, E , (ii) the development of inelastic strain, manifested in a progressive broadening of the hysteresis loop and a reduction in the hysteresis modulus, E_H , and (iii) an increasing permanent strain, ϵ_p . Some typical measured loops illustrating these changes are shown in Fig. 2.

The objective of the present article is to present an analysis of the inelastic deformation of multiply cracked TMCs, incorporating the effects of crack length and fiber bridging. The analysis is conducted

* Corresponding author. Tel.: +1-805-8938699; fax: +1-805-8938486; e-mail: zok@engineering.ucsb.edu.

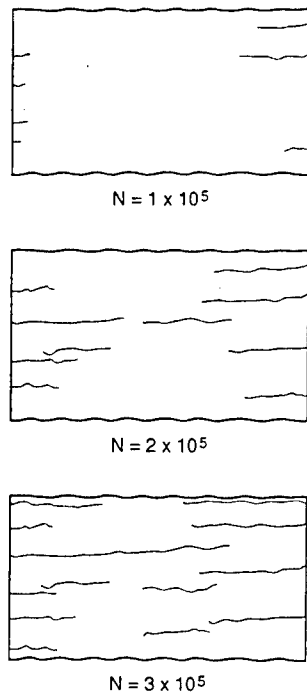


Fig. 1. Crack patterns obtained from surface replicas of a Ti-6Al-4V/SCS-6 SiC composite, following cyclic loading at a stress amplitude, $\Delta\sigma = 800$, and stress ratio, $R = 0$, for various numbers of cycles, N . The specimen width is 6.3 mm.

within the context of continuum fracture mechanics wherein the bridging fibers are treated as a distribution of tractions acting on the faces of the matrix

crack, the magnitude of the tractions being governed by a characteristic bridging law. Comparisons between the analytical results and experimental measurements (of the type shown in Fig. 2) are presented also.

There is a vast body of literature on the use of line spring models to describe the effect of fibers bridging a matrix crack, for a variety of materials and bridging laws. Previous calculations have focused on the reduction in the crack tip stress intensity factor due to fiber bridging, which can be used to address questions about crack stability, toughening behavior, cyclic crack growth and fiber failure. A few notable examples of such work include Marshall et al., 1985; Nemat-Nasser and Hori, 1987; McMeeking and Evans, 1990; Cox and Lo, 1992a,b; Ghosn et al., 1992; Bakuckus and Johnson, 1993; Bao and McMeeking, 1994, 1995; and Begley and McMeeking, 1995. Since bridging traction profiles can be directly related to crack opening profiles via the bridging law, the governing equations outlined in the previous studies provide the background for the work presented here, which focuses on predicting remote displacements via crack opening areas.

Rather than recalculating complete solutions to the integral equations governing fiber bridging, use is made of the asymptotic behavior of these equations in the limit that cracks are very short or very long. The asymptotic behavior of the singular integral equations has been rigorously treated in Willis

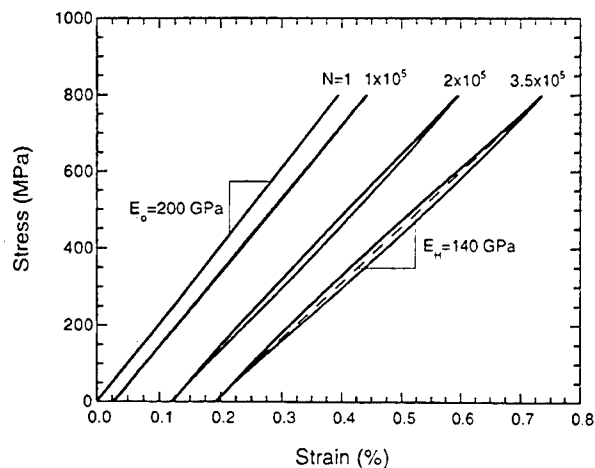


Fig. 2. Changes in the hysteresis loops associated with matrix cracking. (Data correspond to surface replicas shown in Fig. 1). Note the development of inelastic (permanent) strain and the reduction in the hysteresis modulus, E_H , with increasing cycles.

and Nemat-Nasser, 1990 and Hori and Nemat-Nasser, 1990. Such work provides the foundation for the solutions presented here. Relevant asymptotic solutions are presented in terms of the engineering quantities governing crack bridging in TMCs (e.g. moduli, interface sliding stress, fiber diameter, fiber volume fraction, etc.) and explained in terms of how much the near tip behavior dominates the crack opening profile along the crack. Full numerical solutions for a limited number of cases are used to illustrate the error associated with the asymptotic solutions when they are not strictly applicable.

The present results are also applicable to some CMCs: specifically, those that exhibit bridged cracks of *finite* length. The response of composites containing cracks that propagate across the *entire* composite section have been analyzed extensively in the past (see, for example, Aveston et al., 1971; Hutchinson and Jensen, 1990; Evans et al., 1994).

2. Preliminaries

2.1. General

The problem of interest is shown schematically in Fig. 3. A unidirectionally-reinforced fiber composite panel containing a fully bridged through-thickness crack of length, $2a$, is subjected to an applied tensile stress, σ_a , parallel to the fiber axis. The additional remote displacement, δ , associated with the crack is (Tada et al., 1985)

$$\delta_c = A/2W, \quad (1)$$

where $2W$ is the specimen width and A is the crack area, defined by

$$A = 2 \int_0^a u(x) dx \quad (2)$$

with $u(x)$ being the effective crack opening displacement (COD)¹ and x the distance from the crack center.

¹ For cracks bridged by fibers, $u(x)$ represents the additional extension of the fibers associated with fiber-matrix sliding. This differs from the actual crack opening displacement by a factor $E_m(1-f)/E$ (Hutchinson and Jensen, 1990).

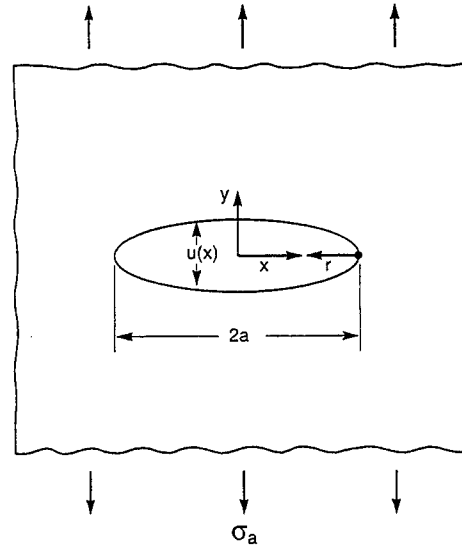


Fig. 3. Schematic diagram showing the crack and specimen geometry.

The governing equation for the crack opening profile for a bridged crack can be written as (Marshall et al., 1985; McMeeking and Evans, 1990).

$$u(x) = f[\sigma_b(x)] = \frac{4\sigma_a a}{\bar{E}} \left(1 - \left(\frac{x}{a}\right)^2\right)^{1/2} - \frac{4}{\bar{E}} \int_0^a \sigma_b(t) H(t, x, a) dt, \quad (3)$$

where σ_a is the applied stress; $H(t, x, a)$ is the Green's function for the specimen geometry (Tada et al., 1985); $f[\sigma_b(x)]$ is the bridging law, usually obtained from a cell model; and \bar{E} is a composite modulus which accounts for plane stress or strain, and possibly orthotropy (Bao and McMeeking, 1994). (\bar{E} is hereafter taken to be equal to the longitudinal composite Young's modulus, E , which is obtained from the rule of mixtures. This assumption is justified on the basis that the degree of orthotropy in TMCs is small. Indeed, calculations by Bao and McMeeking (1994) indicate that the difference between \bar{E} and E is typically only $\sim 4\%$). The first term on the right side of Eq. (3) is the crack opening profile of an unbridged crack, whereas the second term represents the reduction in the crack opening due to bridging. In general, this equation must be

solved numerically because of the dependence on σ_b of both the opening, u , (on the left side) and the argument of the integral (on the right side). Once the solution for u is obtained at each position, x , it is integrated according to Eq. (2) and the result combined with Eq. (1) to obtain the additional displacement due to the crack.

For a dilute array of cracks with a number density per unit area of ρ_c , the additional strain, ε_c , associated with the cracks is obtained by summing the displacements from each individual crack and dividing by the appropriate length. The result is

$$\varepsilon_c = \delta_c \rho_c^{1/2} \quad (4)$$

For the remainder of this article, attention is focused on the crack area, though its connection with the remote displacement for a single crack and the strain for a dilute array of cracks is implied through Eqs. (1) and (4).

2.2. Unbridged cracks

In the absence of fiber bridging (or, equivalently, when the bridging tractions are very small) the COD profile in Eq. (3) reduces to the usual elliptical form which can be integrated to get

$$A_c = 2\pi\sigma_a a^2/E \quad (5)$$

Note that, in this case, A scales linearly with the applied stress, σ_a .

2.3. Bridging law for TMCs

The simplest form of bridging law appropriate for TMCs is obtained by assuming that the interface sliding stress, τ , is constant and subsequently performing a shear lag analysis of a single bridging fiber. Under monotonic loading, the resulting law is (Marshall et al., 1985; Hutchinson and Jensen, 1990; McMeeking and Evans, 1990)

$$u = \lambda \sigma_b^2, \quad (6a)$$

where

$$\lambda = D(1-f)^2 E_m^2 / 4f^2 \tau E_f E^2 \quad (6b)$$

with D being the fiber diameter, f the fiber volume fraction, E_m and E_f the matrix and fiber Young's modulus, respectively, and E the longitudinal com-

posite Young's modulus. Under cyclic loading, an analogous relationship exists between the COD range, Δu , during a loading–unloading cycle and the associated stress range, $\Delta \sigma_b$, given by (McMeeking and Evans, 1990)

$$\Delta u = \frac{1}{2} \lambda (\Delta \sigma_b)^2 \quad (7)$$

3. Bridged crack under monotonic loading

For monotonic tensile loading, the displacement δ_c is obtained by first combining the traction law of Eqs. (6a) and (6b) with Eq. (3), solving numerically for u , and then integrating u over the length of the crack. Details of the method used to solve for u are outlined in Begley and McMeeking (1995).

The COD profiles obtained in this manner exhibit two characteristic shapes (Fig. 4). When cracks are

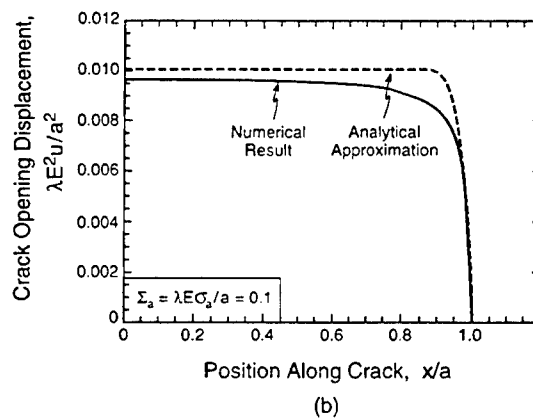
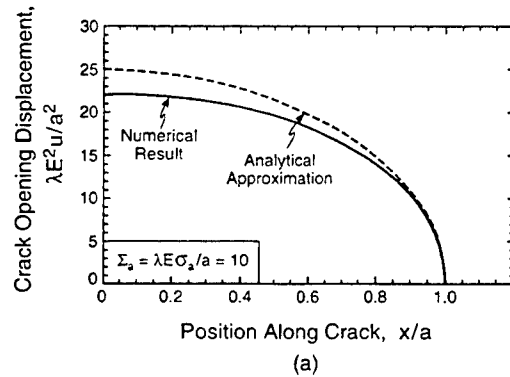


Fig. 4. COD profiles obtained for (a) $\Sigma_a = 10$ (short crack) and (b) $\Sigma_a = 0.1$ (long crack).

short and applied loads are high, the near tip behavior of the crack dominates the COD profile along its entire length. The result is a nearly elliptical crack opening. For longer cracks, the near tip behavior influences only a small portion of the crack, and the crack opening is constant over a large portion of its length. This can also be understood from the viewpoint of bridging tractions; far from the crack tip, the bridging stresses must be equal to the applied load due to equilibrium considerations. This leads immediately via the bridging law to constant crack openings. This scenario is often referred to as a steady state, since the crack tip has no effect on the majority of cracked material and vice versa. Thus, when the crack length is large or the applied stress is small, the profile is comprised of (i) an approximately elliptical region near the crack tip and (ii) a region away from the crack tip in which the opening is essentially constant. It has previously been shown that a steady-state is approached when (Cox and Lo, 1992a,b; Bao and McMeeking, 1994; Begley and McMeeking, 1995)

$$\Sigma_a \equiv \lambda E \sigma_a / a < 1, \quad (8)$$

where Σ_a can be considered as a nondimensional measure of either the applied stress or the inverse of the crack length.

Rather than resorting to numerical methods for evaluating the COD profile exactly, an approximate analytical solution can be obtained by assuming that at least part of the crack is dominated by near tip behavior and is therefore nearly elliptical. In this case, the form of the solution depends on whether steady state conditions have been obtained. The solutions are developed below. The two cases (short cracks vs. long cracks) are considered separately.

3.1. Short cracks ($\Sigma_a > 1$)

In this regime, the entire COD profile is assumed to be elliptical. The profile is of the general form

$$u = u_0 \left(1 - (x/a)^2 \right)^{1/2} = u_0 \left(2r/a - (r/a)^2 \right)^{1/2}, \quad (9)$$

where u_0 is the COD at the crack center ($x = 0$) and r is the distance measured from the crack tip ($r = a$

– x). The corresponding stress distribution (from Eqs. (6a), (6b) and (9)) is

$$\sigma_b = \sigma_0 \left(1 - (x/a)^2 \right)^{1/4}, \quad (10)$$

where σ_0 is the bridging stress at $x = 0$. The near-tip shape must be consistent with the square root profile, given by

$$u = \frac{8K_I}{E} \sqrt{\frac{r}{2\pi}}, \quad (11)$$

where K_I is the crack tip stress intensity factor. K_I is obtained by summing the contributions from the applied stress and from the crack bridging tractions in the standard manner (Tada et al., 1985). Using the assumed bridging stress distribution (Eq. (10)) with the appropriate weight function yields

$$K_I = I_0 \sigma_a \sqrt{\pi a} - 2I_1 \sigma_0 \sqrt{a/\pi} \quad (12)$$

with $I_0 = 1$ and $I_1 = 1.2^2$. The near-tip profile must also be consistent with the traction law (Eqs. (6a) and (6b)), such that

$$u = \lambda (\sigma(r))^2 \approx \lambda \sigma_0^2 \sqrt{2r/a} \quad (13)$$

Combining Eqs. (11)–(13) yields

$$\Sigma_0^2 + \frac{8I_1}{\pi} \Sigma_0 - 4I_0 \Sigma_a = 0, \quad (14)$$

where Σ_0 is a nondimensional parameter that characterizes the maximum bridging stress, defined by

$$\Sigma_0 \equiv \lambda E \sigma_0 / a \quad (15)$$

Note the first term in Eq. (14) reflects the total COD via the bridging law, the second the reduction due to bridging and the third the opening for an unbridged crack. Solving Eq. (14) for Σ_0 yields

$$\Sigma_0 = \frac{4I_1}{\pi} \left\{ \left[1 + \left(\frac{\pi}{2I_1} \right)^2 I_0 \Sigma_a \right]^{1/2} - 1 \right\} \quad (16)$$

Note that Eq. (16) is general in the sense that it applies to any crack configuration coupled with a square root bridging law. Other crack geometries will influence this expression only through the con-

² For an edge crack in an infinite body, the same result applies, with constants $I_0 = 1.12$ and $I_1 = 1.35$.

stants I_0 and I_1 , which are obtained via integration of the appropriate Green's function.

The COD profile can be written in the nondimensional form

$$\lambda Eu/a^2 = \Sigma_0^2 (1 - (x/a)^2)^{1/2} \quad (17)$$

A comparison of the approximate profile with the one calculated numerically for $\Sigma_a = 10$ is shown in Fig. 4(a). The correlation between the two is quite good, though the analytical result generally overestimates the COD, particularly near the crack center. The corresponding crack area is obtained by integrating this profile according to Eq. (12), resulting in

$$\lambda E^2 A / 2 a^3 = \frac{4 I_1^2}{\pi} \left\{ \left[1 + \left(\frac{\pi}{2 I_1} \right)^2 I_0 \Sigma_a \right]^{1/2} - 1 \right\}^2 \quad (18)$$

In the limit of very short cracks ($\Sigma_a \gg 1$), Eq. (18) reduces to

$$\lambda E^2 A / 2 a^3 = \pi \Sigma_a \quad (19)$$

It can be readily shown that this result is identical to the solution for an unbridged crack (Eq. (5)). Note, again, the linear dependence of crack area on the applied stress in this limit.

3.2. Steady state cracks ($\Sigma_a \leq 1$)

In this regime, the crack profile is assumed to consist of two regions: (i) a near-tip region of length a_* where the profile is elliptical (due to the dominance of the tip); and (ii) a steady-state region of length $a - a_*$ where the COD is constant (since it is far removed from the tip).

In the near-tip region ($x < a_*$), the crack opening and bridging stress profiles are given by Eqs. (9) and (10), except that σ_0 is replaced by σ_a and a is replaced by a_* . This represents the limiting case where the maximum bridging stress equals the applied stress. The very near-tip region is again required to be consistent with the square root profile (Eq. (11)) with K_I given by (Tada et al., 1985)

$$K_I = \sqrt{\frac{2}{\pi}} \int_0^{a_*} \frac{\sigma_a - \sigma_b(r)}{\sqrt{r}} dr = I_2 \sigma_a \sqrt{2 a_* / \pi}, \quad (20)$$

where $I_2 = 0.513$. (Note that the crack tip is assumed to be far removed from external influences; hence, the weight function of a semi-infinite geometry is used.) Combining this result with Eq. (11) gives

$$u = 8 I_2 \sigma_a \sqrt{a_*} r / E \pi \quad (21)$$

As before, the near-tip profile must also be consistent with the traction law (Eqs. (6a) and (6b)). The critical length, a_* , is obtained by setting the expressions for u in Eqs. (21) and (13) equal to one another (wherein $\sigma_0 \rightarrow \sigma_a$); the result is

$$a_* = \lambda E \sigma_a \left(\frac{\sqrt{2} \pi}{8 I_2} \right) = \gamma \lambda E \sigma_a, \quad (22)$$

where $\gamma = 1.08 \approx 1$. Comparison of this result with the definition of Σ_a reveals that the critical length is adequately described by the condition $\Sigma_a \approx 1$. That is, for a given crack length a , the critical load at which the near tip zone encompasses the entire crack is given by $\Sigma_a = 1$. Below this load or for crack lengths greater than $\lambda E \sigma_a$, the near tip zone does not dominate the entire crack length and hence a steady state region is obtained.

The crack area in the near-tip portion of the crack is

$$\begin{aligned} A_1 &= 2 \lambda \sigma_a^2 a_* \int_0^1 \left[\frac{2r}{a_*} - \left(\frac{r}{a_*} \right)^2 \right]^{1/2} d(r/a_*) \\ &= I_3 \lambda^2 \sigma_a^3 E \end{aligned} \quad (23)$$

where $I_3 = 1.710$. In the steady state region, $r > a_*$, the crack area is simply

$$A_2 = \lambda \sigma_a^2 (a - a_*) = \lambda \sigma_a^2 a (1 - \gamma \lambda \sigma_a E / a) \quad (24)$$

The total crack area is the sum of A_2 and A_1 which can be written in the nondimensional form

$$\lambda E^2 A / 2 a^3 = \Sigma_a^2 - 0.225 \Sigma_a^3 \quad (25)$$

In the limit of very long cracks ($\Sigma_a \ll 1$), the first term on the right side becomes dominant and the area reduces to

$$\lambda E^2 A / 2 a^3 = \Sigma_a^2 \quad (26)$$

In this limit, the crack area scales with the square of the stress. This result is equivalent to the one ob-

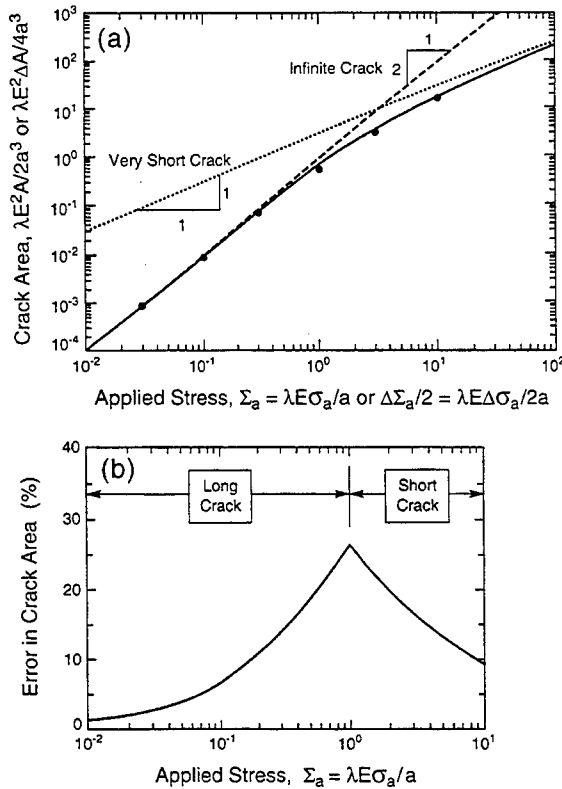


Fig. 5. (a) Variation in crack area (A or $\Delta A/2$) with applied stress (Σ_a or $\Delta \Sigma_a/2$). The solid symbols are the exact numerical results. The solid line is the approximate analytical result. (b) Differences between the numerical and analytical results.

tained from a shear lag analysis of a single bridging fiber (done originally by Aveston et al., 1971).

A comparison of the approximate COD profile with the one obtained numerically for $\Sigma_a = 0.1$ is shown in Fig. 5(b). Once again, the correlation between the two is good, though the analytic result slightly overestimates the numerical one.

Comparisons of the crack areas over a wide range of Σ_a (both in the short crack and the long crack regimes) are presented in Fig. 5(a); the relative differences between the two are plotted in Fig. 5(b). In general, the agreement is good for $\Sigma_a \gg 1$ and $\Sigma_a \ll 1$. The difference is at a maximum ($\sim 30\%$) at the transition between the short and long crack regimes (at $\Sigma_a = 1$) and diminishes as Σ_a either increases above or decreases below unity.

4. Bridged crack under cyclic loading

The integral equation that describes the crack profile under cyclic loading is obtained by replacing u , σ_a and σ_b in Eq. (3) with the corresponding changes in these parameters, Δu , $\Delta \sigma_a$ and $\Delta \sigma_b$, respectively, such that

$$\Delta u(\Delta \sigma_b, x) = \frac{4\Delta \sigma_a}{E} \left(1 - \left(\frac{x}{a} \right)^2 \right)^{1/2} - \frac{4}{E} \int_0^a \Delta \sigma_b(t) H(t, x, a) dt \quad (27)$$

For the traction law of interest, the crack opening range, Δu , under cyclic loading is related to the peak crack opening under monotonic loading through the relation

$$\Delta u = 2u(\Delta \sigma_b/2) \quad (28)$$

Notably, the COD range is twice the value of the peak COD evaluated at a bridging stress equal to half of the bridging stress range. Upon inspection of Eq. (27), it is further recognized that the integral equation for cyclic loading can be made equivalent to the one for monotonic loading by replacing σ_a with $\Delta \sigma_a/2$ and σ_b with $\Delta \sigma_b/2$. (This connection between monotonic and cyclic loading was first identified by McMeeking and Evans (1990), and is extensively detailed by Begley and McMeeking (1995).) Consequently, σ_b and $\Delta \sigma_b$ are related through

$$\Delta \sigma_b(\Delta \sigma_a, x) = 2\sigma_b(\Delta \sigma_a/2, x) \quad (29)$$

Recognizing these connections, the approximate analytical solutions for crack openings developed in the preceding sections can be re-interpreted for cyclic loading. It can be readily shown that the peak normalized bridging stress, Σ_o , is related to the bridging stress range, $\Delta \Sigma_o$, through a relation analogous to Eq. (29), specifically

$$\Delta \Sigma_o(\Delta \Sigma_a) = 2\Sigma_o(\Delta \Sigma_a/2) \quad (30)$$

Similarly, the peak crack area is related to the range in crack area, ΔA , through

$$\Delta A(\Delta \Sigma_a) = 2A(\Delta \Sigma_a/2) \quad (31)$$

Consequently, the results in Fig. 5(a) can be re-interpreted for cyclic loading by replacing A on the ordinate with $\Delta A/2$ and Σ_a on the abscissa with $\Delta \Sigma_a/2$.

These results can also be used to obtain the crack area, $A_m = A - \Delta A$, at the minimum stress, $\sigma_a - \Delta \sigma$. For short cracks ($\Sigma_a > 1$), the minimum crack area is

$$\lambda E^2 A_m / 2 a^3 = \frac{\pi}{4} \left[\Sigma_o^2 - \frac{1}{2} (\Delta \Sigma_o)^2 \right], \quad (32)$$

where Σ_o and $\Delta \Sigma_o$ are given by Eqs. (16) and (30); for long cracks ($\Sigma_a < 1$), it is

$$\lambda E^2 A_m / 2 a^3 = \left[\Sigma_a^2 - 0.225 \Sigma_a^3 \right] - 2 \left[(\Delta \Sigma_a / 2)^2 - 0.225 (\Delta \Sigma_a / 2)^3 \right] \quad (33)$$

5. Slip zone lengths and crack interactions

At sufficiently high stress levels, the slip zones of adjacent cracks begin to overlap. Once this occurs, the average matrix stress within the slip zone reaches a saturation value, independent of additional crack opening. Upon further opening, only the fibers support additional stress and the bridging traction law becomes linear (rather than quadratic). Consequently, the solutions presented in the preceding sections no longer apply. For a periodic array of cracks, the interactions can begin when the maximum slip length, d_s , (at the crack center) reaches one half of the crack spacing, ℓ , measured normal to the crack plane (Zok and Spearing, 1992)³. The slip length is given by

$$d_s = \sigma_b D E_m (1 - f) / 2 \tau E f, \quad (34)$$

where σ_b is the maximum bridging stress.

³ The onset of slip zone overlap depends on the relative offset of neighboring cracks, i.e. the relative locations of the crack centers. The present analysis considers only the case where the crack centers are directly above one another. This assumption yields a lower bound to the stress required for the onset of slip zone overlap.

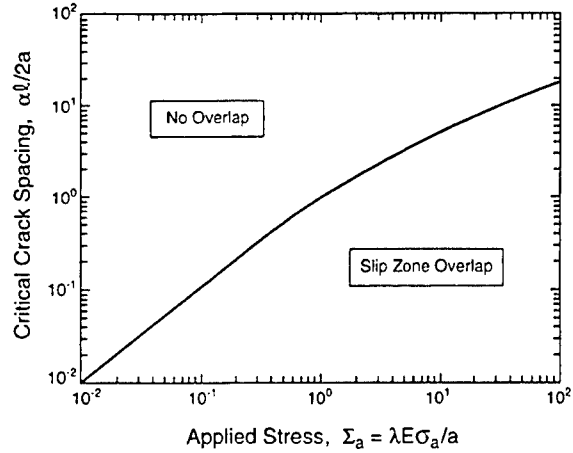


Fig. 6. Effect of applied stress on the critical crack spacing at which overlap occurs between slip zones of neighboring cracks.

In the short crack regime ($\Sigma_a \geq 1$), the maximum slip length occurs at $\sigma_b = \sigma_o$. The result, in nondimensional form, is

$$\alpha d_s / a = \Sigma_o, \quad (35a)$$

where

$$\alpha \equiv (1 - f) E_m / f E_f \quad (35b)$$

and Σ_o is related to Σ_a through Eq. (16). In the limit where $\Sigma_a \gg 1$, Eqs. (35a) and (35b) reduces to

$$\alpha d_s / a = 2 \sqrt{\Sigma_a} \quad (36)$$

The corresponding result in the long crack regime ($\Sigma_a \leq 1$) is obtained by setting $\sigma_o = \sigma_a$ whereupon

$$\alpha d_s / a = \Sigma_a \quad (37)$$

Trends in the critical crack spacing (obtained by setting $d_s = \ell/2$) with applied stress, Σ_a , are plotted in Fig. 6. Below the critical value, the slip zones overlap; above it, the solutions presented in the preceding sections are expected to apply.

When the slip zones overlap and the cracks are within the steady state regime ($\Sigma_a < 1$), a simple limiting solution for the crack area can be obtained in the following way. If $\Sigma_a \ll 1$, then the majority of the crack has a uniform opening. In this limit, the crack area scales with Σ_a^2 up to the critical stress at which the slip zones begin to overlap ($\Sigma_a = \alpha \ell / 2 a$).

Beyond this stress, the bridging traction law is linear, such that the crack area follows the relation

$$A = A_c + 2a\ell(\sigma - \sigma_c)/fE_f, \quad (38)$$

where A_c and σ_c represent the critical values of A and σ at which the slip zones just begin to overlap. Evaluating A_c and σ_c (by setting $\Sigma_a = \alpha\ell/2a$) and substituting the results into Eq. (38) gives the variation in the nondimensional crack area with applied stress as

$$\lambda E^2 A / 2a^3 = \left(\frac{\alpha\ell}{2a} \right)^2 + \frac{2\ell E}{afE_f} \left(\Sigma_a - \frac{\alpha\ell}{2a} \right) \quad (39)$$

The corresponding remote strain in a composite specimen containing a uniform array of cracks stacked directly above one another (such as those shown in Fig. 1) can be calculated by considering the specimen to be comprised of two parallel slabs (one containing cracks and the other uncracked), and assuming that the total tensile strain in each is the same. The inelastic strain within the cracked regions is taken as A/ℓ , where A is given by either Eq. (26) or Eq. (39), as appropriate. An additional elastic strain also arises within the cracked material; it is σ/E_* , where E_* is the elastic modulus of the cracked composite (He et al., 1994). The total strain in this region is the sum of the elastic and inelastic components. In contrast, the response of the uncracked region remains elastic, with a modulus, E . The composite stress is then given by the weighted average of the two strength levels at a prescribed macroscopic strain, with the weighting factors being a/W and $1 - a/W$ for the cracked and uncracked sections, respectively.

6. Comparisons with experiments

A preliminary comparison between the predicted inelastic response and that measured experimentally has been performed. The tested material was a Ti–6Al–4V alloy reinforced unidirectionally with 34% by volume of SCS-6 SiC fibers. Cyclic loading experiments were performed on dog-bone shaped tensile coupons with a gauge length of 50 mm and width of 6.4 mm. The strain was measured using a clip-on extensometer with a 10 mm gauge length.

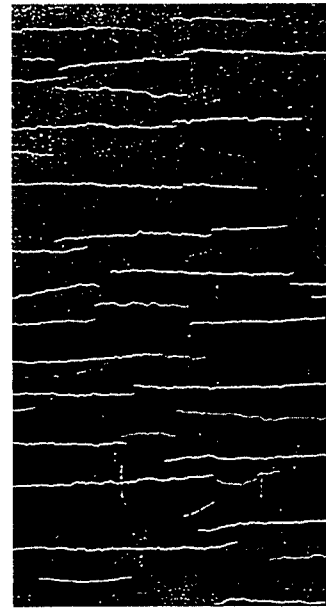


Fig. 7. Scanning electron micrograph showing periodic cracks following fatigue fracture. The specimen width is 6.3 mm.

The test results reported here were obtained at a stress range $\Delta\sigma = 800$ MPa, a stress ratio $R = 0$, and cycling frequency of 10 Hz. The test was interrupted periodically and the hysteresis response measured and recorded over the stress range of 0–800 MPa. Typical hysteresis loops are shown on Fig. 2. In addition, the broad surface of the specimen was replicated using cellulose acetate tape and the replica then examined in an optical microscope. Measurements were made of both the average crack length and the average crack spacing normal to the loading direction. The cracks typically initiated at the specimen corners and propagated stably across the broad face until they linked with cracks emanating from the opposite side. Once the cracks linked, they formed a periodic array with a fixed mean spacing, as shown in Fig. 7. At this point, the crack pattern resembled that seen in unidirectional fiber-reinforced ceramic composites.

In order to assess the model predictions, the values of numerous constituent properties are needed. Most of these are well known (e.g. fiber diameter, fiber volume fraction, matrix modulus and fiber modulus) and are given in Table 1. The property which is subject to the most uncertainty is the inter-

Table 1
Summary of constituent properties of Ti–6Al–4V/SCS-6 fiber composite

Fiber volume fraction f	0.34
Fiber diameter D (μm)	140
Fiber modulus E_f (GPa)	410
Matrix modulus E_m (GPa)	110
Interface sliding stress τ (MPa)	23

face sliding stress, τ . It was evaluated from the hysteresis loops following complete saturation and linkage of cracks. In this regime, the cracks can be treated as being infinitely long and, provided the slip zones of adjacent cracks do not overlap, the axial response is given by (Aveston et al., 1971; Walls et al., 1996)

$$\bar{\varepsilon} = \frac{\bar{\sigma}}{E_*} + \frac{(1-f)^2 E_m^2 D \bar{\sigma}^2}{8\tau E_f f^2 \ell E^2}, \quad (40)$$

where $\bar{\varepsilon}$ and $\bar{\sigma}$ represent the differences in the strain and the stress from those measured at the previous load reversal, ℓ is the mean crack spacing and E_* is the modulus of the cracked material. (Note that Eq. (40) represents the sum of the elastic and inelastic strains, the latter being obtained from Fig. 5(a) in the ‘infinite crack’ regime.) Once the slip zones overlap, the response is linear and given by Eq. (39). In this case, the tangent modulus is simply fE_f because only the fibers support additional stress.

To obtain τ , it is convenient to differentiate Eq. (40) to get

$$\frac{d\bar{\varepsilon}}{d\bar{\sigma}} = \frac{1}{E_*} + \frac{(1-f)^2 E_m^2 D \bar{\sigma}}{4\tau E_f f^2 \ell E^2} \quad (41)$$

A plot of $d\bar{\varepsilon}/d\bar{\sigma}$ vs. $\bar{\sigma}$ is thus predicted to be linear at sufficiently low stresses, with a slope governed by τ (along with the other constituent proper-

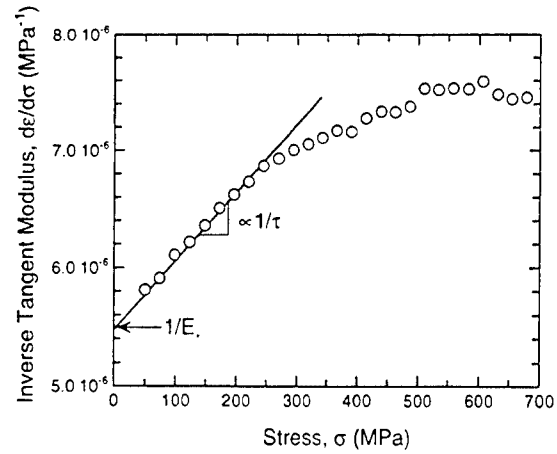


Fig. 8. Variation in $d\bar{\varepsilon}/d\bar{\sigma}$ with stress, σ , for a fully-cracked specimen.

ties) and an intercept given by $1/E_*$. Fig. 8 shows such a plot. In this case, $d\bar{\varepsilon}/d\bar{\sigma}$ varies linearly with $\bar{\sigma}$ over the stress range 0–300 MPa. The slope of this plot along with the constituent properties in Table 1 and the measured mean crack spacing ($\ell = 0.69$ mm) yields a sliding stress of ~ 23 MPa, and a modulus $E^* = 182$ GPa (slightly lower than the modulus of the uncracked TMC $E_0 = 203$ GPa). At higher stress levels, the tangent modulus reaches a saturation value approximately equal to $1/fE_f = 7.2 \times 10^{-6} \text{ MPa}^{-1}$.

In simulating the hysteresis loops, the effects of crack spacing on the elastic modulus, E_* , were taken into account by interpolating between the initial (uncracked) modulus, $E_0 = 203$ GPa, and the one for the fully cracked panel with a crack spacing of 0.69 mm, in accordance with (He et al., 1994; Walls et al., 1996)

$$E_0/E_* = 1 + \phi D/\ell \quad (42)$$

Here ϕ is a nondimensional parameter, determined from the experiments to be $\phi \approx 0.57$. Moreover, the

Table 2
Summary of measurements ($\Delta\sigma = 800$ MPa, $R = 0$)

Cycle number	Average crack length a (mm)	Normalized crack length a/W	Average crack spacing ℓ^*	Measured hysteresis strain $\Delta\varepsilon$ (%) ^a	Simulated hysteresis strain $\Delta\varepsilon$ (%) ^a
1×10^5	0.81	0.25	0.98	0.414	0.422
2×10^5	2.66	0.84	0.84	0.476	0.513
3.5×10^5	3.97	~ 1	0.69	0.543	0.555

^a Maximum–minimum.

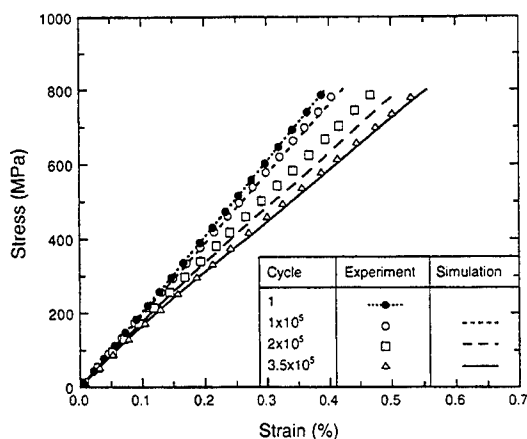


Fig. 9. Comparison of simulated and measured stress-strain curves ($\Delta\sigma = 800$ MPa, $R = 0$, $N = 3 \times 10^5$).

cracks were treated as being in steady-state, wherein the crack opening profile is uniform along its entire length. This assumption is justified on the basis of the calculated range of a_* using the constituent properties in Table 1. The maximum value of a_* (evaluated at the peak stress, $\sigma = 800$ MPa) is ~ 0.5 mm, which is roughly equal to two fiber spacings. Considering that a_* is proportional to σ and hence, on average, is only ~ 0.25 mm, and that the pertinent crack and specimen dimensions are typically more than an order of magnitude greater than a_* , the variation in crack opening near the crack tip can be safely neglected. A summary of the measured crack lengths and crack spacings are presented in Table 2.

The simulated curves are shown on Fig. 9, along with the ones measured experimentally. For clarity, only the change in strains within each loop for the loading portion are presented here. The agreement between experiment and theory appears encouraging, with the maximum difference in the hysteresis strains being $\sim 0.03\%$. The discrepancy is believed to be due to a crack morphology (characterized by its size and spatial distributions) which is somewhat more complex than the idealization. This issue is the subject of current investigations.

7. Concluding remarks

The analysis presented in this paper provides approximate solutions for the area of bridged cracks

in terms of the applied stress, the crack length and the various constituent properties that govern the bridging law. These solutions are based on asymptotically correct solutions to the governing equations which are available in the literature. They are identical to the exact (numerical) results in the limiting cases of very short and very long cracks, and are overestimates near crack lengths at which steady state conditions are obtained. The results can be applied to cyclic loading through a transformation of the relevant parameters. For sufficiently low crack densities, the crack areas can be readily converted to inelastic strains. For higher densities, the conversion is more complicated; an approach for this conversion in the long crack regime has been proposed and compared with experimental results. The results are expected to find utility in modeling the development of permanent (inelastic) strain and the reduction in hysteresis modulus associated with matrix cracks during fatigue of TMCs.

Acknowledgements

Funding for this work was provided by the ARPA University Research Initiative Program at UCSB under ONR contract No. N00014-92-J-1808.

References

- Aveston, J., Cooper, G.A., Kelly, A., 1971. Single and multiple fracture. In: *The Properties of Fiber Composites*. National Physical Laboratory, IPC Science and Technology Press, pp. 15–26.
- Bakuckus, J.W., Johnson, W.S., 1993. Application of fiber bridging models to fatigue crack growth in unidirectional titanium matrix composites. *J. Comp. Tech. Res.* 15, 242–255.
- Bao, G., McMeeking, R.M., 1994. Fatigue crack growth in fiber-reinforced metal matrix composites. *Acta Metall. Mater.* 42, 2415–2425.
- Bao, G., McMeeking, R.M., 1995. Thermomechanical fatigue cracking in fiber reinforced metal–matrix composites. *J. Mech. Phys. Solids* 43, 1433–1460.
- Begley, M.R., McMeeking, R.M., 1995. Fatigue crack growth with fiber failure in metal–matrix composites. *Comp. Sci. Tech.* 53, 365–382.
- Cox, B.N., Lo, C., 1992a. Load ratio, notch and scale effects for bridged cracks in fibrous composites. *Acta Metall. Mater.* 40, 69–80.
- Cox, B.N., Lo, C., 1992b. Simple approximations for bridged cracks in fibrous composites. *Acta Metall. Mater.* 40, 1487–1496.

- Evans, A.G., Domergue, J.M., Vaggagini, E., 1994. Methodology for relating the tensile constitutive behavior of ceramic-matrix composites to constituent properties. *J. Am. Ceram. Soc.* 77, 1425–1435.
- Ghosn, L.J., Kantzos, P., Telesman, J., 1992. Modeling of crack bridging in a unidirectional metal matrix composite. *Int. J. Fract.* 54, 345–357.
- Harmon, D.M., Saff, C.R., 1989. Damage initiation and growth in fiber reinforced metal matrix composites. In: Johnson, W.S. (ed.), *Metal Matrix Composites Testing, Analysis and Failure Modes*. ASTM STP 1032, ASTM, Philadelphia, pp. 237–250.
- He, M.Y., Wu, B.X., Evans, A.G., Hutchinson, J.W., 1994. Inelastic strains due to matrix cracking in unidirectional fiber-reinforced composites. *Mech. Mater.* 18, 213–229.
- Hori, M., Nemat-Nasser, S., 1990. Asymptotic solution of a class of strongly singular integral equations. *SIAM J. Appl. Math.* 50, 716–725.
- Hutchinson, J.W., Jensen, H., 1990. Models of fiber debonding and pullout in brittle composites with friction. *Mech. Mater.* 9, 139–163.
- Marshall, D.B., Cox, B.N., Evans, A.G., 1985. The mechanics of matrix cracking in brittle-matrix fiber composites. *Acta Metall.* 32, 2013–2021.
- McMeeking, R.M., Evans, A.G., 1990. Fatigue crack growth in fiber-reinforced metal-matrix composites. *Mech. Mat.* 9, 217–227.
- Nemat-Nasser, S., Hori, M., 1987. Toughening by partial or full bridging of cracks in ceramics and fiber reinforced composites. *Mech. Mater.* 6, 245–269.
- Steyer, T.E., Zok, F.W., Walls, D.P., 1997. Experimental assessment of fatigue life and failure modes in a SiC/Ti composite. *Comp. Sci. Tech.*, submitted.
- Tada, H., Paris, P.C., Irwin, G.R., 1985. *The Stress Analysis of Cracks Handbook*. Del Research, St. Louis, MO.
- Walls, D.P., McNulty, J.C., Zok, F.W., 1996. Multiple matrix cracking in a fiber-reinforced titanium matrix composite under high-cycle fatigue. *Metall. Mater. Trans. A* 27, 1899–1907.
- Willis, J.R., Nemat-Nasser, S., 1990. Singular perturbation solution of a class of singular integral equations. *Q. Appl. Math.* 48, 741–753.
- Zok, F.W., Spearing, S.M., 1992. Matrix crack spacing in brittle matrix composites. *Acta Metall. Mater.* 40, 2033–2043.

Section B

CONSTITUTIVE LAWS AND DESIGN



THE ROLE OF SCARF ANGLE IN THE PERFORMANCE OF ALUMINUM MATRIX COMPOSITE JOINTS

D. D. BRINK, C. G. LEVI, A. C. F. COCKS† and F. A. LECKIE†

High Performance Composites Center, Departments of Materials and Mechanical Engineering,
 University of California, Santa Barbara, CA 93106-5050, U.S.A.

(Received 18 April 1996; accepted 30 October 1996)

Abstract—The role of geometry on the mechanical performance of scarf joints in Al-matrix composites reinforced with continuous polycrystalline alumina fibers was investigated. Model joints consisting of thin metal interlayers at varying scarf angles between composite sub-elements were designed, manufactured and tested to study the relevant deformation and failure phenomena. Specimens were produced by pressurized infiltration of molten Al-4.5%Mg into fiber preforms containing prescribed discontinuities. In this way, matrix continuity through the interlayer was ensured and defects normally introduced in actual joining operations were minimized. Reference composite specimens were produced in the same manner and exhibited tensile strengths of the order of 700 MPa, compared with a matrix yield strength, σ_0 , of approximately 100 MPa. The strength of the scarf joints with aspect ratios of 17–48 and angles below 45° was relatively constant, $\sim 310 \pm 10$ MPa, but increased at higher angles, reaching over 485 MPa at 75°. Failure of these joints was typically by debonding at the composite–interlayer interface. A simple analytical model suggests that failure occurs when the stress normal to the interlayer reaches a critical value, although the details of the debonding mechanism are still unclear. Conditions leading to a transition from debond failure to plastic collapse in joints of low aspect ratios are also discussed. © 1997 Acta Metallurgica Inc.

1. INTRODUCTION

Metal matrix composites (MMCs) offer strength and stiffness advantages over the corresponding monolithic matrix materials, but the anisotropy introduced by continuous fiber reinforcement creates difficulties in joining MMC elements in order to produce a viable component. Uncertainties in the interface properties have resulted in design paradigms which rely on load transfer solely through shear forces, e.g. Ref. [1]. However, load transfer normal to the interface has been shown to be significant [2], and these design restrictions may forego optimal solutions.

Joint designs should ideally enable the full exploitation of the properties of the composite. Unfortunately, discontinuities of properties, stress concentrations and defects resulting from the joining process frequently render joints the “weakest link” of a structure [3]. Interfaces frequently harbor these strength-limiting defects on both the microscopic (fiber–matrix) and macroscopic (composite–monolith) scales and limit joint performance. Thus, the micromechanisms determining joint strength in the absence of gross defects, as well as the effect of design parameters such as geometry on joint performance are not well understood.

Previous work [2] has demonstrated the feasibility of manufacturing model joints which are free of the

gross interfacial defects often encountered in conventional joining methods [4]. The joints are formed by pressurized infiltration of molten Al alloys into preforms of continuous Al_2O_3 fibers containing prescribed discontinuities. In these specimens, the metal is continuous throughout the joint, minimizing defects at the composite–joint interlayer interface. Using this approach, a baseline for optimum joint performance in different geometries can be established. This work builds on the analysis of butt joints developed by Burr *et al.* [2] and examines the behavior of scarf joints under tension, focusing on the effect of the scarf angle on achievable joint strength.

2. MATERIALS AND JOINT FABRICATION

Model scarf joints utilized in this study consist of thin metal interlayers between two aligned composite sub-elements, as illustrated in Fig. 1. This geometry is similar to that used in other studies on adhesively bonded joints, e.g. Refs [5, 6]. While this particular joint geometry is perhaps too simplistic to be used in a practical design with MMCs, the high constraint in the interlayer provides an avenue for assessing the load-bearing capacity of the composite–monolith interface under different combinations of tensile and shear stresses [2]. The interfacial strength is, in turn, an important parameter in the design of actual joints and attachments [1].

†On sabbatical leave at UCSB from Cambridge University, now at Leicester University, Leicester, England.

Specimen fabrication involves the preparation of a suitable fiber preform followed by pressurized melt infiltration (squeeze casting), as described in detail elsewhere [2]. Briefly, rigid preform bars with a packing density of ~ 60 vol.% are prepared by winding a continuous fiber with a polymer solution binder (PVAc). After hardening, the preforms are sectioned according to the desired joint geometry and encapsulated in a porous ceramic mold. Spacing of the preform halves is maintained through the use of a thin polymer film of appropriate thickness. The assembly is subsequently heated to 750°C to burn off the binder and spacer materials, and placed in a die where it is infiltrated with a molten aluminum alloy at a pressure of ~ 180 MPa. The resulting casting is then machined into suitable specimens, which typically exhibit full infiltration with no significant porosity or inclusions within the matrix or at interfaces. Reference composite specimens are also prepared in this manner, whereas reference matrix specimens can be taken from the alloy surrounding the porous mold to ensure chemical similarity with the composite matrix.

All specimens were fabricated using AlmaxTM (Mitsui Mining Co.) polycrystalline $\alpha\text{-Al}_2\text{O}_3$ fibers, nominally $10\ \mu\text{m}$ in diameter, in untwisted tows containing ~ 1000 filaments. The matrix was Al-4.5 wt% Mg alloy prepared in house by induction melting using 99.98% pure Al and Mg. The primary set of specimens for this work included joints with scarf angles of $0\text{--}75^\circ$ in 15° intervals, with aspect ratios (B/h) ranging from ~ 17 to ~ 48 . A second set with unintended but substantially lower aspect ratios (from ~ 3 to ~ 10) was also analyzed. The low B/h set was the result of earlier efforts in developing the

fabrication technique and, while less suitable from the viewpoint of interlayer constraint, was useful in revealing other aspects of the joint failure behavior. One significant difference between the two sets of specimens was a change in the polymer film used to separate the composite halves, from PVAc in the earlier efforts (as well as in Ref. [2]) to cellulose in the primary set for this work. Comparative tests with both spacer materials revealed no detectable residue in either case when burned in an open crucible, suggesting that the substitution should not have any side effects on the composite microstructure. However, it became evident later that this seemingly small processing change may have had a more significant impact than originally anticipated, as discussed below.

The elastic modulus and mean strength of the Almax fibers are 320 and 1.8 GPa, respectively [7, 8]. The 0.2% offset yield stress and elastic modulus of the matrix are ~ 100 MPa and 70 GPa, respectively [2]. The matrix exhibits mild work hardening, with an ultimate tensile strength of ~ 190 MPa and a failure strain of $\sim 9\%$. The typical stress-strain behavior of the reference composite specimens shows an initial nonlinearity at a strain of $\sim 0.05\%$, consistent with matrix yielding under residual tension, and exhibits brittle failure at ultimate tensile strengths of the order of ~ 700 MPa.

3. PERFORMANCE OF MODEL SCARF JOINTS

3.1. Mechanical behavior

All model joints were tested in an Instron 8562 frame using hydraulic grips which rigidly fixed the ends of the specimens. The strain in the metal interlayer was evaluated from measurements with two strain gages, located as shown in Fig. 1. The gages were set parallel to the fiber direction, one spanning the joint and neighboring composite regions, ϵ_{i+c} , and the other measuring the strain in one of the composite elements, ϵ_c , away from the joint. Assuming that the response of the first gage reflects a weighted average of the elongations in the composite and metal interlayer, one can readily calculate the strain in the latter from its thickness and the strain gage dimensions by subtracting the contribution from the composite. The calculation assumes that there is no significant displacement of the composite elements perpendicular to the fiber direction, which is justified by the rigid gripping and the stiffness of the composite. The assumption was further supported by the absence of significant bending stresses when comparing the response of additional gages placed on the specimen sides near the edge of the grips.

The stress-strain behaviour of a butt joint (0° angle) with an aspect ratio of ~ 36 , depicted in Fig. 2, provides a useful starting point for assessing the effects of scarf angle and relative interlayer thickness. The metal interlayer is more compliant than the

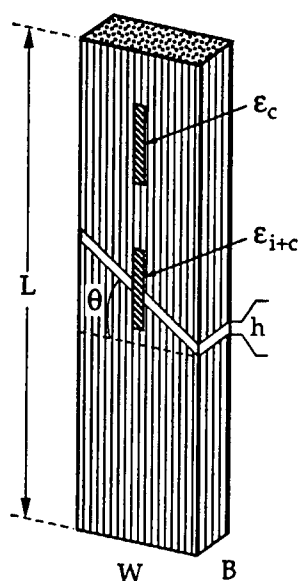


Fig. 1. Schematic of model scarf joint used in the present experiments and location of strain gages.

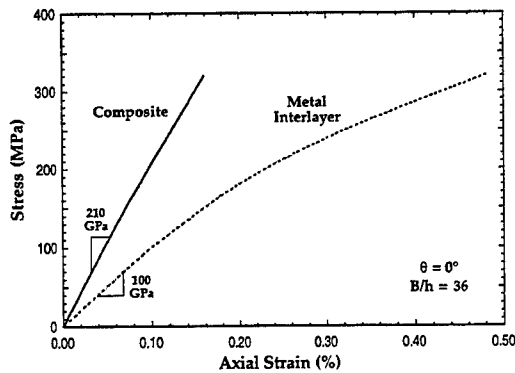


Fig. 2. Stress-strain behavior for the composite elements and the metal interlayer in the 0° (butt) joint.

composite, as expected, but less than the unconstrained monolithic alloy. Moreover, the interlayer exhibits substantial plasticity as well as load-bearing capabilities well beyond the tensile strength of the monolithic matrix. The relative stiffening and strengthening of the metal in the interlayer are clearly a consequence of the constraint provided by the stiffer neighboring composite, as discussed in Ref. [2]. Notwithstanding the higher compliance of the metal, the overall stiffness of the specimen is not greatly compromised by the presence of the joint owing to the small thickness of the interlayer.

The behavior of the metal interlayers for the two sets of scarf joint specimens is compared to that of the 0° butt joint in Figs 3(a) and (b). In all cases the scarf interlayers are more compliant than that corresponding to the butt joint. The stress-strain curves suggest that the compliance reaches a maximum at ~45°, although the dependence of compliance on scarf angle at the lower strains is somewhat erratic. (This is probably a consequence of the uncertainty involved in the calculation of the strains, as the interlayer thicknesses are, in all cases, much smaller than the strain gage lengths.)

The ultimate tensile strengths and corresponding interlayer strains for the specimens in Figs 3(a) and (b) are summarized in Table 1. In general, the strains at the maximum stress increase consistently with scarf angle, except for the last specimen in each series where the failure mode was different. In the lower B/h series the 60° joint did not fracture at the maximum stress but continued to extend under decreasing load until debond failure occurred at ~13% strain. By comparison, the 60° specimen with the higher aspect ratio also went through a load maximum before failure, but the subsequent load drop before failure was much smaller—see Fig. 4. It is also evident in this figure that both 60° specimens appeared to reach

elongations well beyond that observed in the monolithic matrix at failure (~9%).†

The strengths for both sets of specimens in Table 1 appear to be relatively insensitive to orientation at the lower angles, and then increase at the higher angles. The 75° specimen in the higher B/h series failed by fracture of the composite at the grips, suggesting that the actual UTS for this joint angle could have been significantly higher. In all cases, however, the joint strengths are only about half of the UTS of the continuous composite, but ~2.5 to ~5 times higher than the yield stress of the unreinforced matrix.

The strengths of the lower B/h specimens are consistently lower than those obtained with the higher aspect ratio at comparable angles. One might then be tempted to infer that joint strength increases significantly with aspect ratio. Prior analysis of butt joints [2] revealed that there is indeed an effect of aspect ratio on the load-bearing capacity of the joint (see the discussion below), but the predicted increase is much less pronounced than that observed in Table 1. Conversely, butt joints with aspect ratios ranging from 10 to 64, fabricated with the same matrix material and process parameters, were

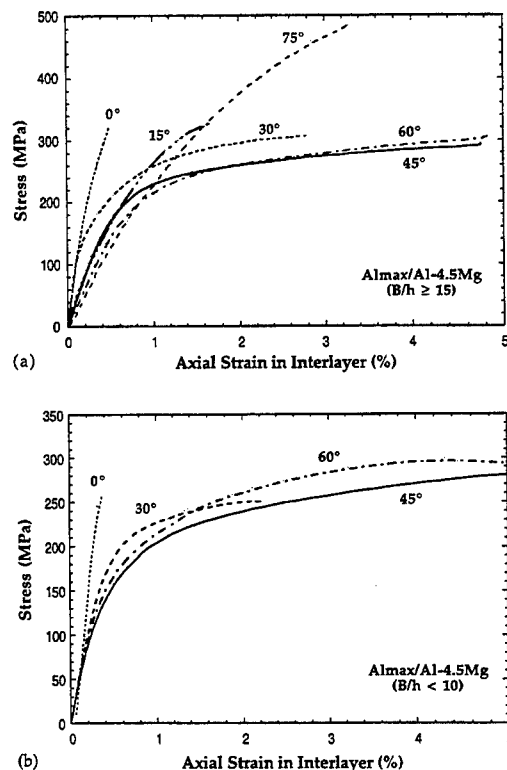


Fig. 3. Stress-strain behavior of the metal interlayers in the two series of joints investigated: (a) higher aspect ratio joints; (b) lower aspect ratio joints. The stress-strain curves for the 45° and 60° specimens extend beyond 5% in both cases (see Table 1).

†It should be noted that strains above ~5% are only semi-quantitative since they exceed the nominal range of the gages used. The failure strain of the matrix was measured with an extensometer.

Table 1. Summary of mechanical performance of joints investigated

Scarf angle	B/h	Higher aspect ratio ($B/h > 15$)		B/h	Lower aspect ratio ($B/h < 10$)	
		UTS (MPa)	ϵ_{UTS} (%)		UTS (MPa)	ϵ_{UTS} (%)
0°	36	319	0.5	9.5	250	0.4
15°	33	329	1.7	—	—	—
30°	48	308	2.8	3.3	253	2.1
45°	22	297	6.0	7.2	298	8.2
60°	17	364	18 ^a	4.4	301	4.3 ^a
75°	27	> 485 ^b	> 3.3 ^b	—	—	—

^aStrain corresponding to maximum load. Strain to failure was substantially higher in both cases. Values above ~5% are only semi-quantitative since they exceed the nominal gage range.

^bSpecimen failed at the grips.

characterized by remarkably consistent strengths in the range of 250–265 MPa, with no apparent correlation with aspect ratio [9].

Although the role of aspect ratio on joint strength is yet to be quantified in a rigorous manner, one might speculate at this point on the source of the unexpected difference in strength between the low and high B/h series. Thermogravimetric analysis of the pyrolysis behavior of the spacer films used in the two specimen groups revealed that the PVAc film oxidizes noticeably more slowly than cellulose, and hence leaves more residue after comparable heating times. This behavior may be further accentuated when the preform is completely encapsulated in the porous ceramic mold. Thus, it is possible that the differences in strength might have arisen from varying levels of carbon contamination, as has been reported for other metal–ceramic interfaces [10]. This hypothesis implies, however, that the rather remarkable consistency in strength (250–265 MPa) observed for earlier butt joints prepared with the PVAc spacer material may be somewhat fortuitous. The issue remains unresolved and clearly deserves further investigation.

3.2. Microstructural analysis of fracture surfaces

With the exceptions noted above, all joints that failed did so by separation at the interface(s) between

the metal interlayer and the composite elements. The typical macroscopic features of the fracture surfaces are illustrated in Fig. 5. In general, cracks appear to evolve on both sides of the interlayer and eventually link by metal shear. There is often one dominant crack on each side of the interlayer, as shown in Figs 5(c) and (d), although patchwork surfaces such as those in Figs 5(a) and (b) suggest that there may be a distribution of interfacial strengths leading to multiple crack initiation sites.

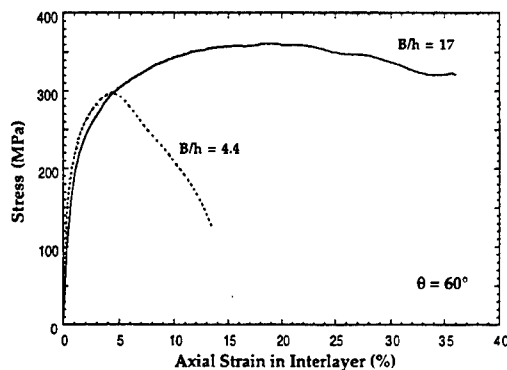


Fig. 4. Stress-strain behavior of the 60° joints with two different aspect ratios. Note the extensive elongation and the load drop prior to debond failure.

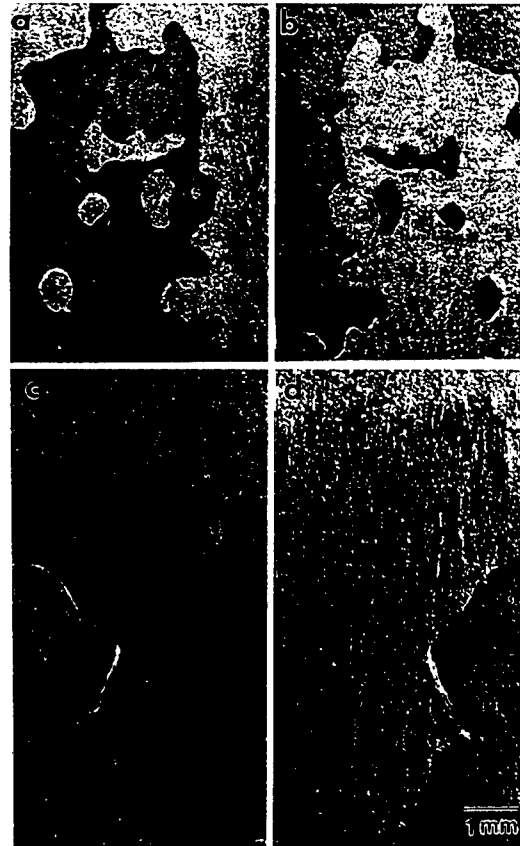


Fig. 5. Macroscopic views of the fracture surfaces of the 0° (a, b) and 45° (c, d) joints. Failure occurs by debonding on both interfaces coupled with metal shear through the interlayer. The brighter regions correspond to the "metal side" of the fracture surface.

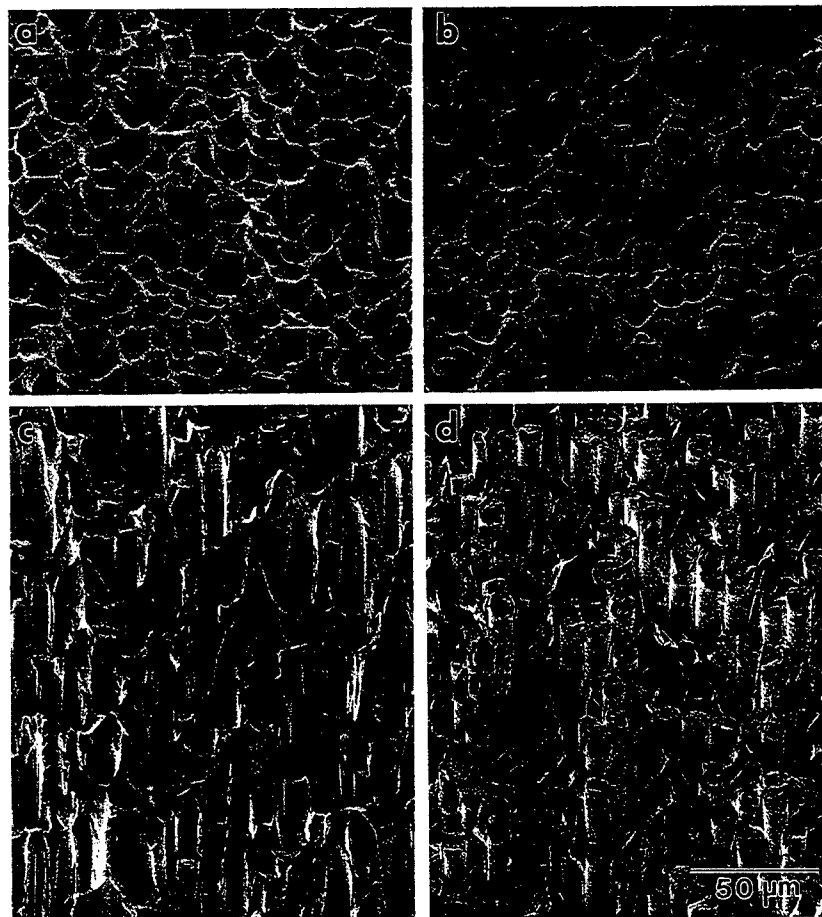


Fig. 6. Closer views of the "metal" and "fiber" sides of the fracture surfaces in Fig. 5. Parts (a, b) correspond to the 0° joint and (c, d) to the 45° joint. Note the relatively clean debonding at the fiber tips and the extensive plasticity accompanying the fracture process.

Closer examination of the fracture surfaces, e.g. Fig. 6, reveals that failure occurs predominantly by debonding at the fiber ends, whereupon the fracture surface can be conveniently described as having a "fiber side" and a "metal side".† Debonding is accompanied by plasticity in the metal regions between the fibers, which show localized extensive deformation prior to failure. In the case of the butt joint the deformation leads to a modest amount of lateral debonding, schematically depicted in Fig. 7(a), which clearly delineates the original fiber "sockets", but is not sufficient to distort significantly the "footprint" of the associated fiber ends. The larger metal ridges observed on the fiber side, Fig. 6(b), correspond to regions of lower fiber packing density

and give rise to the metal side texture observed in the macroscopic views of Fig. 5.

As the scarf angle increases the appearance of the debond surfaces changes, with the exposed fiber area becoming increasingly dominated by the lateral fiber surfaces, rather than the fiber tips, and the sockets assuming a semi-cylindrical shape, e.g. Figs 6(c) and (d). Closer examination of the "metal side" reveals that the lateral debond process involves substantial amounts of interfacial sliding and metal shear, rather than separation normal to the tip surface as suggested by the appearance of the butt joint sockets. One may then infer that some shear deformation parallel to the plane of the joint must be taking place, whereupon the debonding process would evolve as schematically depicted in Fig. 7(b). However, the details of the initiation and propagation of debonding at the microscopic level are still unclear and remain to be elucidated by further work.

4. STRESS ANALYSIS OF JOINTS

The relevant geometry is depicted in Fig. 8, with a uniform remote stress applied along the longitudinal

†Fiber fragments are occasionally found embedded in the metal side, suggesting fiber tip failure, and, rather less frequently, macroscopic metal patches indicative of voidage failure within the metal interlayer may be found on the fiber side. This is consistent with previous observations by Burr *et al.* [2] in butt joints of varying thickness.

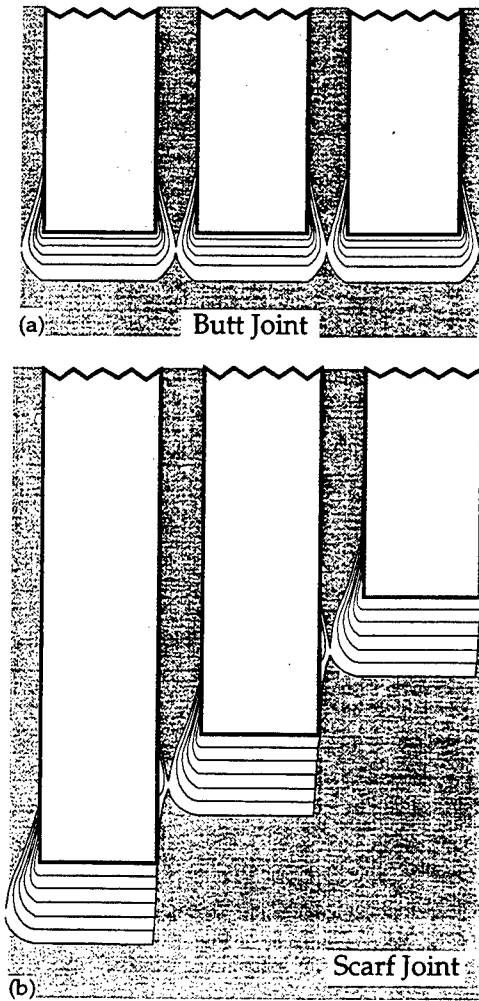


Fig. 7. Schematic of the debond process for the butt and scarf joints. The metal layer moves only in the vertical direction in the top illustration, whereas it experiences a small but finite displacement along the plane of the joint in the bottom diagram.

axis of the specimen, and the reference coordinate system normal to the plane of the metal interlayer. Owing to the rigid constraint of the grips and the higher stiffness of the composite, one may assume as a first approximation that displacements in the transverse direction can be neglected, ($ds \approx 0$), and hence that the lateral surface of the top and bottom composite elements remain perfectly aligned throughout the test. Following Burr *et al.* [2] it is further assumed that the interlayer may be divided into two distinct regions: a core, where the principal stresses are reasonably uniform, and a band surrounding the

core which slides inward as the core stretches.† The constraint imposed by the neighboring composite elements builds up a hydrostatic stress as the slipping band is pulled inward by the core, enabling the development of normal stresses in the interlayer well beyond the yield strength of the unconstrained monolithic metal. Since the projected width of the specimen ($W/\cos \theta$) is always larger than the depth (B), and both are much greater than the thickness (h), the interlayer may be considered to be in plane strain, ($\epsilon_{33} = 0$),‡ whereupon the slipping region may be taken as consisting of two parallel rectangular bars on the sides of the core, as illustrated in Fig. 8.

Using the von Mises criterion for an elastic-perfectly plastic interlayer in plane strain ($\sigma_{33} = \frac{1}{2}(\sigma_{11} + \sigma_{22})$), the relevant yielding condition is

$$\sigma_0^2 = \frac{3}{4}(\sigma_{22} - \sigma_{11})^2 + 3(\tau_{12}^2 + \tau_{23}^2) \quad (1)$$

where σ_0^2 is the yield stress of the unconstrained metal. Within the core region $\tau_{12} \approx 0$, whereupon the yield condition becomes

$$\sigma_0^2 = \frac{3}{4}(\sigma_{22} - \sigma_{11})^2 + 3\tau_{23}^2. \quad (2)$$

The associated plastic strain increments are:

$$d\epsilon_{22} = \lambda \frac{\partial \sigma_0}{\partial \sigma_{22}} = \lambda \frac{3}{4} \frac{(\sigma_{22} - \sigma_{11})}{\sigma_0} \quad (3a)$$

$$d\gamma_{23} = \lambda \frac{\partial \sigma_0}{\partial \tau_{23}} = \lambda \frac{3\tau_{23}}{\sigma_0} \quad (3b)$$

where λ is the plastic multiplier.

If the relative displacement of the composite elements is restricted to the axial direction ($ds \approx 0$), as noted above, and the magnitude of the

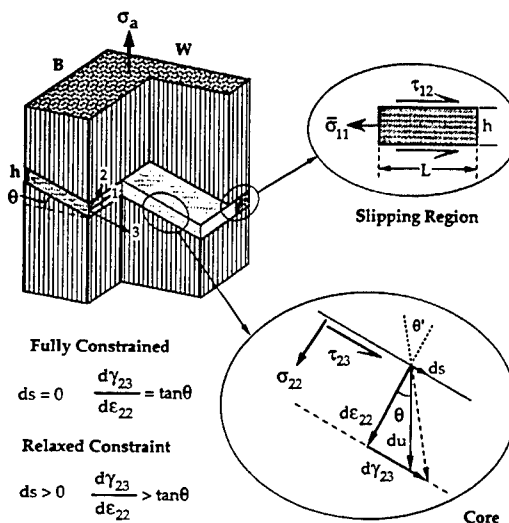


Fig. 8. Schematic of the core and slipping regions in the metal interlayer and the relevant stress and strain relationships in each case. The model in this paper is based on the assumption of no lateral displacement ($ds = 0$).

†Ongoing FEM calculations by Mailand confirm this assumption for the scarf joints, as discussed elsewhere [11].

‡The results are not significantly different if axisymmetric conditions are assumed, as discussed in Ref. [2].

displacement increment is du , the corresponding incremental strains are:

$$d\epsilon_{22} = \frac{du}{h} \cos \theta \quad (4a)$$

$$d\gamma_{23} = \frac{du}{h} \sin \theta. \quad (4b)$$

Combining equations (2)–(4)

$$\frac{d\gamma_{23}}{d\epsilon_{22}} = \frac{2\sqrt{3}\tau_{23}}{\sqrt{\sigma_0^2 - 3\tau_{23}^2}} = \tan \theta \quad (5)$$

and solving for the shear stress component, τ_{23} , gives:

$$\frac{\tau_{23}}{\sigma_0} = \frac{\tan \theta}{\sqrt{3(4 + \tan^2 \theta)}}. \quad (6)$$

Since τ_{23} is dependent only on the scarf angle and the magnitude of the yield stress, the yield condition in equation (2) may be conveniently redefined as:

$$(\sigma_{22} - \sigma_{11}) = \frac{2}{\sqrt{3}} \sqrt{\sigma_0^2 - 3\tau_{23}^2} = \frac{2}{\sqrt{3}} \sigma_{Y0} \quad (7)$$

$$\sigma_{Y0} = \frac{2}{\sqrt{4 + \tan^2 \theta}} \sigma_0 \quad (8)$$

where σ_{Y0} is an *effective* tensile yield stress at a given scarf angle. In the same manner, one may define an *effective* yield stress in shear as:

$$\tau_{Y0} = \frac{\sigma_{Y0}}{\sqrt{3}} = \frac{2}{\sqrt{4 + \tan^2 \theta}} \frac{\sigma_0}{\sqrt{3}}. \quad (9)$$

The solutions developed by Burr *et al.* [2] for the butt (0°) joint may now be extended to the scarf joints with the aid of the above definitions.† The normal stress distribution in the slipping regions is given by:

$$\begin{aligned} \frac{\sigma_{22}}{\sigma_0} &= \frac{2}{\sqrt{3}} \left[\frac{x_1}{h} + \frac{\pi}{4} \right] \frac{\sigma_{Y0}}{\sigma_0} \\ &= \frac{2}{\sqrt{3}} \left[\frac{x_1}{h} + \frac{\pi}{4} \right] \frac{2}{\sqrt{4 + \tan^2 \theta}} \end{aligned} \quad (10)$$

where x_1 is the distance from the free surface, normal to the broad face of the specimen—see Fig. 8. The average normal stress in the slipping regions ($0 \leq x_1 \leq L$) is consequently

$$\begin{aligned} \frac{\bar{\sigma}_{22}}{\sigma_0} &= \frac{2}{\sqrt{3}} \left[\frac{L}{2h} + \frac{\pi}{4} \right] \frac{\sigma_{Y0}}{\sigma_0} \\ &= \frac{2}{\sqrt{3}} \left[\frac{L}{2h} + \frac{\pi}{4} \right] \frac{2}{\sqrt{4 + \tan^2 \theta}} \end{aligned} \quad (11)$$

†In this extension it is assumed that the shear stress component τ_{23} is constant over the composite–interlayer interface. This is confirmed by the calculations in Ref. [11].

and the average in-plane stress in the x_1 direction at the intersection of the core and slipping regions, $\bar{\sigma}_{11}$, is given by:

$$\frac{\bar{\sigma}_{11}}{\sigma_0} = \frac{2L}{h} \frac{\tau_{Y0}}{\sigma_0} = \frac{2}{\sqrt{3}} \left(\frac{L}{h} \right) \frac{2}{\sqrt{4 + \tan^2 \theta}}. \quad (12)$$

The latter stress is essentially the force necessary to pull the slipping elements inward against the shear induced by the upper and lower interfaces with the composite elements (Fig. 8). The ensuing hydrostatic component of stress at the core may then be expressed as:

$$\begin{aligned} \frac{\sigma_H}{\sigma_0} &= \frac{1}{3} [\bar{\sigma}_{11} + \sigma_{22} + \bar{\sigma}_{33}]_{x_1=L} \\ &= \frac{1}{\sqrt{3}} \left[\frac{2L}{h} + \frac{\pi}{4} \right] \frac{2}{\sqrt{4 + \tan^2 \theta}}. \end{aligned} \quad (13)$$

Once plasticity has spread through the entire interlayer, the normal stress in the core, σ_{22}^* , which is approximately constant [2, 11], may be obtained from equations (7), (8) and (12). This results in:

$$\frac{\sigma_{22}^*}{\sigma_0} = \frac{\bar{\sigma}_{11}}{\sigma_0} + \frac{2}{\sqrt{3}} \frac{\sigma_{Y0}}{\sigma_0} = \frac{2}{\sqrt{3}} \left(1 + \frac{L}{h} \right) \frac{2}{\sqrt{4 + \tan^2 \theta}}. \quad (14)$$

This result is slightly different to that obtained by setting $x_1 = L$ in equation (10) owing to the assumption that the boundary between the core and the slipping regions is sharp, as discussed in Ref. [2].

A force balance in the longitudinal direction (Fig. 8), with appropriate consideration for the relationships between the cross-sectional area of the specimen, BW , and the areas of the core and slipping regions in the interlayer, $(B - 2L)W/\cos \theta$ and $2LW/\cos \theta$, respectively, yields

$$\sigma_a = \sigma_{22}^* \left(1 - \frac{2L}{B} \right) + \bar{\sigma}_{22} \left(\frac{2L}{B} \right) + \tau_{23} \tan \theta. \quad (15)$$

Combining equations (6), (11), (14) and (15) yields the relationship between the length of the slipping regions and the applied stress for a given scarf angle

$$\begin{aligned} \frac{L}{h} &= \frac{B}{2h} \left\{ \left[1 - \frac{h}{B} \left(2 - \frac{\pi}{2} \right) - \left[1 - \frac{h}{B} \left(2 - \frac{\pi}{2} \right) \right]^2 \right. \right. \\ &\quad \left. \left. - \frac{h}{B} [3(4 + \tan^2 \theta)]^{1/2} \left[\frac{\sigma_a}{\sigma_0} - \left(\frac{4 + \tan^2 \theta}{3} \right)^{1/2} \right] \right]^{1/2} \right\}. \end{aligned} \quad (16)$$

For a butt joint ($\theta = 0^\circ$) of high aspect ratio, i.e. $B/h \gg [2 - (\pi/2)]$, the above expression reduces to that proposed by Burr *et al.* [2],

$$\frac{L}{h} = \frac{B}{2h} \left\{ 1 - \sqrt{1 - 2\sqrt{3} \frac{h}{B} \left[\frac{\sigma_a}{\sigma_0} - \frac{2}{\sqrt{3}} \right]} \right\}. \quad (17)$$

The applied stress may now be rewritten as:

$$\sigma_a = \sigma_{22}^* + \tau_{23} \tan \theta - \frac{2L}{B} (\sigma_{22}^* - \bar{\sigma}_{22}) \quad (18a)$$

$$\frac{\sigma_a}{\sigma_0} = \frac{\sigma_{22}^*}{\sigma_0} + \frac{\tan^2 \theta}{\sqrt{3(4 + \tan^2 \theta)}} - \frac{4}{\sqrt{3(4 + \tan^2 \theta)}} \left[\left(\frac{L}{h} \right)^2 + \left(2 - \frac{\pi}{2} \right) \frac{L}{h} \right] \frac{h}{B} \quad (18b)$$

where the second term on the RHS represents the load-bearing contribution of the out of plane shear stress, τ_{23} , and the last term represents the knockdown effect associated with the reduced normal stress in the slipping regions relative to the core. The latter effect is minimized by utilizing interlayers with high aspect ratios, B/h , in agreement with the butt joint analysis [2], and is further reduced by increasing the scarf angle.

A significant result of the model is that the shear stress contribution is independent of the applied stress, assuming that plasticity has fully developed through the interlayer. The onset of plasticity is readily deduced from equation (16) as the minimum stress necessary for $L/h > 0$, which is

$$\frac{\sigma_a}{\sigma_0} > \sqrt{\frac{4 + \tan^2 \theta}{3}}. \quad (19)$$

It may also be shown from compatibility that the slip length when the yield condition is satisfied at the core is approximately $L/h \approx 2/3$ [2]. Further analysis reveals that this critical slip length is also relatively insensitive to scarf angle. Therefore, the development of full interlayer plasticity requires a minimum stress given by:

$$\frac{\sigma_a}{\sigma_0} > \sqrt{\frac{4 + \tan^2 \theta}{3}} + \frac{4}{9\sqrt{3}} \frac{[6 - (16 - 3\pi)(h/B)]}{\sqrt{4 + \tan^2 \theta}}. \quad (20)$$

Comparison of equations (8) and (19) reveals that both the effective yield stress, σ_{Y0} , and the applied stress at the onset of interlayer plasticity are only functions of the scarf angle when normalized by the nominal yield stress, σ_0 . However, while σ_{Y0} decreases with increasing angle, the actual onset of plasticity ($L/h > 0$) requires progressively higher applied stresses, as illustrated in Fig. 9(a). This is a direct consequence of the increasing influence of the shear stress contribution, $\tau_{23} \tan \theta$, as θ increases. The actual magnitude of the shear stress is never greater than $\sigma_0/\sqrt{3}$, as shown in Fig. 9(a), but the concomitant increase in joint area with angle makes the net contribution of the projected component of τ_{23} along the tensile axis greater than τ_{23} for values of θ greater than 45° . Figure 9(a) also shows that the stress increment necessary to yield the core after the onset of plasticity near the surface, i.e. the second term on the RHS of equation (20), is of the order of

σ_0 for the 0° joint but decreases significantly with increasing angle above 45° .

Contrary to the terms in Fig. 9(a), the normal and hydrostatic stresses are, as expected, a function of the applied load. These are plotted in Fig. 9(b) for joints with a fixed aspect ratio ($B/h = 30$) and $\sigma_a = 3\sigma_0$, approximately corresponding to the failure stress for the butt joint in Fig. 2. It is immediately evident that as the scarf angle increases the contribution from the shear stress increases, while the normal and hydrostatic stresses decrease. Similar trends have been found in elastic analyses of adhesively bonded scarf joints, e.g. Ref. [5]. It is these latter stresses that, in principle, provide the driving potential for debonding and cavitation processes [12]. Figure 9(b) also reveals that the knockdown effect produced by the slipping regions is relatively small, even for the moderate aspect ratio selected, and decreases further with angle as anticipated from equation (18b).

5. EXPERIMENTAL CORRELATION

Equations (13), (16) and (18a) can be used in conjunction with the ultimate strengths and aspect ratios in Table 1 to calculate the normal and hydrostatic stresses in the interlayer at the moment of failure. The results are summarized in Table 2. The

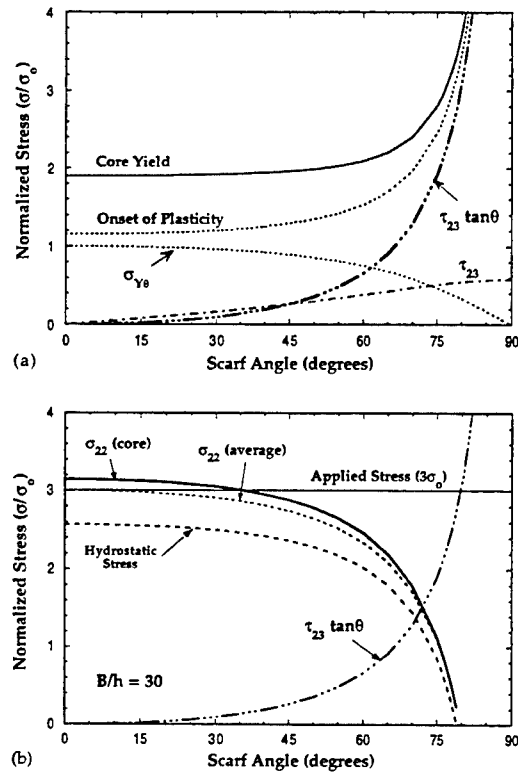


Fig. 9. Relevant terms in the stress analysis of the scarf joints. Part (a) depicts terms independent of the applied stress, whereas (b) shows the variation of the terms that are expected to drive the debond process at a fixed value of the applied stress.

Table 2. Stresses at failure in the joints with higher aspect ratio

Angle	0	15	30	45	60	75 ^a
Failure stress, σ_{UTS}/σ_0	3.19	3.29	3.08	2.97	3.64	4.85
Shear stress cont., $\tau_{23} \tan \theta/\sigma_0$	0.00	0.02	0.09	0.26	0.66	1.90
Aver. normal stress, $\sigma_{23}^{av}/\sigma_0$	3.19	3.27	2.99	2.71	2.98	2.95
Core normal stress, σ_c^*/σ_0	3.33	3.44	3.11	2.90	3.53	3.68
Pressure stress, σ_H/σ_0	2.63	2.74	2.40	2.27	3.00	3.35
Effective breadth $(1-2L/B)$	0.90	0.88	0.93	0.84	0.64	0.57

^aSpecimen failed by composite fracture at the grips.

initial analysis is limited to the higher aspect ratio joints, since those for which $B/h < 10$ and $\theta > 0$ in Table 1 failed at stresses wherein the model would predict plastic collapse in the absence of hardening (see the discussion below).

The peak normal stresses for the specimens that failed by debonding (0–60°) fall within a relatively narrow range ($\pm 10\%$) of $3.25\sigma_0$. This suggests that debond failure occurs when the normal stress at the core reaches a critical value, σ_c , consistent with the behavior of the butt joints [2]. If the aspect ratio is sufficiently high, the knockdown effect of the slipping regions is minimal and the net effect of the scarf angle may be expressed as:

$$\frac{\sigma_f(\theta)}{\sigma_f(0^\circ)} \approx 1 + \frac{\tau_{23} \tan \theta}{\sigma_c}$$

$$\approx 1 + \left(\frac{\sigma_0}{\sigma_c} \right) \frac{\tan^2 \theta}{\sqrt{3(4 + \tan^2 \theta)}}. \quad (21)$$

Hence, the strengthening relative to the butt joint arises then solely from the shear stress contribution, $\tau_{23} \tan \theta$, and the magnitude of the effect depends on the relative debond resistance of the joint, σ_c/σ_0 . Figure 10 depicts the strengthening effect predicted by the model for joints with a critical (debond) stress $\sigma_c = 3.25\sigma_0$, and for aspect ratios representing the bounds of the range investigated. The predictions are reasonably consistent with the experimental results, and confirm that the strengthening is significant only

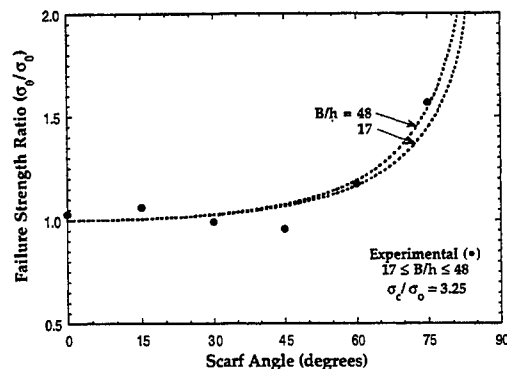


Fig. 10. Comparison between the experimental and predicted strengthening effect of the scarf angle for the average value of the "debond" stress calculated for the 0–60° joints and the relevant range of aspect ratios.

for angles above $\sim 45^\circ$. Moreover, the effect of the aspect ratio (which is already embedded in the magnitude of the butt joint strength) is rather small, even for the moderate B/h values depicted.

The discussion above implies the existence of a critical debond stress, but the physical observations suggest that the failure process is more complicated than a simple interfacial decohesion at a "threshold" value of the normal stress. For example, the failure in Figs 6(c) and (d) appears to occur by debonding of the metal at the fiber tips, probably by interfacial void nucleation and coalescence [13], followed by a form of "pull-out" involving sliding against one half of the lateral surface of the socket and debonding from the other side—see Fig. 7(b). These observations clearly indicate the occurrence of some lateral displacement, i.e. $d\gamma_{23} > d\epsilon_{22} \tan \theta$, which is at variance with the assumptions of the model.

One further complication arises from the estimate of the core normal stress at the moment of failure for the 75° joint in Table 2. This joint reaches the highest value of σ_c^* , yet it fails by composite fracture at the grips rather than by debonding. One possible explanation is that the joint was about to debond when it failed prematurely elsewhere, and that the estimated value of the peak normal stress is still consistent with the concept of a "threshold" debond stress within the limits of experimental error. It is also possible that the value of σ_c^* at failure is overestimated since the composite beams may experience some finite deflection in the transverse direction and partially relax the normal stress at the joint.

Figure 8 shows that the net effect of relaxing the constraint on beam bending and allowing a finite lateral displacement ($ds > 0$) is to make $d\gamma_{23}/d\epsilon_{22} > \tan \theta$. If the ends of the bar are still firmly gripped this would produce a small rotation of the joint plane, which is equivalent to an increase in the scarf angle to $\theta' > \theta$. More importantly, one can readily show from equation (5) that the relaxed constraint produces a net increase in the shear stress component τ_{23} . An accurate estimate of τ_{23} and θ' would require a full elasto-plastic analysis which is beyond the scope of this paper. However, one can estimate an upper bound to the effect of the shear stress increase on the joint strength by noting that the maximum value of τ_{23} for an elastic-perfectly plastic material would be $\tau_0 = \sigma_0/\sqrt{3}$ and by assuming that

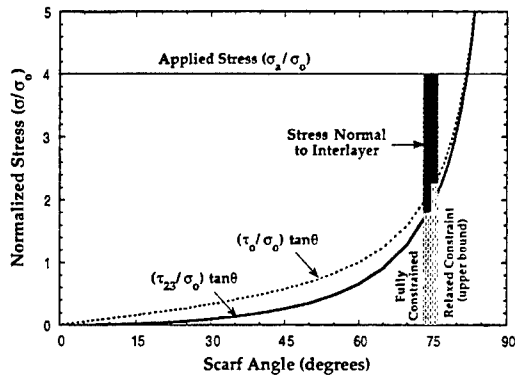


Fig. 11. Illustration of the potential effect of relaxing the rigid constraint assumption, hence allowing lateral displacements during the deformation of the joint specimen, on the shear stress contribution and the average stress normal to the interlayer.

$\theta' \approx \theta$. The result is plotted in Fig. 11 as $\tau_o \tan \theta$, and compared with the value of $\tau_{23} \tan \theta$ for the fully constrained case. The actual value of the shear stress contribution would fall somewhere between these two curves in Fig. 11.

Since the normal stress is essentially the difference between the applied stress and the shear contribution $\tau_{23} \tan \theta$, assuming the joint is fully plastic, the larger shear stress expected under the relaxed constraint conditions in Fig. 11 further decreases the stress available to "drive" the debond process. One might infer that the normal core stress at the moment of failure could be overestimated by as much as $\sim 0.26\sigma_o$ for $\theta = 75^\circ$, which would bring it in line with the range observed for the other specimens ($\theta \leq 60^\circ$), suggesting that the interlayer was indeed near debonding when failure occurred at the grips. (This hypothesis is further supported by microstructural analysis of the 75° specimen, which revealed evidence of sub-critical debonding at some fiber tips.) It is also clear, however, that the debond stresses calculated for the other specimens may also be overestimated, although the differences would be, in all cases, of the order of 10% of the core normal stresses listed in Table 2. Further insight into this problem will be gained by ongoing finite element analyses to be reported in a separate publication [11].

6. DESIGN IMPLICATIONS

If the performance of joints was indeed predominantly controlled by the scarf angle and some critical level of the normal (debond) stress, σ_c , one may use the present model to develop failure regime maps such as those depicted in Fig. 12. For joints with high aspect ratio, Fig. 12(a), the behavior is elastic at the lower stresses with interlayer plasticity developing above the solid curve. The joint will fail by debonding when the curve corresponding to a critical value of σ_c/σ_o is reached. It is also noted that for any given debond stress there is a critical angle above which the

estimated joint strength surpasses that of the composite, allowing the latter to be loaded to its full capacity.

An additional failure mechanism may appear in the map when the joint aspect ratio decreases. Even though the onset of yield is shifted to higher stresses with increasing scarf angle, once the interlayer yields the slipping regions near the surface grow more rapidly with stress owing to the reduced effective yield stress in shear, equation (9). If the slipping lengths overlap before the core stress reaches the critical debond value, a plastic limit load will be reached and the joint will fail by plastic collapse. The limit load may be estimated by setting $L = B/2$ in equation (11) and then adding the shear stress contribution $\tau_{23} \tan \theta$. This gives

$$\frac{\sigma_{LL}}{\sigma_o} = \frac{[(B/h) + \pi + \tan^2 \theta]}{\sqrt{3(4 + \tan^2 \theta)}} \quad (22)$$

The effect of plastic collapse is illustrated in Fig. 12(b), where the debond stress has been fixed and the aspect ratio allowed to vary. As the applied load is increased, the joint will be first elastic and then become plastic upon reaching the onset stress defined by the solid curve. If the aspect ratio is sufficiently

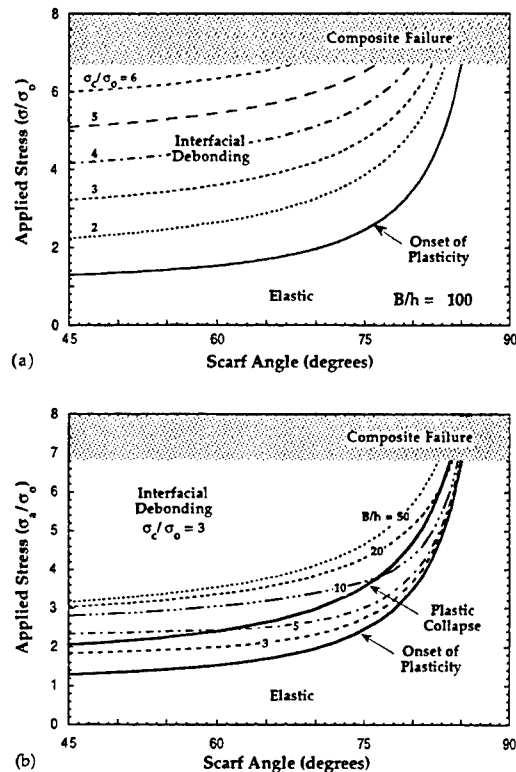


Fig. 12. Failure mechanism maps for the scarf joints calculated with the present model. The top map illustrates the effect of the debond strength for joints of high aspect ratio. The bottom map illustrates the possibility of failure by plastic collapse when the aspect ratio of the joint is reduced.

high, the joint will fail by debonding when the corresponding curve is reached. However, if the aspect ratio is low, the joint will fail by debonding if the angle is to the left of the plastic limit curve in Fig. 12(b), and by plastic collapse if the angle is within the plastic collapse and plastic onset curves in this figure. The map is in qualitative agreement with the observed behavior of the 60° joint with an aspect ratio of ~4, which extended plastically up to ~13% strain prior to debond failure—see Fig. 4. The model also predicts that the 30 and 45° joints with low aspect ratios in Table 1 should have failed by plastic collapse, but they failed instead by debonding, albeit without the load drop observed in the 60° specimen. The observed behavior may be associated with strain hardening effects, which would shift the reference stress σ_0 in Fig. 12(b) but are neglected in the present model. The actual boundary between the debond and plastic collapse mechanisms would then have to be determined by numerical calculations. Alternatively, the problem is easily avoided by selecting an interlayer with sufficiently high aspect ratio.

7. CONCLUDING REMARKS

Investigation of the tensile behavior of thin metal interlayers between composite elements, oriented at different angles relative to the applied stress, has led to an improved understanding of the mechanical performance of interfaces relevant to the design of composite-monolith transitions. The typical failure mode is separation at the metal-composite interfaces, apparently initiated by debonding at the fiber tips. Because of the constraint imposed by the neighboring composite, the interlayers may be loaded well beyond the normal tensile strength of the constituent metal. Significant plasticity is observed in all cases, increasing from ~0.5% strain for the 0° joints to well over 10% at ~60°, wherein the applied stress goes through a maximum prior to debond failure. The joint strengths are relatively insensitive to scarf angle below 45°, but increase substantially for the higher angles.

A simple model for the plastic behavior of a thin metal interlayer between two fully rigid composite elements was found to be reasonably consistent with the experimental results. For interlayers with sufficiently high aspect ratios debonding appears to occur at a relatively constant value of the tensile stress normal to the macroscopic composite-metal interface. The observed strengthening arises primarily from the increased fraction of the applied load carried by the shear stress as the scarf angle increases, which is predominated by the concomitant increase in

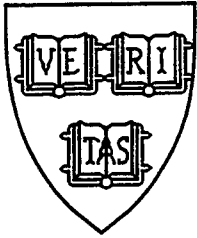
the interfacial (load-bearing) area. The model may be used to develop failure maps which reflect the interplay between different failure mechanisms as a function of interfacial strength and the geometric parameters of the joint. It is shown that for any level of interfacial (debond) strength there should be a critical angle above which the joint can reach a strength comparable to that of the composite.

The analysis also shows that the relaxation of the rigid constraint assumption may have important implications in the relative magnitudes of the normal and shear stresses in the interlayer. These issues are currently under investigation.

Acknowledgements—The studies in this paper were sponsored by the National Science Foundation, Mechanics and Materials Program, under grant MSS 93-02053 monitored by Drs O. Dillon and W. Spitzig. Additional support was provided by the High Performance Composites Centre through the university Research Initiative grant N00014-92-J-1808 from the Advanced Research Projects Agency, supervised by Dr W. Coblenz and monitored by Dr S. G. Fishman of the Office of Naval Research. Expert assistance of Dr J. Y. Yang in developing the specimen preparation techniques, and Dr F.-C. Dary and Mr K. Fields in developing the testing techniques, is gratefully acknowledged.

REFERENCES

1. Zok, F. W., He, M. Y., Evans, A. G., Leckie, F. A. and Déve, H. E., *Composites Part A*, in press.
2. Burr, A., Yang, J. Y., Levi, C. G. and Leckie, F. A., *Acta metall. mater.*, 1995, **43**(5), 3361.
3. Clyne, T. W. and Withers, P. J., *An Introduction to Metal Matrix Composites*. Cambridge University Press, Cambridge, 1993, pp. 236, 359, 441, 442.
4. Messler, Jr, R. W., *Joining of Advanced Materials*. Butterworth-Heinemann, Stoneham, MA, 1993, pp. 270–274, 492–496.
5. Chen, D. and Cheng, S., *J. Appl. Mech.*, 1990, **57**, 78.
6. Ikegami, K., Takesha, T., Matsuo, K. and Sugibayashi, T., *Int. J. Adhesion Adhesives*, 1990, **10**(3), 199.
7. Saitow, Y., Iwanaga, K., Itou, S., Fukumoto, T. and Utsunomiya, T., in *Proceedings of the 37th International SAMPE Symposium*, 9–12 March, 1992.
8. Private communication from Mitsui Chemical Co., 1994.
9. Yang, J. Y., Levi, C. G. and Leckie, F. A., unpublished work.
10. Dalgleish, B. J., Saiz, E., Tomsia, A. P., Cannon, R. M. and Ritchie, R. O., *Scripta metall. mater.*, 1994 **31**(8), 1109.
11. Mailand, J., M.S. thesis, University of California, Santa Barbara, 1996.
12. Huang, Y., Hutchinson, J. W. and Tvergaard, V., *J. Mech. Phys. Solids*, 1991, **39**, 223.
13. Tvergaard, V., *Failure by Ductile Cavity Growth at a Metal Ceramic Interface*. Danish Center for Applied Mathematics and Mechanics, June 1990, Report No. 406.



MECH 305

ON KINK-BAND PROPAGATION IN FIBER COMPOSITES

B. Budiansky[†], N. A. Fleck[°] and J. C. Amazigo^{*}

[†]Division of Engineering and Applied Sciences
Harvard University
Cambridge, MA 02138

[°]Engineering Department
Cambridge University
Cambridge CB2 1PZ, England

^{*}Department of Mathematics
University of Nigerai
Nsukka, Nigeria

ON KINK-BAND PROPAGATION IN FIBER COMPOSITES

B. Budiansky[†], N.A. Fleck[°], and J.C. Amazigo^{*}

[†]Division of Engineering and Applied Sciences, Harvard University, Cambridge, MA 02138

[°]Engineering Department, Cambridge University, Cambridge CB2 1PZ, England

^{*}Department of Mathematics, University of Nigeria, Nsukka, Nigeria

ABSTRACT

Two kinds of kink-band propagation in the compression of aligned-fiber composites are studied analytically: band broadening, discovered experimentally by Moran, Liu and Shih in 1995, in which a uniform kink band grows in the direction of loading at constant stress under increasing deformation; and transverse kink propagation, in which a kink band traverses a specimen quasi-statically under constant overall shortening. The analysis is based on a 1D, geometrically nonlinear couple-stress theory of composite kinking that takes elastic fiber bending resistance into account together with idealized nonlinear stress-strain relations, but assumes non-breaking fibers. Simple results for the band-broadening and transverse propagation stresses are deduced, and their significance is discussed.

INTRODUCTION

Elementary analyses of localized kinking under compression of aligned-fiber polymer-matrix composites (Budiansky and Fleck, 1993), considered together with experimental data, provide compelling evidence that compressive kinking strength is governed primarily by the yield strength in shear of the composite, and by fiber misalignment. The indeterminacy of misalignments accounts for the notorious scatter in kinking data. (For some general reviews of kinking studies, see Budiansky and Fleck, 1994; Schultheisz and Waas, 1996, Waas and Schultheisz, 1996; Fleck, 1997). On the basis of various geometrical and physical models of the composite, detailed 2D finite-element calculations have recently been used to study the initiation, metamorphosis, and propagation of kink-bands in the presence of various initial distributions of fiber misalignment or notches (e.g., Fleck and Shu, 1995; Kyriakides et al, 1995; Sutcliffe and Fleck, 1996; Kyriakides and Ruff, 1996). Such numerical studies provide useful insights into the kinking process, and also serve to assess the accuracy and relevance of elementary analyses. We note that fiber fracture has not yet been incorporated into 2D finite-element calculations; but fiber fracture can generally be expected to occur only *after* the peak compressive stress has been attained (Fleck et al, 1995).

In this paper we use *one-dimensional* analyses to explore two kinds of steady-state kink propagation: *band broadening*, in which an established kink band grows in the direction of loading, and *transverse propagation*, in which a kink band travels across the width of a composite

specimen. Remarkably, band broadening without fiber fracture was discovered experimentally only recently by Moran et al (1995). On the other hand, transverse propagation (which precedes band broadening) is ubiquitous, though often dynamic, and not usually steady-state. Both types of propagation have been studied theoretically on the basis of various physical models. (e.g. Fleck and Budiansky, 1991; Sutcliffe and Fleck, 1994; Moran et al, 1995; Liu and Shih, 1996). Our aim here is to present some fairly rigorous studies of the mechanics of band broadening and transverse propagation, including the effects of fiber bending resistance. With the further use of idealized constitutive models, succinct results will be shown for both types of kink propagation. Because compressive kinking strength is a random variable sensitive to initial imperfections, we will discuss briefly the possibility (Moran et al, 1995) of adopting one or another of the kink propagation stresses as a rational working stress for design purposes.

REVIEW OF BASIC KINKING THEORY

To set the stage, we will summarize briefly some basic results of the elementary theory of kinking (Budiansky and Fleck, 1993). We show in Fig. 1 the conventional picture of a kink band oriented at an angle β , within which the fibers, originally misaligned by $\bar{\phi}$ with respect to the direction of loading, have rotated by the additional angle ϕ under the compressive stress σ . For ϕ

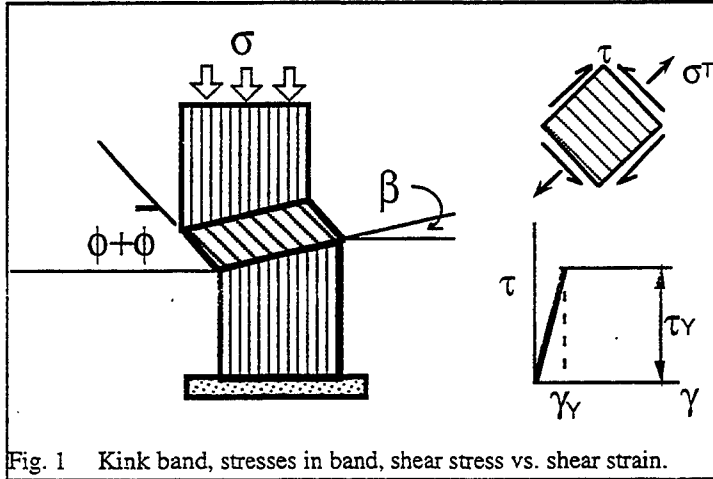


Fig. 1 Kink band, stresses in band, shear stress vs. shear strain.

and $\bar{\phi}$ small, equilibrium requires that the shear stress τ and the tensile transverse stress σ_T defined in Fig. 1 be related to the applied compressive stress σ by

$$\sigma = \frac{\tau + \sigma_T \tan \beta}{\bar{\phi} + \phi} \quad (1)$$

and, for inextensional fibers, the shear strain γ and the transverse strain ϵ_T are given by

$$\begin{cases} \gamma = \phi \\ \epsilon_T = \phi \tan \beta \end{cases} \quad (2)$$

Dropping the contribution of σ_T to σ , and adopting the elastic-ideally-plastic relation between τ and γ sketched in Fig. 1, we find that σ maximizes at $\phi = \gamma_Y$; this gives the lower-bound estimate

$$\sigma_c = \frac{\tau_Y}{\bar{\phi} + \gamma_Y} \quad (3)$$

for the critical kinking stress. In the limiting case $\bar{\phi} = 0$, this gives the Rosen (1965) result $\sigma_c = G$, where G is the elastic shear modulus of the composite; for $\gamma_Y = 0$, we get the Argon (1972) estimate $\sigma_c = \tau_Y / \bar{\phi}$.

Two points deserve emphasis. Even though Eq. (3) does not contain β , comparisons made by Budiansky and Fleck (1993) indicate that over a reasonable range (say, up to $\beta=40^\circ$) it provides a fair approximation to critical stresses derived for strain-hardening composites, with interactive effects of τ and σ_T taken into account, and τ_Y equal to a nominal yield stress. Second, the compressed composite is very imperfection-sensitive. For example, with $\bar{\phi} \approx 1.7^\circ$ and $\gamma_Y \approx .01$, Eq. (3) gives $\sigma_c/G \approx 1/4$ and $\sigma_c/\tau_Y \approx 25$; small changes in $\bar{\phi}$ overwhelm the effects of σ_T and β .

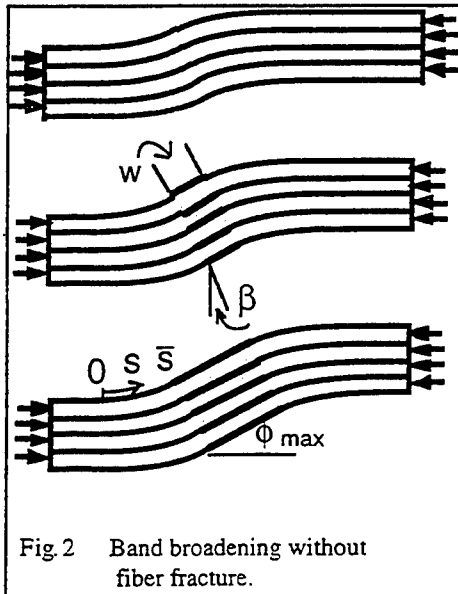
Another fact to be noted is that fiber fracture does not influence σ_c . The detailed studies of Fleck et al (1995), in which fiber bending resistance is considered, show that fiber fracture occurs while the compressive load is dropping, at rotations much larger than those corresponding to the attainment of maximum load. This holds even if the fibers have no tensile strength; for this case, a simple approximate formula for the fiber rotation at fiber fracture, that follows from the analyses by Budiansky (1983) and Fleck et al (1995), gives

$$\phi_{\text{fracture}} \approx \left(\frac{2\tau_Y}{E} \right)^{1/3} \quad (4)$$

where E is the Young's modulus of the composite. For the plausible value $\tau_Y/E = .0004$, this gives $\phi_{\text{fracture}} = .09$ --- much larger than the value $\phi = \gamma_Y$ at which σ_c is reached.

BAND BROADENING: OBSERVATIONS

In recent tests, Moran et al (1995) and Moran and Shih (1996) observed the longitudinal



kink-band broadening shown schematically in Fig. 2. The composite was composed of 60% IM7 fibers in a PEEK matrix and the broadening evidently occurred without fiber fracture and at constant applied stress. The growing band of straight fibers, shown shaded, remained inclined at an angle ϕ approximately equal to twice the band orientation $\beta \approx 20^\circ$. This kind of fracture-free broadening was later seen by Fleck et al (1997) in an IM8/PEEK composite.

Band broadening of the type illustrated in Fig. 3, in which the straight portion of the broadening band consists of broken segments of approximately equal length, has recently been observed by Sivashanker et al (1996), Kyriakides and Ruff (1996), and Vogler and Kyriakides (1996). In these cases the composite contained AS4 carbon fibers, less strong and less stiff

than IM7 and IM8. We will study only fracture-free band broadening in this paper, but we will also determine the magnitudes of fiber strength that permit its occurrence.

In the experiments of Vogler and Kyriakides (1996) the fiber rotation during broadening was found to exceed 2β somewhat. We will nevertheless use $\phi_{\max}=2\beta$ as a reasonable approximation, based on the idea of "lock-up", to be discussed.

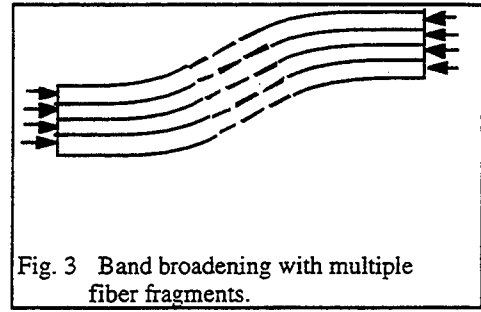


Fig. 3 Band broadening with multiple fiber fragments.

LARGE-ROTATION, ONE-DIMENSIONAL BENDING THEORY

We will develop here equations governing the response to compression of an aligned-fiber composite, appropriate for the study of band-broadening, and later, transverse kink propagation. The theory embodies couple stresses that account for the bending resistance of the fibers, but extends the linear analyses by Budiansky (1983) and Fleck et al (1995) to large rotations. Small initial misalignments will be neglected in comparison with the much larger rotations that occur during the development of the broadening configuration.

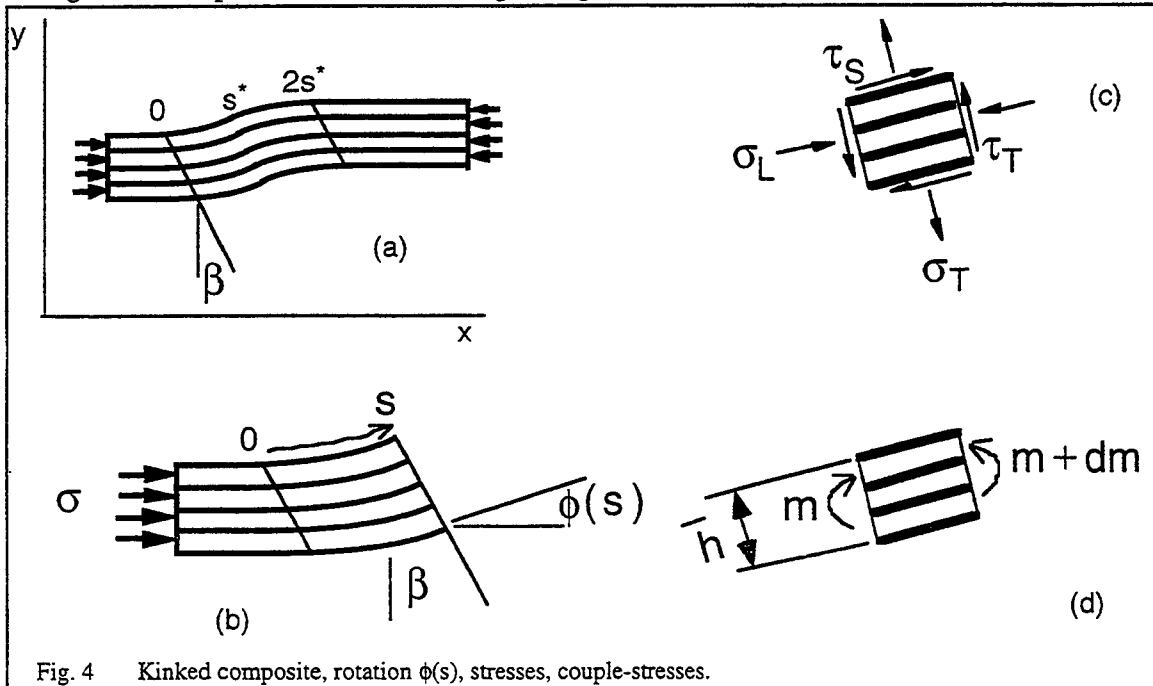


Fig. 4 Kinked composite, rotation $\phi(s)$, stresses, couple-stresses.

We contemplate a geometry in which the kinking orientation is pre-set at β and (see Fig. 4) the fiber rotation ϕ is invariant along β -lines $x+y\tan\beta=\text{constant}$. Assuming inextensional fiber deformations, we can introduce the one-dimensional function $\phi(s)$, where s is distance along an arbitrary fiber, and define the longitudinal stress σ_L , transverse stress σ_T , sliding shear stress τ_s ,

transverse shear stress τ_T , and couple stress m , as shown in Fig. 4. These are all smeared-out *true* stresses, and are considered to be functions of s ; σ_L and τ_S are parallel to the fibers, σ_T and τ_T act normal to the fibers, and m is the couple stress on the deformed plane normal to the fibers.

Distances along β lines do not change, but the rotated portions of the composite undergo transverse stretching. Let h denote the original thickness in the y -direction of a portion of the composite, and let \bar{h} be the stretched thickness normal to the fibers (Fig. 4(d)). Then the transverse stretch ratio is

$$\frac{\bar{h}}{h} \equiv g(\beta, \phi) = \frac{\cos(\beta - \phi)}{\cos \beta}. \quad (5)$$

The function $g(\beta, \phi)$ will appear frequently in the derivations that follow.

The assumptions of inextensionality and plane strain, i.e. zero strain in the thickness direction normal to the x - y plane, imply that the composite suffers a volumetric increase, also given by the ratio $g(\beta, \phi)$. (It is generally believed that this dilatation is accommodated by microcracking in the polymeric matrix.)

Force equilibrium in the direction normal to the fibers at the right end of the free body in Fig. 4(b) implies that

$$\sigma \cos \beta \sin \phi = \tau_T \cos(\beta - \phi) + \sigma_T \sin(\beta - \phi). \quad (6a)$$

and equilibrium in the fiber direction gives

$$-\sigma \cos \beta \cos \phi = \tau_S \sin(\beta - \phi) + \sigma_L \cos(\beta - \phi) \quad (6b)$$

These agree with the equilibrium equations given by Budiansky and Fleck (1993) for a constant-rotation kink, in which there is no bending and $\tau_S = \tau_T$. But now moment equilibrium of the element in Fig. 4(c,d) requires that

$$\frac{d}{ds}(mg) = (\tau_S - \tau_T)g \quad (7)$$

and this permits the elimination of τ_T from (6a) to give

$$\sigma \cos \beta \sin \phi + \cos \beta \frac{d}{ds}(mg) = \tau_S \cos(\beta - \phi) + \sigma_T \sin(\beta - \phi) \quad (8)$$

We will soon drop σ_T , but we keep it temporarily, in order to define strains via the principle of virtual work. For convenience (this is not crucial) say that ϕ vanishes at each end of the composite specimen in Fig. 4(a), and note that the shortening is Δ is

$$\Delta = \int (1 - \cos \phi) ds \quad (9)$$

where the integration is over the original specimen length. We assert that strain variations $\delta\gamma$ and $\delta\epsilon_T$, and bending-strain variations $\delta\kappa$, conjugate in the work sense to τ_S , σ_T , and m , satisfy the principle of virtual work

$$\sigma \delta \int (1 - \cos \phi) ds = \int (\tau_S \delta\gamma + \sigma_T \delta\epsilon_T + m \delta\kappa) g(\beta, \phi) ds \quad (10)$$

for strain variations compatible with $\delta\phi(s)$ and all combinations of stresses (τ_S, σ_T) and couple

stresses m that satisfy equilibrium. Eliminating σ via Eq. (8), and doing one integration by parts, leads to

$$\int \left\{ \tau_s [\delta\gamma - \delta\phi] + \sigma_T [\delta\varepsilon_T - \delta\phi \tan(\beta - \phi)] + m \left[\delta\kappa - \delta \frac{d\phi}{ds} \right] \right\} g(\beta, \phi) ds = 0. \quad (11)$$

This implies the energetically consistent strain-rate definitions

$$\begin{cases} \dot{\gamma} = \dot{\phi} \\ \dot{\varepsilon}_T = \dot{\phi} \tan(\beta - \phi) \\ \dot{\kappa} = d\dot{\phi}/ds \end{cases} \quad (12)$$

which integrate to the strains

$$\begin{cases} \gamma = \phi \\ \varepsilon_T = \log \frac{\cos(\beta - \phi)}{\cos\beta} \equiv \log g(\beta, \phi) \\ \kappa = d\phi/ds \end{cases} \quad (13)$$

The first two of these agree with the results derived by Fleck and Budiansky (1991) for ϕ independent of s and $\bar{\phi} = 0$; the expression for ε_T is also consistent with the stretch ratio (5).

To complete the theoretical set-up we need constitutive relations. Transverse tension tests point to early failure at transverse strains less than 1% (e.g. Fleck and Jelf, 1995; Kyriakides et al, 1995), and so at this point we will drop σ_T from the equilibrium Eq. (8) *as long as the transverse strain ε_T is positive*. We then consider τ_s to be a function only of $\gamma = \phi$. (Here we abandon the unrealistic assumption made by Fleck and Budiansky (1991) that τ_s becomes zero when transverse failure occurs.) We note further that the transverse compressive strains that would want to occur for $\phi > 2\beta$ will be resisted elastically, at least initially, because matrix cracks will have closed, and so henceforth we make the simplifying "lock-up" assumption (Fleck and Budiansky, 1991), and say that ϕ can not exceed 2β .

The bending will be presumed to be resisted elastically only by the fibers, with the bending moment M in each circular fiber given by

$$M = E_f \frac{\pi d^4}{64} \frac{d\phi}{ds} \quad (14)$$

where E_f is the fiber modulus and d its diameter. In terms of the fiber volume concentration c_f of the undeformed composite, the couple stress m in the deformed material is

$$m = \frac{c_f M}{g(\beta, \phi)(\pi d^2/4)} \quad (15)$$

and so, with the approximation $E \approx c_f E_f$ for the initial composite modulus, we get the bending constitutive relation

$$m = \frac{E d^2}{16 g(\beta, \phi)} \frac{d\phi}{ds}. \quad (16)$$

Using (16) in (8), with σ_T dropped, gives

$$\frac{Ed^2}{16} \frac{d^2\phi}{ds^2} + \sigma \sin \phi = \tau_S(\phi)g(\beta, \phi) \quad (17)$$

for $\phi < 2\beta$. We will now neglect elastic strains in the relation $\tau_S(\phi)$, and suppose that τ_S jumps to a finite value for $\phi=0^+$. We can then expect rotations $\phi(s)$ confined to a finite domain $(0, 2s^*)$, symmetrical about $s=s^*$, and satisfying $\phi(0)=\phi'(0)=0$; this would lead to the picture in Fig. 4a, with ϕ identically zero for $s < 0$ and $s > 2s^*$, and continuity of displacement, rotation, and bending moment maintained.

A first integral of (17), valid in $(0, s^*)$ for $\phi < 2\beta$, gives

$$\frac{Ed^2}{32} \left(\frac{d\phi}{ds} \right)^2 + \sigma(1 - \cos \phi) = \int_0^\phi \tau_S(\tilde{\phi})g(\beta, \tilde{\phi})d\tilde{\phi} \quad (18)$$

and since $d\phi/ds$ vanishes at $s=s^*$, the connection between σ and $\phi_{\max}=\phi(s^*)$ is

$$\sigma = \frac{\int_0^{\phi_{\max}} \tau_S(\phi)g(\beta, \phi)d\phi}{1 - \cos \phi_{\max}}. \quad (19)$$

Note that σ is generally a monotonically decreasing function of ϕ_{\max} , starting at $\sigma=\infty$, and so the kinking stress, which occurs at small $\phi=O(\gamma_Y)$, is not captured by the theory. But as long as $\beta \gg \gamma_Y$, this should not matter much in the analysis of either band broadening or transverse kink propagation, both of which involve large rotations, up to $\phi=2\beta$.

BAND BROADENING: CALCULATIONS

Lock-up will first occur when ϕ_{\max} reaches the value 2β . The corresponding value of the applied stress σ given by Eq. (19) is

$$\sigma_b = \frac{\int_0^{2\beta} \tau_S(\phi) \cos(\beta - \phi) d\phi}{\sin \beta \sin 2\beta}. \quad (20)$$

This is the band broadening stress! With the loading held constant at $\sigma = \sigma_b$, the successive configurations shown in Fig. 2 can evolve, with bent shapes identical to those at the initiation of lock-up emerging from a straight, locked interval of increasing size. All requirements of equilibrium and continuity remain fully satisfied during this band broadening. (It also has to be verified that in the locked region, where $m=0$, the transverse stress given by

$$\sigma_T = [-\sigma_b \sin 2\beta + \tau_S(2\beta)] \cot \beta \quad (21)$$

according to Eq. (8), is negative. This will always be true for $\tau'(\gamma) \geq 0$ and $\tau''(\gamma) \leq 0$.)

Because the basic equations of the theory were formulated to be consistent with virtual work principles, the result for the band-broadening stress should emerge from a simple energy

calculation. Let w represent the length along the fibers in the locked portion of the kink band (see Fig. 2). The shortening during an increment δw during broadening is $\delta\Delta = \delta w(1 - \cos 2\beta)$, and the additional work done by the sliding shear stresses is $\delta w \int_0^{2\beta} \tau_S(\phi)g(\beta, \phi)d\phi$ per unit thickness of the composite. The virtual work equality

$$\sigma_b \delta w(1 - \cos 2\beta) = \delta w \int_0^{2\beta} \tau_S(\phi)g(\beta, \phi)d\phi \quad (22)$$

recovers Eq. (20).

Finally, we will display a convenient explicit result for the band-broadening stress, corresponding to the rigid-ideally-plastic idealization $\tau_S(\gamma) \equiv \tau_L$. (Here we distinguish τ_L from the value τ_Y (Fig. 1) that appears in the estimate (3) for the kinking stress. The yield stress τ_Y corresponds to very small shear strains, whereas τ_L should be regarded as representative of the stresses associated with the large rotations that occur during the evolution of band-broadening, and may be substantially higher than τ_Y . See, for example, the composite shear stress-strain curves measured by Kyriakides et al (1995)). With $\tau_S(\phi) \equiv \tau_L$, Eq. (22) becomes

$$\sigma_b \delta w(1 - \cos 2\beta) = \delta w(2\tau_L \tan \beta) \quad (23)$$

and we get

$$\sigma_b = \frac{2\tau_L}{\sin 2\beta} \quad (24)$$

for the band-broadening stress. The transverse stress (21) in the locked region reduces to

$$\sigma_T = -\tau_L \cot \beta. \quad (25)$$

FIBER FRACTURE CRITERION

In order to assess the validity of the assumption that fiber fracture does not occur, we will calculate the maximum fiber tensile strain during band broadening. As before, we take the datum for distance s along a fiber to be the left-hand end of its curved region, as shown in Fig. 2. Fiber rotation begins at $s=0$ and the fibers have rotated through 2β to a locked-up state at $s=\bar{s}$. The fiber tensile strain due to bending and longitudinal stress is given by

$$\varepsilon = \frac{d}{2} \frac{d\phi(s)}{ds} + \frac{g(\beta, \phi)\sigma_L(s)}{E} \quad (26)$$

for s in $(0, \bar{s})$. (The factor g in the second term reflects the effect of transverse stretching on the local composite stiffness in the fiber direction.) We will use the rigid-ideally plastic relation $\tau_S(\phi) \equiv \tau_L$, and introduce the nondimensional coordinate

$$S \equiv \frac{4s}{d} \sqrt{\frac{\tau_L}{E}} \quad (27)$$

to rewrite ε as

$$\varepsilon = 2\sqrt{\frac{\tau_L}{E}} \phi' + \frac{g\sigma_L}{E} \quad (28)$$

where ϕ and σ_L are now functions of S , and the primes denotes differentiation with respect to S . Setting $\sigma = \sigma_b$ and $\tau_S(\phi) \equiv \tau_L$ in Eq. (18) gives the connection

$$\phi' = \sqrt{2 \cot \beta [g(\beta, \phi) - 1]} \quad (29)$$

between ϕ' and ϕ in the curved portion of the kink during band broadening, and Eq. (6b) provides

$$\frac{g\sigma_L}{E} = -\frac{\tau_L}{E} \left[\frac{\cos \phi}{\sin \beta \cos \beta} + \frac{\sin(\beta - \phi)}{\cos \beta} \right]. \quad (30)$$

For each τ_L/E , the maximum strain ε_t can now be found by maximizing (28) with respect to ϕ in $(0, 2\beta)$; the maximum occurs for $\phi > \beta$, giving the curves shown in Fig. (5). Actually, the peak strain occurs so close to the point where $\phi = \beta$ that these results are indistinguishable from those given by explicit formula

$$\varepsilon_t = 2\sqrt{\frac{2\tau_L}{E} \tan \frac{\beta}{2}} - \frac{\tau_L}{E} \csc \beta \quad (31)$$

obtained by substituting $\phi = \beta$ in Eqs. (28-30).

Fig. (5) indicates combinations of β and τ_L/E for which fracture-free broadening would be

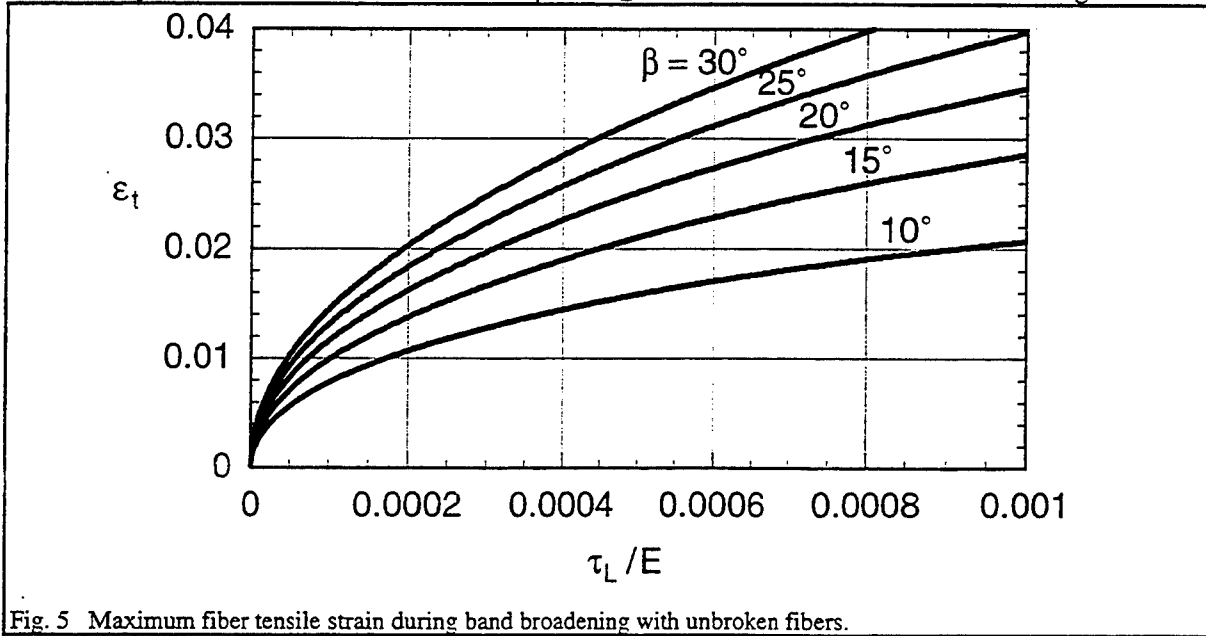


Fig. 5 Maximum fiber tensile strain during band broadening with unbroken fibers.

possible for a given fiber breaking strain. For example, for a nominal fracture strain ε_f of $1\frac{1}{2}\%$, fracture-free band broadening with $\beta = 30^\circ$ could occur only for τ_L/E less than the unreasonably low value .0001; but for $\varepsilon_f = 2\%$ and $\beta = 15^\circ$, we would only need $\tau_L/E < .00045$.

TRANSVERSE KINK PROPAGATION

We now contemplate a kink band propagating transversely at an angle β across a uniformly compressed specimen (Fig. 6a) into an unkinked region. Since the height L of the specimen is finite, the inclined kink would eventually have to run into the upper edge of the

specimen. But we presume that the propagation will be essentially steady-state under constant end shortening Δ as long as the kink front remains far from the boundaries. Alternatively, the analysis that follows is also applicable (perhaps more so) to the horizontal steady-state propagation of a kink band inclined at β in the thickness direction (Fig. 6b).

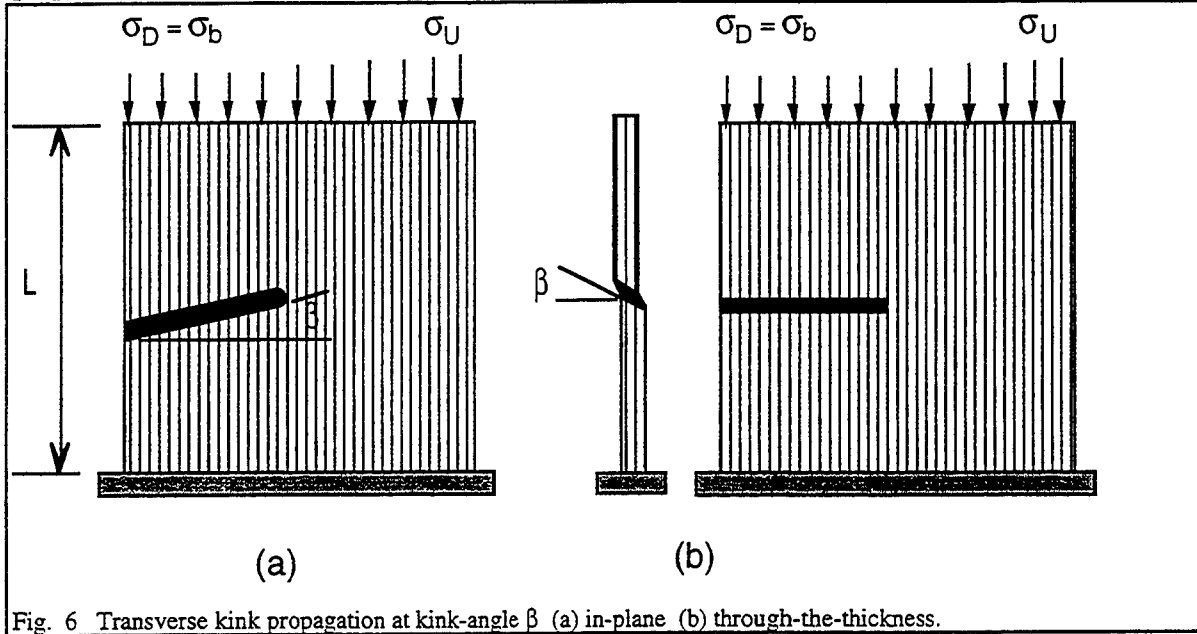


Fig. 6 Transverse kink propagation at kink-angle β (a) in-plane (b) through-the-thickness.

We must now partially relinquish the assumption of fiber inextensibility, because the elastic shortening of the composite specimen due to fiber compression is likely to dominate the shortening Δ_{kink} associated with the fiber rotations, which occur over very small distances compared with the specimen length L . However, far back from the leading edge of the kink, the total shortening Δ may be approximated by

$$\Delta = \sigma_D L / E + \Delta_{\text{kink}} \quad (32)$$

where σ_D is the downstream boundary stress, E is the composite modulus, and Δ_{kink} is based on the inextensibility, one-dimensional bending theory that we have developed. We anticipate that lock-up will occur downstream, and therefore, as indicated in Fig. 6, the downstream stress σ_D will be equal to the broadening stress σ_b . The downstream shortening Δ_{kink} will be written as the sum

$$\Delta_{\text{kink}} = \Delta_{\text{bend}} + w(1 - \cos 2\beta) \quad (33)$$

where Δ_{bend} is the shortening due to fiber bending, and the last term is provided by the rotation of the locked portion of the kink. Then, for a kink propagating statically under a fixed shortening Δ , the upstream boundary stress σ_U must satisfy

$$\sigma_U L / E = \sigma_b L / E + \Delta_{\text{bend}} + w(1 - \cos 2\beta) \quad (34)$$

During steady kink propagation, upstream strain energy is converted to downstream strain energy and plastic shear dissipation. Accordingly, in units of energy per unit original width, per unit composite thickness

$$\frac{1}{2} \frac{\sigma_U^2 L}{E} = \frac{1}{2} \frac{\sigma_b^2 L}{E} + W_m + W_\tau + \sigma_b w (1 - \cos 2\beta) \quad (35)$$

where W_m is the bending strain energy, W_τ is the work done by the sliding shear stresses in the bent portions of the kink, and the last term (see Eq. (22)) is the work that has been done by the shear stress τ_L in the locked kink segment of length w . We can eliminate w from Eqs. (34-35) to get the result

$$\sigma_U = \sigma_b + \sqrt{\frac{2E}{L} (W_m + W_\tau - \sigma_b \Delta_{\text{bend}})} \quad (36)$$

for the upstream propagation stress.

To make this explicit, we adopt the rigid-plastic idealization $\tau_s(\phi) \equiv \tau_L$. The shortening due to bending is

$$\Delta_{\text{bend}} = 2 \int_0^{\bar{s}} (1 - \cos \phi) ds = 2 \int_0^{2\beta} \frac{1 - \cos \phi}{d\phi/ds} d\phi \quad (37)$$

and making use of the nondimensionalization (27) as well as the connection (29) between $d\phi/ds$ and ϕ leads to

$$\Delta_{\text{bend}} = d \sqrt{\frac{E}{\tau_L}} \sqrt{\frac{\tan \beta}{2}} \int_0^\beta \frac{1 - g(\beta, \phi) \cos^2 \beta}{\sqrt{g(\beta, \phi) - 1}} d\phi \quad (38)$$

Similarly (see Eq. (16)) we have

$$W_m = 2 \int_0^{\bar{s}} \frac{1}{2} mg \frac{d\phi}{ds} ds = \frac{Ed^2}{16} \int_0^{2\beta} \frac{d\phi}{ds} d\phi = \frac{\tau_L d}{2\sqrt{\tau_L/E}} \sqrt{2 \cot \beta} \int_0^\beta \sqrt{g(\beta, \phi) - 1} d\phi \quad (39)$$

and

$$W_\tau = 2\tau_L \int_0^{\bar{s}} \int_0^\phi g(\beta, \theta) d\theta ds = 2\tau_L \int_0^{2\beta} \frac{\tan \beta - \frac{\sin(\beta - \phi)}{\cos \beta}}{d\phi/ds} d\phi = \frac{\tau_L d (2 \tan \beta)^{3/2}}{4\sqrt{\tau_L/E}} \int_0^\beta \frac{d\phi}{\sqrt{g(\beta, \phi) - 1}} \quad (40)$$

Putting (38)-(40) into Eq. (36) yields the result

$$\frac{\sigma_U}{\tau_L} = \frac{\sigma_b}{\tau_L} + \left(\frac{d}{L}\right)^{1/2} \left(\frac{\tau_L}{E}\right)^{-3/4} \left(\frac{8}{\tan \beta}\right)^{1/4} \left\{ \int_0^\beta \sqrt{g(\beta, \phi) - 1} d\phi \right\}^{1/2} \quad (41)$$

for the propagation stress, illustrated in Fig. 7 for several values of β .

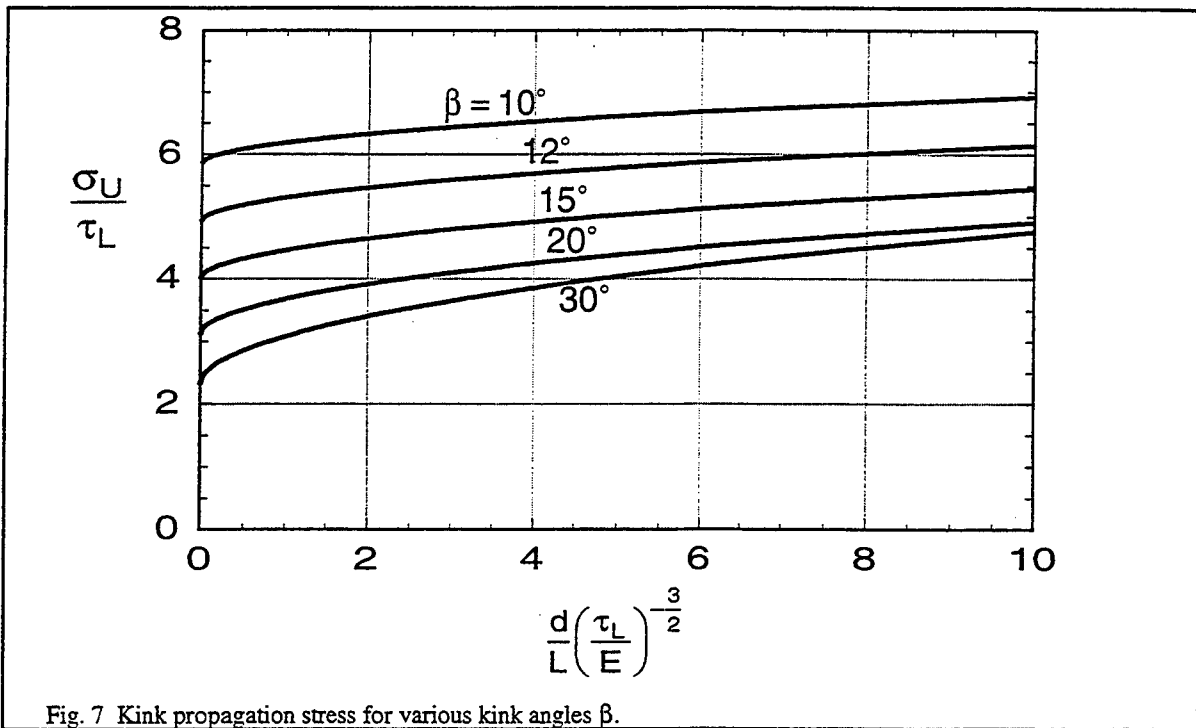


Fig. 7 Kink propagation stress for various kink angles β .

The size w of the locked part of the downstream kink may now easily be found from Eq. (34). For the range of parameters in Fig. 7, w does indeed turn out positive, verifying the presumption of downstream lock-up. The results are shown non-dimensionally in Fig. 8.

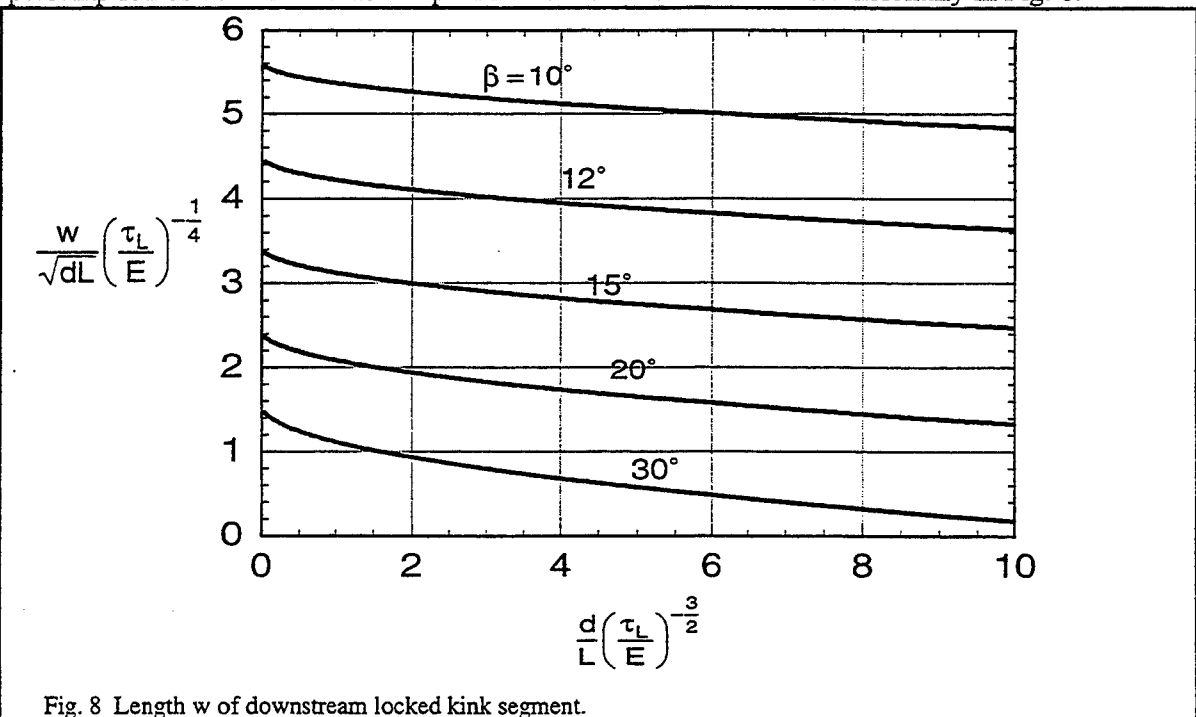


Fig. 8 Length w of downstream locked kink segment.

A few remarks follow about these calculations and results, before we discuss their significance, or lack thereof, vis-a-vis design.

(a) An asymptotic approximation to (41) for small β gives

$$\frac{\sigma_U}{\tau_L} \approx \frac{\sigma_b}{\tau_L} + \left(\frac{\pi B}{2} \right)^{1/2} \beta^{3/4} \quad (42)$$

where

$$B \equiv \frac{d}{L} \left(\frac{\tau_L}{E} \right)^{-3/2} \quad (43)$$

Remarkably, if we retain the exact result (24) for σ_b in (42), the difference from the exact answers (41) plotted in Fig. 7 stays well under 1% throughout the range shown.

(b) The small- β results for Δ , W_m and W_τ are

$$\frac{\Delta_{\text{bend}}}{d} \sqrt{\frac{\tau_L}{E}} \approx \frac{3\pi\beta^{5/2}}{8}, \quad \frac{4W_m\sqrt{\tau_L/E}}{\tau_L d} \approx \frac{\pi\beta^{3/2}}{2}, \quad \text{and} \quad \frac{4W_\tau\sqrt{\tau_L/E}}{\tau_L d} \approx 2\pi\beta^{3/2}. \quad (44)$$

In this approximation the bending strain energy is one-fourth the work of shear stress in the curved part of the kink; the exact ratio W_m/W_τ given by Eqs. (39-40) is only slightly less than 1/4 at $\beta=30^\circ$. It can be verified that Eqs. (36) and (44) are consistent with (42).

(c) The calculation of σ_U on the basis of Eqs. (34-35) is entirely equivalent to that implied by the Maxwell stress-displacement diagram shown schematically in Fig. 9. The dots denote the upstream and downstream states of the propagating kink, each at the same shortening Δ , consistent with Eq. (34). Equality of the shaded regions ensures that the work done per unit width downstream is the same as that upstream, as specified by Eq. (35).

(d) Locked kink widths predicted in Fig. 8 for steady-state transverse propagation can be much greater than the sizes of kink segments bounded by fiber breaks studied by Fleck et al (1995). For example, $\tau_L/E=.0008$, $\beta=15^\circ$, and $d/L=10^{-4}$ give $w/d \approx 48$; from Fleck et al (1995), we find that for $\tau_Y/E=.0004$ and a fiber failure strain equal to .015, the broken-segment size is $w/d \approx 16$.

(e) If kinking does not occur until a shortening Δ larger than the critical value $\sigma_U L/E$ for steady propagation has been imposed, we can expect *accelerating* transverse kink propagation under this fixed Δ . When the process is completed, the stress will have dropped to σ_b , and a locked-up, broadened kink can be expected to extend transversely across the full width of the specimen. The size of the locked portion of the kink could then be estimated by

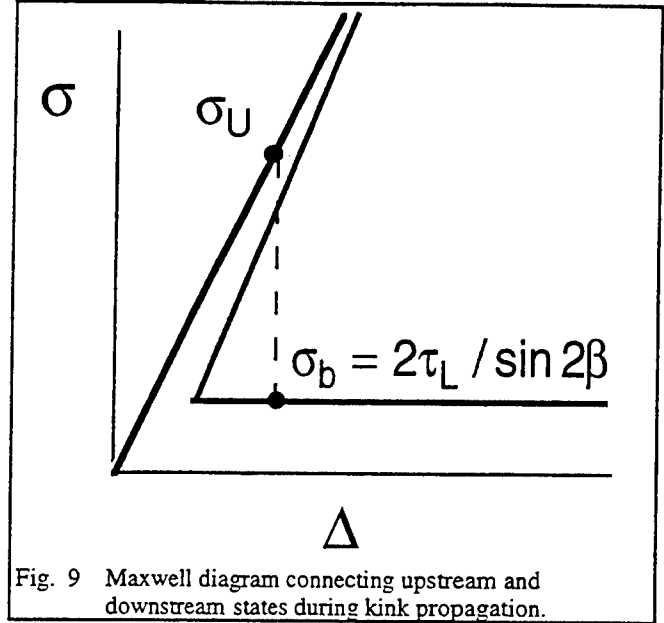


Fig. 9 Maxwell diagram connecting upstream and downstream states during kink propagation.

$$w = \frac{\bar{\Delta} - \sigma_b L / E - \Delta_{\text{bend}}}{1 - \cos 2\beta} \approx \frac{\bar{\Delta} - \sigma_b L / E - (3\pi d / 8)\beta^{5/2}(\tau_L / E)^{-1/2}}{1 - \cos 2\beta}. \quad (45)$$

(f) We have so far ignored the possible effects of testing-machine compliance in the analysis of transverse propagation. This extra compliance can be roughly taken into account by replacing the specimen length L , wherever it appears in any of the results, by a larger effective length L' .

DISCUSSION AND CONCLUDING REMARKS

It will not have escaped the reader's attention that we have taken the kink angle β as a prescribed quantity in our treatments of both band broadening and transverse propagation, but have said nothing about how β is to be chosen. The β question has come up repeatedly in the literature, and suggestions of varying degrees of plausibility have been offered to predict kink angles. A wide variety of β 's have actually been observed, and simple theoretical criteria for β based only on analyses of final, uniform kinked states are not promising. Sutcliffe and Fleck (1997) have made extensive numerical 2D finite element studies of kink initiation, evolution, and propagation, showing clearly how kink fronts reorient themselves naturally as they propagate in order to point in stabilized β directions. But while the dependence of β on various physical parameters was studied, and trends discerned, easy recipes are not yet available. So in the present work, we leave β unspecified.

But this may not matter much when we consider what roles the band-broadening stress or the transverse propagation stress might play in design. Because both are deterministic quantities, not sensitive to initial imperfections, waviness, or notches, it is enticing to adopt one or the other as a design limit, but a glance at their magnitudes is sobering. Assuming $\beta < 20^\circ$, we could say (Fig. 7) that kink propagation could not occur if we kept $\sigma/\tau_L < 3$. But this would constitute a severe restriction. For example, take $\tau_L = 2\tau_Y$ and $\gamma_Y = .01$; then, the propagation stress $\sigma = 6\tau_Y$ is substantially less than the peak kinking stresses $\sigma_c \approx 16\tau_Y$ given by Eq. (3) for an imperfection $\bar{\phi} = 3^\circ$. This is just an example, but it highlights the dilemma facing the composites designer: he or she must come to grips with the statistics and control of imperfections, echoing the similar situation long faced by engineers who must design shells against buckling. Picking σ_U , or the even lower band-broadening stress σ_b , as the design stress is unduly conservative. On the other hand, the availability of continued deformation at the band-broadening stress confers a welcome pseudo-ductility on the composite after its initial kinking stress is reached.

Finally, we suggest that the present results found for the band-broadening stress, derived on the assumption that there is no fiber fracture, remain approximately applicable when multiple fiber fracture occurs (Fig. 3). During band broadening under increasing shortening, the applied stress can be expected to oscillate if fibers break and lock-up proceeds in discrete steps, not

necessarily in unison all along the kink band; but the *average* stress during broadening should be about the same as that for intact fibers.

ACKNOWLEDGEMENTS

This work was supported by NSF (award 92161350), DARPA (subagreement KK3007 with the University of California at Santa Barbara), ONR (contract 0014-91-J-1916), the Division of Engineering and Applied Sciences, Harvard University, and the Department of Engineering, Cambridge University.

REFERENCES

- Argon A.S. (1972) Fracture of composites. *Treatise of Materials Science and Technology*, Vol. 1, Academic Press, New York.
- Budiansky, B. and Fleck, N.A. (1993) Compressive failure of fibre composites. *J Mech. Phys. Solids* **41**(1) 183-211.
- Budiansky, B. and Fleck, N.A. (1994) Compressive kinking of fiber composites: A topical review. *Applied Mechanics Reviews*, **47**(6), part 2.
- Fleck, N.A. (1997) Compressive failure of fibre composites. *Advances in Applied Mechanics*, Academic Press, New York, **33**, 43-117.
- Fleck, N.A., and Budiansky, B. (1991) Compressive failure of fibre composites due to microbuckling. *Proc 3rd Symp on Inelastic Deformation of Composite Materials*, Troy, New York, 29 May-1 June, 1990, (ed. G. Dvorak), Springer Verlag, New York, 235-273.
- Fleck, N.A., Deng, L. and Budiansky, B. (1995) Prediction of kink width in fiber composites. *J. Appl. Mech.*, **62**, 329-337.
- Fleck, N.A. and Jelf, P.M. (1995) Deformation and failure of a carbon fibre composite under combined shear and transverse loading. *Acta Metall. et Mater.*, **43**(8), 3001-3007.
- Fleck, N.A. and Shu, J.Y. (1995) Microbuckle initiation in fibre composites: a finite element study. *J. Mech. Phys. Solids*, **43**(12), 1887-1918.
- Fleck, N.A., Sivashankar, S., and Sutcliffe, M.P.F. (1997) Compressive failure of composites due to microbuckle growth. *Eur. J. Mech. A/Solids* (to be published).
- Kyriakides, S, Arseculeratne, R., Perry, E.J., and Liechti, K.M. (1995) On the compressive failure of fiber reinforced composite. *Int. J. Solids Structures*, **32**(6/7), 689-738.
- Kyriakides, S. and Ruff (1996) Aspects of the failure and postfailure of fiber composites in compression. *J. Composite Materials* (to be published).
- Liu, X.H., Moran, P.M., and Shih, C.F. (1996) The mechanics of compressive kinking in unidirectional fiber reinforced ductile matrix composites. *Composites Part B (Engineering)*,

27B(6), 553-60.

Liu, X.H. and Shih, C.F. (1996) Micromechanics of compressive kinking in composites. Brown University report.

Moran, P.M., Liu, X.H., and Shih, C.F. (1995) Kink band formation and band broadening in fiber composites under compressive loading. *Acta Metall. et Mater.* **43**(8), 2943-2958.

Moran, P.M. and Shih, C.F. (1996) Kink band propagation and broadening in ductile matrix fiber composites: experiments and analysis. *Int. J. Solids Structures* (submitted).

Rosen, B.W. (1965) Mechanics of composite strengthening. In *Fibre Composite Materials*, Am. Soc. Metals Seminar, Chapter 3.

Schultheisz, C.R. and Waas, A.M. (1996) Compressive failure of composites, Part I: Testing and micromechanical theories. *Prog. Aerospace Sci.*, **32**, 1-42.

Sivashankar, S., Fleck, N.A. and Sutcliffe, M.P.F. (1996) Microbuckle propagation in a unidirectional carbon fibre - epoxy matrix composite. *Acta Mater.* **44**(7), 2581-2590.

Sutcliffe, M.P.F. and Fleck, N.A. (1994) Microbuckle propagation in carbon fibre - epoxy composites. *Acta Metall. et Mater.*, **42**(7), 2219-2231.

Sutcliffe, M.P.F. and Fleck, N.A. (1997) Microbuckle propagation in fibre composites, *Acta Mater.* **45**(3), 921-932.

Vogler, T.J. and Kyriakides, S. (1996) Initiation and axial propagation of kink bands in fiber composites. *Acta Mater.* (to be published).

Waas, A.M. and Schultheisz, C.R. (1996) Compressive failure of composites, Part II: Experimental studies. *Prog. Aerospace Sci.*, **32**, 43-78.

27 JUN 1997

Eur. J. Mech., A/Solids, 16, n° 5, 000-000, 1997

IRIS
EJMA
No 5-97
A822
26 June 1997

Singularities in bi-materials: parametric study of an isotropic/anisotropic joint

R. DESMORAT*, ** and F. A. LECKIE*

ABSTRACT. – Problems in fracture mechanics are frequently solved in terms of crack tip singularities. Geometries other than cracks also exhibit singular stresses at points such as corners, edges and interfacial joints. Corners occurring in monolayers or multilayered media have been studied under the assumption that each layer is isotropic. For general elastic plane problems, the present study extends the earlier results to anisotropy. For orthotropic joints, generalized Dundurs parameters are introduced. Isotropic results are a limiting case of the present analysis.

In the vicinity of a singular point, the displacements and stresses may be expressed as a function of the polar coordinates $r - \theta$ by:

$$u = hr^\delta g(\theta), \quad \sigma = hr^{\delta-1} F(\theta)$$

where h is the intensity factor and δ the singularity exponent ($0 < \delta < 1$). The values of h and δ reduce to the stress intensity factor k and the complex exponent $0.5 + i\varepsilon$ for the limiting case of cracks at the interface of dissimilar media.

Using an anisotropic complex potential method, the present analysis gives δ as the solution of an eigenvalue problem and as the root of a nonlinear equation $\det \underline{A}(\delta) = 0$. It leads to a closed-form expression for g and F . The matrix \underline{A} depends on the number of layers at the singular point, their relative elastic properties and the boundary conditions such as free surface or bonded interface close to the singularity corner. A closed-form expression is derived for \underline{A} which depends on 3 generalized Dundurs parameters for a metal matrix composite isotropic metal interface joint. This compares to the 2 Dundurs parameters needed for joints with isotropic layers.

The intensity factor h of any singularity is determined from a path independent integral, using an extraction function which is more singular than that defining the actual stress state.

1. Introduction

Singular solutions are used to solve linear elastic fracture mechanics problems and the procedures are illustrated fully in standard texts such as Liebowitz (1968), Kanninen and Popelar (1985). The singular crack solutions for power-law hardening plasticity were studied by Hutchinson (1968) and Rice and Rosengren (1968). Geometries other than cracks also exhibit singular stresses at corners, edges and interfacial joints. They have been studied for angular corners of isotropic materials by Williams (1952), Bogy (1968), England (1971), Stern and Soni (1976) and Reedy (1990) and for multilayered media by

* Department of Mechanical and Environmental Engineering, University of California, Santa Barbara CA 93106-5070, U.S.A.

** On leave from Laboratoire de Mécanique et Technologie, E.N.S. de Cachan/C.N.R.S./Université Paris 6, 61 avenue du Président Wilson, F-94235 Cachan Cedex, France.

Schmauder (1989), Kelly *et al.* (1992), Reedy (1993). The study has been extended to anisotropic layers by Leguillon and Sanchez Palencia (1987) using a numerical method and then by Desmorat (1996) who derives the closed-form fields. The main results of these studies is that the singular fields for displacement and stress can be expressed as a function of the polar coordinates $r - \theta$ as (vectors are represented by bold characters and tensors are underlined):

$$(1) \quad \mathbf{u} = hr^\delta \mathbf{g}(\theta), \quad \underline{\sigma} = hr^{\delta-1} \underline{F}(\theta)$$

where the singularity exponent δ is the solution of an eigenvalue problem defined by the boundary conditions close to the tip. The intensity factor h of the problem depends on the external load and the geometry of the structure. Obviously for cracks in isotropic materials, $\delta = 0.5$ and h is the stress intensity factor K . For interfacial cracks between dissimilar materials (Rice, 1988), $\delta = 0.5 + i\varepsilon$ where ε is the oscillatory index. For interfacial cracks, ε is generally small and has a very localized effect at the crack tip on a scale smaller than the scale of the occurrence of plasticity.

A knowledge of the existence and the strength of a singularity is important in *FE* computations because it is easy to misjudge a singularity as a stress concentration even with a refined mesh of the zone close to the singular corner. The singular fields also provide a means of obtaining additional information about the stress, strain and displacement fields by using the theoretical singular solution as an input to a very detailed *FE* computation (Mc Meeking, 1977).

In the present paper, we will focus on joints consisting of anisotropic layers and particularly on the composite joint described in Figure 2 when a bar of metal matrix composite (MMC) is embedded in a uniform isotropic metal. For our application the MMC considered is the $\text{Al}_2\text{O}_3/\text{Al}$ composite (materials properties in appendix), with the direction of the fibers coinciding with the longitudinal direction of the bar. The isotropic metallic joint is an aluminium alloy (Young's modulus $E_a = 70$ GPa, Poisson's ratio $\nu_A = 0.3$). The geometry of the joint is a particular case of Figure 1 with an isotropic layer A and with $b = 180^\circ\text{C}$.

The closed-form singular expression of the stress and displacement fields is derived from an anisotropic complex potential method in plane elasticity. Generalized Dundurs parameters are introduced for joints consisting of two orthotropic layers. The exponent δ is shown to be the solution of an eigenvalue problem and is the root of a nonlinear equation. The intensity factor h may be derived from a path-independent integral using the reciprocal elastic theorem and a singular function (Stern and Soni, 1976; Babuska and Miller, 1984; Leguillon and Sanchez-Palencia, 1987). The expression for h will be derived in the present analysis, but its evaluation is left to a later paper.

1.1. INTENSITY FACTOR AND MIXED MODES

As it is for the crack problem, the intensity factors are defined for each mode, 1 or 2 as:

$$(2) \quad \lim_{r \rightarrow 0} r^{1-\delta} \sigma_{\theta\theta}|_{\theta=0} = h_1, \quad \lim_{r \rightarrow 0} r^{1-\delta} \sigma_{r\theta}|_{\theta=0} = h_2$$

The factors h_j play a role similar to that of the stress intensity factors k_j of interfacial crack problems (Rice, 1988), with the same property of mixed modes as we will see later. The factors h_1 and h_2 are related to the global intensity factor h for which the dependence on the structure size L and the applied load σ_∞ is given by Reedy (1990):

$$(3) \quad h = \sqrt{h_1^2 + h_2^2} = \tilde{h} \sigma_\infty L^{1-\delta}$$

where \tilde{h} is a dimensionless shape factor. The mixity angle ψ is classically defined as:

$$(4) \quad \tan \psi = \frac{h_2}{h_1}$$

and is not size dependent.

1.2. DUNDURS PARAMETERS

Following Dundurs (1967, 1969) for bi-materials composed of elastic isotropic layers A and B with in-plane loading and no applied displacement (Fig. 1), the material parameters which define the stress field are reduced to two Dundurs parameters α_{iso} , β_{iso} defined as:

$$(5) \quad \alpha_{iso} = \frac{\Gamma(1 + \kappa_A) - 1 - \kappa_B}{\Gamma(1 + \kappa_A) + 1 + \kappa_B}, \quad \beta_{iso} = \frac{\Gamma(\kappa_A - 1) - \kappa_B + 1}{\Gamma(1 + \kappa_A) + 1 + \kappa_B}$$

where Γ is the ratio of the shear moduli G_B/G_A and κ is the plane deformation parameter, $\kappa = 3 - 4\nu$ for plane strain and $\kappa = (3 - \nu)/(1 + \nu)$ for plane stress state, ν being the Poisson's ratio. With these notations, the value of the oscillatory index ε is given by:

$$(6) \quad \varepsilon = \frac{1}{2\pi} \ln \left(\frac{1 - \beta_{iso}}{1 + \beta_{iso}} \right)$$

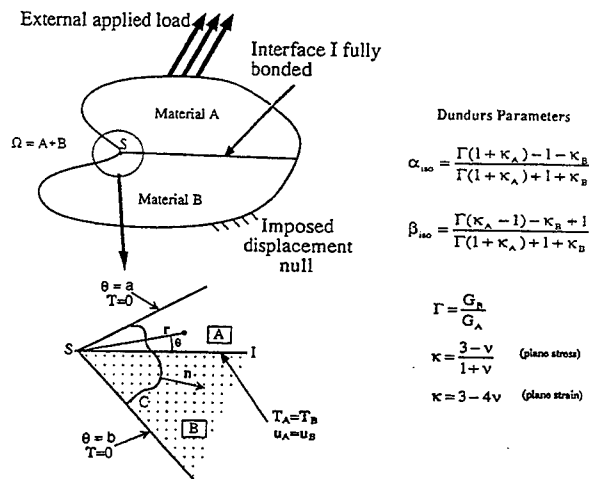


Fig. 1. – Bi-material consisting of layers A and B : local geometry and Dundurs parameters.

For pairs of materials with the same Poisson's ratio, $\kappa_A = \kappa_D = \kappa$, the relationship between the mismatch parameters is simply $\beta_{iso} = \alpha_{iso}(\kappa - 1)/(\kappa + 1)$. It is illustrated by Schmauder (1986) and Kelly *et al.* (1992) that two large classes of joints exists for which either:

$$(7) \quad a) \quad \beta_{iso} = 0 \quad \text{or} \quad b) \quad \beta_{iso} = \frac{\alpha_{iso}}{4}$$

depending on the material combinations. This means for such circumstances the number of independent material parameters can be reduced to one.

2. The complex potential method for anisotropic elasticity or L.E.S. representation – in-plane loading

The complex potentials for anisotropic bodies have been introduced by Lekhnitskii (1963), Eshelby *et al.* (1953), Stroh (1958) and summarized by Suo (1990). For convenience the works of Lekhnitskii, Eshelby and Stroh are referenced to as the (L.E.S.) representation. The complex potentials formally satisfy the equilibrium, the compatibility equations and the elastic stress/strain laws but the specific form of the solution is gained by matching boundary conditions.

For a general anisotropic material the elastic behavior may be written as a linear relationship between the generalized strains ε and stress σ :

$$(8) \quad \varepsilon_i = \sum_{j=1}^6 s_{ij} \sigma_j \quad \text{or} \quad \sigma_i = \sum_{j=1}^6 c_{ij} \varepsilon_j$$

with the standard notations,

$$(9) \quad \{\varepsilon_i\} = [\varepsilon_{11}, \varepsilon_{22}, \varepsilon_{33}, \gamma_{23}, \gamma_{31}, \gamma_{12}]^T, \quad \{\sigma_i\} = [\sigma_{11}, \sigma_{22}, \sigma_{33}, \sigma_{23}, \sigma_{31}, \sigma_{12}]^T$$

$(\cdot)^T$ being the transpose. The 6×6 matrices $[c_{ij}]$ and $[s_{ij}]$ are the compliance and stiffness matrices respectively.

For two dimensional problems with in-plane loading of orthotropic materials, the strains and stresses reduce to:

$$(10) \quad \{\varepsilon_i\} = [\varepsilon_{11}, \varepsilon_{22}, \gamma_{12}]^T, \quad \{\sigma_i\} = [\sigma_{11}, \sigma_{22}, \sigma_{12}]^T$$

where $[c_{ij}]$ and $[s_{ij}]$ are,

$$(11) \quad [c_{ij}] = \begin{pmatrix} c_{11} & c_{12} & 0 \\ c_{12} & c_{22} & 0 \\ 0 & 0 & c_{66} \end{pmatrix}, \quad [s_{ij}] = \begin{pmatrix} s_{11} & s_{12} & 0 \\ s_{12} & s_{22} & 0 \\ 0 & 0 & s_{66} \end{pmatrix}$$

For an isotropic material under plane stress or plane strain deformation, $s_{11} = s_{22} = (1 + \kappa)/8G$, $s_{12} = (\kappa - 3)/8G$ and $s_{66} = 1/G$.

For the in-plane loading condition, the elastic field may be represented by two holomorphic functions $f_1(z_1)$ and $f_2(z_2)$, where,

$$(12) \quad z_j = x + \mu_j y$$

are the complex coordinates (for orthotropic materials these two coordinates are usually different). The complex numbers μ_j depend on the materials properties. The means of obtaining those numbers have been proposed by Eshelby *et al.* (1953) and Lekhnitskii (1963) and are summarized by Suo (1990). For orthotropic materials, μ_j are the roots with positive imaginary part of the fourth order equation.

$$(13) \quad \lambda \mu^4 + 2\rho \lambda^{1/2} \mu^2 + 1 = 0$$

which is valid for both plane stress and plane strain states. For plane stress, the constants λ and ρ which measure the material anisotropy are given by:

$$(14) \quad \lambda = \frac{s_{11}}{s_{22}}, \quad \rho = \frac{1}{2}(2s_{12} + s_{66})(s_{11}s_{22})^{-1/2}$$

General expressions for the complex numbers are

$$(15) \quad \begin{cases} \mu_1 = i\lambda^{-1/4}(n+m), & \mu_2 = i\lambda^{-1/4}(n+m) & \text{for } 1 < \rho < \infty \\ \mu_1 = \lambda^{-1/4}(in+m), & \mu_2 = \lambda^{-1/4}(in+m) & \text{for } -1 < \rho < 1 \\ \mu_1 = \mu_2 = i\lambda^{-1/4} & & \text{for } \rho = 1 \end{cases}$$

where,

$$(16) \quad n = \left[\frac{1}{2}(1+\rho) \right]^{1/2}, \quad m = \left[\frac{1}{2}(1-\rho) \right]^{1/2}$$

The positiveness of the strain energy requires that $\lambda > 0$ and $-1 < \rho < \infty$. For isotropic materials, $\lambda = \rho = 1$, $\mu_1 = \mu_2 = i$. Plane strain deformation can be treated by a simple change of compliance with:

$$(17) \quad s'_{ij} = s_{ij} - \frac{s_{i3}s_{j3}}{s_{33}}$$

The value of the different parameters of the FP/A1 layer (see appendix) shown in Figure 2 for a plane strain state are:

$$(18) \quad \lambda = 0.699, \quad \rho = 1.388, \quad \mu_1 = 1.676i, \quad \mu_2 = 0.714i$$

The displacements u , stresses $\underline{\sigma}$ and resultant forces on an arc \mathbf{T} (the medium being kept on the left hand side as the observer travel in the positive direction of the arc, Fig. 1) can be derived from the complex potentials and are:

$$(19) \quad u_i = 2\text{Re} \left\{ \sum_{j=1}^2 A_{ij} f_j(z_j) \right\}, \quad T_i = -2\text{Re} \left\{ \sum_{j=1}^2 L_{ij} f_j(z_j) \right\}$$

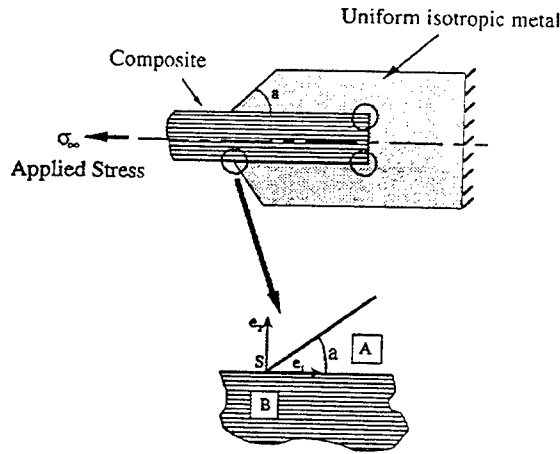


Fig. 2. - MMC Joint: bar of FP/Al embedded in an aluminium body.

$$(20) \quad \sigma_{2i} = 2\text{Re} \left\{ \sum_{j=1}^2 L_{ij} f'_j(z_j) \right\}, \quad \sigma_{1i} = -2\text{Re} \left\{ \sum_{j=1}^2 L_{ij} \mu_j f'_j(z_j) \right\}$$

where f' is the derivative of f . For arbitrary anisotropic materials, general expressions for \underline{A} and \underline{L} are given by Lekhnitskii (1963). For orthotropic materials, they simplify as:

$$(21) \quad \underline{A} = \begin{pmatrix} s_{11}\mu_1^2 + s_{12} & s_{11}\mu_2^2 + s_{12} \\ s_{21}\mu_1 + \frac{s_{22}}{\mu_1} & s_{22}\mu_2^2 + \frac{s_{22}}{\mu_2} \end{pmatrix}, \quad \underline{L} = \begin{pmatrix} -\mu_1 & -\mu_2 \\ 1 & 1 \end{pmatrix}$$

In order to define the stress and displacement field for isotropic materials (Stroh, 1958) introduced the connection between the (L.E.S.) and isotropic complex potentials (Muskhelishvili, 1963) by the means of the positive hermitian matrix

$$(21) \quad \underline{B} = i\underline{A}\underline{L}^{-1} = \begin{pmatrix} 2n\lambda^{1/4}(s_{11}s_{22})^{1/2} & i[(s_{11}s_{12})^{1/2} + s_{12}] \\ -i[(s_{11}s_{12})^{1/2} + s_{12}] & 2n\lambda^{1/4}(s_{11}s_{22})^{1/2} \end{pmatrix}$$

which comes from the (L.E.S.) representation but remains defined for isotropy. We will later use the \underline{B} matrices to derive the generalized Dundurs parameters.

For isotropic materials, $\rho = 1$ and the matrices \underline{A} and \underline{L} of eq. (16)-(17) can no longer be inverted. In this circumstance, another complex representation has to be considered (Suo *et al.*, 1990). The connection between both degenerate and anisotropic stress field is done in paragraph 4.4.

3. Bi-material matrices and generalized Dundurs parameters

For joints consisting of two orthotropic layers A and B (Fig. 1), two bi-material matrices \underline{H} and \underline{G} , which are hermitian, positive-definite and involve material elastic constants of both layers are defined as:

$$\underline{H} = \underline{B}_A + \overline{\underline{B}}_B, \quad \underline{G} = \underline{B}_B + \underline{B}_A$$

For a pair of materials with symmetries as high as those defining orthotropy, the expression of the \underline{H} -matrix simplifies and reveals the constant β which is the generalization of the second Dundurs parameter β_{iso} (Suo, 1990),

$$(24) \quad \begin{cases} \underline{H} = H_{11} \begin{pmatrix} 1 & -i\beta \left(\frac{H_{22}}{H_{11}} \right)^{1/2} \\ i\beta \left(\frac{H_{22}}{H_{11}} \right)^{1/2} & \frac{H_{22}}{H_{11}} \end{pmatrix} \\ H_{11} = [2n\lambda^{1/4}(s_{11}s_{22})^{1/2}]_A + [2n\lambda^{1/4}(s_{11}s_{22})^{1/2}]_B \\ H_{22} = [2n\lambda^{-1/4}(s_{11}s_{22})^{1/2}]_A + [2n\lambda^{-1/4}(s_{11}s_{22})^{1/2}]_B \end{cases}$$

$$(25) \quad \beta = \frac{[(s_{11}s_{12})^{1/2} + s_{22}]_B - [(s_{11}s_{12})^{1/2} + s_{12}]_A}{(H_{11}H_{22})^{1/2}}$$

For orthotropic materials, the second b-material matrix \underline{G} becomes (Eq. 23):

$$(26) \quad \underline{G} = H_{11} \begin{pmatrix} \alpha_1 & i\beta \left(\frac{H_{22}}{H_{11}} \right)^{1/2} \\ -i\beta \left(\frac{H_{22}}{H_{11}} \right)^{1/2} & \alpha_2 \end{pmatrix}$$

where two additional generalized Dundurs parameters α_1, α_2 appear. They reduce to α_{iso} when both A and B are isotropic. A fourth parameter $\chi = H_{22}/H_{11}$ also appears in the expressions of \underline{H} and \underline{G} which reduces to unity for isotropic layers. For the orthotropic bimaterial, we define

$$(27) \quad \alpha_1 = \frac{[2n\lambda^{1/4}(s_{11}s_{12})^{1/2}]_B - [2n\lambda^{1/4}(s_{11}s_{12})^{1/2}]_A}{H_{11}}$$

$$(28) \quad \alpha_2 = \frac{[2n\lambda^{-1/4}(s_{11}s_{12})^{1/2}]_B - [2n\lambda^{-1/4}(s_{11}s_{12})^{1/2}]_A}{H_{11}}$$

Generally for orthotropic materials $\lambda^{1/4}$ is close to unity (for the FP/Al $\lambda^{1/4} = 0.915$), and thus the parameters α_1 and α_2 are almost equal, leading to $\chi \approx 1$, and may be approximated by a mean value α . The expression for α is the average value of α_1 and α_2 ,

$$(29) \quad \alpha = \frac{[n(\lambda^{1/4} + \lambda^{-1/4})(s_{11}s_{12})^{1/2}]_B - [2n(\lambda^{1/4} + \lambda^{-1/4})(s_{11}s_{12})^{1/2}]_A}{H_{11}}$$

and using $\lambda^{1/4} + \lambda^{-1/4} \approx 2$ gives the simpler form which be used in the following development:

$$(30) \quad \alpha = \frac{2n_B(s_{11}s_{12})_B^{1/2} - 2n_A(s_{11}s_{12})_A^{1/2}}{H_{11}}$$

This expression for α and those for $\alpha_1, \alpha_2, \beta$ reduce naturally for isotropic layers to the corresponding classical mismatch parameters $\alpha_{iso}, \beta_{iso}$.

Let us consider now the condition when A is isotropic B is isotropic. Then the matrix \underline{B}_A and the expression of \underline{H} and \underline{G} (Eq. 27 and 26) remain valid, with the equality.

$$(31) \quad [2n\lambda^{1/4}(s_{11}s_{12})^{1/2}]_A = [2n\lambda^{-1/4}(s_{11}s_{12})^{1/2}]_A = (1 + \kappa_A)/4G_A$$

The generalized Dundurs parameters for the joint α_1, α_2 are still given by Eq. (27)-(28) leading to the important simplification which will be used for the parametric study of the composite joint,

$$(32) \quad \chi = \frac{H_{22}}{H_{11}} = 1 + \alpha_2 - \alpha_1$$

In case of two isotropic layers A and B Eq. (32) becomes $\chi = 1$, with $\alpha_1 = \alpha_2 = \alpha = \alpha_{iso}$.

4. Singular solutions for corners in bi-materials

We now consider the singularities in stress and strain which occur when a corner is formed with two completely anisotropic elastic materials A and B (Fig. 1). Perfect bonding between A and B is assumed.

For general anisotropy, the most general expressions for the matrices \underline{A} and \underline{B} have to be considered. For the particular case of orthotropic layers, \underline{A} and \underline{B} are defined by Eq. (21). Isotropic results will be obtained as a limiting case of the general anisotropic study (paragraph 4.4).

The singular solutions exhibit a major term close to the singular point S for which the stresses are proportional to $r^{\delta-1}$, and the displacements to r^δ . In case of complex δ , the real part of the expressions containing δ is selected in order to give real fields. The magnitude of the exponent δ must be positive for the strain energy to remain finite and smaller than 1 for the stress field to be singular. Its value depends on the local geometry (by the angles a and b) and on the material properties of each layer (by the matrices \underline{B}). Using the L.E.S. representation, the complex potentials of materials A and B are of the form:

$$(32) \quad f_k^A(z_k^A) = \phi_k^A \cdot (z_k^A)^\delta, \quad f_k^B(z_k^B) = \phi_k^B \cdot (z_k^B)^\delta$$

where ϕ_k^A, ϕ_k^B ($k = 1, 2$) are complex coefficients, introducing four real constants to be determined for each component of the joint. They are related to the normalizing h -factor (Eq. 1). Using polar coordinates, the complex coordinates are (Eq. 12):

$$(34) \quad z_k^A = r(\cos \theta + \mu_k^A \sin \theta), \quad z_k^B = r(\cos \theta + \mu_k^B \sin \theta)$$

Defining for each layer:

$$(35) \quad \Phi = [\phi_1, \phi_2]^T, \quad \underline{Z} = \text{diag}[z_1, z_2], \quad \mathbf{f} = [f_1, f_2]^T$$

then the complex potentials may be represented by the vector:

$$(36) \quad \mathbf{f} = \underline{Z}^\delta \Phi$$

The various field quantities are now from Eq. (16):

$$(37) \quad \mathbf{u} = \{u_i\} = \underline{A} \mathbf{f} + \overline{\underline{A}} \overline{\mathbf{f}} = \underline{A} \underline{Z}^\delta \Phi + \overline{\underline{A}} \overline{\underline{Z}}^\delta \overline{\Phi}$$

$$(38) \quad -\mathbf{T} = \{-T_i\} = \underline{L} \mathbf{f} + \overline{\underline{L}} \overline{\mathbf{f}} = \underline{L} \underline{Z}^\delta \Phi + \overline{\underline{L}} \overline{\underline{Z}}^\delta \overline{\Phi}$$

4.1. SINGULARITY EXPONENT AS AN EIGENVALUE PROBLEM

It proves convenient to introduce the 2×2 matrices \underline{X} , \underline{Y} , $\underline{1}$, $\underline{0}$ defined by

$$(39) \quad \underline{X} = \underline{L} \underline{Z}^\delta \underline{L}^{-1}, \quad \underline{Y} = \overline{\underline{X}}^{-1} \underline{X}, \quad \underline{1} = \begin{pmatrix} 1 & 0 \\ 0 & 1 \end{pmatrix}, \quad \underline{0} = \begin{pmatrix} 0 & 0 \\ 0 & 0 \end{pmatrix}$$

The equilibrium and the compatibility equations are automatically satisfied by Eq. (37)-(38). The boundary conditions of the joint of Figure 1 are of two kinds. At the free surfaces where $\theta = a$ and $\theta = -b$, $\mathbf{T} = 0$ and since the interface I is assumed fully bonded, $\mathbf{u}_A = \mathbf{u}_B$ and $\mathbf{T}_A = \mathbf{T}_B$ for $\theta = 0$. The application of these conditions leads to a set of linear equations which can be written:

$$(40) \quad \underline{K}(\delta) \mathbf{V} = 0$$

\underline{K} is an 8×8 matrix depending on the matrix \underline{B}_A , \underline{B}_B , $\underline{Y}_A = \underline{Y}(\theta = a, \delta)$, $\underline{Y}_B = \underline{Y}(\theta = b, \delta)$ and \mathbf{V} depends on 8 real constants to be determined,

$$(41) \quad \underline{K} = \begin{pmatrix} \underline{Y}_A & \underline{1} & \underline{0} & \underline{0} \\ \underline{0} & \underline{0} & \underline{Y}_B & \underline{1} \\ \underline{1} & \underline{1} & -\underline{1} & -\underline{1} \\ \underline{B}_A & -\underline{B}_A & -\underline{B}_B & \underline{B}_B \end{pmatrix}, \quad \mathbf{V} = \begin{pmatrix} (\underline{L}\Phi)_A \\ (\overline{\underline{L}}\Phi)_A \\ (\underline{L}\Phi)_B \\ (\overline{\underline{L}}\Phi)_B \end{pmatrix}$$

The matrices \underline{Y} generally depends on the angle a (or $-b$), the exponent δ and on the complex numbers μ_k of the considered layer. From Eq. (39),

$$(42) \quad \begin{cases} \underline{Y}_A = \underline{L}_A(\underline{Z}_A(a))^{-\delta} \underline{L}_A^{-1} \underline{L}_A(\underline{Z}_A(a))^{-\delta} \underline{L}_A^{-1}, \\ \underline{Y}_B = \underline{L}_B(\underline{Z}_B(-b))^{-\delta} \underline{L}_B^{-1} \underline{L}_B(\underline{Z}_B(-b))^{-\delta} \underline{L}_B^{-1}. \end{cases}$$

The search of nontrivial solution leads to an eigenvalues problem which gives the singularity exponent δ as the smallest positive root of $\det \underline{K}(\delta) = 0$. By defining

$$(43) \quad \mathbf{v} = \frac{(\underline{L}\Phi)_A}{h}, \quad \mathbf{v} = \frac{(\underline{L}\Phi)_B}{h}$$

it is possible to reduce the size of the determinant from 8×8 to 2×2 , the eigenvalue problem (40)-(41) becoming

$$(44) \quad \underline{A}\mathbf{v} = \underline{0}, \quad \underline{Y}_A\mathbf{v} + \underline{v} = \underline{0}$$

where \underline{A} is the 2×2 matrix defined by

$$(45) \quad \underline{A} = \underline{B}_A + \underline{B}_A\underline{Y}_A - [\underline{B}_B + \underline{B}_B\underline{Y}_B] \cdot (\underline{1} - \underline{Y}_B)^{-1} \cdot (\underline{1} - \underline{Y}_A)$$

and the singularity exponent is now found as the smallest positive root of the 2×2 determinant:

$$(46) \quad \det \underline{A}(\delta) = 0$$

For each layer, \underline{B} and \underline{Y} are functions of the stiffness s_{11} , s_{22} , s_{12} , s_{66} . Thus, the singularity exponent δ depends on 8 material parameters (for a bi-material) when the geometry is represented by the two angles a and b . Singular solutions also exist for which $\delta^* < 0$ and use shall be of one of them later to determine the h -factor. It should be noticed that if δ is a solution then $\delta^* = -\bar{\delta}$ is also a solution (Leguillon and Sanchez-Palencia, 1987).

If the composite joint consists of a pair of isotropic materials, or if just one of them is isotropic, Eq. (45)-(46) still define the singular exponent δ . This will be justified by unifying the writing of the boundary conditions at the interface for both isotropic and anisotropic representations (paragraph 4.4).

4.2. DETERMINATION OF THE EIGENMODE

The complex eigenvector \mathbf{v} solution of Eq. (44) is found by solving the eigenvalue problem:

$$(47) \quad \underline{A} \cdot [\underline{1} - (\underline{Y}_A - \underline{1})^{-1} \cdot (\underline{Y}_A + \underline{1})] \cdot \text{Re}\{\mathbf{v}\} = \underline{0}$$

where $\text{Re}\{\mathbf{v}\}$ means the real part of \mathbf{v} . The imaginary part is then given by

$$(48) \quad \text{Im}\{\mathbf{v}\} = i(\underline{Y}_A - \underline{1})^{-1} \cdot (\underline{Y}_A + \underline{1}) \cdot \text{Re}\{\mathbf{v}\}$$

We normalize \mathbf{v} by considering the definition of the intensity factor h (Eq. 2-3) as well as the expressions of the stresses at the interface (Eq. 20 with $\theta = 0$). This ends up to $||\text{Re}\{\mathbf{v}\}||/2\delta$. The eigenvector \mathbf{w} is finally found to be:

$$(49) \quad \mathbf{w} = (\underline{1} - \underline{Y}_B)^{-1} \cdot (\underline{1} - \underline{Y}_A)\mathbf{v}$$

It should also be noticed that the mixity angle is a function of the singularity exponent,

$$(50) \quad \psi(\delta) = \tan^{-1} \left(\frac{\text{Re}\{v_1\}}{\text{Re}\{v_2\}} \right)$$

4.3. STRESSES AND DISPLACEMENTS IN ANISOTROPIC LAYERS

The knowledge of the eigenvector \mathbf{v} directly leads to the determination of the complex potentials \mathbf{f} . From Eq. (36) and (43),

$$(51) \quad \mathbf{f}_A = h \underline{Z}_A \underline{L}_A^{-1} \mathbf{v}, \quad \mathbf{f}_B = h \underline{Z}_B \underline{L}_B^{-1} \mathbf{w}$$

We get the closed-form expression of the vector \mathbf{g} and the tensor \underline{F} for each layer from Eq. (19)-(20). We only give here the full results for material B , because those for A are found by replacing \mathbf{w} by \mathbf{v} (for convenience the subscripts B are omitted),

$$(52) \quad \mathbf{g} = 2\text{Re}\{\underline{A} \underline{\tilde{Z}}^\delta \underline{L}^{-1} \mathbf{w}\}$$

$$(53) \quad F_{1i} = 2\delta \text{Re}\{(\underline{L} \underline{\tilde{Z}}^{\delta-1} \underline{L}^{-1} \mathbf{w})_i\}$$

$$(54) \quad F_{2i} = -2\delta \text{Re}\{(\underline{L} \underline{\mu} \underline{\tilde{Z}}^{\delta-1} \underline{L}^{-1} \mathbf{w})_i\}$$

with $\underline{\tilde{Z}} = \text{diag}[\cos \theta + \mu_1 \sin \theta, \cos \theta + \mu_2 \sin \theta]$, $\underline{\mu} = \text{diag}[\mu_1, \mu_2]$.

For isotropic layers the Muskhelishvili's formulation has to be considered. The related isotropic potentials complex are derived in next paragraph.

4.4. DEGENERATE CASE AND ISOTROPY

For the degenerate case when $\rho = 1$ (which includes isotropy when $\lambda = n = 1$), the complex numbers μ_j are double roots of Eq. (13) and the complex coordinates reduce to the single value,

$$(55) \quad z = x + i\lambda^{-1/4}y$$

Furthermore the matrices \underline{A} and \underline{L} of Eq. (21) can no longer be inverted, so that the L.E.S. representation is unable to define the various fields. In this circumstance, another complex representation may be used. It was introduced for layers with $\rho = 1$ and is the basis of the rescaling method introduced by Suo *et al.* (1990a) in order to convert an anisotropic elasticity problem to an equivalent isotropic problem. The resulting complex potential formulation is analogous to Muskhelishvili's representation and the holomorphic functions $\omega(z)$ and $\Omega(z)$ define the displacements \mathbf{u} , stresses $\underline{\sigma}$ and resultant forces as follow:

$$(56) \quad \lambda^{1/2} \sigma_{11} + \sigma_{22} = 4\text{Re}\{\omega'\}$$

$$(57) \quad \sigma_{22} - \lambda^{1/2} \sigma_{11} + 2i\lambda^{1/4} \sigma_{12} = 2[\bar{z}\omega'' + \Omega']$$

$$(58) \quad 2\bar{G}(u_1 + i\lambda^{1/4}u_2) = \bar{\kappa}\omega - z\bar{\omega}' - \bar{\Omega}$$

$$(59) \quad i(\lambda^{1/4}T_1 + iT_2) = \omega + z\bar{\omega}' + \bar{\Omega}$$

where $\overline{(\cdot)}$ is the conjugate and the isotropically equivalent shear modulus \tilde{G} and plane deformation parameter $\tilde{\kappa}$ are defined for plane stress by:

$$(60) \quad \tilde{G} = \frac{1}{s_{66}} = \frac{1}{2((s_{11}s_{22})^{1/2} - s_{12})}, \quad \frac{1 + \tilde{\kappa}}{4} = \frac{(s_{11}s_{22})^{1/2}}{(s_{11}s_{22})^{1/2} - s_{12}} = \frac{2(s_{11}s_{22})^{1/2}}{s_{66}}$$

and their value for plane strain are obtained by the change of compliance of Eq. (14). For isotropic materials we need to find the complex potentials $\omega(z)$ and $\Omega(z)$ corresponding to a stress singularity of exponent $\delta - 1$. These potentials have the following form,

$$(61) \quad \left(\frac{\omega(z)}{\Omega(z)} \right) = hbz^\delta$$

Knowing that the L.E.S. representation gives the correct boundary conditions even for isotropic layers, we just have to match those at the interface for both methods, anisotropic and isotropic. Along the interface I , the displacements and resultant forces can be rewritten as ($x > 0$):

$$(62) \quad \mathbf{u} = -ix^\delta(\underline{B}\mathbf{v} - \overline{\underline{B}}\overline{\mathbf{v}}), \quad \mathbf{T} = -hx^\delta(\mathbf{v} = \overline{\mathbf{v}}) \quad \text{anisotropic}$$

$$(63) \quad \mathbf{u} = hx^\delta(\underline{D}\mathbf{b} + \overline{\underline{D}}\overline{\mathbf{b}}), \quad \mathbf{T} = hx^\delta(\underline{C}\mathbf{b} + \overline{\underline{C}}\overline{\mathbf{b}}) \quad \text{isotropic}$$

where:

$$(64) \quad \underline{C} = \frac{1}{2} \begin{pmatrix} i(\delta - 1) & i \\ -(1 + \delta) & -1 \end{pmatrix}, \quad \underline{D} = \frac{1}{4G} \begin{pmatrix} \kappa - \delta & -1 \\ -i(\kappa + \delta) & -i \end{pmatrix}$$

Matching displacements and forces of both methods gives:

$$(65) \quad \mathbf{b} = [\overline{\underline{D}}^{-1}\underline{D} - \overline{\underline{C}}^{-1}\underline{C}]^{-1} \cdot [(\overline{\underline{C}}^{-1} - i\overline{\underline{D}}^{-1}\underline{B})\mathbf{v} + (\overline{\underline{C}}^{-1} + i\overline{\underline{D}}^{-1}\underline{B})\overline{\mathbf{v}}]$$

Finally, for an isotropic layer, \mathbf{g} and \underline{F} are such as:

$$(66) \quad 2G(g_1 + ig_2) = \kappa b_1 e^{i\delta\theta} - \delta \bar{b}_1 e^{-i(\delta-2)\theta} - \bar{b}_2 e^{-i\delta\theta}$$

$$(67) \quad F_{11} + F_{22} = 2\delta(b_1 e^{i(\delta-1)\theta} + \bar{b}_1 e^{-i(\delta-1)\theta})$$

$$(68) \quad F_{22} - F_{11} + 2iF_{12} = 2\delta((\delta - 1)(b_1 e^{i(\delta-3)\theta} + \bar{b}_2 e^{i(\delta-1)\theta}))$$

Thus, we verify here that for isotropic materials (or degenerate materials if only $\rho = 1$) the elastic solution may be gained by using the anisotropic complex representation in order to derive the eigenvalue problem based on the boundary conditions. By using the degenerate representation (56)-(59), we obtain the stress and displacement fields.

4.5. REMARK ON THE LIMITING CASE OF A CRACK

The singular solution at a crack tip between two dissimilar anisotropic elastic materials is obtained here as the limiting case of the corner problem, with $a = -b = \pi$. The eigenvalue problem to be considered is still (44), but the matrix \underline{A} can be expressed in terms of bi-material matrices: $\underline{A} = \underline{H} + e^{2i\delta\pi}\overline{\underline{H}}$ as shown by Suo (1990) who completed the stress analysis.

For a crack between orthotropic materials, the oscillatory index ε has formally the same expression as for the isotropic case (Eq. 6), where β_{iso} is replaced by its orthotropic generalization β . For a crack between aluminum and FP/Al the value is $\varepsilon = 0.035$.

5. Composite joint

The expressions which have been developed are now applied to the joint geometry shown in Figure 2 which consists of a bar of the MMC FP/AL (material B) embedded in a body of aluminium (material A). The loading is assumed to be in-plane (traction on the bar with an applied stress σ_∞) and we will consider a plane strain state. The design parameters are the elastic properties of each layer, the global geometry of the joint, defined by the inclination angle a , the embedded length L , the thickness of the bar and the total length of the aluminium body.

In the particular case of this joint, $b = \pi$, we show here that the singularity exponent is a function of only the 3 generalized Dundurs parameters α_1 , α_2 , β . Furthermore, for most material combinations they may be reduced to a single parameter.

Several different type of failure have been observed (Zok *et al.*, 1995):

- (i) Interfacial cracks may initiate at any of the singular point S , S' , S'' , leading to failure by delamination of the joint interface,
- (ii) Damage may be induced in the composite B , leading to a crack starting at the corner S and propagating normally to the interface I ,
- (iii) Global failure of the butt joint by delamination, ductile failure at the right hand end of the MMC or by void growth inside the plain metal close to the end.

We will focus on the design of the inclined part for which a failure type (i) or (ii) may occur. The singularity corner S is taken as the origin. The design parameters then reduce to the single value of the angle a , since b is now equal to π . The same study could be done for the other singularity corners S' and S'' .

5.1. USE OF THE GENERALIZED DUNDURS PARAMETERS

The singularity exponent for the composite joint is given by Eq. (45)-(46), but the expression of \underline{A} can be simplified. Because of the free edge at $\theta = -\pi$, z_1^B and z_2^B are both equal to $x = re^{-i\pi}$ and the expression of the matrix \underline{Y}_B (Eq. 42) becomes,

$$(69) \quad \underline{Y}_B = \underline{Y}(\theta = -\pi) = e^{-2i\delta\pi} \underline{1}$$

For any other angle than $b = \pi$, the imaginary parts of the complex coordinates z_1^B and z_2^B do not vanish and the two parameters μ_1^B and μ_2^B have to be taken into account. The material A being isotropic, \underline{Y}_A is defined as the limit of Eq. (42) for $\mu_k \rightarrow i$ and only depends on the angle a and the exponent δ ,

$$(70) \quad \underline{Y}_A = e^{2i\delta a} \begin{pmatrix} 1 - 2s^2\delta^2 + 2i\delta sc & 2i\delta(1 - \delta)s^2 \\ 2i\delta(1 + \delta)s^2 & 1 - 2s^2\delta^2 - 2i\delta sc \end{pmatrix}$$

where $c = \cos a$, $s = \sin a$. For the composite joint, with $b = \pi$, the matrix \underline{A} may be now expressed in terms of bi-materials matrices (\underline{H} , \underline{G}) and reduces to

$$(71) \quad \underline{A} = \underline{H} + e^{2i\delta\pi} \underline{\overline{H}} - [e^{2i\delta\pi} \underline{\overline{H}} - + \underline{G}] \frac{\underline{Y}_A - e^{2i\delta\pi} \underline{1}}{1 - e^{2i\delta\pi}}$$

The matrix \underline{B}_A as well as the expressions of \underline{H} and \underline{G} (Eq. 24 and 26) remain valid for an isotropic material A . Equations (24), (26), (32) show that the matrix \underline{A}/H_{11} is a function of the exponent δ , of the angle a and of the 3 generalized Dundurs parameters. Thus, from $\det \underline{A} = 0$, the singularity exponent δ only on α_1 , α_2 , β and a .

5.2. PARAMETRIC STUDY OF THE SINGULARITY EXPONENT

For orthotropic MMC's, $\lambda^{1/4}$ is generally close to unity, so that the parameters α_1 and α_2 are almost equal to α . It means that the singularity exponent depends roughly on the two parameters α and β (Eq. 25 and 30). For the Al-FP/Al joint (of the category for which $\beta \approx \alpha/4$),

$$(72) \quad \alpha_1 = -0.442, \quad \alpha_2 = -0.387, \quad \alpha = -0.416, \quad \beta = -0.109$$

The fact that layer B is a bar (and that $z_1^B z_2^B = z$ for $\theta = -\pi$) has played a major role in the simplification in the number of independent parameters of the eigenvalue problem. For the case of two orthotropic materials bonded together with the local geometry generally defined by the angles a and b , the singularity exponent was a function of 8 independent material parameters (6 if layer A is isotropic). For the composite joint with A isotropic and $b = 180^\circ$, β is a function only of 3 generalized Dundurs parameters, and in most cases only of α and β or if we assume the relation $\beta = \alpha/4$ of the single α (Fig. 3). This reduction is of course helpful for designing the joint and makes the parametric study quite simple.

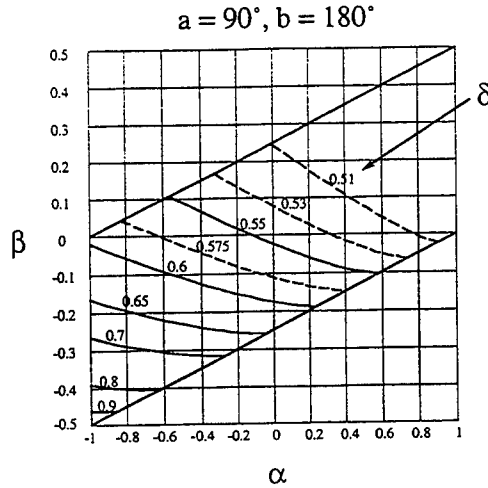
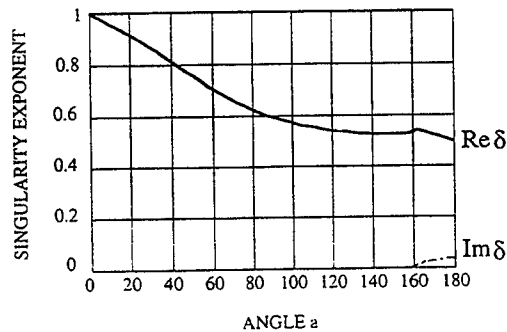
Fig. 3. - Contours of constant δ in the α - β plane.

Figure 4 illustrates the various of the singularity exponent for the composite joint as a function of the angle a for the exact value of the generalized Dundurs parameters and for their approximate value $\alpha_1 \approx \alpha_2 \approx \alpha$. Another way to represent the result is to plot the isovalue of δ in the α - β plane for different angles a (Fig. 3, $a = 90^\circ$). For any positive α or any positive β it can be seen that the corner almost behaves as a crack ($\delta \approx 0.5$). The α -approximation makes it possible to use pre-existing results of isotropic layers joints (see for instance the review done by Kelly (1992) in the α_{iso} - β_{iso} plane). The correct value of the singularity exponent for joints with $\beta = \pi$ will be found by replacing α_{iso} by α and β_{iso} by β .

Fig. 4. - Singularity Exponent δ vs Angle a ($\alpha = -0.416$, $\beta = -0.109$).

By considering the general properties $\beta \approx 0$, $\beta \approx \alpha/4$ valid for most of the joints of dissimilar materials, we can plot the curve Singularity Exponent versus Angle a for

different values of the parameter $\alpha = [-0.75, -0.5, -0.25, 0, 0.25, 0.5, 0.75]$ (Fig. 5). It shows that the singularity exponent depends mostly (for a given geometry) on the single material parameter α . For angles smaller than 90° , the value of δ decreases almost linearly and for angles larger than 90° , the singular behavior is almost the same as that for a crack $\delta \approx 0.5$).

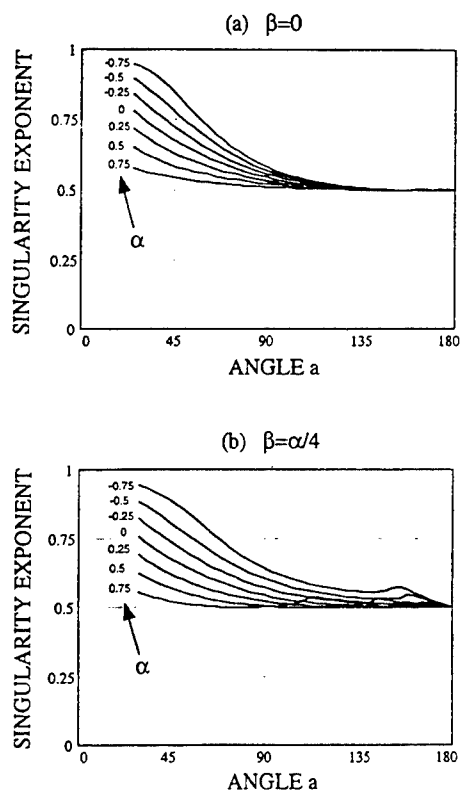


Fig. 5. – Exponent δ vs Angle α curves for different value of α and β (with $h = 180^\circ$).

6. Determination of h : the ψ -integral

Considering two solutions of an elasticity problem, displacements \mathbf{u}^a , \mathbf{u}^b , associated stresses $\underline{\sigma}^a$, $\underline{\sigma}^b$, satisfying the same boundary conditions but obtained by different methods, one of which may come from a global finite element solution and the other from the study of the singular solution, the difference of stored energy $W^a - W^b$ in the body Ω (Fig. 1) due to these different solutions may be expressed as a path independent integral form:

$$W^a - W^b = \psi(\mathbf{u}^a, \mathbf{u}^b) = \frac{1}{2} \int_C (\underline{\sigma}^a \mathbf{n} \cdot \mathbf{u}^b - \underline{\sigma}^b \mathbf{n} \cdot \mathbf{u}^a) dS$$

where the stored energy W in the whole body each solution is:

$$(74) \quad W^k = \frac{1}{2} \int_{\Omega} \underline{\sigma}^k : \underline{\varepsilon}^k dV$$

and C is any contour around the corner O , inside which no external load is applied.

The path independence of ψ was demonstrated by Stern (1976) and was used to determine the stress intensity at fixed-free corners. Leguillon (1993). Leguillon and Sanchez-Palencia (1987, 1991) extended this method to any geometry including 2- or 3-D singularities. The main idea is to compare the singular solution $\mathbf{u} = hr^{\delta} \mathbf{g}$, $\underline{\sigma} = hr^{\delta-1} \underline{F}$ to a reference solution (displacements \mathbf{U} , associated stresses $\underline{\Sigma}$ coming for example from a FE computation), by the introduction of the extraction solution $\mathbf{u}^* = r^{\delta^*} \mathbf{g}^*$, $\underline{\sigma}^* = r^{\delta^*-1} \underline{F}^*$, $\delta^* = -\bar{\delta}$ (Babuska and Miller, 1984). This last solution is more singular than that which describes the state in the vicinity of the corner and has the property to make the integral $\psi_{C_1}(\mathbf{u}, \mathbf{u}^*)$ finite. The solution \mathbf{u}^* , $\underline{\sigma}^*$ is fully determined by the foregoing analysis from the knowledge of the singularity exponent δ^* (eigenproblem 45-46). Using the path independence, the comparison between \mathbf{u} and \mathbf{U} may be written

$$(75) \quad \psi_{C_1}(\mathbf{u}, \mathbf{u}^*) = \psi_{C_2}(\mathbf{U}, \mathbf{u}^*)$$

which leads to:

$$(76) \quad h = \frac{\psi_{C_2}(\mathbf{U}, \mathbf{u}^*)}{\psi_{C_1}(r^{\delta} \mathbf{g}, \mathbf{u}^*)}$$

The two contours C_1 and C_2 may be any contour of course but it seems judicious to take for C_1 a circle of center O and of radius going to zero. The integral $\psi_{C_1}(r^{\delta} \mathbf{g}, \mathbf{u}^*)$ can be accurately calculated. It has been shown that even a crude reference solution for \mathbf{U} can still give a good estimation of the intensity factor (Stern and Soni, 1976). It is also recalled that the scaling law (Eq. 3) can be used to extend the knowledge of the intensity factor for a given sample to any specimen having the same shape but a different size: in that case the shape factor h remains constant.

Conclusion

The present analysis allows fast calculations of 2D-elastic singular strains, stresses and displacements close to corners, edges or interface ends of joints constituted of anisotropic layers. The exact expression of the singular fields is given. isotropic results are derived as a limiting case of the general anisotropic study.

The singularity exponent of the MMC joint studied here depends on the local geometry defined by the angle α and on the materials properties defined by the three generalized Dundurs parameters, one of which was known previously and two have been introduced in the present study. They make the design of the joint quick and the use of previous knowledge on joints constituted of isotropic layers can be extended to the MMC joint. Figure 3 shows the plot of constant singularity exponent δ in the α - β plane (eqs. 25

and 30) while Figure 5 represents the variation of δ with respect to the local geometry (defined by the angle α) for different bi-materials (represented by the single mismatch parameter α under the assumptions $\beta \approx 0$ and $\beta = \alpha/4$. For angles smaller than 90° , the value of δ decreases almost linearly and for angles larger than 90° , the singular behavior is almost the same as that for a crack $\delta \approx 0.5$).

The intensity factor h is determined from a path independent integral valid not only for cracks but for any other geometry. We may need *FE* computations to find h , but not necessarily: analytical solutions giving an idea of a high stress concentration may be sufficient.

An infinite stress is not really physical: at high level of stress, plasticity and damage are induced, limiting or erasing the singularity. The present analysis does not give directly the final stress state but may be a useful tool for computing the plastic or damaged zones (Desmorat, 1996; Desmorat and Lemaitre, 1996):

- An estimation of the plastic zone shape and size can easily found by introducing the yield stress.
- Neglecting the stress redistribution, it is possible to make local post-calculations of the nonlinear evolution laws of the material. The final stress state will take into account plastic and damage. These calculations do not need any *FE* computations.
- One can use the linear singular solution as an input to a very detailed *FE* computation: in a zone localized around the singular point, the nonlinear behavior is taken into account and the singular stress field is used as boundary condition.
- Fatigue behavior may be also studied by assuming that the stress field under cyclic loading may be derived from the present analysis.

Appendix

For a transversely isotropic composite, such as FP/Al system, the stiffness matrix \underline{s} introduces the five longitudinal (L) and transverse (T) elastic properties E_L , E_T , G_L , G_T , ν_L , ν_T the longitudinal direction being parallel to the fibers.

$$(A1) \quad \underline{s} = \begin{pmatrix} \frac{1}{E_L} & \frac{\nu_L}{E_L} & \frac{\nu_L}{E_L} & 0 & 0 & 0 \\ -\frac{\nu_L}{E_L} & \frac{1}{E_T} & -\frac{\nu_T}{E_T} & 0 & 0 & 0 \\ -\frac{\nu_L}{E_L} & -\frac{\nu_T}{E_T} & \frac{1}{E_T} & 0 & 0 & 0 \\ 0 & 0 & 0 & \frac{1}{G_T} & 0 & 0 \\ 0 & 0 & 0 & 0 & \frac{1}{G_L} & 0 \\ 0 & 0 & 0 & 0 & 0 & \frac{1}{G_L} \end{pmatrix}, \quad G_T = \frac{E_T}{2(1 + \nu - T)}$$

where these elastic properties have been determined experimentally by Jansson (1991):

$$(A2) \quad E_L = 225 \text{ GPa}, \quad G_L = 58 \text{ GPa}, \quad \nu_L = 0.28$$

$$(A3) \quad E_T = 150 \text{ GPa}, \quad G_T = 55 \text{ GPa}, \quad \nu_T = 0.31$$

REFERENCES

- BABUSKA I. and MILLER A., 1984, The Post-Processing Approach in the Finite Element Method, Part 2: The Calculation of Stress Intensity Factors. *Int. J. Num. Meth. Engng.*, **20**, 1111-1129.
- BOGY D. B., 1968, Edge Bonded Dissimilar Orthogonal Wedges under Normal and Shear Loading, *J. Appl. Mech.*, **35**, 460-466.
- BOGY D. B., 1971, Two Edge-Bonded Elastic Wedges of Different Materials and Wedge Angles under Surface Traction, *J. Appl. Mech.*, **38**, 377-386.
- DUNDURS J., 1967, Effect of Elastic Constants on Stress in a Composite under Plane Deformation, *J. Composite Materials*, **1**, 310-322.
- DUNDURS J., 1969, Discussion, *J. Appl. Mech.*, **36**, 650-652.
- DESMORAT R., 1996, Singular Field for a Bi-material in Anisotropic Plane Elasticity, *C. R. Acad. Sci. Paris*, **322**, Série IIB.
- DESMORAT R. and LEMAITRE J., 1996, Stress singularities applied to crack initiation by damage of multimaterial joints. *Proc. ASME Winter Congress*, Atlanta.
- ENGLAND A. H., 1971, On Stress Singularities in Linear Elasticity, *Int. J. Engng Sci.*, **9**, 571-585.
- ESHELBY J. D., READ W. T. and SHOCKLEY W., 1953, Anisotropic Elasticity with Applications to Dislocation Theory, *Acta Metall.*, **1**, 251-259.
- HUTCHINSON J. W., 1968, Singular Behavior at the End of a Tensile Crack in a Hardening Material, *J. Mech. Phys. Solids*, **16**, 13-31.
- JANSSON S., 1991, Mechanical Characterization and Modeling of Non-linear Deformation and Fracture of a Fiber Reinforced Matrix Composite, *J. Mech. Mater.*, **12**, 47-62.
- KANNINEN M. F., and POPELAR C. H., 1985, *Advanced Fracture Mechanics*, New York.
- KELLY P. A., HILLS D. A. and NOWELL D., 1992, The Design of Joints Between Elastically Dissimilar Components (with special reference to ceramic/metal joints), *J. Strain Anal.*, **27**(1), 15-20.
- LEGUILLON D. and SANCHEZ-PALENCIA E., 1987, *Computation of Singular Solutions in Elliptic Problems and Elasticity*, Masson, Paris, J. Wiley, New York.
- LEGUILLON D. and SANCHEZ-PALENCIA E., 1991, *Crack Phenomena in Heterogeneous Media*.
- LEGUILLON D., 1993, *Computation of 3D-Singularities in Elasticity*. In CIRM, Luminy, 3-7, May, France.
- LEKHNITSKII S. G., 1963, *Theory of Elasticity of an Anisotropic Body*, Holden-Day, San Francisco.
- LIEBOWITZ H., 1968, *Fracture*, New York and London, Academic Press.
- MC MEEKING R. M., 1977, Finite Deformation Analysis of Crack Tip Opening in Elastic-Plastic Materials, *Calculations and Implications for Fracture*, *J.M.P.S.*, **25**, 357-381.
- MUSKHELISHVILI N. I., 1963, *Some basic problems of the mathematical theory of elasticity*, 4th Edn, Noordhoff, Groningen.
- REEDY JR E. D., 1990, Intensity of the Stress Singularity at the Interface Corner between a Bonded Elastic and Rigid Layer, *Engng Fract. Mech.*, **36**(4), 575-583.
- REEDY JR E. D., 1993, Asymptotic Interface Corner Solutions for Butt Tensile Joints, *Int. J. Solids Structures*, **30**(6), 767-777.
- RICE J. R., 1988, Elastic Fracture Mechanics Concepts for Interfacial Cracks, *J. Appl. Mech.*, **55**, 98-103.
- RICE J. R. and ROSENGREN G. F., 1968, Plane Strain Deformation near a Crack Tip in a Power-Law Hardening Material, *J. Mech. Phys. Solids*, **16**, 1-12.
- SCHMAUDER S., 1986, *Cer. Forum Int.*, **2**, 101.
- SCHMAUDER S., 1989, Influence of Elastic Anisotropy on the Edge Problem, *Metal-Ceramic Interfaces*, **4**, 413-419.
- STERN M. and SONI M. L., 1976, On the Computation of Stress Intensities at Fixed-Free Corners, *Int. J. Solids Structures*, **12**, 331-337.
- STROH A. N., 1958, Dislocations and Cracks in Anisotropic Elasticity, *Phil. Mag.*, **7**, 625-646.

- SUO Z., BAO G., FAN B. and WANG T. C., 1990, Orthotropy Rescaling and Implications for Fracture in Composites, *Int. J. Solids Structures*, **28**(2), 235-248.
- SUO Z., 1990, Singularities, Interfaces and Cracks in Dissimilar Anisotropic Media, *Proc. R. Soc. London*, **A427**, 331-358.
- VROONHOVEN J. C. W., 1992, Stress Singularities in Bi-Materials Wedges with Adhesion and Delamination, *Fatigue Fract. Engng Mater. Struct.*, **15**(2), 159-171.
- WILLIAMS M. L., 1952, Stress Singularities Resulting from Various Boundary Conditions in Angular Corners of Plates in Extensions, *J. Appl. Mech.*, **19**, 526-528.
- ZOF F., DU Z. Z., and EVANS A. G., LECKIE F. A., 1995, Strength Limited Design of AMC/Al Transitions.

(Manuscript received February 27, 1996;
revised and accepted June 2, 1997.)



OVERVIEW No. 125

DESIGN AND LIFE PREDICTION ISSUES FOR HIGH-TEMPERATURE ENGINEERING CERAMICS AND THEIR COMPOSITES

A. G. EVANS

Division of Applied Science, Harvard University, Cambridge, MA 02138, U.S.A.

(Received 9 November 1995; accepted 4 April 1996)

Abstract—Perspectives are presented on ceramics and ceramic matrix composites (CMCs) as high-temperature materials. The emphasis is on design and life prediction requirements and their role in directing research. Important themes include the relative roles of fracture toughness and inelastic strain (ductility), as well as scaling and stochastic effects caused by manufacturing defects. Ceramics with high toughness have been developed. However, because they are inductile, design with such materials is based on elastic stresses, combined with weakest link scaling and extreme value statistics. Procedures that ensure reliable performance under these circumstances are inherently constrained. Opportunities to mitigate these restrictions by matching mechanisms to design are explored. By contrast CMCs exhibit inelastic strain mechanisms that provide an efficient means of redistributing stress. These mechanisms eliminate stress concentrations and suppress scaling effects, enabling design procedures similar to those used with metals. The sources and mechanisms of inelastic strain are described, as well as the ensuing constitutive models. Examples of their finite element implementation in design are presented. A life prediction methodology requires a robust procedure for characterizing fatigue effects in conjunction with manufacturing and machining flaws. A lifing approach is described having commonality between ceramics and CMCs. Copyright © 1996 Acta Metallurgica Inc.

1. INTRODUCTION

A goal for many decades has been the creation of affordable structural materials capable of reliable operation at 1200–1400°C, subject to oxidizing conditions as well as tensile loading. This goal has yet to be realized. The strategy has been to begin with stable materials, inherently deformation resistant at these temperatures. Such materials are typically ceramics or intermetallics. Because of brittleness, components made from these materials have not exhibited acceptable reliability upon tensile loading. The addition of reinforcements has provided damage tolerance. Various approaches have been successful, although each has degraded stability and deformation resistance. To exploit this promise, coherent engineering objectives are essential. Guidelines needed for this purpose have yet to be clarified. The consequence has been minimal engineering experience, and few applications. The intent of this overview is to identify the technical problems as well as explore strategies which might enable such materials to be implemented extensively in commercial systems. To facilitate this objective, methodologies that have close analogies with those currently practiced on metals are emphasized. Two parallel themes address mechanism-based concepts in engineering design and life prediction: (i) the relative roles of ductility and toughness; (ii) engineering design and life prediction methodologies.

The earliest goal was to create ductility by inducing dislocation plasticity [1–17]. But, even when plasticity was achieved, the materials still had a low fracture toughness and were prone to catastrophic rupture. This paradox arose because cracks in ceramics do not exhibit plastic blunting [11–17]. Subsequently, the research realigned into two conceptual directions: one concerned with the development of toughness; the other emphasized inelastic deformation mechanisms and ‘ductility’. These research efforts have resulted in major discoveries of mechanisms with theories capable of characterizing the principal effects. An excellent overview is given in the book by Wachtman [18]. However, the technological ramifications have still been minimal. One reason has been an ineffectual translation of the physics and mechanics concepts into design and life prediction methodologies.

The central technical problem for ‘toughened’ materials, is their lack of ductility. That is, these materials have no mechanism for redistributing stress: therefore, strain concentration sites are also regions of high stress. There is an associated notch sensitivity, coupled with a scale dependence caused by weakest link behaviour. These factors impose stringent demands on design, and engineering exploitation has been seriously impeded. Conversely, materials designed to induce ‘ductility’, through inelastic deformation mechanisms, enable stress redistribution and, in some cases, exhibit notch

insensitivity [19]. Equally important, the ultimate tensile strengths become scale insensitive, because local stress concentrations are alleviated [10–23]. These characteristics allow a design strategy similar to that used with metals. Such merits have given a stimulus to the continued development of materials that exhibit 'ductility', particularly ceramic matrix composites (CMCs).

Having a life prediction capability is an equally important requirement for the reliable implementation of new materials. Fatigue, creep, stress corrosion and their interactions are all involved. Here, some issues that arise in fatigue and its interaction with stress corrosion are presented with a focus on approaches for realizing a life prediction methodology.

2. DESIGN APPROACHES

Design procedures used in practice are straightforward and robust. They are based on rigorous mechanics principles, but simplified to allow ready implementation at acceptable precision. They use the theories of elasticity and plasticity, combined with Gaussian statistics. The engineering challenge for ceramics and their composites is to provide analogous strategies that can be applied with similar confidence. Central to the challenge is the approach used to address the roles of inelastic strain and fracture toughness.

In the absence of macroscopic inelastic strain, stress concentrations persist at slots, attachments, impact sites, etc. The consequent design procedure requires that the 'strength' be compared with the concentrated stresses [26–28]. This design strategy has deficiencies, associated with the acquisition of high-fidelity strength data. The problem is caused by weakest link scaling and the extreme value nature of the stochastics. It can be alleviated, but not obviated, by using higher toughness materials. A more robust design strategy can be implemented if the material has a capacity to exhibit inelastic strain. Such strain diminishes stress concentrations, leading to a decreased sensitivity to manufacturing flaws, notches and impacts [19, 29]. The effects are analogous to plasticity in metals. Further confidence is achieved if weakest link scaling can be suppressed by imparting damage tolerance to the material, through mechanisms that stabilize sub-critical cracks. The following discussion summarizes these design issues and makes a preliminary attempt to understand the opportunities for enhancing the 'design friendliness' by optimizing toughness, by inducing inelastic strain and by suppressing weakest link scaling.

2.1. Weakest link design

A consequence of material linearity is that stress concentrations are overwhelmingly important. This difficulty is exacerbated by weakest link scaling of the strength, as well as the extreme value stochastics.

These issues are elaborated. Designing a load bearing component using a linear elastic material involves two steps: (1) an elastic analysis is performed in order to obtain the stresses; (2) the survival probability of each element is evaluated using the principles of weakest link statistics [23–25, 27–33]. The procedure is understood and has been implemented in software programs compatible with finite element codes. The codes calculate the survival probability, ϕ , of volume elements δV using the weakest link expression [27].

$$\begin{aligned}\phi_s &= 1 - \delta V \int_0^{\sigma_D} g_s(S) dS \\ &\equiv 1 - \delta V G_s(\sigma_D)\end{aligned}\quad (1a)$$

where $g_s(S) dS$ is the number of flaws in a unit volume having strength between S and $S + dS$, σ_D is the average stress within the element at the design load and G_s is the cumulative distribution. There is a corresponding formula for the surface elements. The survival probability of the component is the product of the survival probabilities of all elements (volume plus surface), $\Pi(\phi_s)$ [25, 27]. Usually, G_s is approximated by a power law (Weibull distribution) with a scale parameter, S_0 , and a shape parameter, m ,

$$G_s(S) \approx (S/S_0)^m. \quad (1b)$$

The practical utilization of these codes is limited by the procedures used to obtain data. The integration of equation (1a) is between zero and the design stress. However, strength data are normally obtained using flexure tests or tension tests on small specimens. These provide information about the flaw populations at stresses above σ_D , because of weakest link scaling [3] (Fig. 1). A robust procedure for extrapolating has not been provided. It is often asserted that the scale and shape parameters obtained from a power law fit to laboratory data at high strength levels apply at stresses below σ_D . Such assertions are not justified. A polynomial fit to the data could be made with equal fidelity, resulting in large differences in the predicted survival probability upon data extrapolation. A key question is whether it might ever be feasible to establish a robust, affordable design procedure for systems having these characteristics. A corollary is whether the situation can be ameliorated by creating materials with relatively high toughness. The following two approaches address these problems.

(1) Provide data which ensure acceptable confidence in the scale and shape parameters at the design stress. For this purpose, tests must be performed on relatively large tension specimens in order to obtain data close to σ_D (Fig. 1). However, the gathering of such data is costly. These costs might be justified when the processing and machining have been standardized and subjected to a rigorous control regimen, such that the flaw populations are

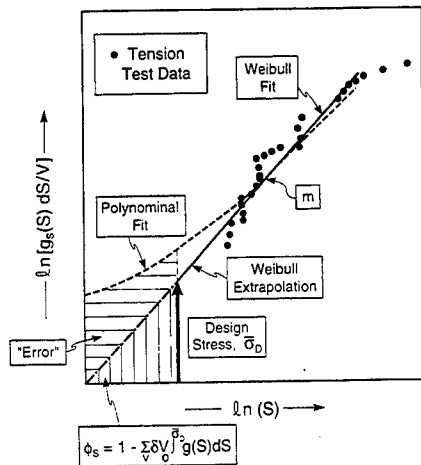


Fig. 1. Typical statistical data obtained upon tension testing of ceramics. The extrapolation from the (linear) Weibull fit is shown, as well as the extrapolation from a polynomial fit. These indicate the large difference in the projected survival probability (note that the axes are logarithmic).

stable and consistent. Otherwise, batch-to-batch variations and deviations among machining runs result in population changes that have to be recalibrated in order to provide the level of confidence required for the design. The associated costs are usually prohibitive.

(2) With these problems, diminishing the sensitivity of the strength to processing and machining flaws appears to be the preferred alternative. In principle, improving the toughness should result in these attributes. However, the resistance-curve behaviour inherent in the toughening mechanisms limits exploitation, because toughening cannot be utilized by the small flaws typically introduced upon processing [34–36]. Nevertheless, the scaling difficulties can be diminished by matching the design to the crack growth resistance.

2.2. Stress redistribution and design

The design situation is completely different for 'ductile' materials exhibiting inelastic deformation modes such as CMCs (Fig. 2). Such deformations redistribute stress [26, 37]. Two fundamentally different stress redistribution mechanisms operate (Fig. 3). (a) One derives from the inelastic strain produced by multiple matrix cracking accompanied by interface debonding and friction. This mechanism is subject to strain hardening [19, 26]. (b) The other involves fibre pull-out, beyond the Ultimate Tensile Strength (UTS) after localization [19, 38]. This mechanism is subject to strain softening. It is associated with frictional tractions enabled by the pull-out of the failed fibres. These mechanisms are so efficient at dissipating energy by internal friction that the materials become notch insensitive [37]. Inelastic constitutive laws associated with these

mechanisms have been developed and implemented in finite element codes [26]. Stress redistribution is illustrated by two representative design calculations: one for tensile plates containing holes or slots (Fig. 4a); the other for pin-loaded holes (Fig. 4b), which simulate mechanical attachments. These calculations demonstrate that the inelastic strain spreads out the stress concentrations and diminishes their peak magnitudes [26]. In design these peak stresses are compared with the ultimate tensile strength [19, 26]. The UTS is scale insensitive and its distribution is Gaussian, because it is controlled by stable damage modes [20, 21].

The consequence of this stress distribution capability is that components can be designed with small holes and slots, without concern for stress concentrations. That is, a net-section stress calculation is often adequate. This feature has been used to advantage in the design of combustors and other thermally-loaded components. Another consequence is that mechanical attachments can be used, with the loads transferred through holes drilled in the material, again without concern for stress concentrations. A dramatic illustration of this behaviour is notch insensitivity (Fig. 5) and the immunity of the strength to impact damage, etc.

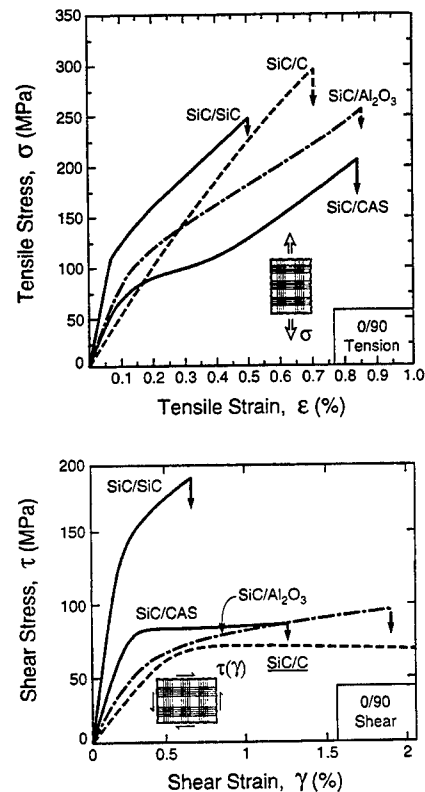


Fig. 2. Typical stress-strain curves for CMCs in tension and shear.

PULL-OUT AFTER LOCALIZATION

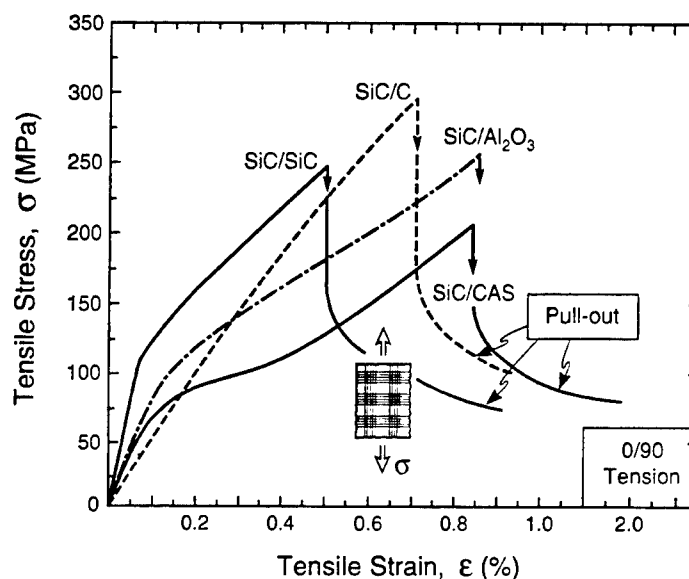


Fig. 3. Tensile stress-strain curves showing the pull-out origin at stresses beyond the UTS.

2.3. Illustration of differences

The consequence of weakest link scaling is that the strength S of a component, at specified survival probability, decreases as its stressed volume, V , increases [30]. Large components have much lower strength than laboratory test specimens, even when the flaw populations are calibrated and invariant. Moreover, if a strain concentration is introduced, such as a small hole or attachment, the stress concentration interacts with the flaws and further diminishes the strength. A large component with an attachment thus has a tensile strength about one-quarter of that of a smooth tensile bar and one-eighth of that of a flexure beam. The corresponding strength requirements for a 'ductile' material are considerably less stringent, since there are minimal scaling and stress concentration effects [22]. That is, a large component with a small hole has about the same load capacity as a laboratory tensile coupon. Moreover, most ceramic and CMC components are designed primarily to withstand thermal loads, with minimal pressure. In such cases, design is strain-based, such that the failure strain of the material is most relevant. For CMCs, these strains are typically 0.8% [19–20, 43] well in excess of design strains which are typically <0.2%.

3. THE ROLE OF TOUGHENING

3.1. Reliability through enhanced toughness

The fracture toughness has no direct affect on the design of elastic materials. Its influence is These reflected in the magnitudes of the stochastic strength parameters, m and S_0 , through their effect on strengthening and reliability. An approach that provides insights about these effects is developed and presented. Toughening is manifest as a fracture resistance, Γ_R , that increases with crack extension, Δa (Fig. 6) [44–51]. Concepts of initiation toughness, Γ_0 , steady-state toughness, $\Delta\Gamma$, and tearing index, λ are needed to characterize this behaviour. To bring out the concepts in the most straightforward manner, the simplest relation for transient toughening ($\Delta a \leq L$) having a sound theoretical basis is used. It is given by [51],

$$\Delta\Gamma_R = \Gamma_R - \Gamma_0 \approx \Delta\Gamma_0(\Delta a/L)^{1/2} \quad (2a)$$

and for steady-state ($\Delta a \geq L$),

$$\Delta\Gamma_R = \Delta\Gamma, \quad (2b)$$

where L is a reference length related to the inelastic zone size. The tearing index is a measure of the slope of the resistance curve and is defined as

$$\lambda = (\Delta\Gamma_0/\Gamma_0^2)/L. \quad (3)$$

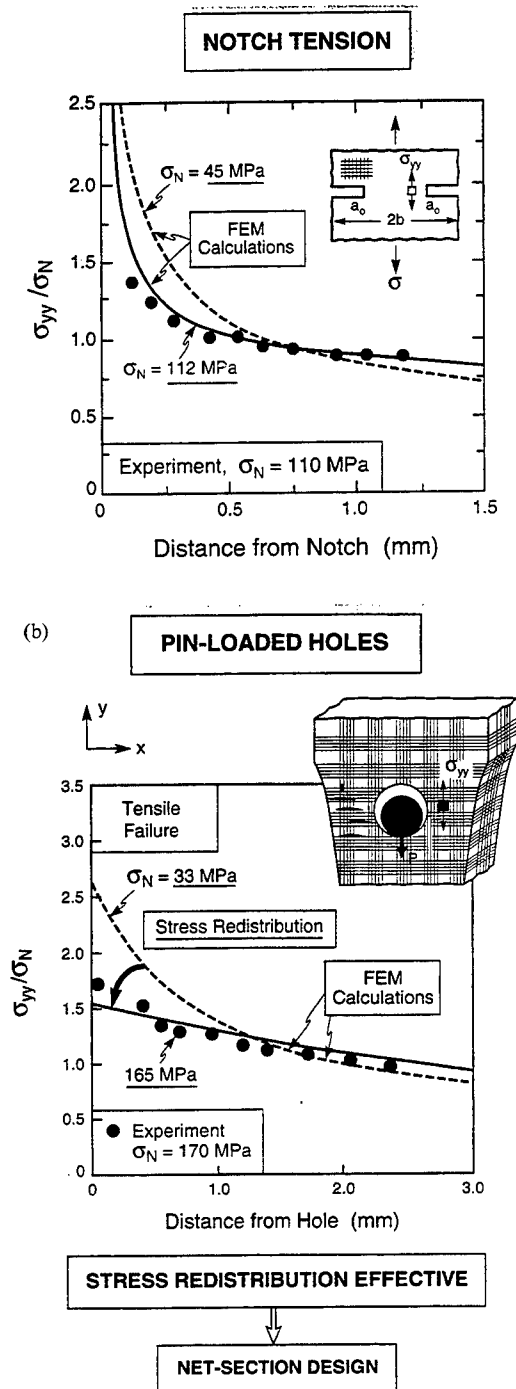


Fig. 4. (a) A notched tension test showing the stress ahead of the notch. The measured values are indicated as well as those calculated by FEM using equation (28). (b) A pin-loaded hole test performed on SiC/CAS showing the stress across the net section. The measured values are compared with those calculated by FEM using the inelastic constitutive law (equation (28)).

It has units of reciprocal length. Reliability is dictated by the product of λ with the size a_0 of the flaws responsible for component survival at the design stress.

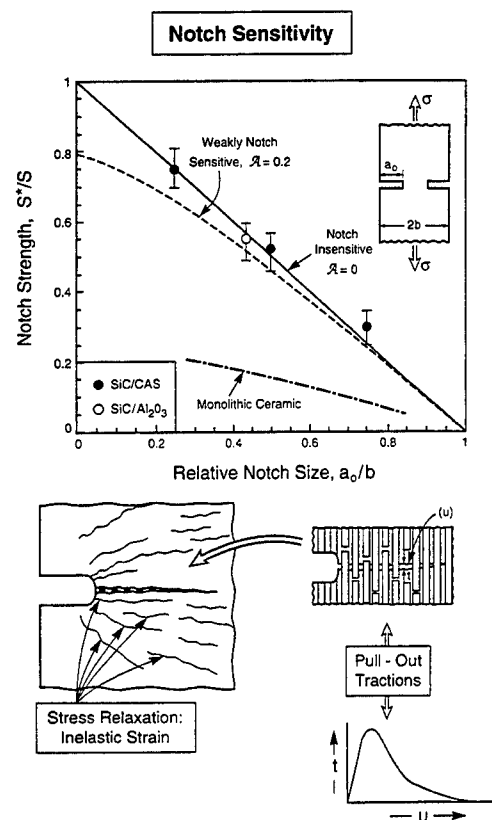


Fig. 5. The notch insensitive behaviour found for SiC/CAS and SiC/Al₂O₃. The inset shows the pull-out mechanism.

To develop understanding, the energy release rate for the small processing and machining flaws that typically control strength is used

$$\mathcal{G} = 4\sigma^2 a / \pi E \quad (4)$$

where a is the crack radius, ($a = a_0 + \Delta a$), with a_0 being the initial crack radius and σ the applied stress. The ultimate tensile strength S is obtained from these equations ((2) and (4)) by requiring that $G = \Gamma_R$ and $dG/da = d\Gamma_R/da$. Accordingly, S is determined to vary with the tearing index in accordance with,

$$S/S^* = [\Lambda/2((1 + \Lambda)^{1/2} - 1)]^{1/2} \quad (5)$$

where Λ is related to the tearing index by

$$\Lambda = \lambda a_0 \quad (6)$$

and S^* is the UTS of the untoughened material: that is,

$$S^* = (\sqrt{\pi}/2)(E\Gamma_0/a_0)^{1/2} \quad (7)$$

The corresponding crack extension Δa_c when it becomes critical is,

$$\Delta a_c/a_0 = [(1 + \Lambda)^{1/2} - 1]^2/\Lambda \quad (8)$$

The larger Λ , the more beneficial the effect of the toughening on the strength and reliability. The inference is that the attainment of 'beneficial'

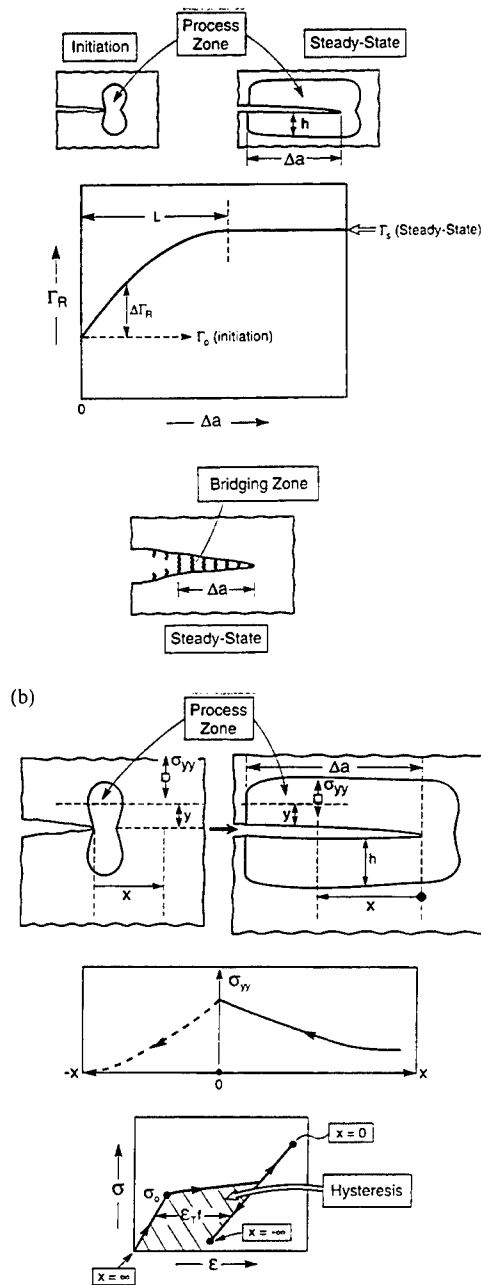


Fig. 6. (a) A schematic of a resistance curve showing the evolution of the inelastic zones and the parameters that characterize the behaviour. (b) A schematic of crack extension in the presence of a process zone and the strain-stress history experienced by an element of material within the zone.

toughening requires an optimization based on L , as well as $\Delta\Gamma_s$, through λ and Λ .

The key importance of Λ is illustrated in Fig. 7. When the flaws a_0 are very small ($\Lambda \ll 1$), fracture occurs unstably and the strength stochastics are unaffected by the toughening. Conversely, larger flaws are able to experience stable crack growth such that the strength exceeds the untoughened magnitude

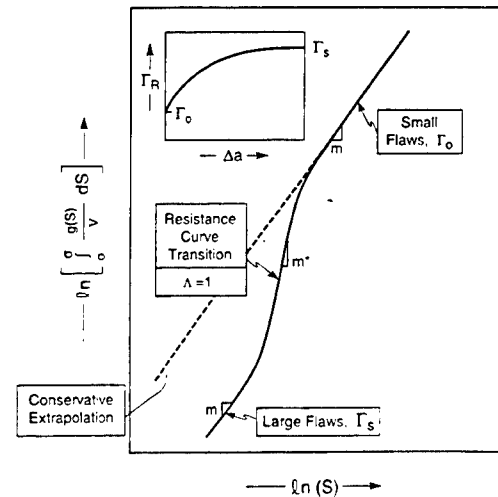


Fig. 7. Superior confidence associated with extrapolation when a toughened ceramic is used at the optimum value of the strengthening index, $\Lambda \approx 1$. That is, the slope which governs the shape parameter increases above m when the tearing behaviour becomes significant.

[34, 35], and the Weibull shape parameter increases ($m^* > m$, Fig. 7). That is, the material has a diminished sensitivity to processing and machining flaws and size scaling effects are alleviated. Toughening mechanisms that achieve a reliability enhancement require: $\Lambda = \lambda a_0 \geq 1$. The means for attaining this objective are addressed next.

3.2. Toughening configurations

The known toughening mechanisms involve inelastic deformation zones having two distinct configurations (Fig. 6): (i) zones that concentrate in a thin region around the crack plane which rupture as the crack extends: referred to as either bridging or Dugdale zones; (ii) regions that extend normal to the crack plane and remain in a deformed but intact state after the crack has propagated through the material: these are designated process zones. Process and bridging zone mechanisms may operate simultaneously and synergistically [50–53].

Toughening by bridging is caused by tractions along the crack surface induced by intact inelastic material ligaments. Usually, the tractions soften as the crack extends. Then, in steady-state, the toughening $\Delta\Gamma_s$ is [50, 51]

$$\Delta\Gamma_s = b[t_0 u_c] \quad (9)$$

where u_c is the crack opening at the edge of the bridging zone, t_0 is the peak traction and $b \approx 1/2$. The inelastic zone length is [51]

$$L \approx c[Eu_c/t_0] \quad (10)$$

where $c \approx 0.12\pi$. The tearing index is thus

$$\lambda = (b^2 c)^{-1} [t_0^2 u_c / E \Gamma_0^2] \quad (11)$$

Note the particularly strong influence of the traction t_0 . Ductile reinforcements, as well as brittle fibres and

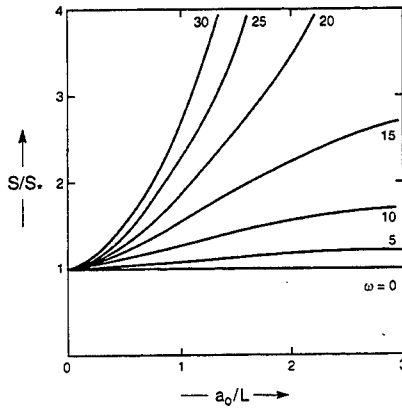


Fig. 8. The effect of crack length on the strengths enabled by transformation toughening: w is a parameter related to the tearing index.

anisotropic grains, toughen by means of bridging tractions. Some typical magnitudes are described below.

Process zone toughening may be characterized by the product of the critical stress for activating the inelastic strain mechanism, σ_0 , the associated stress-free strain, ϵ_T , and the zone height, h , in accordance with the stress-strain hysteresis of material elements within the process zone (Fig. 6b) [48, 52–54].

$$\Delta\Gamma_s = 2h\sigma_0\epsilon_T. \quad (12)$$

The inelastic zone length is governed by the zone height,

$$L = c_0 h \quad (13)$$

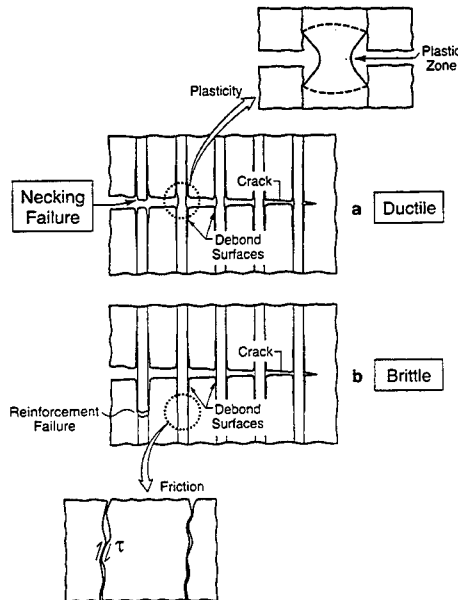


Fig. 9. A schematic indicating the dissipation that occurs with a bridging zone: (a) ductile ligaments, (b) brittle reinforcements.

where $c_0 \approx 3$. Moreover, the zone height is related to the critical stress by

$$h = d_0[E\Gamma_0/\sigma_0^2] \quad (14)$$

where d is a mechanism dependent coefficient of order 0.1 [54]. The tearing index is thus,

$$\lambda = (4d_0/c)[\epsilon_T^2 E/\Gamma_0] \quad (15)$$

Note that at this level of simplification, the only inelastic material property affecting the tearing and strengthening is the transformation strain, ϵ_T . The critical stress and the zone height are of secondary importance, in contrast to their primary influence on the steady-state toughening. Because of this, the strengthening flexibility for process zone toughening is appreciably less than that for the bridging mechanisms. Moreover, strengthening predictions are often optimistic, because there are important short crack effects. For crack lengths, $a_0 < 2L$, interactions between the inelastic zones at the opposite crack tips, reduce the toughening. Some appreciation for the effect is provided by results obtained for transformation toughening [54] (Fig. 8).

3.3. Bridging mechanisms

Reinforcing elements can be either ductile or brittle. The former rely on plasticity to create ligaments and dissipate energy [51, 55–56] (Fig. 9). When the elements are brittle, bridging requires either microstructural residual stresses or weak interfaces. Residual stresses caused by thermal expansion mismatch can suppress local crack propagation and, thereby, allow intact ligaments to exist behind the crack front [57]. When these ligaments eventually fail in the crack wake, energy is dissipated through acoustic waves and causes toughening [36]. Low fracture energy interfaces are more effective. They cause the crack to deflect and debond the interfaces [58]. The debonds acquire mode II (shear) characteristics, leading to friction, stability, and intact ligaments [19]. As the crack extends, further debonding occurs, subject to friction [19]. Eventually, the bridging material fails, either by debonding around the ends or by fracture. Following reinforcement failure, additional friction may occur along the debonded surfaces. The dissipation thus includes terms from the debonded interfaces, the acoustic energy upon reinforcement failure, and friction [36] (Fig. 9). The latter is typically dominant. Moreover, the internal friction can become exceptionally large, resulting in toughnesses approaching those for ductile metals (Section 4) [19].

3.3.1. Ductile phases. There are three distinct ductile phase microstructures: (a) isolated ductile reinforcements in an elastic matrix; (b) interpenetrating ductile/elastic networks; and (c) a ductile matrix with a dispersed elastic phase [36, 50, 55, 59, 60]. An important difference between the first two microstructures and the third concerns the potential for macroscopic plastic strain. Plastic strain in the former is limited by the elastic network, such that the only

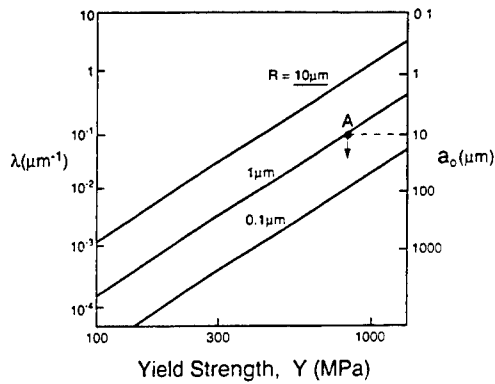


Fig. 10. Effect of yield strength on the tearing index for several reinforcement radii in ductile phase toughened materials (with $f = 0.2$ and $\Gamma_0 = 20 \text{ Jm}^{-2}$). For a $10 \mu\text{m}$ initial crack and $1 \mu\text{m}$ reinforcements (A), the yield strength needed to achieve appreciable strengthening is $Y \approx 800 \text{ MPa}$.

ductile material experiencing extensive strain is that stretching between the crack surfaces in the bridging zone [55, 56, 60]. The latter develop an additional plastic zone which enables further, often substantial, inelastic dissipation [61, 62].

Ductile phase toughening in an otherwise elastic material is contingent upon the ligament failure mechanism, through the stress/stretch relation. Such toughening can be re-expressed by noting that the traction scales with the uniaxial yield strength, Y , of the ligaments and that the plastic stretch is proportional to the radius of the cross-section of the reinforcements, R . Consequently, the asymptotic toughening is

$$\Delta\Gamma_c = \chi f R Y \quad (16a)$$

and the zone length is

$$L = \beta R E / Y f \quad (16b)$$

where f is the volume fraction of the reinforcement; χ and β are 'ductility' parameters, which also depend on the extent of the interface debonding d . Without debonding, the traction attains high levels, because of the elastic constraint of the matrix, but then decreases as the crack opens because of necking

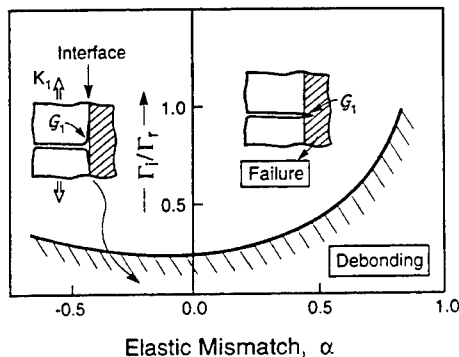


Fig. 11. A debond diagram for brittle reinforcements [58].

[55, 60]. Debonding reduces the constraint, but increases the plastic stretch to failure [55, 63]. The latter dominates, causing the dissipation to increase as the debond length increases. Values of χ and β have been obtained both by calculation and by experiment [55–63]. For well-bonded interfaces with ductile phases that fail by necking to a point, $\chi \approx 0.5$ and $\beta \approx 0.1$, both increasing as the strain hardening increases. Less-ductile ligaments that rupture prematurely have correspondingly smaller χ and β . With debonding, χ and β depend on the reinforcement morphology. For interpenetrating or continuous reinforcing phases, χ and β are both increased by debonding, because the dissipation is spread laterally away from the crack plane: χ approaches 8 for large d/R . For discontinuous phases, debonding around the ends of the reinforcement diminishes χ and β .

The tearing index for such materials is obtained from equations (3) and (16) as

$$\lambda = [\chi^2/\beta][R/E\Gamma_0^2](Yf)^{-1}. \quad (17)$$

The important implication is that the scaling that controls strength and reliability is most strongly affected by the yield strength of the reinforcing material Y and its ductility, through χ . Other factors are relatively unimportant. A plot of λ against Y^2 for various R (Fig. 10) indicates the range in toughening parameters needed as a function of the flaw size. For example, when the manufacturing and machining flaws responsible for component performance at the design stress are typically $\sim 10 \mu\text{m}$, and the reinforcements are in the $1 \mu\text{m}$ range, Y should exceed 800 MPa if effective strengthening is to be achieved. Such results guide material design for engineering performance.

3.3.2. Brittle reinforcements. The highest toughnesses are achievable in systems containing 'weak' interfaces, which enable debonding and allow dissipation by internal friction [19, 35]. There are major effects of the morphology of the debond planes

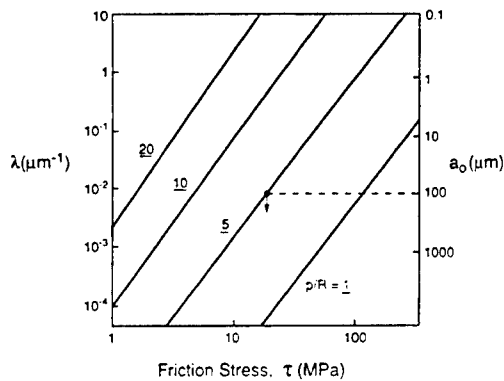


Fig. 12. Effect of friction stress on the tearing index at several pull-out lengths for reinforcements with radii, $R = 10 \mu\text{m}$ (for $f = 0.4$ with $\Gamma_0 = 20 \text{ Jm}^{-2}$). Note the relatively small values of τ needed to achieve strengthening with $100 \mu\text{m}$ flaws.

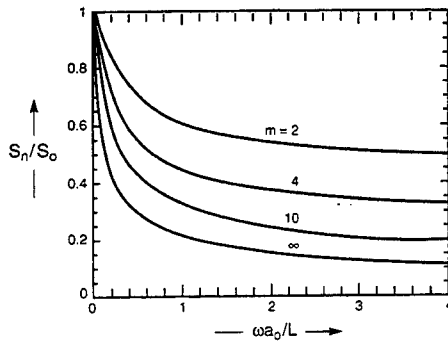


Fig. 13. The notch properties of materials reinforced with short aligned, brittle reinforcements: m is the Weibull shape parameter [69].

(roughness), the residual stresses, the failure stochastics of the reinforcements and the stiffnesses of the constituent phases [64]. A prerequisite to toughening is that the debond criterion be satisfied. That is, Γ_i/Γ_f be small enough to lie within the debond zone depicted in Fig. 11 (typically $\leq 1/4$) [58]. The extent of initial debonding is small. However, further debonding is induced in the crack wake, as the crack extends, having an extent governed largely by the residual field, the debond surface roughness and the friction coefficient [65]. Reinforcement failure involves stochastics, subject to a friction stress τ [20–21, 66–69]. Large τ causes the stress to vary rapidly and induces reinforcement failure close to the crack, leading to a small pull-out length, p , and vice versa [66, 67, 69]. The consequent tractions are relatively complex. Insight is gained from solutions for short, strong, aligned reinforcements, subject to friction. For this case [36, 69],

$$\Delta\Gamma_s = f\tau(p/R)^2 R$$

$$L = (c/2)ER/f\tau \quad (18)$$

where R is the reinforcement radius, p is their length, such that p/R is the aspect ratio. The corresponding tearing index is

$$\lambda = (2/c)[R/EG\Gamma_s^2](f\tau)^3(p/R)^4. \quad (19)$$

Note the major influences of the aspect ratio and the friction stress. This toughening and strengthening is only attained provided that the reinforcement strength, S , satisfies [69]

$$S > \tau(p/R). \quad (20)$$

A plot of λ as a function of the aspect ratio for various friction stresses (Fig. 12) establishes the potential for strengthening. A comparison with Fig. 10 indicates the relatively greater efficiency of the internal friction mechanism with aligned, brittle reinforcements than the plasticity mechanism with ductile reinforcements. That is, strengthening by friction is attained with $\tau \sim 10$ MPa, whereas the comparable effect achievable with yielding requires $Y \sim 500$ MPa. The difference is attributable to the enhanced influence zone achieved by spreading of the friction normal to

the crack, resulting in greater dissipation. The implication is that frictional toughening is more effective than ductile phase toughening.

When the reinforcements are long and aligned, but susceptible to fracturing as the crack extends, the tractions are more complex [19]:

$$t/fS_L = \sqrt{w} \exp[-\alpha w^{(m+1)/2}] \quad (21)$$

where m is the Weibull shape parameter associated with the reinforcements, S_L is their average strength at length L_r , and [19]

$$w = 8\zeta^2(u/L_r)$$

$$\alpha = [\Gamma(1 + 1/m)]^m/[m + 1]$$

$$\zeta = [E/2E_m(1 - f)](E_t/S_L)^{1/2}$$

$$L_r = S_L R/\tau$$

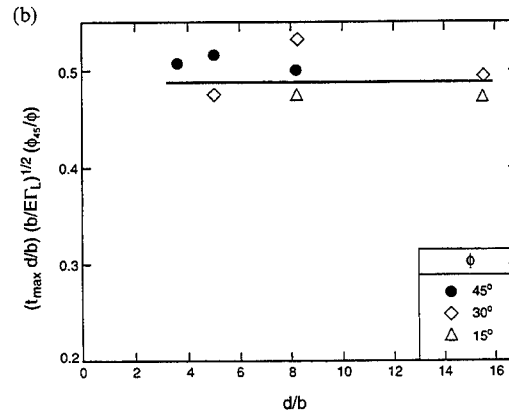
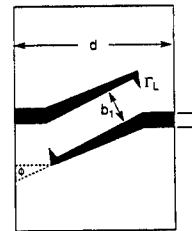
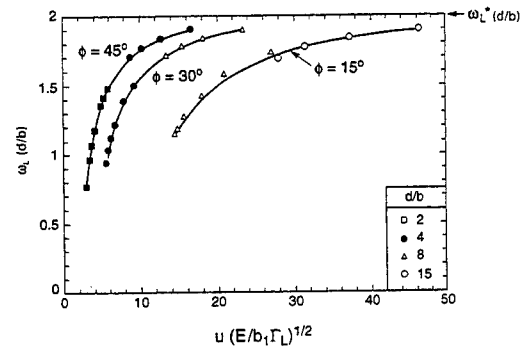


Fig. 14. Non-dimensional parameters that affect ligament toughening [72]. (a) The toughening as a function of opening u , with ω_L^* being steady-state. (b) A tearing coefficient and its dependence on ligament dimensions.

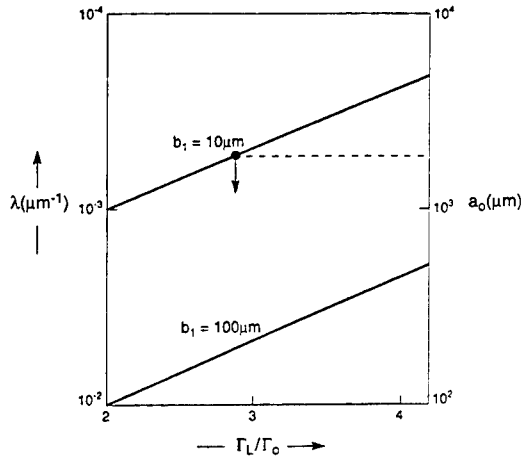


Fig. 15. Tearing index for elastic ligament toughening ($d/b_1 = 4$).

with the subscripts m and r referring to the matrix and reinforcements, respectively, and here Γ is the gamma function. Even in this simplified case, the friction stress and reinforcement strength have interactive effects on toughening and strengthening which are not evident without detailed analysis. Consequently, for practical implementation, the integrated effect of these variables on the notch sensitivity, is more useful. The notch behaviour predicted by equation (21) for short, aligned reinforcements is plotted in Fig. 13. It demonstrates how variability in the reinforcement strength (low m) alleviates the notch sensitivity.

3.3.3. Anisotropic grains. Low fracture energy planes or grain boundaries can allow debonding, as in reinforced materials with weak interfaces.

such that toughening involves the same considerations. Certain anisotropic ceramics with elongated grains exhibit such toughening (particularly alumina and silicon nitride [47, 49, 70]). The dominant effect is the friction that operates along the rough, non-aligned, debonded grain boundaries. The trends are broadly consistent with the above results for short, strong reinforcements. That is, the toughening and the strengthening increase as the grain radius R and their aspect ratio, p/R increase [70]. Intermetallics such as TiAl also toughen in this manner [71, 72], because of extreme anisotropy in the cleavage energies. But, in this case, the energy of the additional surface created by debonding and ligament formation appears to be more important than the friction. The relevant toughening and strengthening parameters are controlled entirely by the extra surface energy and are given by [72].

$$+ \Delta\Gamma_r/\Gamma_L = \omega_L^* \quad (22)$$

and

$$L = 2cb_1\omega_L^*/\chi^2$$

such that

$$\lambda = (\Gamma_L/\Gamma_o)^2\omega_L^*\chi^2/2cb_1$$

where Γ_L is the cleavage energy on the 'tough', transverse planes, b_1 is the ligament width (Fig. 14) and ω_L^*, χ are non-dimensional quantities. The inverse dependence of λ on size b_1 , contrasts with that for the other mechanisms. This dependence arises because more surface is created per unit area of crack growth as b_1 decreases. The consequence is a strengthening effect that can become very large as

CERAMIC MATRIX COMPOSITES Microstructural Design Concepts

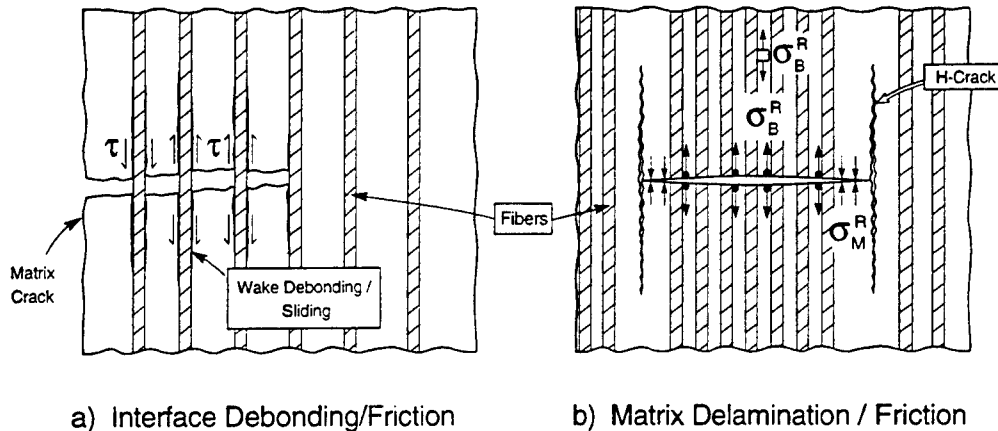


Fig. 16. The two concepts for deviating cracks and inducing frictional dissipation along debonded surfaces. (a) Debonding within fibre coatings. (b) Debonding within the (porous) matrix.

b_1 becomes smaller. A plot of the strengthening achievable as the anisotropy increases for different b_1 (Fig. 15) quantifies the importance of the size scale.

In summary, when such a mechanism prevails, there can be no effect of the ligament width on the steady-strain toughening. The only quantities affecting this behaviour are the aspect ratio and orientations of the ligaments that form, as well as the cleavage energies. Conversely, the strengthening is influenced by the ligament size, with the opposite trend to that associated with frictional toughening. That is, the strengthening increases as the microstructure is refined (Fig. 15).

4. THE ROLE OF 'DUCTILITY'

4.1. Inelastic strains

A mechanism-based strategy for calculating stress redistribution is illustrated using results for CMCs. These composites exhibit inelastic deformations when matrix microcracks are stabilized [19, 58, 73]. This is achieved by using either fibre coatings [42, 74, 75] or porous matrices [73] that deviate cracks toward the loading axis (Fig. 16). The resultant composite microstructure and the ensuing mechanical responses resemble those found in various naturally occurring materials. The fundamental requirement is that the crack deviating sites be homogeneously dispersed throughout the body and that these regions have a low debond energy relative to the fracture energy of the reinforcements [58, 76]. Once the deviation criterion has been satisfied, the inelastic strain is governed primarily by the number density of

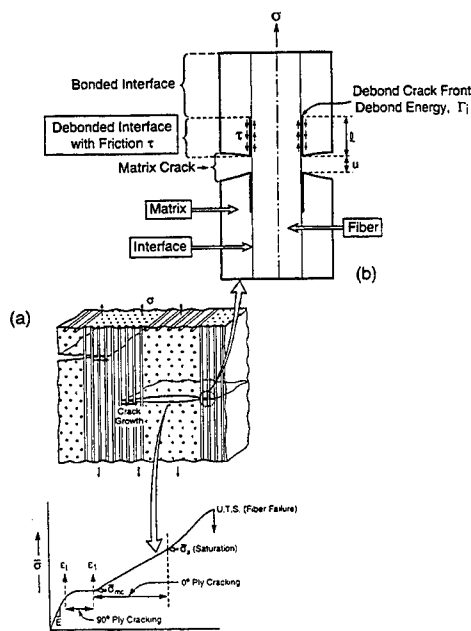


Fig. 17. (a) The ply cracking model and the associated stress-strain curve. (b) The cell model for inelastic strains in the 0° plies.

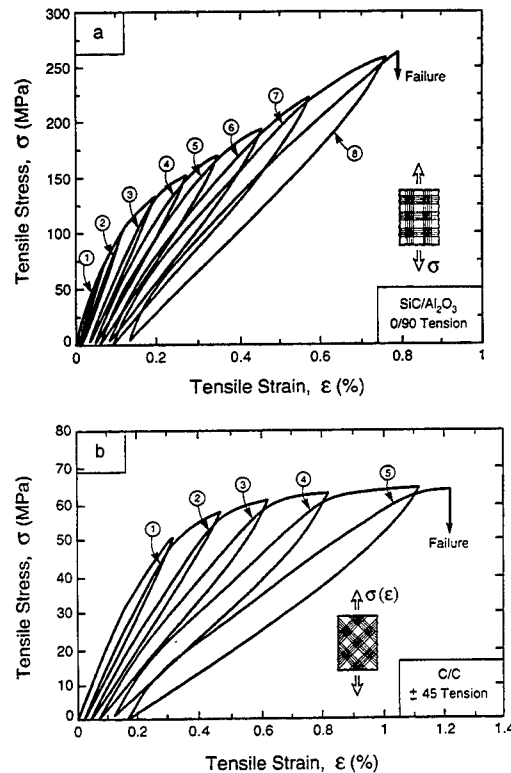


Fig. 18. Hysteresis loops measured on (a) SiC/Al₂O₃ tested $0/90$ in tension, (b) C/C tested in $\pm 45^\circ$ tension.

cracking sites and the friction stress that operates along the debonded crack surfaces [64].

Debonding and friction are commonly encountered in thin brittle layers. They occur by the formation and eventual coalescence of microcracks *en echelon* within a cohesive zone [77]. The associated fracture energy is about four times the mode I fracture toughness of the material in the layer. When debonding occurs, the microcracks coalesce behind the debond and fragment the layer. This process results in a slip zone subject to a friction stress, τ . Models and experiments indicate that τ is affected primarily by the roughness amplitude behind the debond [64]. The residual stress, the elastic compliance of the circumventing material and the friction coefficient are also important [19].

4.2. Stress-strain curves

Two cell models represent most of the important physical relationships between the inelastic strains and the mechanisms of matrix cracking, friction and debonding. One model applies to cracks that first form on the 90° plies (Fig. 17(a)) [78–80]. The other represents cracks that penetrate the 0° plies [81] (Fig. 17(b)). Cracks form first in the 90° plies by tunnelling with an associated inelastic strain [19, 80] (Fig. 17(a)). Upon subsequent loading, as the cracks penetrate the 0° plies, they interact with the fibres and the coatings [79]. When debonding and slip occur within the coating, two stresses

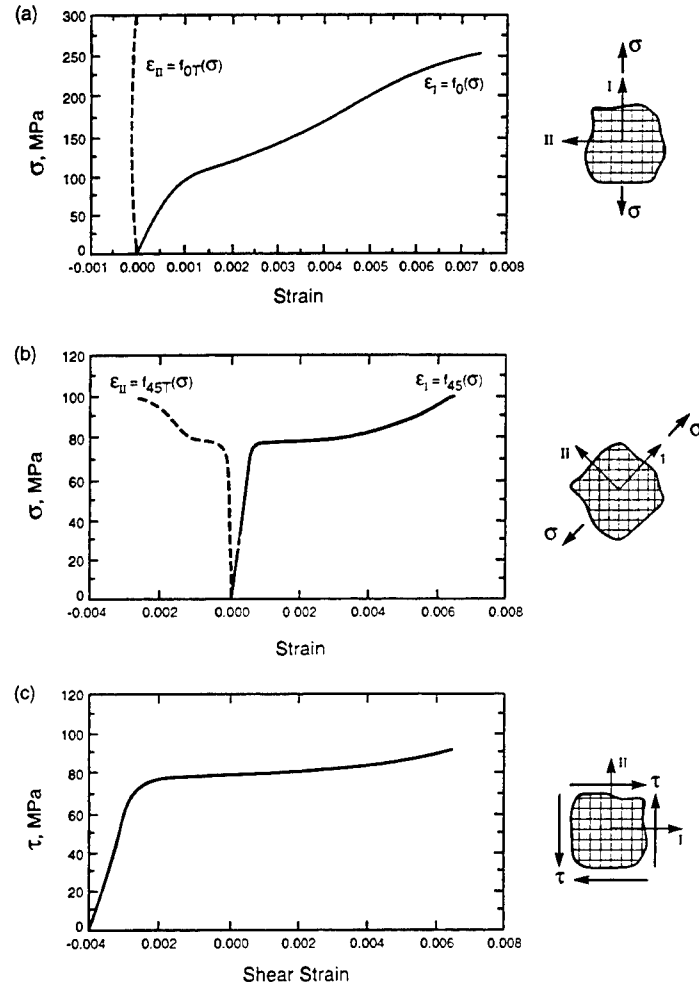


Fig. 19. Stress-strain curves for SiC/CAS materials: (a) 0°/90° longitudinal and transverse strains; (b) $\pm 45^\circ$ axial and transverse strains; (c) shear stress-strain.

characterize the inelastic strain: a friction stress τ , and a debond stress σ_i [81] (Fig. 17(b)). The latter is related to the debond toughness for the coating and the residual stress. The consequent inelastic tensile strain ϵ depends on the stress σ acting on the 0° plies. It has linear and parabolic terms, given by [81, 82]

$$\epsilon = (1 + \Sigma^T)\sigma/E_* + 2\mathcal{L}\sigma^2(1 - \Sigma_i) \times (1 + \Sigma_i + 2\Sigma^T) - \sigma^T/E \quad (23)$$

where Σ_i is the non-dimensional debond stress, ($\Sigma_i = \sigma_i/\sigma$), E_* is the diminished elastic modulus caused by matrix cracking, σ^T is the residual stress ($\Sigma^T = \sigma^T/\sigma$) and \mathcal{L} is an interface friction index, given by [82]

$$\mathcal{L} = \frac{(1-f)^2 R}{4f\tau d E_m} \quad (24)$$

with d being the crack spacing. The parameters E_* , \mathcal{L} and Σ_i , evaluated from hysteresis loops [82]

(Fig. 18) provide understanding about the separate influences of debonding, friction and matrix cracking on the inelastic strain. They also provide the insight needed to develop a constitutive law compatible with finite element codes. Simulations, as well as hysteresis measurements have established the influences of friction and debonding on the stress-strain behavior of CMCs [65, 82]. The principal effects associated with (23) are as follows. The inelastic strain and the hysteresis loop width increase as the friction stress τ decreases (or \mathcal{L} increases). Small τ accounts for the wide hysteresis loops in SiC/CAS. A large debond stress σ_i limits the role of friction and diminishes both the inelastic strain and the hysteresis. Large σ_i accounts for the narrow hysteresis loops in SiC/SiC and SiC/MAS.

These insights have led to the formulation of a constitutive law. The plane stress relation for the stresses and strains in directions (1, 2) obtained by expressing the inelasticity through the stress drops that occur upon matrix cracking in (Fig. 19) [26],

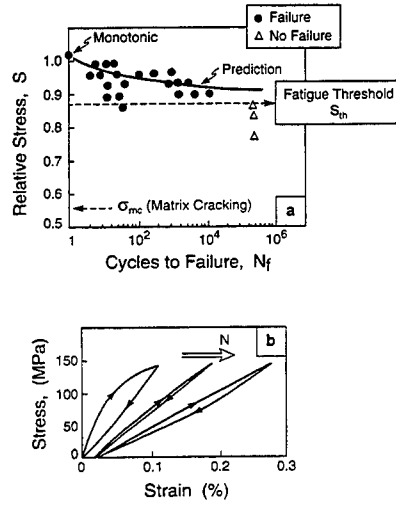


Fig. 20. (a) The S/N curve for a SiC/SiC composite. (b) Hysteresis loop measurements.

$$\sigma_1 = \frac{E_0}{1 - \nu_0^2} (\epsilon_1 + \nu_0 \epsilon_2) + \Delta\sigma_1 \cos^2 \theta + \Delta\sigma_{11} \sin^2 \theta$$

$$\sigma_2 = \frac{E_0}{1 - \nu_0^2} (\epsilon_2 + \nu_0 \epsilon_1) + \Delta\sigma_1 \sin^2 \theta + \Delta\sigma_{11} \cos^2 \theta$$

$$\tau = \frac{E_{45}}{2(1 - \nu_{45})} \gamma_{12} - (\Delta\sigma_1 - \Delta\sigma_{11}) \sin \theta \cos \theta \quad (25)$$

where τ is now the macroscopic shear stress, $\epsilon_{1,2}$ the normal strains and γ_{12} the shear strain; $\Delta\sigma_{1,11}$ are the stress drops upon matrix cracking at fixed strain, parallel and normal to the fibre directions, θ is the angle between (1) and the fibre direction. Some calculations of stress redistribution in a pin loaded configuration have been summarized on Fig. 4. These calculations use (25) with the data for SiC/CAS on Fig. 19. A comparison with experiment is also shown. These results establish that appreciable stress reduction is enabled by the inelastic strain, resulting in a response insensitive to the strain concentration caused by the hole. Other configurations have also been analysed, in some cases demonstrating notch insensitivity [26, 83, 84].

4.3. The ultimate tensile strength (UTS)

The UTS of CMCs is not subject to weakest link have limited susceptibility, because of the stress redistribution enabled by internal friction. The important consequence is that these materials are scale insensitive and subject to Gaussian statistics [20, 21, 68]. Design practice is thus essentially the same as that used in metals. Namely, the peak tensile stress obtained through FEM calculations is equated to the UTS.

The underlying phenomena governing the UTS reside in the effects of internal friction on the dimension, δ , over which the stress concentrations in failed fibres are eliminated. This length becomes an internal scale parameter, enabling the UTS to be

independent of the actual size of the body [22]. The stress evolution of fibre failures still satisfies extreme value statistics and is characterized by a shape parameter, m . Hence, m appears in the expression representing the UTS [22]. For CMCs in which the fibre/matrix interfaces enable stress redistribution through debonding and friction, fibre failures occur in a spatially uncorrelated manner, resulting in global load sharing (GLS) characteristics. In consequence, beyond a slip transfer length, the stress in the fibres is unaffected by the existence of the failure [22]. This length dictates the dimension δ governing the fibre bundle strength. For materials of infinite size, the UTS is given by [22]

$$S_u = f S_c F(m) \quad (26)$$

where

$$F(m) = [2/(m+1)]^{1/(m+1)} [(m+1)/(m+2)]$$

and

$$S_c = S_0 \left[\frac{\tau \delta}{S_0 R} \right]^{1/m}$$

where

$$\delta = [L_0 (S_0 R / \tau)^m]^{1/(m+1)}$$

with L_0 being a reference gauge length (normally 25 mm). The main features described by this result are that the UTS is affected by friction, which sets the 'internal gauge length' and that there is a weak dependence on the shape parameter m , but a strong effect of the reinforcement scale parameter, S_0 (or equivalently, the mean reinforcement strength, S_L).

Even when the friction is less effective and some concentrated stresses persist upon fibre failure, resulting in local load sharing (LLS), the effects on the UTS are not especially deleterious. Actual composites having finite size, subject to LLS, exhibit strengths slightly smaller than that predicted by equation (26). They also exhibit a moderate dependence of the UTS on the gauge length characterised by a Weibull shape parameter over an order of magnitude larger than that for the fibres alone [21, 68]. Moreover, the strength distribution is essentially Gaussian, rather than an extreme value. The 'design friendliness' is thus retained.

Large manufacturing flaws could have a more profound effect on the UTS. These flaws induce a stress concentration governed by the following index, [54, 85],

$$\eta = \frac{\pi f^2 E_f E_a \tau}{(1-f)^2 E_m^2 R S_A} \quad (27)$$

such that the composite strength S becomes [85],

$$S/S_u = (1 + \eta^{2/3})^{-1/2} \quad (28)$$

where a is the size of the largest manufacturing flaw, f is again the fibre volume fraction, A is an anisotropy

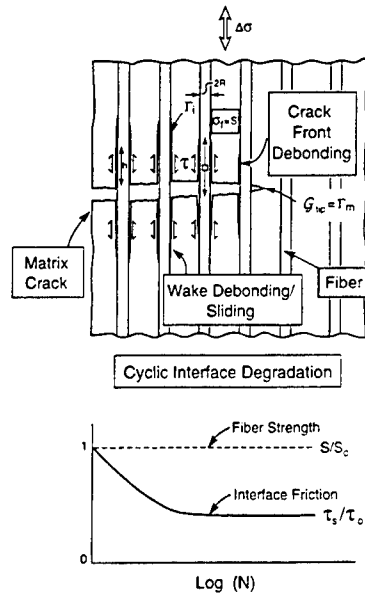


Fig. 21. The phenomena accompanying cyclic loading of CMCs at maximum stresses above that needed to introduce matrix cracks.

coefficient of order unity. When $\eta \rightarrow 0$, there is no effect of manufacturing flaws. Otherwise, such flaws could degrade the UTS. Note that materials with a high friction stress and relatively weak fibres are most prone to degradation by flaws.

Usually, the damaging flaws are limited in size by the ply dimension, h [19, 79, 80]. For typical fibre strengths, this results in a maximum acceptable τ that ensures flaw insensitivity and enables attainment of the GLS strength. This value is, $\tau_{\max} \approx 50$ MPa. Otherwise, the UTS would be lower than the GLS magnitude and the material would have a diminished inelastic tensile strain capacity. Decisions regarding the behaviour of 'ductile' materials need to be made subject to this level of understanding.

5. FATIGUE LIFE PREDICTION

Cyclic degradation acts upon the mechanisms that provide the toughening and the inelastic deformation, causing the materials to embrittle. An understanding of the degradation mechanisms and of their roles in diminishing either toughness or inelastic strain enables development of a fatigue life prediction methodology. In contrast to metals, there is no cyclic growth mechanism operating at the crack front, because there is no plastic blunting [86]. Instead, fatigue operates in the crack wake. For materials toughened by bridging, two principal mechanisms are involved: (i) the friction stress τ diminishes by a 'wear' phenomenon acting along the debonded interfaces [86–93]; (ii) the reinforcement strength decreases by an abrasion mechanism, exacerbated by environmental interactions. Diagnosis of these two factors is achieved with hysteresis and retained strength

measurements (Figs 20–22). The method is particularly well-developed for CMCs [86–93]. By measuring and analysing hysteresis strains, changes in the friction stress and the debond energy upon cycling can be determined [86]. Changes in the reinforcement strengths are obtained by measuring the UTS retained after cycling.

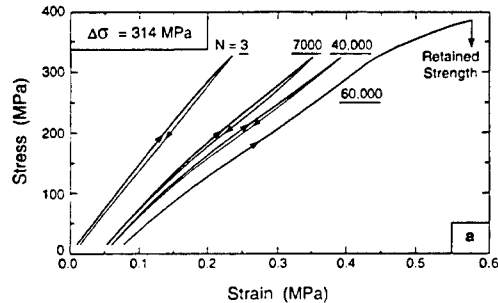
Typically, τ decays after cycling from the initial value τ_0 to a steady-state value τ_s (of order 5–10 MPa). An empirical function that represents the experimental measurements is (Fig. 22),

$$(\tau - \tau_s)/(\tau_0 - \tau_s) = (1 + b_0)(1 + b_0 N)^{-1} \quad (29)$$

where b_0 is a coefficient; j is an exponent which determines the rate at which τ drops with the number of cycles N . It is dependent upon the properties of the interface. Both b_0 and j must be obtained by experiment. The reasons for steady-state friction, τ_s , are not understood, but its existence is crucial to the presence of a threshold stress, S_{th} (Fig. 20). When there is no reinforcement degradation, the ambient temperature fatigue threshold for CMCs becomes [86, 93],

$$S_{th}/S_0 = (\tau_s/\tau_0)^{1/(m+1)} \quad (30)$$

Because the power law exponent, $1/(m+1)$, is small,



EFFECTS OF CYCLING ON FRICTION

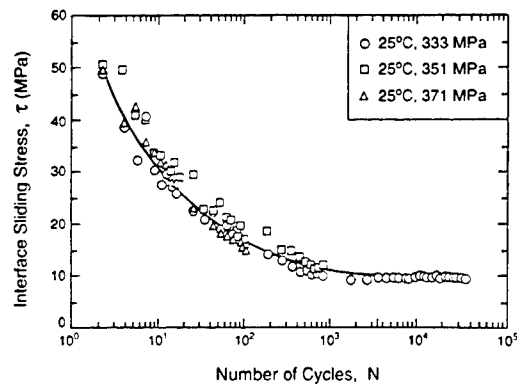


Fig. 22. (a) Hysteresis and retained strength measurements upon fatigue testing of SiC/MAS composites. (b) The change in friction stress upon cycling evaluated from the hysteresis measurements.

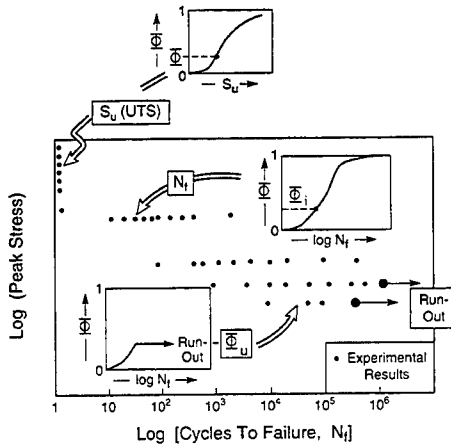


Fig. 23. An approach for measuring the fatigue threshold stress for ceramics.

S_{th} is a large fraction of the UTS: typically 0.7 to 0.8 (Fig. 20). Consequently, for lower temperature applications, where the fibres retain their strength, fatigue does not present life prediction challenges for CMCs. Design of the threshold provides a robust strategy.

Similar characteristics arise in ceramics toughened by a bridging zone. Changes in the bridging tractions upon cycling lead to crack growth. A simple model again identifies the predominant characteristics. In the model, cyclic degradation proceeds uniformly in accordance with equation (29), whereupon it will be shown that $\Lambda(N)$ fully characterizes cyclic crack growth. The energy release rate at the maximum stress is always equal to the current fracture resistance Γ_R and the tip energy release rate remains at Γ_0 . That is, for the crack to extend,

$$G_{max}/\Gamma_0 - 1 = (\Lambda/a_0)^{1/2} \quad (31)$$

But Λ is now cycle dependent and given by equations (19) and (16) with τ as a variable:

$$\Lambda = \Lambda_0(\tau/\tau_0)^3[1 + \Delta a/a_0] \quad (32)$$

with Λ_0 being the magnitude of Λ after the first cycle, when $\tau = \tau_0$. Fracture is considered to occur in accordance with the same requirements used for monotonic loading: that is, when Δa reaches a critical magnitude Δa_c , still given by equation (8). Combining equation (31) with (5) and (7), gives the fracture relation,

$$(S/S_0)^2[1 + \Delta a_c/a_0] = (\Lambda \Delta a_c/a_0)^{1/2} + 1 \quad (33)$$

With equation (8), this becomes,

$$\Lambda = 4(S/S_0)^4[1 - (S/S_0)^2] \quad (34)$$

The cycle dependence of Λ is now invoked, by combining equation (32) with (29),

$$\Lambda = \Lambda_0[(1 + b_0)(1 + N_f)]^{-1} \quad (35)$$

Combining equations (34) and (35), the cycles to failure N_f becomes,

$$N_f = \left\{ (1 + 1/b_0) \frac{(S_{th}/S)^{4/3}[1 - \Omega^2]^{1/3}}{\Omega^{4/3}[1 - (S_{th}/S)^2]^{1/3}} - 1 \right\}^{1/2} \quad (36)$$

There is a threshold stress, S_{th} , as $N_f \rightarrow \infty$. The parameter, $\Omega = S_{th}/S_0$, is a reference stress ratio, with S_0 being the UTS. The S/N behaviour associated with these results is summarized in Fig. 23. The straightforward dependence on a few parameters that can be calibrated by selected experiments provides a basis for a life prediction methodology. A relatively few test data calibrate the key quantities, particularly the threshold stress parameter, Ω . This life prediction approach is analogous to that developed for stress corrosion cracking [94–102]. More complexity could be added to the model, but the methodology then becomes less tractable.

Cyclic tests are performed at three or more peak stress S levels, and the cycles to failure measured. The results at each S are ordered to obtain the survival probability Φ_s as a function of N_f , by using order statistics. Then, the data at given Φ_s are correlated and plotted as a function of S to obtain the slope of the S/N plot. Specimens that exhibit run-out (no failure after a designated number of cycles) provide particularly important information. These data give the threshold stress, at the associated Φ_s . These S_{th} may be compared with the initial strengths S_0 at the same Φ_s to determine the reference threshold stress, $\Omega(\Phi_s)$. This is the crucial quantity, because it scales all other data required for life prediction.

Most non-oxide materials are susceptible to stress oxidation [19, 104–105]: a high-temperature manifestation of stress corrosion (Fig. 24). Again, the phenomenon degrades the toughening. It is particularly debilitating for very tough non-oxide CMCs, especially at intermediate temperature (700–900°C);

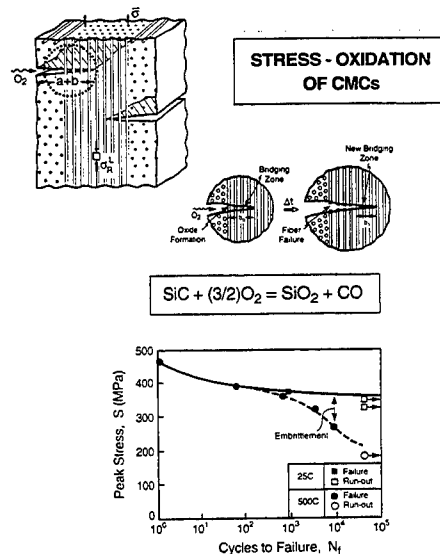


Fig. 24. A schematic of the stress oxidation mechanism that operates in non-oxide CMCs.

that is, 'pest' behavior applies. Matrix cracks created upon loading become pathways for the relatively rapid ingress of oxygen. The oxygen reacts to form both solid and gaseous products. There is a threshold stress below which the phenomenon does not occur, given by [104]

$$S_{th} = \left(\frac{2E_m \Gamma_0}{\pi h} \right)^{1/2} \quad (37)$$

For CMCs, this stress is typically small, of order 10–50 MPa, and too low to enable efficient, lightweight design. Degradation when $\sigma > S_{th}$ occurs according to two rate-limiting phenomena [104]. (i) When the oxygen flow within the cracks is relatively rapid, all reinforcements bridging surface-connected cracks oxidize and weaken simultaneously. When they have degraded sufficiently to fail, the surface cracks extend across the weakened zone and form new crack segments bridged by pristine reinforcements (Fig. 24). This new bridged region again gradually weakens and fails. The process continues in a manner resembling reaction-controlled, stress corrosion cracking. This is the more important regime, because it governs the rupture life at long times. (ii) When the matrix crack opening is narrow, oxygen gradients develop along the crack, resulting in a degradation front that progresses into the material. This process is similar to diffusion controlled, stress corrosion cracking (Fig. 24).

In order to provide a life prediction methodology, three principal phenomena must be addressed [104]: (a) the reduced strength of the reinforcements with an oxide reaction layer; (b) the stress concentration on the reinforcements at the perimeters of unbridged crack segments, (28); (c) the oxygen concentration within the matrix cracks, which is coupled with the thickness of the oxide reaction product on the reinforcements. Analysis of these effects leads to an expression for the failure time Δt_c [104]

$$\Delta t_c \approx t_0 \left[\frac{S_0^4 \sqrt{E \Gamma_0} R^{2/3}}{(\sigma^{13/6} \tau^{1/3}) h^{7/6}} \right] \quad (38)$$

The features emphasized by (38) are the explicit effects of the applied stress and the friction stress as well as the fibre strength. However, the major issue relates to the chemistry, which determines the reference time t_0 . The basic kinetic factors are presently unresolved. An alternative approach is to implement all-oxide systems, which use a porous matrix to stabilize cracks and to induce internal friction (Fig. 16(b)).

6. CHALLENGES AND OPPORTUNITIES

Ceramics have the disadvantage that weakest link statistics must be used for design. The associated size scaling causes practical difficulties in the acquisition of design data, since the survival probabilities at design stress levels must be specified with high

confidence. Such testing becomes prohibitively costly unless either proof testing can be performed on every component or the manufacturing is so consistent that batch-to-batch variability in the stochastic parameters is within a narrow range. The latter would require a processing regimen that regulates the stochastic strength parameters. The stringency of the testing and control regimen can be ameliorated by using reinforcing schemes that toughen the material. The toughening goals are set by requirements for diminished variability in the stochastic parameters governing component survival probabilities at the design stresses. These goals are manifest in the tearing index for the toughening process. This index has explicit forms for each important toughening mechanism. Derivation and discussion of these indices has demonstrated preferences for two mechanisms. (i) Internal friction, achievable through the use of aligned, strong reinforcements with 'weak' interfaces. Materials that optimize this mechanism can become sufficiently tough that ductility is achieved. The thermomechanical phenomena that dictate design and reliability change, are elaborated next. (ii) Microstructures having fine scale cleavage anisotropy sufficient to form elastic ligaments, such as lamellar TiAl, have a tearing index that increases as the microstructure is refined, resulting in potent strengthening. There are opportunities to exploit these toughening and strengthening mechanisms in a manner that enhances 'design friendliness'.

Materials that develop inelastic deformation have the advantage that these strains enable stress redistribution and the implementation of familiar design rules used for metals. Such materials are exemplified by ceramic matrix composites reinforced with continuous, aligned fibres. Moreover, the damage stabilization mechanisms that operate in such materials lead to an 'internal' scaling, which causes the UTS to be insensitive to size and to be distributed in a Gaussian manner. The remaining problems with these materials concern high-temperature degradation and cost. For non-oxide CMCs, oxidation embrittlement is debilitating. Retarding the degradation requires research on multiple coating concepts, as well as on the development of fibres having high purity, at acceptable manufacturing costs.

Implementation requires a robust life prediction methodology in addition to design strategies. One component of such a methodology involves fatigue. Some of the principles governing development of fatigue life prediction methods have been discussed, through phenomena common to toughened ceramics and CMCs, especially those that rely on internal friction to impart toughness and ductility. It is predicated on the interplay between cyclic friction and reinforcement degradation. However, much additional analysis and modelling is needed to establish a comprehensive lifing methodology. The

phenomena still to be addressed include stress oxidation, cyclic creep and thermomechanical fatigue.

REFERENCES

1. R. J. Stokes, *Trans. Met. Soc. of AIME* **222**, 1227 (1962).
2. R. J. Stokes, *J. Am. Ceram. Soc.* **48**, 60 (1965).
3. R. J. Stokes, *J. Am. Ceram. Soc.* **49**, 39 (1966).
4. R. J. Stokes, in *Ceramic Microstructures* (edited by J. M. Fulrath and J. A. Pask), pp. 379. John Wiley & Sons, New York (1968).
5. R. J. Stokes and C. H. Li, *Acta metall.* **10**, 535 (1962).
6. R. J. Stokes and C. H. Li, in *Fracture of Solids* (edited by D. C. Drucker and J. J. Gilman), pp. 289. Interscience Publishers, John Wiley & Sons, New York (1963).
7. J. B. Wachtman, Jr and L. H. Maxwell, *J. Am. Ceram. Soc.* **37**, 291 (1954).
8. J. B. Wachtman, Jr and L. H. Maxwell, *J. Am. Ceram. Soc.* **40**, 377 (1954).
9. J. B. Wachtman, Jr and L. H. Maxwell, *J. Am. Ceram. Soc.* **42**, 432 (1959).
10. S. M. Wiederhorn, *Ann. Rev. Mater. Sci.* **14**, 374 (1984).
11. F. J. P. Clarke, R. A. J. Sambell and H. G. Tattersall, *Phil. Mag.* **7**, 393 (1962).
12. P. B. Hirsch and S. G. Roberts, *Phil. Mag.* **A64**, 55 (1991).
13. B. J. Hockey, *J. Am. Ceram. Soc.* **54**, 223 (1971).
14. M. L. Kronberg, *Acta metall.* **5**, 507 (1957).
15. F. R. N. Nabarro, (editor), *Dislocations in Solids 1-8* (1979-1989).
16. J. R. Rice and G. E. Beltz, *J. Mech. Phys. Solids* **42**, 333 (1994).
17. G. Xu, A. S. Argon and M. Ortiz, *Phil. Mag.* (1995) in press.
18. J. B. Wachtman, *Mechanical Properties of Ceramics*, to be published.
19. A. G. Evans and F. W. Zok, *J. Mater. Sci.* **29**, 3857 (1994).
20. W. A. Curtin, *Appl. Phys. Lett.* **58**, 1155 (1991).
21. R. B. Henstenburg and S. L. Phoenix, *Polym. Compos.* **10**, 389 (1989).
22. W. Curtin, *J. Am. Ceram. Soc.* **74**, 2837 (1991).
23. J. Lamon, *J. Am. Ceram. Soc.* **71**, 106 (1988).
24. A. G. Evans, *J. Am. Ceram. Soc.* **61**, 302 (1978).
25. J. R. Matthews, W. J. Shack and F. A. McClintock, *J. Am. Ceram. Soc.* **59**, 304 (1976).
26. G. Genin and J. W. Hutchinson, *Trans. Am. Ceram. Soc.* (1995) in press.
27. A. Freudenthal, *Fracture* (edited by H. Liebowitz), pp. 341. Academic Press, New York (1967).
28. W. Weibull, *Ingeniorsvetenskapakademiens*, p. 153. Handlingar, Nr (1939).
29. S. B. Batdorf and J. G. Crose, *J. Appl. Mech.* **459** (1974).
30. S. B. Batdorf and D. J. Chang, *Int. J. Frac.* **15**, 191 (1979).
31. S. B. Batdorf and H. L. Heinisch, Jr, *J. Am. Ceram. Soc.* **61**, 355 (1978).
32. S. B. Batdorf and G. Sines, *J. Am. Ceram. Soc.* **63**, 214 (1980).
33. CARES. Software, NASA Lewis Research Center.
34. K. Kendall, N. McNallford, S. R. Tan and J. D. Birchall, *J. Mater. Sci.* **1**, 120 (1986).
35. R. F. Cooke and D. R. Clarke, *Acta metall.* **36**, 555 (1988).
36. A. G. Evans, *J. Am. Ceram. Soc.* **73**, 187 (1990).
37. C. Cady, T. J. Mackin and A. G. Evans, *J. Am. Ceram. Soc.* **78**, 77 (1995).
38. G. Bao and Z. Suo, *Appl. Mech. Rev.*, **45**, 355 (1992).
39. C. Cady, F. E. Heredia and A. G. Evans, *J. Am. Ceram. Soc.* **78**, 2065 (1995).
40. K. M. Prew, *J. Mater. Sci.* **22**, 2595 (1987).
41. D. C. Phillips, *J. Mater. Sci.* **9**, 1874 (1974).
42. J. J. Brennan, *Tailoring of Multiphase Ceramics* (edited by R. Tressler), p. 549. Plenum, New York (1986).
43. J. Aveston, G. A. Cooper and A. Kelly, in *Properties of Fiber Composites: Conf. Proc. National Physical Laboratories*, pp. 15-26. IPC Science and Technology Press, Surrey, UK (1971).
44. P. Becher, *J. Am. Ceram. Soc.* **74**, 255 (1991).
45. R. M. McMeeking and A. G. Evans, *J. Am. Ceram. Soc.* **65**, 242 (1982).
46. D. J. Green, R. H. Hanninck and M. V. Swain, *Transformation Toughening of Ceramics*. CRC Press, Boca Raton, FL (1989).
47. P. R. Becher and T. N. Tieg, *J. Am. Ceram. Soc.* **70**, 651 (1987).
48. A. G. Evans and R. M. Cannon, *Acta metall.* **34**, 761 (1986).
49. C.-W. Li and J. Yamanis, *Ceram. Eng. Sci. Proc.* **10**, 632 (1989).
50. G. Vekinis, M. F. Ashby and P. W. R. Beaumont, *Acta metall. mater.* **38**, 1151 (1990).
51. G. Bao and C. Y. Hui, *Int. J. Solids & Structures* **26**, 631 (1990).
52. B. Budiansky and J. C. Amazigo, *Int. J. Solids & Structures* **24**, 7 (1988).
53. B. Budiansky and J. C. Amazigo, *J. Mech. Phys. Solids* **36**, 5 (1988).
54. B. Budiansky and D. M. Stump, *Acta metall.* **37**, 12 (1989).
55. M. F. Ashby, F. J. Blunt and M. Bannister, *Acta metall.* **37**, 1947 (1989).
56. A. G. Evans and R. M. McMeeking, *Acta metall.* **34**, 2435 (1986).
57. J. W. Hutchinson and D. K. M. Shum, *Mechanics of Materials* **9**, (1990).
58. M. Y. He and J. W. Hutchinson, *J. Applied Mechanics* (Trans. ASME), **56**, 270 (1989).
59. B. D. Flinn, C. S. Lo, F. W. Zok and A. G. Evans, *J. Am. Ceram. Soc.* **76**, 369 (1993).
60. P. A. Mataga, *Acta metall.* **37**, 3349 (1989).
61. J. W. Hutchinson and V. Tvergaard, *J. Mech. Phys. Solids* **40**, 6 (1992).
62. J. W. Hutchinson and V. Tvergaard, *J. Mech. Phys. Solids* **41**, 1119 (1993).
63. H. Deve, A. G. Evans and R. Mehrabian, *Mat. Res. Soc. Symp. Proc.* **170**, 33 (1990).
64. R. Kerans, *Scripta metall. mater.* **32**, 1075 (1994).
65. J. W. Hutchinson, M. Y. He, B.-X. Wu and A. G. Evans, *Mechanics of Materials* **18**, 213 (1994).
66. M. D. Thouless and A. G. Evans, *Acta metall.* **36**, 517 (1988).
67. M. Sutcu, *Acta metall.* **37**, 651 (1989).
68. W. A. Curtin and S. J. Zhou, *J. Mech. Phys. Solids* **43**, 343 (1995).
69. B. Budiansky and J. C. Amazigo, *IUTAM Symposium on Nonlinear Analysis of Fracture*, Cambridge, Sept. (1995).
70. P. F. Becher, *J. Am. Ceram. Soc.* **73**, 255 (1991).
71. K. S. Chan and Y. W. Kim, *Met. Trans.* **24A**, 113 (1993).
72. D. J. Wisnuck, M. Y. He and A. G. Evans, *Acta mater.*, in press.
73. W. Tu, F. F. Lange and A. G. Evans, *J. Am. Ceram. Soc.* **79**, 417 (1996).
74. P. E. D. Morgan and D. B. Marshall, *J. Am. Ceram. Soc.* **78**, 113 (1995).
75. J. B. Davis, J. P. A. Löfvander and A. G. Evans, *J. Am. Ceram. Soc.* **76**(5), 1249 (1993).

76. J. E. Gordon, *The New Science of Strong Materials*. Penguin, London (1968).
77. J. W. Hutchinson and Z. C. Xia, *Int. J. Solids Structures* **31**, 1133 (1994).
78. C. Xia, J. W. Hutchinson, B. Budiansky and A. G. Evans, *J. Mech. Phys. Solids* **42**, 1139 (1994).
79. C. Xia and J. W. Hutchinson, *Acta metall. mater.* **42**, 1935 (1994).
80. C. Xia, R. R. Carr and J. W. Hutchinson, *Acta metall. mater.* **41**, 2365 (1993).
81. J. W. Hutchinson and H. Jensen, *Mech. of Mater.* **9**, 139 (1990).
82. J.-M. Domergue, E. Vagaggini, A. G. Evans and J. Parenteau, *J. Am. Ceram. Soc.* **78**, 2721 (1995).
83. C. M. Cady, T. J. Mackin and A. G. Evans, *J. Am. Ceram. Soc.* **78**, 1 (1995).
84. F. A. Heredia, A. G. Evans and C. E. Anderson, *J. Am. Ceram. Soc.* **78**, 2790 (1995).
85. B. Budiansky and L. Cui, *J. Mech. Phys. Solids* **42**, 1 (1994).
86. A. G. Evans, F. W. Zok and R. M. McMeeking, *Acta metall. mater.* **43**, 859 (1995).
87. J. E. Ritter, Jr, K. Jakus, A. Batakis and N. Bandyopadhyay, *J. Non-Crystalline Solids* **38-39**, 419 (1980).
88. C. J. Gilbert, R. H. Dauskardt and R. O. Ritchie, *J. Am. Ceram. Soc.* **78**, 2291 (1995).
89. S. Lathabai, J. Rödel and B. Lawn, *J. Am. Ceram. Soc.* **74**, 1360 (1991).
90. R. H. Dauskardt, *acta metall. mater.* **41**, 2765 (1993).
91. H. C. Cao, E. Bischoff, O. Sbaizero, M. Rühle, A. G. Evans, D. B. Marshall and J. J. Brennan, *J. Am. Ceram. Soc.* **73**, 1691 (1990).
92. C. J. Gilbert, R. H. Dauskardt, R. W. Steinbrech, R. N. Petrany and R. O. Ritchie, *J. Mater. Sci.* **30**[3], 643 (1995).
93. D. Rouby and P. Reynaud, *Compos. Sci. Technol.* **48**, 109 (1993).
94. A. G. Evans and S. M. Wiederhorn, *Int. J. Frac.* **10**, 379 (1974).
95. A. G. Evans and E. R. Fuller, *Metall. Trans.* **5**, 27 (1974).
96. K. Jakus, D. C. Coyne and J. E. Ritter, Jr, *J. Mater. Sci.* **13**, 2071 (1978).
97. K. Jakus and J. E. Ritter, Jr, *Res. Mechanica* **2**, 39 (1981).
98. K. Jakus, J. E. Ritter, Jr, T. Service and D. Sonderman, *J. Am. Ceram. Soc.* **64**, C174 to C-175 (1981).
99. K. Jakus, J. E. Ritter, Jr and J. M. Sullivan, *J. Am. Ceram. Soc.* **64**, 372 (1981).
100. J. E. Ritter, Jr, in *Fracture Mechanics of Ceramics*, Vol. 4 (edited by R. C. Bradt, D. P. H. Hasselman and F. F. Lange), pp. 667-686. Plenum, New York (1978).
101. J. E. Ritter, Jr, N. Bandyopadhyay and K. Jakus, *J. Am. Ceram. Soc.* **62**, 542 (1979).
102. J. E. Ritter, Jr, N. Bandyopadhyay and K. Jakus, *Bulletin of the Am. Ceram. Soc.* **60**, 7989 (1981).

APPENDIX I: NOMENCLATURE

a	flaw size	A	anisotropy factor (about unity)
a_0	initial flaw size	b_0	interface fatigue coefficient
Δa	crack extension	b	toughening coefficient (9)
Δa_c	critical crack extension	c	inelastic zone length coefficient (10)
		d_0	process zone size coefficient (14)
		d	crack spacing
		E	Young's modulus for composite
		E_0	longitudinal modulus of ply
		E_T	transverse Young's modulus
		E_m	Young's modulus for matrix
		E_f	Young's modulus for fibres
		E_c	Young's modulus of CMC with matrix microcracks
		f	reinforcement volume fraction
		g	attachment factor between fibre and matrix
		g_s	frequency function for strength
		G	strain energy release rate
		G_{max}	maximum G
		h	ply thickness in CMCs
		h	process zone size
		j	fatigue exponent
		\mathcal{L}	interface friction index
		L	inelastic zone size
		m	Weibull shape factor
		N	number of cycles
		N_f	number of cycles to failure
		p	reinforcement pull-out length
		R	reinforcement radius
		S	tensile strength
		S_c	reference fibre strength
		S_{th}	threshold stress for fatigue
		S_u	ultimate tensile strength
		S_0	strength scale factor
		t	time
		t_0	reference time for oxide growth on reinforcements
		Δt_c	rupture time
		t	traction
		t_0	maximum traction
		u	crack opening displacement
		δV	volume element
		δ	stress transfer length
		ϵ	tensile strain
		ϵ_T	transformation strain
		ν_0	Poisson's ratio for 0° loading
		ν_{45}	Poisson's ratio for 45° loading
		Ω	ratio of cyclic threshold stress to UTS
		Γ_R	fracture resistance
		Γ_0	initiation fracture energy
		Γ_i	interface toughness
		Γ_f	reinforcement toughness
		$\Delta \Gamma_R$	transient toughening
		η	stress concentration index
		Λ	strengthening index
		λ	tearing index
		σ	applied stress
		σ_R	ply level residual stress
		σ_c	debond stress
		σ_T	misfit stress
		$\Delta \sigma_{I,II}$	stress drops upon matrix cracking in the I and II orientations
		Σ_i	non-dimensional debond stress
		Σ_T	non-dimensional misfit stress
		τ	friction stress at interface
		τ_0	initial value of τ
		τ_s	steady-state τ after cycling
		ω_L	ligament toughening coefficient
		χ	ligament strengthening coefficient

EFFECT OF INTERFACE UNDULATIONS ON THE THERMAL FATIGUE OF THIN FILMS AND SCALES ON METAL SUBSTRATES

A. G. EVANS¹, M. Y. HE² and J. W. HUTCHINSON¹

¹Division of Engineering and Applied Sciences, Harvard University, Pierce Hall, Cambridge, MA 02138
and ²Department of Materials Engineering, University of California, Santa Barbara, CA 93106, U.S.A.

(Received 12 November 1996; accepted 28 January 1997)

Abstract—Oxide scales that form on superalloys eventually spall, especially upon thermal cycling. This phenomenon is motivated by the large residual *compression* in the oxide. Buckling and interface crack propagation are known aspects of this behavior, but the origin of the interface separation that precedes and activates buckling is not understood. One mechanism is described and analyzed in this article. It relies on the observation that the interfaces are typically non-planar. Such non-planarity can result in cyclic straining of the substrate, near the interface, leading to crack initiation by fatigue. The conditions that lead of cyclic plasticity are analyzed for a typical range of parameters. © 1997 Acta Metallurgica Inc.

1. INTRODUCTION

Thermally grown oxide thin films on metal alloy substrates are known to spall from the substrate upon thermal cycling, particularly Al_2O_3 on Ni or Fe-based alloys [1–4]. The oxide is typically in residual compression, caused primarily by the thermal expansion mismatch between the oxide film and the substrate. Recent measurements suggest that at room temperature these stresses are of the order of 3–5 GPa [5, 6]. In some cases, growth stresses are superposed, but they are relatively small. It has been surmised that these stresses motivate the spalling event. One key connection between the stresses and the spalling mechanism is addressed in this article.

It is established that large compressive stresses can cause buckling when an initial decohesion exists at the interface. The critical requirement for a circular decohesion is that its radius, b , satisfy [8]

$$b > 1.11h \sqrt{\frac{E_i}{(1 - \nu_i^2)\sigma}} \quad (1)$$

where σ is the residual compressive stress, h the film thickness, E_i and ν_i are the Young's modulus and Poisson's ratio of the film. Moreover, upon buckling, there is an energy release rate that can extend the crack and, thereby, cause spalling. The critical requirement for this to occur is expressible through a non-dimensional parameter [7]

$$\Omega = \frac{\sigma^2 h}{E_i \Gamma_i} \quad (2)$$

where Γ_i is the interface toughness. For the buckled configuration to extend, it is required that Ω exceed a critical magnitude, Ω_c , of the order of 6 [8]. Often

the buckles propagate in a linear or “telephone cord” morphology [9] (see Fig. 1).

While the buckling and crack growth aspects of the spalling phenomenon are quite well understood, and experimentally validated [10] it is not known how the initial decohesions needed to satisfy the buckling condition (1) are created. Since the pre-existence of decohesions this large is unlikely, there have been various speculations about their formation, such as void formation and coalescence by diffusion [2, 11], but most of these are kinetic processes which occur at a rate governed primarily by the time spent at the highest temperature. The practical experience is that thermal cycling is often more important than prolonged isothermal exposure [12, 13]. The implication is that thermal fatigue is involved, embodied in cyclic plastic strains occurring either at the interface or in the substrate close to the interface. This realisation provides the basis for engineering models that characterise the cycles to failure, but a mechanistic basis has yet to be established. Such mechanism-based models are needed to identify the key variables and to understand scaling effects with those variables. The objective of this article is to provide a plausible cyclic mechanism with the associated analysis.

For a perfectly planar interface between the oxide and the substrate, there are no shear stresses along the interface, except near free edges and terminations [14–16]. Consequently, for typical thick substrates the yield condition can only be attained in these regions and spalls that occur remote from edges and features could not be explained. Thus, the idea that cyclic plastic strain at the interface could be important has been largely discounted. However, most interfaces

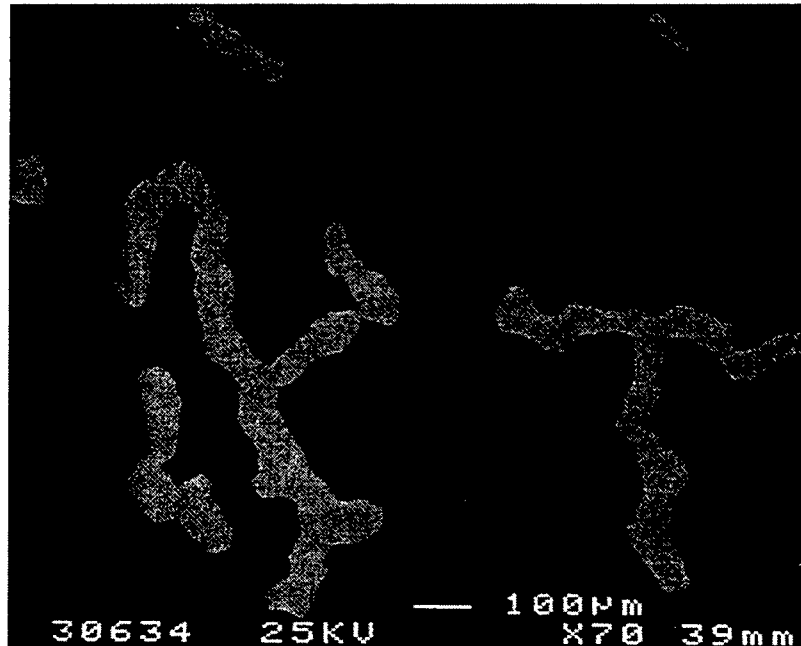


Fig. 1. A spalled region of an oxide scale formed at 1000°C on a Ni aluminide bond coat indicating the telephone cord morphology. The light grey areas are the spalled regions, while the dark grey areas are still attached (J. S. Wang, unpublished research).

with thermally grown oxides are non-planar, because of growth instabilities (Fig. 2) [17]. It will be shown that even small morphological perturbations from planarity have a surprisingly large effect on the stresses at the interface, as well as in the substrate. The conditions under which these stresses can induce cyclic plastic strains are analysed as a possible source of the initial interface decohesions that precede buckling. An elastic perturbation solution is presented first in order to elucidate trends and to identify the salient variables. These results are also used to estimate the plastic zone morphology and the shakedown conditions. Thereafter, detailed finite element results are obtained that embrace the full range of conditions expected in practice.

2. PERTURBATION SOLUTION

An elastically isotropic coating with Young's modulus E_1 , Poisson's ratio ν_1 and average thickness h is bonded to an infinitely deep substrate which is also isotropic with E_2 and ν_2 . The upper surface of the coating is assumed to be planar, but its interface with the substrate is wavy having amplitude A and wavelength L , varying according to $y = (A/2)\cos(2\pi x_1/L)$ (Fig. 3). The substrate/coating system is taken to be infinite in extent in the x_1 and x_2 directions. Gao [18] considered the same type of wavy interfaces, but for the case where both the substrate and the region above the interface are semi-infinite in extent in the direction perpendicular to the interface. Let T_0 be the temperature at which the coating is deposited on the substrate, and define ϵ_0^T to be the

thermal mismatch strain of the coating at any other temperature T as

$$\epsilon_0^T = \int_{T_0}^T (\alpha_1 - \alpha_2) dT \quad (3)$$

where α_1 and α_2 are the coefficients of thermal expansion of the coating and substrate. If the interface is planar ($A = 0$), the substrate is unstressed and two non-zero components of stress in the coating are

$$\sigma_{11}^0 = \sigma_{33}^0 = -\frac{E_1}{1 - \nu_1} \epsilon_0^T \equiv \sigma_0. \quad (4)$$

If the undulation amplitude A is non-zero, the stress and strain *changes* relative to the case with $A = 0$ satisfying the equations of plane strain. In what follows, a perturbation solution for the stresses and strains in the coating and substrate is given with A as the perturbation parameter. The solution, which is obtained to lowest order in A , will be seen to be reasonably accurate for surprisingly large non-planarities. It remains valid as long as the maximum slope of the interface, which is proportional to A/L , is not too large. There is no restriction on the magnitude of h/L . Denote components of stress, strain and displacement in the (x_1, x_2) plane using Greek subscripts in the standard manner, and write the perturbation expansion of the in-plane quantities according to

$$u_i = u_i^0 + A\tilde{u}_i + O(A^2)$$

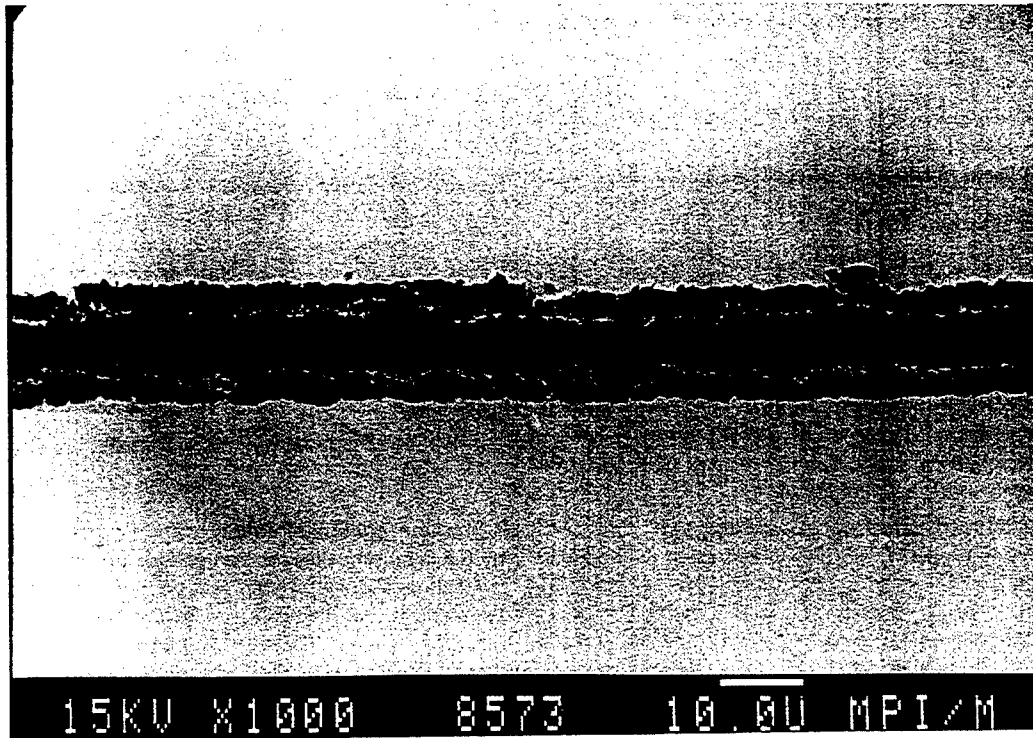


Fig. 2. Scanning electron microscopy of a double cross section of an alumina scale on an iron-based superalloy (FeAlCr) (M. Rühle, unpublished research). The sections are attached by an epoxy bond (black). The dark grey regions are the oxide and the light grey the alloy. Note the undulations at the oxide/alloy interface and the protuberances into the alloy.

$$\begin{aligned}\epsilon_{\alpha\beta} &= \epsilon_{\alpha\beta}^0 + A\tilde{\epsilon}_{\alpha\beta} + O(A^2) \\ \sigma_{\alpha\beta} &= \sigma_{\alpha\beta}^0 + A\tilde{\sigma}_{\alpha\beta} + O(A^2).\end{aligned}\quad (5)$$

All the zeroth order quantities vanish in the substrate, while in the coating $\sigma_{12}^0 = \sigma_{22}^0 = 0$, σ_{11}^0 is given by equation (4), and

$$u_1^0 = 0, \quad u_2^0 = x_2 \epsilon_{22}^0, \quad \epsilon_{11}^0 = 0, \quad \epsilon_{22}^0 = \frac{(1 + \nu_1)}{(1 - \nu_1)} \bar{\epsilon}_0. \quad (6)$$

The first order perturbations in equations (5) must satisfy equilibrium, $\tilde{\sigma}_{\alpha\beta,\beta} = 0$, the strain-displacement

relations, $\tilde{\epsilon}_{\alpha\beta} = \frac{1}{2}(\tilde{u}_{\alpha,\beta} + \tilde{u}_{\beta,\alpha})$, and the plane strain stress and strain relations

$$\begin{aligned}\tilde{\sigma}_{\alpha\beta} &= \frac{E}{1 + \nu} \left(\tilde{\epsilon}_{\alpha\beta} + \frac{\nu}{1 - 2\nu} \tilde{\epsilon}_{\kappa\kappa} \delta_{\alpha\beta} \right) \\ \text{or } \tilde{\epsilon}_{\alpha\beta} &= \frac{1 + \nu}{E} (\tilde{\sigma}_{\alpha\beta} - \nu \tilde{\sigma}_{\kappa\kappa} \delta_{\alpha\beta})\end{aligned}\quad (7)$$

with $(E, \nu) \equiv (E_1, \nu_1)$ in the coating and $(E, \nu) \equiv (E_2, \nu_2)$ in the substrate. Equilibrium is satisfied by stresses generated from an Airy stress function:

$$\tilde{\sigma}_{11} = \Phi_{,22}, \quad \tilde{\sigma}_{22} = \Phi_{,11}, \quad \tilde{\sigma}_{12} = -\Phi_{,12}. \quad (8)$$

Compatibility of the strains, with equation (7), requires that the Airy stress function satisfy

$$\nabla^4 \Phi = 0. \quad (9)$$

Continuity of displacements and tractions must be maintained across and along the wavy interface, $x_2 = y(x_1)$. It is these conditions which produce the non-homogeneous terms in the perturbation procedure. First, consider the continuity condition for displacements, $u_i^{(1)}(x_1, y(x_1)) = u_i^{(2)}(x_1, y(x_1))$, where superscripts (1) and (2) will be used to denote

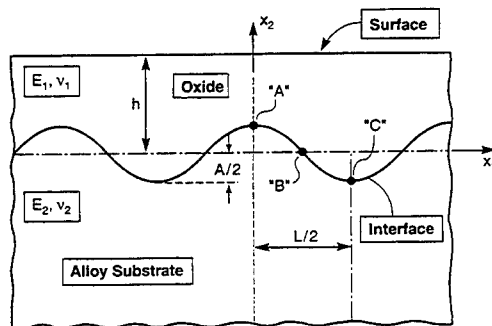


Fig. 3. A schematic of the configuration analysed, indicating the relevant parameters.

quantities in the coating and substrate, respectively. From

$$u_x^{(B)}(x_1, y(x_1)) = u_x^{(B)}(x_1, 0) + \frac{\partial u_x^{(B)}}{\partial x_2}(x_1, 0)y(x_1) + \dots,$$

it follows from displacement continuity that

$$u_x^{(1)}(x_1, 0) - u_x^{(2)}(x_1, 0) = -\left[\frac{\partial u_x^{(1)}}{\partial x_2}(x_1, 0) - \frac{\partial u_x^{(2)}}{\partial x_2}(x_1, 0)\right]y(x_1) + \dots \quad (10)$$

Conditions along the wavy interface are thereby replaced by conditions along $x_2 = 0$. When terms of the order of A are retained in these two equations after having been expressed in terms of the expansions (5), one obtains

$$\tilde{u}_1^{(1)}(x_1, 0) - \tilde{u}_1^{(2)}(x_1, 0) = 0$$

and

$$\tilde{u}_2^{(1)}(x_1, 0) - \tilde{u}_2^{(2)}(x_1, 0) = -\frac{1}{2}\epsilon_{22}^0 \cos(2\pi x_1/L). \quad (11a,b)$$

Similar treatment of traction continuity gives

$$\begin{aligned} \tilde{\sigma}_{12}^{(1)}(x_1, 0) - \tilde{\sigma}_{12}^{(2)}(x_1, 0) &= -(\pi/L)\sigma_{11}^0 \sin(2\pi x_1/L) \\ \text{and } \tilde{\sigma}_{22}^{(1)}(x_1, 0) - \tilde{\sigma}_{22}^{(2)}(x_1, 0) &= 0. \end{aligned} \quad (12a,b)$$

The Airy stress function will be used to generate the perturbation solution in each of the two regions. It is therefore expedient to obtain conditions equivalent to those in equations (11) and (12) expressed in terms of Φ . Conditions from equations (12a,b) follow immediately:

$$\begin{aligned} \Phi_{,12}^{(1)} - \Phi_{,12}^{(2)} &= (\pi/L)\sigma_{11}^0 \sin(2\pi x_1/L) \\ \text{and } \Phi_{,11}^{(1)} - \Phi_{,11}^{(2)} &= 0 \quad \text{on } x_2 = 0 \end{aligned} \quad (13a,b)$$

where $\Phi^{(1)}$ governs in $x_2 > 0$ and $\Phi^{(2)}$ in $x_2 < 0$. It is less straight forward to obtain replacements for equations (11a,b). It is useful at this juncture to anticipate the general result of Dundurs [19] which states that the inplane stresses, $\tilde{\sigma}_{\alpha\beta}$, can be expected to depend on the elastic mismatch between the coating and the substrate through only two mismatch parameters, α_D and β_D . For plane strain, the Dundurs mismatch parameters are

$$\begin{aligned} \alpha_D &= \frac{\bar{E}_1 - \bar{E}_2}{\bar{E}_1 + \bar{E}_2} \\ \text{and } \beta_D &= \frac{1}{2} \frac{\mu_1(1-2\nu_2) - \mu_2(1-2\nu_1)}{\mu_1(1-\nu_2) + \mu_2(1-\nu_1)} \end{aligned} \quad (14)$$

where $\bar{E} = E/(1-\nu^2)$ and $\mu = E/(2(1+\nu))$. The following steps are required to express equation (11a) in terms of Φ . Take the derivative of the equation with respect to x_1 ; note that $\tilde{u}_{1,1} = \tilde{\epsilon}_{11}$; express the strains in terms of stresses via equation (7); and express the stresses in terms of Φ via equation (8).

The final step is to make use of equation (14) and identities derived from equation (14), to arrive at

$$(1 - \alpha_D)\Phi_{,12}^{(1)} - (1 + \alpha_D)\Phi_{,12}^{(2)} + 2(\alpha_D - 2\beta_D)\Phi_{,11} = 0 \quad \text{on } x_2 = 0. \quad (15)$$

The first step in the reduction of equation (11b) starts with two derivatives of the equation with respect to x_1 , permitting displacement quantities to be replaced by strains. From this point on, the procedure parallels that just described, except in the final step when equation (13a) is used to eliminate the non-homogeneous term. The result is

$$\begin{aligned} (1 - \alpha_D)\Phi_{,112}^{(1)} - (1 + 5\alpha_D - 4\beta_D)\Phi_{,112}^{(2)} \\ + (1 - \alpha_D)\Phi_{,222}^{(1)} - (1 + \alpha_D)\Phi_{,222}^{(2)} = 0 \quad \text{on } x_2 = 0. \end{aligned} \quad (16)$$

The four continuity conditions are supplemented by the condition that the top surface of the coating is traction-free ($\Phi_{,11}^{(1)} = \Phi_{,12}^{(1)} = 0$ on $x_2 = h$) and the requirement that the stresses in the substrate decay to zero as $x_2 \rightarrow -\infty$. The system of equations admits a separable solution of the form

$$\begin{aligned} \Phi^{(1)} &= (\sigma_0/\lambda)f^{(1)}(x_2)\cos(2\pi x_1/L) \\ \text{and } \Phi^{(2)} &= (\sigma_0/\lambda)f^{(2)}(x_2)\cos(2\pi x_1/L) \end{aligned} \quad (17)$$

where $\lambda = 2\pi/L$. The general solution to equation (9) satisfying the traction-free condition on $x_2 = h$ and zero stress as $x_2 \rightarrow -\infty$ is

$$\begin{aligned} f^{(1)} &= a_1[\sinh \lambda(x_2 - h) - \lambda(x_2 - h)\cosh \lambda(x_2 - h)] \\ &\quad + a_2\lambda(x_2 - h)\sinh \lambda(x_2 - h) \\ f^{(2)} &= a_3e^{\lambda x_2} + a_4\lambda x_2 e^{\lambda x_2}. \end{aligned} \quad (18)$$

The four continuity conditions, (13a,b), (15) and (16), provide the equations for the four coefficients, a_i :

$$\sum_{j=1,4} M_{ij}a_j = b_i \quad (i = 1, 4) \quad (19)$$

where $b_1 = 1/2$ with $b_i = 0$ for $i = 2, 4$ and

$$M_{11} = \lambda h S, \quad M_{12} = S + \lambda h C,$$

$$M_{13} = 1, \quad M_{14} = 1,$$

$$M_{21} = -S + \lambda h C, \quad M_{22} = \lambda h S,$$

$$M_{23} = -1, \quad M_{24} = 0,$$

$$M_{31} = (1 - \alpha_D)(S + \lambda h C),$$

$$M_{32} = (1 - \alpha_D)(2C + \lambda h S),$$

$$M_{33} = -1 - 3\alpha_D + 4\beta_D, \quad M_{34} = -2(1 + \alpha_D),$$

$$M_{41} = -2(1 - \alpha_D)C, \quad M_{42} = -2(1 - \alpha_D)S,$$

$$M_{43} = 4(\alpha_D - \beta_D), \quad M_{44} = -1 + 2\alpha_D - 4\beta_D \quad (20)$$

with $S \equiv \sinh(\lambda h)$ and $C \equiv \cosh(\lambda h)$. Formulas for the a_i are too lengthy to be revealing, and, therefore, numerical solution of equation (19) is used to

generate results. Note that the a_i depend on the two Dundurs parameters and $\lambda h = 2\pi h/L$.

2.1. Stress at the interface in the substrate

The solution provides stresses to the order of A/L in the coating and in the substrate, for which the stresses vanish when $A = 0$. The emphasis here will be on the stresses in the substrate at the interface, which are given by

$$\begin{aligned}(\sigma_{11}, \sigma_{22}) &= \sigma_0 A \lambda \cos(2\pi x_1/L)(a_3 + 2a_4, -a_3), \\ \sigma_{12} &= \sigma_0 A \lambda \sin(2\pi x_1/L)(a_3 + a_4).\end{aligned}\quad (21)$$

The associated out-of-plane stress is $\sigma_{33} = \nu_2(\sigma_{11} + \sigma_{22})$, which brings in a dependence on ν_2 in addition to the Dundurs parameters. The von Mises effective stress in the substrate just below the interface is

$$\begin{aligned}\sigma_e &= \left\{ \frac{1}{2} [(\sigma_{11} - \sigma_{22})^2 + (\sigma_{11} - \sigma_{33})^2 \right. \\ &\quad \left. + (\sigma_{22} - \sigma_{33})^2] + 3\sigma_{12}^2 \right\}^{1/2} \\ &= |\sigma_0 A/L| \{ [Q_n \cos(2\pi x_1/L)]^2 \\ &\quad + [Q_s \sin(2\pi x_1/L)]^2 \}^{1/2}\end{aligned}\quad (22)$$

where

$$\begin{aligned}Q_n &= 2\pi \{ (1 - \nu_2 + \nu_2^2) [(a_3 + 2a_4)^2 + a_3^2] \\ &\quad + (1 + 2\nu_2 - 2\nu_2^2) a_3(a_3 + 2a_4) \}^{1/2} \\ Q_s &= 2\pi \{ 3(a_3 + a_4)^2 \}^{1/2}\end{aligned}\quad (23)$$

Note that $\sigma_e = |\sigma_0 A/L| Q_n$ is the effective stress in the substrate at the peaks and valleys of the interface undulation where the shear stress vanishes, while $\sigma_e = |\sigma_0 A/L| Q_s$ is the corresponding value at the midpoints where the maximum magnitude of the shear stress occurs and the normal components of stress vanish.

Plots of Q_n and Q_s as functions of α_D are given in Fig. 4 for five values of h/L with $\beta_D = \alpha_D/4$ and $\nu_2 = 0.3$. The dependence of these quantities on β_D was established by repeating the calculations with $\beta_D = 0$, which produces only small numerical changes from the results in Fig. 4. Since $0 < \beta_D < \alpha_D/4$ for most bi-material systems, it follows that β_D is of secondary importance. Similarly, the effect of ν_2 has been determined to be relatively small. More importantly, it can be seen that Q_n and Q_s are not only nearly equal, but they have little dependence on h/L over the probable range of interest for this parameter. It follows from these two observations that the von Mises effective stress in the substrate just below the interface is nearly independent of x_1 and can be approximated by

$$\begin{aligned}\sigma_e &= |\sigma_0 A/L| Q(\alpha_D) \\ \text{where } Q &\cong 3(1 - \alpha_D) - \frac{1}{2}(1 - \alpha_D)^2.\end{aligned}\quad (24)$$

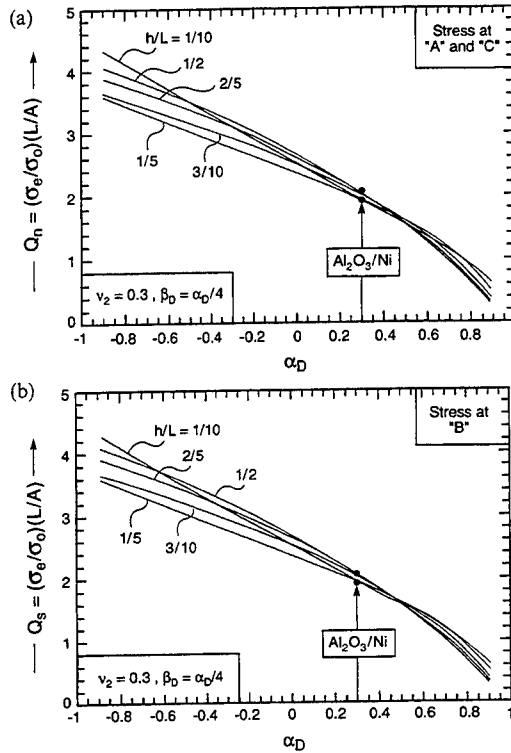


Fig. 4. Effect of the Dundurs parameter α_D on the non-dimensional factors in equation (22) for a range of normalized film thicknesses, h/L : ($\beta_D = \alpha_D/4$ and $\nu_2 = 0.3$): (a) Q_n (b) Q_s . (Note that there is little effect of the film thickness.) The α_D relevant to the $\text{Al}_2\text{O}_3/\text{Ni}$ system used for numerical analysis is indicated by the arrow.

2.2. Application of the perturbation solution to substrate yielding and shakedown

To provide a specific example, suppose the coating is deposited at T_0 and subsequently cooled to T . The thermal expansion mismatch, $\Delta\alpha = \alpha_1 - \alpha_2$, is imagined to be negative such that the thermal reference stress σ_0 in equation (4) is negative (compressive). In addition, to simplify the discussion, the yield strength of the substrate σ_Y will be assumed to be independent of temperature, but this restriction will be lifted in Section 3.

By equating σ_e to the yield strength of the substrate, the effect of the interface roughness on the incidence of substrate yielding can be estimated. By equation (24), the temperature drop at first yield corresponds to

$$\sigma_0 = -\frac{\sigma_Y}{Q(\alpha_D)} \left| \frac{L}{A} \right|. \quad (25)$$

Note that yielding is essentially independent of h/L , but there is a strong dependence on the elastic mismatch through α_D . Higher modulus films ($E_1 > E_2$ with positive α_D) decrease Q , but the effect is counteracted by the larger misfit stress as E_1 increases. There is an explicit inverse dependence on

the relative amplitude of the interface undulations, A/L . These trends are used to establish the scope of selected numerical calculations presented in Section 3.

Upon thermal cycling with amplitude $\Delta T = T_0 - T$, it can be asserted that some plastic straining will occur in each cycle if the change $\Delta\sigma_e$ in the effective stress, due to ΔT , exceeds $2\sigma_Y$ predicted by an elastic analysis [20]. Elastic shakedown is only possible if $\Delta\sigma_e \leq 2\sigma_Y$. In Section 3 it will be established that the shakedown limit for coating/substrate systems is well approximated by the condition $\Delta\sigma_e = 2\sigma_Y$. Based on the perturbation result (4), the shakedown condition for the idealized case of a temperature-independent substrate yield stress is therefore that ΔT be

$$-\sigma_0 \leq \frac{2\sigma_Y}{Q(\alpha_D)} \left| \frac{L}{A} \right|. \quad (26)$$

The significance of equation (26) is that, when satisfied, the substrate response becomes elastic after the first cycle. Consequently, there can be no fatigue, rendering this mechanism incapable of creating initial decohesions at the interface. Condition (26) thus becomes a benchmark for ascertaining the thermal range, ΔT , and roughness amplitude, A/L , above which thermal fatigue can be anticipated.

3. NUMERICAL RESULTS

The numerical calculations are performed for a thin film on a very thick substrate, so that bending of the substrate is excluded. Symmetry permits a unit cell of width $L/2$ to be analysed, extending from $x_1 = 0$ to $L/2$ in Fig. 3, with periodic boundary conditions imposed. A finite element mesh designed to resolve the stresses near the coating/substrate interface was used in carrying out the calculations. A difference in thermal expansion coefficient, $\Delta\alpha = \alpha_1 - \alpha_2$, between the film and substrate is imposed. In the numerical calculations, the elastic properties are chosen to represent Al_2O_3 on Ni alloys (Table 1), such that the Dundurs' parameters are: $\alpha_D = 0.31$ and $\beta_D = 0.06$. The Poisson's ratio in the substrate is $\nu_2 = 0.3$. The film thickness is kept constant at $h/L = 1$, since the preceding analytical results have indicated that this dimension has only a second order influence on the stresses. (Selected numerical results for smaller values of h/L were obtained to further verify this assertion.)

Elastic calculations of the effective stress in the substrate have been made at the point where it is largest (point "A" in Fig. 3, just below the interface

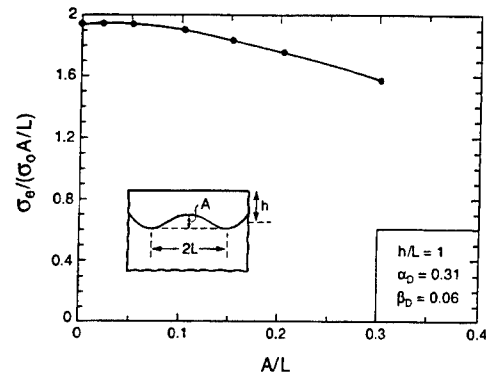


Fig. 5. Dependence of normalized effective stress at point "A" determined from an elastic computation, as a function of A/L . Note the extensive range of accuracy of the perturbation solution. Compare the results as $A \rightarrow 0$ with the analytic results for $\alpha_D = 0.31$ from Fig. 4.

at $x_1 = 0$) as a function of A/L . The solution depends linearly on the reference stress σ_0 in equation (4). The result is normalized in a way that brings out the accuracy of the perturbation solution. The numerical results (Fig. 5) approach the perturbation result as A/L becomes small, evident upon comparing the asymptote $A/L \rightarrow 0$ with Q_e or Q_n from Figs 4(a) and (b) (for $\alpha_D = 0.31$). This consistency provides a check on the accuracy of the finite element model. Moreover, the two sets of results continue to approximate each other reasonably well, even for undulation amplitudes as large as $A/L = 0.3$.

Contours corresponding to constant values of effective stress in the substrate as computed by the finite element model, assuming that the *substrate remains elastic*, are displayed in Fig. 6 for three values of A/L . The significance of these stress levels can be appreciated by noting that σ_0 for the $\text{Al}_2\text{O}_3/\text{Ni}$ system at room temperature is about -3 GPa [6]. At the smallest undulation amplitude, $A/L = 0.1$, the contour of constant effective stress is almost parallel to the interface in close accord with the approximate perturbation result in equation (24). This characteristic is attributed to the largely deviatoric nature of the deformations arising at all locations along the interface. That is, at the peaks and valleys of the undulations (points "A" and "C" in Fig. 3), yielding is encouraged by a combination of either tensile σ_{11} and compressive σ_{22} stresses, or vice versa, while at the mid-position (point "B"), shear stresses σ_{12} are dominant. Some variation of σ_e along the interface becomes apparent at $A/L = 0.3$. The largest value is attained just below the interface at the peak of the undulation (point "A"), and the smallest value at point "B". The effective stress at the valley of the undulation (point "C") is intermediate between the other two values. These trends are further emphasised at the largest amplitude shown, $A/L = 0.5$. It is apparent from this numerical example that effective stresses, large enough to produce plastic staining in the substrate, must be expected when interface

Table 1. Material properties summary

Material	E (GPa)	ν	α ($10^{-6} \text{ } ^\circ\text{C}^{-1}$)
Al_2O_3	400	0.2	8
Ni alloy	200	0.3	15

undulations are not tightly controlled. By this example and the results in Fig. 5, it has also been demonstrated that the perturbation results can be used with confidence to predict elastic stresses for undulation amplitudes as large as about $A/L = 0.3$.

3.1. Temperature-independent yield strength

To establish limits on temperature variations corresponding to initial plastic yielding and to elastic shakedown for thermal cycling, an elastic-perfectly plastic substrate with a temperature-independent yield strength, σ_y , is considered first. The following history is prescribed in accordance with the notation in Fig. 7, which depicts the effective stress variation at a point in the substrate such as "A". The coating is assumed to be deposited stress-free at temperature T_0 . The temperature T is then lowered to $T_4 \equiv RT_0$, generating a compressive thermal reference stress σ_0 defined in equations (3) and (4). The results presented below in terms of σ_0 do not require that the mismatch in the coefficients of thermal expansion be temperature independent, but when it is,

$$\sigma_0 = -\frac{E_1 \Delta \alpha (T_4 - T_0)}{(1 - \nu_1)} \quad (27)$$

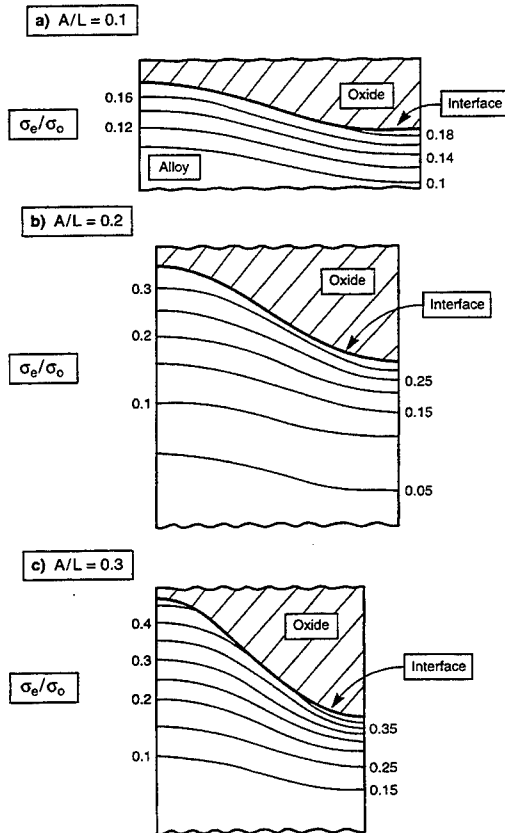


Fig. 6. Equivalent stress contours in the substrate at three undulation amplitudes as determined by an elastic analysis using the finite element model ($\alpha_D = 0.31$, $\beta_D = 0.06$, $\nu_2 = 0.3$, $h/L = 1$).

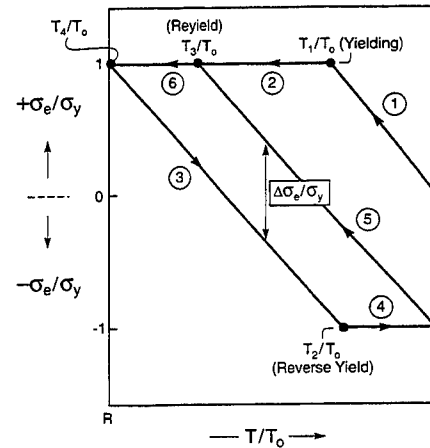


Fig. 7. History of effective stress at a point such as "A" in an elastic-perfectly plastic substrate with a temperature-independent yield strength σ_y . The film/substrate system is subject to a temperature history with cycles from T_0 to T_4 , where the initial stress is taken to be zero at the start of the history at T_0 . The case illustrated involves plastic straining in each cycle. For the purposes of displaying the effective stress history it is convenient to plot the variation by changing the sign of σ_e at each T where it becomes zero, in the manner illustrated here. This reflects the fact that individual components of stress change sign when T is varying monotonically and σ_e vanishes.

At this point the temperature is raised back to T_0 , and the temperature history is repeated, cycling between T_0 and T_4 . The same two questions examined in Section 2.2 are first readdressed here: (i) Is R sufficiently large that no plastic yielding occurs in the entire history? (ii) If not, is R in the range such that plastic deformation occurs in the first few cycles but subsequently shakes down with only an incremental elastic response (i.e. the hysteresis loop, $3 \rightarrow 4 \rightarrow 5 \rightarrow 6 \rightarrow 3$, in Fig. 7 has zero width)?

Results of the numerical calculations are shown in Fig. 8 for the elastic-perfectly plastic substrate with a temperature independent yield strength σ_y . The solid line curve labelled "initial yielding" corresponds to the largest magnitude of σ_0 such that no yielding occurs during the thermal history at a given undulation amplitude A/L . The solid line labelled "elastic shakedown" represents the largest magnitude of σ_0 at a given A/L such that after one or more thermal cycles, no subsequent plastic yielding occurs. Note that the shakedown reference stress is approximately twice the reference stress at initial yield. Moreover, the predictions based on the perturbation analysis, equations (25) and (26), which are plotted as dashed curves, provide a good approximation to the numerical results even at interface undulation amplitudes as large as $A/L = 0.3$. With due account for the temperature dependence of σ_y , the results from the perturbation analysis can be used to establish conditions on the thermal cycles which ensure shakedown.

When σ_0 lies between the curves labelled "initial yield" and "elastic shakedown" in Fig. 8, plastic yielding occurs as the temperature drops toward T_4 , but upon reheating to T_0 , there is no reverse yielding and the substrate experiences only elastic deformation in the subsequent thermal cycles. When σ_0 lies above the elastic shakedown threshold, reversed plastic flow occurs in the first cycle as the temperature is brought back up to T_0 . Figure 9 displays the active plastic zones in the *first cycle*, at $T = T_4$ and then at the end of the cycle at $T = T_0$. After one or more subsequent cycles, plastic straining settles down to steady hysteretic behavior, as illustrated by two sets of numerical results in Fig. 10 for ϵ_2^p at "A". Included in Fig. 8(b) are curves associated with two levels of effective plastic strain increment,

$$\Delta \epsilon_c^p = \int_{T_2}^{T_0} \sqrt{\frac{2}{3} \dot{\epsilon}_{ij}^p \dot{\epsilon}_{ij}^p} dt, \quad (28)$$

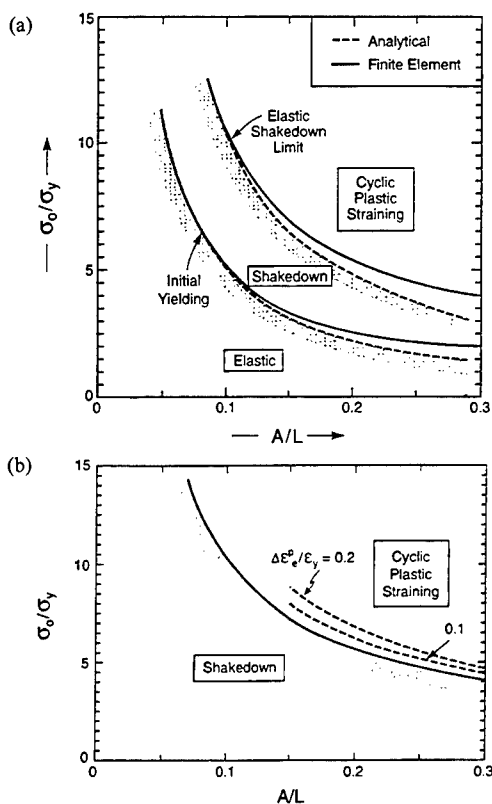


Fig. 8. Thermal fatigue maps characterising the regions in which initial yielding, shakedown and cyclic plasticity occur. The ordinate is the ratio of the reference thermal stress to the substrate yield strength and the abscissa is the ratio of the amplitude to the wavelength of the roughness, A/L . (a) Estimates obtained from the perturbation analysis (dashed curves) and from the finite element analysis (solid curves) are both shown. (b) Above the shakedown threshold, curves corresponding to specified effective plastic strain amplitudes characterizing the width of the hysteresis loop are also plotted, as obtained from the numerical calculations. The yield strength is independent of temperature, $\alpha_D = 0.31$, $\beta_D = 0.06$, $\nu_2 = 0.3$ and $h/L = 1$.

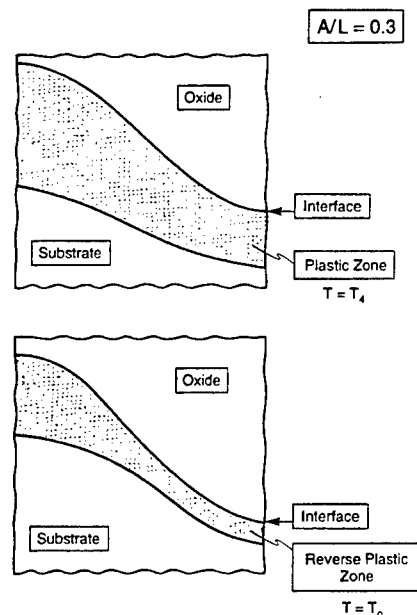


Fig. 9. Typical active plastic zones in the first thermal cycle from the numerical calculations when σ_0 exceeds the shakedown threshold. (a) Initial zone on cooling to T_4 ; (b) reverse plastic zone on reheating to T_0 . The results correspond to $\sigma_0/\sigma_Y = 7$. The temperature T_4 and T_0 are defined in Fig. 7.

normalized by the elastic yield strain $\epsilon_Y = \sigma_Y/E_2$. This measure characterizes the width of the cyclic hysteresis loop (c.f. Figs 7 and 10) when σ_0 exceeds the shakedown threshold. The values in equation (28) were calculated at point "A", but the equivalent stresses and strains calculated at this location closely represent the behavior found at all other locations along the interface. Thermal fatigue is expected to be related to the level of reversed plastic strain per cycle in the substrate at the interface if this is the operative mechanism.

3.2. An example for a substrate with a temperature-dependent yield strength

The yield strength of the substrate can vary significantly over the temperature cycle, as illustrated by data for a superalloy and an intermetallic in Fig. 11 [21]. To illustrate how such temperature-dependent yielding affects the deformation history of the substrate, numerical computations have been carried out for a hypothetical case where the substrate is again elastic-perfectly plastic with $\sigma_Y(T)$ varying linearly from 700 MPa at 0°C to 220 MPa at 1000°C. The other properties of the film and the substrate are temperature-independent and taken to be the same as those used in the previous sub-section. The imposed temperature variation starts at $T = 1000^\circ\text{C}$, where the stress in the substrate is assumed to be zero, and is subsequently cycled between 0 and 1000°C. The effective stress history at point "A" is plotted in Fig. 12(a) in the same manner

as for the earlier case. Now, as the temperature drops and yielding occurs, the effective stress increases in accordance with the temperature-dependent yield stress. As the temperature reverses in the second half of the cycle, the opposite happens. The history of the dominant plastic strain component at "A" is displayed in Fig. 12(b). After the first cycle, a steady hysteresis sets in with reversed plastic straining in each cycle.

4. SOME USEFUL APPROXIMATIONS

The preceding results suggest approximations that might be used for the development of a mechanism-based life prediction methodology. The underlying principles are illustrated by graphical presentations which commence with the construction of Fig. 13. Let T_U and T_L denote the upper and lower limits, respectively, of the repeated temperature cycle. Plot the curves for the substrate yield strength, $\pm\sigma_y(T)$, over this temperature range. Attention will focus on whether or not cyclic plastic straining occurs, and not

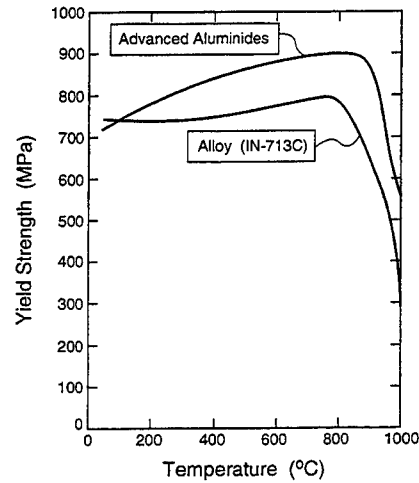


Fig. 11. Temperature dependence of yield strength for a typical superalloy, as well as for an intermetallic that might be used as bond coat.

on the less important issue of initial yield following coating or scale growth. It should be evident from the two previous numerical examples that development of a steady hysteresis cycle is tied to T_U and T_L and not the deposition temperature, T_0 , which need not coincide with T_L . Construct the hysteresis loop in

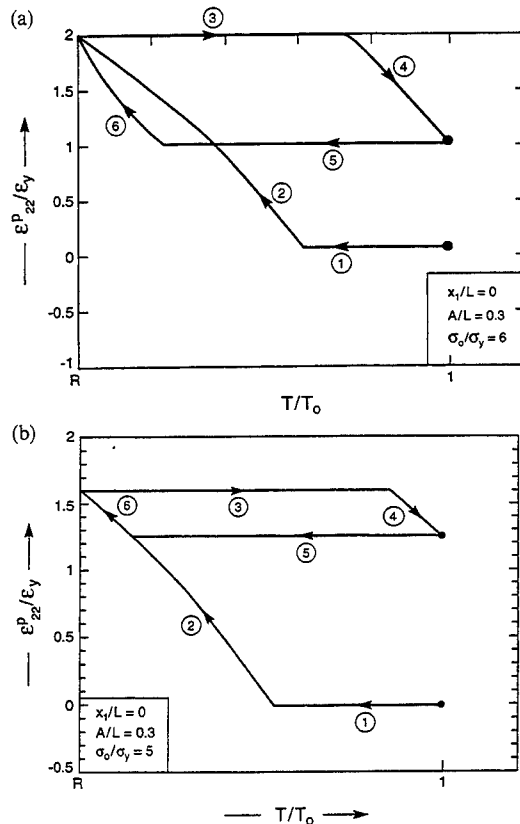


Fig. 10. The history of the plastic strain component, ϵ_{zz}^p , at point "A". The segments of the history are numbered to correspond with the numbering in Fig. 7. Beyond the first cycle, the history of ϵ_{zz}^p repeats itself. Similar plots pertain to other plastic strain components and to other locations. The results have been computed for the case: (a) $\sigma_0/\sigma_y = 6$ and (b) $\sigma_0/\sigma_y = 5$.

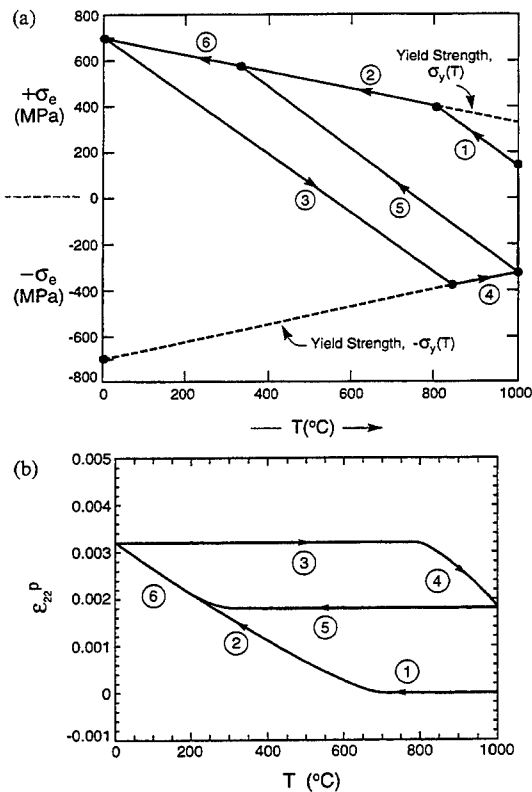


Fig. 12. A numerical example illustrating the effect of a temperature-dependent substrate yield strength. (a) Effective stress history, and (b) history of ϵ_{zz}^p at point "A".

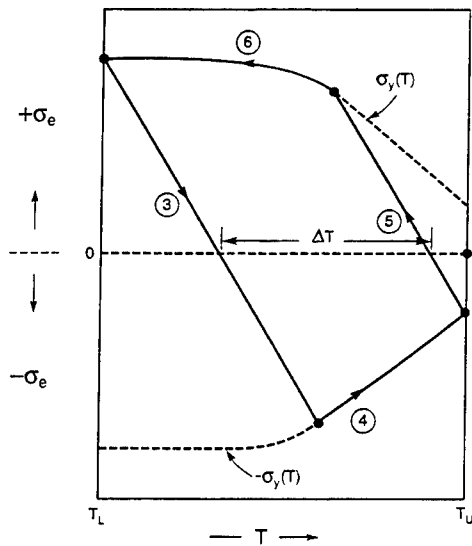


Fig. 13. Plot of effective stress history at the interface in the substrate in steady thermal cycling between T_U and T_L for an elastic-perfectly-plastic substrate with a temperature-dependent yield strength. The width of the loop, ΔT , is taken at the axis $\sigma_e = 0$, as shown.

Fig. 13 by drawing line #3 starting at $\sigma_y(T_L)$. In this segment of the cycle the response of the substrate is elastic, and thus, from equation (24), the slope of the line is well approximated by

$$\frac{d\sigma_e}{dT} = - \left| \frac{E_1 \Delta \alpha}{(1 - \nu_1)} \frac{A}{L} \right| Q(\alpha_D). \quad (29)$$

In plotting Fig. 13, the mismatch in thermal expansion coefficients was taken to be independent of temperature, such that line #3 is straight. In a similar manner, draw in line #5 starting at $-\sigma_y(T_U)$, also with slope (29). The case depicted in Fig. 13 illustrates a history with reversed plastic straining in each cycle. If it had been the case that

$$\left| \frac{E_1 \Delta \alpha}{(1 - \nu_1)} \frac{A}{L} \right| Q(\alpha_D) [T_U - T_L] < [\sigma_y(T_U) + \sigma_y(T_L)], \quad (30)$$

then the loop would have zero width and elastic shakedown would pertain.

If elastic shakedown is not predicted, it is expected that the fatigue life of the coating will depend on the level of the plastic straining (28) in each thermal cycle at the interface in the substrate. Insight into the magnitude of plastic strains occurring in each cycle when the shakedown limit (30) is exceeded can be obtained from an understanding of the stresses and strains which develop along the interface in an elastic cycle. Were no tractions to be exerted by the substrate on the coating (away from the substrate edges), equilibrium would result in higher inplane stress and strain where the coating is thinner. The film would

clearly undergo in-plane straining incompatible with the substrate. The stresses and strains which develop at the interface in the substrate arise to enforce strain compatibility and to counteract the force imbalance in the coating. The shear traction on the interface is largest midway between the peaks and valleys of the interface undulation, alternating in sign so as to consistently stretch or compress the respective thin and thick sections of the coating. The normal traction attains the largest magnitude at the peaks and valleys of the undulation, also alternating in sign. Plastic deformation at the interface in the substrate tends to relax the requirement of local in-plane strain compatibility between the coating and the substrate. It is to be expected, therefore, that the plastic strain induced once yielding starts should be of the order of the elastic strain which would otherwise occur.

An approximate expression for the width of the plastic hysteresis loop, $\Delta \epsilon_p^*$, is developed based on the above reasoning. Consider first substrates with a temperature-independent yield strength. Let $\Delta \sigma_0$ denote the change in the thermal reference stress (4) occurring after the yield in the substrate starts in any cycle. That is, if Δx is temperature-independent and ΔT denotes the width of the loop in a plot such as Fig. 13, then

$$\Delta \sigma_0 = \frac{E_1 \Delta \alpha \Delta T}{(1 - \nu_1)}. \quad (31)$$

Using equation (24) to estimate the associated increment in the effective strain, $(\Delta \epsilon_e)_{\text{elastic}}$, as predicted by an elastic analysis, gives i.e.

$$(\Delta \epsilon_e)_{\text{elastic}} = \left| \frac{\Delta \sigma_0}{E_2} \frac{A}{L} \right| Q. \quad (32)$$

As an approximation, the effective plastic strain increment $\Delta \epsilon_p^*$ can be expressed as

$$\frac{\Delta \epsilon_p^*}{(\Delta \epsilon_e)_{\text{elastic}}} = F \left[\frac{(\Delta \epsilon_e)_{\text{elastic}}}{\epsilon_Y} \right] \quad (33)$$

where F is a function. Numerical results for $\Delta \epsilon_p^*$ from the finite element calculations for substrates with a temperature-independent yield stress are plotted in this manner in Fig. 14. The function

$$F(x) = 1.32x - 0.668x^2 + 0.123x^3 \quad (34)$$

gives a good fit to the data for $A/L = 0.3$ over the range plotted. The formula (33) clearly fails to capture the full A/L dependence, but in conjunction with equation (34) should provide a useful approximation. Any formula such as equation (33) must necessarily over-simplify the cyclic plastic strain dependencies. In a given cycle, yielding starts at point "A" and spreads along the interface. Formula (33) reflects the fact that there will be more constraint to plastic flow when $(\Delta \epsilon_e)_{\text{elastic}}/\epsilon_Y$ is small than when it is of order unity with yielding occurring all along the interface.

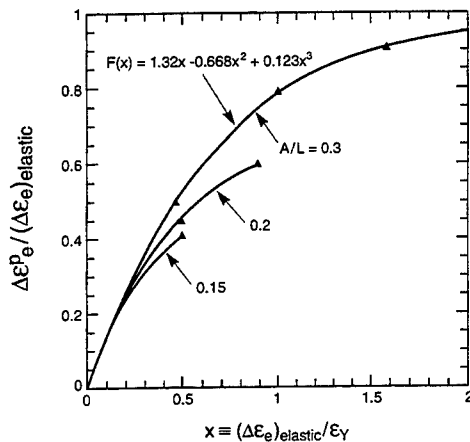


Fig. 14. Selected numerical results for the width of the hysteresis loop as measured by $\Delta\epsilon_p^p$ and the function $F(\cdot)$ in equation (33).

Accurate prediction of $\Delta\epsilon_p^p$ for substrates with temperature-dependent yielding will require further research. In the interim, the following approach based on equation (33) is suggested. Two additional complications now arise in using equation (33) to predict $\Delta\epsilon_p^p$: (i) the temperature increment ΔT during which yield occurs differs for the heating and cooling segments of the cycle (c.f. Fig. 13); and (ii) ϵ_Y depends on T . With ΔT identified as shown in Fig. 13, the largest estimate of $\Delta\epsilon_p^p$ from equation (33) would be obtained with $\epsilon_Y = \epsilon_Y(T_U)$, while the smallest estimate would be obtained using $\epsilon_Y = \epsilon_Y(T_L)$. These values should bracket $\Delta\epsilon_p^p$, subject to the accuracy of equation (33) itself. In a steady cyclic hysteresis loop, the effective plastic strain increment must be the same for the heating and cooling segments. This suggests that the average of the two estimates may be a reasonable choice, i.e.

$$\frac{\Delta\epsilon_p^p}{(\Delta\epsilon_e)_{\text{elastic}}} = \frac{1}{2} \left\{ F \left[\frac{(\Delta\epsilon_e)_{\text{elastic}}}{\epsilon_Y(T_U)} \right] + F \left[\frac{(\Delta\epsilon_e)_{\text{elastic}}}{\epsilon_Y(T_L)} \right] \right\}. \quad (35)$$

5. IMPLICATIONS AND CONCLUSIONS

The results identify explicit ranges in material properties that separate shakedown from cyclic plastic straining. The principal factors are the thermal expansion misfit between the scale and the substrate, $\Delta\alpha$, the scale modulus, E , the substrate yield strength, σ_Y , the cyclic temperature range, ΔT , and the amplitude, A , of the undulations that develop at the scale/substrate interface. The thickness of the scale, h , has only a secondary importance. The effects of $\Delta\alpha$, ΔT , E and σ_Y are consistent with engineering models and practical experience. The roles of A and h require some discussion. While h increases with dwell time at high temperature, this thickening has little effect on the thermal fatigue, so that there is no obvious role of the dwell, in apparent contradiction with the

practical findings. However, the interfaces also change with dwell time, usually developing larger amplitude undulations as the scale thickens. This effect of time on A could be the source of the dwell time effect. The reasons for changes occurring in A as the scale develops are not well-documented, but will be addressed in future research.

One way in which the above results can be used to understand the initial stages of spalling once cyclic plastic straining commences is to relate $\Delta\epsilon_p^p$ to the number of reversals needed to initiate fatigue, designated N_i . For this purpose, the Coffin-Manson relation [22, 23] is assumed to apply:

$$N_i = (1/2)(\Delta\epsilon_p^p/2\epsilon_f)^{1/c} \quad (36)$$

where ϵ_f is a ductility measure that calibrates the behavior and the exponent c is in the range -0.5 to -0.7 . Combining equations (31)–(34) with equation (36) gives

$$N_i = (1/2) \left[\frac{E_1 \Delta\alpha \Delta T A}{2E_2 \epsilon_f (1-\nu)L} Q \right]^{1/c} F^{1/c} \quad (37)$$

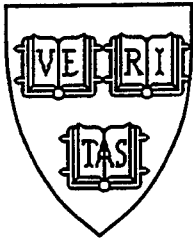
where it is recalled that ΔT denotes the width of the hysteresis loop as identified in Fig. 13. This result contains parameters that can be verified and experimentally tested in order to evaluate the importance of cyclic plasticity in the initiation of interface separations. Such evaluations are in progress. However, as noted above, a full life prediction model would need to include the subsequent buckling and buckle propagation, as well as possible high temperature interface crack initiation and growth processes.

Acknowledgements—This work was supported in part by the DARPA University Research Initiative through grant N00014-92-J-1808, by the NSF through grant DMR-94-00396 and by the Division of Engineering and Applied Sciences at Harvard University.

REFERENCES

1. Miller, R. A., *Thin Solid Films*, 1982, **95**, 265.
2. Meier, S. M., Nissley, D. M., Sheffler, K. D. and Cruse, T. A., *J. Engng Gas Turbines and Power*, 1992, **114**, 258.
3. Sheffler, K. D. and Gupta, D. K., *J. Engng Gas Turbines and Power*, 1988, **110**, 605.
4. Brindley, W. J. and Miller, R. A., *Surf. Coat. Technol.*, 1990, **43**, 446.
5. Christensen, R. J., Lipkin, D. M. and Clarke, D. R., *Appl. Phys. Lett.*, 1996, **69**, 3754.
6. Lipkin, D. M. and Clarke, D. R., *Oxidation of Metals*, 1996, **34**, 125.
7. Evans, A. G. and Hutchinson, J. W., *Acta metall. mater.*, 1995, **43**, 2507.
8. Hutchinson, J. W. and Suo, Z., *Adv. Appl. Mech.*, 1992, **29**, 63.
9. Hutchinson, J. W., Thouless, M. D. and Liniger, E. G., *Acta metall. mater.*, 1992, **40**, 295.
10. Thouless, M. D., Jensen, H. M. and Liniger, E. G., *Proc. R. Soc., London*, 1994, **A447**, 271.
11. Evans, A. G., Crumley, G. B. and Demaray, R. E., *Oxidation and Metals*, 1983, **20**, 193.

- | | | |
|--|---------------------|---|
| 12. Wright, K., 1996, unpublished research at General Electric. | b | critical radius for buckling |
| 13. Miller, R. A., <i>J. Am. Ceram. Soc.</i> , 1984, 67 , 517. | C | cosh (λh) |
| 14. Chen, K. S., He, M. Y. and Hutchinson, J. W., <i>Mater. Sci. Engng.</i> 1993, A167 , 57. | E | Young's modulus |
| 15. Bak, M. and Koenig, H. A., <i>Engng Fracture Mech.</i> , 1994, 48 , 583. | F | function [see equation (34)] |
| 16. Kuo, A. Y., <i>J. appl. Mech.</i> , 1978, 56 , 585. | h | film thickness |
| 17. Ruhle, M., 1996, unpublished research at Max Planck Institut, Stuttgart. | L | undulation wavelength |
| 18. Gao, H., <i>Int. J. Solids Struct.</i> , 1991, 28 , 703. | N | number of cycles |
| 19. Dundurs, J., <i>J. appl. Mech.</i> , 1969, 36 , 650. | Q | stress scaling coefficient |
| 20. Drucker, D. C. and Palgen, L., <i>J. appl. Mech.</i> , 1981, 48 , 479. | S | sinh (λh) |
| 21. Liu, C. T. and White, C. L., <i>High Temperature Ordered Intermetallic Alloys</i> , Materials Research Society, 1985, 39 , 365. | T | temperature |
| 22. Coffin, L. F., <i>Trans. ASME</i> , 1954, 76 , 931. | u | displacements |
| 23. Manson, S. S., National Advisory Commission on Aeronautics, Report 1170, Cleveland Lewis Propulsion Laboratory, 1954. | u^0 | displacements in film |
| | x | coordinate |
| | α | thermal expansion coefficient |
| | α_D | Dundur's parameter [see equation (14)] |
| | β_D | Dundur's parameter |
| | ϵ_y | yield strain |
| | ϵ_δ^T | thermal misfit strain |
| | ϵ_f^0 | strains in film |
| | ϵ_f^p | plastic strain |
| | Γ_i | interface toughness |
| | ν | Poisson's ratio |
| | λ | $2\pi/L$ |
| | σ | residual compressive stress |
| | σ_v^0 | stresses in film |
| | σ_0 | misfit stress [see equation (4)] |
| | σ_e | equivalent stress [see equation (22)] |
| | σ_s | yield strength of substrate |
| | Ω | cracking coefficient [see equation (2)] |
- APPENDIX**
- Nomenclature*
- | | |
|-----|----------------------|
| A | undulation amplitude |
|-----|----------------------|



MECH-316

FAILURES AT ATTACHMENT HOLES IN BRITTLE MATRIX LAMINATES

Guy M. Genin and John W. Hutchinson

Division of Engineering and Applied Sciences
Harvard University
Cambridge, MA 02138

October 1997

Failures at Attachment Holes in Brittle Matrix Laminates

GUY M. GENIN AND JOHN W. HUTCHINSON

Division of Engineering and Applied Science

Harvard University

29 Oxford Street

Cambridge, MA 02138

ABSTRACT: Mechanical attachments for a brittle-matrix fiber-reinforced cross-ply composite are analyzed. Two model problems are considered: first, a bolt-loaded strut, and second, an infinitely-wide plate with evenly-spaced bolts. The possible failure mechanisms for the strut are identified, and the influence of bolt size, bolt location, bolt elasticity, and interfacial friction on these failure mechanisms and the associated failure loads are evaluated. The bolt spacing for the plate is identified that best takes advantage of a SiC/MAS cross-ply's ability to redistribute stresses through the mechanism of matrix cracking.

Boundary value problems are solved using the finite element method. The cross-ply's constitutive behavior is described by the model of Genin and Hutchinson [1].

KEY WORDS: "ductile" ceramic matrix composites, mechanical attachments, bolt-loaded hole, failure mechanisms, failure loads, stress redistribution due to matrix cracking

1. INTRODUCTION

A fundamental difficulty faced when incorporating ceramic matrix composite (CMC) components into design is the attachment of the CMC components to each other and to components made of other materials. Drilling a hole through a CMC laminate and applying force to the laminate through a bolt leads to stress concentrations that accelerate matrix cracking. Since matrix cracking can affect failure by either relieving or intensifying stresses near stress-concentrating features [1], design with ceramic matrix composites must be based on analysis that accounts for the stress redistribution caused by matrix cracking.

The focus of this study is development of an understanding of how CMC's perform in the vicinity of bolts, with an emphasis on the influence of matrix cracking on this performance. Two model problems are considered: a bolted CMC strut serves as a model for identifying the influence of geometric and material parameters on failure mechanisms in the vicinity of fasteners, and an infinitely-wide, uniformly-loaded plate fastened with evenly-spaced bolts is studied to determine how these competing mechanisms influence optimal design.

The laminate strut is loaded axially through bolts inserted into holes near the ends of the strut, as shown in Figure 1a. The infinite laminate plate, shown in Figure 2a, is loaded similarly. Three sets of parameters are relevant to the problems: (1) the specimen dimensions h/r and w/r (s/r for the plate); (2) the material properties of the bolt and the laminate; and (3) friction at the interface between the bolt and the laminate. In both problems, the laminate's constitutive behavior is modelled using the model of Genin and Hutchinson [1], which will be reviewed in Section 2. The bolts are assumed either to be rigid, or to remain linear-elastic at all loads.

Previous work on the model strut that addresses some of the above factors is reviewed in the following two sections. Section 1.1 reviews the results of analytical and numerical investigations of how of the aforementioned parameters influence the stress distribution at the bolt-strut interface for a linear elastic strut, and also describes some attempts to model the "ductility" of the strut due to matrix cracking. Section 1.2 reviews the failure mechanisms observed in components of this type.

1.1 Previous Analytical Work on Bolted Joints in CMC's

The fastener illustrated in Figure 1 has been studied extensively [2-14]. Analyses typically employ plane stress to model the laminate's behavior. The vast majority of work on fasteners is based on linear elastic analyses, and has focussed on determining the stress field along the boundary between the bolt and the strut. In finite element analyses, the radial stress distribution along the boundary between an isotropic strut and a rigid, frictionless bolt is commonly modelled with a cosine distribution over a 180° region of contact [e.g., 2-4] after Bickley [5]. The actual distribution of normal stresses is fairly close to this for mildly orthotropic struts loaded with rigid bolts when the interface between the bolt and the strut is frictionless [3, 6-10]. The tangential stresses in the strut at the hole boundary are compressive beneath the bolt (the point $(0,-r)$ in Figure 1a for a strut loaded in tension), and tensile above the bolt. The peak tensile stresses typically occur near the point $(r,0)$. Several authors have noted that friction relieves stresses above the bolt (at $(0,r)$) and intensifies the maximum stress concentration [3,8,9]. Hyer, et al., [3] concluded from an analysis neglecting interfacial friction that the elastic properties of the bolt only mildly affect the stress distribution in the strut; the maximum tangential stress along the hole boundary decreases slightly as the elastic modulus of the bolt decreases.

Two efforts to model material nonlinearity in the cross-ply from which the strut in Figure 1 is constructed have used a phenomenological approach, and have qualitatively reproduced experimental observations. Both Serabian and Oplinger [10] and Chang, et al., [11] used the linear elastic behavior of a cross-ply in tension and a curve fit of the cross-ply's behavior in shear in their constitutive relations. Serabian and Oplinger's analysis produced a strain field qualitatively similar to that which they observed experimentally. Chang, et al., found that the stresses from their analysis, when entered into a failure criterion, predicted the failure loads they observed more accurately than did the stresses from their linear elastic analysis, reported in [4].

1.2 Identification of Failure Mechanisms

CMC struts like that of Figure 1 can fail in three modes, as depicted in Figure 3 a-c [e.g., 12, 13]. A fourth possible mode of failure, depicted in Figure 3d, has never been observed in CMC's, but has been observed in a polymer matrix composite [14].

Cady, et al. [12], mapped the range of specimen sizes over which each of the first three mechanisms in Figure 3 is most likely to occur through experiments on struts of a SiC/CAS cross-ply. The shear mode of failure shown in Figure 3a occurs in struts with a large width w compared to the distance h from the center of the bolt to the top edge of the strut. The normal mode of failure in Figure 3b occurs for narrow struts in which the ratio h/w is large. Bearing failure as shown in Figure 3c occurs when h and w are both large compared to the diameter of the bolt.

The "bending" failure shown in Figure 3d was observed by Matthews, et al., in a fiber-reinforced polymer matrix cross-ply composite comprised of woven graphite fibers in an epoxy matrix [14]. This mode of failure occurred only in specimens which first failed with a bearing failure like that of Figure 3c.

1.3 Overview

The material model used to describe the behavior of the CMC is discussed in Section 2. The strut depicted in Figure 1 will be analyzed in Section 3. The effect of relative strut dimensions, bolt elasticity, and interfacial friction on failure mechanisms and failure loads for a CMC strut is determined. Design optimization based on the nonlinear behavior exhibited by CMC's is performed in Section 4 for the plate shown in Figure 2, where the optimum spacing for bolts supporting a CMC plate will be ascertained. The influence of material nonlinearity on optimal design is highlighted.

2. MATERIAL MODEL

This section discusses the material model used to describe the behavior of the CMC. Section 2.1 section reviews the plane stress constitutive framework for symmetrically-stacked brittle-matrix laminates developed in [1]. This framework will be specialized to the case of a laminate stacked with a [0/90] configuration, and fit to uniaxial stress-strain data gathered for a SiC/MAS laminate by McNulty and Zok [15,16]. The failure criterion which will be used is discussed in Section 2.2.

2.1 Constitutive Model

The constitutive model of Genin and Hutchinson [1], specialized to the case of a cross-ply laminate, is considered. For a cross-ply, the constitutive model is based on the three uniaxial curves shown in Figure 4. The stress-strain curve for a test performed parallel to the fibers in a cross-ply laminate is denoted by $\epsilon_I = f_0(\sigma_I)$, and the transverse strain from this same test is written as $\epsilon_{II} = f_{0T}(\sigma_I)$. The strain in the loading direction for a uniaxial tension test conducted at 45° to the fiber directions is expressed as $\epsilon_I = f_{45}(\sigma_I)$. The function describing strain transverse to the loading direction in this test, $f_{45T}(\sigma_I)$, is a function of the other three input curves:

$$f_{45T}(\sigma) = f_0(\sigma) + f_{0T}(\sigma) - f_{45}(\sigma) \quad (1)$$

The model begins with the following proposal for proportional multiaxial loading when the principal axes of stress and strain are aligned with the fibers in the crossply:

$$\begin{aligned} \epsilon_I &= f_0(\sigma_I) + f_{0T}(\sigma_{II}) \\ \epsilon_{II} &= f_0(\sigma_{II}) + f_{0T}(\sigma_I) \end{aligned} \quad (2)$$

For loading in which the principal axes of stress are aligned in the symmetry axes 45° from the fibers in a cross-ply, the strains share the same principal axes, and are given by:

$$\begin{aligned} \epsilon_I &= f_{45}(\sigma_I) + f_{45T}(\sigma_{II}) \\ \epsilon_{II} &= f_{45}(\sigma_{II}) + f_{45T}(\sigma_I) \end{aligned} \quad (3)$$

Define $\Sigma_0(\epsilon_I, \epsilon_{II})$ as the inverse of Equations (2), such that

$$\begin{aligned} \sigma_I &= \Sigma_0(\epsilon_I, \epsilon_{II}) \\ \sigma_{II} &= \Sigma_0(\epsilon_{II}, \epsilon_I) \end{aligned} \quad (4)$$

The reduction in stresses due to matrix cracking at prescribed ϵ_I and ϵ_{II} , when the principal loading axes coincide with the fiber directions, is the difference between the stresses that would

result if no cracking occurred and Σ_0 . The “stress deficits” for loading in the fiber axes are defined as:

$$\begin{aligned}\Delta\sigma_I^0 &= \frac{E_0}{(1-\nu_0^2)}(\epsilon_I + \nu_0\epsilon_{II}) - \Sigma_0(\epsilon_I, \epsilon_{II}) \\ \Delta\sigma_{II}^0 &= \frac{E_0}{(1-\nu_0^2)}(\epsilon_{II} + \nu_0\epsilon_I) - \Sigma_0(\epsilon_{II}, \epsilon_I)\end{aligned}\quad (5)$$

where E_0 and ν_0 are the elastic modulus and Poisson's ratio for uniaxial loading parallel to the fibers.

When the principal axes of loading lie at 45° to the fiber directions, the stress deficits in these axes are given by:

$$\begin{aligned}\Delta\sigma_I^{45} &= \frac{E_{45}}{(1-\nu_{45}^2)}(\epsilon_I + \nu_{45}\epsilon_{II}) - \Sigma_{45}(\epsilon_I, \epsilon_{II}) \\ \Delta\sigma_{II}^{45} &= \frac{E_{45}}{(1-\nu_{45}^2)}(\epsilon_{II} + \nu_{45}\epsilon_I) - \Sigma_{45}(\epsilon_{II}, \epsilon_I)\end{aligned}\quad (6)$$

Here, E_{45} is the elastic modulus for uniaxial loading in the axes at 45° to the fiber directions, $\nu_{45} = 1 - \frac{E_{45}}{E_0}(1 - \nu_0)$, and the combined equations $\sigma_I = \Sigma_{45}(\epsilon_I, \epsilon_{II})$ and $\sigma_{II} = \Sigma_{45}(\epsilon_{II}, \epsilon_I)$ form the inverse of (3).

For principal strains $(\epsilon_I, \epsilon_{II})$ in principal axes oriented at an arbitrary angle θ from the fiber directions, the principal axes of the stress deficits are taken to coincide with the principal strain axes. The stress deficits in these axes are assumed to be given by interpolation between the stress deficits in the 0° and 45° orientations according to:

$$\begin{aligned}\Delta\sigma_I &= \Delta\sigma_I^0 \cos^2 2\theta + \Delta\sigma_I^{45} \sin^2 2\theta \\ \Delta\sigma_{II} &= \Delta\sigma_{II}^0 \cos^2 2\theta + \Delta\sigma_{II}^{45} \sin^2 2\theta\end{aligned}\quad (7)$$

Upon rotating back to the fiber axes, one obtains the plane stress relation for stresses associated with proportional straining to $(\epsilon_1, \epsilon_2, \gamma_{12}=2\epsilon_{12})$:

$$\begin{aligned}\sigma_1 &= \frac{E_0}{(1-\nu_0^2)}(\epsilon_1 + \nu_0\epsilon_2) - \Delta\sigma_I \cos^2 \theta - \Delta\sigma_{II} \sin^2 \theta \\ \sigma_2 &= \frac{E_0}{(1-\nu_0^2)}(\epsilon_2 + \nu_0\epsilon_1) - \Delta\sigma_I \sin^2 \theta - \Delta\sigma_{II} \cos^2 \theta \\ \tau &= \frac{E_{45}}{2(1+\nu_{45})}\gamma_{12} - (\Delta\sigma_I - \Delta\sigma_{II})\sin\theta\cos\theta\end{aligned}\quad (8)$$

2.1.1 Model CMC

The material studied in this paper is a cross-ply laminate that exhibits an apparent "ductility" when loaded in uniaxial tension, as shown in Figure 4. The laminae are constructed of aligned SiC fibers embedded in a glass (MAS) matrix, and the laminate is constructed of a series of these laminae stacked such that the fiber directions of neighboring layers are perpendicular to one another. The curves in Figure 4 for loading parallel to one set of fibers are from McNulty and Zok [15]; the curve for loading at 45° to the fiber directions is derived from the results of a Iosipescu shear test performed by McNulty and Zok [16] using a formulation that is presented in [17]. In this paper, all stresses are normalized by the proportional limit for loading parallel to one set of fibers in the cross-ply, $\sigma_{mc}^0 = 90$ MPa.

The nonlinear material behavior is modeled in the analyses that follow by fitting the constitutive model described above to the stress-strain curves in Figure 4. Linear elasticity is used for all compressive stresses. The stress-strain curves are extrapolated linearly for stresses and strains that exceed the limits of the data in tension.

2.2 Failure Criterion

The criterion adopted in this paper is that the laminate will fail when the normal strain in the direction of one set of fibers at some point equals the uniaxial failure strain observed in a tensile specimen. This is equivalent to a maximum normal stress criterion for the fibers in the material. Compressive failure is not modeled, so the bearing failure mechanism of Figure 3c is ignored.

The justification for this criterion is as follows: when a brittle matrix laminate is saturated with matrix cracks, the fibers carry the entire applied load, and are largely debonded from the matrix material. The strain in the fibers once the matrix is saturated with cracks is thus the difference between the macroscopic strain as predicted by the continuum constitutive model and the initial residual strain in the fibers from the manufacturing process for the laminate. If the fibers remain linear-elastic until the failure load, then a maximum strain failure criterion for the fibers is equivalent to a maximum normal stress criterion. Therefore, assuming the matrix material saturates with cracks before the laminate fails, the level of strain necessary to raise the fibers from their initially compressive stress state to their *in situ* failure stress is the failure strain for a uniaxial specimen of the material. The uniaxial failure strain from a tensile specimen is thus used in this study as the critical failure strain.

The failure criterion is based on the premise that a laminate fails when the first fibers in the laminate break in tension. This assumption oversimplifies actual conditions in a cross-ply [e.g., 18, 19].

Predictions of the displacements necessary to stretch plates of the SiC/MAS cross-ply to failure are plotted in Figure 5 as a function of the angle ϕ between the loading direction and the

orientation of one set of the cross-ply's fibers. The predicted axial strain level necessary to fail the composite stretched in directions $\pm 45^\circ$ to the fiber axes is much higher relative to the failure strain for loading parallel to the fibers than expected for a typical cross ply, indicating that a mechanism other than fiber failure is dominant for these loading directions. Accordingly, the shear strength of the cross-ply and thus the resistance to the "shear" mode of failure is overpredicted in the analyses in this paper.

3. PREDICTION OF FAILURE MECHANISMS IN CMC STRUTS

The failure criterion described in Section 2.2 is applied to the results of finite element analyses of the bolted strut of Figure 1. The failure loads and failure mechanisms predicted by these analyses are compared for struts of varying geometries, and the effects of elasticity in the bolt and friction at the interface between the bolt and the strut are investigated.

3.1 Numerical Model

The influence of strut geometry, bolt elasticity, and interfacial friction on failure modes and failure loads is assessed through finite element analyses. The mathematical model chosen for the analyses exploits the symmetry of the strut about both its horizontal and vertical mid-planes, as depicted in Figure 1b. Along the bottom of the model in Figure 1b, the vertical (x_2 -direction) displacements are constrained to be the same, and the shear traction vanishes. The lower boundary carries a net vertical force of $P/2$. The left-hand boundary of the model in Figure 1b is free of shear-traction, and is constrained from moving in the x_1 -direction.

For analyses in which the bolt is not assumed rigid, the boundary conditions on the bolt approximate a loading apparatus used in the experiments of Cady, et al.[12], in which the bolt rests in a 90° notch in a rigid loading fixture. To model this fixture, nodes on the finite element mesh for the bolt that lie close to the contact point between the bolt and the loading apparatus are constrained to move along the 45° line shown in Figure 1b. The bolt is assumed to fit perfectly into the hole in the unloaded state.

Because of the interface between the bolt and the plate, the finite element mesh and its boundary conditions at each loading increment must be found as part of the solution; iteration is required even for loads in the linear range. The numerical procedure begins with a guess as to which nodes on the plate will be "in contact" with corresponding nodes on the bolt after a load is applied.

Stresses and displacements are calculated for this initial mesh, and are checked to ensure that none of the elements assumed to be in contact are predicted to carry tension normal to the contact plane. Nodes in regions assumed to be free of contact are checked to verify that no interpenetration occurs. Interpenetration occurs if the displacement component of a node on the bolt boundary in the direction of the initial outward normal to the bolt boundary exceeds that of the corresponding node on the strut boundary in this direction. If the check reveals that a portion of the bolt-strut boundary is in tension, the analysis is repeated with that portion of the boundary assumed to be traction-free; if the check reveals that nodes from the bolt and the plate interpenetrate, the analysis is repeated with those nodes assumed to be in contact. Once the closest approximation to the proper mesh is determined, the analysis continues with the next loading increment.

3.2 Influence of Strut Geometry on Failure Load and Failure Mechanism

Finite element analyses are run to gain insight into the material response for a range of strut geometries. In these analyses, the bolt is assumed to be rigid, and the interface between the bolt and the strut is assumed to be frictionless.

3.2.1 Bolt Depth, h/r

To illustrate the effect of varying the distance h from the center of the bolt to the top of the specimen, two analyses are run with the above procedure for SiC/MAS struts of identical widths $w/r = 4$, but different pin depths h/r . Contours of the maximum principal stresses and of the density of matrix cracks for the loads at which each of the two struts are predicted to fail are shown in Figure 6. The measure of the intensity of matrix cracking $\Delta\sigma$ is the square root of the sum of the squares of the "principal stress deficits" defined in Equation (8).

As shown in Figure 6, the two regions of the strut with largest bolt depth h ($h/r = 4$) that carry the most load are the hole boundary by the thinnest section of the strut, and the top of the specimen. Cracking for this strut is most intense at the point of maximum stress on the hole boundary. Slight cracking in shear is indicated above the hole. When the failure criterion is met, the entire strut is predicted to have undergone matrix cracking at points lower than a few bolt radii beneath the hole. The location at which the failure criterion is first met is on the hole boundary, where the tensile stresses are highest, and the strut will clearly fail by a "tensile"-type failure originating from this point.

Halving the bolt depth h significantly alters the way the strut carries load. As can be seen from the contour plots in Figure 6 for the strut with $h/r = 2$, moving the bolt closer to the top of the specimen reduces the bending stiffness of the section of material above the hole, and as a consequence moves the point of maximum stress to the top of the strut. The failure criterion is met here, and this strut will fail by the "bending" mode of failure. The plot of cracking intensity

reveals that the reduction in cross-sectional area caused by raising the bolt also increases the prevalence of shear cracking above the hole. This suggests that the mechanism of shear failure is also possible when little clearance exists between the bolt and the upper boundary of the strut.

The analyses indicate that a strut with $h/r = 4$ fails at a remote stress $P/(2w)$ of $1.14 \sigma_{mc}^0$, where P is the force per unit thickness. The failure load predicted for the strut with $h/r = 2$ is just over half of this, at $P/(2w) = 0.64 \sigma_{mc}^0$, and this strut fails while matrix cracking is still fairly localized.

3.2.2 Strut Width, w/r

To assess the effect of strut width on the way SiC/MAS struts carry loads, a strut is analyzed with $h/r = 2$, as above, but with $w/r = 10$. Again, the bolt is taken to be rigid, and the interface is frictionless. Since increasing the width of the strut increases the bending stiffness of the material above the bolt, the stress concentration at the top of the strut is somewhat mitigated in the wider specimen, as is illustrated by Figure 7. The failure mechanism predicted by the maximum normal strain criterion for the wide strut is a tensile failure at the hole boundary. However, the plot of matrix cracking for this strut shows that cracking is most intense in shear above the hole; this failure mechanism might be close to activation.

While the narrower strut withstands a higher average stress $P/2w$ at failure than does the wider specimen, the analysis predicts that the force per unit depth of $P/h = 2.7 \sigma_{mc}^0$ necessary to break the wider strut just exceeds the failure strength $P/h = 2.6 \sigma_{mc}^0$ of the narrower strut.

3.2.3 Discussion

The predicted failure mechanism of a strut changes with the strut's relative dimensions. The trends of this section are qualitatively similar to the analyses of Cady, et al. [12] for the shear and tensile modes of failure: the shear mode of failure becomes increasingly dominant over the tensile mode of failure as the strut width increases. The bending mode of failure is predominant when the bolt is near the upper edge of the strut and when the strut is too narrow to contribute significantly to the bending stiffness of the material above the bolt.

3.3 Interfacial Friction

The role of interfacial friction is assessed by analyzing a strut with dimensions $h/r = 4$ and $w/r = 4$ identical to that analyzed in Section 3.2.1, but with the condition imposed that nodes which are in contact with the rigid pin remain fixed. This provides an upper bound on the frictional force along the interface.

Interfacial friction constrains material directly above the bolt from stretching horizontally (i.e., perpendicular to the direction of loading), and thereby significantly reduces stresses above the bolt, as is shown in Figure 8. However, the reduction in stresses above the bolt means a

reduction in stress redistribution by matrix cracking, and results in an overall decrease in the load-carrying capacity of this strut. Friction intensifies the stress concentration at the hole boundary, and reduces the failure load by about 50%.

For this strut, a no-slip boundary condition along the interface completely suppresses the bending mode of failure, and also reduces the level of shear cracking, as can be seen from Figure 8. The strut will fail in the tensile mode, with a high degree of certainty.

3.4 Bolt Elasticity

A strut with dimensions $h/r = 4$ and $w/r = 4$ is again loaded, this time with soft, frictionless bolts having an elastic modulus one tenth that of the strut. The region of contact between bolt and strut is broadened by allowing the bolt to deform, and this causes a slight reduction in stresses above the hole. The failure mechanism is unaffected by the elasticity of the bolt. This result concurs with that of Hyer, et al. [3], for linear elastic struts.

The elasticity of the bolt plays a larger role when interfacial friction is incorporated into the problem. Two identically dimensioned specimens, both with no slippage allowed for surfaces in contact, are pictured at their failure loads in Figure 9. One specimen is loaded by a rigid bolt, while the other is loaded by a soft bolt, with $E_{\text{bolt}}/E_{\text{strut}} = 0.1$. As can be inferred from Figure 9, the soft bolt moves the end of the region of contact and the point of maximum stress closer to the thinnest section of the strut, and thereby raises the stress concentration. The pin elasticity results in over a 10% drop in the failure load of the specimen. This is likely to be a larger effect than would be seen in a real strut, as the model of friction applied here is idealized.

3.5 Discussion

Bolt-loaded struts analyzed in this section are predicted to fail through the "shear," "tensile," and "bending" modes illustrated in Figure 3. The "shear" and "tensile" modes match qualitative experimental observations, but the "bending" mode has little observational support. The bending failure has most likely eluded experimental observation partially through interfacial friction, which completely precludes this failure mechanism for the extreme case evaluated here, and partially through the common sense of those who have sought to characterize these failure mechanisms experimentally: achieving this failure mechanism requires drilling a hole far closer to the top of the strut than any engineer would realistically consider.

Comparisons of the predicted failure mechanisms to the locations of intense matrix cracking indicates that the failure criterion used in this section either overpredicts the shear strength of the SiC/MAS composite, or underpredicts its tensile strength. The former is likely. Regardless of which is the case, the design engineer forced to utilize this failure criterion would now seek to design a strut that avoids the nonconservatively predicted "shear" mode, and optimize this design based on the specific material properties of the SiC/MAS laminate.

Interfacial friction should be avoided to the extent possible when designing attachments for the SiC/MAS cross-ply. If friction is minimized, the elasticity of the bolt has no significant bearing on design.

4. DESIGN OPTIMIZATION BASED UPON MATERIAL PROPERTIES

Rather than continue with the bolted strut analyzed in Section 3, attention is turned to the more interesting, but mathematically similar problem of a bolted plate illustrated in Figure 2. A plate is loaded by bolts in the direction shown. The infinitely-wide plate is long compared to the bolt spacing $2s$, and is symmetric about a horizontal line through its center. The bolts are allowed to slide freely in the lateral direction, and are each pulled vertically with a force $(2s)\sigma$. The goal here is find the bolt spacing s that best utilizes the nonlinearity of the SiC/MAS composite to maximize the plate's strength. Based on the analysis of the strut in Section 3, a depth $h/r = 4$ is used, as this was a bolt depth for the strut at which a tensile failure in the strut was very probable. Once an optimal spacing is ascertained, the failure mechanism corresponding to this spacing is carefully checked.

4.1 Numerical Procedure

The boundary value problems are once more solved using the finite element method in conjunction with the constitutive model presented in Section 2. The model is again fit to McNulty and Zok's material data for the SiC/MAS cross-ply.

For each bolt spacing s considered, a finite element mesh is generated according to the model in Figure 2b. This model is identical to that used for the strut, except here the nodes on the right-hand boundary are constrained to move together in the horizontal direction. This models both the periodicity of the problem, and the condition that the bolts may move laterally.

The bolts are taken to be rigid, and the interface carries no friction. As before, the boundary conditions are part of the solution, and iteration is required even for loads to which the plate responds linearly.

4.2 Results

Failure loads for plates with a range of bolt spacings are calculated, and are plotted in Figure 10, normalized by the highest failure load that can be achieved by a bolted SiC/MAS plate. This peak load of $\sigma = 1.4 \sigma_{mc}^0$ occurs when the bolt spacing $2s$ is approximately six times the bolt radius.

To highlight how stress redistribution related to matrix cracking influences the optimum dimensions of a bolted plate, a similar analysis is run with the plate taken as linear elastic. The failure loads for a linear elastic plate having the elastic constants of SiC/MAS are plotted with a dashed line in Figure 10, normalized by the highest possible failure load that can be attained with such a plate. For a brittle plate with same failure strain as the SiC/MAS composite, this peak load is $\sigma = 3.1 \sigma_{mc}^0$. The optimum bolt spacing $2s$ for the linear elastic plate is four times the bolt radius: the strongest SiC/MAS plate is constructed with two times as much material between edges of neighboring bolts as the strongest elastic plate.

The optimum bolt spacing for the SiC/MAS plate is reached by the following trade-off. As the bolt spacing decreases, the cross-sectional area between neighboring bolts decreases. However, the average stress across this area increases as the bolt spacing decreases for two reasons: first, the elastic stress concentration drops (relative to the mean stress across the ligament), and second, the redistribution of stresses away from these concentrations due to the mechanism of matrix cracking increases. This is illustrated in Figure 11, which shows the increase in the average stress between neighboring bolts for decreasing bolt spacing. As s approaches the bolt radius, the net section stress at failure approaches the uniaxial failure stress of $3.5 \sigma_{mc}^0$.

Analysis of an SiC/MAS plate with a nearly optimal bolt spacing indicates that at the optimum dimensions, the plate fails in the "tensile" failure mode. As can be seen from Figure 12, which displays contours of principal stresses and matrix cracking at the failure load for material in close proximity to the bolts, the increase in the bending stiffness of material above the bolts caused by the periodic boundary conditions eliminates any chance of a "bending" failure. Since shear cracking is also not prevalent, the predicted failure mechanism is likely to be the only possible failure mechanism for this configuration.

5. SUMMARY

Assuming a simple failure criterion, this work explored the effect of geometric and material parameters on failure loads and mechanisms of a bolted CMC strut undergoing matrix cracking. As the position of a bolt in a fairly wide strut nears the end of the strut, the likely failure mode shifts from a tensile mode to a shear mode. For more narrow struts, a "bending" mode can occur. Friction along the interface promotes the tensile failure mode, and also significantly reduces a strut's load-carrying capacity. The elastic properties of the bolt have little bearing on load-carrying capacity, especially if friction is minimized.

The analysis technique used herein can be used to optimize design of fasteners. In the case examined here, the optimal design of a uniformly-fastened CMC plate is reached through a trade-

off between decreasing area between neighboring bolts, and increasing stress redistribution due to matrix cracking.

6. ACKNOWLEDGEMENTS

The authors would like to thank Carl Cady and Tony Evans for helpful discussions of their experimental observations [12], and John McNulty and Frank Zok for furnishing essential material data for the model CMC used in this study.

This work was supported in part by the ARPA University Research Initiative (Sub-agreement P.O. KK-3007 with the University of California, Santa Barbara, ONR Prime Contract N00014-92-J1808) and the Division of Applied Sciences, Harvard University.

REFERENCES

- [1] G.M. Genin and J.W. Hutchinson. "Composite Laminates in Plane Stress: Constitutive Modeling and Stress Redistribution due to Matrix Cracking." *J. Am. Ceram. Soc.*, **80** [5] 1245-55 (1997).
- [2] J.P. Waszczack, and T.A. Cruse. "Failure Mode and Strength Prediction of Anisotropic Bolt Bearing Specimens." *J. Compos. Mater.*, **5**, 421-423 (1971).
- [3] M.W. Hyer, E.C. Klang, and D.E. Cooper. "The Effects of Pin Elasticity, Clearance, and Friction on the Stresses in a Pin-Loaded Orthotropic Plate." *J. Compos. Mater.*, **21**, 190-206 (1987).
- [4] F.-K. Chang, R.A. Scott, and G.S. Springer. "Failure Strength of Composite Laminates Containing Pin Loaded Holes — Method of Solution." *J. Compos. Mater.*, **18**, 255-278 (1984).
- [5] W. Bickley. "The Distribution of Stress Round a Circular Hole in a Plate." *Phil. Trans. Roy. Soc. A*, **227**, 383 (1928).
- [6] T. De Jong. "Stresses Around Pin-Loaded Holes in Elastically Orthotropic or Isotropic Plates." *J. Compos. Mater.*, **11**, 313-331 (1977).
- [7] B.L. Agarwal. "Static Strength Prediction of Bolted Joint in Composite Material." *AIAA Journal*, **18**, 1345-1375 (1980).
- [8] R.E. Rowlands, M.U. Rahman, T.L. Wilkinson, and Y.I. Chang. "Single- and Multiple-Bolted Joints in Orthotropic Materials." *Composites* **13**, 273-278 (1982).
- [9] K.-D. Zhang and C.E.S. Ueng. "Stresses Around a Pin-Loaded Hole in Orthotropic Plates." *J. Compos. Materials*, **18**, 432-446 (1984).
- [10] S.M. Serabian and D.W. Oplinger. "An Experimental and Finite Element Investigation into the Mechanical Response of 0/90 Pin-Loaded Laminates." *J. Compos. Mater.*, **21**, 631-49 (1987).
- [11] F.-K. Chang, R.A. Scott, and G.S. Springer. "Failure Strength of Nonlinearly Elastic Composite Laminates Containing a Pin Loaded Hole." *J. Compos. Mater.*, **18**, 464-477 (1984).
- [12] C.M. Cady, A.G. Evans, and K.E. Perry. "Stress Redistribution Around Mechanical Attachments in Ceramic Matrix Composites." To appear in *J. Am. Ceramic Soc.*
- [13] M.Y. Tsai and J. Morton. "Stress and Failure Analysis of a Pin-Loaded Composite Plate: An Experimental Study." *J. Compos. Mater.*, **24**, 1101-1120 (1984).
- [14] F.L. Matthews, A.A. Roshan, and L.N. Phillips. "The Bolt Bearing Strength of Glass/Carbon Hybrid Composites." *Composites*, **13**, 225-227 (1982).
- [15] J.C. McNulty and F.W. Zok. "Application of Weakest-Link Fracture Statistics to Fiber-Reinforced Ceramic Matrix Composites." To appear in *J. Am. Ceramic Soc.* (1997).

- [16] J.C. McNulty and F.W. Zok. Private communication.
- [17] G.M. Genin, J.W. Hutchinson, J.C. McNulty, and F.W. Zok. "Shear Characterization of Brittle Matrix Cross-Ply Laminates using the Iosipescu Shear Test." In preparation.
- [18] B. Budiansky. "On the Theoretical Toughness and Strength of Ceramic Composites." **Proceedings of IUTAM Symposium on Fracture of Brittle Disordered Materials: Concrete, Rock, Ceramics.** Brisbane, September 20-24, 1993.
- [19] B. Budiansky and J.C. Amazigo. "Notch Strength of Ceramic Composites: Long Fibers, Stochastics, Short Fibers." Harvard University Solid Mechanics Report MECH-269.

LIST OF CAPTIONS

- Figure 1.** (a) A CMC strut, and (b) the model used in the analyses.
- Figure 2.** (a) A CMC plate, and (b) the model used in the analyses.
- Figure 3.** Failure mechanisms for fastened struts.
- Figure 4.** Uniaxial stress-strain curves for a cross-ply ceramic matrix composite (SiC/MAS). Data is from McNulty and Zok [15,16].
- Figure 5.** Axial failure strain for SiC/MAS stretched at an angle ϕ from one set of fibers, as predicted by a maximum normal strain criterion.
- Figure 6.** Effect of bolt depth h on (a) matrix cracking and (b) stress distribution at failure load, P_{ult} . $w/r = 4$.
- Figure 7.** Effect of strut width w on (a) matrix cracking and (b) stress distribution at failure load, P_{ult} . $h/r = 2$.
- Figure 8.** Effect of interfacial friction on (a) matrix cracking and (b) stress distribution at failure load, P_{ult} . $h/r = 4$; $w/r = 4$.
- Figure 9.** Effect of bolt elasticity on (a) matrix cracking and (b) stress distribution at failure load, P_{ult} , when no slippage is allowed between the bolt and the strut $h/r = 4$; $w/r = 4$.
- Figure 10.** Ultimate load of a fastened SiC/MAS plate as a function of bolt spacing s/r , compared to the ultimate loads for a linear plate having the elastic properties of SiC/MAS. $h/r = 4$.
- Figure 11.** Performance of a fastened SiC/MAS plate as a function of bolt spacing s/r . $h/r = 4$.
- Figure 12.** (a) Intensity of matrix cracking and (b) stress distribution at failure, σ_{ult} , for optimal bolt spacing $s/r \approx 3$. $h/r = 4$.

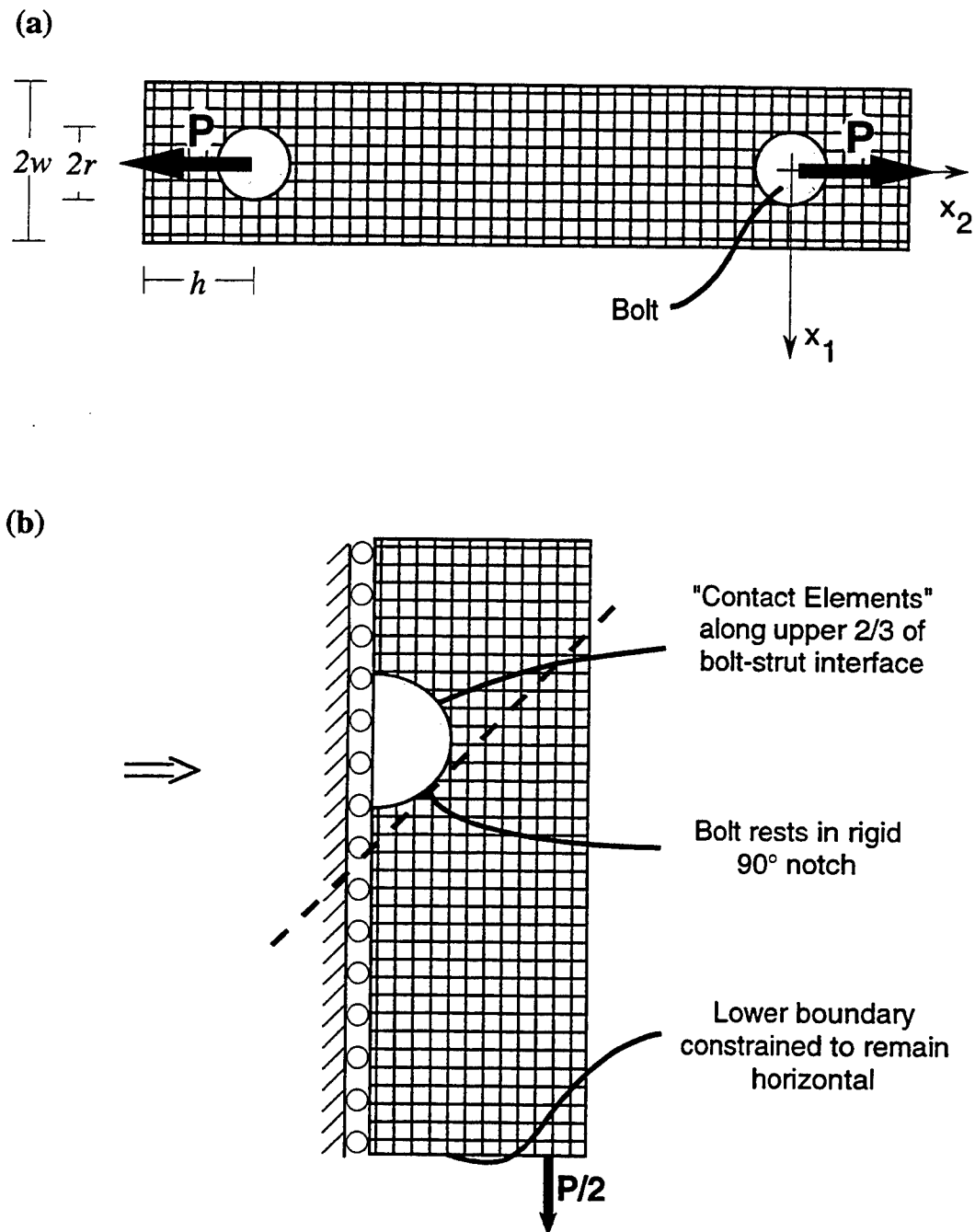


Figure 1. (a) A CMC strut, and (b) the model used in the analyses.

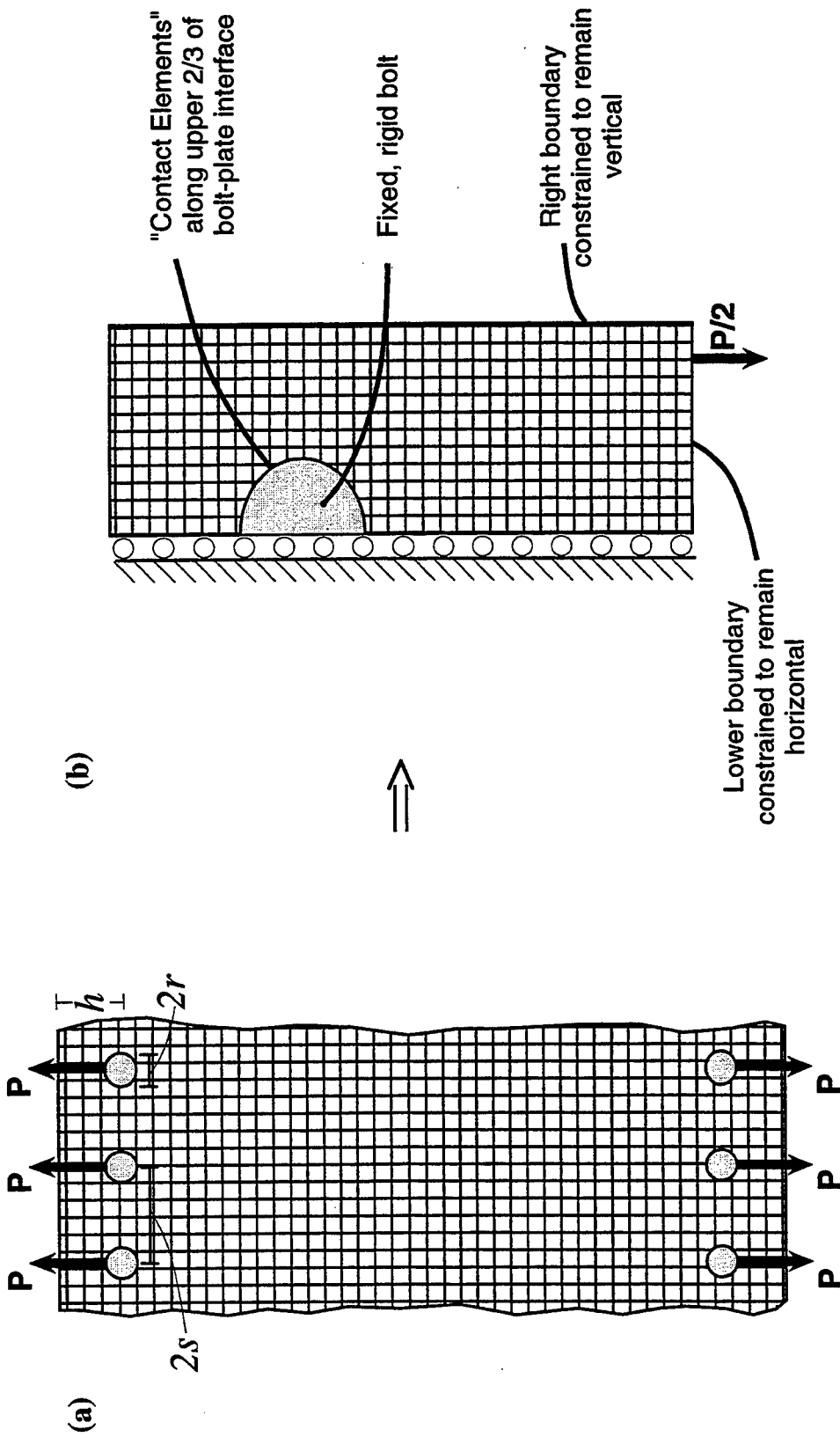
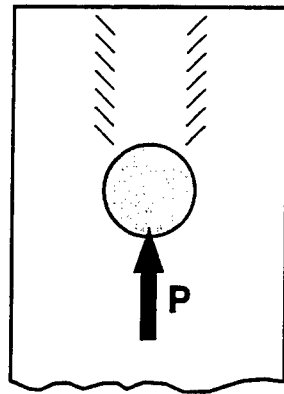
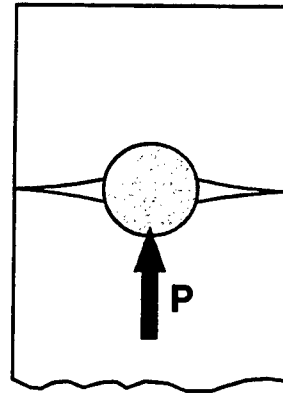


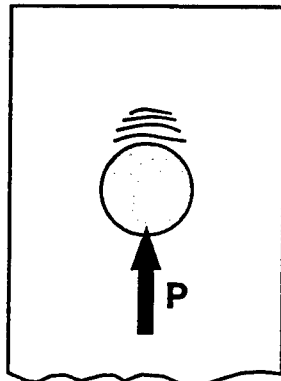
Figure 2. (a) A CMC plate, and (b) the model used in the analyses.



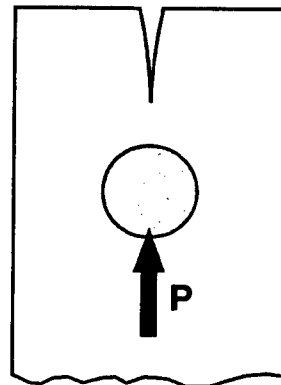
(a) shear failure



(b) tensile failure



(c) bearing failure



(d) bending failure

Figure 3. Failure mechanisms for fastened struts.

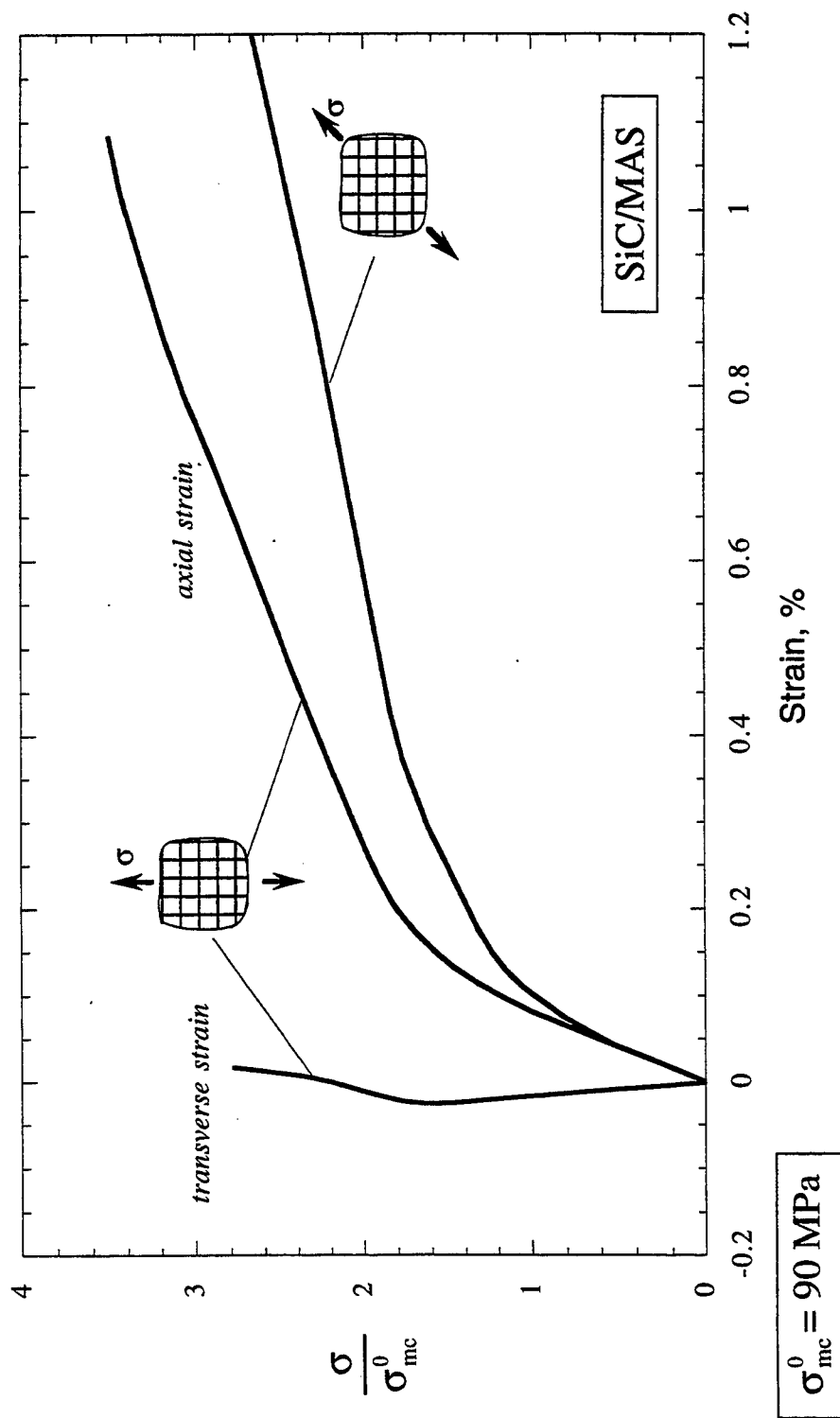


Figure 4. Uniaxial stress-strain curves for a cross-ply ceramic matrix composite (SiC/MAS). Data is from McNulty and Zok [15,16].

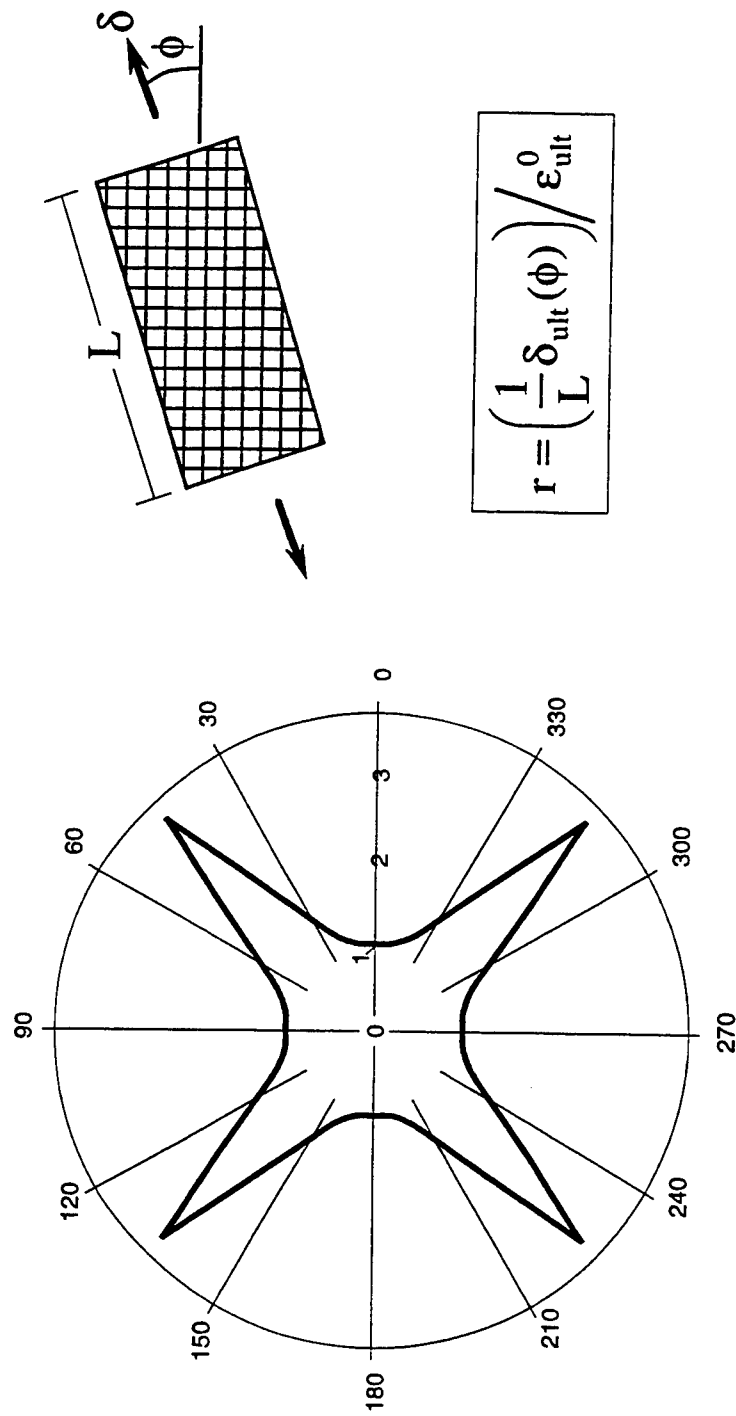


Figure 5. Axial failure strain for SiC/MAS stretched at an angle ϕ from one set of fibers, as predicted by a maximum normal strain criterion.

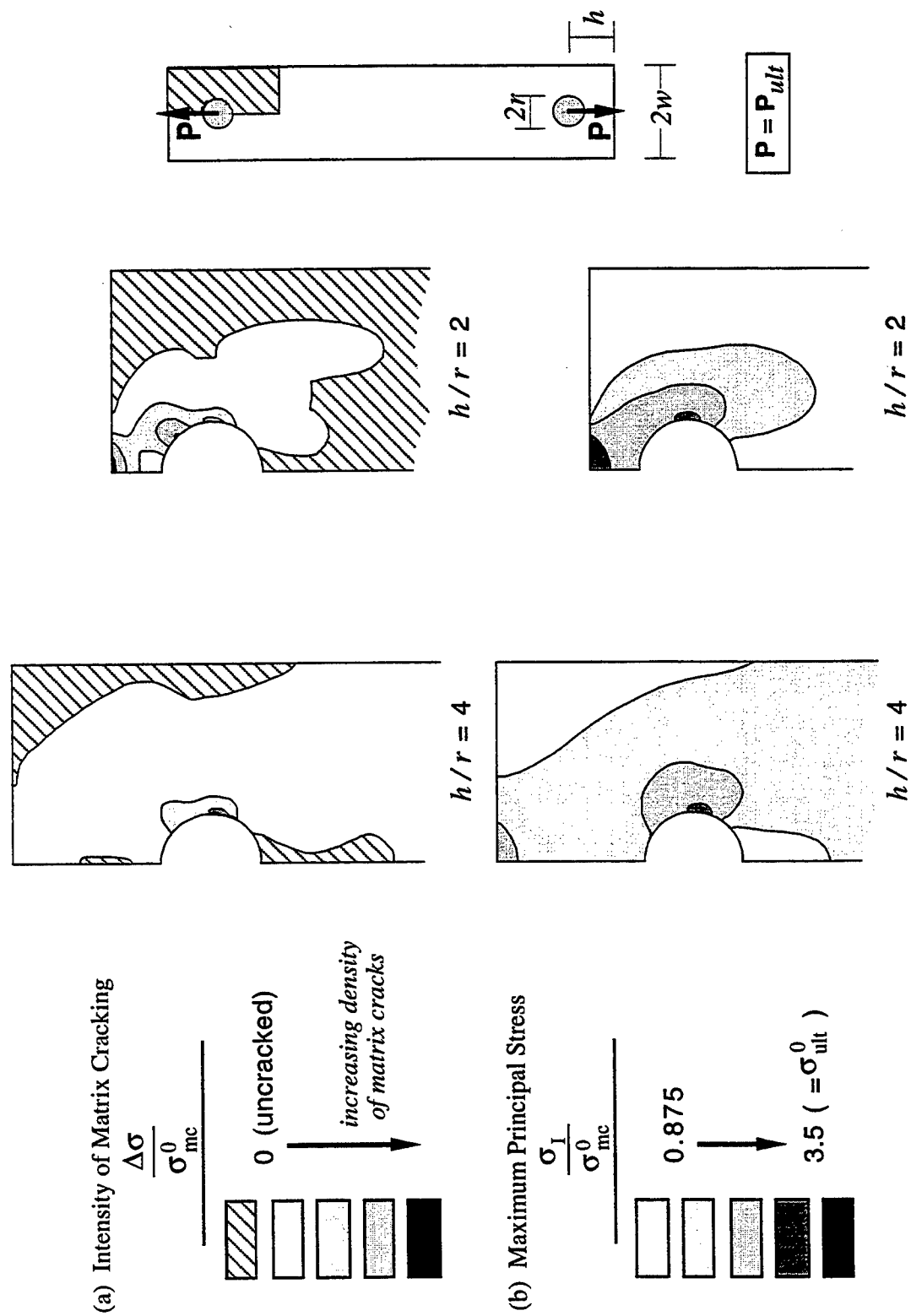
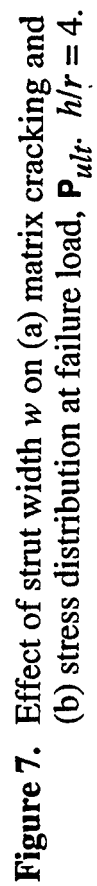


Figure 6. Effect of bolt depth h on (a) matrix cracking and (b) stress distribution at failure load, P_{ult} . $w/r = 4$.



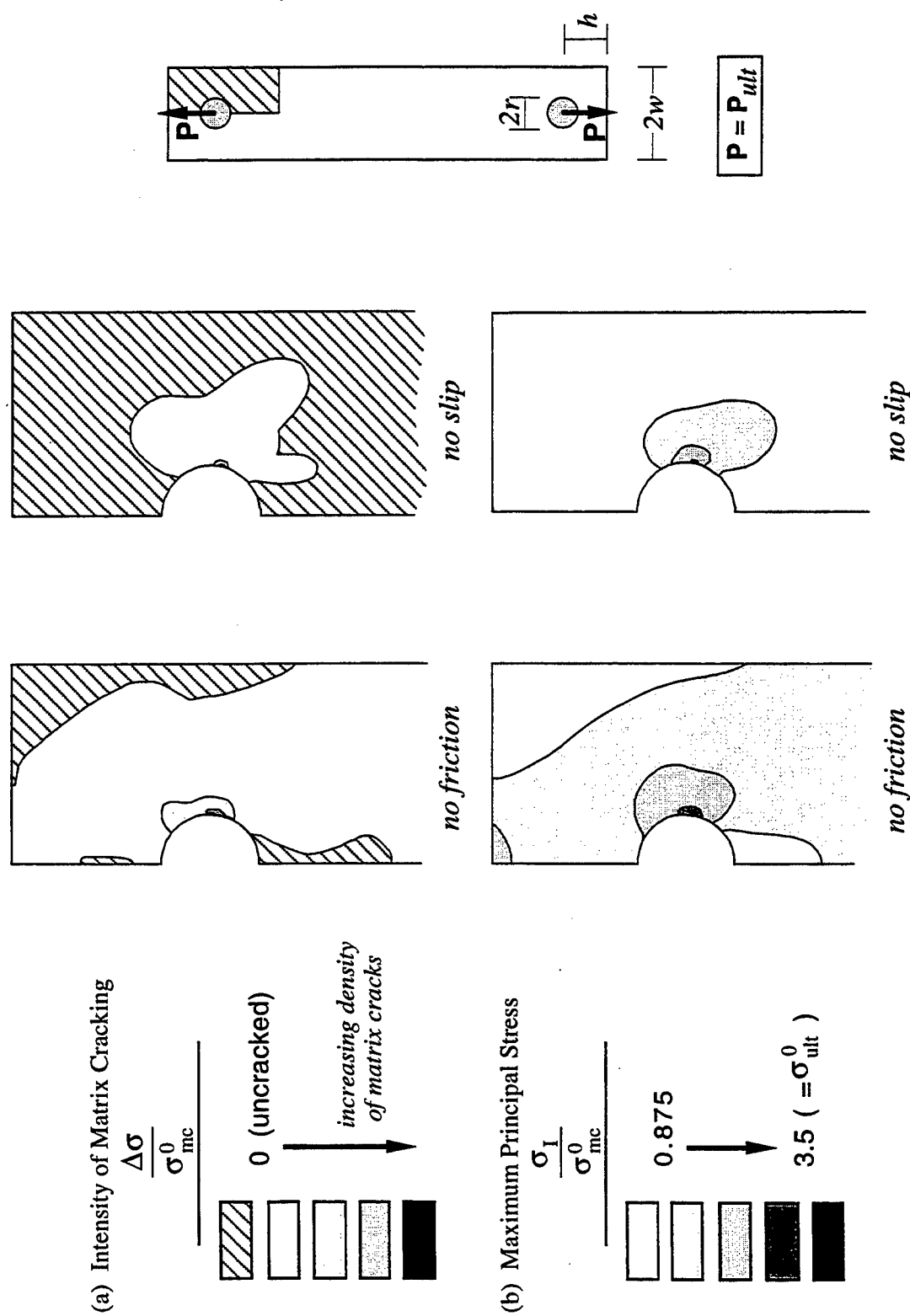


Figure 8. Effect of interfacial friction on (a) matrix cracking and (b) stress distribution at failure load, P_{ult} . $h/r = 4$; $w/r = 4$.

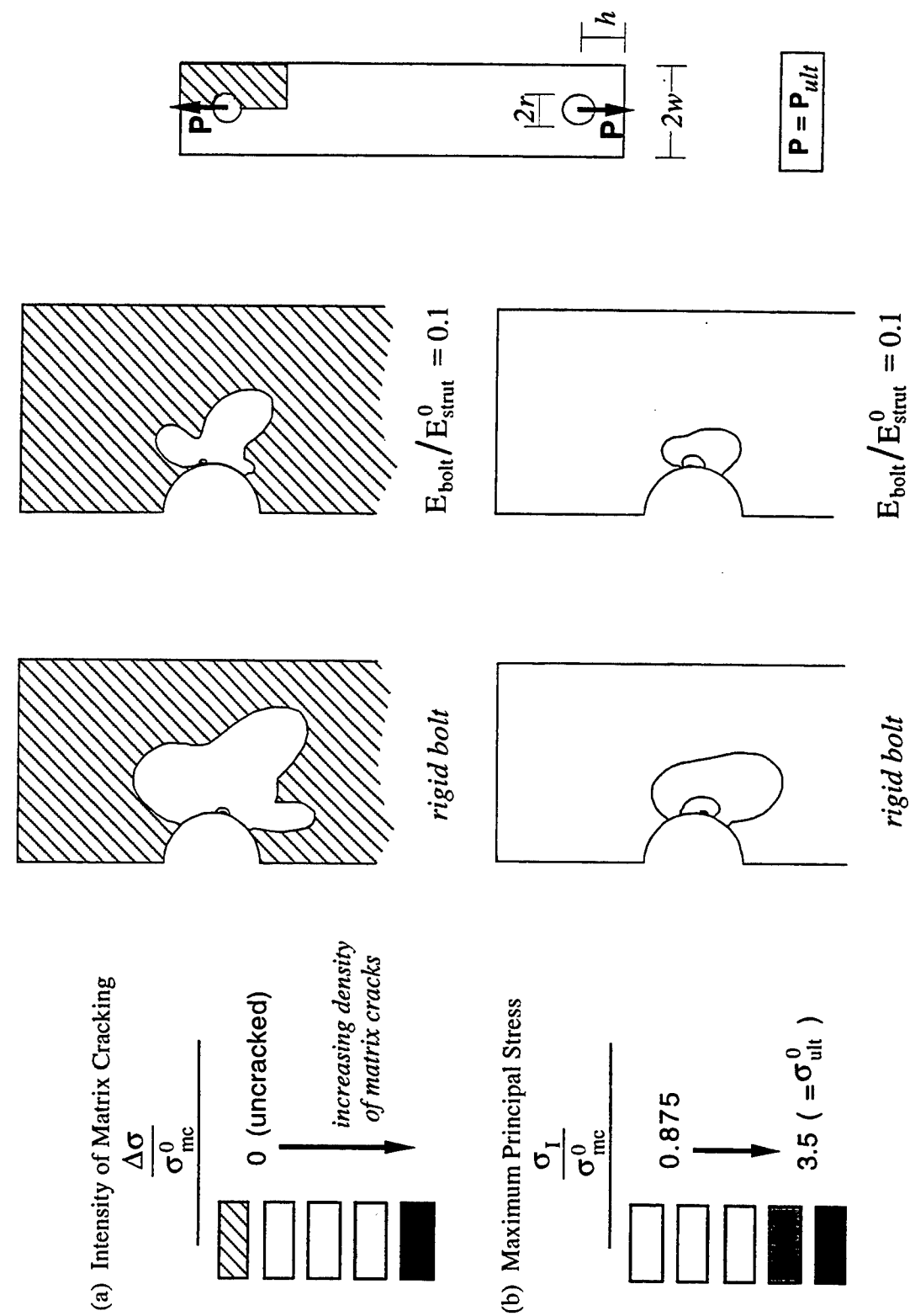


Figure 9. Effect of bolt elasticity on (a) matrix cracking and (b) stress distribution at failure load, P_{ult} , when no slippage is allowed between the bolt and the strut. $h/r = 4$; $w/r = 4$.

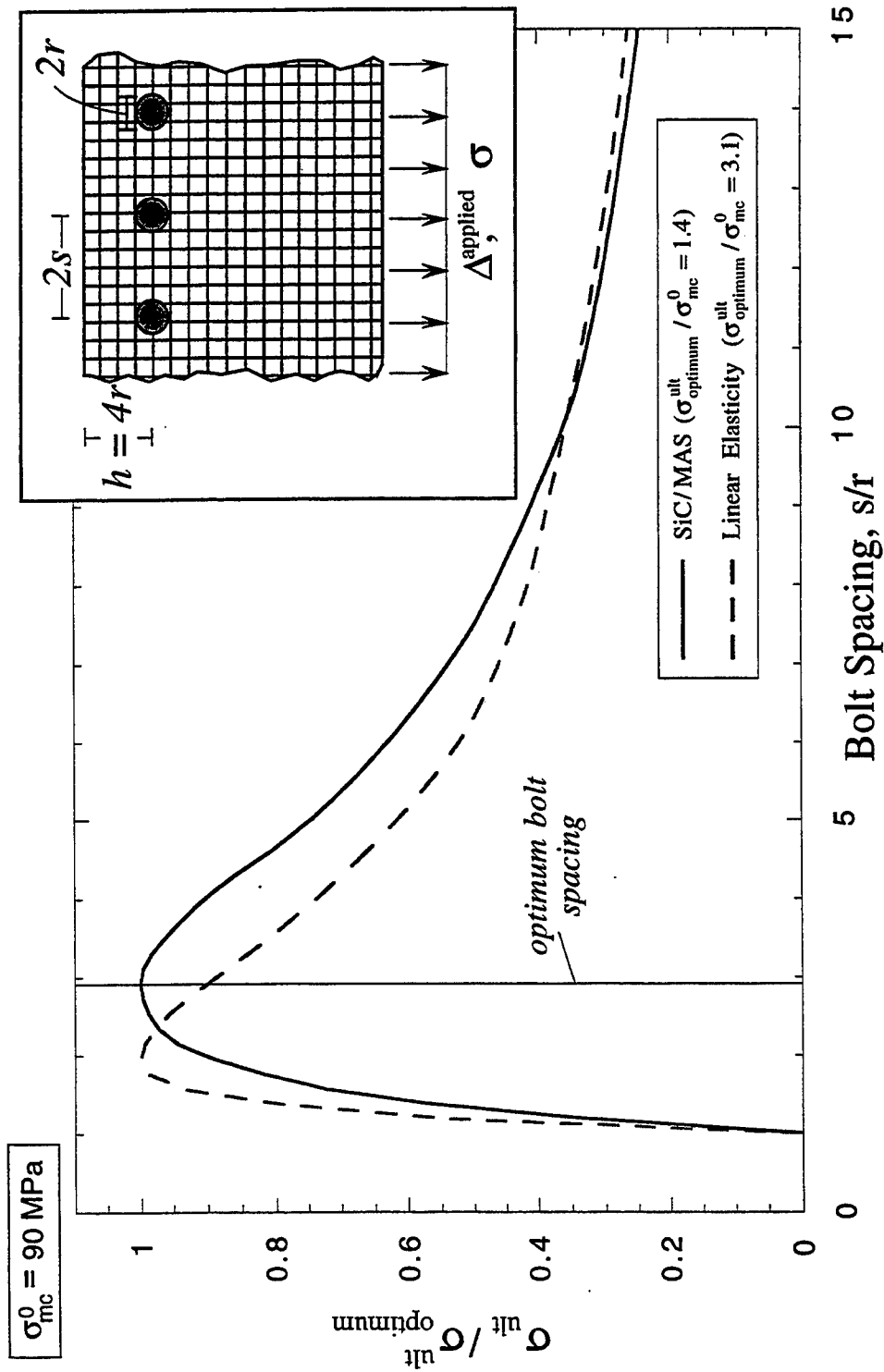


Figure 10. Ultimate load for a fastened SiC/MAS plate as a function of bolt spacing, s/r , compared to the ultimate loads for a linear plate having the elastic behavior of SiC/MAS. $h/r = 4$.

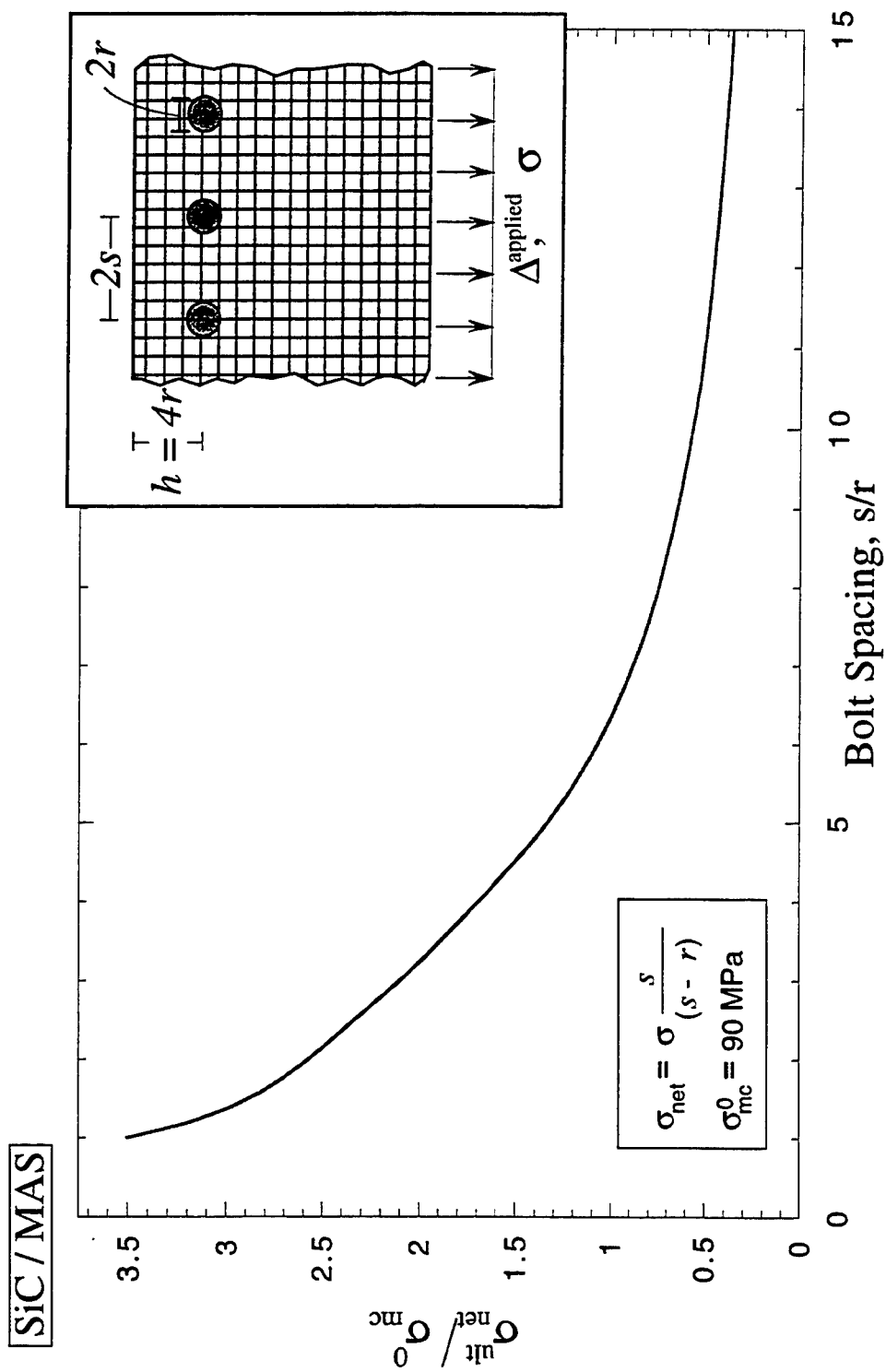
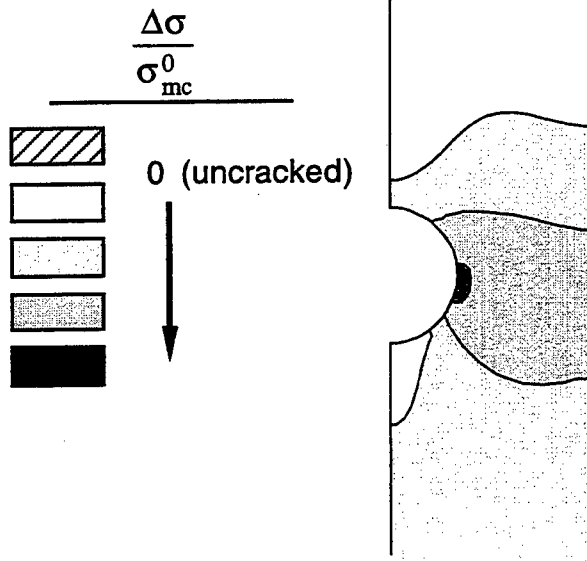
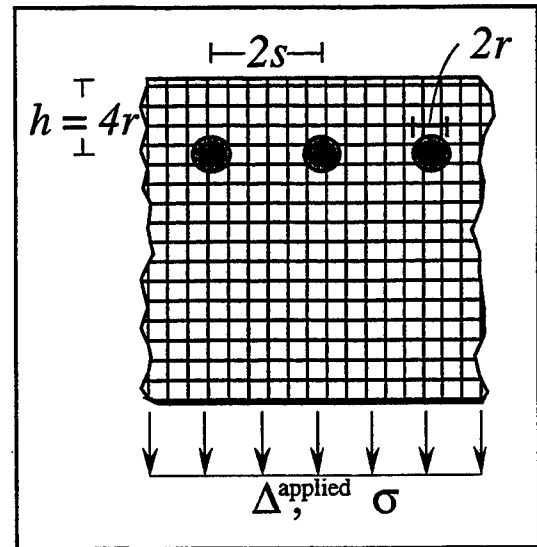
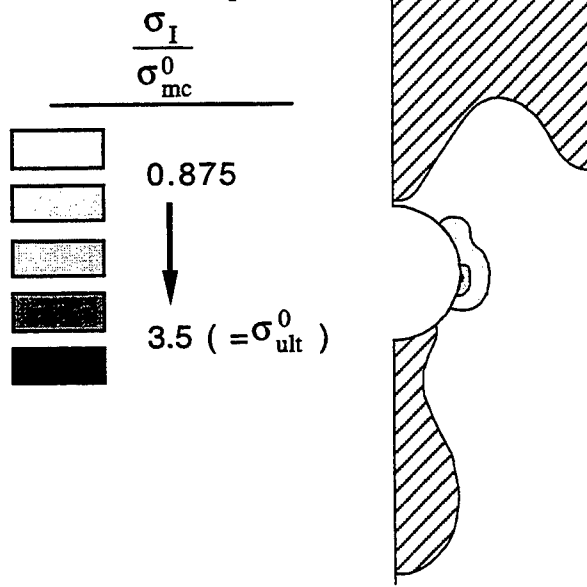


Figure 11. Performance of a fastened SiC/MAS plate as a function of bolt spacing s/r . $h/r=4$.

(a) Intensity of Matrix Cracking



(b) Maximum Principal Stress



$$\sigma = \sigma_{ult}$$

Figure 12. (a) Intensity of matrix cracking and (b) stress distribution at failure load, σ_{ult} , for optimal bolt spacing $s/r \approx 3$. $h/r = 4$.

Effect of cyclic thermal loading on the inplane shear strength of fiber reinforced MMC's

S. JANSSON* and F. LECKIE*

ABSTRACT. – The effect of cyclic thermal loading on the inplane shear strength of fiber reinforced metal matrix composites is investigated. An improved upper bound is given for the limit strength of randomly distributed fibers in the transverse plane. The limit load calculation are used in conjunction with shakedown theorems to assess the effect of thermal loading on the composite strength.

1. Introduction

When structural components made of metal matrix composites (MMC's) are subjected to fluctuations in operating temperature, the differential coefficients of thermal expansion of fiber and matrix give rise to microstructural stresses. The behavior of the composite is complex when the combination of thermal and mechanical loading result in plastic deformation in the matrix. It is possible in principle to perform an incremental analysis that determines the microscopic and macroscopic stress state simultaneously for a given loading history. This is hardly a practical approach since it does not offer the insight that is so essential in developing an understanding of material behavior and component performance. In this paper an approach is presented which is readily trackable and give results with a well defined interpretation.

The mechanical behavior of an aluminium alloy matrix reinforced with continuous Al_2O_3 fibers when subjected to a constant load transverse to the fibers and cyclic thermal load was studied by Jansson and Leckie (1992). It was determined experimentally that a shakedown condition exists, which has the form given in Figure 1. When the operating condition exceeded the shakedown criterion, each thermal cycle was accompanied by an increment of plastic strain, even for operating conditions which were only slightly in excess of the shakedown condition. When no noticeable plastic strain can be accepted in a composite structure the operating conditions are limited by the shakedown condition. In situations where substantial plastic strains can be accepted the number of operating cycles can be determined from the incremental cyclic strain rate given in Figure 1. It

* Department of Mechanical Engineering, University of California, Santa Barbara, CA 93106, USA.

has also been observed by Youda *et al.*, 1978) that severe distortion of fiber reinforced composites occurs for pure thermal cycling when the operating conditions are in excess of shakedown. Referring to the interaction diagram in Figure 1, for a given temperature range $\Delta\theta$ the available strength to support a mechanical load without accumulation of plastic strain is reduced to σ_{\max} . This type of representation is simple to use in design and provides an efficient tool in the communication between material scientists and designers.

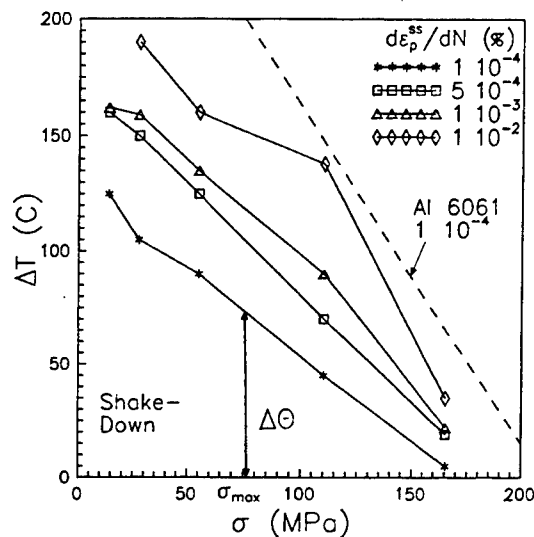


Fig. 1. – Experimentally determined interaction diagram for transverse tension.

The shakedown condition for transverse loading was also determined by Jansson and Leckie (1992) using homogenization techniques in conjunction with the finite element method. This is a rather extensive calculation and is unsuitable for routine calculations. Alternative methods developed by Gokhfeld and Cherniavsky (1980), Ponter and Karadeniz (1985) were applied by Cocks *et al.* (1992) to determine the shakedown condition of a simple fiber distribution subjected to transverse loading. These methods permit analytical solutions and provide good insight into the shakedown phenomenon.

In this paper the methods of Gokhfeld and Ponter, which utilize the limit load and a cyclic thermo-elastic solutions, will be used to study the reduction in shear strength for inplane loading of a fiber reinforced MMC when subjected to cyclic thermal loading.

2. Problem description

The composite is assumed to consist of long elastic fibers orientated in the 3-direction and randomly distributed in the 1-2 plane, as shown in Figure 2a. A perfect bond exists between fiber and matrix and the matrix is elastic-perfectly plastic with a yield stress σ_{ym} in uniaxial tension. For randomly distributed fibers the area fraction of fibers on arbitrary planes orientated in the 3-direction is equal to the fiber volume fraction, *cf.* Underwood

(1970). This implies that the portion of the straight line $\Sigma l_1 + \Sigma l_2 = l$ in Figure 2a that cuts through the fibers is given by

$$(1) \quad \Sigma l_2 = lf$$

where f is the fiber volume fraction. A concentric cylinder model of the same composite is shown in Figure 3. It can be noted that the average ratio of L_2/l , taken for all possible locations, for the cylinder mode is the same as given by Eq. (1) for the randomly distributed fibers. This feature will be used later.

3. Limit load solution

The classical limit load theorem of perfect plasticity state that a lower bound on the limit load is given by a statically admissible stress field that does not exceed the yield

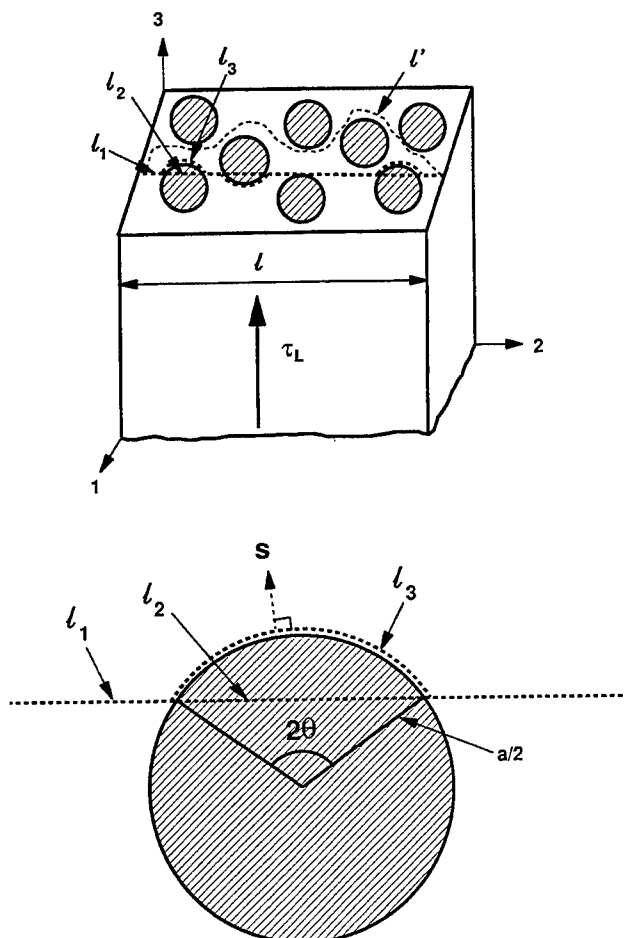


Fig. 2. – a) Slip surface for inplane shear loading of composite with randomly distributed fibers; b) Detailed view of slip surface near a fiber.

strength of the material. A trivial lower bound is given by assuming a constant stress distribution throughout the composite. This implies that

$$(2) \quad \tau_L \geq \tau_{ym}$$

where τ_L is the applied macroscopic shear stress and τ_{ym} is the yield strength in shear of the matrix. For the von Mises yield condition the yield stress in shear is related to the yield stress in uniaxial tension by the relation as $\tau_{ym} = \sigma_{ym}/\sqrt{3}$. It is hard to improve the lower bound without making more precise statements about the fiber distribution.

An upper bound on the limit strength is given by the work balance of a kinematically admissible displacement field. The classical bounding theorem states

$$(3) \quad \int_s P_i^s du_i^c \leq \int_v \sigma_{ij}^m d\varepsilon_{ij}^c dV$$

where $du_i^c, d\varepsilon_{ij}^c$ is the assumed compatible deformation mechanism and σ_{ij}^m is the point on the yield surface which corresponds to $d\varepsilon_{ij}^c$ by the normality rule. Since the fibers remain elastic the slip is limited to the matrix. Referring to Figure 2a, the deformation is assumed to be confined to slip on a surface given by the 3-direction and the line l' in the 1-2 plane. For slip in the 3 direction, the dissipation in the matrix is given by the work of the shear stress distributed along the line l' and the external work is given by the macroscopic stress distributed on the surface of width l . Applying the upper bound for this situation gives

$$(4) \quad \tau_L \leq \frac{l'}{l} \tau_{ym}$$

The lowest upper bound is given by the shortest distance l' . By choosing $l' = \Sigma l_1 + \Sigma l_3$ Eq. (4) reads

$$(5) \quad \tau_L \leq \tau_{ym} \left[1 + f \left(\frac{\Sigma l_3}{\Sigma l_2} - 1 \right) \right]$$

by use of Eq. (1). Since the slip surface is forced to circumvent the fiber $l_3/l_2 > 1$ and this is the source of strengthening. The increase in length due to a single fiber can be determined from Figure 2b as

$$(6) \quad \frac{l_3}{l_2} = \frac{\theta}{\sin \theta}$$

when θ is defined in the figure. The plane can intersect the fiber at any position and the ratio given by Eq. (5) can take any value in the range $1 \leq l_3/l_2 \leq \pi/2$. Shu and Rosen (1967) found this range and used the upper value of $\pi/2$ in Eq. (5). For randomly distributed fibers the line l_2 will cut through the individual fibers at different locations with equal probability and $0 \leq \Theta \leq \pi/2$. Including all these possibilities for the ratio in Eq. (5) gives

$$(7) \quad K = \frac{\Sigma l_3}{\Sigma l_2} = \frac{a \int_0^{\pi/2} \theta d\theta}{a \int_0^{\pi/2} \sin \theta d\theta} = \frac{\pi^2}{8}$$

so that Eq. (5) can be written as

$$(8) \quad \tau_L \leq (1 + f(K - 1)) \tau_{ym}$$

The same value of the upper bound can also be derived for the concentric cylinder model given in Figure 3. A macroscopic slip involves many cylinders and the macroscopic slip plane will cut through each individual cylinder at different locations. A possible slip surface is indicated by the lines l_1 and l_3 in Figure 3. This gives

$$(9a) \quad \tau_L (l_1 + l_2) \leq \tau_{ym} (l_1 + l_3)$$

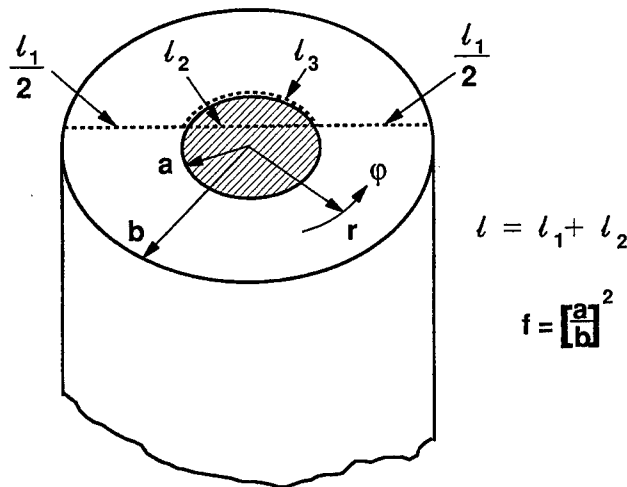


Fig. 3. - Concentric cylinder model of composite.

Including all the possible locations of the slip plane in the work balance equation gives

$$(9b) \quad \tau_L \Sigma (l_1 + l_2) \leq \tau_{ym} \Sigma (l_1 + l_3)$$

Proceeding in the same manner as for Eq. (7) gives

$$(10) \quad \tau_L \pi b^2 \leq \tau_{ym} [\pi b^2 (I - f)] + \tau_{ym} K f \pi b^2$$

This result is identical to the upper bound given by Eq. (8). The present upper bounds are compared with previous bounds given by Shu and Rosen (1967) and Majumdar and McLaughlin (1973) in Table 1 for fiber volume fraction of 50%. The present bound is

the lowest for randomly distributed fibers and has the same lowest value for the cylinder model, but a simpler expression than the bound by Majumdar and McLaughlin (1973). In practice the highest achievable fiber volume fraction for MMC's is approximately 55%, which is close to the random dense parking limit; *cf.* Bouvard and Lange (1992). The bound, Eq. (8), then implies that the practical maximum strengthening is 13%. The present upper bounds for randomly distributed fibers and the cylinder model are identical and this suggests that the cylinder model can be used with some confidence in the subsequent analysis. The cylinder model is used in the thermo-mechanical analysis because of the simplicity of the expression for the thermo-elastic stress field.

TABLE. - Upper bounds for inplane shear strength $\tau_L \sqrt{3}/\sigma_{ym}$ for $f = 50\%$.

Randomly distributed			Composite cylinder		
Shu	Majumdar	Present	Shu	Majumdar	Present
Rosen	McLaughlin		Rosen	McLaughlin	
1.29	1.14	1.12	1.13	1.12	1.12

4. Thermo-elastic stress field

The cylinder model, Figure 3, consists of a linear elastic fiber and an elastic perfectly plastic matrix. It is stress free at a temperature T_0 and for a temperature change from T_0 to $T_0 + \Delta T$ the thermo-elastic stress field which develops in the matrix is:

$$(11a) \quad \sigma_{rr}^T = \sigma_{ym} A \left[\frac{1}{r^2} - 1 \right]$$

$$(11b) \quad \sigma_{\varphi\varphi}^T = -\sigma_{ym} A \left[\frac{1}{r^2} + 1 \right]$$

$$(11c) \quad \sigma_{33}^T = -\sigma_{ym} AB$$

where the constant A is defined by

$$A = \frac{\frac{f}{1-f} (1 + \nu_m) + \beta (1 + \nu_f)}{\frac{1+\nu_m}{1-f} [1 + f (1 - 2\nu_m)] + \beta [1 + \frac{1+f}{f} (1 + \nu_m) - \nu_f (1 - 4\nu_m)]} + \frac{1}{\beta^2 \frac{1+f}{f} [1 - \nu_f (1 + 2\nu_f)]} \cdot \frac{E_m \Delta\alpha \Delta T}{\sigma_{ym}}$$

and the constant B by

$$B = \frac{\beta (1 + \nu_f) (1 - f) + (1 + \nu_m) (1 + f)}{\beta (1 + \nu_f) (1 - f) + (1 + \nu_m) f}$$

Here $\beta = E_m/E_f$, ν_m and ν_f are the Poisson's ratio of the matrix and fiber respectively, $\Delta\alpha$ is the difference in CTE between matrix and fiber and the dimensionless radius is defined by

$$\bar{r} = \frac{r}{b}$$

where b is the outer radius of the concentric cylinder model, Figure 3, and $f = (a/b)^2$.

When the fiber is rigid, $\beta \ll 1$, and the expressions for A and B simplify to

$$A = \frac{f}{1 + f(1 - 2\nu_m)} \frac{E_m \Delta\alpha \Delta T}{\sigma_{ym}}$$

$$B = \frac{1 + f}{f}$$

For the present problem the von Mises yield condition for the matrix can be written in the form

$$(12) \quad (\sigma_r - \sigma_{\varphi\varphi})^2 + (\sigma_{33} - \sigma_{\varphi\varphi})^2 + (\sigma_r - \sigma_{33})^2 + 6\tau_s^2 - 2\sigma_{ym}^2 = 0$$

when τ_{S3} is the shear stress on the slip surface and σ_{ym} is the yield strength of the matrix.

5. Elastic shakedown

The kinematical shakedown theorem for constant mechanical and time-dependent thermal loading states that an upper bound of the mechanical loading that the system can support at shakedown is given by

$$(13) \quad \int_s P_i^s \Delta u_i^c \leq \int_v \int_0^{\Delta t} (\sigma_{ij}^m - \sigma_{ij}^T) \dot{\epsilon}_{ij}^c dt dv$$

cf. Koiter (1956) or Gokhfeld and Chernaivsky (1980). Here Δt is the cycle time, σ_{ij}^m is associated with the strain rate $d\epsilon_{ij}^c$ which satisfies the condition over the cycle

$$(14) \quad \Delta\epsilon_{ij}^c = \int_0^{\Delta t} \dot{\epsilon}_{ij}^c dt$$

and that $\Delta\epsilon_{ij}^c$ is compatible with the displacement field Δu_i^c . This bound can be quite cumbersome to apply directly and a convenient way to determine the load carrying capacity at shakedown has been devised by Gokhfeld, cf. Gokhfeld and Chernaivsky (1980). The calculation is divided into two steps by assuming that plastic straining can occur at the two extremes of the thermal cycle. This implies that a modified yield surface $\phi(\sigma^*) = 0$ can be introduced. The modified yield surface is defined by translating the thermo-elastic stress field of Eq. (11) so it touches the inside of the matrix yield surface given by Eq. (12). The locus of points at the center of the cyclic stress vector are mapped

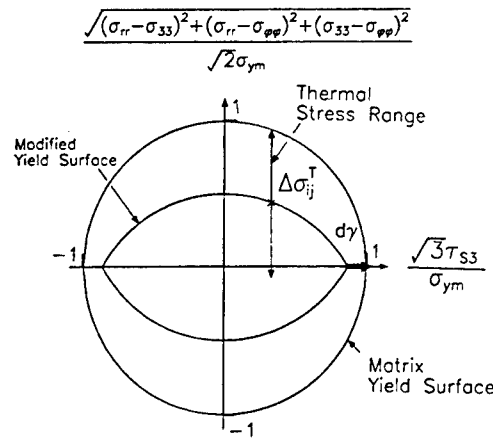


Fig. 4. - Modified yield surface.

out to form the modified yield surface indicated in Figure 4. The load carrying capacity at shakedown is then found by using a regular limit load calculation based on the modified yield surface and a static collapse mechanism so that,

$$(15) \quad \int_s P_i^s \Delta u_i^c \leq \int_v \sigma_{ij}^* \Delta \varepsilon_{ij}^c dV$$

The analysis is particularly amenable for the present case because the mechanical stresses due to the shear loading and the thermo-elastic stresses are orthogonal. Slip along the surface indicated by the line $l_1 - l_3$ in Figure 2 is given by the strain increment at the vertex of the modified yield surface as shown in Figure 4. The yield stress in shear at the vertex can be determined by use of the thermo-elastic stress field (11) and the yield condition (12) as

$$(16) \quad \tau_{S3} = \frac{\sigma_{ym}}{\sqrt{3}} \sqrt{I - \frac{A^2}{4} \left[\frac{3}{\bar{r}^4} + (1-B)^2 \right]}$$

The shear strength during thermal cycling can now be determined by using the yield stress in shear or the modified yield surface, Eq. (13), and performing a limit load calculation with use of Eq. (15). Proceeding in the same manner as in the derivation of Eq. (10) gives

$$(17) \quad \tau_L \pi b^2 = 2 \pi b^2 \int_{\sqrt{f}}^1 \tau_{S3}(\bar{r}) \bar{r} d\bar{r} + \pi a^2 K \tau_{S3}(\sqrt{f})$$

Evaluation of the integral and rearranging terms gives the final expression for the shake down condition:

$$(18) \quad \frac{\tau_L \sqrt{3}}{\sigma_{ym}} = f(K-1) \sqrt{1 - \frac{A^2}{4} \left[\frac{3}{f^2} + (1-B)^2 \right]} + \sqrt{1 - \frac{A^2}{4} [3 + (1-B)^2]} \\ + \frac{\sqrt{3}}{2} A \left[\sec^{-1} \left(f \sqrt{\frac{4 - A^2(1-B)^2}{3A^2}} \right) - \sec^{-1} \sqrt{\frac{4 - A^2(1-B)^2}{3A^2}} \right]$$

The expression is valid until a cyclic plastic zone starts to develop at the fiber-matrix interface. The highest equivalent stress in the matrix of the cyclic thermal then reaches twice the value of the yield stress. This condition is given by letting $\tau_{s3} = 0$ and $r = \sqrt{f}$ in Eq. (16), to give

$$A = \frac{2f}{\sqrt{3 + f^2(1 - B)^2}}$$

The shakedown condition is shown graphically in Figure 5 for rigid fibers and a fiber matrix modulus ratio representative of aluminium matrix composite with Al_2O_3 fibers. The fiber volume fraction $f = 0.5$ and the poisson's ratios $\nu_m = 0.32$ and $\nu_f = 0.26$.

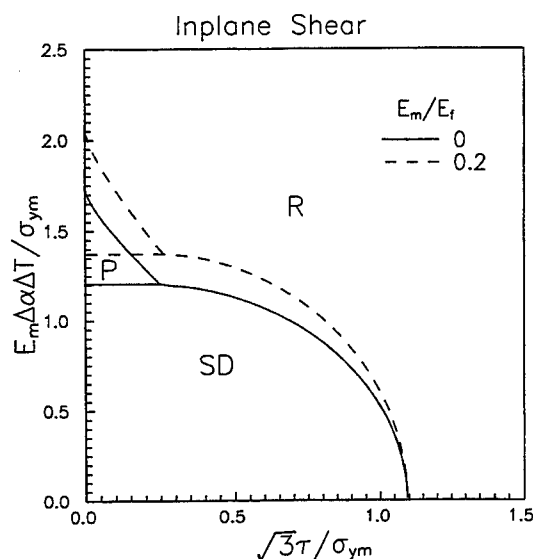


Fig. 5. - Interaction diagram for inplane shear where the ShakeDown, Ratchetting and reversed Plasticity regions are indicated.

6. Plastic shakedown

The result by Ponter and Karadeniz (1985) are used to estimate the boundary between reversed plastic straining and ratchetting. In the procedure the bound of Eq. (15) is applied as demonstrated previously except for the regions in which the equivalent von Mises stress of the elastic stress range exceeds $2\sigma_{ym}$. The only contribution that could come from these regions is given by a residual hydrostatic stress field. It could not have an in-plane shear component and hence these regions do not contribute to the load carrying capacity for the present case. The largest cyclic thermo-elastic stresses are adjacent to the fiber and from Eq. (16) it can be determined that the cyclic plastic zone extends from the fiber matrix interface to the radius r^* given by

$$(19) \quad \frac{\bar{r}^{*2}}{f} = \sqrt{\frac{3A^2}{A^2(I - B)^2 - 4}}$$

Using the work relation given by Eq. (15) as previously gives

$$(20) \quad \pi b^2 \tau_L = \pi b^2 \int_{\bar{r}^*}^1 \tau_s 3(\bar{r}) \bar{r} d\bar{r}$$

An evaluation of the integral gives the final expression for the reversed plasticity shakedown condition

$$(21) \quad \frac{\tau_L \sqrt{3}}{\sigma_{ym}} = \sqrt{1 - \frac{A^2}{4} (3 + (1 - B)^2)} - \frac{\sqrt{3}}{2} A \sec^{-1} \sqrt{\frac{4 - A^2 (1 - B)^2}{3 A^2}}$$

The reversed plasticity shakedown boundary is also shown in Figure 5.

7. Temperature dependent modulus and yield strength

No rigorous shakedown theorem exists for systems for which the elastic modulus is temperature dependent. An appreciation for the effect of temperature dependent moduli may be obtained by using moduli for different temperatures in the shakedown calculations. The most conservative result is usually given by the temperature that has the lowest E_m/E_f ratio. The effect is modest, since a temperature change of 200 C for an aluminium matrix causes a reduction of only 5% in the ratio.

A general consideration of a temperature dependent yield stress that gives the shape of the elastic and plastic shake down boundaries would require a numerical integration of Eqs. (14) and (17). However, a simple result can be obtained for pure thermal loading which corresponds to the interception of the shakedown boundaries with the axis for thermal loading, Figure 5. Following Gokhfeld and Chernaivsky (1980) it is assumed that plastic deformation only occurs at the two extremes of the cycle so that only the yield stress at the lowest and highest temperature need be considered. This implies at shakedown that

$$\sigma_{ym}(T_{\max}) = \sigma^e (\rho_{ij} + \Delta\sigma_{ij})$$

at the highest temperature of the cycle and

$$\sigma_{ym}(T_{\min}) = \sigma^e (\rho_{ij} - \Delta\sigma_{ij})$$

at the lowest temperature of the cycle. Choosing the local residual stress field ρ_{ij} to be of the form

$$\rho_{ij} = \beta \Delta\sigma_{ij}$$

maximizes the shakedown condition to give

$$\frac{\sigma_{ym}(T_{\max}) + \sigma_{ym}(T_{\min})}{2} = \sigma^e (\Delta\sigma_{ij})$$

This implies that the effect of a temperature dependent yield stress can be assessed by using the mean value of the yield stress for the two extremes of the cycle in the calculations for temperature independent yield stress. This is correct for pure thermal

loading and gives an estimate of the effect of temperature dependent yield stress for thermal and mechanical loading.

8. Discussion

It has been found that the limit strength in plane shear is bounded as

$$1 \leq \frac{\tau_L}{\tau_{ym}} \leq 1 + 0.24 f$$

This implies that the shear strength of a composite with a strong interface cannot be expected to be much higher than the yield stress of the matrix. Failure strains of 20% have been observed (Jansson, 1991) for the in-plane shear response of a fiber reinforced aluminium matrix composite. This implies that limit load calculations can clearly be used to predict the strength under these circumstances. The non-linear response for a composite with a matrix exhibiting nonlinear hardening can be estimated by use of the reference stress method, *cf.* Boyle and Spence (1983), that utilizes the limit load calculation. The linear elastic response can be determined by methods readily available in textbooks.

The results for the interaction of mechanical and thermal loading are summarized in Figure 5 which indicate regions of ShakeDown (SD), Ratchetting (R) and reversed Plasticity (P). In the shakedown region the final response is elastic after an initial response in which elastic and plastic deformation may occur. In the ratchetting region an increment of irreversible plastic strain occurs over each cycle. Because of this ratchetting behavior such loading conditions would lead to a very rapid accumulation of strain resulting in failure or excessive deformations. In the reversed plasticity region, reversed plastic straining occurs which does not have any incremental accumulation of strain. Operating in this regime introduces concerns of low cycle fatigue.

The procedure is straight forward and can be extended readily by finite elements to deal with more complex problems. An appreciation for an interaction diagram of the type given in Figure 5 can be obtained quite readily by calculating the key points. The intersection of the shakedown boundary and the axis for mechanical loading is given by a limit load calculation. The intersection of the shakedown boundary and the axis for thermal loading is given by a linear thermo-elastic calculation where the highest equivalent stress is equal to twice the yield stress of the matrix. The intersection of the reversed plasticity boundary and the axis for thermal loading is given by a similar calculation where the lowest equivalent stress, based on the elastic thermal stress, in the matrix along the slip line is equal to twice the matrix yield stress. The effect of a temperature dependent yield stress can also readily be assessed by using the mean value of the yield stress for the two extremes of the cycle in the calculations.

Acknowledgement

This work was supported by grant from Sandia National Laboratories at Livermore.

REFERENCES

- BOUVARD B., LANGE F. F., 1992, Correlation Between Random Dense Packing for Determining Particle Coordination Number in Binary Systems, *Physical Review A*, **42**, No. 2.
- BOYLE J. T., SPENCE J., 1983, *Stress Analysis for Creep*, Butterworths, London.
- COCKS A. C. F., JANSSON S., LECKIE F. A., 1992, Effect of Cyclic Thermal Loading on the Properties of Metal Matrix Composites, *Journal of Thermal Stresses*, **15**, 175-184.
- GOKHFELD D. A., CHERNIAVSKY O. F., 1980, *Limit Analysis of Structures at Thermal Cycling*, Sijthoff and Noordhoff, Amsterdam.
- JANSSON S., 1991, Mechanical Characterization and Modeling of Non-Linear Deformation and Fracture of a Fiber Reinforced Metal Matrix Composite, *Mechanics of Materials*, **12**, 47-62.
- JANSSON S., LECKIE A., 1992, Mechanical Behavior of a Continuous Fiber Reinforced Aluminium Matrix Composite Subjected to Transverse and Thermal Loading, to appear in *Journal of the Mechanics and Physics of Solids*.
- KOITER W. T., 1960, General Theorems for Elastic-Plastic Solids, in *Progress in Solid Mechanics*, SNEDDON I. N. and HILL R. Eds., North-Holland, Amsterdam, 1960, 165-221.
- MAJUMDAR S., MCLAUGHLIN P. V., J. R., 1973, Upper bounds to In-Plane Shear Strength of Unidirectional Fiber-Reinforced Composites, *Journal of Applied Mechanics*, **40**, 824-825.
- PONTER A. R. S., KARADENIZ S., 1985, An Extended Shakedown Theory for Structures that Suffed Cyclic Thermal Loading, Part I: Theory, *Journal of applied Mechanics*, **52**, 877-882.
- SHU S. S., ROSEN B. W., 1967, Strength of Fiber-Reinforced Composites by Limit Analysis Methods, *Journal of Composite Materials*, **1**, 366-381.
- UNDERWOOD E. E., 1970, *Quantitative Stereology*, Addison-Wesley, Reading, MA.
- YODA S., KURIHARA N., WAKASHIMA and UMEKAWA S., 1978, Thermal Cycling-Induced Deformation of Fibrous Composites with Particular Reference to the Tungsten Copper System, *Metallurgical Transactions*, **9A**, 1229-1236.

(Manuscript received August 8, 1995;
revised and accepted December 22, 1995.)

Design considerations and mechanical properties of SCS6/Ti 15-3 metal matrix composite after debond

S. Jansson & K. Kedward

Department of Mechanical and Environmental Engineering, University of California, Santa Barbara, Santa Barbara, CA 93106, USA

The anisotropic mechanical behavior of a continuous SiC fiber reinforced Ti alloy-matrix composite which possesses a weak fiber-matrix interface is investigated experimentally and modeled analytically. It is found that the transverse tensile and in-plane shear moduli are reduced drastically when the compressive residual stresses at the fiber-matrix interface are relaxed. It is shown that this change in elastic properties can cause a dramatic stress redistribution in components. This implies that design calculations based on properties for the pristine composite can be un-conservative and this possible stress redistribution has to be incorporated into the design procedures. © 1997 Published by Elsevier Science Ltd.

INTRODUCTION

Continuous fiber reinforced metal matrix composites (MMCs) are attractive because of excellent longitudinal properties and a relatively high transverse strength and stiffness. These type of MMCs can readily be utilized efficiently when the loading is predominantly uniaxial with primary stresses in the longitudinal direction and only secondary stresses in transverse directions. However, most structural components are subjected to complex multiaxial stress states. The efficient use of composite materials in such situations requires an understanding of the overall anisotropic mechanical behavior of the composite. A substantial amount of data have recently been generated for titanium matrix composites (TMCs) and are available in the literature [1-4]. Present TMC systems have a weak fiber-matrix bond to maintain a high fiber strength in the fabricated composite. This implies that the fibers are mainly held in place by the residual compressive stresses induced during the consolidation of the composite and the surface roughness of the fibers. These composites systems are candidates for medium-

temperature applications and can be exposed to in-service temperature variations such that inelastic deformation occurs in the matrix. Complex components are manufactured by diffusion bonding of sub-components at temperatures sufficiently high to cause inelastic deformation in the matrix. During these temperature excursions the compressive residual stress at the fiber-matrix interface can relax and change the performance of the composite.

Experimental and numerical procedures have been applied previously by Gunawardena *et al.* [5] to establish the pristine anisotropic behavior of TMC SCS6/Ti 15-3. The numerical simulations indicated that the residual stress state affects the longitudinal response modestly, while the transverse and in-plane shear responses are changed substantially. In a subsequent study by Jansson *et al.* [6], the transverse behavior of this system was studied for loadings with cyclic temperature histories. In particular, it was found, experimentally and theoretically, that the transverse modulus was reduced to a third of the value of the pristine composite after a small accumulation of transverse inelastic strain. The interfacial sliding stress, determined

from push-out tests of fibers, was found to be reduced to a fifth of the value for the pristine composite.

In this paper transverse tensile and in-plane shear responses are investigated for a composite that had accumulated 0.5% transverse creep strain before the final testing. This strain is sufficiently high to relax the compressive normal stress at the interface. These responses are representative of a system that has debonded and are compared with responses for a pristine composite. A detailed micromechanical finite-element simulation that incorporates the influence of a weak interface, residual stresses from fabrication and matrix plasticity is used to evaluate the responses.

COMPOSITE MATERIAL

The material used in this study is SCS6/Ti 15-3 made by Textron. It consists of continuous SiC fibers with a complex carbon and SiC coating in a eight-ply uniaxial lay-up. The fiber volume fraction is 35% and the average fiber diameter is 140 μm . The matrix is a β -Ti alloy, Ti-15V-3Cr-3Al-3Sn. The composite is fabricated by vacuum hot pressing a fiber-matrix foil lay-up, but no detailed information on the processing is available. However, the composite is consolidated at approximately 900°C. In the subsequent cool down, the mismatch in coefficients of thermal expansion of fibers and the matrix causes residual stresses to form.

EXPERIMENTAL PROCEDURES

The ambient tensile properties of the matrix were obtained by Jansson *et al.* [7] from tensile tests on matrix foil extracted from the composite. The fiber modulus was determined from cantilevered bend tests on fibers extracted from the composite. The matrix stress-strain curve is shown in Fig. 1 together with the fiber response estimated from the bend tests.

The initial transverse creep tests were conducted at 480°C until a creep strain of 0.5% was accumulated. This strain is sufficient to relax the residual stresses at the fiber-matrix interface, cf. Jansson *et al.* [6]. The strain was measured with an extensometer and the heating was applied with an induction heater and a steel susceptor in a servohydraulic test system. The

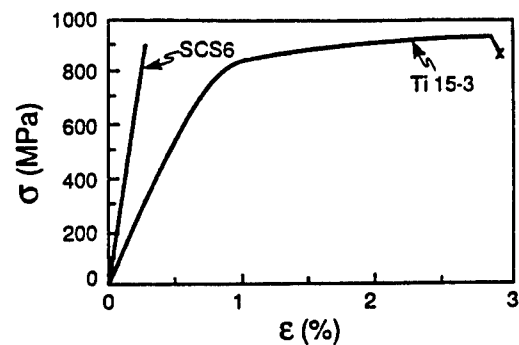


Fig. 1. Uniaxial stress-strain behavior of Ti 15-3 matrix and SCS6 fibers.

notches on the shear specimens were machined after the initial creep test.

The tensile and shear tests at ambient temperature were conducted at nominal strain rates of 10^{-5} s^{-1} in a servohydraulic test system.

The transverse properties were determined using specimens of dog-bone type. The specimen (Fig. 2a) has a relatively wide gauge section of 20 mm to ensure constant conditions at the center of the specimen. The longitudinal and transverse strains were measured with 3.2-mm long strain gauges, while the out-of-plane strain was measured with a 2-mm long strain gauge.

A specimen of the Iosipescu type (Fig. 2b), was used to determine the in-plane shear response. The specimen has a reduced gauge section of 60% and a notch angle of 110°. The notch angle is larger than the critical angle so high stress concentrations at the notch root are

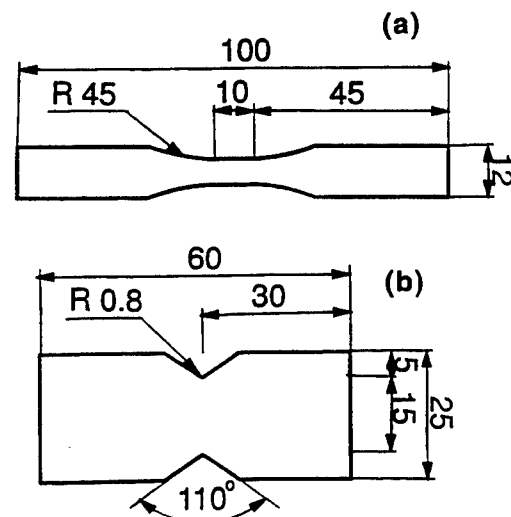


Fig. 2. (a) Specimen type for transverse tests. (b) Specimen of Iosipescu type for shear tests.

avoided. A singularity exists at the notch root for a notch angle smaller than the critical angle [8]. Too large a notch angle causes the stress distribution to be parabolic. The shear strain was measured with two 1.62-mm long strain gauges mounted on opposite sides of the specimen in the $\pm 45^\circ$ directions.

MICROMECHANICAL MODELING

Numerical simulations were performed using homogenization techniques in conjunction with the general purpose finite-element package ABAQUS [9]. In the computations the fibers are assumed to be long parallel cylinders arranged in a hexagonal array (Figs 3a and b). This is the simplest periodic array for which the linear elastic properties are transversely isotropic. The non-linear response of the array has a slight deviation from transverse isotropy. It

was demonstrated by Jansson [10] that the array can be used to predict the properties of a transversely isotropic system with randomly distributed fibers, if care is exercised when selecting the loading directions. For a system with randomly distributed fibers the matrix area fraction, on any plane cut through the composite, is equal to the matrix volume fraction (see Underwood [11]). However, the matrix area fraction is strongly dependent on the orientation and location for a periodic array. The present system has some form of arrangement resulting from the fiber-foil consolidation process, but it is difficult to identify any definite simple array type as the distribution pattern differs from point to point. However, it was found that an important feature of the weakly bonded systems for transverse tension is the matrix area fraction on the weakest planes. This was found to be 40%, which is substantially lower than the value of 65% for randomly distributed fibers. The corresponding value for the hexagonal array is 38% when loaded in one direction (Fig. 3a). The hexagonal array was selected in this case because it models the correct volume fraction and matrix area fraction on the weak planes that dictates the transverse strength.

In the homogenization technique (see Jansson [12]) the displacement field is assumed to have the form

$$u_i = u_i^0 + \langle \epsilon_{ij} \rangle x_j + u_i^p \quad (1)$$

where u_i^0 is an arbitrary constant displacement, $\langle \epsilon_{ij} \rangle$ is the average strain in the composite and u_i^p is an unknown displacement field which is periodic on the unit cell. The average stress $\langle \sigma_{ij} \rangle$ can conveniently be determined from the traction T_i on surface S of the unit cell by use of the mean stress theorem as

$$\langle \sigma_{ij} \rangle = \frac{1}{S} \int_S T_i x_j dS \quad (2)$$

All the loading cases considered are symmetric with respect to the x_1 and x_2 axes in Fig. 3(a) and the displacement field has an inversion symmetry about the point $(x_1 = a\sqrt{3}/2, x_2 = a/2)$. This implies that only the unit cell A-B-C-D in Fig. 3(a) need be analyzed. Ten-node quadratic generalized plane-strain elements with reduced integration were used to model the longitudinal and transverse behavior. The boundary conditions at the interface were selected to satisfy the interface bond characteristics. A fully bonded interface was modeled by

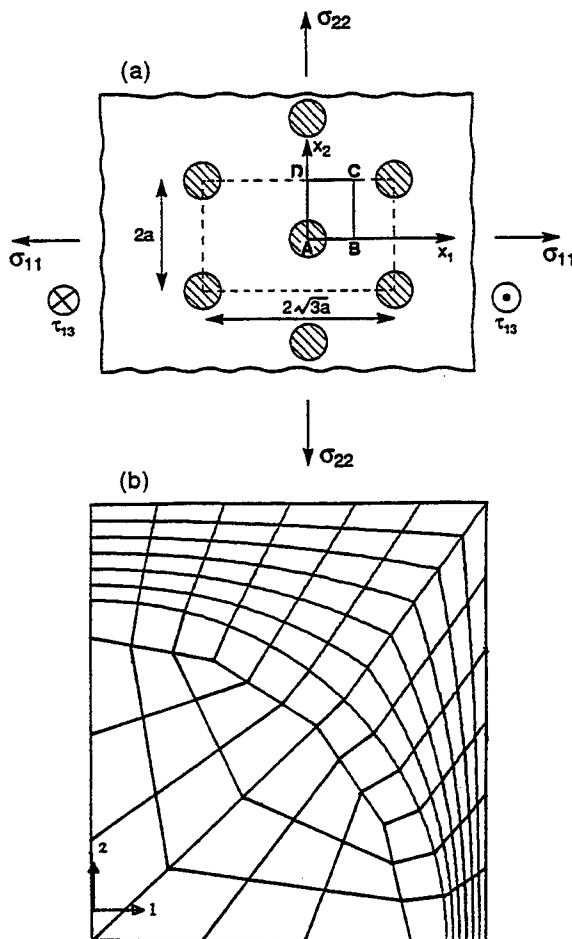


Fig. 3. (a) Hexagonal array with unit cell indicated. (b) Finite-element mesh for unit cell.

enforcement of displacement continuity across the interface. The weak interface was modeled by a three-node sliding interface element available in ABAQUS [9]. The interface is assumed to debond when the normal stresses become tensile and the interface is thereafter traction-free. Normal compressive stresses can be accompanied by shear stresses given by Coulomb's law of friction. Restrictions of the code meant that direct modeling of the in-plane shear response required a three-dimensional analysis using a 20-node brick element. Boundary conditions, which ensured generalized plane-strain behavior, and the symmetries on the unit cell were imposed. These conditions reduce the degrees of freedom in the model substantially and results in reasonable solution times. Because of limitations in the code the interface was modeled in the three-dimensional calculations as a thin elastic-perfectly plastic solid layer whose yield strength was selected to be equal to the sliding resistance of the interface.

The fibers were assumed to be isotropic linear elastic and the matrix is assumed to be elastic-plastic with isotropic hardening. The ambient elastic properties of fiber and matrix are given in Table 1. It was found by Gunawardena *et al.* [5] that the simplified temperature dependence of the yield stress given in Fig. 4 together with temperature-independent moduli gave the same residual stress distribution as that found in more refined models.

EXPERIMENTAL OBSERVATIONS AND NUMERICAL SIMULATIONS

Residual stresses after fabrication

The residual stresses following fabrication are likely to influence the mechanical behavior of

Table 1. Matrix and fiber properties at ambient temperature

	Matrix	Fiber
Young's modulus (GPa)	115	360
Poisson's ratio	0.33	0.17
Tensile strength (MPa)	950	4300
Strain to failure in tension (%)	3	1.2
Coefficient of thermal expansion (1/C)	9.7×10^{-6}	4.5×10^{-6}

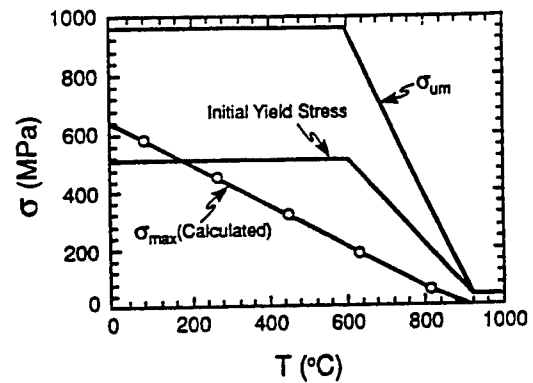


Fig. 4. Temperature dependence of matrix properties.

weakly bonded composites. When calculating the residual stress fields the composite is assumed to be stress-free at the consolidation temperature and subsequently cooled down to room temperature. The exact details of the process are unknown and consequently no time-dependent viscous behavior was included in the analysis. It was found in Gunawardena *et al.* [5] that an assumed consolidation temperature of 900°C gave excellent agreement between the calculated and experimentally observed behavior for the pristine composite. The residual stress in the fiber consists of a compressive axial stress of 720 MPa and almost uniform compressive radial and hoop stresses of 220 MPa. The residual hoop and radial stresses in the matrix vary substantially and the highest magnitudes are found near the interface with a compressive radial stress of 200 MPa and a tensile hoop stress of 500 MPa. The axial stress is tensile and is almost constant, varying between 390 and 420 MPa.

Transverse tension

The transverse tensile response is shown in Fig. 5(a) for the pristine ($\epsilon_1^c = 0$) and debonded composite ($\epsilon_1^c = 0.5$) together with numerical simulations. It was found by Gunawardena *et al.* [5] that the response of the pristine composite was modeled well by including the residual stresses from a fabrication temperature of 900°C and an interface that can only transfer compressive normal stresses and has a coefficient of friction of $\mu = 0.8$. It is interesting to note that the initial linear response for the composite is slightly more compliant than for a composite with a fully bonded interface. After the initial linear response a substantial decrease

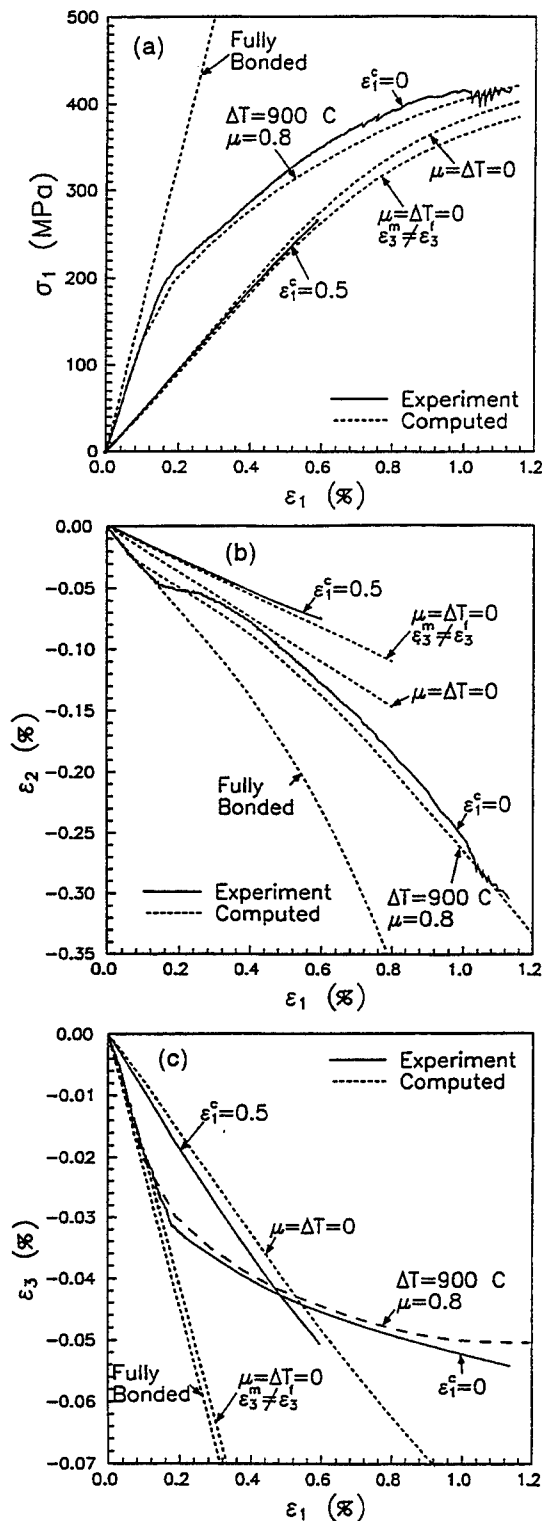


Fig. 5. (a) Experimentally determined and calculated transverse tensile stress-strain behavior for different interface characteristics. (b) Experimentally determined and calculated contractions in unloaded transverse for different interface characteristics. (c) Experimentally determined and calculated contractions in the longitudinal direction for different interface characteristics.

occurs in the slope of the stress-strain curve and this is caused by debond at the fiber-matrix interface. The computations also indicate that some localized yielding occurs in the matrix at the initial portion of the debond. Finally, the interface is fully debonded in the loading direction and the load-carrying capacity is dictated by the matrix ligaments between the fibers. A simple estimate for the transverse limit strength [7] gives

$$\sigma_{TL} = \frac{2}{\sqrt{3}} A_{fm} \sigma_{Lm} \quad (3)$$

where A_{fm} is the matrix area fraction at the weakest plane and σ_{Lm} is the limit strength of the matrix. The strain to failure is approximately 40% of the matrix failure strain of 3.2%. This reduction in failure strain is caused by a concentration of strain in the matrix ligaments between the fibers because they are subjected to a higher stress. The response for the debonded composite, $\epsilon_1^c = 0.5$, has a much more compliant initial linear response. The modulus is only a third of the modulus for the pristine composite and is of the same magnitude as was observed for the same composite after cyclic thermo-mechanical load [6]. It can be deduced that this response is modeled closely by assuming an initially stress-free interface, $\Delta T = 0$. The calculated response after debond is insensitive to the value of the coefficient of friction at the interface and quite insensitive to the constraint in the longitudinal direction. The response for the case where the fiber and matrix have the same longitudinal strain is only slightly stiffer than the response for the case where the matrix is assumed to be fully decoupled from the fiber in the longitudinal direction, $\epsilon_3^m \neq \epsilon_3^f$.

The contraction in the unloaded transverse direction is shown in Fig. 5(b). The response of the pristine composite is modeled closest, as previously, by including the residual stress state from fabrication and the friction at the interface. The decrease in contraction rate after the initial linear response is caused by the debond at the interface and the subsequent increases are caused by general yielding in the matrix.

The experimental response for the debonded composite has approximately the same slope as the center portion of the curve for pristine composite. This response agrees well with the calculated response for the case of no residual stress and decoupled longitudinal strain of fiber

and matrix. The assumption of a decoupled longitudinal strain is close to the condition at the side of the specimen where the out-of-plane strain gauge is mounted. However, it is likely that the longitudinal strain in the matrix and fiber are equal at the center of the specimen, and the response there is given by the case $\mu = \Delta T = 0$. At the free edge of the specimen the fiber and matrix can deform independently in the longitudinal direction. If the distance is sufficiently long only a small frictional stress is needed at the interface to build up a longitudinal strain compatibility between fiber and matrix away from the free edge. The later condition can be expected to dominate the response in a large component where dimensions are much larger than a fiber diameter.

The contraction in the longitudinal direction is depicted in Fig. 5(c). The response for the pristine composite has initial linear response with a decrease in contraction after matrix yield as the deformation tends to plane strain in the fiber direction. This response is also modeled well by a consolidation temperature of 900°C and friction at the interface.

The response for the debonded composite has a initially lower contraction than the pristine composite. The matrix yields at a lower transverse strain for the pristine composite than for the debonded composite and this cause the contraction rate to decrease at a lower strain for the pristine composite than for the debonded composite. The response for the debonded composite is modeled well with an initially stress-free interface and equal longitudinal strain in fiber and matrix. It surprising to see that the response for decoupled longitudinal strain in the fiber and matrix is almost identical to the fully bonded case.

The strain to failure strain in the tensile test for the debonded composite is 0.6%. It had previously accumulated a creep strain of 0.5%, giving it a total strain of 1.1%. This total strain at failure is very close to the observed failure strain for the pristine composite, indicating that a constant strain criteria could be used as a failure condition for this type of loading.

In-plane shear

Shear tests have been performed with the fibers orientated in the direction of the two notches. It was shown by Jansson *et al.* [7] that the limit strength is dependent on the orientation of the

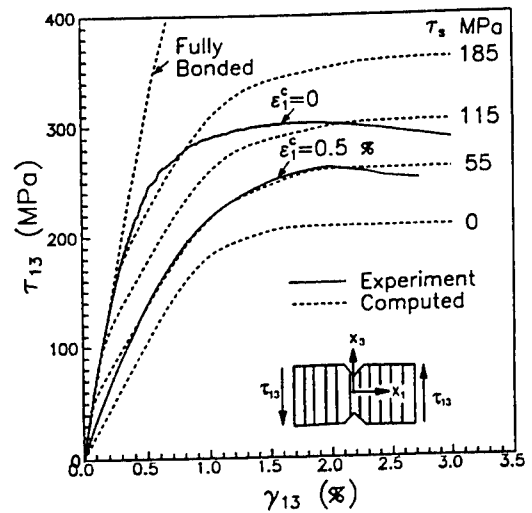


Fig. 6. Experimentally determined and calculated in-plane shear-stress response for different interface characteristics.

fibers for composites with weak interfaces in this type of test. The present loading subjects a long portion along the fibers to constant conditions and is representative of loading that occurs in practice. It has a lower limit strength than the case where the fibers are orientated perpendicular to the notches. The experimental and computed stress strain curves are shown in Fig. 6.

The response for the pristine composite has a initial linear response followed by a gradual transition that reaches a limit condition with no increase in stress. A comparison with the numerical simulations indicated that no sliding occurs initially at the interface. This is followed by a response that corresponds to a sliding with a shear stress of 185 MPa at the interface. The sliding stress thereafter gradually decreases with an increase in strain to a saturation value of 115 MPa. A simple model for the limit strength was proposed by Jansson *et al.* [7]

$$\tau_L = \frac{1}{\sqrt{3}} \sigma_{Lm} A_{fm} + \tau_y^i \frac{\pi}{2} \times (1 - A_{fm}) \quad (4)$$

where τ_y^i is the sliding stress at the interface. This model predicts a sliding resistance of 95 MPa at the interface for the limit state, which is close to the computed value of 115 MPa. The debonded composite has a lower modulus and limit strength than the pristine composite. The value of the initial modulus is approximately half the value for the pristine composite. This is higher than that predicted for a stress-free interface with no sliding resist-

ance, indicating that some contact is present at the interface for this type of loading. The computations indicate that final limit strength corresponds to a sliding resistance of 55 MPa at the interface, also approximately half the value of the pristine composite. A modest reduction in failure strain that is close to the sample-to-sample variation is observed.

CONSEQUENCES IN DESIGN

Stress redistribution

Titanium matrix composites (TMCs) can be used efficiently in unidirectional lay-ups with the dominating loading in the fiber direction. A MMC turbine disk represents a candidate component that features this type of loading. It has fibers orientated in the most highly stressed direction, the hoop direction. For simplicity, the disk is assumed to be of constant thickness and only a uniform blade loading on the outer radius (Fig. 7a) will be considered. The stress distribution can readily be found in Lekhnitskii [13] as

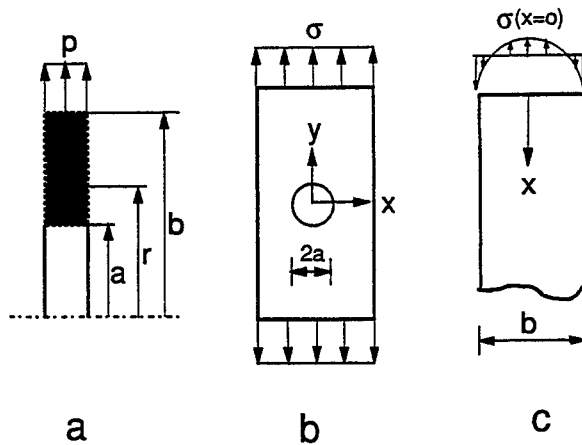


Fig. 7. (a) Fiber reinforced ring with loading on the outer surface. (b) Plate with a hole. (c) Stress decay in a strip subjected to a self-equilibrating edge load.

$$\sigma_r = \frac{p}{1-c^{2k}} \left[\left(\frac{r}{b} \right)^{k-1} - C^{2k} \left(\frac{b}{r} \right)^{k+1} \right] \quad (5a)$$

$$\sigma_\phi = \frac{p}{1-c^{2k}} \left[\left(\frac{r}{b} \right)^{k-1} + C^{2k} \left(\frac{b}{r} \right)^{k+1} \right] \quad (5b)$$

where $C = (a/b)$, $k = \sqrt{E_\phi/E_r}$, a is the inner radius, b is the outer radius and p is the equivalent blade loading on the outer surface. The hoop and radial stress distribution are shown in Fig. 8 for a ring with $a/b = 0.5$ and different anisotropy ratios k . The case $k = 1.2$ corresponds to the elastic properties for the pristine composite and $k = 2.1$ corresponds to the properties for a debonded composite (see Table 2). The pristine composite has a very low anisotropy and the stress distribution is accurately given by the isotropic solution with the highest hoop stress at the inner radius. However, the loss of residual stresses at the interface and the associated debond causes a substantial reduction in the transverse modulus and an increase in the anisotropy of the composite. This causes

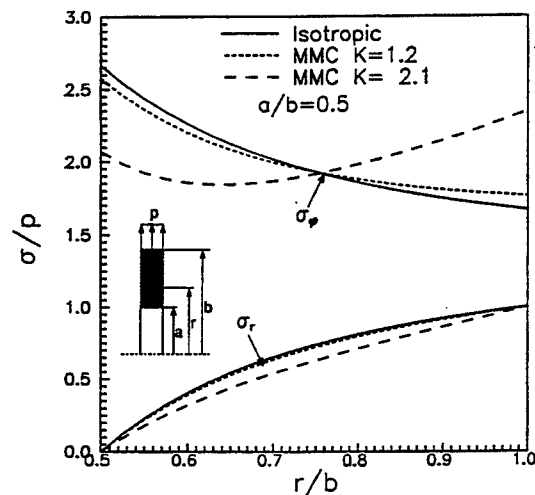


Fig. 8. Stress distribution in a ring with $a/b = 0.5$ for different degrees of anisotropy.

Table 2. Comparison of experimental and calculated elastic properties for a pristine and debonded composite

		E_{33} (GPa)	ν_{31}	E_{11} (GPa)	ν_{23}	ν_{13}	G_{13} (GPa)
Pristine	Experiment	196	0.25	129	0.34	0.20	62
	Computed	202	0.27	133	0.36	0.17	64
Debonded	Experiment	—	—	46	0.13 [†]	0.095	38
	Computed	202	0.25	47	0.14 [†]	0.085	20 [‡]

[†]These values are for the free edge of the specimen. The calculated value for the center is 0.18.

[‡]Based on the assumption of a frictionless interface.

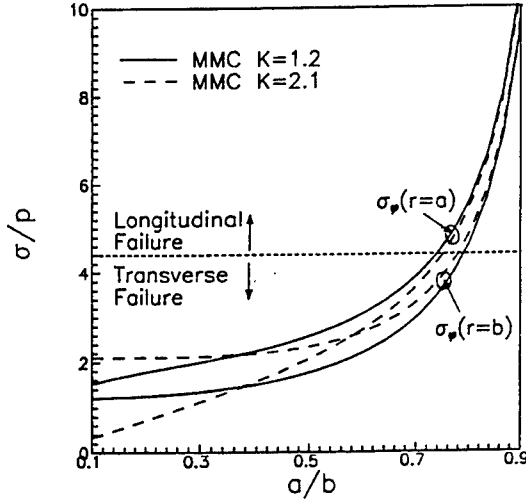


Fig. 9. Maximum and minimum hoop stress in an externally loaded ring for different hole sizes and anisotropy ratios.

a dramatic change in the hoop stress distribution and the hoop stress attains its maximum value at the outer radius rather than at the inner radius. The value of the hoop stress at the inner and outer radius are shown in Fig. 9 for different ring dimensions a/b . It can be deduced that a tremendous stress distribution occurs when the interface debonds for small a/b ratios and the maximum hoop stress can even increase. However, this can be avoided by choosing a larger a/b ratio and it can be seen that the stress redistribution is modest for $a/b > 0.7$. This implies that this type of stress redistribution can sometimes be avoided by choosing configurations such that the geometry dictates the stress distribution more than the constitutive properties.

Stress concentration

The highest tensile stress concentration for a hole in a infinite plate (Fig. 7b) is given by the tensile hoop stress at the ends of the diameter perpendicular to the loading direction (cf. Lekhnitskii [13]) as

$$\sigma_{\max} = \sigma_y^{\infty} \left[1 + \sqrt{2} \left(\frac{E_y}{E_x} - \nu_{yx} \right) + \frac{E_y}{G_{yx}} \right] \quad (6)$$

For a pristine composite loaded in the longitudinal direction the stress concentration is 3.4. After the residual stresses have relaxed at the interface the stress concentration increases to

4.6. For loading in the transverse direction the stress concentration for the pristine composite is 2.7 and it decreases to 2.1 for the debonded composite.

Stress decay

An interesting issue for composites is how far an edge effect propagates into a component (Saint-Venant's Principle). It can propagate much further into highly anisotropic materials than into isotropic materials. This was studied by Horgan *et al.* [14] for the self-equilibrating loading shown in Fig. 7(c). The stress decay is approximately given by

$$|\sigma| \leq Ae^{-\lambda x}, \quad x \geq 0 \quad (7a,b)$$

where

$$\lambda \approx \frac{2\pi}{b} \sqrt{\frac{G_{xy}}{E_x}} \quad (7c)$$

Equation (7a,b) and (7c) indicates that the edge effect has its slowest decay rate in the stiffest direction. For the present composite, the longitudinal modulus can be expected to be unaffected by the debond. An appreciation for the difference in decay rate for the debonded and pristine composite is given by the ratio of the lengths required to achieve the same stress level. Use of eqn (7a, b) and (7c) gives

$$\frac{x^d}{x^p} = \sqrt{\frac{G_{xy}^p}{G_{xy}^d}} \quad (8)$$

This implies that the load diffusion length increases by 40% for the debonded material.

CONCLUSIONS

It has been found that the relaxation of the residual compressive stresses at the fiber-matrix interface causes a reduction in the transverse modulus to a third of the value for the pristine composite.

The initial in-plane shear response is not affected as strongly as the transverse tensile response. The shear modulus is reduced to half the value of the pristine material. Calculations

indicate that the sliding resistance at the interface reduced to half the value of the pristine material. The limit strength in shear is dictated by a combination of the matrix strength and the sliding resistance at the interface. This implies that the limit strength of the composite is only reduced by a factor 2/3.

Some loadings, such as longitudinal tension, will tend to close the fiber-matrix interface and cause the debonded composite to have the same elastic properties as the pristine composite. Other loadings, such as transverse tension, will cause portions of the interface to open up more during loading. This will cause the debonded composite to have elastic properties that are dependent on the loading, and some of the elastic symmetry relations do not apply for constants determined from these different loadings.

It was demonstrated that micromechanical simulations can be used as an efficient tool to evaluate the experimental observations. This experience also adds confidence to the approach to be used to predict composite behavior.

The present TMC systems with weak interfaces are candidates for components with complex shapes. The components will be manufactured through complex processes and assemblies of sub-components. The individual sub-components can therefore be subjected to a number to thermal cycles with high temperature before service. This can lead to a relaxation of the compressive stresses at the fiber-matrix interface. The relaxation leads to a drastic reduction in the transverse modulus. A reduction in transverse modulus causes an increase in the anisotropy of the material, and the stress distribution in a component consisting of a debonded composite can be substantially different to the stress distribution for the pristine composite. Hence, design calculations should be performed on the pristine and debonded composite properties to ensure that the component has the required performance.

ACKNOWLEDGEMENTS

Funding for this work has been provided by contracts NASA NAG 1-1376 and NCEL N 47408/93R7308.1

REFERENCES

1. NASA, *Hitemp Review*. NASA CP 10082, 1991.
2. Harmon, D.M., Finfield, M.A., Harter, J.A. and Buchanan, D.L., Differences in fatigue and fracture behavior of woven-mat and acrylic binder SCS6/Ti 15-3 composites. *J. Composites Technol. Res.* 1993, **15**, (3), 225-233.
3. Johnson, W.S., Damage development in titanium metal-matrix composites subjected to cyclic loading. *Composites* 1993, **24**, (3), 187-196.
4. Russ, S. M., Nicholas, T., Bates, M. and Mall, S., Thermomechanical fatigue of SCS6/Ti 24-AL-11Nb metal matrix composite. In *Failure Mechanisms in High Temperature Composite Materials*, ASME AD, Vol. 22/MD, Vol. 122, 1991, pp. 63-6.
5. Gunawardena, S.R., Jansson, S. and Leckie, F.A., Modeling of anisotropic behavior of weakly bonded fiber reinforced MMC's. *Acta Metall.* 1993, **41**, 3147-3156.
6. Jansson, S., Dal Bello, D.J. and Leckie, F.A., Transverse and cyclic thermal loading of the fiber reinforced metal matrix composite SCS6/Ti-51-3. *Acta Metall.* 1994, **42**, 4015-4024.
7. Jansson, S., Deve, H.E. and Evans, A.G., The anisotropic mechanical properties of a Ti matrix composite reinforced with SiC fibers. *Metall. Trans. A* 1991, **22A**, 2975-2983.
8. Wang, S. S. and Dasgupta, A., Development of Iosipescu-type test for determining in-plane shear properties of fiber composite materials. UILU-ENG-86-5021. Department of Theoretical and Applied Mechanics, University of Illinois, 1986.
9. *ABAQUS Finite Element Program*. Hibbitt, Karlson and Sorensen, Inc., 1988.
10. Jansson, S., Mechanical characterization and modeling of non-linear deformation and fracture of a fiber reinforced metal matrix composite. *J. Mech. Mater.* 1991, **12**, 47-62.
11. Underwood, E. E., *Quantitative Stereology*. Addison-Wesley, Massachusetts, 1970, pp. 25-7.
12. Jansson, S., Homogenized non-linear constitutive properties and local stress concentration for composites with periodic internal structure. *Int. J. Solids Struct.* 1992, **29**, 2181-2200.
13. Lekhnitskii, S. G., *Anisotropic Plates*. Gordon and Breach, New York, 1944.
14. Horgan, C., Saint-Venant end effects in composites. *J. Composite Mater.* 1992, **16**, 411-422.

**ON THE BEHAVIOUR OF METAL MATRIX COMPOSITES
SUBJECTED TO CYCLIC THERMAL LOADING**

A. R. S. Ponter,

Department of Engineering, University of Leicester, LE1 7RT, UK

and

F. A. Leckie,

Department of Mechanical Engineering, University of California, Santa Barbara,
California, 93106, USA

ABSTRACT

The mechanical properties of metal matrix composite materials are strongly effected by thermal cycling. Through the study of the experimental data of Jansson and Leckie (1992), for an aluminium /alumina continuous fibre composite, the paper investigates the relationship between the observed behaviour and the predictions, using simplified methods of analysis, of classical plasticity models for the matrix material. This comparison shows that many of the features of the data can be understood in this way but the long term cyclic growth of strain, when the material has reached a stabilised state, cannot be so understood. This effect is due to material ratchetting. The conclusion of this study is that the inelastic deformation of machine components when composed of such a material and subject to many cycle of temperature depends upon an understanding of the stress dependance of material ratchetting.

November 1997

1. INTRODUCTION

Fibre reinforced metal matrix composites provide a means of producing materials with high uniaxial strength and stiffness and, at the same time, resistance to brittle fracture. Their high strength-to-weight ratio make them attractive for a range of applications such as the dynamically loaded components of internal combustion engines and gas turbines. However, in both these applications a major component of the load history arises from local temperature fluctuations and thermal stresses arising from temperature gradient. Such thermal effects can cause cyclic strain growth in the matrix even in the absence of other forms of loading. The phenomenon is particularly pronounced for growth activated by stresses transverse to the direction of the fibre. The capacity of metal matrix composites to withstand thermal fluctuations is an important limit to their use.

This paper is concerned with methods of understanding the behaviour of an element of a composite subjected to constant stress and cyclic temperature. The composite is modelled as an inhomogenous body composed of elastic fibres and an elastic-plastic matrix. Fluctuations in temperature induce thermo-elastic stresses produced by the difference between the coefficient of thermal expansion of the two component materials. When the thermal stresses are sufficiently large, plastic strains occur in the matrix resulting in either cyclic strain growth (ratchetting) or growth of strain to some asymptotic value. The problem is inherently very complex and the interpretation of the behaviour of the composite in terms of the properties of the component materials poses considerable computational problems. A number of separate phenomena are involved and a complete understanding of observed behaviour requires insight into the ways plastic strain growth results from the stress cycles occurring in the matrix.

An important step in the development of such an understanding has been provided by Jansson and Leckie (1992). The results of tests on a continuous fibre composite with stress applied in a direction perpendicular to the fibres have been interpreted in terms of shakedown

concepts, assuming the matrix is an elastic-perfectly plastic material. These tests involved moderate temperature fluctuations (up to about 100°C) and the tests were terminated when high rates of ratchetting were experienced. Jansson and Leckie (1992), in their interpretation of the data, concentrated on the terminal rate of strain ratchetting occurring after a number of cycles of temperature fluctuation. They showed that the stress dependency of this terminal rate was related to shakedown concepts but differed from the stress dependency of the shakedown boundary predicted by finite element calculations.

In contrast, Daehn et al (1991) and Zhang et al (1990,1991) have extensively studied particulate and whisker reinforced MMC's where the amplitude of temperature cycle (typically 350°C) results in high rates of ratchet for small applied stress. In such cases the entire volume of the matrix material experiences substantial reversed plasticity in the absence of applied stress and the form of ratchetting phenomenon is comparable to, for example, the cyclic thermal ratchetting of polycrystalline uranium. In this paper we study the moderate cycling case which defines the onset of inelastic strain growth with increasing applied stress and temperature amplitude.

The purpose of this paper is to study the various modes of behaviour which occurred in the Jansson and Leckie tests and to relate them to characteristic modes of behaviour of an elastic plastic body. The behaviour is inherently complex and this case study is an attempt to provide a framework within which cyclic strain growth of composites may be understood.

The paper consists of three sections. We first revisit the data of the Jansson Leckie tests and interpret regions of an interaction diagram where distinct modes of behaviour are observed to take place. These modes fall into two classes; structural plasticity phenomena which are predictable by the classical plasticity models and; material ratchetting. The former modes are; elastic behaviour, elastic shakedown, plastic shakedown, ratchetting limited by strain hardening, and unlimited ratchetting. All these phenomena can be understood in terms of shakedown concepts for perfect plasticity with extensions to the behaviour outside the

shakedown limit taking into account the strain hardening of the matrix. Material ratchetting, however, is an inherent property of the matrix material, in this case aluminium, and shows stress dependency which is distinctly different to the structural plasticity phenomenon as was observed by Jansson and Leckie (1992). For each mode of behaviour we discuss the predictions which can be made on the basis of simple plasticity constitutive equations and assumptions of kinematic determinacy of the micro strain fields. In the last section we interpret the material data in terms of these simple theories. We conclude that most aspects of the flow behaviour can be interpreted in this way, giving a reasonable coherent model for the ratchetting of MMCs subjected to moderate temperature fluctuations. The most significant conclusion, however, is that for situations where many thousands of thermal cycles are involved, the strain growth becomes dominated by material ratchetting, a phenomenon currently poorly understood.

2. EXPERIMENTAL PHENOMENA

Figure (1) shows an interaction diagram for the Jansson and Leckie tests with axis given by the constant macro applied stress Σ and the amplitude of temperature variation $\Delta\theta$. The test sequence for five tests are shown where the applied macrostress is maintained constant and the amplitude of temperature is maintained at a fixed level and then increased by increments of 5°C or 10°C . At each stage thermal cycling was continued until either strain growth terminated or ratchetting strain growth at a constant rate was achieved. The tests were terminated when high rates of strain growth were observed. The diagram also contains two boundaries which delimit distinct modes of behaviour:

E : Elastic Region: the micro thermoelastic stresses lies within the yield condition for the initial yield point of the material assuming zero initial micro residual stresses. Some plastic strain growth was observed in the data as the composite possessed initial micro residual stresses from the forming process.

ES : Elastic Shakedown: This region is bounded by the shakedown boundary for a

perfectly plastic material using the initial yield stress of the aluminium as reported by Jansson and Leckie (1992) from finite element calculations. In this region a small amount of strain growth occurs terminating in a low rate of material ratchetting.

PS : Plastic Shakedown: For higher ranges of temperature amplitude and low applied stress no cyclic strain growth occurs and the observed behavior is similar to shakedown. Figure (2) shows the growth of strain in Tests (1) and (2) with increasing $\Delta\theta$. Strain growth is primarily confined to the shakedown region (S) and becomes stabilised in the plastic shakedown region (PS). The upper limit of this region is defined by the onset of high rates of ratchet which is discussed below.

LR : Ratchetting Limited by Strain Hardening: In this region the material shows an initial high rate of ratchet which then declines over a substantial number of cycles to either a low or zero rate of strain growth per cycle. During this transient significant strain growth occurs. For each cycling sequence it is possible to identify the number of cycles N_{99} when 99% of the ultimate strain growth had been achieved in the transient. For tests 3,4 and 5 the value of N_{99} is shown in Figure (3) as a function of the total accumulated plastic strain. Although there is some scatter, there is a distinct trend where the number of cycles increase with increased strain. The predictions shown in the figure are discussed below. In this region it is possible to plot the total accumulated strain against an effective macrostress Σ^* as shown in Figure (4) with the experimental monotonic stress strain curve for the composite for constant temperature, i.e. for $\Sigma^* = \Sigma$. We will show in the next section that this behaviour is consistent with classical plasticity behaviour assuming that the microstrains exhibit the same pattern as in the constant temperature monotonic test.

R : Unlimited Ratchetting: Once the temperature difference exceeds the boundaries between the limited ratchetting (LR) region and the ratchetting (R) region, the rate of terminal strain growth per cycle increases rapidly to high values. As we mentioned earlier, this was the stage at which the tests were terminated. The steady state ratchet rate for all the tests is shown in

Figure (5) where the temperature axis is normalized by a value $\Delta\theta^*$ near or on this outer boundary. The value of $\Delta\theta^*$ used for each test is shown in Figure (1) as a star. It can be seen that within the width of the transition shown as a double line in Figure (1), corresponding to approximately $10^0 C$, the ratchet rate changes from very low values to a consistent high values. In Figure (5) we show a pair of bound on this high rate which is discussed in the next section. It is interesting to note that this ratchet rate appears to be independent of the value of the applied load, Test (1) and Test (5) show remarkably similar rates.

Material Ratchetting: Within the outer boundary all the tests show some residual ratchet rate at the end of each test sequence. Jansson and Leckie (1992) showed that the rate seemed to be governed by a parameter beta given by,

$$\beta = \frac{\Delta\theta}{\Delta\theta^*} + \frac{\Sigma}{\Sigma_L} - 1 \quad (2.1)$$

where $\Delta\theta^* \approx 100^0 C$ and Σ_L is the limit stress value. A plot of the terminal rates against β is shown in Figure (6) with the high rates in the ratchetting (R) region excluded. A reasonable fit to the data is given by,

$$\frac{dE^p}{dN} = 1.79.10^{-7} e^{9.82\left(\frac{\Delta\theta}{\Delta\theta^*} + \frac{\Sigma}{\Sigma_L} - 1\right)} \quad (2.2)$$

In the following section we relate these observed phenomena to predictions base upon classical plasticity.

3. GENERAL RESULTS

Consider an element of composite material of volume V , subject to a constant uniaxial macrostress Σ in a direction orthogonal to the fibre direction. The microstructure consists of a volume V_f , assumed to be linearly elastic, and matrix V_m , assumed to be an elastic plastic solid. A uniform temperature θ fluctuates cyclically between extremes θ_0 and $\theta_0 + \Delta\theta$. The

microstresses will involve a thermo-elastic stress field $\hat{\sigma}_{ij}^\theta$ arising from the differences in thermal expansion between the fibre and the matrix with a maximum value of the Von Mises effective stress of $\bar{\sigma} = \sigma_t$.

3.1 Shakedown

The location of the shakedown boundary for the geometry of the tests was evaluated from a sequence of cyclic finite element calculations for an elastic perfectly plastic material with a Von Mises yield condition and reported in Jansson and Leckie (1991). The shakedown boundary was located as the stress level at which continuous strain growth begins to occur. The boundary is shown in Figure (1) and it can be seen that there are two distinct portions, both of which are near linear. From the upper bound shakedown theorem it can be shown that this is consistent with a constant ratchet mechanism within each region; the proof is given in Appendix A. The equations of the two lines are;

$$\frac{\Sigma_s}{\Sigma_L} = 1 - A \frac{\sigma_t}{\sigma_y} \quad (3.1)$$

and

$$\frac{\sigma_t}{\sigma_y} = 2 \quad (3.2)$$

where $A = 0.29$.

3.2 Ratchetting in Excess of Shakedown for Perfect Plasticity

For $\Sigma \geq \Sigma_s$, Ponter and Cocks (1984) derived a linearised relationship between the ratchet rate and the increment of load above shakedown. In the present context the result relates the increment of plastic macro-strain per cycle dE^p / dN and the excess macro-stress $\Delta\Sigma = \Sigma - \Sigma_s$ in the form

$$\frac{dE^p}{dN} = B \frac{\Delta \Sigma}{E_c} \quad (3.3)$$

where E_c is the elastic modulus of the composite in the direction of Σ . For a proportional temperature history the constant B is bounded from below by (Ponter and Cocks (1984)),

$$B \geq 4 \quad (3.4)$$

There are three important characteristics of this bound;

- 1) The result is independent of the yield stress distribution, and is a function only of the elastic properties.
- 2) As a result of the inequality (3.4), the rates predicted by equation (3.3) are always high. If $\Delta \Sigma / \Sigma_s = 0.1$, the accumulated ratchet strain in 25 cycles is greater than 10 elastic deflections due to Σ_s . This form of ratchetting is referred to as unlimited as it is the highest rate achievable in time independent plasticity. Essentially, in each cycle the strain increases at each temperature change by the release of elastic deformation which occurs when the stress in some part of the matrix volume becomes limited by the yield condition.
- 3) Contours of constant ratchet rate are lines parallel to the shakedown limit; equation (3.3) can be expressed in terms of either an increment of stress or temperature above shakedown.

3.3 Ratchetting Limited by Strain Hardening

In the LR region, when the amplitude of the temperature is increased transient strain growth occurs which reduces to a low value associated with material ratchetting after a number of cycles. In the stabilized state prior to this increase the load point in Figure (1) may be regarded as lying on the shakedown boundary corresponding to the previously acquired state of strain hardening; the renewed cyclic increase in strain occurs because the load point has increased above this boundary but insufficient strain has been accumulated for a new stabilized state to occur. During this transient state the rate of ratchet is given by equation (3.3) where Σ_s

is now interpreted as the current shakedown boundary taking prior strain accumulation into account. An analysis of the transient is given in appendix B where we make the assumption that the pattern of plastic strain in the region LR is given by the pattern that develops during monotonic loading. With this assumption the stabilized growth in strain is given by the equations;

$$E^p = f(\Sigma^*) \quad (3.5)$$

where
$$\Sigma^* = \Sigma - \Sigma_s + \Sigma_L = \Sigma - \Sigma_L A(\sigma_t / \sigma_y) \quad (3.6)$$

and $E^p = f(\Sigma)$ is the equation of the stress strain curve of the composite at constant temperature. A linearized description of the transient, derived in Appendix B, indicates that the number of cycles to the stabilized state is given by;

$$N_{99} \leq k \quad (3.7)$$

where

$$k = \frac{d\Sigma}{dE^p} \frac{1}{E_c} \quad (3.8)$$

4. APPLICATION OF THE SIMPLIFIED THEORY TO EXPERIMENTAL DATA

Figure (4) shows the relationship between Σ^* and E^p for the test points within the LP region. The kinematic assumptions in Appendix B would predict that the stabilized accumulated plastic strain curves would fall on the isothermal stress strain curve and the comparison is satisfactory. In Figure (3) the number of cycles to the stabilized state are compared with the bound (3.7) which underestimates the experimental data. The data is, however, bounded by the upper curve, $N_{99} = 2k$. It seems likely that the presence of material ratchetting delays the achievement of the stabilized state and this accounts for this disparity between the theory and the data.

In Figure (5) the prediction of the rate of unlimited ratchetting is shown where the

commencement of the ratchetting is assumed to occur on each of the two outer boundaries shown in Figure (1). Although the number of data points in this region are limited the general tendency for the rates to increase to these high values is clear. The corresponding range of values of Σ^* where this transient takes place is shown in Figure (4) and corresponds to a range of stress and strain where strain hardening is continuing to take place in the monotonic curve.

5. CONCLUSIONS

The interpretation of the experimental data of Jansson and Leckie (1992) can be understood in two stages.

If we assume that the matrix of the composite conforms to a classical elastic plastic material and we also assume that the microstrain distribution remains relatively unchanged in form, as it cyclically accumulates, we can predict the macro plastic strain accumulation of the composite with reasonable accuracy, provided we ignore the terminal material ratchet rate. The phenomenology of shakedown and ratchetting are reproduced. Limited plastic strain, of the order of elastic strains, occurs in the elastic, shakedown and plastic shakedown regions. In excess of shakedown in the ratchetting region for moderate increases of stress above shakedown, plastic strain accumulates and the rate of ratchet reduces as strains increase. The total accumulation of strain and the number of cycles in this transient are reasonably represented by the prediction of an isotropic strain hardening model although a kinematic model would have given the same answer. For sufficiently large increases of stress above shakedown, ratchetting occurs at a rate which is consistent with perfect plasticity for an increased yield stress. The onset of this high rate occurs, however, when the uniaxial isothermal data still shows significant strain hardening. As these high rates occur at the end of each test there is a distinct possibility that micro damage of the composite could have had a significant effect. The Ponter Cocks ratchet rate, eqn. (3.3) and (3.4), appears to provide a limiting value at high stress.

However such an analysis fails to predict the terminal ratchet rates at the end of transients in the S, PS and LR regions. This is attributable to material ratchetting, the cyclic growth of strain in a stabilised dislocation structure. The phenomenon is observed in other materials. For example, a study of material ratchetting in copper has been given by Megahed Morrison and Ponter (1983,1984) in the context of simple structures. In the tests under discussion here there are two distinct features of note. The strain rates are generally low, of the order of 10^{-6} per cycle or of the

order of 10% of the elastic strain at yield per cycle. This rate is also typical of the values observed in copper by Megahed et al (1983,1984), the reason being that the phenomenon arises from the same process in both materials, the instability of the dislocation structure when subjected to cyclic stress. Contours of constant macro strain rate predicted by equation (2.2) are superimposed upon the shakedown boundary in Figure (7) where it can be seen that the dependance on the thermal stress is more severe for material ratchetting than for shakedown and this feature, again, was observed by Megahed et al.. Whereas in classical plasticity the production of plastic strains depends upon the maximum stress in a cycle it seems clear (see Megahed et al.) that the rate of material ratchetting depends not only on the maximum stress but also the stress variation.

The phenomenon of material ratchetting is not well understood but it can have a dominant effect upon the total strain growth when the number of thermal cycles are sufficiently large. In the type of applications which have been envisaged for composite materials the numbers of cycles would normally be expected to extend to close to the fatigue limit of the material and in such circumstances the geometric stability of the component will be defined by accumulation of material ratchet strain. There is, therefore, an inherent weakness in metal matrix composite materials where thermal cycling occurs. The presents of micro thermo-elastic stresses activate material ratchetting mechanisms which would not occur in a homogeneous material. The rate of material ratchetting depends upon the magnitude of the micro thermo-elastic stresses, which are large in the aluminium /alumina system, and also the matrix material. It also seems likely that it also depends on the alloy structure of the matrix material. Hence the design of geometrically stable metal matrix composites requires the development of an understanding of material ratchetting on the microscale and it's consequences when placed in a a body with thermal gradients. The development of a theory capable of predicting material ratchetting in such circumstances will be the subject of a forthcoming paper.

6. ACKNOWLEDGEMENTS

The final preparation of this paper was carried out during a visit of the first author to the Department of Materials, University of California, Santa Barbara in the Spring of 1997. He would like to acknowledge the support of the department during the visit.

7. REFERENCES

Daehn G. S., Zhang H., Chen Y-C and Wagoner R. H., (1991), "Approaches to Modeling the Plastic Deformation of Metals Matrix Composites under Thermal Cycling Conditions", In: *Modeling the Deformation of Crystalline Solids: Physical Theory, Applications, and Experimental Comparisons*, Ed. Lowe T. c. et al, TMS, New Orleans, Louisiana

Jansson, S and Leckie, F.A., (1992), "Mechanical Behaviour of a Continuous Fibre Reinforced Aluminium Matrix Composite Subjected to Transverse and Thermal Loading", *Jn. Mech. Phys. Solids*, **12**, 593-612

Koiter W. T.,(1960) General Theorems for Elastic-Plastic Solids, *Progress in Solid Mechanics*, Ed. Hill R. and Sneddon I. North Holland Press, 167.

Martin J. B. (1975), Plasticity, MIT Press.

Megahed M., Ponter A.R.S. and Morrison C.J., (1983), "A Theoretical and Experimental Investigation of Material Ratchetting in a Bree Beam Element", *Int. J. Mech. Sci.*, **25**, 917-933.

Megahed M., Ponter A.R.S. and Morrison C.J., (1984), Experimental investigation into the influence of cyclic phenomena of metals on structural ratchetting behaviour, *Int. J. Mech. Sci.*, **26**, pp.625-638.

Ponter A.R.S., "A General Shakedown Theorem for Inelastic Materials", Proc. 3rd International Conference on Structural Mechanics in Reactor Technology, Imperial College, September 1976.

Ponter, A.R.S. and Cocks, A.C.F., (1984), "The Incremental Strain Growth of an Elastic-plastic Body Loaded in Excess of the Shakedown Limit", *Trans ASME, Jn. Appl. Mech.* , **51**,465-469

Ponter, A.R.S. and Karadeniz, S.(1985), "An Extended Shakedown Theory for Structures that Suffer Cyclic Thermal Loading, Part I, Theory", *Trans ASME, Jn. Appl. Mech.*, **52**, 877-882. Part II, Applications: Ibid, 883-889.

Ponter, A.R.S., and Carter, K.F.,(1988) "The Ratchetting Behaviour of Shells Subjected to Severe Thermal Loading", *Applied Solid Mechanics-2*, Ed. Tooth, A.S., and Spence, J., Elsevier Applied Science, London, 303-320.

Ponter, A.R.S., Karadeniz, S., and Carter, K.F.,(1990) " The Computation of Shakedown Limits for Structural Components Subjected to Variable Thermal Loading", Commission of the European Communities Office for Official Publications, Luxembourg, 1990, Report EUR 12686 EN, 178 pages.

Zhang H., Daehn G.S., and Wagoner R. H.,(1990), "The Temperature-Cycling Deformation of Particle Reinforced Metal Matrix Composites - A Finite Element Study", *Scripta Met.*, **24**, 2151-2155.

Zhang H., Daehn G.S., and Wagoner R. H. , (1991), "Simulation of the Plastic Response of Whiskers reinforced Metal Matrix Composites under Thermal Cycling Conditions", *Scripta Met.*, **25**

APPENDIX A

Shakedown Boundaries for Perfect Plasticity

Consider, initially, the problem of the body composed of an elastic-perfectly plastic material with a Von-Mises yield condition within V_m

$$f(\sigma_{ij}) = \bar{\sigma} - \sigma_y \leq 0 \quad (A1)$$

where

$$\bar{\sigma} = \sqrt{\frac{3}{2} \sigma'_{ij} \sigma'_{ij}}$$

and σ'_{ij} denotes the deviatoric stress.

The material element is subjected to constant macro-stress Σ and a uniform thermal temperature history $\theta(\underline{x}, t)$ where

$$\theta(t) - \theta_0 = \Delta\theta h(t), \quad 0 \leq h \leq 1, \quad h(t) = h(t + \Delta t) \quad (A2)$$

Here $\Delta\theta$ is the maximum temperature fluctuation during a cycle.

In the following, we interpret the relationship between micro and macro stresses as those of an homogenized solid, so that

$$\Sigma_{ij} = \frac{1}{V_e} \int_{V_e} \sigma_{ij} dV \quad \text{and} \quad E_{ij} = \frac{1}{V_e} \int_{V_e} \epsilon_{ij} dV$$

and hence the Hill relationship holds;

$$\Sigma_{rs} E_{rs} = \frac{1}{V_m} \int_{V_m} \sigma_{ij} \epsilon_{ij} dV$$

The corresponding micro-thermoelastic stresses $\hat{\sigma}_{ij}^\theta$ are given by

$$\hat{\sigma}_{ij}^\theta = \Delta\theta h(t) \tilde{\sigma}_{ij}(\underline{x}) \quad (\text{A3})$$

and the trajectory of $\hat{\sigma}_{ij}^\theta$ in stress space is a line between

$$\text{and} \quad \left. \begin{aligned} \hat{\sigma}_{ij}^\theta &= 0 & \text{at } t = t_1 \text{ when } h(t_1) &= 0 \\ \hat{\sigma}_{ij}^\theta &= \Delta\theta \tilde{\sigma}_{ij}^\theta & \text{at } t = t_2 \text{ when } h(t_2) &= 1 \end{aligned} \right\} \quad (\text{A4})$$

The maximum effective micro-thermo-elastic stress is denoted by

$$\sigma_t = \max \{ \bar{\sigma}(\hat{\sigma}_{ij}^\theta(\underline{x}, t_1)) \} = \Delta\theta \max \{ \bar{\sigma}(\tilde{\sigma}_{ij}^\theta) \} \quad (\text{A5})$$

Under isothermal conditions the load at which plastic collapse would take place is given by $\Sigma = \Sigma_L$, and we can characterise the behaviour in terms of an interaction diagram with axis Σ / Σ_L and either $\Delta\theta$ or σ_t / σ_0 as shown in Figure (1).

The shakedown limit of the macro-stress Σ_s is the maximum load for which purely elastic behaviour is possible, when a constant residual stress field is superimposed on the elastic stress history. Alternatively it can be defined as the minimum of the following upper bound.

$$\Sigma_s \Delta E^c \leq \frac{1}{V} \int_{V_m} \int_0^{\Delta t} (\sigma - \Delta\theta h(t) \tilde{\sigma}_{ij}) \dot{\epsilon}_{ij}^c dt dV \quad (\text{A6})$$

see, for example, Koiter (1960), Martin (1975), Ponter and Karadeniz (1984). Here $\dot{\epsilon}_{ij}^c$ is a micro-strain rate history which satisfies the condition that

$$\Delta \epsilon_{ij}^c = \int_0^{\Delta t} \dot{\epsilon}_{ij}^c dt \quad (\text{A7})$$

is compatible with a displacement field Δu_i^c which satisfies the periodicity condition of the

homogenised problem and gives rise to macrostrain ΔE^c . The stress state σ_{ij}^c is associated with $\dot{\epsilon}_{ij}^c$ at yield. For the thermal loading history (A4) plastic strains can only occur at time $t = t_1$ and $t = t_2$ when (incompatible) strain components $\Delta \epsilon_{ij}^1$ and $\Delta \epsilon_{ij}^2$ occur, where

$$\Delta \epsilon_{ij}^c = \Delta \epsilon_{ij}^1 + \Delta \epsilon_{ij}^2 \quad (A8)$$

For the case $\Delta \theta = 0$, $\Delta \epsilon_{ij}^c = \Delta \epsilon_{ij}^L$, where $\Delta \epsilon_{ij}^L$ is the mechanism of plastic collapse and $\Sigma = \Sigma_L$, the limit load. For $\Delta \theta \neq 0$ we can now construct the upper bound

$$\Sigma_s \Delta E^P \leq \frac{1}{V} \int_{V_m} (\sigma_{ij}^c - \Delta \theta h(t_0) \tilde{\sigma}_{ij}) \Delta \epsilon_{ij}^L dV \quad (A9)$$

where the time t_0 is chosen so that the upper bound is minimised. This is achieved by choosing

$$t_0 = t_1 \quad \text{if} \quad \tilde{\sigma}_{ij} \Delta \epsilon_{ij}^L < 0$$

or

$$t_0 = t_2 \quad \text{if} \quad \tilde{\sigma}_{ij} \Delta \epsilon_{ij}^L > 0$$

As

$$\Sigma_L \Delta E^P = \int_{V_m} (\sigma_{ij}^c \Delta \epsilon_{ij}^L) dV \quad (A10)$$

the upper bound (A9) can be written as,

$$\frac{\Sigma_s}{\Sigma_L} = 1 - A \frac{\sigma_t}{\sigma_y} \quad (A12)$$

where

$$A = \left\{ \frac{1}{V} \int_{V_m} h(t_0) \frac{\tilde{\sigma}_{ij} \Delta \epsilon_{ij}^L}{\bar{\sigma}(\tilde{\sigma}_{ij})} dV \right\} \frac{\Sigma_L \Delta E^P}{\sigma_y} \quad (A12)$$

Hence for a given $\tilde{\sigma}_{ij}$ and $\Delta \varepsilon_{ij}^L$, A is a constant and the upper bound describes a straight line in the interaction diagram.

A second upper bound on the shakedown limit, corresponding to reverse plasticity at the position of maximum thermal stress fluctuation, is given by the condition

$$\sigma_t \leq 2\sigma_y \quad (A13)$$

This result can be derived from the upper bound (A6) by postulating a mechanism

$$\Delta \varepsilon_{ij}^1 = \tilde{\sigma}_{ij} \lambda, \quad \Delta \varepsilon_{ij}^2 = -\Delta \varepsilon_{ij}^1, \quad \Delta \varepsilon_{ij}^c = 0, \quad \Delta E_{ij}^P = 0 \quad (A14)$$

where λ is an arbitrary constant. The bound is, in fact, the exact solution when $\Sigma = 0$, as the choice of the residual stress field

$$\bar{p}_{ij} = \Delta \theta \tilde{\sigma}_{ij} / 2 \quad (A15)$$

ensures that

$$\bar{\sigma}(\hat{\sigma}_{ij}^\theta + \bar{p}_{ij}) \leq \sigma_y, \quad \text{if} \quad \sigma_t \leq 2\sigma_y \quad (A16)$$

We have now defined two straight lines in the interaction diagram, equality in (A11) and (A13), which are upper bounds but are exact at the two axes. We will adopt these lines as an exact solution with the knowledge that this procedure is usually exactly true or a reasonable approximation in many known solutions. For example, in a survey of shakedown solutions for shells subjected to cyclic thermal loading (Ponter and Carter (1988) and Ponter, Karadeniz and Carter (1990)), this approximation is close to computed solutions in all cases where a PS region exists in the interaction diagram.

APPENDIX B

Ratchetting Limited by Strain Hardening

Shakedown theorems for strain hardening constitutive model have been given by a number of authors and, perhaps the earliest were given by Ponter (1976). When such theories are applied to the LR region of Figure (1) very similar results are obtained for either kinematic or isotropic hardening models as the stress history, for increasing Σ , causes increasing plastic strain at a near constant position on the hardening yield surface. In the following analysis we make a seemingly rather restricting kinematic assumptions but ones which appears to provide answers which are close to observed behaviour. We assume that the pattern of microplastic strain is determined by the value of the macro strain E^p and that contours of constant E^p when transient effects have ceased are parallel to the shakedown boundary. The relationship between Σ and E^p within the region LR is given, therefore, by;

$$E^p = f(\Sigma^*) \quad (\text{B1})$$

where
$$\Sigma^* = \Sigma - \Sigma_s + \Sigma_L = \Sigma - \Sigma_L A(\sigma_i / \sigma_y) \quad (\text{B2})$$

During transient strain growth following an increase in $\Delta\theta$, the material will exhibit unlimited ratchetting strain growth according to the difference between the current macrostress and the stabilized state given by Σ^* according to (3.3), i.e.

$$\frac{dE^p}{dN} = \frac{B}{E_c} (\Sigma - \Sigma^*(E^p)) \quad (\text{B3})$$

For the small increases in temperature in the tests we may make the approximation

$$\frac{d\Sigma^*}{dE^p} = kE_c \quad (\text{B4})$$

where the variation of k with plastic strain can be obtained from the monotonic stress strain curve. Combining (B3) and (B4) we obtain the first order differential equation;

$$\frac{dE^p}{dN} = \frac{B}{k}(E_f^p - E^p) \quad (B5)$$

where E_f^p is the plastic strain in the stabilized state and $E^p = E_0^p$ when $N=0$. The solution of (B5) is given by;

$$\frac{E^p(N)}{E_0^p} = \frac{E_f^p}{E_0^p} + \left(\frac{E_f^p - E_0^p}{E_0^p} \right) \exp\left(-\frac{BN}{k}\right) \quad (B6)$$

where E_0^p and E_f^p are the initial and final plastic strains during the transient strain growth. The characteristic decay cycle number is therefore given by $N = k/B$ and 99% of convergence to the final strain is given by $N \simeq 4k/B$. As $B \geq 4$ then

$$N_{99} \leq k \quad (B7)$$

Figure Captions

- Figure 1 Regions of the interaction diagram associated with distinct modes of behaviour. The load points of the tests of Jansson and Leckie [1] are shown.
- Figure 2 Growth of strain in Tests 1 and 2 of Jansson and Leckie [1] as the load point passes from the shakedown region (S) to the plastic shakedown region (PS).
- Figure 3 The number of cycles to 99 per cent stabilisation compared with the predictions of the linearized theory.
- Figure 4 Variation of normalised stress Σ^* with stabilised plastic strain.
- Figure 5 Variation of ratchet rate with increasing temperature amplitude across the boundary between the limited ratchetting (LR) and ratchetting (R) regions of Figure (1).
- Figure 6. Variation of material ratchet rates with $\beta = \frac{\Delta\theta}{\Delta\theta^s} + \frac{\Sigma}{\Sigma_L} - 1$. The dashed line corresponds to eqn. (2.2).
- Figure 7. Contours of constant material ratchet rate as predicted by eqn. (2.2), superimposed upon the shakedown boundary. Note that material ratchetting has a greater sensitivity to temperature variation than shakedown.

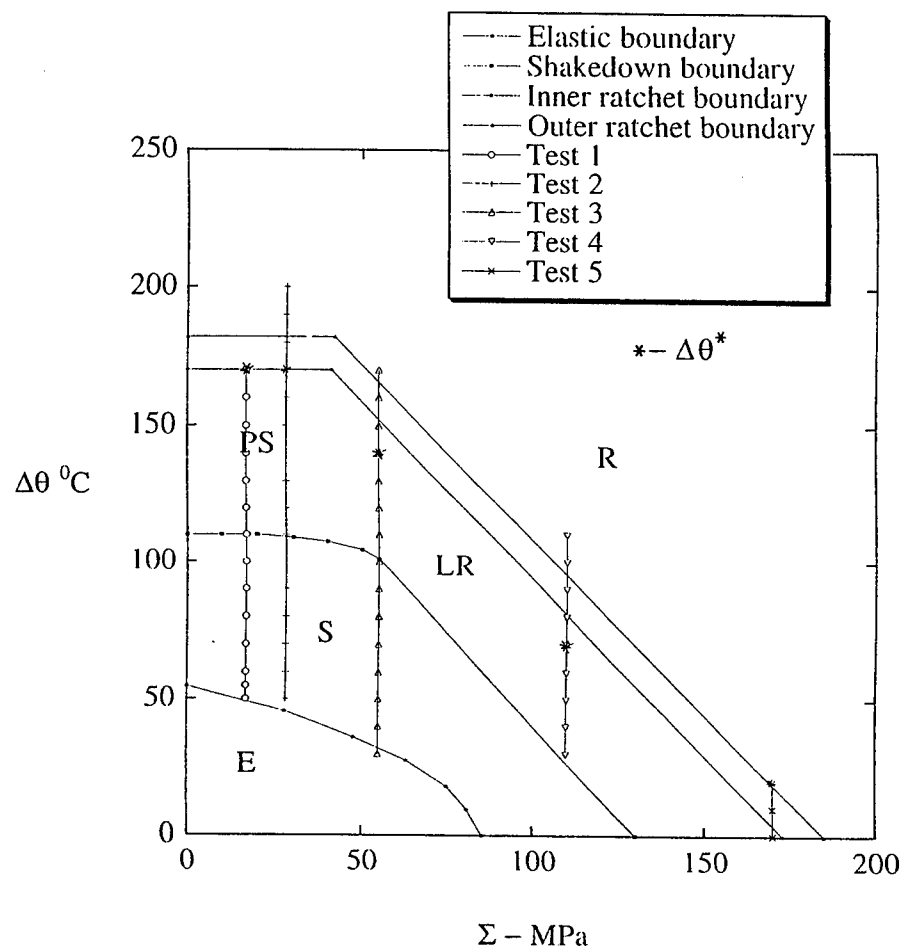


Figure 1 Regions of the interaction diagram associated with distinct modes of behaviour. The load points of the tests of Jansson and Leckie [1] are shown.

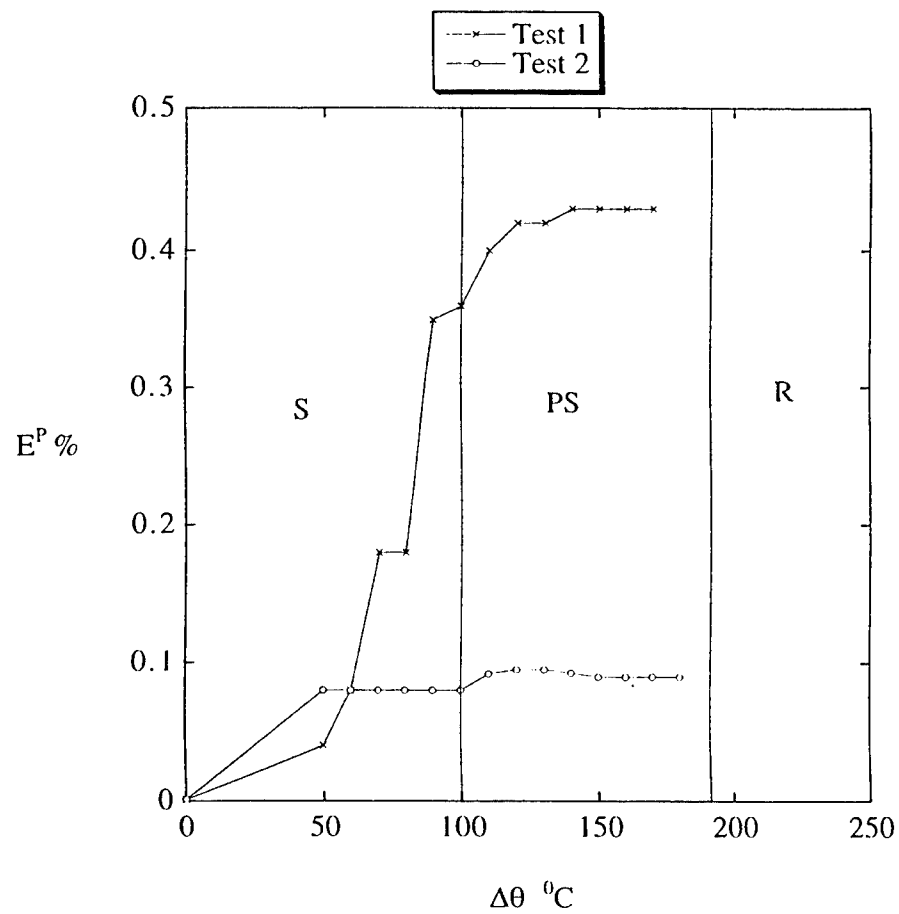


Figure 2 Growth of strain in Tests 1 and 2 of Jansson and Leckie [1] as the load point passes from the shakedown region (S) to the plastic shakedown region (PS).

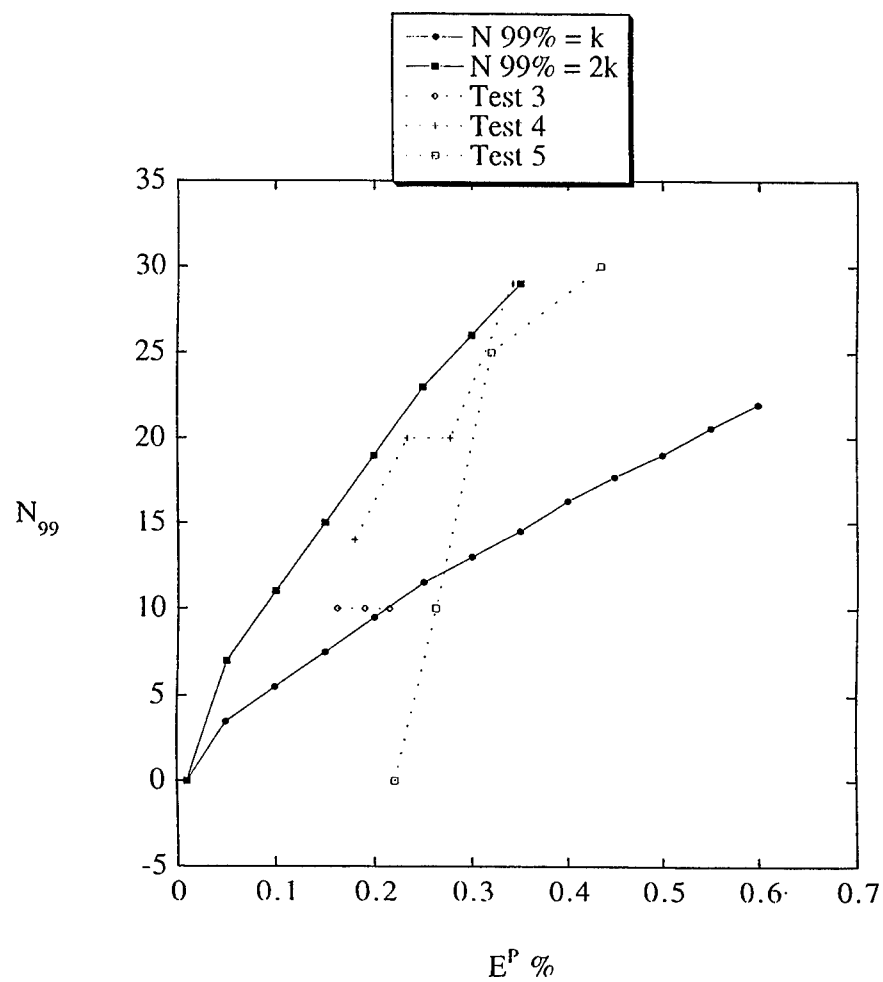


Figure 3 The number of cycles to 99 per cent stabilisation compared with the predictions of the linearized theory.

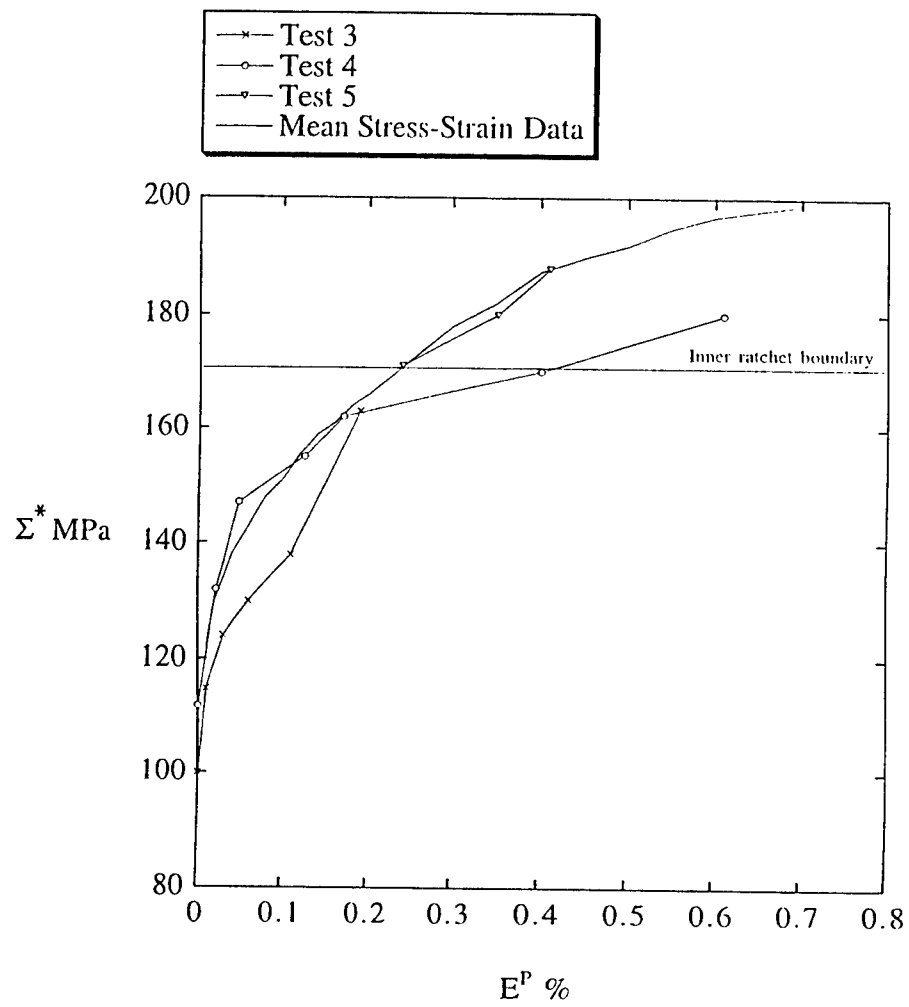


Figure 4 Variation of normalised stress Σ^* with stabilised plastic strain.

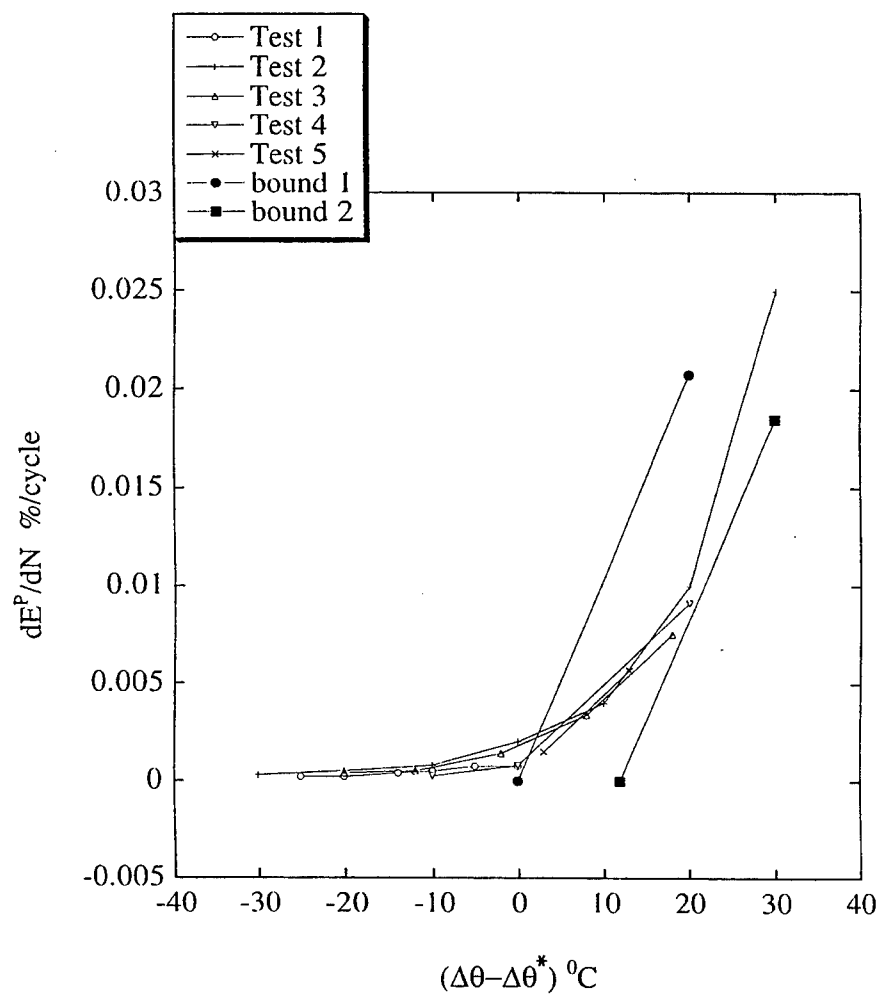


Figure 5 Variation of ratchet rate with increasing temperature amplitude across the boundary between the limited ratchetting (LR) and ratchetting (R) regions of Figure (1).

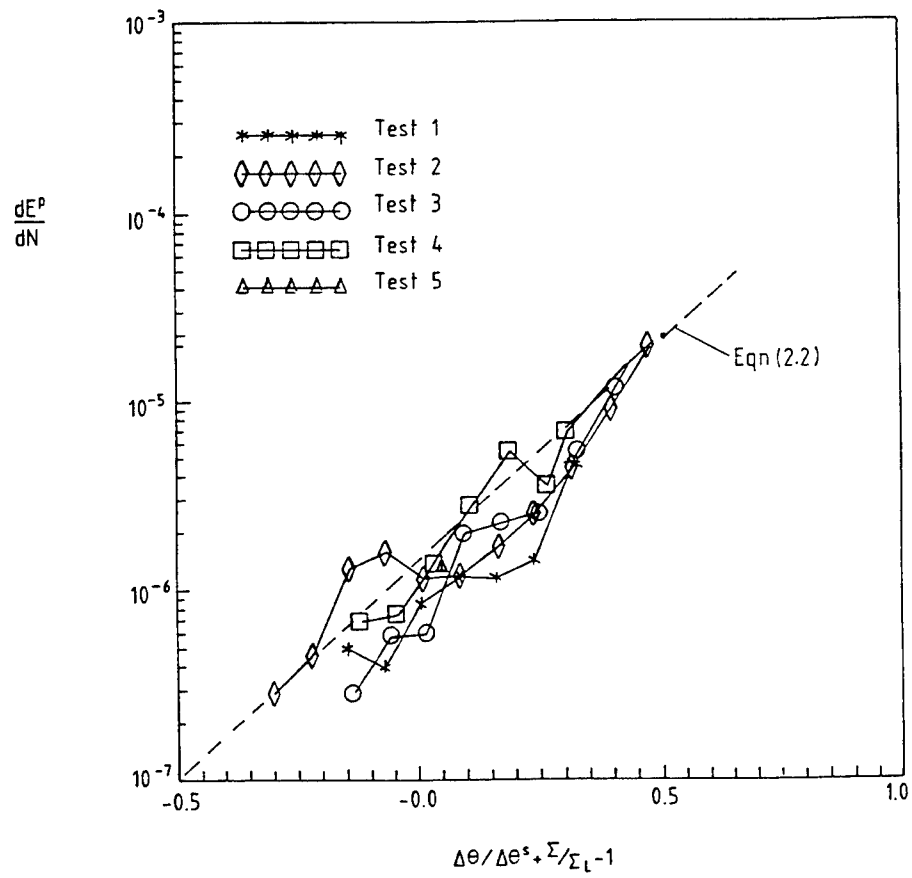


Figure 6. Variation of material ratchet rates with $\beta = \frac{\Delta\theta}{\Delta\theta^s} + \frac{\Sigma}{\Sigma_L} - 1$. The dashed line corresponds to eqn. (2.2).

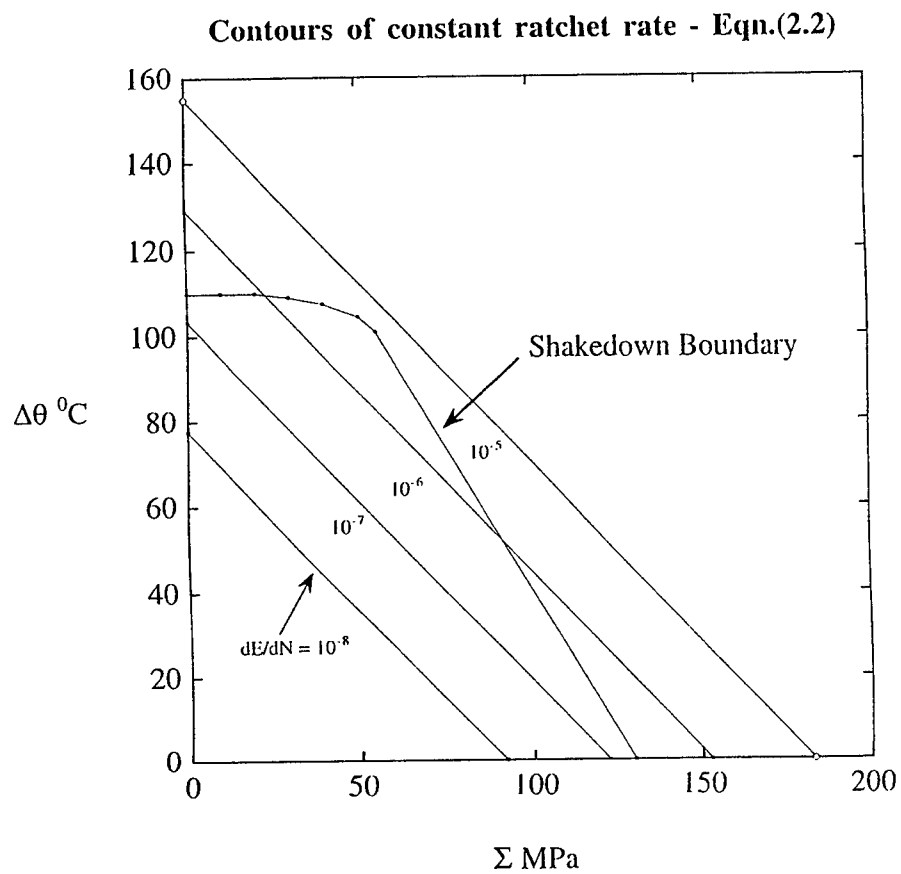


Figure 7. Contours of constant material ratchet rate as predicted by eqn. (2.2), superimposed upon the shakedown boundary. Note that material ratchetting has a greater sensitivity to temperature variation than shakedown.

Submitted to *Composites Tech
and Research*, ASTM
Nov '97

Shakedown Limits for a Metal Matrix Composite

A. R. S. PONTER, K. F. CARTER and J. M. DUGGAN

*Department of Engineering, University of Leicester,
Leicester, LE1-7RH, United Kingdom*

Abstract

The paper discusses a method for the evaluation of the reduction of the yield values of a metal matrix composite material when subjected to a variation in temperature. A direct shakedown analysis method is described which produces a shakedown stress value as a result of a sequence of incompressible linear elastic solutions with a spatially varying elastic modulus. The process converges to the minimum upper bound associated with the class of displacement fields when implemented in a finite element method (Ponter and Carter [7]). The solutions for an Aluminium/alumina system loaded in a direction perpendicular to the direction of the fibres demonstrates the high sensitivity of this material to fluctuations in temperature. Simple approximate equations for strength values are presented in terms of non-dimensional variables.

1 Introduction

In contrast to homogeneous materials, composite materials gain their mechanical properties from the interaction between material elements with markedly differing properties. This allows the development of materials with high strength and stiffness and acceptable fracture properties. However, if the constituent material components have markedly differing coefficients of thermal expansion, micro ther-

moelastic stresses are set up when the temperature fluctuates and this can give rise to a deterioration in the composites strength properties when compared with isothermal properties. The nature of the problem has been demonstrated by Jansson and Leckie [4] for the behaviour of an Aluminium/Alumina fibre reinforced composite when loaded in a direction perpendicular to the direction of the fibres. The combination of mean stress and temperature variation when cyclic strain growth is initiated in material tests was correlated with the shakedown limit evaluated from finite element analyses, with the assumption that the matrix was elastic/perfectly plastic and the fibres remained elastic. Subsequently Cocks et al [3] used shakedown theory to directly compute, approximately, the onset of cyclic strain growth. Estimates of the rate of ratchet in excess of the shakedown limit for thermally loaded bodies has been given by Ponter and Cocks [9,10]. Other studies by Zhang et al [13] have used finite element methods to understand cyclic strain growth.

In recent years there has been a developing interest in the development of computational methods for the direct computation of shakedown limits. Most of such methods tend to use linear and non-linear programming techniques and have been developed for applications to the design of large-scale structure, resulting in computer codes with rather specialist applications. However, recent theoretical studies (Ponter and Carter [7,8]) demonstrate that a method, used for a number of years in industry, may be formulated to provide a monotonically reducing convergent sequence of upper bounds. A sequence of incompressible linear elastic solutions with a spatially varying elastic modulus simulate the stress history which occurs at the shakedown limit. Ponter and Carter [7,8] contain formal proofs that such a method is convergent to the limit load and shakedown limit when the elastic solutions are evaluated exactly and converge to a minimum upper bound when the elastic solutions are evaluated by a Rayleigh-Ritz method such as the finite element method.

In this paper we investigate the application of this method to the shakedown of a fibre reinforced metal matrix composite when stressed in a direction perpendicular to the fibres and subjected to a cycle of temperature with amplitude $\Delta\theta$. For a prescribed $\Delta\theta$ the method evaluates a sequence of mechanisms of ratchetting which provide a monotonically reducing set of upper bounds which converge to the least upper bound to the shakedown limit associated with the class of displacement field defined by the finite element mesh. The method is described in the following section which also includes the extension to plane strain problems not given by Ponter and Carter [8]. This is followed by the evaluation of the shakedown limit for both a square and an hexagonal array of fibres for a range of fibre concentrations for

an aluminium/alumina system. The results, which are discussed in Section (5), demonstrate the high sensitivity of this particular composite to varying temperature. The increase in lateral strength provided by the fibres is lost when quite small temperature variations occur. However, for a square array for high concentrations the strengthening effect of the fibres is significant and the loss due to temperature variation saturates. The composite will then tolerate higher temperature fluctuations, up to 70°C , before its strength reduces to the plane strain strength of the matrix. A simple non-dimensional equation is proposed as a conservative estimate of the loss of strength due to thermal cycling.

2 Shakedown Analysis

In the following we consider the following problem. Consider a body with volume V and surface S which is subjected to loads $P\bar{p}(\underline{x})$ where P is a scalar parameter of the total load, and $\bar{p}(\underline{x})$ is the shape description of a unit load, operating on part of the surface S , namely S_T . A separate part of S , namely S_u , is assumed to suffer displacement rates $\dot{u}_i = 0$, and the remainder of the surface, where zero surface tractions apply, belongs to S_T . The material is assumed to be linear elastic/perfectly plastic with uniaxial yield stress σ_Y and satisfies the Von-Mises yield condition;

$$f(\sigma_{ij}) = \bar{\sigma}(\sigma'_{ij}) - \sigma_Y = 0 \quad (1)$$

where $\bar{\sigma}$ is the Von Mises effective stress expressed in terms of the deviatoric stress σ'_{ij} . Plastic strain rates at yield are given by the associated flow rule, the Prandtl-Reuss equations (Martin [5]),

$$\dot{\epsilon}_{ij}^p = \dot{\lambda} \sigma'_{ij} \quad (2)$$

where $\dot{\lambda}$ is a scalar plastic multiplier.

In addition the body is subjected to a cycle of temperature $\theta(x_i, t)$ with cycle time Δt . We assume the temperature history is proportional so that the thermo-elastic stress history follows a straight line path in stress space and achieves extreme values at two distinct instances t_1 and t_2 at each point of the body. It is possible to develop the method for a much wider class of problems, but the relevant equations are in their simplest form in this case.

The shakedown limit solution for an elastic perfectly plastic body has the following

properties (see, for example Koiter [1], Martin [5] and Ponter and Karadeniz [6]). At a limit state there exists a constant residual stress field \bar{p}_{ij} so that the sum with the elastic solution;

$$\sigma_{ij}^* = P\hat{\sigma}_{ij}^p(x_i) + \hat{\sigma}_{ij}^g(x_i, t) + \bar{p}_{ij}(x_i) \quad (3)$$

satisfies the yield condition everywhere within V . Associated with σ_{ij}^* there exists a history of plastic strain $\hat{\epsilon}_{ij}^p$ which has the following properties:

At each instant when $\dot{\epsilon}_{ij}^p \neq 0$, σ_{ij}^* lies on the yield surface at the point associated with $\hat{\epsilon}_{ij}^p$. The total accumulated plastic strain over the cycle;

$$\int_0^{\Delta t} \dot{\epsilon}_{ij}^p dt = \Delta \epsilon_{ij}^p \quad (4)$$

is compatible with a displacement field Δu_i which is zero on S_u . For the class of problems under discussion two possible local situations can occur, in distinct regions V_0 and V_1 of the body;

In V_0 : All the plastic strain occurs at either t_1 or t_2 so that either;

$$\Delta \epsilon_{ij}^p = \Delta \epsilon_{ij}^1 \quad \text{or} \quad \Delta \epsilon_{ij}^p = \Delta \epsilon_{ij}^2 \quad (5)$$

where $\Delta \epsilon_{ij}^l$ is associated with time t_l .

In V_1 : Plastic strains occur at both t_1 and t_2 and;

$$\Delta \epsilon_{ij}^p = \Delta \epsilon_{ij}^1 + \Delta \epsilon_{ij}^2 \quad (6)$$

In a particular problem any of the three conditions can occur at some point in the volume and, generally at least two of the conditions will occur somewhere. The purpose of the method, therefore, is to simulate this solution, using linear elastic solutions, taking into account that all three conditions can occur and in such a way that both upper and lower bounds can be constructed during an iterative process which converges to the shakedown solution. For the class of shakedown problems under consideration here, we assume that the temperature history is prescribed and we seek the value of the load parameter $P = P_s$ which corresponds to the shakedown limit. The general bounds are given in Ponter and Karadeniz [6] and take the following form;

Lower Bound Shakedown Theorem

For the stress history of the form of eqn.(3), if there exists a \bar{p}_{ij} which satisfies the yield condition throughout the cycle for $P = P_{LB}$, then $P_{LB} \leq P_s$.

Upper Bound Shakedown Theorem

For any history of plastic strain rate $\dot{\epsilon}_{ij}^c$ for which the total accumulated strain $\Delta\epsilon_{ij}^c$, given by;

$$\int_0^{\Delta t} \dot{\epsilon}_{ij}^c dt = \Delta\epsilon_{ij}^c \quad (7)$$

and compatible with a displacement field Δu_i^c which satisfies the boundary condition on S_u , then the value of P_{UB} derived from;

$$P_{UB} \int_{S_T} p_i \Delta u_i^c dS = \int_V \int_0^{\Delta t} (\sigma_{ij}^c - \hat{\sigma}_{ij}) \dot{\epsilon}_{ij}^c dt dV \quad (8)$$

satisfies $P_{UB} \geq P_s$; σ_{ij}^c is the stress at yield associated with $\dot{\epsilon}_{ij}^c$.

3 The Iterative Process for Shakedown Limit Solutions

In essence the method consists of defining a linear material so that the potential energy of the body is matched to the local slope of the functional eqn.(8) at the current strain distribution. The solution of the linear problem produces a minimum of the potential energy and, at the same time, a strain distribution with a reduced upper bound to the shakedown limit.

For the limit state solution, the iterative process involves the evaluation of a sequence of incompressible linear elastic solutions with a spatially varying shear modulus;

$$\epsilon_{ij} = \frac{1}{\mu(x_i)} \sigma_{ij} \quad (9)$$

For the shakedown problem we evaluate a sequence of such solutions but including an initial stress;

$$\epsilon_{ij} = \frac{1}{\mu(x_i)} (\sigma_{ij} + \sigma_{ij}^m) \quad (10)$$

where σ_{ij}^{in} is derived from the thermoelastic solution. The iterative scheme then becomes;

In V_0 :

$$\mu_{k+1} = \mu_k \frac{\sigma_Y}{\bar{\sigma}(\sigma_{ij}^k + \hat{\sigma}_{ij}(t_0))} \quad (11)$$

and

$$\sigma_{ij}^{\text{in}} = \hat{\sigma}_{ij}(t_0) \quad (12)$$

where $t_0 =$ either t_1 or t_2 .

In V_1 :

$$\mu_{k+1}^1 = \mu_k^1 \frac{\sigma_Y}{\bar{\sigma}(\sigma_{ij}^k + \hat{\sigma}_{ij}(t_1))} \quad (13)$$

$$\mu_{k+1}^2 = \mu_k^2 \frac{\sigma_Y}{\bar{\sigma}(\sigma_{ij}^k + \hat{\sigma}_{ij}(t_2))} \quad (14)$$

$$\frac{1}{\mu_{k+1}} = \frac{1}{\mu_{k+1}^1} + \frac{1}{\mu_{k+1}^2} \quad (15)$$

and

$$\sigma_{ij}^{\text{in}} = \beta \hat{\sigma}_{ij}(t_1) + (1 - \beta) \hat{\sigma}_{ij}(t_2) \quad (16)$$

where

$$\beta = \frac{\mu_k}{\mu_k^1} \quad \text{and} \quad (1 - \beta) = \frac{\mu_k}{\mu_k^2} \quad (17)$$

In Ponter and Carter [8] we prove that the upper bound evaluated from the substitution of the strain fields generated by the sequence of solutions defined by eqn.(10) to eqn.(17) into eqn.(8) produces a sequence of reducing upper bounds which converge to either the shakedown limit, when the elastic solutions are evaluated exactly, or the the least upper bound when a finite element method is used, provided $P^{k+1} = P_{UB}^k$. The proof assumes that the volumes V_0 and V_1 are fixed during this process. In the application of the method it is necessary to use a consistency condition for assigning a material point to either V_0 or V_1 and this is discussed in Ponter and Carter [8]. Initially we assume all point lie within V_0 and then reassign points to V_1 once an initial solution has been evaluated. In practice we find that the material points remain within either V_0 or V_1 after the first few iterations .

4 Plane Strain Shakedown Solutions

For plane strain solutions we need to take into account the kinematic constraint

$$\Delta \varepsilon_{zz} = \Delta \varepsilon_{zz}^1 + \Delta \varepsilon_{zz}^2 = 0 \quad (18)$$

As plane strain finite element solutions are evaluated through the relationship between the in-plane stresses and strains, the relationships eqn. (10) to eqn. (17) must be expressed entirely in terms of such quantities. For simplicity we define a new variable;

$$s_{ij} = \sigma_{ij} - \sigma_{ij}^m \quad (19)$$

The kinematic constraint eqn.(18) in V_1 implies;

$$s_{zz} = s_{xx} + s_{yy} \quad (20)$$

Substituting eqns. (20), (19) and (15) to (17) into (10) leads to the explicit plane strain equations;

$$\varepsilon_{xx} = \frac{1}{2\mu_k} (\sigma_{xx} - \sigma_{yy}) + \frac{1}{2\mu_k^1} [\hat{\sigma}_{xx}(t_1) - \hat{\sigma}_{yy}(t_1)] + \frac{1}{2\mu_k^2} [\hat{\sigma}_{xx}(t_2) - \hat{\sigma}_{yy}(t_2)] \quad (21)$$

$$\varepsilon_{yy} = \frac{1}{2\mu_k} (\sigma_{yy} - \sigma_{xx}) + \frac{1}{2\mu_k^1} [\hat{\sigma}_{yy}(t_1) - \hat{\sigma}_{xx}(t_1)] + \frac{1}{2\mu_k^2} [\hat{\sigma}_{yy}(t_2) - \hat{\sigma}_{xx}(t_2)] \quad (22)$$

$$\varepsilon_{xy} = \frac{1}{2\mu_k} \sigma_{xy} + \frac{1}{2\mu_k^1} [\hat{\sigma}_{xy}(t_1)] + \frac{1}{2\mu_k^2} [\hat{\sigma}_{xy}(t_2)] \quad (23)$$

$$\varepsilon_{zz} = 0 \quad (24)$$

and the Von Mises effective stress becomes;

$$\bar{\sigma} (\sigma_{ij} + \sigma_{ij}^m) = \sqrt{\frac{3}{2} (s_{xx}'^2 + s_{yy}'^2 + s_{zz}'^2 + 2s_{xy}'^2)} \quad (25)$$

For the volume V_0 the relevant equations are obtained by removing the terms which relate to either time t_1 or t_2 .

5 Shakedown Limits for a Metal Matrix Composite

The relationship between the observed behaviour of metal matrix composites and the shakedown limit has been discussed by Jansson and Leckie [4] for the case when stress is applied in a direction perpendicular to the direction of the fibres. Assuming an elastic perfectly plastic matrix and elastic fibres they carried out a sequence of step by step finite element analysis of a material element with the usual homogenization boundary condition. The shakedown boundary was then located as the level of loading at which a steady growth in strain began to occur. The boundary, so defined, corresponded well to the level of loading at which inelastic strain growth became significant in experimental study of an Alumina/Aluminium system.

The shakedown boundary, as defined by shakedown theory, locates this boundary exactly. Using the method described in the previous section a survey of the shakedown boundaries for the same system as studied by Jansson and Leckie [4] has been carried out for a range of fibre concentrations. The procedure was as follows. For a particular fibre concentration the thermo-elastic stress were evaluated for an arbitrarily chosen temperature amplitude ($\Delta\theta = 50^\circ\text{C}$). A sequence of shakedown limits for the applied stress were then evaluated for a sequence of scaled distributions of thermoelastic stresses corresponding to a range of temperature amplitude. The elastic and plastic properties of the matrix and fibres were the same as in the study by Leckie et al and are given in Table 1. The material constants were all assumed to be constant with temperature.

Both hexagonal and a square array of fibres were studied and typical FE meshes, of eight noded rectangular elements, are shown in Figure (1). The implementation of the method is that described by Ponter and Carter [7] in the finite element code BERSAFE. The direction of the application of macro stress for a square array is in the direction where the yield value is at a maximum. For an hexagonal array the composite is near isotropy for rotations about the fibre direction.

The variation of the applied macro stress $\bar{\sigma}_m$ with fibre volume ratio V_f for isothermal conditions is shown in Figure (2). The results are very similar to those given by Du, McMecking and Schmauder [11]. For an hexagonal array there is a near linear increase in yield value. For a square array the yield value increases rapidly when the volume fraction exceeds about 35 percent.

A typical convergence sequence for the iterative method is shown in Figure(3) where it can be seen that a converged value is obtained in less than ten cycles. The number of cycles to produce a converged solutions was similar for both the limit stress and shakedown solutions. Some fluctuation in the lower bound may be observed and this is due to numerical error. The values shown in this paper are all upper bound values.

The variation of the shakedown limit with both the fibre volume ration and the temperature fluctuation are shown in Figure (4) and Figure (5). The same results are replotted in Figure (6) and Figure(7) using nondimensional variable which display the results in the typical Bree diagram form (see Bree [2]).

In Figure (4) and (5) the value of the plane strain yield value of the matrix is shown as a horizontal dotted line. Hence points above this line indicate a net strengthening of the composite due to the presence of the fibres and points below indicate a net weakening, resulting from the increase in strength for $\Delta\theta = 0$ and the reduction in strength due to the fluctuating thermo-elastic stresses. It can be seen that for an hexagonal array the two effects cancel each other for a temperature difference of about $\Delta\theta_c = 30^\circ C$ over the entire range of fibre volume fractions V_f . A similar tendency is shown for square array for V_f less than 30 percent. For the higher values of V_f the increase in strength for $\Delta\theta = 0$ means that the composite will tolerate a much higher temperature fluctuation before it's strength is reduced to the matrix plane strain value. For both of the fibre volumes shown this increased temperature variation is near to $70^\circ C$. Overall the results shown the sensitivity of this particular system to variation in temperature.

In Figure (6) and (7) the variation of normalised strength $\bar{\sigma}_m/\sigma_0$ with variation in the normalised maximum effective thermoclastic stress $\hat{\sigma}_{max}^{\Delta\theta}/\sigma_0$ shows a relatively simple near linear form. For higher levels of V_f the square array shows a saturation effect where near identical results are obtained for V_f in excess of 0.3, the value at which the isothermal yield value increases rapidly. This combination of effects explains the difference between the values of $\Delta\theta_c$ for a square and an hexagonal array.

To a first approximation the results in Figure (6) and (7) may be represented by the equation;

$$\frac{\bar{\sigma}_m}{\sigma_0} + A(V_f) \frac{\hat{\sigma}_{max}^{\Delta\theta}}{\sigma_0} = 1 \quad (26)$$

The variation of the parameter $A(V_f)$ with V_f is shown in Figure (8) for both arrangements of fibres. For the square array a saturation value of $A = 0.266$ may be observed. The values for the hexagonal array are slightly lower. A conservative estimate of A is given by;

$$A = 0.0316 + 0.782V_f \quad \text{for} \quad V_f \leq 0.30 \quad (27)$$

$$A = 0.266 \quad \text{for} \quad V_f \geq 0.30 \quad (28)$$

6 Conclusions

The results discussed above demonstrate that direct shakedown analysis solutions are capable of giving insight into the variation of strength properties of metal matrix composites. The method discussed in Section (3) is reliable, rapidly convergent and may be implemented in a standard finite element code.

The set of results presented in Section (5) for an Aluminium/Alumina system demonstrates the high sensitivity of the strength properties of this material perpendicular to the fibre direction to variation in temperature. The presence of fluctuating micro thermal stresses results in a reduction in the yield strength which is greater than the strengthening effects of the fibres for quite moderate amplitudes of temperature variation, of less than 30°C for both a square and hexagonal arrays. However for higher fibre volumes, in excess of 30 percent, for a square array this effect begins to saturate and a larger temperature variation, near to 80°C , is required before the strength properties has reduced to the plane strain yield strength of the matrix. Approximate analytic expressions for these variations have been given for practical application.

The application of this direct shakedown limit method demonstrates that important characteristic of the behaviour of composite materials can be evaluated in this way. All the solutions in this paper were generated from the solution of about 600 linear solutions. At this level of computational effort it is possible to carry out parametric surveys of material characteristics as a guide to material scientists. This paper provides a preliminary demonstration of this potential.

7 Acknowledgements

The development of the computational techniques described in this paper was supported by the Science and Engineering Research Council of the UK (now the Engineering and Physical Sciences Research Council) and Nuclear Electric Ltd which is gratefully acknowledged. The final preparation of the paper was completed while visiting the Department of Materials at the University of California , Santa Barbara in 1997. The authors would like to thank Bob McMeeking and Fred Leckie for assistance during this period.

8 References

1. Koiter, T. (1960), *Progress in Solid Mechanics*, Ed. Sneddon, I.N. and Hill, R., North Holland Press, Amsterdam, 167-221
2. Bree, J. J., (1967) *J. Strain Analysis*, **2**, 226-238
3. Cocks, A.C.F., Jansson, S. and Leckie, F. A. (1992), *J. Thermal Stresses*, **15**, 175-184
4. Jansson, S. and Leckie, F.A.(1992) *J.Mech, Phys. Solids*, **40**, 593-612
5. Martin, J.B. (1975), "Plasticity", MIT Press.
6. Ponter, A.R.S., Karadeniz, J. (1985) *J. Applied Mech*, **52**, Part I, 877-882 Part II 883-889
7. Ponter, A. R. S. and Carter K. F.(1997a), Limit state solutions, based upon linear elastic solutions with a spatially varying elastic modulus, *Comput. Methods Appl. Mech. Engrg.*, **140**, 237-258.
8. Ponter, A. R. S. and Carter K. F.(1997b), Shakedown state simulation techniques, based upon linear elastic solutions, *Comput. Methods Appl. Mech. Engrg.*, **140**, 259-279.
9. Ponter, A.R.S., Cocks, A.C.F. (1984) *J. Applied Mech*, **51**, 465-469
10. Ponter, A.R.S., Cocks, A.C.F. (1984) *J. Applied Mech*, **51**, 470-474
11. Du, Z.-Z., McMecking R.M., and Schmauder, S. (1995), *Mechanics of Materials*, **21**, 159-167.
12. Zahl, D. B., Schmauder S., and McMecking, (1994), *Acta Metall. Mater.*, **42**, 2983 .
13. Zhang H., Daehn S.S , and Wagoner, (1990), *Scripta Met.*, **24**, 2151-2155

Table 1 Material Constants used in the Finite Element Calculations.

	Al	Al_2O_3
Young's Modulus (E)	70GPa	370GPa
Thermal expansion coeff (α)	22MK ⁻¹	8MK ⁻¹
(E α)	1540	2960
Yield stress (σ_y)	80MPa	2000MPa
Density (ρ)	2.7Mgm ⁻³	4.0Mgm ⁻³
Poissons ratio (ν)	0.3	0.3

Figure Captions

Figure 1 Typical finite element mesh for symmetric region of unit cell of square and hexagonal arrangement of fibres.

Figure 2 Variation of isothermal yield stress $\bar{\sigma}_m$ with fibre volume fraction V_f for both the hexagonal and square arrangement of fibres.

Figure 3 A typical convergence sequence for the iterative method. Convergence was normally obtained in about 10 cycles (i.e. ten linear elastic solutions). $V_f = 44.58\text{percent}$, $\Delta\theta = 80^\circ\text{C}$.

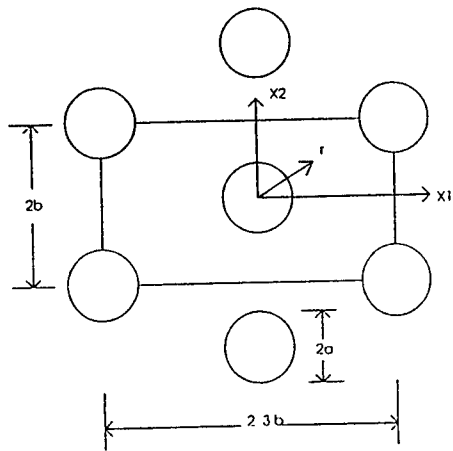
Figure 4 Variation of shakedown limit $\bar{\sigma}_m^s$ with amplitude of temperature variation $\Delta\theta$ for a range of values of fibre volume ratio V_f for a square array of fibres.

Figure 5 Variation of shakedown limit $\bar{\sigma}_m^s$ with amplitude of temperature variation $\Delta\theta$ for a range of values of fibre volume ratio V_f for an hexagonal array of fibres.

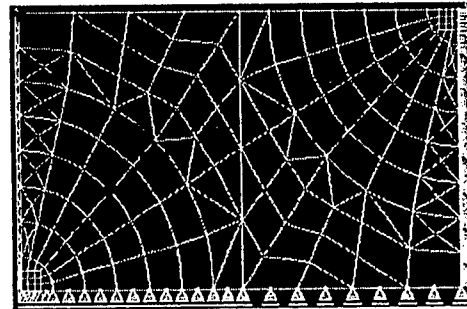
Figure 6 Variation of the normalised shakedown limit $\bar{\sigma}_m^s/\sigma_0$ with normalised maximum thermoelastic stress for a range of values of fibre volume ratio V_f for a square array of fibres.

Figure 7 Variation of the normalised shakedown limit $\bar{\sigma}_m^s/\sigma_0$ with normalised maximum thermoelastic stress for a range of values of fibre volume ratio V_f for an hexagonal array of fibres.

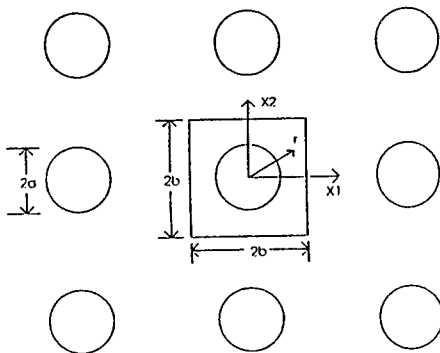
Figure 8 Variation of the thermal stress sensitivity parameter A in eqn.(26) with fibre volume ratio V_f for both a square an hexagonal array of fibres. Eqns. (27) and (28) are shown as dotted lines.



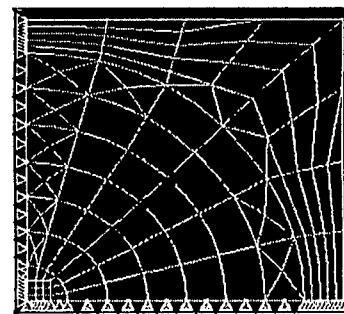
THE HEXAGONAL ARRAY



THE HEXAGONAL UNIT CELL MESH



THE SQUARE ARRAY



THE SQUARE UNIT CELL MESH

Figure 1 Typical finite element mesh for symmetric region of unit cell of square and hexagonal arrangement of fibres.

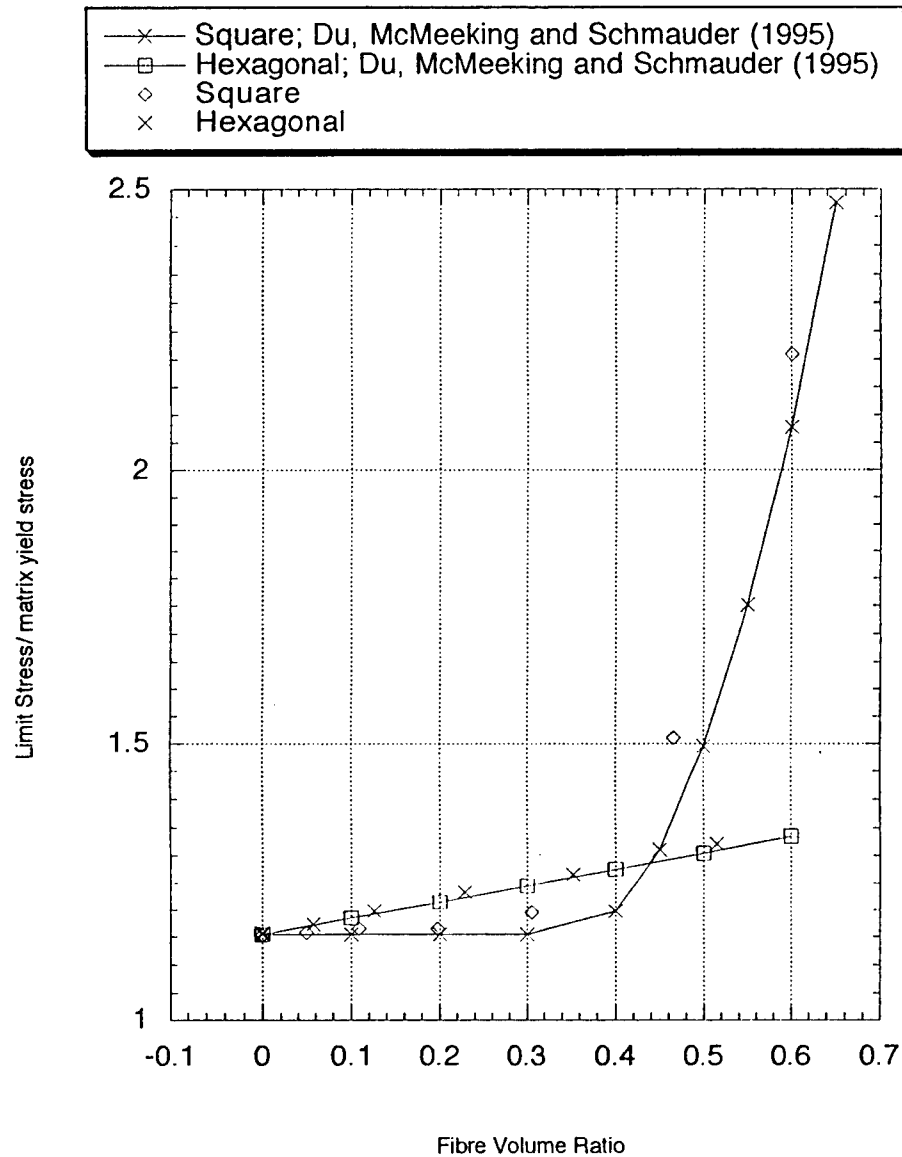


Figure 2 Variation of isothermal yield stress $\bar{\sigma}_m$ with fibre volume fraction V_f for both the hexagonal and square arrangement of fibres.

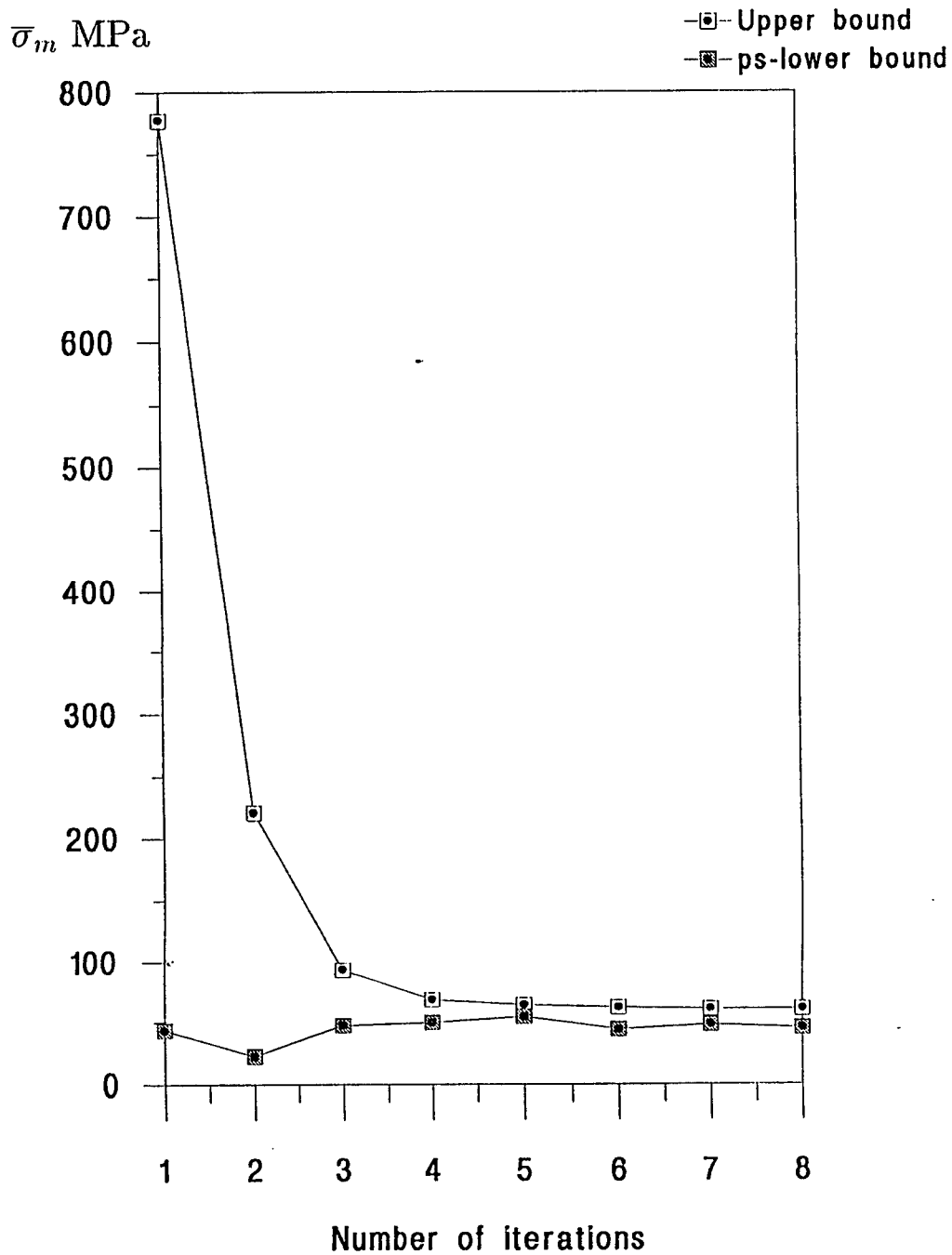


Figure 3 A typical convergence sequence for the iterative method. Convergence was normally obtained in about 10 cycles (i.e. ten linear elastic solutions). $V_f = 44.58\text{percent}$, $\Delta\theta = 80^\circ\text{C}$.

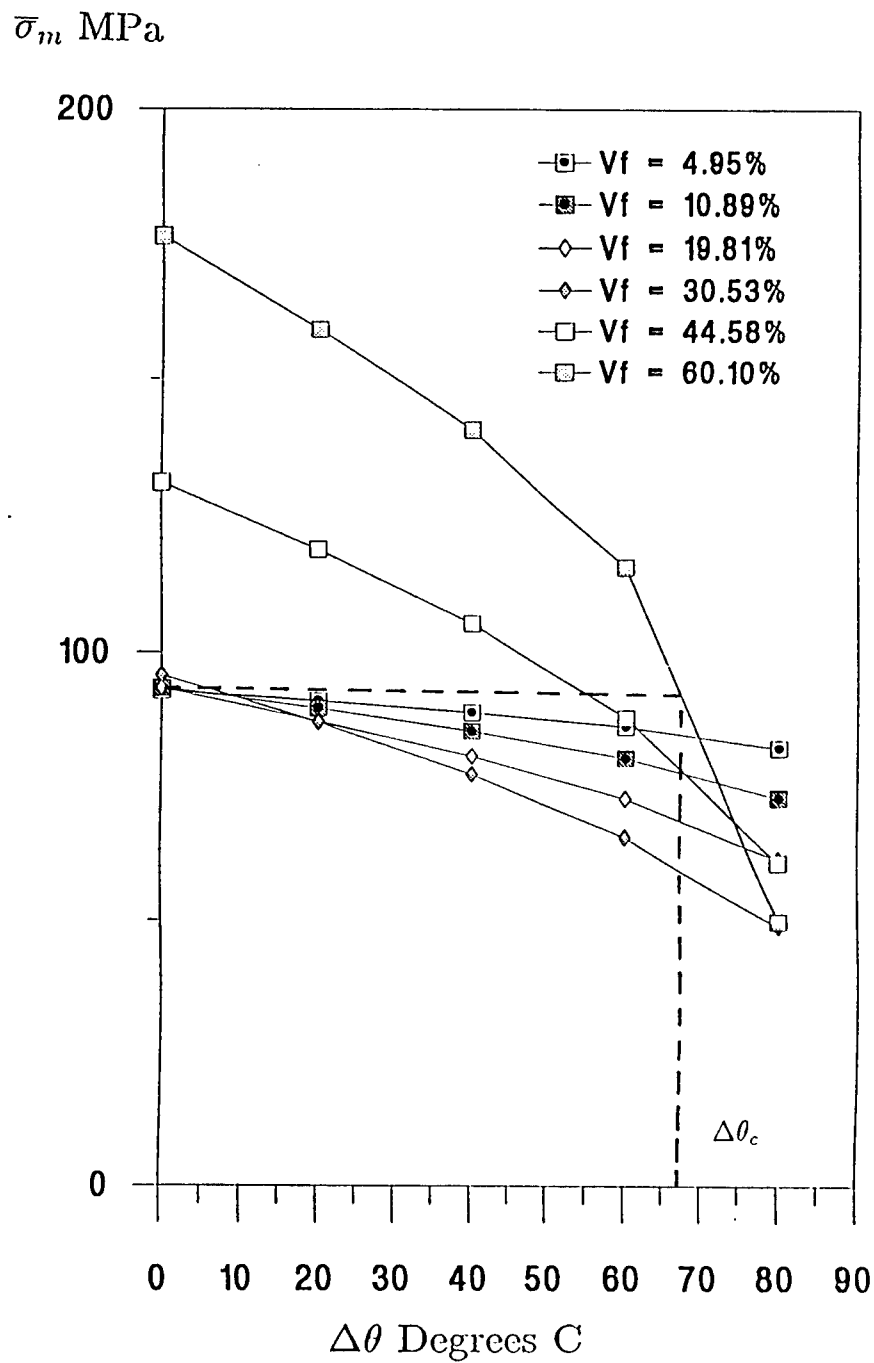


Figure 4 Variation of shakedown limit $\bar{\sigma}_m^s$ with amplitude of temperature variation $\Delta\theta$ for a range of values of fibre volume ratio V_f for a square array of fibres.

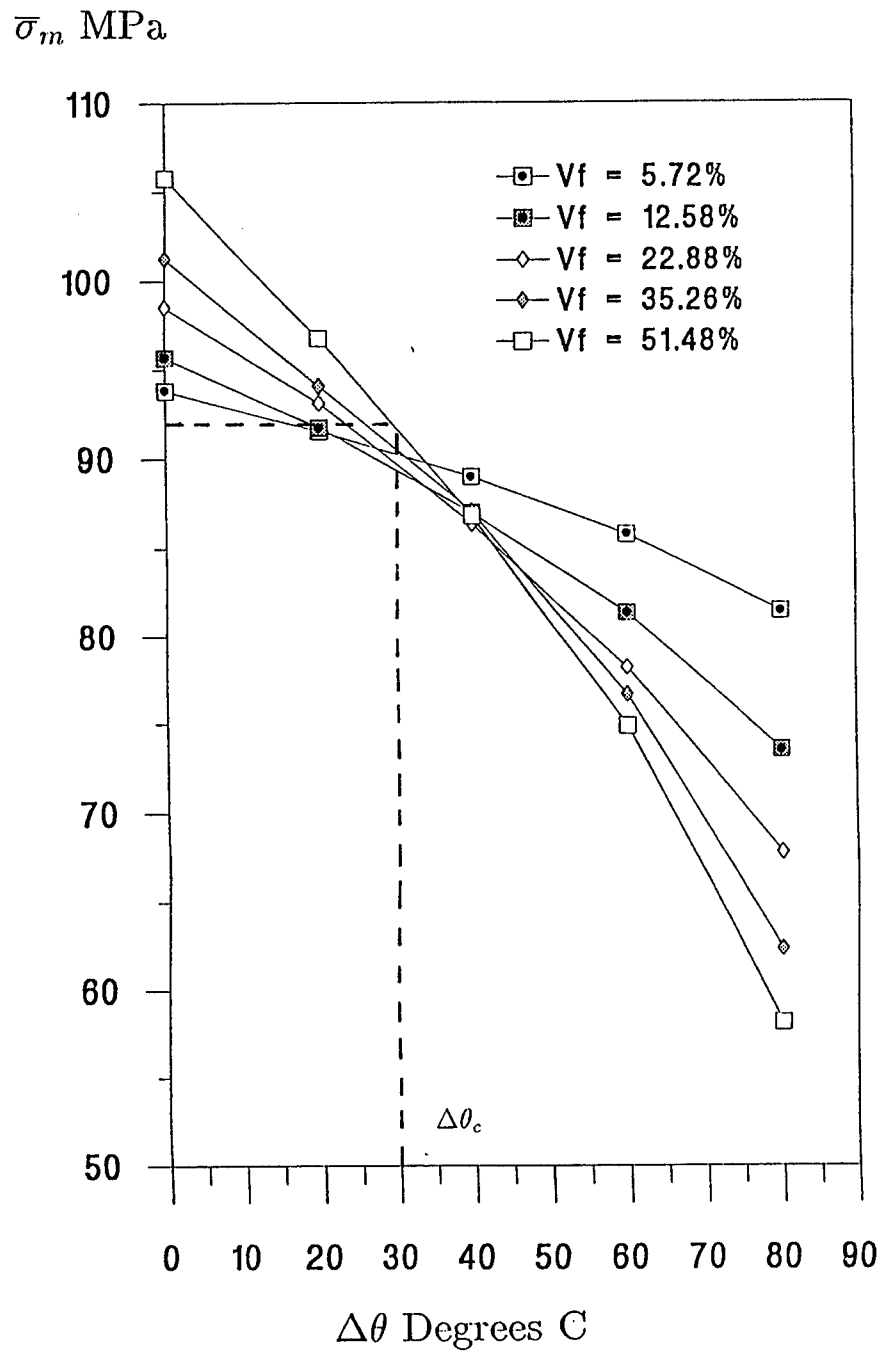


Figure 5 Variation of shakedown limit $\bar{\sigma}_m$ with amplitude of temperature variation $\Delta\theta$ for a range of values of fibre volume ratio V_f for an hexagonal array of fibres.

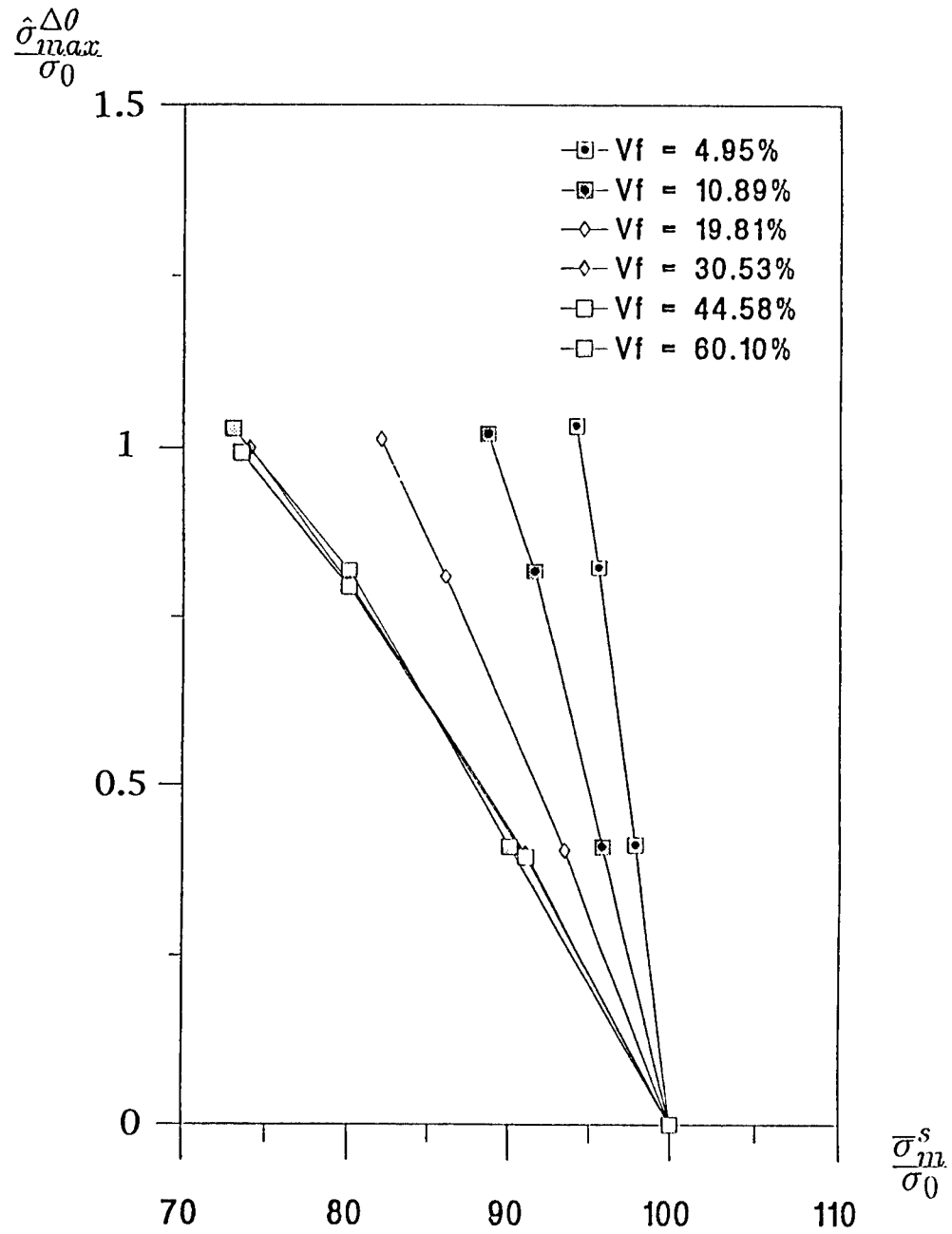


Figure 6 Variation of the normalised shakedown limit $\bar{\sigma}_m^s/\sigma_0$ with normalised maximum thermoelastic stress for a range of values of fibre volume ratio V_f for a square array of fibres.

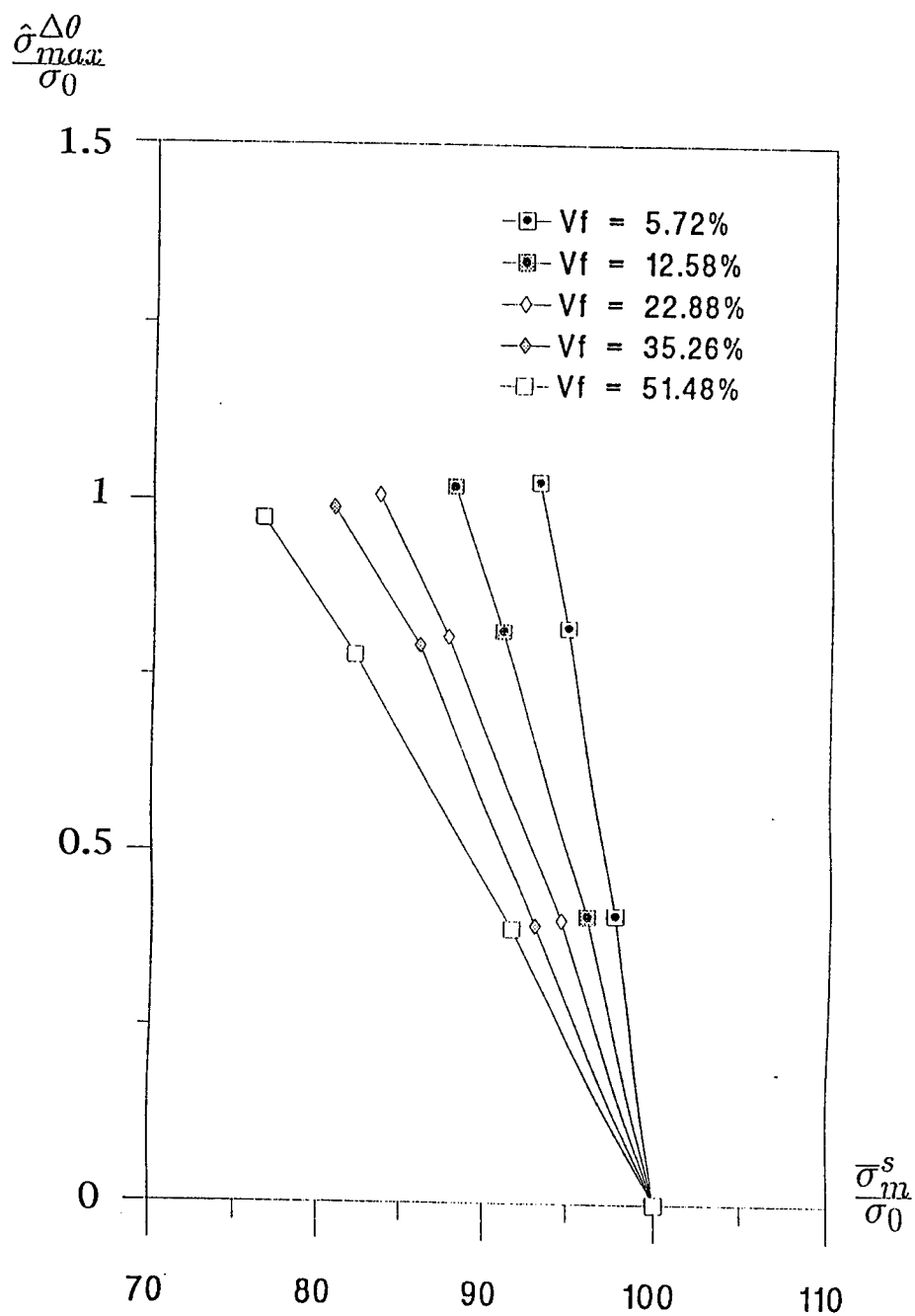


Figure 7 Variation of the normalised shakedown limit $\bar{\sigma}_m^s / \sigma_0$ with normalised maximum thermoelastic stress for a range of values of fibre volume ratio V_f for an hexagonal array of fibres.

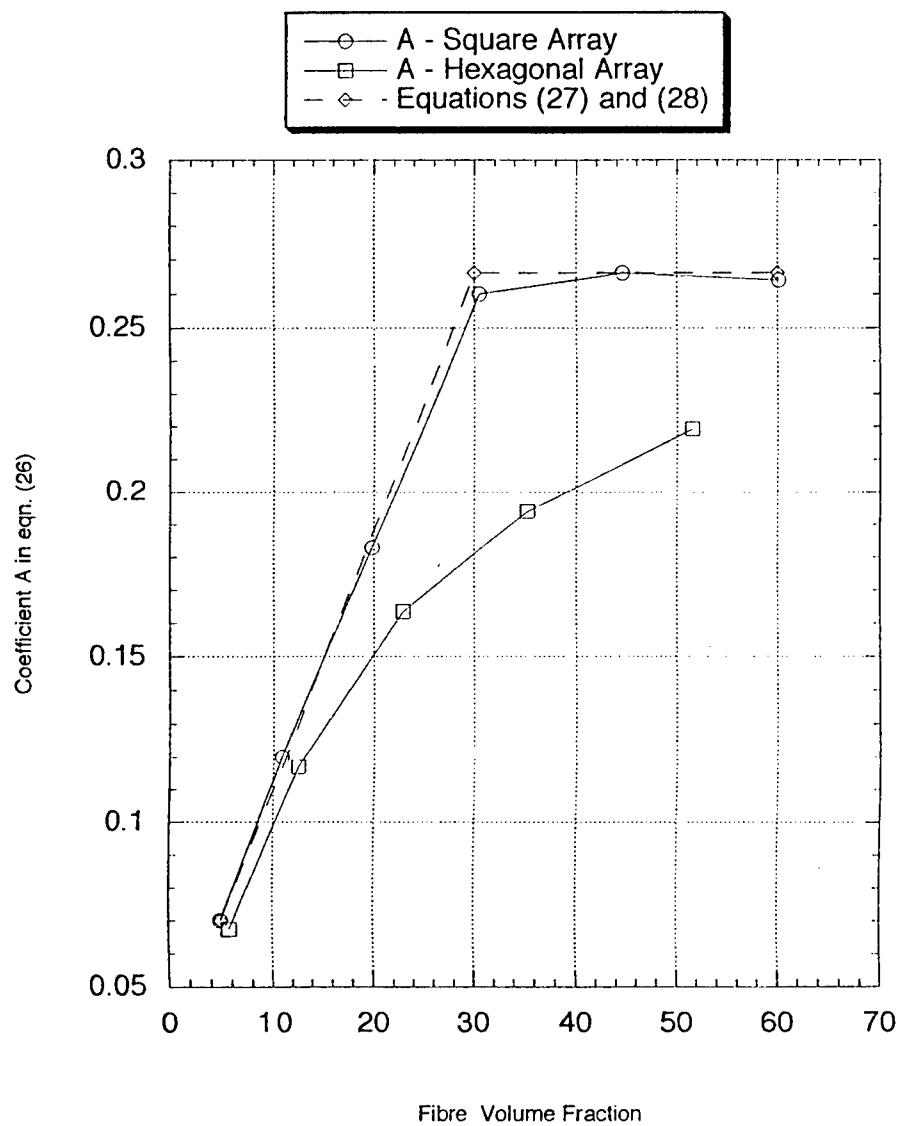


Figure 8 Variation of the thermal stress sensitivity parameter A in eqn.(26) with fibre volume ratio V_f for both a square an hexagonal array of fibres. Eqs. (27) and (28) are shown as dotted lines.

Effects of cladding on the tensile properties of titanium matrix composites

U. Ramamurty^a, F.W. Zok^a, F.A. Leckie^b

^a*Materials Department, University of California, Santa Barbara, CA 93106, USA*

^b*Mechanical and Environmental Engineering Department, University of California, Santa Barbara, CA 93106, USA*

Received 8 December 1995; revised 22 February 1996

Abstract

The effects of monolithic titanium cladding on the tensile properties of fiber-reinforced titanium matrix composites (TMCs) have been studied. The work is motivated by the realization that most TMC components currently under development will be clad with monolithic titanium alloys in order to prevent damage to the fibers during component manufacture and in service. The focus has been on the elastic modulus, the yield strength, and the failure stress and strain. Experiments have been conducted on panels with two different clad thicknesses as well as a panel without cladding. The experimental results have been compared with predictions of models based on an effective (average) fiber volume fraction. The correlations between the experiments and the model predictions indicate that these properties are insensitive to the spatial distribution of fibers.

Keywords: Cladding; Titanium; Tensile behaviour

1. Introduction

Fiber-reinforced titanium matrix composites (TMCs) are under development for use in a number of components in the next generation of aircraft engines, including actuator piston rods, fan blades and fan frames. The main motivations for these efforts are the high specific stiffness and strength of unidirectionally reinforced TMCs in the longitudinal direction. In these applications, it is envisaged that the TMC will be used to selectively reinforce the structure; the regions of the structure which are to be attached to other components will be manufactured from monolithic Ti alloys [1]. Moreover, the reinforced sections will be clad with monolithic Ti alloys in order to prevent damage of the fibers during component manufacture and in service. The concepts are driven partly by the high cost of the TMCs as well as considerations associated with the manufacturability and the performance of all TMC components.

An example of a preliminary design of a hollow Ti/SiC actuator piston rod that utilizes Ti cladding is shown in Fig. 1. In this design, the inner and outer walls of the TMC are clad with ~ 1 and 0.5 mm, respectively, of the Ti-alloy matrix. Since the fibers cannot be aligned perfectly over the entire length of the

rod, the excess Ti will allow machining of the inner and outer diameters with adequate tolerances to prevent contact between the cutting tool and the fibers. Similar thicknesses of cladding are also expected to be used on fiber-reinforced fan blades.

The objective of the present study was to assess the effects of cladding on the tensile mechanical properties of TMCs. For this purpose, experiments have been conducted on composite panels with two different clad thicknesses, as well as a panel without cladding. The experimental results have been compared with models for stiffness, strength and ductility. The effect of notches and holes on the tensile strength and fatigue resistance are presented elsewhere [2]. Background on the mechanical properties of unclad unidirectional TMCs, including fatigue, creep and tensile fracture, can be found in Refs. [3–12].

2. Experimental procedures

2.1. Materials

The materials used in this study were comprised of a Ti–6Al–4V alloy matrix reinforced with 6 plies of SCS-6 SiC fibers (produced by Textron Specialty Mate-

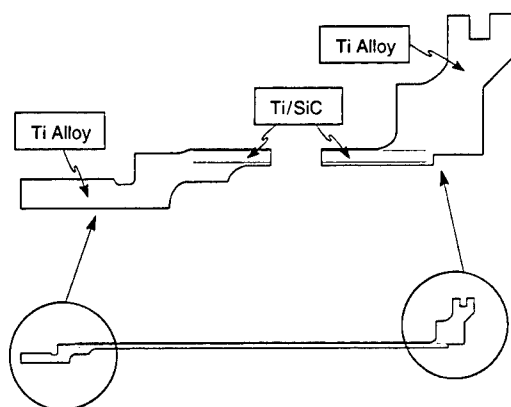


Fig. 1. Preliminary design of a hollow nozzle actuator piston rod utilizing Ti/SiC composites (courtesy D.P. Walls and R. Tucker, United Technologies, Pratt & Whitney).

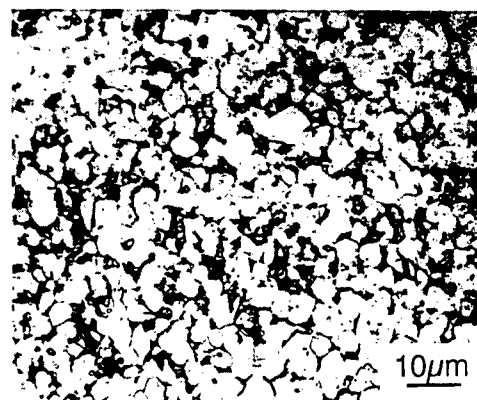


Fig. 3. Optical micrograph of the matrix microstructure (etched with Knoll's reagent).

rials). Monotapes were fabricated by induction plasma spraying of the Ti alloy onto fiber mats. Six plies of the monotapes were subsequently laid-up between monolithic foils of the Ti alloy and consolidated by hot-isostatic pressing. The thickness, $2t_o$, of the central region of the panels (comprising the 6 ply TMC) was ~ 1.3 mm. The fiber volume fraction within this region was $\sim 32\%$. Two different Ti foil thicknesses were used, yielding clad thicknesses, t_c , of either 0.37 or 0.64 mm, with relative thicknesses, $t_c/t_o \sim 0.5$ and 1. The two panels are denoted as A and B. Micrographs of cross-sections through the two panels are shown in Fig. 2. To evaluate the properties of the TMC alone (without cladding), some of the specimens were ground, leaving a Ti layer $\sim 50 \mu\text{m}$ thick adjacent to the outer fibers (comparable with that found in conventional TMC panels). A cross-section through a ground panel is also shown in Fig. 2. This panel is denoted as O. The matrix material (both within the composite and the cladding) is comprised of equiaxed α grains, $\sim 10 \mu\text{m}$ in diameter, with intergranular β -phase (Fig. 3). There was no evidence of an "interface" between the cladding and the TMC nor of any differences in matrix microstructure in these two regions.

2.2. Mechanical tests

Dog-bone shaped tensile specimens were cut from the panels parallel to the fiber direction using electro-discharge machining (EDM). The gage section was 55 mm long and 4 mm wide. To facilitate gripping, beveled stainless steel tabs were bonded to the specimen ends using an epoxy adhesive. Monotonic tension tests were performed at a rate of 0.02 mm min^{-1} . Axial strains were measured using both a 12.7 mm contacting extensometer and a pair of 3.2 mm strain gauges mounted on opposite faces.

An estimate of the matrix strength was obtained using the Vickers hardness test. The measurements were made with a load of 500 g, yielding indent sizes of $\sim 50 \mu\text{m}$. Care was taken to ensure that the corners of the indents were situated at least one indent size away from the nearest fiber. The hardness measurements were converted to strengths using a plastic constraint factor of 3. The strengths determined this way are considered to be representative of the ultimate tensile strength, σ_m^u , of the matrix (rather than the initial yield stress).

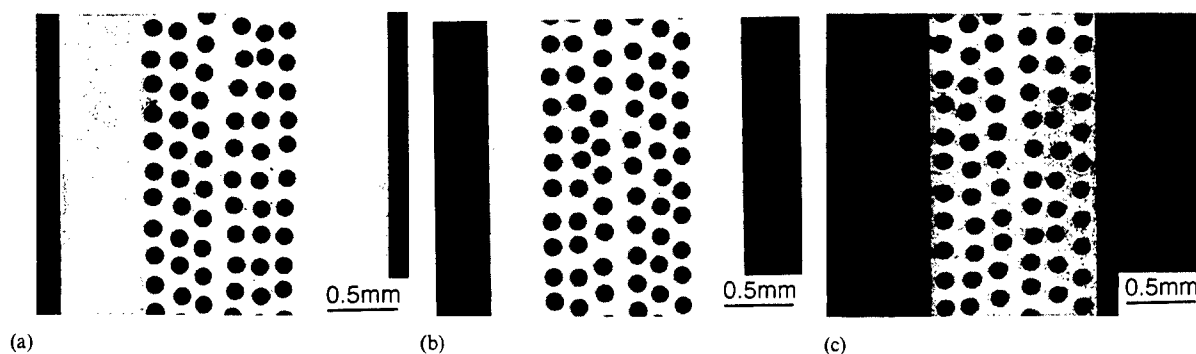


Fig. 2. Micrographs of transverse sections through the three Ti/SiC composites, with clad thickness, t_c/t_o , of (a) 1.0, (b) 0.5 and (c) ~ 0 .

2.3. Residual strains

As described in a subsequent section, the yield strength and the failure strain depend on the thermal residual strain in the fibers. The residual strains in the clad materials were measured using a selective etching procedure, detailed in Ref. [13]. The specimen used for these measurements was ~ 15 mm wide (transverse to the fibers) and ~ 75 mm long (parallel to the fibers). Two narrow slits, ~ 2 mm apart and 50 mm long, were machined along the length of the specimen. The region outside of the narrow tongue between the slits was masked with silicone rubber. The entire specimen was immersed in a 50% HF solution to dissolve the matrix between the slits, allowing the fibers to relax. The heights, z , of the tops of the fibers were then measured using confocal microscopy, with a precision of ~ 1 μ m. The extension of the fibers, Δ , was evaluated from the difference in positions of the exposed fibers and the adjacent embedded fibers. Typically, measurements were made on ~ 20 –40 fibers embedded within the composite and almost all of the exposed fibers (~ 20 –30). The positions, (x, y) , of the fibers on the plane normal to the beam were also recorded.

Since the top surface of the panel could not be aligned perfectly normal to the beam axis, a slight but systematic variation in the heights of the embedded fibers was found along both the x and y directions. To account for this variation, the measurements on the embedded fibers were used to define a reference plane, corresponding to the top surface of the specimen prior to matrix dissolution. This was accomplished by performing a least squares fit of the data to the equation of a plane. Typically, this surface was tilted by $\leq 0.5^\circ$. The average fiber extension, $\bar{\Delta}$ was then calculated as the difference between the average height of the exposed fibers and the average height of the reference plane within the dissolved section. The corresponding fiber strain, ϵ_f^R , was calculated using the relation

$$\epsilon_f^R = -\bar{\Delta}/l \quad (1)$$

where l is the length of the exposed fibers (~ 50 mm).

3. Experimental results

Fig. 4 shows the tensile stress–strain curves. As the clad thickness is increased, the Young's modulus, E , and the ultimate strength, σ_u , decrease whereas the ductility increases. These trends are summarized in Fig. 5. Evidently, the changes in these properties with clad thickness are relatively modest, ranging from $\sim 10\%$ –25%.

The yield point in these materials is somewhat ill-defined. Deviations from linearity begin to occur at relatively low stress levels (~ 800 MPa for $t_c = 0$),

though the changes in the tangent modulus, $d\sigma/d\epsilon$, are initially small. The tangent modulus eventually reaches a saturation value, indicating that the matrix has completely yielded and all additional stress is supported solely by the fibers. For $t_c = 0$, the saturation value is obtained at a stress of ~ 1400 MPa: considerably higher than the stress at the onset of yielding. The strain range over which yielding is effected (from the first non-linearity to the point of saturation in the tangent modulus) is typically $\sim 0.3\%$ – 0.4% .

In order to interpret the changes in yield point with clad thickness, a practical definition of yielding is required. One approach is to use the stress at a prescribed offset strain. In monolithic metals, the offset strain is usually taken to be 0.2%. In the Ti/SiC composites, this offset produces yield stresses that are comparable with the ultimate tensile strength and have little physical meaning. A lower value of the offset strain could potentially be used, though the computed yield stress would be sensitive to the choice of this strain. An alternate approach is to identify an "average" strain at which yielding occurs and take the yield stress as the product of the yield strain and the composite Young's modulus. This can be accomplished by extrapolating the two linear portions of the stress–strain curve and taking their intersection as the yield point (Fig. 4(a)). This approach is considered to have more physical meaning than the one involving an offset strain and is used in the interpretation of the present results. Fig. 5(b) shows that the yield stress, defined in this manner, decreases with increasing clad thickness.

The residual fiber strains, ϵ_f^R , in Panels A and B were -0.19% and -0.22% , respectively (Table 1). The Vickers indentation tests gave matrix strengths in the range 1000–1060 MPa, with an average value of 1030 MPa. These values are comparable to the tensile strengths of Ti–6Al–4V alloys with similar equiaxed microstructures (~ 950 – 1050 MPa) [14]. Because these materials exhibit minimal strain hardening, the yield

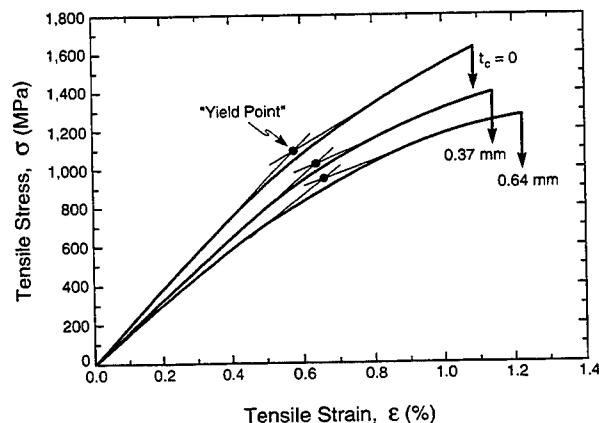


Fig. 4. Results of the tensile tests.

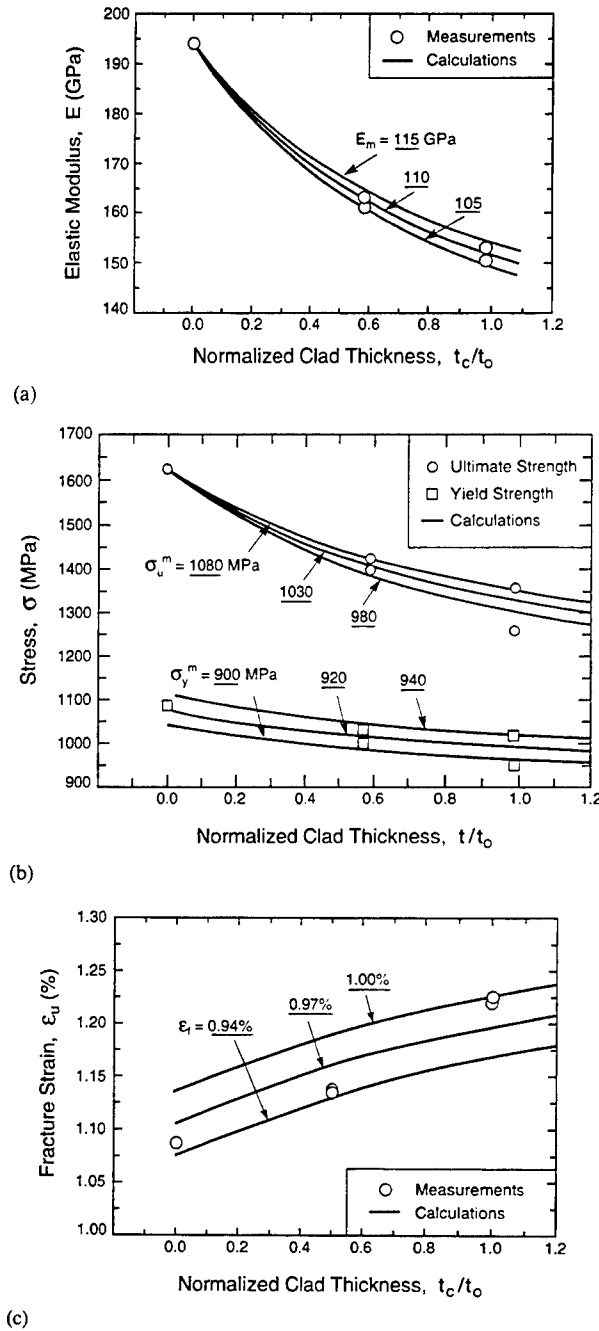


Fig. 5. Trends in (a) Young's modulus, (b) yield and ultimate tensile strength and (c) failure strain, with the normalized clad thickness \hat{t} .

stress is expected to be only slightly lower than the ultimate strength.

4. Analysis and discussion

The trends in the mechanical properties with clad thickness can be rationalized using existing micromechanical models, assuming that (i) iso-strain conditions

exist in the fibers and the matrix, and (ii) the fibers in the clad materials are distributed uniformly throughout the panel with a reduced, effective volume fraction (all quantities pertaining to the clad materials are denoted by an overbar), \bar{f} .

4.1. Young's modulus

Following this approach, the initial elastic modulus of the unclad material is given by

$$E_o = f_o E_f + (1 - f_o) E_m \quad (2)$$

where f_o is the fiber volume fraction and E_f and E_m are the Young's moduli of the fiber and matrix, respectively. The moduli of \bar{E} , the clad materials, can be calculated in a similar fashion, replacing f_o with the average fiber volume fraction, \bar{f} :

$$\bar{E} = f_o / (1 + \hat{t}) \quad (3)$$

where \hat{t} is the normalized clad thickness,

$$\hat{t} \equiv t_c/t_o \quad (4)$$

Thus the elastic modulus can be written as

$$\bar{E} = E_o \frac{(1 + \hat{t} E_m/E_o)}{(1 + \hat{t})} \quad (5)$$

4.2. Yield stress

The yield stress of the unclad material is

$$\sigma_y^o = (\sigma_y^m - \sigma_R^m) (E_o/E_m) \quad (6)$$

where σ_y^m is the (unconstrained) yield stress of the matrix alloy and σ_R^m is the average axial residual stress within the matrix¹. The axial stress obtained from the concentric cylinder model is [15]

$$\sigma_R^m = \frac{f_o E_f E_m^* (E_f + E_o^*) \Omega}{E_o^* (E_f + E_o^* (1 - 2\nu))} \quad (7)$$

where ν is the Poisson's ratio (assumed to be the same for the fibers and the matrix) E_m^* is the average matrix modulus over the appropriate temperature range, E_o^* is the longitudinal composite modulus calculated using E_m^* and Ω is the misfit strain,

$$\Omega = (\alpha_f - \alpha_m) \Delta T \quad (8)$$

with ΔT being the temperature change from processing and α_f and α_m being the thermal expansion coefficients of the fibers and matrix, respectively. The yield stress of the clad materials is obtained by replacing f_o with \bar{f} in the expressions for E_o , E_o^* and σ_R^m .

The misfit strain, Ω , is obtained by combining the residual fiber strains with the concentric cylinder model, yielding the result

¹ 3D finite element calculations show that the average value of the effective residual stress is similar to the axial component [16].

Table 1
Summary of measured mechanical properties

Thickness of cladding, t_c (mm)	Fiber volume fraction, \bar{f} (%)	Young's modulus, E (GPa)	Yield stress, σ_y (MPa)	Tensile strength, σ_u (MPa)	Failure strain, ε_u (%)	Residual strain, ε_r^R (%)	Misfit strain, Ω (%)
0	32	194	1090	1620	1.087	—	—
0.37	21	163, 161	1030, 1000	1420, 1400	1.135, 1.138	–0.191	0.420
0.64	16	153, 151	1010, 950	1330, 1260	1.219, 1.224	–0.222	0.412

Table 2
Summary of constituent properties

Property	Value
Fiber volume fraction in central region, f_o	0.32
Matrix yield stress, σ_m^y	920 MPa
Matrix ultimate strength, σ_m^u	1030 MPa
Matrix modulus (20 °C), E_m	110 GPa
Average matrix modulus (20–600 °C), E_m^*	90 GPa
Fiber modulus, E_f	360 GPa
Misfit strain, Ω	0.42%

$$\Omega = -\frac{\varepsilon_R^f(\bar{f}E_f + (1-\bar{f})E_m^*)}{(1-\bar{f})E_m^*} \quad (9)$$

The values of Ω calculated for the two panels A and B are essentially identical to one another (Table 1): $\Omega = 0.42\%$

4.3. Fracture stress and strain

The tensile strength, σ_u , of the unclad composite is

$$\sigma_u = f_o S_f + (1-f_o)\sigma_u^m \quad (10)$$

where S_f is the fiber bundle strength. The corresponding failure strain is

$$\varepsilon_u = \varepsilon_f - \varepsilon_R^f \quad (11)$$

where ε_f is the failure strain of the fiber bundle in the absence of residual strain. The failure stress, $\bar{\sigma}_u$, and strain, $\bar{\varepsilon}_u$, of the clad materials are obtained by replacing f_o with \bar{f} , as before, yielding the results

$$\bar{\sigma}_u = \sigma_u \frac{(1 + \hat{f} \sigma_u^m / \sigma_u)}{(1 + \hat{f})} \quad (12)$$

and

$$\bar{\varepsilon}_u = \varepsilon_u + \frac{f_o E_f E_m^* \Omega}{E_o^*(E_o^* + \hat{f} E_m^*)} \quad (13)$$

4.4. Comparisons between experiment and theory

Fig. 5 shows comparisons between the predicted and measured properties. A summary of the constituent properties used in the predictions is in Table 2.

The middle curve in Fig. 5(a) is based on the reported Young's modulus for the Ti alloy (110 GPa); the other two curves are calculated using values of E_m that differ from the average by ± 5 GPa. The average value is consistent with the one inferred from the elastic modulus of the unclad composite (assuming a fiber modulus, $E_f = 360$ GPa), as well as with the trends in modulus with.

The composite yield stress has been obtained by fitting the model to the data through adjustments in the matrix yield stress (Fig. 5(b)). The fitting procedure gives a matrix yield stress of $\sim 920 \pm 20$ MPa. As

expected, the matrix yield stress is slightly lower than the ultimate tensile strength obtained from the hardness measurements (1030 MPa).

Similar procedures were followed to obtain the curves in Fig. 5(c) and (d). The average matrix tensile strength was taken to be the one inferred from the hardness measurements (1030 MPa); the upper and lower curves were obtained by varying the matrix strength by ± 50 MPa. The inferred fiber bundle failure strain from Fig. 5(d) is $0.97\% \pm 0.03\%$.

In all cases, good correlations are obtained between the calculated and measured properties, demonstrating that the tensile properties can be modeled using the effective fiber volume fraction. Moreover, they suggest that these properties are insensitive to the spatial distribution of fibers.

5. Concluding remarks

The monotonic tensile properties of the clad TMCs are governed by the fiber volume fraction averaged over the entire cross-section. However, it is anticipated that other properties will be sensitive to the fiber distribution. For example, under cyclic loading, cracks will initiate within the cladding and propagate through the central reinforced region. At low stress levels, the cracks will be bridged by fibers within the composite, though, clearly, they will not be bridged within the cladding. The portion of the crack in the cladding will act essentially as a notch, concentrating the stress within the bridged fibers in the plies closest to the cladding and causing premature fiber fracture. Such effects are currently under investigation.

Acknowledgements

Funding for this work was provided by the ARPA University Research Initiative Program at UCSB under ONR contract No. N00014-92-J-1808. The authors would like to thank S.A. Kraus and P. Nagy of Textron Specialty Materials for generously providing the materi-

als used in this study and D.P. Walls and R. Tucker of United Technologies, Pratt & Whitney, for providing the design in Fig. 1 as well as numerous stimulating discussions regarding cladding of Ti/SiC composites.

References

- [1] D.P. Walls, *personal communication*, United Technologies, Pratt & Whitney.
- [2] U. Ramamurty, F.W. Zok and F.A. Leckie, *Acta Metall. Mater.*, 1995, submitted for publication.
- [3] B.N. Cox and D.B. Marshall, *Fatigue Fract. Eng. Mater. Struct.*, 14 (1991) 847.
- [4] M.D. Sensmeier and P.K. Wright, in P.K. Liaw and M.N. Gungor (eds.), *Fundamental Relationships Between Microstructure and Mechanical Properties of Metal Matrix Composites*, The Minerals, Metals and Materials Society, 1990, p. 441.
- [5] D.M. Harmon and C.R. Saff, in W.S. Johnson (ed.), *Metal Matrix Composites: Testing, Analysis and Failure Modes*, ASTM STP 1032, ASTM, Philadelphia.
- [6] J.G. Bakuckas, Jr. and W.S. Johnson, *J. Comp. Tech. Res.*, 15 (1993) 242.
- [7] D.P. Walls, G. Bao and F. Zok, Mode I Fatigue Cracking in a Fiber Reinforced Metal Matrix Composite, *J. Eng. Mater. Tech.*, 115 (1993) 314–318.
- [8] S.J. Connell, F.W. Zok, Z.Z. Du and Z. Suo, On the tensile properties of a fiber reinforced titanium matrix composite: II. Influence of notches and holes, *Acta Metall. Mater.*, 42 (10) (1994) 3451–3461.
- [9] C.H. Weber, X. Chen, S.J. Connell and F.W. Zok, *Acta Metall. Mater.*, 42 (1994) 3443.
- [10] S. Jansson, H. Dève and A.G. Evans, *Metall. Trans.*, 22A (1991) 2975.
- [11] C.H. Weber, Z.Z. Du and F.W. Zok, High temperature deformation and fracture of a fiber-reinforced titanium matrix composite, *Acta Metall. Mater.*, 1996, in press.
- [12] F.W. Zok, Z.Z. Du and S.J. Connell, On the development of fatigue failure maps for titanium matrix composites, *Mech. Sci. Eng.*, A200 (1995) 103–113.
- [13] U. Ramamurty, F.-C. Dary and F.W. Zok, *Acta Metall. Mater.*, in press.
- [14] D.J. Maykuth, R.E. Monroe, R.J. Favor and D.P. Moon, *Titanium-Base Alloys: 6Al-4V*, Battelle Memorial Institute, Columbus, OH, 1971.
- [15] B. Budiansky, J.W. Hutchinson and A.G. Evans, *J. Mech. Phys. Solids*, 34 (1986) 164.
- [16] R.P. Nimmer, R.J. Bankert, E.S. Russell, G.A. Smith and P.K. Wright, *J. Comp. Tech. Res.*, 13 (1) (1991) 3–13.

Role of Cladding in the Notched Tensile Properties of a Titanium Matrix Composite

U. RAMAMURTY, F.W. ZOK, and F.A. LECKIE

The utility of Ti cladding in alleviating the notch sensitivity of both the monotonic and cyclic tensile properties of Ti matrix composites (TMC) has been examined. Experiments have been conducted on panels with two different clad thicknesses as well as on the TMC alone. Crack bridging models have been used to describe the composite behavior, incorporating explicitly the effects of the cladding. It is demonstrated that the notched strength can be raised up to the level corresponding to the un-notched TMC alone, with a critical clad thickness that depends on the fracture properties of the TMC and the notch size. The fatigue threshold can be elevated also, though it cannot reach the threshold of the un-notched TMC. The bridging models have been used to calculate the trends in the strength and the fatigue threshold with the clad thickness.

I. INTRODUCTION

THE ultimate tensile strength of fiber-reinforced titanium matrix composites (TMCs) is relatively notch sensitive. Typically, for specimens containing circular holes or sharp notches ~3 to 6 mm in size, the strength is reduced by as much as a factor of 2.^[1] Such a high degree of notch sensitivity may preclude the design of TMC components that contain holes or other stress concentrating features.

The fatigue resistance of TMCs is also notch sensitive. Under cyclic loading, fatigue cracks initiate and grow within the matrix, leaving the fibers intact in the crack wake. There exists a critical peak stress below which the crack growth rate approaches a steady-state value, independent of crack length. Above the critical stress, fiber failure occurs in the crack wake, leading to an acceleration in the crack growth rate and, ultimately, catastrophic fracture. This critical stress represents a threshold below which the fatigue life is infinite. Both experiments^[2] and calculations^[3,4] indicate that the threshold stress decreases dramatically with increasing notch size. The fatigue notch sensitivity is an additional concern in the design of components containing stress concentrations.

One approach to alleviating the notch sensitivity of TMCs is to reinforce components locally in regions surrounding the stress concentrating features. Through judicious selection of the reinforcing material and the geometry, it is anticipated that the local strength and fatigue resistance could be brought up to the levels corresponding to the TMC alone, rendering the material notch insensitive.

A simple approach to manufacturing reinforced panel structures involves hot pressing TMC plates between monolithic sheets of the Ti alloy itself and subsequently machining away the excess Ti remote from the stress concentrating features. Figure 1 shows a schematic illustration

of this reinforcement scheme for a panel containing a through-thickness hole. Similar schemes have been used in the past in repairing aluminum aircraft components that contain fatigue cracks, using either boron/epoxy or graphite/epoxy composites.^[5]

The objective of the present study is to assess the utility of Ti cladding in improving the notched properties of TMCs. For this purpose, experiments have been conducted on composite panels with two different clad thicknesses as well as a panel without cladding. The focus of the work is on the ultimate tensile strength and the resistance to fatigue cracking. The un-notched tensile properties of these materials have been reported elsewhere.^[6]

Section II provides an overview of models that have been developed to describe the effects of notches on both the static tensile strength and the fatigue resistance of TMCs. The models are used to identify the constituent properties that govern the mechanical behavior of the composites and to provide guidance for the selection of critical experiments to assess the models. The overview is followed by a description of the materials and test procedures, the experimental results, and comparisons with model predictions.

II. BACKGROUND

A. Notched Strength

In the presence of notches or holes, catastrophic fracture of TMCs is preceded by the formation of a localized plastic strip in which the matrix is fully yielded and most of the fibers are broken.^[1] As the remote stress is increased, the plastic strip extends away from the notch tip, in a manner analogous to a bridged crack in a ceramic matrix composite. Consequently, the notched strength can be rationalized in terms of a bridging (or cohesive zone) model. The bridging traction law relevant to TMCs is illustrated in Figure 2(a). At the simplest level, it is comprised of two rectilinear parts, each characterized by a strength and a critical displacement. The strength level σ_1 of the first part is essentially the un-notched tensile strength of the composite. At this stress, the fiber bundle fails but the matrix remains intact. The corresponding displacement, u_1 , depends on the width of the plastic strip and the fiber bundle failure strain.

U. RAMAMURTY, formerly Post-graduate Researcher with the Materials Department, University of California, is Lecturer, School of Mechanical and Production Engineering, Nanyang Technological University, Singapore, 2263. F.W. ZOK Professor, Materials Department, and F.A. LECKIE, Professors, are with the Department of Mechanical and Environmental Engineering, University of California, Santa Barbara, CA 93106.

Manuscript submitted October 10, 1996.

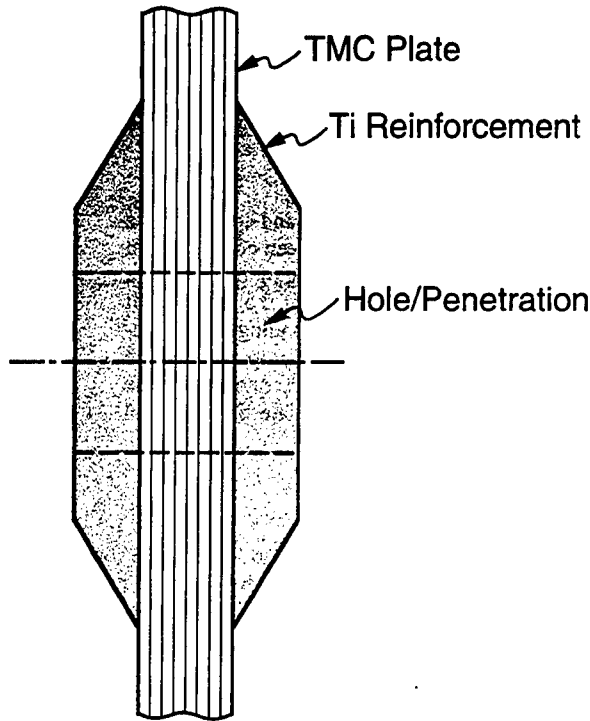


Fig. 1—Schematic illustration of the local reinforcement concept for a panel containing a through-thickness hole.

The bridging stress, σ_2 , in the second part of the traction law is dictated by the strength of the matrix. At a critical crack opening displacement, u_2 , the local strain reaches the matrix failure strain, leading to the formation of an unbridged matrix crack. The notched strength is simulated by incorporating the two-level bridging law into a fracture mechanics model, as described in Reference 1. Moreover, the total (or steady-state) fracture energy is taken to be the area under the traction law.

A simpler solution to the strength in the "long notch" regime can be obtained using a single-level rectilinear law, similar to the one attributed to Dugdale^[7] and Barenblatt^[8] and developed by Bilby *et al.*^[9] This law is characterized by a single-valued strength, σ_0 , and a critical displacement, u_0 , with a toughness, $\Gamma = \sigma_0 u_0$. The notched strength σ_N is predicted to vary with notch length, $2a_0$, in accordance with^[9]

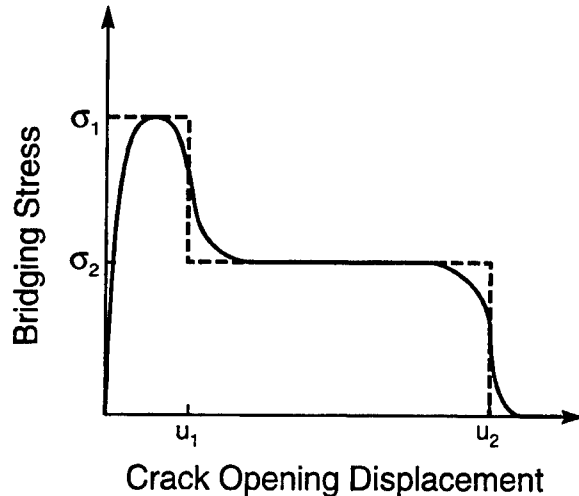
$$\sigma_N = \sigma_0 \frac{2}{\pi} \cos^{-1} \left[\exp \left(\frac{-\pi \Gamma E}{8a_0 \sigma_0^2} \right) \right] \quad [1]$$

where E is the Young's modulus.

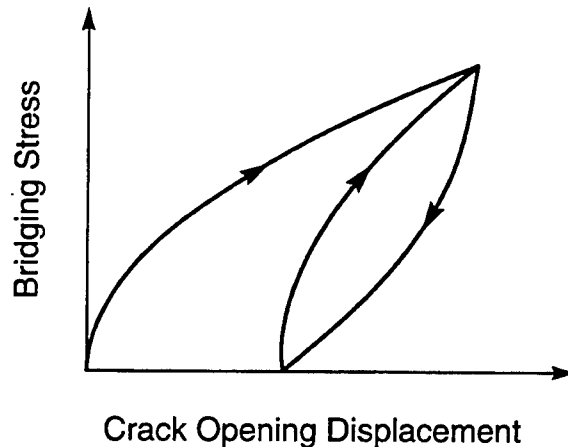
From these bridging models, a characteristic bridging length emerges, defined by

$$a_b \equiv \Gamma E / \sigma_0^2 \quad [2]$$

For TMCs, a_b is typically ~ 5 to 10 mm.^[1] The size of the notch or hole relative to a_b determines the degree of notch sensitivity. When $a_0/a_b \ll 1$, the bridging zone length is large in relation to the notch size and the material is *notch insensitive*, the strength being comparable to the un-notched tensile strength. Conversely, when $a_0/a_b \gg 1$, the strength diminishes as $a_0^{-1/2}$, in accordance with the Griffith equa-



(a)



(b)

Fig. 2—Schematic of the traction laws pertinent to (a) the notched tensile strength and (b) the fatigue resistance of TMCs.

tion. In the intermediate regime, the solution based on the single-level rectilinear law is expected to provide a reasonable estimate of notched strength.

B. Fatigue Cracking

Under cyclic loading, cracks initiate and propagate through the matrix, but the fibers initially remain intact. The effects of these fibers on the crack tip stress intensity amplitude, ΔK_r , can also be modeled using crack bridging concepts. Assuming that the fibers are frictionally coupled to the matrix through a constant interfacial sliding stress, τ , the relevant *cyclic* bridging traction law is^[10]

$$\Delta u = \frac{1}{2} \lambda \Delta \sigma_b^2 \quad [3a]$$

where Δu is the crack opening displacement amplitude, $\Delta \sigma_b$

Table I. Summary of Constituent Properties

Fiber volume fraction, $f_0 = 0.32$
Fiber diameter, $D = 140 \mu\text{m}$
Young's modulus of matrix, $E_m = 110 \text{ GPa}$
Young's modulus of fibers, $E_f = 400 \text{ GPa}$
Poisson's ratio, $\nu \approx 0.2$
Orthotropy factor, $A = 0.925^{[3]}$
Interface sliding stress, $\tau = 10 \text{ to } 15 \text{ MPa}$
Paris law exponent, $n = 4$
Paris law prefactor, $\beta \approx 3 \times 10^{-36} \text{ m}^7/\text{N}^4$
Fiber bundle strength, $S_f = 2500 \text{ MPa}$

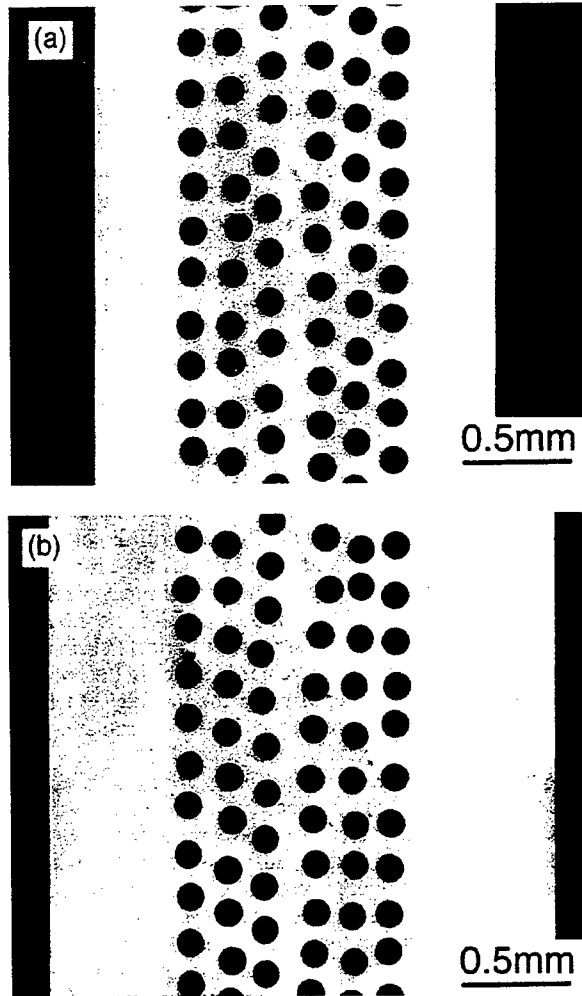


Fig. 3—Cross sections of the clad TMCs.

is the corresponding amplitude in the bridging stress, and λ is a bridging parameter, defined by

$$\lambda \equiv \frac{D(1-f)^2 E_m^2}{4 E E_f \tau f^2} \quad [3b]$$

with D being the fiber diameter; f the fiber volume fraction; E_m and E_f the Young's moduli of the matrix and fibers, respectively; and E the longitudinal composite modulus.

This traction law is shown schematically in Figure 2(b). An extensive set of solutions for the crack tip stress intensities in terms of the bridging parameter, λ , the notch size, $2a_0$, and the applied stress amplitude, $\Delta\sigma$, have been developed^[4,11] and used to simulate fatigue cracking in TMCs over a range of loading conditions and notch geometries.^[2,12]

The preceding bridging model has also been used to calculate the threshold stress amplitude, $\Delta\sigma_{th}$, below which fiber failure does not occur for any crack length.^[3,4] Within this regime, the crack growth rate approaches a steady-state value, independent of crack length. The numerical results for $\Delta\sigma_{th}$ can be accurately described by the relation^[3]

$$\frac{6\pi\xi a_0\tau}{DS_f} = \left[\left(\frac{\Delta\sigma_{th}}{fS_f(1-R)} \right)^{-4/3} - \left(\frac{\Delta\sigma_{th}}{fS_f(1-R)} \right)^{2/3} \right]^{3/2} \quad [4a]$$

where S_f is the fiber strength (assumed to be deterministic), R is the stress ratio (minimum/maximum), and ξ is a dimensionless parameter defined by

$$\xi = \frac{fE_f E (1-\nu^2)}{(1-f)^2 E_m^2 A} \quad [4b]$$

with ν being Poisson's ratio and A an orthotropy factor of order unity.

Inspection of Eq. [4] yields a second characteristic bridging length, a'_b , defined by

$$a'_b = DS_f/6\pi\xi\tau \quad [5]$$

The ratio a_0/a'_b dictates the degree of notch sensitivity under cyclic loading conditions, in essentially the same manner that a_0/a_b dictates the monotonic strength. For typical values of the parameters in Eq. [4] (Table I), the bridging length, a_b , is ~ 0.2 to 1 mm , about an order of magnitude smaller than a'_b . Consequently, failure of TMCs is expected to be more sensitive to the presence of flaws under cyclic loading than under monotonic loading.

III. EXPERIMENTS

The materials used in this study were comprised of a six-ply Ti-6Al-4V alloy reinforced unidirectionally with ~ 32 vol pct of SCS-6 SiC fibers (produced by Textron Specialty Materials, Lowell, MA). The thickness of the composite, $2t_0$, was 1.3 mm . The panels were clad on both sides with the Ti-6Al-4V alloy, with the clad thickness t_c being either 0.37 or 0.64 mm (Figure 3). The relative clad thicknesses were $\hat{t} = t_c/t_0 = 0.5$ or 1 . In some instances, the cladding was removed by grinding and the properties of the TMC alone were measured also.

Uniaxial tension tests were performed on straight-sided, 15-mm -wide specimens containing either a through-thickness circular hole or through-thickness sharp notch at the specimen center, all produced by electrodischarge machining. The holes were either 0.6 or 3.2 mm in diameter and the notches were 3-mm long. The results of these tests, as

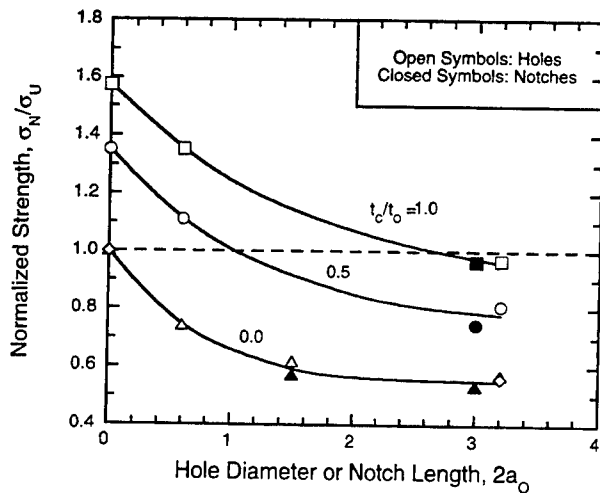


Fig. 4—Trends in tensile strength with notch size. The triangles correspond to data on a Ti-6Al-4V alloy reinforced with 32 pct Sigma SiC fibers;^[1] all other data are for the composites with SCS-6 SiC fibers.

well as the fatigue tests described subsequently, are presented in terms of the stresses calculated on the basis of the area of the *unclad TMC material alone*, the relevant thickness being $2t_0$ rather than $2(t_0 + t_c)$.^{*} Upon perform-

^{*}Although in the present experiments the cladding is present along the entire length of the specimen, it is envisaged that local reinforcement could be accomplished by machining the excess cladding in regions remote from the stress concentration, as illustrated schematically in Fig. 1. The values of notched strength presented in terms of the area of the unclad composite are therefore representative of the load bearing capacity of locally reinforced structures.

ing a force balance, the *remote* stress, σ_∞ , can be related to the *local* net-section stress, σ_N , through

$$\sigma_\infty = \sigma_N (1 + t_c/t_0) \quad [6]$$

The critical crack opening, u_2 , was obtained by measuring the width of the notch prior to testing and then repeating the measurement after fracture. These measurements were made in an optical microscope at a magnification of 200 times. In addition, the width of the plastic zone normal to the loading direction was measured using optical microscopy. This was accomplished by locating the point at which the broad side surface near the fracture plane was no longer in focus with the rest of the surface.

Measurements of toughness were made using the edge-notched work-of-rupture specimen, loaded by four-point bending. The toughness, Γ , was calculated from the relation^[13]

$$\Gamma = \frac{\int_0^{v_c} P(v) dv}{t(w - a_0)} \quad [7]$$

where P is the applied load, v is the load-point displacement, v_c is the displacement at fracture, t is the panel thickness, w is the specimen width (7 mm), and a_0 is the notch depth (4 mm).

Fatigue crack growth experiments were conducted on 15-mm-wide specimens containing 3-mm-long center notches. Experiments were conducted at several stress ranges, $\Delta\sigma$. The stress ratio (minimum/maximum) was $R = 0.1$ and the cycling frequency was 5 Hz. Crack extension was measured

using a traveling stereomicroscope connected to a video recorder. To determine whether the crack front was straight through the thickness of the clad panels, some of the fatigued specimens were given a heat-tinting treatment (2 hours at 400 °C), pulled to fracture, and subsequently examined. In some instances, the matrix material around the crack plane was dissolved in a 50 pct HF solution following testing, and the specimen subsequently examined in a scanning electron microscope in order to establish the degree of fiber failure in the crack wake.

The interface sliding stress, τ , was measured using a multiple fiber pullout technique. In the technique, two coplanar notches were machined into the cladding of a straight tensile specimen, with care taken not to cut or damage the fibers. The specimen was then loaded cyclically at a low stress level ($\Delta\sigma = 300$ MPa) such that fatigue cracks initiated and propagated from the notches, but not in regions remote from the notches. Following ~50,000 loading cycles, the two cracks linked together to form a single crack across the entire section, with all fibers remaining intact. The test was then interrupted and a 12.7-mm extensometer mounted across the crack faces. Additional cycling was performed at progressively increasing stress levels until the fiber bundle failed. The measured stress-displacement loops were subsequently used to determine τ .^[14] The analysis is presented in the Appendix.

IV. NOTCHED STRENGTH

Figure 4 shows the trends in notched tensile strength, σ_N , with notch or hole size, $2a_0$. The results obtained in a previous study on a similar TMC are also shown for comparison.^[1] The results indicate that there is a critical notch size below which the notched strength exceeds the un-notched strength σ_U of the TMC alone. The critical notch sizes are -1 and -3 mm for clad thicknesses, t , of 0.5 and 1.0 mm, respectively. Alternatively, there exists a critical clad thickness for a prescribed notch size needed to raise the notched strength of the clad material up to the un-notched tensile strength of the TMC alone. A method for interpolating between these results is detailed subsequently.

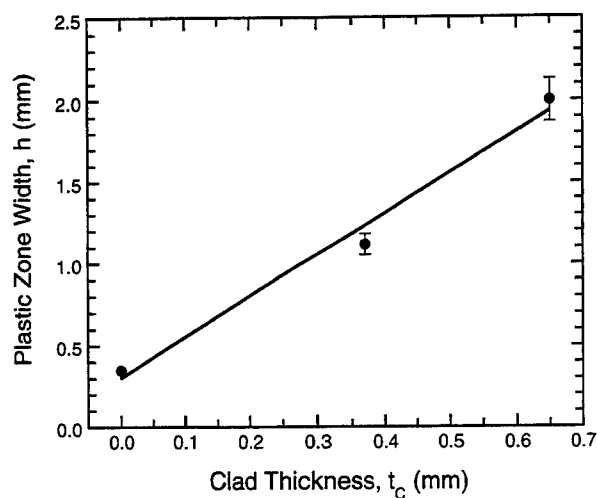
Figure 5 shows trends in the plastic zone width, h , and the critical notch tip displacement, u_2 , with the panel thickness, t . Both h and u_2 increase approximately linearly with t . These trends are consistent with the expected behavior of thin ductile sheets subject to plane *stress* conditions. (Under plane strain conditions, h would be *independent* of t .) The critical displacement, in turn, varies linearly with h (Figure 5(c)). In essence, h represents an effective gage length within the plastic zone and the critical displacement is expected to follow in accordance with

$$u_2 \sim \epsilon_m h \quad [8]$$

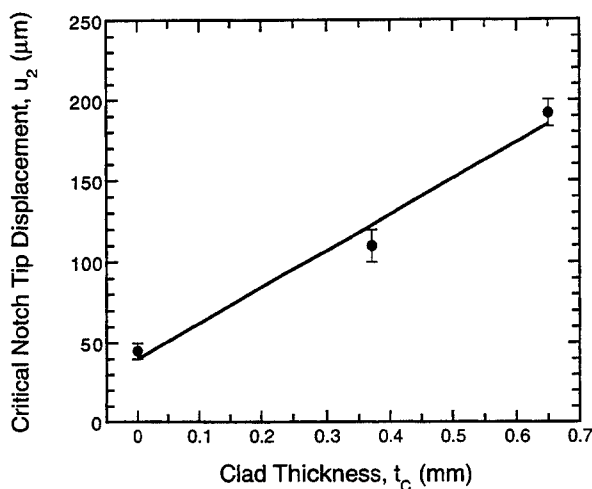
where ϵ_m is the failure strain of the matrix. The failure strain obtained from the experiments (Figure 5(c)) is $\epsilon_m = u_2/h \sim 0.09$, essentially the same as the reported failure strain for Ti alloys.^[15]

The results of the work-of-rupture tests are summarized in Figure 6. The trend in fracture energy with clad thickness can be described by a "rule-of-mixtures" relation:

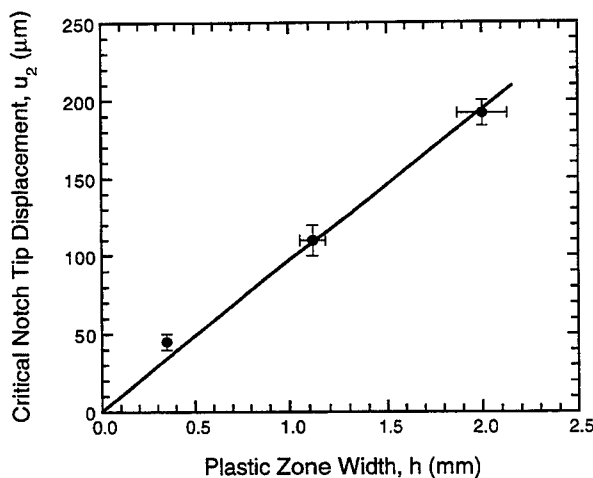
$$\Gamma = (\Gamma_m t_c + \Gamma_0 t_0)/(t_c + t_0) \quad [9]$$



(a)



(b)



(c)

Fig. 5—Influence of clad thickness on (a) the plastic zone width and (b) the critical notch tip displacement. (c) The data in (a) and (b) plotted as critical displacement vs plastic zone width.

where Γ_0 and Γ_m are the contributions from the TMC and the cladding, respectively. This equation implicitly assumes that the two contributions are independent of one another. A least-squares curve fit of Eq. [9] to the data in Figure 6(b) yields the results $\Gamma_0 = 43 \text{ kJ/m}^2$ and $\Gamma_m = 106 \text{ kJ/m}^2$. The latter result is consistent with the plane-stress fracture toughness of Ti alloys (typically ranging from 100 to 120 kJ/m^2 [15]).

To assess the utility of the Dugdale–Barenblatt model, the notched strength, σ_N (calculated on the basis of the total thickness $2(t_c + t_0)$ within the clad region), is plotted against the parameter, a_0/TE , as suggested by the form of Eq. [1] (Figure 7). The experimental results are compared with the predictions, using σ_0 as a fitting parameter. For sufficiently high values of a_0/TE ($\geq 0.5 \times 10^{-7} \text{ MPa}^{-2}$), a reasonable correlation is obtained between the measurements and the theory, using a bridging stress of $\sigma_0 = 900 \pm 100 \text{ MPa}$, comparable to the yield strength of Ti alloy matrix.* Interestingly, the strengths calculated using the to-

*The strengths for low values of a_0/TE are predicted more accurately using the two-level bridging law. However, in light of the additional complexity of these calculations, along with the expectation that hole sizes relevant to engineering components will be $\geq 5 \text{ mm}$, only the Dugdale–Barenblatt solution is presented here. Additional details of the two-level bridging law are found in Ref. 1.

tal composite thickness are insensitive to the clad thickness, t_c/t_0 , as evidenced by the collapse of the data in Figure 7 onto essentially a single band. This result indicates that the bridging processes that determine the notch sensitivity are not strongly affected by the cladding. The main effect of the cladding is to simply increase locally the thickness of material that can support load around the hole, leaving σ_N unchanged for a prescribed notch length. The strength calculated on the basis of the remote stress, σ_∞ , thus increases proportionally with the clad thickness, t_c/t_0 , in accordance with Eq. [6].

The critical clad thickness, t_c^* , required to attain a notched strength equal to the un-notched ultimate tensile strength of the TMC has been calculated using Eqs. [1] and [6], and the results are plotted in Figure 8. For this calculation, the effective composite modulus, \bar{E} , is calculated assuming the fibers to be distributed uniformly through the cross section of clad region, with an effective fiber volume fraction, \bar{f} : [6]

$$\bar{f} = f_0 / (1 + \hat{t}) \quad [10]$$

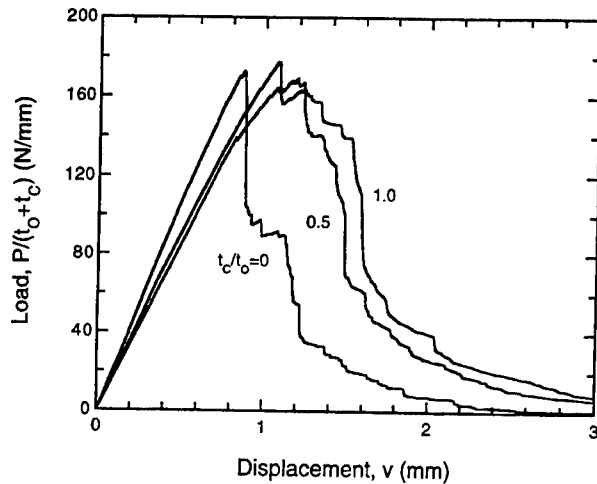
where f_0 is the fiber volume fraction in the unclad TMC. Thus, the modulus is, [6]

$$E = E_0 (1 + \hat{t} E_m / E_0) / (1 + \hat{t}) \quad [11]$$

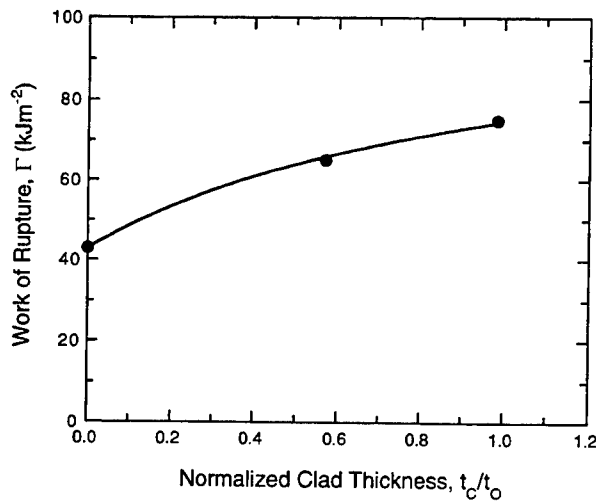
where E_0 is the Young's modulus of the TMC alone. For hole sizes of 5 to 20 mm, the critical clad thickness is predicted to be in the range $t_c/t_0 \sim 1$ to 2.

V. FATIGUE CRACKING

The fatigue characteristics of both the unclad and the clad materials were similar to those previously reported for other TMCs. [2,12] Notably, fatigue cracks were initiated readily at the notch root. The cracks grew stably through the matrix and initially were accompanied by fiber bridging.



(a)



(b)

Fig. 6—(a) Load-displacement curves obtained from the work of rupture tests. (b) Variation in fracture energy with clad thickness. The solid line is a fit of Eq. [8].

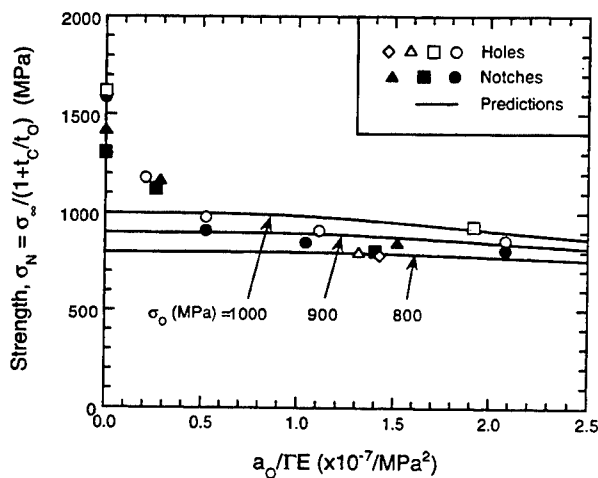


Fig. 7—Notched strength, σ_N , plotted against $a_0/\Gamma E$. The solid lines are predictions of the Dugdale-Barenblatt model.

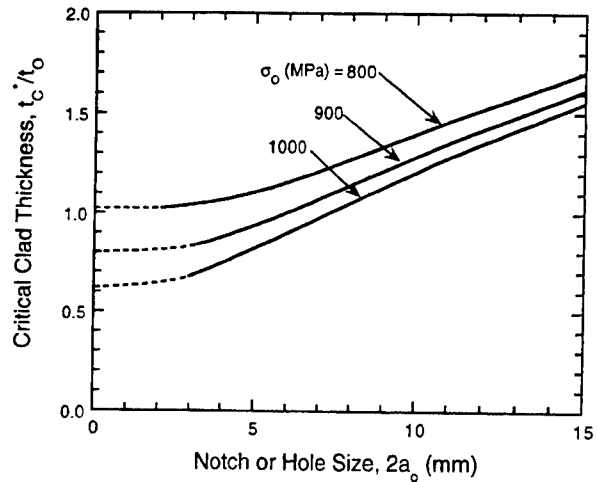


Fig. 8—Effects of notch size on the critical clad thickness. The predictions in the short notch regime overestimate the critical clad thickness and are thus shown as dashed lines.

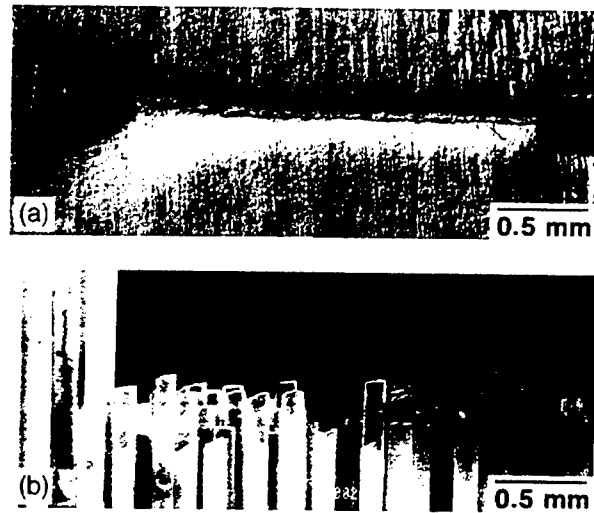


Fig. 9—(a) A matrix fatigue crack and (b) the underlying fibers, showing extensive fiber failure in the crack wake.

In some specimens, all of the underlying fibers were found to be intact; in others, the fibers had fractured over either part or all of the crack wake. An example of the latter is shown in Figure 9. Moreover, the heat-tinting treatments indicated that the crack front was essentially straight, despite the nonuniformity of the fiber distribution (Figure 10). Evidently, crack trapping associated with the higher fatigue resistance of the TMC is negligible.

The main effect of fiber bridging was to cause a reduction in the crack growth rate with increasing crack length. Several representative crack growth curves are shown in Figure 11. At high stress levels, the onset of fiber fracture resulted in a subsequent acceleration in crack growth and, in some instances, led to catastrophic fracture. The curves also indicate that the fatigue resistance increases with increasing clad thickness, as manifested in both a slight reduction in the crack growth rate in the initial stages of cracking (when the fibers are intact) and an elevation in the number of cycles needed to initiate fiber fracture. The com-

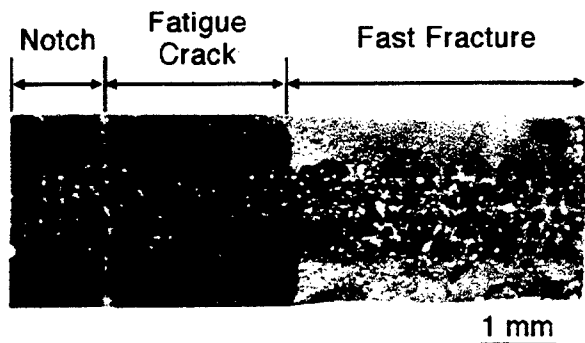


Fig. 10—Surface of specimen that was fatigued, heat tinted, and fractured.

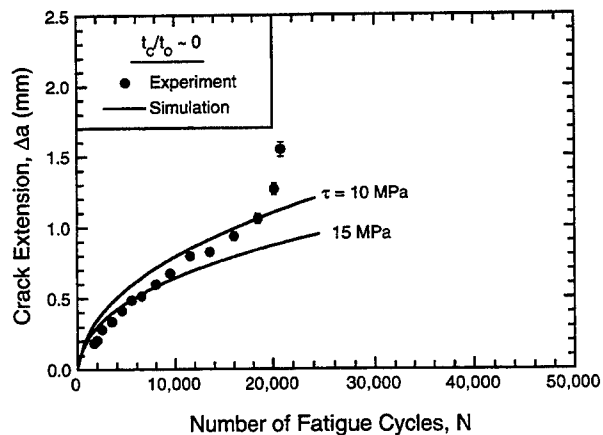
parisons are made at a fixed stress amplitude, again calculated on the basis of the composite thickness, $2t_c$.

Also shown in Figure 11 are crack growth simulations based on a crack bridging model developed by McMeeking and co-workers.^[4,10,11] In this model, the fibers are assumed to be frictionally coupled to the matrix through a constant interface sliding stress, τ , and the bridging traction law then obtained using a shear lag analysis. In turn, the spatial distribution of fiber stresses along the plane of the matrix crack and the crack tip stress intensity range are calculated, treating the fibers as a series of line springs acting along the crack plane. The sliding stress, measured from the fiber bundle pullout tests, is in the range of 10 to 15 MPa (refer to the Appendix for details). The crack growth simulations have been performed using the measured range of sliding stresses along with the material properties summarized in Table I. The fatigue resistance of the composite was assumed to follow the Paris law, with numerical coefficients equal to those of the matrix alloy. These, too, are given in Table I. Good correlations are obtained between the experimental data and the simulated curves. It should be noted that the beneficial effects of the cladding are rather modest; over the range of clad thicknesses examined here, the crack growth rate was reduced by a maximum of a factor of ~ 2 .

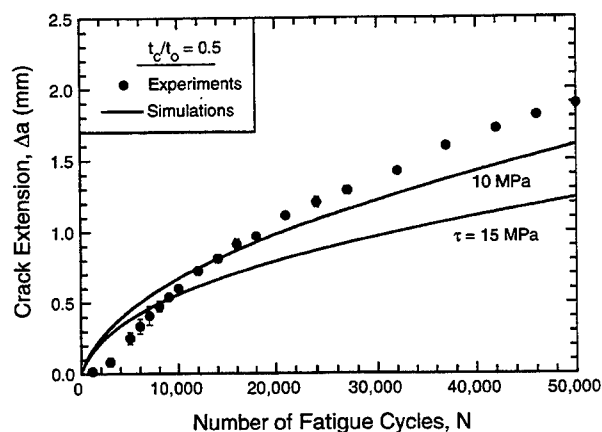
The cladding also plays a role in enhancing the fatigue threshold. The effects can be incorporated into Eq. [4], assuming the fibers are distributed uniformly within the clad region and reinterpreting the parameters accordingly. In doing this, Eq. [4] becomes

$$\frac{a_0}{a_b} = \left(\frac{\xi}{\xi_c} \right) \left[\left(\frac{\Delta \sigma_{th}}{f_0 S_f (1-R)} \right)^{-4/3} - \left(\frac{\Delta \sigma_{th}}{f_0 S_f (1-R)} \right)^{2/3} \right]^{3/2} \quad [12]$$

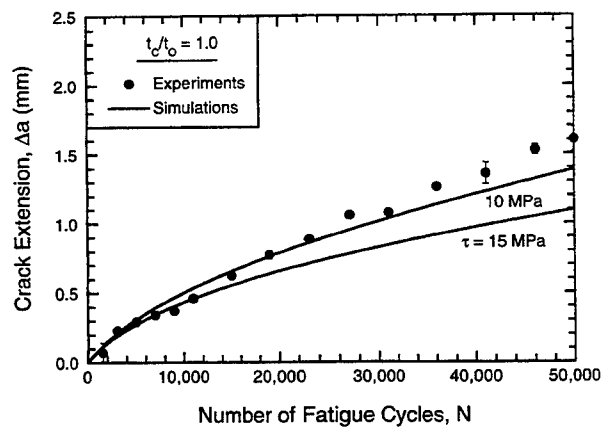
where ξ is the dimensionless parameter defined in Eq. [4b], evaluated using the effective fiber volume fraction, f , and the effective modulus, \bar{E} , through Eqs. [10] and [11]. Figure 12(a) shows the trend in the calculated threshold stress with normalized notch size, $a_0 \xi / a_b \xi$. At stress levels above this line, fiber fracture is predicted to occur at some point during crack growth; below the line, the fibers are predicted to remain intact indefinitely. Also shown are the data from the experiments, the open symbols representing tests in which no significant fiber failure was observed and the



(a)



(b)



(c)

Fig. 11—(a) through (c) Influence of clad thickness on fatigue crack growth rate.

closed symbols representing tests in which some or all of the bridging fibers had broken. The fiber strength (2.5 GPa) was obtained from the fiber bundle pullout tests. The data are consistent with the predicted boundary between the “fiber fracture” and “no fiber fracture” regimes, as indicated on the figure.

An alternate representation of the predicted effects of cladding on the fatigue threshold is obtained by replotting the results in Figure 12(a) against a_o/a_b , rather than $a_o\xi_i/a_b\xi$. (The parameter $a_o\xi_i/a_b\xi$ is a function of the clad thickness, t_c/t_o , and, consequently, the effects of t_c/t_o are not evident. Such effects are illustrated more clearly by plotting the results against a_o/a_b since it does not depend on t_c/t_o .) In this form, a series of threshold lines are obtained, each corresponding to a prescribed value of clad thickness, t_c/t_o , and, through Eqs. [4b], [10], and [11], to a fixed value of ξ_i/ξ (Figure 12(b)). Though it is evident that the cladding enhances the fatigue threshold, the threshold cannot be raised to the level corresponding to the un-notched TMC (at $\Delta\sigma_{th}/f S_f(1-R) = 1$), except in the limit of $t_c/t_o \rightarrow \infty$. Therefore, cladding cannot render the composite completely notch insensitive under cyclic loading conditions.

VI. CONCLUDING REMARKS

The experiments and calculations demonstrate that cladding can be an effective means of local reinforcement around stress concentrations, raising both the tensile strength and the fatigue threshold. For notch sizes of ~ 1 cm, the tensile strength of the clad region can be brought up to the level corresponding to the TMC alone using a relative clad thickness of $t_c/t_o \sim 1.2$. For this notch size and clad thickness, the fatigue threshold is elevated by a factor of ~ 2 , though it remains well below the threshold of the un-notched TMC alone. Moreover, the associated changes in fatigue crack growth rate at stresses below the threshold are modest. Clearly, the cladding is more effective in improving the notch sensitivity of the ultimate strength than that of the fatigue resistance.

These differences can be understood in terms of the mechanical properties of the cladding and their role in determining the efficacy of the bridging processes. Under monotonic loading, the load bearing capacity of the cladding is high, the ultimate strength (~ 1000 MPa) being comparable to that of the TMC (~ 1500 MPa). Consequently, the cladding provides a substantial enhancement in the notched strength, σ_∞ ; the enhancement is proportional to the strength of the cladding and its thickness. Evidently, the cladding does not have a strong effect on the characteristic bridging length, a_b , because of the similarities in the mechanical properties of the Ti cladding and the TMC under monotonic loading. Conversely, under cyclic loading, the cladding cracks along with matrix within the TMC and therefore does not support any load in the crack wake. Consequently, the fatigue resistance is dominated by the properties of the TMC. The main effect of the cladding on the fatigue threshold comes from its role in the characteristic bridging length, a_b' , through Eqs. [4] and [5]. Specifically, a_b' increases with increasing t_c/t_o , which, in turn, reduces the degree of notch sensitivity. However, the changes in the threshold stress with the clad thickness are considerably smaller than those involving the monotonic strength.

One potential approach for further enhancing the fatigue resistance while maintaining a high monotonic strength is to replace the Ti cladding with the TMC itself (essentially increasing the cross section of the entire composite in the region around the stress concentration). However, this approach is expected to be more difficult to implement fol-

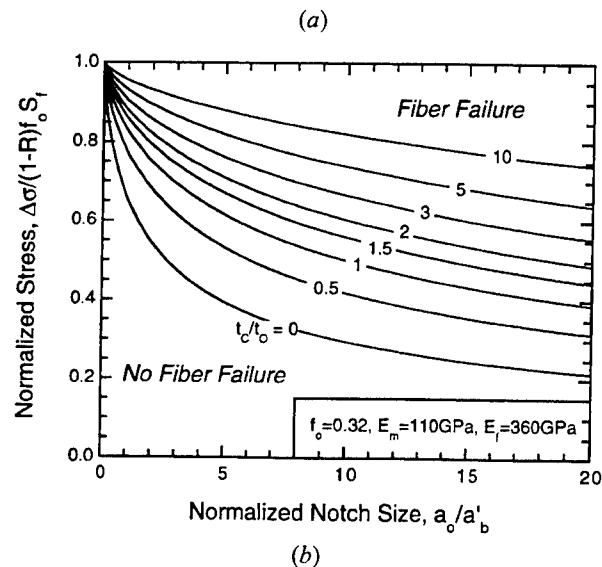
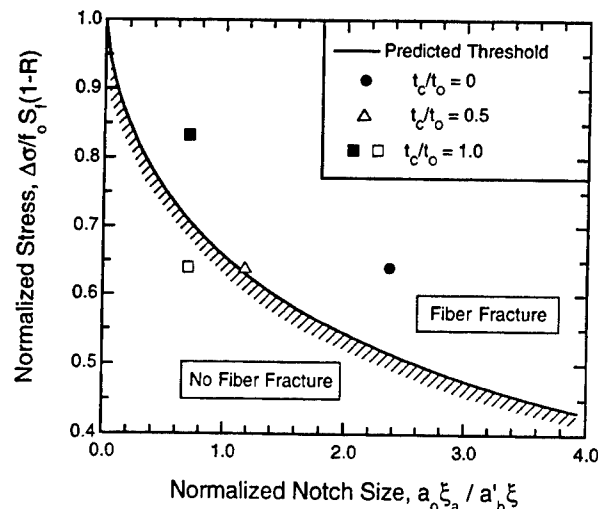


Fig. 12—(a) and (b) Influences of clad thickness and notch size on the fatigue threshold.

lowing the manufacturing route used to make the present panels, mainly because of difficulties associated with machining the excess TMC in the regions remote from the stress concentration and the potential problems associated with the exposed fibers at the ends of the cladding. Alternate manufacturing routes would need to be developed to alleviate these problems. Moreover, problems of stress concentrations associated with the transition region need to be addressed.

APPENDIX Analysis of hysteresis loops

Assuming that τ is constant, the slip length, l , along the fiber-matrix interface is given by

$$l = \frac{\sigma_f (1 - f) E_m D}{4 \tau E} \quad [A1]$$

where σ_f is the fiber stress in the crack plane. The far-field

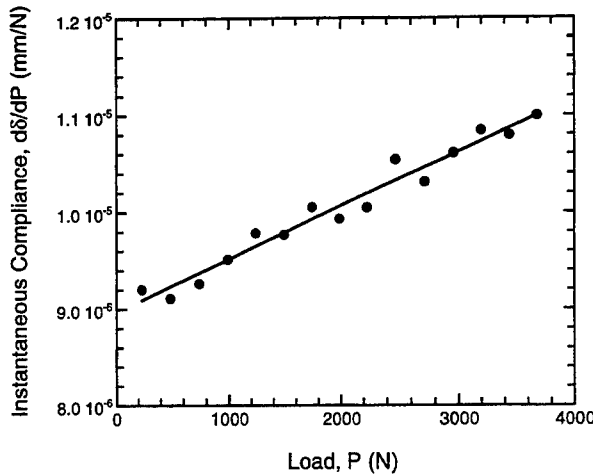


Fig. A1—Variation of instantaneous compliance with applied load.

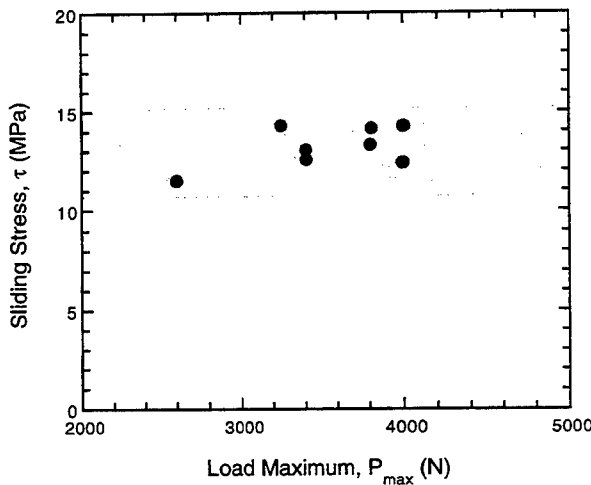


Fig. A2—Summary of sliding stress measurements.

displacement, δ_p , due to fiber sliding is obtained by integrating the additional fiber strain over the slip length, yielding^[14]

$$\delta_p = \frac{D \alpha^2 (\sigma_f)^2}{4 E_f \tau (1 + \alpha)^2} \quad [A2]$$

where

$$\alpha \equiv \frac{E_m (1 - f)}{E_f f} \quad [A3]$$

Upon load reversal, the pullout displacement becomes

$$\delta_p' = \delta_{\max} - \frac{D \alpha^2 (\sigma_{\max} - \sigma_f)^2}{8 E_f \tau (1 + \alpha)^2} \quad [A4]$$

where δ_{\max} is evaluated at the maximum fiber stress, σ_{\max} , prior to unloading, using Eq. [A2]. Upon reloading, it is

$$\delta_p'' = \delta_{\min} + \frac{D \alpha^2 (\sigma_{\min} + \sigma_f)^2}{8 E_f \tau (1 + \alpha)^2} \quad [A5]$$

with δ_{\min} evaluated at the minimum fiber stress σ_{\min} .

The measured displacement, δ , is the sum of two components: (1) an elastic one, δ_e , proportional to the applied load, P ; and (2) the inelastic one, δ_p , proportional to P^2 . Thus,

$$\delta = C_1 P + C_2 P^2 \quad [A6]$$

where C_1 is the elastic compliance of the cracked body over the relevant gage length and C_2 is a material property, related to τ by

$$C_2 = \frac{D \alpha^2}{4 E_f \tau (1 + \alpha^2) A^2 f^2} \quad [A7]$$

with A being the cross-sectional area of the composite. Differentiating Eq. [A6] with respect to P yields

$$d\delta/dP = C_1 + 2 C_2 P \quad [A8]$$

The instantaneous compliance $d\delta/dP$ is thus predicted to be proportional to the applied load, subject to the assumption of a constant sliding stress.

A typical plot of the instantaneous compliance is shown in Figure A1. The linearity in the curve validates the assumption of a constant sliding stress. The sliding stress measurements are summarized in Figure A2. All of the measurements lie in the range of ~10 to 15 MPa. This range is comparable to the values previously measured in fatigued specimens by both fiber pushout (~20 MPa in a SCS-6 SiC/Ti-15V-3Cr-3Al-3Sn composite^[2,16]) and fiber pullout (~10 MPa in a Sigma SiC/Ti-6Al-4V composite^[17]), but is considerably lower than values measured in pristine composites (typically, ~70 to 80 MPa when measured by pullout^[2,18] and ~120 to 140 MPa when measured by pushout^[16] in systems reinforced with SCS-6 fibers). The reduction in the sliding stress has been correlated with damage of the fiber coatings following repeated sliding.^[2,14,16-18]

ACKNOWLEDGMENTS

Funding for this work was provided by the ARPA University Research Initiative Program at UCSB under ONR Contract No. N00014-92-J-1808. Additional support was provided by NSF Grant No. MSS 93-02053. The authors are grateful to S.A. Kraus and P. Nagy, Textron Specialty Materials, for providing the materials used in this study. The authors also acknowledge Z.-Z. Du for assistance with the fatigue crack growth simulations.

REFERENCES

1. S.J. Connell, F.W. Zok, Z.-Z. Du, and Z. Suo: *Acta Metall. Mater.*, 1994, vol. 42, pp. 3451-3461.
2. D.P. Walls, G. Bao, and F.W. Zok: *Acta Metall. Mater.*, 1993, vol. 41, pp. 2061-2071.
3. B. Budiansky and L. Cui: *J. Mech. Phys. Solids*, 1994, vol. 42, pp. 1-19.
4. G. Bao and R.M. McMeeking: *Acta Metall. Mater.*, 1994, vol. 42, pp. 2415-2425.
5. A.A. Baker: *Composites*, 1978, vol. 9, pp. 1-7.
6. U. Ramamurty, F.W. Zok, and F.A. Leckie: *Mater. Sci. Eng. A*, 1996, vol. A214, pp. 62-67.
7. D.S. Dugdale: *J. Mech. Phys. Solids*, 1960, vol. 8, pp. 100-104.
8. G.I. Barenblatt: *Adv. Appl. Mech.*, 1962, vol. 7, pp. 55-131.
9. B.A. Bilby, A.H. Cottrell, and K.H. Swinden: *Proc. R. Soc. A*, 1963, vol. 272, pp. 304-314.

10. R.M. McMeeking and A.G. Evans: *Mech. Mater.*, 1990, vol. 9, pp. 217-227.
11. M.R. Begley and R.M. McMeeking: *Comp. Sci. Technol.*, 1995, vol. 53, pp. 365-382.
12. F.W. Zok, Z.-Z. Du, and S.J. Connell: *Mater. Sci. Eng.*, 1995, vol. A200, pp. 103-113.
13. H.G. Tattersall and G. Tappin: *J. Mater. Sci.*, 1966, vol. 1, pp. 296-301.
14. D.P. Walls and F.W. Zok: *Acta Metall. Mater.*, 1994, vol. 42, pp. 2675-2681.
15. U. Ramamurty, F.-C. Dary, and F.W. Zok: *Acta Mater.*, 1996, vol. 44, pp. 3397-3406.
16. T.J. Mackin, P.D. Warren, and A.G. Evans: *Acta Metall. Mater.*, 1992, vol. 40, pp. 1251-57.
17. S.J. Connell and F.W. Zok: *Acta Mater.*, in press.
18. D.B. Marshall, M.C. Shaw, and W.L. Morris: *Acta Metall. Mater.*, 1992, vol. 40, pp. 443-54.

Strength-limited design of composite/monolith transitions in metallic structures

F. W. Zok*, M. Y. He, A. G. Evans and F. A. Leckie
Materials Department, University of California, Santa Barbara, CA 93106, USA

and H. E. Déve
3M Company, Mendota Heights, MN 55120, USA
(Received October 1995; revised 9 August 1996)

The failure modes expected for transitions between metal-matrix composites and monolithic metals have been analysed, with special emphasis on aluminium-matrix (AMC) materials. The results have been displayed as mechanism maps that identify parameter ranges within which each failure mode predominates: the variables are the relative dimensions and the material properties. Both metallurgically-bonded and mechanically-bonded attachments have been considered. The implementation of the maps for strength optimization has been illustrated for AMC/Al transitions, with emphasis on the avoidance of modes that cause abrupt (rather than gradual) failure. © 1997 Elsevier Science Limited

(Keywords: metal-matrix composites; composite/monolith transitions; analytical modelling)

INTRODUCTION

The choice of materials for load-bearing structures is controlled by a series of performance indices based on such properties as stiffness, density, strength, toughness, cost, etc.¹. These indices are qualified by geometric or shape factors, which provide an important additional contribution to the structural stiffness or strength¹. In some cases, the structural design can be augmented by using reinforcements, such as fibres, in judiciously selected regions of the structure². The reinforcements increase the stiffness and strength in critical regions. However, the effectiveness of the concept is material- and shape-dependent. These benefits are counteracted (partially or fully) by degradation mechanisms, especially those associated with the transitions between the reinforced and unreinforced regions of the structure. These mechanisms must be identified and quantified and used as input to analysis of the performance benefits of selective reinforcement concepts.

The objective of the present investigation was to develop guidelines for the design of monolith/composite transitions, with emphasis on strength-critical structures. This was accomplished by: (1) identifying the mechanisms of failure in transitions subject to monotonic tensile

loading; (2) devising simple models based on net-section yielding, shear sliding and cracking to determine the conditions under which each of the mechanisms operate, with a view to developing mechanism maps and generic 'design rules' for transitions; and (3) conducting detailed finite element method (FEM) calculations to assess the fidelity of the analytical models (Appendix A). Examples are developed for Al alloys selectively reinforced with unidirectional Al₂O₃ fibres^{2,3} (designated AMCs).

Two transition configurations have been analysed (Figures 1 and 2). In the first configuration, the broad faces of the composite panel are assumed to be well bonded to the alloy. This configuration is subsequently referred to as a *metallurgically-bonded transition*. However, the interface between the end of the composite panel and the alloy is expected to be weaker than the monolithic material itself: a result of processing flaws. To ensure conservative designs, this interface is assumed to be fully debonded following processing. The second configuration utilizes monolithic inserts through the composite panel. The inserts behave as pins that transfer load from the alloy to the composite. This configuration is referred to as a *mechanical attachment*. A worst-case situation is considered, wherein the interfaces between the broad faces of the composite panel and the alloy are assumed to be fully debonded, such that all of the load is transferred through the pins.

*To whom correspondence should be addressed

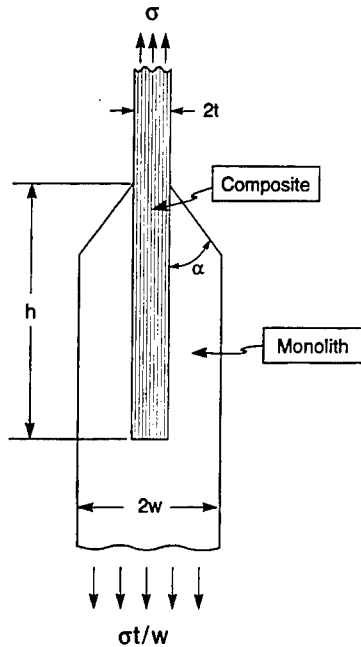


Figure 1 Schematic of metallurgically-bonded transition

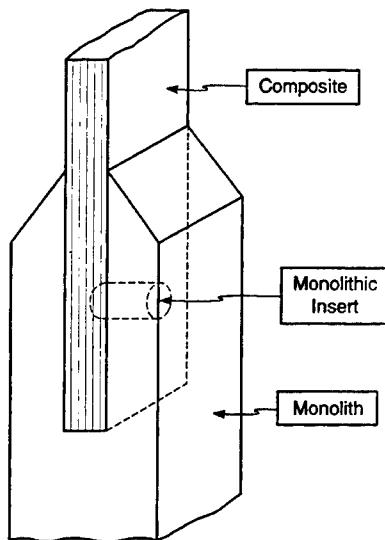


Figure 2 Schematic of mechanical attachment

Simple analytical models provide information regarding the relevant non-dimensional parameters involving both geometry and the constituent properties that govern the failure mechanisms. These enable the construction of a mechanism map that represents the regions within which each of the failure modes dominates, with material properties and geometry as variables. The emphasis of the analysis is on composites with well-bonded fibre-matrix interfaces, such as AMCs^{2,3}. Some modifications would be required for composites with weakly-bonded interfaces.

METALLURGICALLY-BONDED TRANSITIONS

Failure mechanisms

For strength-controlled design of the configuration depicted in Figure 1, four potential failure mechanisms must be considered. Other mechanisms that operate in fatigue, creep and thermomechanical fatigue are not addressed in this assessment. The four mechanisms are: (1) shear-out along a boundary layer at the composite-monolith interface; (2) fracture of the monolith following debonding at the reinforcement ends; (3) plastic yielding of the monolith, resulting in a limit load; and (4) tensile failure of the composite. For the analyses, yielding of the matrix within the composite near the interface was simulated by using a thin ductile interlayer. The interlayer was taken to have a modulus and yield strength equivalent to that of the matrix in the composite. Its thickness was taken to be 1% of the reinforcement thickness, $2t$. Since the layer thickness is much smaller than all other dimensions, it does not influence the failure stress. This approach is consistent with the shear behaviour of these composites⁴.

Shear-out. A critical parameter governing the effectiveness of the load transfer within the attachment is the ratio of composite embedded length, h , to the composite thickness, $2t$. A high value of h/t is most desirable for a high load capacity. However, elevations in h/t increase the amount of monolithic material needed in the structure. This, in turn, increases the structural weight. Consequently, an optimal value of h/t must exist. This optimum is dependent on the properties of both the reinforcement and the monolith.

A simple criterion for shear failure requires that the average shear stress along the interfaces exceed the shear yield strength, $\sigma_y/\sqrt{3}$, with σ_y being the lower of the tensile yield strengths of either the monolith, σ_y^m , or the matrix within the composite, σ_y^A . The corresponding strength of the joint, $\bar{\sigma}_1$, is

$$\bar{\sigma}_1 = \sigma_y h / \sqrt{3} t, \quad (1)$$

independent of the overall width, $2W$. Comparisons with numerical results (Figure 3, Appendix A) validate use of this simple premise.

Monolith fracture. Some load transfer occurs normal to the reinforcement ends. However, the interfaces with the monolith are expected to be weaker than the monolithic material itself, because of processing flaws causing interfacial debonding at moderate stresses, especially upon cyclic loading. The principal influence of the debond is the development of a stress intensity, leading to either fatigue cracking or fracture across the monolith. Dimensional considerations indicate that the magnitude of the energy release rate, \mathcal{G} , for a fully debonded interface is

$$\mathcal{G} E_m W^2 / \sigma^2 t^3 = g(E_m/E_{11}, t/W, \Omega_L, \Omega_T) \quad (2)$$

where σ is the stress on the composite, E_m and E_{11} are

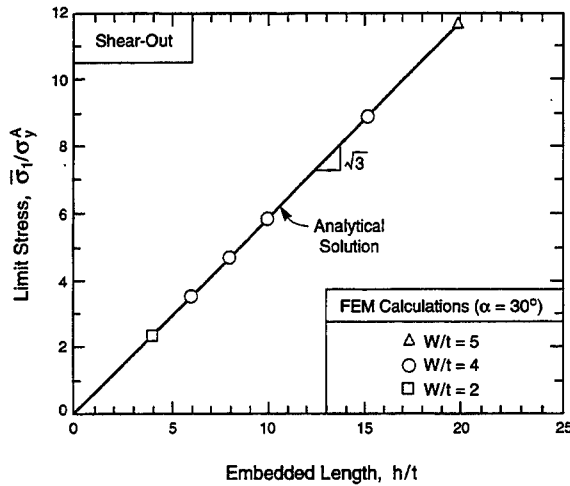


Figure 3 Influence of embedded length, h/t , on limit stress for shear-out. The analytical solution is based on equation (1)

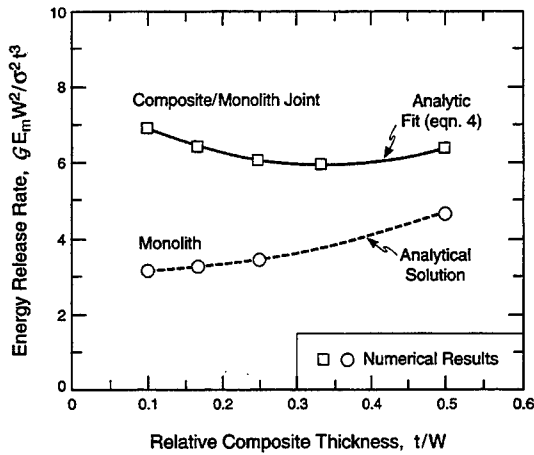


Figure 4 Energy release rate for crack growth from a debonded joint. Also shown for comparison are the FEM results for monolithic materials, and corresponding analytical results, from ref. 5

elastic moduli (Appendix A), Ω_L and Ω_T are the misfit strains arising from thermal expansion mismatch (Appendix A), and g is a function to be determined by calculation. Setting $\mathcal{G} = \mathcal{G}_m$ (the monolith toughness) leads to a prediction for the strength $\bar{\sigma}_2$ of the joint

$$\bar{\sigma}_2 = \sqrt{\mathcal{G}_m E_m W^2 / t^3 g} \quad (3)$$

Note that for a fixed ratio, t/W , the fracture stress decreases with increasing t . The results of calculations for AMC/Al joints (Appendix A, Figure 4) are accurately described by the fitting function

$$\mathcal{G}_m E_m W^2 / \sigma^2 t^3 = 7.93 - 11.8t/W + 17.2(t/W)^2 \quad (4)$$

Comparison with results for monolithic materials⁵ confirms the accuracy of the FEM results over the range $0.1 \leq t/W \leq 0.5$.

Limit load. An alternative failure process is one in

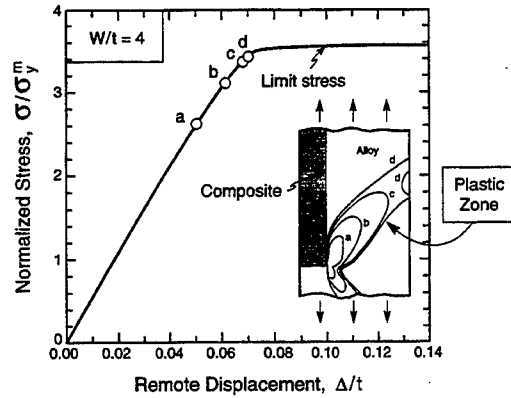


Figure 5 The stress-displacement response of a metallurgically-bonded transition which fails by plastic collapse. The inset shows the development of the plastic zone

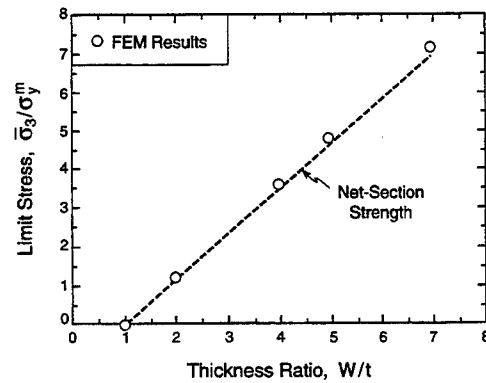


Figure 6 Trends in plastic collapse stress with thickness ratio, W/t

which the monolithic section undergoes yielding. An estimate of the stress at which this occurs is obtained by equating the net-section stress within the monolith to its yield strength, giving the result

$$\bar{\sigma}_3 = \sigma_y^m (2/\sqrt{3}) (W/t - 1) \quad (5)$$

In the absence of work hardening, $\bar{\sigma}_3$ represents a limit load for plastic failure. The FEM model has been used to evaluate the extent of plasticity in the monolith as well as the limit load associated with complete yielding. A typical result is shown on Figure 5. Comparison between the FEM calculations (Figure 6) and equation (5) again establishes the utility of the simple model.

Reinforcement failure. Another possible failure mode is tensile fracture of the composite. This is expected to occur in the region where the reinforcement enters the monolith. The associated load capacity, $\bar{\sigma}_4$, is governed by the ultimate tensile strength (UTS) of the composite and the stress concentration around the entry. The stress concentration, in turn, is governed by the entry angle α , the modulus mismatch, the monolith thickness, the misfit strain Ω , and the degree of plasticity near the entry.

The misfit strain usually results in a residual tensile

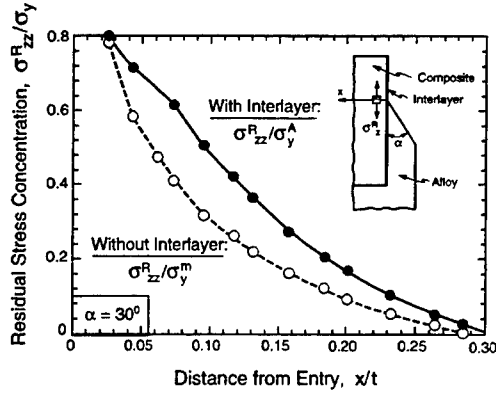


Figure 7 Residual stress concentration, both in the presence and the absence of a soft interlayer

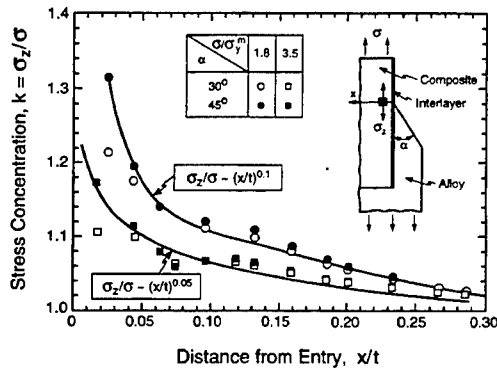


Figure 8 Influence of applied stress and entry angle on stress concentration around entry line

stress σ_z^R within the composite near the entry. This stress scales with the yield strength of either the interlayer or the monolith (Figure 7). For $\alpha = 30^\circ$, the maximum residual stress (calculated in the element adjacent to the interlayer) is $\sigma_z^R/\sigma_y^A \approx 0.8$. This stress decays rapidly with distance from the entry. For typical yield strengths (Appendix A) the maximum residual tension is substantially lower than the UTS of the composite^{2,3}.

Upon tensile loading, additional stress concentrations, k_m , arise at the entry (Figure 8). These concentrated stresses are confined to a relatively small region near the entry and decrease in relative magnitude as the applied load increases, because of yielding along the interlayers.

Predicting the stress at which the composite fails requires knowledge of the statistical parameters that govern the UTS and models of stress redistribution around failed fibres. A conservative approach would equate the peak stress to the composite UTS, designated S , such that the failure strength becomes

$$\bar{\sigma}_4 = S/k_m \quad (6)$$

with k_m obtained from Figure 8. For local load sharing (LLS) materials, such as AMCs, the most extreme situation causes the UTS to scale in accordance with

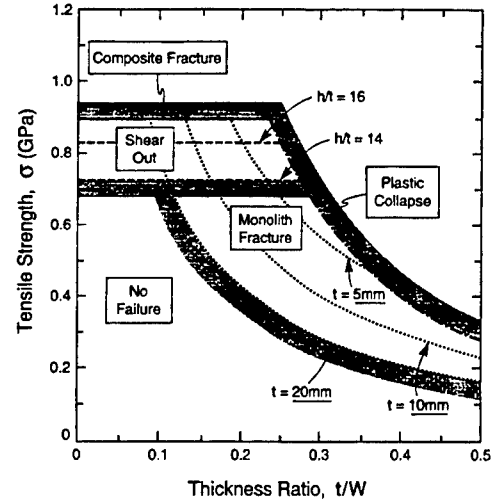


Figure 9 Failure mechanism map for a metallurgically-bonded transition

weakest link statistics^{6,7}. A procedure for estimating k_m in such cases is presented in Appendix B. Typically, k_m is appreciably smaller than the peak stress concentration.

Failure maps

One method of representing the various failure modes and their dependence on the attachment geometry is through a *failure mechanism map*. Such a map has been constructed for Al/AMC transitions (Figure 9). The map shows the stresses required for failure and the transitions in failure mechanisms. At small values of t/W and h/t , when failure occurs, it happens by shear out, bounded by the lower dashed horizontal lines. Smaller h/t result in earlier onset of this failure mode, with correspondingly lower strength levels. Above $h/t \approx 17.5$, failure occurs by composite fracture: the solid horizontal line. Further increases in h/t have no influence on strength. As t/W increases, the mechanism changes to monolith fracture. The transition now depends on h/t as well as the absolute thickness, t . At yet higher t/W , a transition occurs to plastic collapse of the monolith. Note that for sufficiently small t ($< 3\text{mm}$), fracture of the Al never occurs. Instead, there is a direct transition to plastic collapse.

Strength optimization

The preceding map can be used to develop guidelines for geometries that maximize strength. The preferred failure mode is composite fracture, since it provides the highest load-bearing capacity for a prescribed reinforcement thickness. However, composite failure is catastrophic and the failure stress is stochastic. It is then preferable to design within a range that assures gradual progression in eventual failure.

To prevent shear-out, the criterion is

$$\bar{\sigma}_1 \geq \bar{\sigma}_4 \quad (7)$$

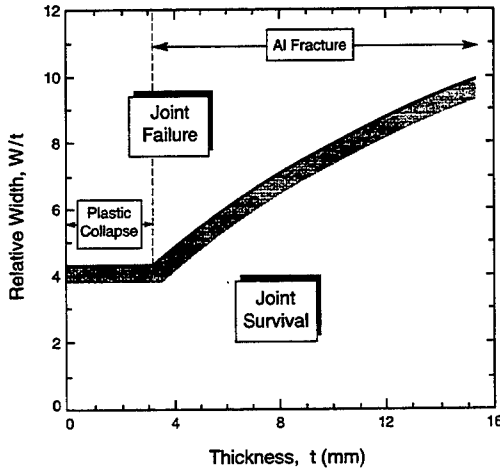


Figure 10 Trends in critical value of W/t needed to prevent both fracture of the composite and plastic collapse of the alloy

which, combined with equations (1) and (6), gives

$$\frac{h}{t} \geq \frac{\sqrt{3}}{k} \left(\frac{S}{\sigma_y^A} \right) \quad (8)$$

In the present case, $h/t \geq 17.5$.

To prevent fracture of the alloy

$$\bar{\sigma}_2 \geq \bar{\sigma}_4 \quad (9)$$

which, combined with equations (3), (4) and (6), yields

$$\frac{W}{t} \geq \left(\frac{S}{k} \right) \sqrt{\frac{tg}{E_m \mathcal{G}_m}} \quad (10)$$

Note that this condition involves both W/t and t .

To prevent plastic collapse,

$$\bar{\sigma}_3 \geq \bar{\sigma}_4 \quad (11)$$

or

$$\frac{W}{t} \geq 1 + \frac{\sqrt{3}}{2} \left(\frac{S}{\sigma_y^m} \right) \quad (12)$$

Trends in the critical value of W/t with t obtained from equations (10) and (12) are plotted in Figure 10, assuming a matrix toughness $\sqrt{E_m \mathcal{G}_m} \approx 30 \text{ MPa m}^{1/2}$. Note that for low values of t ($\leq 3 \text{ mm}$), the critical value is independent of t and is dictated by equation (12). Conversely, at higher values of t , the critical value of W/t increases with increasing t , in accordance with equation (10).

MECHANICAL ATTACHMENTS

Failure mechanisms

For the configuration in which monolithic inserts are used, three alternative, though analogous, failure mechanisms may operate. These are governed by the stresses associated with the pin load and the geometry (Figure 2). The mechanisms are: (1) shear-out of the composite along the fibre direction; (2) tensile fracture of

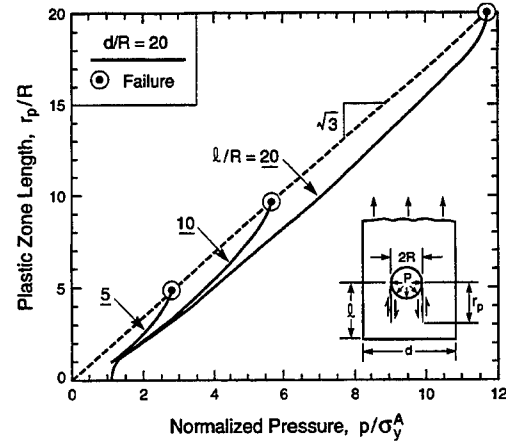


Figure 11 Development of plastic zone with pin pressure in a mechanical attachment

the composite; and (3) shear failure of the pin. Bearing failure of the composite has been excluded as an unlikely mode because of the high compressive strength of AMCs relative to the tensile and shear strengths². The failure loads neglect the shear resistance of the composite–monolith interface and are thus conservative. Such contributions could be incorporated by modelling the interface as a frictional surface.

Shear-out. The pressure exerted by the pin causes shear yielding within the composite, parallel to the fibre axis. The length of the associated slip zone, r_p , can be estimated by equating the average pin pressure, p , to the shear force supported by the yielded material. The result is

$$r_p = \sqrt{3} R p / \sigma_y^A \quad (13)$$

where R is the pin radius. Shear failure occurs when the slip zone reaches the end of the composite panel, a distance l from the centre-line of the pin. The pressure at failure is

$$\bar{p}_1 = \sigma_y^A l / \sqrt{3} R \quad (14)$$

The corresponding remote stress on the composite is

$$\bar{\sigma}_{1,p} = (2/\sqrt{3}) \sigma_y^A l / d \quad (15)$$

Shear yielding of the composite has been simulated in the FEM model by introducing two thin, ductile, interlayers between the equatorial plane of the pin and the end of the panel having the properties of the matrix (Figure 11). The slip zone length increases in approximate proportion with the pin pressure. As the slip zone approaches the end of the panel [within $\sim 2R$], it interacts with the free surface and its growth is accentuated. The corresponding pin pressures (Figure 12) conform well with the analytical result [equation (14)].

Pin failure. When the pin is sufficiently ductile, its failure is expected to occur in shear, parallel to the broad

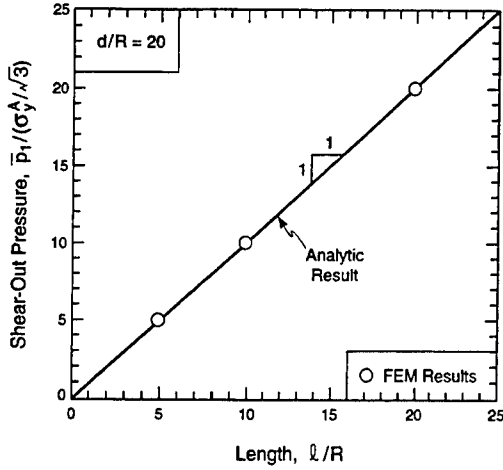


Figure 12 Critical stress for shear-out of a pin joint

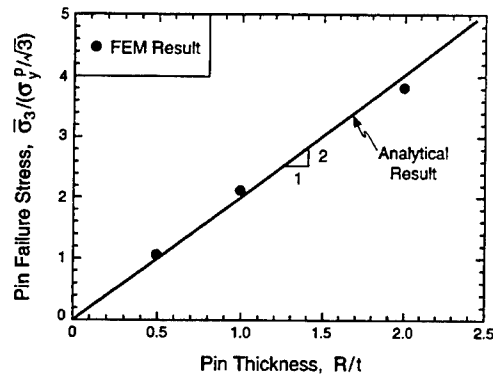


Figure 13 Trends with pin size of the pressure needed for pin failure

faces of the composite panel. An estimate of the pressure \bar{p}_2 at which this occurs is obtained by equating the net-section shear stress within the pin to its shear yield strength, $\sigma_y^A/\sqrt{3}$. The result is

$$\bar{p}_2 = \frac{\pi}{2\sqrt{3}} \sigma_y^P \left(\frac{R}{t} \right) \quad (16)$$

The corresponding remote stress is

$$\bar{\sigma}_{2,p} = (\pi/8\sqrt{3}) \sigma_y^P (2R/d)^2 (d/2t) \quad (17)$$

A numerical simulation has been performed for a related 2D problem in which the pin was assumed to be square in cross-section (with dimension $2R$) and in a state of plane strain (Figure A3, Appendix A). The calculated failure pressures (Figure 13) compare closely with those required for net-section yielding of a square pin

$$\bar{p}_2 = \frac{2}{\sqrt{3}} \sigma_y^P \left(\frac{R}{t} \right) \quad (18)$$

Tensile fracture. Another failure process involves tensile fracture of the composite. Should efficient stress redistribution mechanisms exist, the load capacity would be insensitive to stress concentrations and failure would

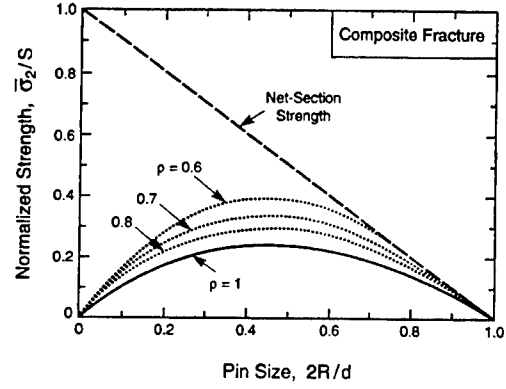


Figure 14 Comparison of model predictions for composite fracture from a mechanical attachment

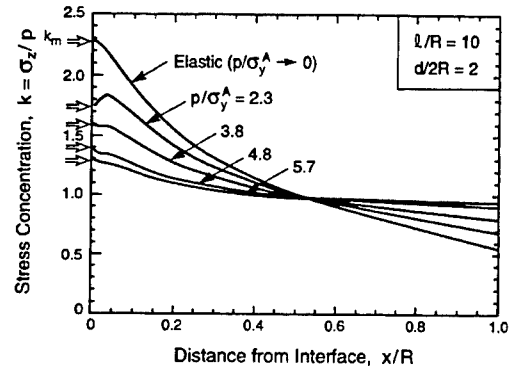


Figure 15 Distribution in the axial tensile stress within the composite around the pin, for $2R/d$

occur when the net-section stress exceeds this strength. The corresponding failure pressure would be

$$\bar{p}_3 = S(d/2R - 1) \quad (19)$$

with the associated remote stress being (Figure 14)

$$\bar{\sigma}_{3,p} = S(1 - 2R/d) \quad (20)$$

For LLS materials, the load capacity would be smaller and the stress concentrations need to be calculated. For this purpose, the distributions in the axial stress, σ_z/p , around the pin have been computed for several geometries (Figure 15). The maximum stress concentration, k_m , near the pin-composite interface (Figure 16) increases as the pin size ($2R/d$) increases, but decreases as yielding develops, upon increasing p/σ_y^A , in accordance with ($p/\sigma_y^A \leq 1.6$)

$$k_m \approx (0.84 + R/d)/(1 - 2R/d) \quad (21a)$$

$$\equiv k_0$$

and ($p/\sigma_y^A > 1.6$)

$$k_m \approx k_0 [1 - 0.16(p/\sigma_y^A - 1.6)^{2/3}] \quad (21b)$$

As with metallurgically-bonded joints, a conservative

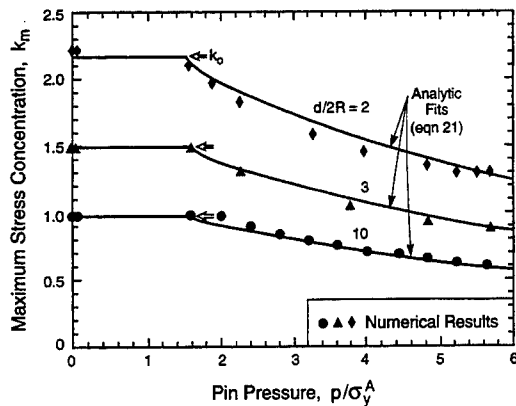


Figure 16 Trends in the maximum stress concentration with applied pressure, p/σ_y^A , and pin size, $2R/d$. The points are FEM results and the solid lines are curve fits [equation (21)]

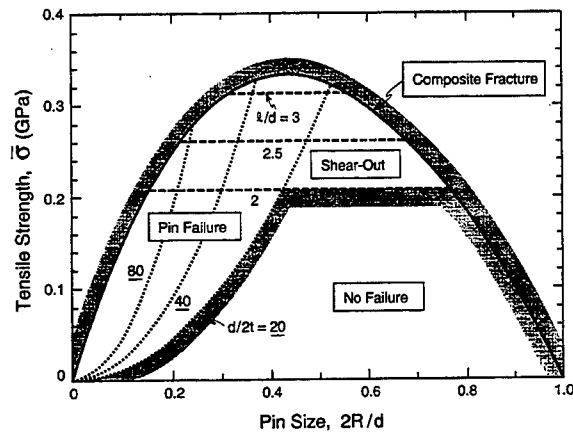


Figure 17 Failure mechanism map for the mechanical attachment

criterion for composite fracture would be

$$\bar{\sigma}_{3,p} = S/k_m \quad (22)$$

as plotted on Figure 14, with $\rho = k_m/k_0$.

Failure maps

A failure mechanism map has been constructed for the mechanical attachment, analogous to that for the metallurgically-bonded transition (Figure 17). In the present case, the map is constructed using coordinates of strength, $\bar{\sigma}$, and normalized pin size, $2R/d$. The three mechanisms described in the preceding section are considered separately. (1) The conditions for shear-out [equation (15)] are independent of $2R/d$ and are thus represented by a family of horizontal lines: each for a prescribed value of l/d . (2) The stress for pin failure [equation (22)] increases monotonically with pin size. This failure mode is represented by a series of dashed lines, for $d/2t = 20, 40$ and 80 . In this case, the mechanical properties of the pin are assumed to be the same as those of the monolithic alloy. (3) The conditions for composite fracture have been computed using a stress concentration, represented by $\rho = 0.7$.

There is an optimum pin size for the attainment of peak strength, in the range $2R/d = 0.5-0.7$. At larger pin sizes, failure occurs by composite fracture. At smaller pin sizes, the pin itself causes failure. Note that, in the optimum size range, the strength can be elevated by increasing l/d . However, for this optimum to be realized, $d/2t$ must also be sufficiently large, i.e. $d/2t \geq 40$. When these dimensions have been achieved, the peak strength of the joint reaches ~ 330 MPa. Such strengths are considerably lower than those for the metallurgically-bonded joints.

CONCLUDING REMARKS

Failure mechanism maps have been developed for both metallurgically-bonded and mechanically-bonded attachments, with special emphasis on AMC materials. The maps indicate that metallurgically-bonded transitions are preferred over mechanical attachments for maximum strength. However, in instances where metallurgical bonds cannot be produced reliably, the mechanical attachment can provide a viable alternative, subject to judicious selection of the dimensions. Moreover, in order to achieve an overall optimum, the two approaches may be combined. It is anticipated that the combination attains strengths exceeding that of the mechanical attachment alone, as well as enabling improvement in reliability.

ACKNOWLEDGEMENTS

Funding for this work was supported by the Advanced Research Projects Agency both through the University Research Initiative at UCSB under ONR Contract N00014-92-J-1808 and through a sub-contract (Order No. 7306) issued under Contract MDA972-90-C-0018.

REFERENCES

1. Ashby, M.F., *Material Selection in Mechanical Design*. Pergamon Press, Oxford, 1992.
2. Dève, H.E. and McCullough, C., *J. Metals*, 1995, 7, 33.
3. Hu, M. S., Yang, J., Cao, H.C. and Evans, A.G., *Acta Metall. Mater.*, 1992, 40, 2315.
4. Jansson, S. and Leckie, F.A., *J. Mech. Phys. Solids*, 1992, 40, 593.
5. Tada, H., Paris, P.C. and Irwin, G.R., *The Analysis of Cracks Handbook*, 2nd edn. Paris Productions, St. Louis, MI, 1985.
6. He, M.Y., Evans, A.G. and Curtin, W., *Acta Metall. Mater.*, 1993, 41, 871.
7. Curtin, W., *J. Mech. Phys. Solids*, 1993, 41, 217.
8. Xia, Z.C., Carr, R.R. and Hutchinson, J.W., *Acta Metall. Mater.*, 1995, 41(8), 2361-2376.
9. Lu, T.J. and Hutchinson, J.W., *Phil. Trans. Roy. Soc.*, 1995, A351, 595-610.
10. Desmorat, R. and Leckie, F.A., to be published.
11. Freudenthal, A., in *Fracture*, ed. H. Liebowitz. Academic Press, New York, 1967.
12. Hutchinson, J.W., *J. Mech. Phys. Solids*, 1968, 16, 13-31.
13. Rice, J.R., *Int. J. Fract. Mech.*, 1968, 4, 41-47.
14. Rice, J.R. and Rosengren, G.F., *J. Mech. Phys. Solids*, 1968, 16, 1-12.

APPENDIX A

Materials properties and numerical procedures

The monolithic material was assumed to be a 357 Al casting alloy in the T6 condition, with a modulus $E = 70$ GPa, a yield strength $\sigma_y = 240$ MPa, a work hardening coefficient $N = 10$, and a thermal expansion coefficient $\alpha = 20 \times 10^{-6} \text{ K}^{-1}$. The composite comprised Al-2% Cu matrix reinforced unidirectionally with 55% of Al_2O_3 fibres. The relevant constituent properties are: (i) fibre modulus $E_f = 380$ GPa, (ii) matrix yield strength $\sigma_y = 90$ MPa, (iii) longitudinal composite strength $\text{UTS} = 1000$ MPa, (iv) fibre thermal expansion coefficient $\alpha_f = 7.1 \times 10^{-6} \text{ K}^{-1}$ and (v) matrix thermal expansion coefficient $\alpha_m = 20 \times 10^{-6} \text{ K}^{-1}$. The composite was assumed to be transversely isotropic, with the following thermal and elastic constants^{8,9}.

- 1) Longitudinal modulus, E_{11} :

$$E_{11} = f E_f + (1 - f) E_m \quad (\text{A1})$$

where f is the fibre volume fraction.

- 2) Transverse modulus, E_{22} :

$$E_{22} = \frac{1 + 2\eta f}{1 - \eta f} E_m \quad (\text{A2})$$

where

$$\eta = \frac{E_f/E_m - 1}{E_f/E_m + 2} \quad (\text{A3})$$

- 3) In-plane shear moduli, G_{12} and G_{13} :

$$G_{12} = G_{13} = \frac{E_{22}}{2(1 + \nu)} \quad (\text{A4})$$

- 4) Out-of-plane shear modulus, G_{23} :

$$G_{23} = \frac{E_f(1 + f) + E_m(1 - f)}{E_f(1 - f) + E_m(1 + f)} \left[\frac{E_m}{2(1 + \nu)} \right] \quad (\text{A5})$$

- 5) Poisson's ratios:

$$\nu_{12} = \nu_{23} = \nu = 0.27 \quad (\text{A6})$$

- 6) Longitudinal thermal expansion coefficient, α_L :

$$\alpha_L = [f E_f \alpha_f + (1 - f) E_m \alpha_m] / E_{11} \quad (\text{A7})$$

- 7) Transverse thermal expansion coefficient, α_T :

$$\alpha_T = (1 - f) \alpha_m + f \alpha_f - \frac{(\alpha_f - \alpha_m) f (1 - f) (E_f - E_m) [\nu E_f + (3\nu - 2) E_{11}]}{E_{11} [E_f + (1 - 2\nu) E_{11}]} \quad (\text{A8})$$

- 8) Misfit strains, Ω_L and Ω_T :

$$\Omega_L = (\alpha_m - \alpha_L) \Delta T \quad (\text{A9})$$

$$\Omega_T = (\alpha_m - \alpha_T) \Delta T$$

where ΔT is taken to be 200°C .

Typical FEM meshes used to perform the calculations are illustrated in *Figures A1, A2 and A3*.

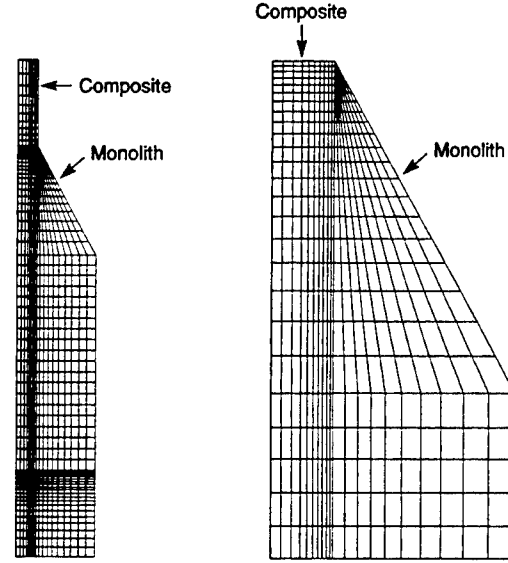


Figure A1 (a) Typical FEM mesh used to analyse the metallurgically-bonded transition. (b) Detail of entry point ($\alpha = 30^\circ$, $W/t = 4$, $h/t = 15$)

APPENDIX B

Stress distributions and failure near corners

When the constituent materials are elastic, the stress $\bar{\sigma}$ near a corner is singular and has the general form¹⁰

$$\bar{\sigma} = H x^{-\lambda} F(\theta) \quad (\text{A10})$$

where x is the distance from the corner, F is a function of the polar orientation, λ is a singularity exponent that depends on the elastic mismatch and the angle, α (*Figure 1*), while H is a stress intensity factor that also depends on α and the elastic properties. It has the form

$$H = \tilde{H} \sigma L^\lambda \quad (\text{A11})$$

where σ is the applied stress, \tilde{H} is a dimensionless parameter and L is a length scale given for *Figure 1* by

$$L = W - t \quad (\text{A12})$$

To extract the scaling behaviour, further assessment makes the simplification that $\bar{\sigma}$ depends only on radial distance r from the corner. Then

$$\frac{\bar{\sigma}}{\sigma} = \left(\frac{L}{r} \right)^\lambda \tilde{H} F \quad (\text{A13})$$

where F is now a constant. The weakest link expression for the failure probability, Φ , of a unidirectional composite subject to longitudinal stress when the flaw population satisfies a two-parameter Weibull form is¹¹

$$-\ln(1 - \Phi) = \frac{2\pi b}{V_0 S_0^m} \int r \sigma_z^m(r) dr \quad (\text{A14})$$

where b is the width of the composite, V_0 the reference volume, S_0 the scale parameter and m the shape parameter. Inserting the singular field from (A13), the

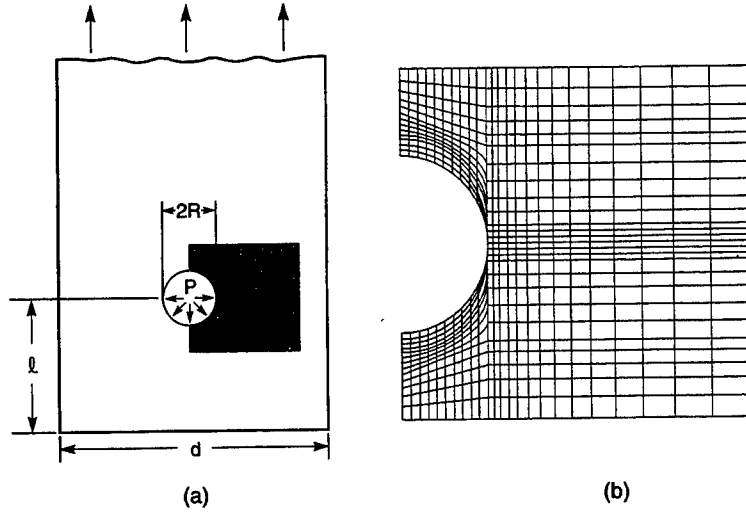


Figure A2 (a) Schematic of mechanical attachment. (b) FEM mesh surrounding the pin [shaded region in (a)]

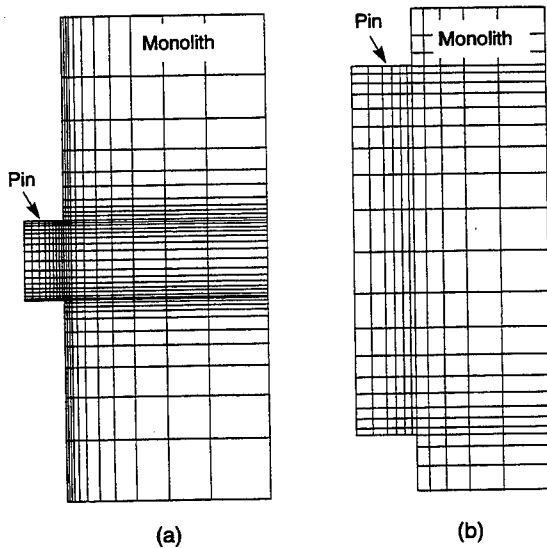


Figure A3 (a) FEM model used to calculate the pressure for pin failure. (b) Detail of the pin-composite interface region

survival probability, $d\Phi$, within an element dr is

$$-\ln(1 - d\Phi) = \left[\frac{2\pi b}{V_0} \left(\frac{\bar{\sigma}}{S_0} \right)^m (\bar{H}F)^m \right] \left(\frac{L}{r} \right)^{m\lambda} r dr \quad (\text{A15})$$

For $m\lambda < 2$, $d\Phi$ increases as r increases. In this case, the singular stress is relatively benign, because the failure sites having highest failure likelihood are located furthest from the entry corner. Conversely, for $m\lambda > 2$, $d\Phi$ increases as r decreases, causing the failure site to be localized to the corner.

For the Al/Al₂O₃ system (and for α between 30° and 45°), $\lambda \approx 0.1$ in the elastic range¹¹. Yielding in the Al would diminish λ , analogous to the HRR field¹²⁻¹⁴. A fit

to Figure 8 gives $\lambda \approx 0.1$ for $\sigma/\sigma_y = 1.8$ and $\lambda \approx 0.05$ for $\sigma/\sigma_y \approx 3.5$, consistent with the expected role of plasticity in reducing λ . Moreover, for Al₂O₃ fibres, $m \approx 5$ (ref. 2). The condition $m\lambda < 2$ thus applies.

The survival probability within a range r_b from the entry corner when $m\lambda < 2$ becomes

$$-\ln(1 - \Phi) = \left[\frac{2\pi b r_b^2}{(2 - m\lambda) V_0} \left(\frac{\bar{\sigma}}{S_0} \right)^m (\bar{H}F)^m \right] \left(\frac{L}{r_b} \right)^{m\lambda} \quad (\text{A16})$$

The range r_b within which the singular stress exceeds the applied stress can be estimated from (A13) (with $\bar{\sigma} \rightarrow \sigma$) as

$$r_b \approx L(\bar{H}F)^{1/\lambda} \quad (\text{A17})$$

such that (A16) becomes

$$-\ln(1 - \Phi) = \frac{2\pi b r_b^2}{(2 - m\lambda) V_0} \left(\frac{\bar{\sigma}}{S_0} \right)^m \quad (\text{A18})$$

The corresponding survival probability within r_b when the stress is uniform ($\bar{\sigma} = \sigma$) is

$$-\ln(1 - \Phi) = \frac{2\pi b r_b^2}{V_0} \left(\frac{\bar{\sigma}}{S_0} \right)^m \quad (\text{A19})$$

Equating the survival probabilities, with and without a singular field, the strength ratio becomes

$$k_m \equiv \sigma/\bar{\sigma} = (2 - m\lambda)^{1/m} \quad (\text{A20})$$

which applies when $1 \leq m\lambda \leq 2$, and

$$k_m = 1 \quad (\text{A21})$$

when $m\lambda < 1$. Hence, for Al₂O₃/Al, there is no significant effect of the stress concentration on the strength. That is, there is a negligibly small likelihood of preferential failure of the composite within the zone affected by the corner stress concentration.

